U.PORTO

FEUP FACULDADE DE ENGENHARIA
UNIVERSIDADE DO PORTO

Master's Dissertation in Mechanical Engineering

Faculty of Engineering of University of Porto

Multi-scale Modelling and Analysis of the Behaviour of PC/ABS Blends with Emphasis on Interfacial/Bulk Damage

Author:
Alexandre David Costa Amaro

Supervisor:
Dr. Francisco Manuel Andrade Pires

Co-Supervisor:
Ana Francisca Carvalho Alves

Submitted in fulfilment of the requirements
for the degree of Master in Mechanical Engineering by
Faculty of Engineering of the University of Porto

Porto, June 2023



CM2S

Computational Multi-Scale
Modeling of Solids and Structures

Dedicado aos meus pais,
Fátima David e Joaquim Amaro

Page intentionally left blank

ABSTRACT

Multi-scale Modelling and Analysis of the Behaviour of PC/ABS Blends with Emphasis on Interfacial/Bulk Damage

The PC/ABS blends, ternary blends of polycarbonate (PC) and acrylonitrile-butadiene-styrene (ABS), are one of the most successful commercial polymer blends, finding their main applications in the automotive sector and consumer electronics. The key factor contributing to their success is the "synergistic effect" observed under specific compositions, combining both the excellent thermal and mechanical properties of PC, and the toughness ABS.

This dissertation focuses on the in-depth study of deformation mechanisms and their impact on the behaviour of PC/ABS blends, with the objective of enabling the development of customised materials and predicting their ideal composition for specific applications. Specifically, internal particle cavitation of the rubber particles, debonding at the PC/ABS interface and shear-yielding of the PC matrix play significant roles. To accurately predict the thermomechanical behaviour of these blends, a multi-scale modelling approach based on computational homogenisation is empoyed, offering an alternative to continuum modelling methods that rely on simplifying assumptions. Besides the proper establishment of a Representative Volume Element (RVE) of the microstructure and the constitutive description of both material phases, it is expected that accounting for the explicit modelling of the PC/ABS interfaces and damage in the matrix is crucial to achieving accurate predictions.

The research presents the development of a Python program capable of efficiently generating and incorporating zero-thickness cohesive interface elements around the ABS particles into preexisting discretised finite element RVEs. The behaviour of the interface elements is characterised using a PPR potential-based cohesive model. The homogenised thermomechanical response of the PC/ABS blends is then inferred through first-order hierarchical multi-scale analyses based on computational homogenisation. To evaluate the influence of explicitly considering the interface phase in the blend's microstructure, several numerical analyses are conducted. Moreover, to address the shear-yielding damage mechanism controlling the behaviour of the PC matrix, its visco-elastic

visco-plastic constitutive model is extended to incorporate a damage variable that quantifies the accumulation of defects in the PC matrix. A synergistic effect between the PPR cohesive model and the damage model extension is then found in capturing the blend's behaviour.

An alternative approach to coupled multiscale finite element analysis is also proposed, which aims to achieve an accurate determination of material parameters for the referred models while considering the interactions between different scales. To accomplish this, the proposed approach integrates numerical calibration grounded on experimental tests.

Overall, this research contributes to the broader understanding of PC/ABS blend behaviour and highlights the importance of considering the damage phenomenon in both the PC matrix (shear-yielding) and the interfaces between the PC and the ABS (cohesive elements). Although only a qualitative understanding of the predominant damage mechanism in the blend's response is achieved, the findings pave the way for future studies in the field with broader applicability beyond PC/ABS blends.

Keywords: Multi-scale modeling; Computational homogenisation; Finite Element Method; Material parameter identification; Material constitutive modelling; Cohesive zone model; PC/ABS polymer blends; Microstructure generation

RESUMO

Análise e Modelação Multi-Escala de Misturas Poliméricas PC/ABS com Ênfase no Comportamento do Dano nos seus Constituintes e Interface

As misturas de PC/ABS, misturas ternárias de policarbonato (PC) e acrilonitrila-butadieno-estireno (ABS), são uma das misturas poliméricas comerciais mais bem-sucedidas, encontrando as suas principais aplicações no setor automóvel e na eletrônica. O principal fator que contribui para o seu sucesso é o "efeito sinérgico" observado para composições específicas, combinando tanto as excelentes propriedades térmicas e mecânicas do PC quanto a resistência do ABS.

Esta tese concentra-se no estudo aprofundado dos mecanismos de deformação e seu impacto no comportamento das misturas de PC/ABS, com o objetivo de permitir o desenvolvimento de materiais personalizados e prever sua composição ideal para aplicações específicas. Especificamente, a cavitação interna das partículas de borracha, o descolamento na interface PC/ABS e o escoamento por corte da matriz de PC desempenham papéis significativos. Para prever com precisão o comportamento termomecânico destas misturas, é proposta uma abordagem de modelação multi-escala baseada em homogeneização computacional, oferecendo uma alternativa aos métodos de modelação contínua que dependem de simplificações. Além do estabelecimento adequado de um Elemento de Volume Representativo (RVE) e da descrição constitutiva de ambas as fases do material, espera-se que a consideração explícita da modelação das interfaces do PC/ABS e do dano na matriz seja crucial para a obtenção de previsões precisas.

A investigação apresenta o desenvolvimento de um programa em Python capaz de gerar e incorporar eficientemente elementos coesivos de interface de espessura nula em redor das partículas de ABS em RVEs previamente discretizados. O comportamento dos elementos de interface é caracterizado usando o modelo coesivo PPR (Park-Paulino-Roesler). A resposta termomecânica homogeneizada das misturas de PC/ABS é então inferida por meio de análises hierárquicas de múltiplas escalas de primeira ordem baseadas em homogeneização computacional. Para avaliar a influência da consideração

explícita da interface na microestrutura da mistura, várias análises numéricas são conduzidas. Adicionalemnte, para lidar com o mecanismo de dano por corte que controla o comportamento da matriz de PC, o seu modelo constitutivo visco-elástico visco-plástico é extendido para incorporar uma variável de dano que quantifica o acumular de defeitos na matriz de PC. Um efeito sinérgico entre o modelo coesivo PPR e a extensão do modelo de dano é então encontrado na captura do comportamento da mistura.

Uma abordagem alternativa para análise de elementos finitos acoplada em múltiplas escalas também é proposta, visando alcançar a precisa determinação dos parâmetros materiais para os modelos referidos, levando em consideração as interações entre diferentes escalas. Para isso, a abordagem proposta integra-se com calibração numérica fundamentada em testes experimentais.

No global, esta tese contribui para uma compreensão mais ampla do comportamento das misturas de PC/ABS e destaca a importância de considerar o fenômeno de dano tanto na matriz de PC (corte) quanto nas interfaces entre o PC e o ABS (elementos coesivos). Embora apenas uma compreensão qualitativa do mecanismo de dano predominante na resposta da mistura seja alcançada, as descobertas abrem caminho para futuros estudos no campo com uma aplicabilidade mais ampla além das misturas de PC/ABS.

Palavras-Chave: Multi-escala; Homogeneização computacional; Método dos Elementos Finitos; Identificação de parâmetros de material; Modelação constitutiva de materiais; Modelo de zona coesiva; Misturas poliméricas PC/ABS; Geração de microestrutura.

AGRADECIMENTOS

Na impossibilidade de nomear todos aqueles que contribuíram, direta ou indiretamente, para que esta investigação se concretizasse, gostaria de expressar a todos os meus sinceros agradecimentos. Uma palavra de particular reconhecimento e gratidão ao meu orientador, Professor Doutor Francisco Andrade Pires, pela oportunidade de integrar o seu grupo de investigação e pelo voto de confiança nas minhas capacidades. A sua orientação exemplar, pautada por um elevado e rigoroso nível científico, a sua constante disponibilidade e os seus conselhos foram fundamentais para o sucesso e enriquecimento deste trabalho. Gostaria também de expressar a minha profunda gratidão à minha Coorientadora, Francisca Alves, pela paciência e ajuda indispensáveis, que culminaram em muitas horas do seu preciso tempo. Agradeço o enorme entusiasmo que me contagiou, bem como a amizade e apoio em todos os momentos que moldaram positivamente esta última etapa.

A toda a equipa de investigação CM2S, António, Bernardo, Igor, José, Rodrigo, Rui e Tiago, agradeço por toda a colaboração e troca de ideias, as quais a partilha de conhecimentos e experiências foi essencial para aprimorar o meu trabalho, pelo que sou grato por ter tido a oportunidade de fazer parte deste grupo de excelência.

Aos meus amigos de longa data, Alberto, Francisco, José, Manuel e Pedro, e à minha família de curso, Cai, Élio, Gonçalo, Henrique e Tomás, um obrigado especial por todo o apoio e por sempre terem estado presentes para ouvir as minhas preocupações e dúvidas, mas também as minhas vitórias, ao longo deste processo. Vocês foram, e são, uma fonte de força e inspiração, e não posso expressar o quão grato sou por ter cada um de vocês ao meu lado.

Por último, mas certamente não menos importante, quero agradecer à minha família, em particular aos meus pais, a quem dedico este trabalho, pois sempre apoiaram as minhas decisões; por todo o seu amor, carinho e interesse pelo meu trabalho. Sempre foram a minha base e, por isso, sou-lhes profundamente grato pelo apoio incondicional que me deram ao longo de todos estes anos e, sem o qual, não poderia atingir metas tão ambiciosas.

Page intentionally left blank

CONTENTS

Abstract iii

Resumo v

Agradecimentos vi

Contents xii

List of Figures xxviii

List of tables xxx

Notation xxxi

1 Introduction 1
- 1.1 Motivation . . . 1
- 1.2 Objectives . . . 4
- 1.3 Computational Framework . . . 5
- 1.4 Document Structure . . . 6

2 Continuum Mechanics Theory and Finite Element Method 11
- 2.1 Deformation Kinematics . . . 12
  - 2.1.1 Deformation Mapping Function . . . 12
  - 2.1.2 Material and Spatial Descriptions . . . 14
  - 2.1.3 Deformation Gradient . . . 15
  - 2.1.4 Isochoric/Volumetric Decomposition . . . 16
  - 2.1.5 Polar Decomposition . . . 18
- 2.2 Strain Tensors . . . 19
- 2.3 Forces and Stresses . . . 21
  - 2.3.1 Cauchy Stress Tensor . . . 22
  - 2.3.2 Piola-Kirchhoff Stress Tensors . . . 22
  - 2.3.3 Kirchhoff Stress Tensor . . . 23
  - 2.3.4 Deviatoric/Hydrostatic Decomposition . . . 23
- 2.4 Fundamental Laws of Thermodynamics . . . 24

2.4.1 Principle of Mass Conservation . . . 24
2.4.2 Principle of Linear Momentum Conservation . . . 24
2.4.3 First Law of Thermodynamics . . . 25
2.4.4 Second Law of Thermodynamics . . . 26
2.4.5 Clausius-Duhem Inequality . . . 26
2.5 Constitutive Theory . . . 27
2.5.1 Constitutive Axioms . . . 27
2.5.2 Thermodynamics with Internal Variables . . . 29
2.5.3 Mechanical Constitutive Initial Value Problem . . . 32
2.6 Weak Equilibrium Equations . . . 34
2.6.1 Spatial Formulation . . . 34
2.6.2 Material Formulation . . . 34
2.6.3 Quasi-Static Formulation . . . 35
2.7 Quasi-Static Initial Value Problem . . . 35
2.8 Finite Element Method . . . 37
2.8.1 Time Discretisation . . . 37
2.8.2 Spatial Discretisation . . . 40
2.8.3 Numerical Integration . . . 46
2.8.4 Proportional Loading . . . 47
2.8.5 Newton-Raphson Method . . . 48

3 First-order Computational Homogenisation Multi-Scale Models 55
3.1 First-order Computational Homogenisation . . . 56
3.1.1 Representative Volume Element . . . 57
3.2 Large Strain Multi-Scale Constitutive Models . . . 58
3.2.1 Homogenisation . . . 59
3.2.2 RVE Kinematics . . . 60
3.2.3 Hill-Mandel Principle . . . 61
3.2.4 Micro-Scale Boundary Conditions . . . 63
3.3 Numerical Formulation . . . 69
3.3.1 Time Discretisation . . . 69
3.3.2 Spatial Discretisation . . . 70
3.3.3 Newton-Raphson Algorithm . . . 71
3.3.4 Dependency Matrix . . . 73
3.3.5 Homogenised Stress Tensor . . . 76
3.3.6 Homogenised Consistent Tangent Modulus . . . 76

4 PC/ABS Polymer Blend **79**
4.1 Polycarbonate (PC) . . . 80
4.1.1 Properties . . . 81
4.2 Acrylonitrile-Butadiene-Styrene (ABS) . . . 82
4.2.1 Rubber-Toughened Polymer Blends . . . 83
4.2.2 Properties . . . 84
4.3 PC/ABS Blends . . . 84
4.3.1 Morphology . . . 85
4.3.2 Deformation and Damage Mechanisms . . . 87
4.3.3 Process-Structure-Property-Performance Dimensions . . . 88

5 Size of the Representative Volume Element (RVE) **91**
5.1 High-Fidelity RVE . . . 92
5.2 Material Model . . . 94
5.2.1 Rheological Model . . . 96
5.2.2 Kinematics . . . 97
5.2.3 Prediction of Damage Linked to the Rubber Particles' Internal Cavitation . . . 98
5.2.4 The Visco-Plastic Constitutive Formulation . . . 100
5.2.5 Strain Hardening . . . 103
5.2.6 No Rubber Phase Model . . . 103
5.2.7 Material Properties . . . 104
5.3 RVE Size . . . 106
5.3.1 2D RVE Size . . . 108
5.3.2 2D RVE Size - Discussion . . . 123
5.3.3 2D RVE Mesh . . . 126
5.3.4 3D RVE Size . . . 130
5.3.5 3D RVE Size - Discussion . . . 136
5.3.6 3D RVE Mesh . . . 137
5.3.7 Remark on the Periodic Boundary Condition - 3D . . . 140

6 Cohesive Zone Model **143**
6.1 Model for Onset and Propagation of Fracture . . . 143
6.2 Boundary Value Problem . . . 144
6.3 Cohesive Elements . . . 146
6.4 Constitutive Cohesive Model . . . 148
6.4.1 Loading Modes . . . 149
6.4.2 Traction-Separation Laws . . . 150
6.4.3 PPR (Park-Paulino-Roesler) Potential-Based Model . . . 151

6.4.4 Unloading/Reloading Model . . . 155
6.4.5 Contact . . . 156
6.4.6 Model Parameters . . . 157
6.4.7 Damage Variable for Post-Processing . . . 157

7 Cohesive Elements Generation in an RVE 159
7.1 RVE Generation . . . 159
7.1.1 Output File . . . 161
7.2 Cohesive Elements Generation . . . 162
7.2.1 Adjacent Elements Detection . . . 162
7.2.2 Cohesive Elements Creation . . . 167
7.2.3 Output File . . . 170
7.3 Numerical Assessment . . . 171
7.3.1 Analysis 1 - Number of Elements . . . 171
7.3.2 Analysis 2 - Number of Materials . . . 174
7.4 Application Examples . . . 175

8 Numerical Analysis on the Influence of Cohesive Elements 181
8.1 Constitutive Cohesive Model Properties . . . 181
8.1.1 Fracture Energy . . . 182
8.1.2 Cohesive Strength . . . 184
8.1.3 Remaining Parameters . . . 185
8.2 CZM Properties Analysis . . . 187
8.3 Loading Schemes Analysis . . . 191

9 Cohesive Zone Model Parameters Calibration 195
9.1 Experimental Testing Setup . . . 198
9.2 Calibration Procedure . . . 199
9.2.1 Optimisation Problem . . . 200
9.2.2 Loss Functions . . . 201
9.2.3 Integration with Finite Element Analysis . . . 201
9.2.4 Optimisation Algorithm . . . 201
9.3 Computational Setting . . . 202
9.3.1 Macro-scale Analysis . . . 202
9.3.2 Micro-scale Analysis . . . 203
9.3.3 Coupled Multi-scale Analysis . . . 205
9.4 Results and Discussion . . . 205
9.4.1 Macro-scale Analysis . . . 205
9.4.2 Micro-scale Analysis . . . 207

9.4.3 Coupled Multi-scale Analysis 214

10 Visco-Elastic Visco-Plastic Constitutive Model: Damage Variable 217
10.1 Explicit Local Damage Model 218
10.2 Computational Implementation 219
10.2.1 Numerical Integration Scheme 220
10.2.2 Fully Implicit Elastic Predictor/Return Mapping Algorithm . 223
10.2.3 State Update 224
10.2.4 Consistent Tangent Modulus 228
10.2.5 Damage Variable Computation 230
10.3 Results and Discussion 231
10.3.1 PC Matrix with Voids under Mixed Tensile-Shear 231
10.3.2 PC/ABS under Mixed Tensile-Shear 235

11 Conclusions 241
11.1 Conclusions 241
11.2 Future Research 245

References 258

Conference Talks 260

Appendixes 261

A Representative Volume Element Size 263
A.1 Two-dimensional RVEs 263
A.2 Three-dimensional RVEs 275

B Finite Elements 279
B.1 Two-dimensional Elements 280
B.1.1 TRI3: 3-node linear element 280
B.1.2 TRI6: 6-node quadratic element 281
B.1.3 QUAD4: 4-node linear element 282
B.1.4 QUAD8: 8-node quadratic element 283
B.1.5 QUAD9: 9-node quadratic element 284
B.2 Three-dimensional Elements 285
B.2.1 TETRA4: 4-node linear element 285
B.2.2 TETRA10: 10-node quadratic element 286
B.2.3 PYRA5: 5-node linear element 287
B.2.4 WEDGE6: 6-node linear element 288

B.2.5 HEXA8: 8-node linear element 289
B.2.6 HEXA20: 20-node quadratic element 290

C Cohesive Elements **291**
C.1 Two-dimensional Elements 291
C.1.1 COH2D4: 4-node linear element 291
C.1.2 COH2D6: 6-node quadratic element 292
C.2 Three-dimensional Elements 293
C.2.1 COH3D6: 6-node linear element 294
C.2.2 COH3D12: 12-node quadratic element 295
C.2.3 COH3D8: 8-node linear element 296
C.2.4 COH3D16: 16-node quadratic element 297

D Smooth Round Bar **299**

E PC/ABS material: Technical Specifications **301**

F Visco-Elastic Visco-Plastic Constitutive Model Linearisation **307**
F.1 State Update Residual Derivative 309
F.1.1 First Residual Derivatives 309
F.1.2 Second Residual Derivatives 310
F.1.3 Third Residual Derivatives 310
F.1.4 Fourth Residual Derivatives 311
F.2 Consistent Tangent Modulus Derivatives 311

LIST OF FIGURES

1 Introduction **1**

1.1 Research group and finite element program logotypes. 5

2 Continuum Mechanics Theory and Finite Element Method **11**

2.1 Deformation of a generic continuum body $\mathscr{B}$. 13
2.2 Schematic of the two types of rigid-body motion of a continuum body: a) rigid translation; b) rigid rotation. 14
2.3 Deformation gradient: deformation of two neighbouring particles 16
2.4 Isochoric and volumetric decompositions. 17
2.5 Polar decompositions of the deformation gradient. 18
2.6 Representation of the initial boundary value problem. 36
2.7 Schematic representation of the different tools (left column) and steps (right column) of the FEM. 38
2.8 Finite element interpolation - element shape function. 41
2.9 Finite element interpolation - global shape function. 42
2.10 Representation of the mapping from the local/natural normalised domain onto the element domain, for a 4-noded bilinear quadratic element. 47
2.11 Representation of the Newton- Raphon Method iterative cycle for a given increment n of the equilibrium equation - one degree of freedom. 53

3 First-order Computational Homogenisation Multi-Scale Models **55**

3.1 Schematic of multi-scale model based on first-order homogenisation models. 59
3.2 Micro-scale Taylor boundary condition model. 65
3.3 Micro-scale linear boundary condition. 66
3.4 Micro-scale periodic boundary condition. 67
3.5 Micro-scale uniform traction boundary condition. 68

3.6 Convergence of homogenised characteristics at varied boundary conditions and RVE sizes. 69

4 PC/ABS Polymer Blend **79**

4.1 Schematic representation of a PC/ABS (70/30) microstructure, evidencing the three phases of the ternary blend. SEM micrograph (PC matrix etched with a NaOH aqueous solution) taken from Greco (1996). 79
4.2 Schematic of the molecular structure of the Bisphenol-A Polycarbonate (PC) - repeat unit (molecular conformation is not considered). 80
4.3 SEM pictures of fracture surfaces of notched PC specimens, notch at the top. a) ductile, test conditions: 10^{-5} m/s, -50 °C; b) brittle, test conditions: 1 m/s, -20 °C; c) mixed mode, test conditions: 10^{-5} m/s, -60 °C. 81
4.4 Schematic of the molecular structure of the Acrylonitrile-Butadiene-Styrene (ABS) - repeat unit (molecular conformation is not considered). 83
4.5 Schematic representation of two different types of PC/ABS morphologies. A sea-island structure is shown for PC/ABS (70/30) and a co-continuous lamellar structure for PC/ABS (50/50). 86
4.6 Schematic of the deformation and damage mechanisms occurring in a PC/ABS blend with sea-island structure. 87

5 Size of the Representative Volume Element (RVE) **91**

5.1 PC/ABS high-fidelity 2D RVEs for various ABS(%) contents with a particulate morphology using AMINO. The RVEs have the same side length of 50μm. 93
5.2 PC/ABS high-fidelity 3D RVEs for various ABS(%) contents with a particulate morphology using AMINO. The RVEs have a side length of 20 μm. 94
5.3 Typical constitutive behaviour of amorphous thermoplastics when subjected to uniaxial compression loading. 95
5.4 Rheological model of the formulated visco-elastic visco-plastic constitutive model. 97
5.5 Various 2D realisations with volume fraction equal to 10% and different volume element sizes. 110

5.6 Homogenised First Piola Kirchhoff shear stress, P_{xy}, for the 50 μm RVE size with 10% volume fraction and linear boundary condition. Shaded bounds: standard deviation; and dashed line: standard deviation 10% limit. 111
5.7 Comparison of the Homogenised First Piola Kirchhoff shear stress, P_{xy}, for different RVE sizes with 10% volume fraction and linear boundary condition. 111
5.8 Variance in behaviour between one RVE size and the next closest RVE size. 111
5.9 Average CPU time of the samples with 10% volume fraction and linear boundary condition under shear across *xy* for different RVE sizes. 111
5.10 Homogenised First Piola Kirchhoff shear stress, P_{xy}, for the 50 μm RVE size with 10% volume fraction and uniform boundary condition. Shaded bounds: standard deviation; and dashed line: standard deviation 10% limit. 112
5.11 Comparison of the Homogenised First Piola Kirchhoff shear stress, P_{xy}, for different RVE sizes with 10% volume fraction and uniform boundary condition. 112
5.12 Variance in behaviour between one RVE size and the next closest RVE size. 112
5.13 Average CPU time of the samples with 10% volume fraction and uniform boundary condition under shear across *xy* for different RVE sizes. 112
5.14 Homogenised First Piola Kirchhoff shear stress, P_{xy}, for the 50 μm RVE size with 10% volume fraction and periodic boundary condition. Shaded bounds: standard deviation; and dashed line: standard deviation 10% limit. 113
5.15 Comparison of the Homogenised First Piola Kirchhoff shear stress, P_{xy}, for different RVE sizes with 10% volume fraction and periodic boundary condition. 113
5.16 Variance in behaviour between one RVE size and the next closest RVE size. 113
5.17 Average CPU time of the samples with 10% volume fraction and periodic boundary condition under shear across *xy* for different RVE sizes. 113

5.18 Homogenised First Piola Kirchhoff shear stress, P_{xy}, computed with distinct boundary conditions, for different RVE sizes with 10% volume fraction at four time instants. 114
5.19 Homogenised First Piola Kirchhoff shear stress, P_{xy}, for the 50 μm RVE size with 20% volume fraction and periodic boundary condition. Shaded bounds: standard deviation; and dashed line: standard deviation 10% limit. 115
5.20 Comparison of the Homogenised First Piola Kirchhoff shear stress, P_{xy}, for different RVE sizes with 20% volume fraction and periodic boundary condition. 115
5.21 Variance in behaviour between one RVE size and the next closest RVE size. 115
5.22 Average CPU time of the samples with 20% volume fraction and periodic boundary condition under shear across *xy* for different RVE sizes. 115
5.23 Homogenised First Piola Kirchhoff shear stress, P_{xy}, for the 50 μm RVE size with 30% volume fraction and periodic boundary condition. Shaded bounds: standard deviation; and dashed line: standard deviation 10% limit. 116
5.24 Comparison of the Homogenised First Piola Kirchhoff shear stress, P_{xy}, for different RVE sizes with 30% volume fraction and periodic boundary condition. 116
5.25 Variance in behaviour between one RVE size and the next closest RVE size. 116
5.26 Average CPU time of the samples with 30% volume fraction and periodic boundary condition under shear across *xy* for different RVE sizes. 116
5.27 Homogenised First Piola Kirchhoff shear stress, P_{xx}, for the 50 μm RVE size with 10% volume fraction and periodic boundary condition. Shaded bounds: standard deviation; black dashed line: standard deviation 10% limit; red data: 5 samples; and blue data: 3 samples. 117
5.28 Comparison of the Homogenised First Piola Kirchhoff shear stress, P_{xx}, for different RVE sizes with 10% volume fraction and periodic bc. Solid line: 5 samples; and dashed line: 3 samples 117
5.29 Variance in behaviour between one RVE size and the next closest RVE size. 117

5.30 Average CPU time of the samples with 10% volume fraction and periodic boundary condition under uniaxial loading along xx for different RVE sizes. 117
5.31 Homogenised First Piola Kirchhoff shear stress, P_{xx}, for the 50 μm RVE size with 20% volume fraction and periodic boundary condition. Shaded bounds: standard deviation; and dashed line: standard deviation 10% limit. 118
5.32 Comparison of the Homogenised First Piola Kirchhoff shear stress, P_{xx}, for different RVE sizes with 20% volume fraction and periodic boundary condition. 118
5.33 Variance in behaviour between one RVE size and the next closest RVE size. 118
5.34 Average CPU time of the samples with 20% volume fraction and periodic boundary condition under uniaxial loading along xx for different RVE sizes. 118
5.35 Homogenised First Piola Kirchhoff shear stress, P_{xx}, for the 50 μm RVE size with 30% volume fraction and periodic boundary condition. Shaded bounds: standard deviation; black dashed line: standard deviation 10% limit; red data: 5 samples; and blue data: 3 samples. 119
5.36 Comparison of the Homogenised First Piola Kirchhoff shear stress, P_{xx}, for different RVE sizes with 30% volume fraction and periodic bc. Solid line: 5 samples; and dashed line: 3 samples. 119
5.37 Variance in behaviour between one RVE size and the next closest RVE size. 119
5.38 Average CPU time of the samples with 30% volume fraction and periodic boundary condition under uniaxial loading along xx for different RVE sizes. 119
5.39 Homogenised First Piola Kirchhoff shear stress, P_{yy}, for the 50 μm RVE size with 10% volume fraction and periodic boundary condition. Shaded bounds: standard deviation; black dashed line: standard deviation 10% limit; red data: 5 samples; and blue data: 3 samples. 120
5.40 Comparison of the Homogenised First Piola Kirchhoff shear stress, P_{yy}, for different RVE sizes with 10% volume fraction and periodic bc. Solid line: 5 samples; and dashed line: 3 samples. 120
5.41 Variance in behaviour between one RVE size and the next closest RVE size. 120

5.42 Average CPU time of the samples with 10% volume fraction and periodic boundary condition under uniaxial loading along *yy* for different RVE sizes. 120
5.43 Homogenised First Piola Kirchhoff shear stress, P_{yy}, for the 50 μm RVE size with 20% volume fraction and periodic boundary condition. Shaded bounds: standard deviation; black dashed line: standard deviation 10% limit; red data: 5 samples; and blue data: 3 samples. 121
5.44 Comparison of the Homogenised First Piola Kirchhoff shear stress, P_{yy}, for different RVE sizes with 20% volume fraction and periodic bc. Solid line: 5 samples; and dashed line: 3 samples. 121
5.45 Variance in behaviour between one RVE size and the next closest RVE size. 121
5.46 Average CPU time of the samples with 20% volume fraction and periodic boundary condition under uniaxial loading along *yy* for different RVE sizes. 121
5.47 Homogenised First Piola Kirchhoff shear stress, P_{yy}, for the 50 μm RVE size with 30% volume fraction and periodic boundary condition. Shaded bounds: standard deviation; and dashed line: standard deviation 10% limit. 122
5.48 Comparison of the Homogenised First Piola Kirchhoff shear stress, P_{yy}, for different RVE sizes with 30% volume fraction and periodic boundary condition. 122
5.49 Variance in behaviour between one RVE size and the next closest RVE size. 122
5.50 Average CPU time of the samples with 30% volume fraction and periodic boundary condition under uniaxial loading along *yy* for different RVE sizes. 122
5.51 Time evolution of the nucleation phenomenon and deformation of a 10% volume fraction RVE under uniaxial loading along *xx*. . . 124
5.52 Time evolution of the nucleation phenomenon and deformation of a 10% volume fraction RVE under uniaxial loading along *xx*. . . 124
5.53 Time evolution of the nucleation phenomenon and deformation of a 10% volume fraction RVE under uniaxial loading along *xx*. . . 124
5.54 Comparison of the Homogenised First Piola Kirchhoff shear stress, P_{xy}, of RVEs with different mesh discretisation levels for 10% volume fraction and periodic boundary condition. 128

5.55 Standard deviation of the Homogenised First Piola Kirchhoff shear stress, P_{xy}, of RVEs with different mesh discretisation levels for 10% volume fraction and periodic boundary condition. 128
5.56 Variance in behaviour between one level of mesh discretisation and the next closest level. 128
5.57 Average CPU time of the samples with 10% volume fraction and periodic boundary condition under shear across *xy* for different mesh discretisation levels. 128
5.58 Comparison of the Homogenised First Piola Kirchhoff shear stress, P_{yy}, of RVEs with different mesh discretisation levels for 10% volume fraction and periodic boundary condition. Solid line: 5 samples; and dashed line: 3 samples. 129
5.59 Standard deviation of the Homogenised First Piola Kirchhoff shear stress, P_{yy}, of RVEs with different mesh discretisation levels for 10% volume fraction and periodic boundary condition. 129
5.60 Variance in behaviour between one level of mesh discretisation and the next closest level. 130
5.61 Various 3D realisations with volume fraction equal to 10% and different volume element sizes. 131
5.62 Homogenised First Piola Kirchhoff shear stress, P_{xy}, for the 15 μm RVE size with 10% volume fraction and mortar periodic boundary condition. Shaded bounds: standard deviation; black dashed line: standard deviation 10% limit; red data: 5 samples; and blue data: 3 samples. 133
5.63 Comparison of the Homogenised First Piola Kirchhoff shear stress, P_{xy}, for different RVE sizes with 10% volume fraction and mortar periodic boundary condition. 133
5.64 Variance in behaviour between one RVE size and the next closest RVE size. 133
5.65 Average CPU time of the samples with 10% volume fraction and mortar periodic boundary condition under shear across *xy* for different RVE sizes. 133
5.66 Homogenised First Piola Kirchhoff shear stress, P_{xy}, for the 15 μm RVE size with 20% volume fraction and mortar periodic boundary condition. Shaded bounds: standard deviation; black dashed line: standard deviation 10% limit; red data: 5 samples; and blue data: 3 samples. 134

5.67 Comparison of the Homogenised First Piola Kirchhoff shear stress, P_{xy}, for different RVE sizes with 20% volume fraction and mortar periodic boundary condition. 134
5.68 Variance in behaviour between one RVE size and the next closest RVE size. 134
5.69 Average CPU time of the samples with 20% volume fraction and mortar periodic boundary condition under shear across xy for different RVE sizes. 134
5.70 Homogenised First Piola Kirchhoff shear stress, P_{xy}, for the 15 μm RVE size with 30% volume fraction and mortar periodic boundary condition. Shaded bounds: standard deviation; and dashed line: standard deviation 10% limit. 135
5.71 Comparison of the Homogenised First Piola Kirchhoff shear stress, P_{xy}, for different RVE sizes with 30% volume fraction and mortar periodic boundary condition. 135
5.72 Variance in behaviour between one RVE size and the next closest RVE size. 135
5.73 Average CPU time of the samples with 30% volume fraction and mortar periodic boundary condition under shear across xy for different RVE sizes. 135
5.74 Time evolution of the nucleation phenomenon and deformation of a 10% volume fraction RVE under shear across xy. 136
5.75 Comparison of the Homogenised First Piola Kirchhoff shear stress, P_{xy}, of RVEs with different mesh discretisation levels for 10% volume fraction and periodic mortar boundary condition. 139
5.76 Standard deviation of the Homogenised First Piola Kirchhoff shear stress, P_{xy}, of RVEs with different mesh discretisation levels for 10% volume fraction and periodic mortar boundary condition. . . 139
5.77 Variance in behaviour between one level of mesh discretisation and the next closest level. 139
5.78 Average CPU time of the samples with 10% volume fraction and periodic mortar boundary condition under shear across xy for different mesh discretisation levels. 139
5.79 Comparisons between the average stress-deformation of the samples with 10% volume fraction for the mortar periodic and periodic boundary conditions. 140

5.80 Comparison between the standard deviation of the average stress-deformation of the samples with 10% volume fraction for the mortar periodic and periodic boundary conditions. 140
5.81 Variance in behaviour between the mortar periodic and periodic boundary conditions. 141
5.82 Comparison between the average CPU time of the samples with 10% volume fraction for the mortar periodic and periodic boundary conditions. 141
5.83 Comparisons between the stress-deformation of the samples with 10% volume fraction for the mortar periodic and periodic boundary conditions; (a) With small particle on the border; (b) Without small particle on the border. 142

6 Cohesive Zone Model **143**

6.1 Continuum and cohesive elements and respective constitutive laws.144
6.2 Continuum body with a crack in the deformed configuration. . . . 145
6.3 Schematic representation of 2D and 3D cohesive elements with respective node displacements defined in the local coordinate system. 147
6.4 Schematic representation of the three fracture modes. 149
6.5 Different formulations to implement cohesive zone models. 150
6.6 Graphic representation of the cohesive interaction zones for the different fracture toughness combinations. The black and blue regions, respectively, define the domains where the normal and tangential tractions are positive and acceptable. 153
6.7 Graphical depiction of the PPR cohesive zone model for varying values of α and β. 154

7 Cohesive Elements Generation in an RVE **159**

7.1 Admissible particle types generated by AMINO. From left to right: a disk, an ellipse, a sphere, an ellipsoid and a cylinder. 160
7.2 Flowchart illustrating the primary blocks of the program. 163
7.3 Flowchart depicting the basic logic underlying the interface detection block. 163
7.4 Representation of the identification matrix of the interface nodes. 164
7.5 Schematic representation of the admissible 2D linear continuum element types read by the code. From left to right: TRI3 and QUAD4164

7.6 Schematic representation of the admissible 2D quadratic continuum element types read by the code. From left to right: TRI6, QUAD8 and QUAD9 165
7.7 Schematic representation of the admissible 3D linear continuum element types read by the code. From left to right: TETRA4 and PYRA5; WEDGE6 and HEXA8. 165
7.8 Schematic representation of the admissible 3D quadratic continuum element types read by the code. From left to right: TETRA10 and HEXA20. 166
7.9 Graphical representation of a 2D linear element with interface nodes that does not form an interface. 166
7.10 Graphic representation of the cohesive elements generation process - 2D analysis. 168
7.11 Graphic representation of the cohesive elements generation process - 3D analysis. 169
7.12 Schematic representation of a 2D case when empty spaces are generated. 170
7.13 Average CPU time (over ten realisations for each case) for generating the cohesive elements - Analysis 1. 173
7.14 Ratio between the average CPU time (over ten realisations for each case) for generating the RVE and the cohesive elements - Analysis 1.173
7.15 Average CPU time (over ten realisations for each case) for generating the cohesive elements - Analysis 2. 175
7.16 Example of a 3D RVE with two material phases. Different colours correspond to different material phases. 176
7.17 Example of a 2D RVE with two material phases. Different colours correspond to different material phases. 176
7.18 Example of a 2D RVE with twenty material phases. Different colours correspond to different material phases. 177
7.19 Example of a 2D RVE with two hundred material phases. Different colours correspond to different material phases. 177
7.20 Example of a 3D RVE with twenty material phases. Different colours correspond to different material phases. 178
7.21 Example of a 3D RVE with two hundred material phases. Different colours correspond to different material phases. 178
7.22 Example of a 3D RVE with two hundred material phases and a random geometry. Different colours correspond to different material phases. 179

7.23 Example of a 2D RVE with twenty material phases, with the cohesive elements normals depicted. Different colours correspond to different material phases. 179
7.24 Example of a 2D RVE with twenty material phases being tractioned in the X and Y directions. Different colours correspond to different material phases. 180
7.25 Example of a 2D RVE with two material phases being tractioned in the Z direction. Different colours correspond to different material phases. 180

8 Numerical Analysis on the Influence of Cohesive Elements 181

8.1 Geometry of the asymmetric double-cantilever beam test used in the calculation of the interfacial fracture toughness. 183
8.2 Fracture toughness, and respective standard deviation, for PC/SAN adhesive joint as a function of AN content of SAN copolymers. . . 183
8.3 Standard dumbbell specimen with a weld line in the centre, to determine the interfacial strength. 184
8.4 Relation between weld line strength and PC/ABS blend ratio. . . . 185
8.5 Influence of injection moulding temperature on the weld line strength of PC/ABS. 185
8.6 Comparison of the microscopic response of PC/ABS with and without cohesive elements. 188
8.7 Time evolution of the nucleation and debonding phenomena and deformation of a 10% volume fraction RVE under uniaxial loading along *xx*. 188
8.8 Effect of the cohesive strengths on the microscopic response of PC/ABS. 189
8.9 Effect of the fracture energies on the microscopic response of PC/ABS. 190
8.10 Effect of the initial slope indicators on the microscopic response of PC/ABS. A total of 9 different combinations are represented. . . 191
8.11 Effect of the shape parameters on the microscopic response of PC/ABS. A total of 9 different combinations are represented. 191
8.12 Sensitivity analysis of the loading schemes most impacted by incorporating cohesive elements at the interface between PC and ABS: (a) Traction along *xx*; (b) Traction along *yy*. 193

8.13 Comparison of the microscopic response of PC/ABS with and without cohesive elements under compression along *yy*. Specifically, C1 = −0.5 and C2 = 0.0. 194
8.14 Comparison of the microscopic response of PC/ABS with and without cohesive elements under traction along *xx*. Specifically, C1 = 0.5 and C2 = 0.0 or 1.0. 194

9 Cohesive Zone Model Parameters Calibration 195

9.1 Cohesive Zone Model parameters calibration procedure. 197
9.2 Uniaxial tensile tests: MTS 810 servo-hydraulic testing system. . . 198
9.3 Geometry of tensile test specimen - smooth round bar. 198
9.4 Thermal cycle used for the thermal treatment of the PC/ABS test specimens. 199
9.5 Finite element model of one-eighth of the tensile test specimen - smooth round bar; and selected Gauss points. 203
9.6 Geometry of the unit cell with a side length of 5.813 μm and an ABS volume fraction of 20%. 204
9.7 Geometry of the RVE with a side length of 15 μm and an ABS volume fraction of 20%. 204
9.8 Comparison between the force-displacement response of the smooth round bar specimen predicted by the proposed constitutive model and the experimental results conducted by Macedo (2023). 207
9.9 Distribution of the Cauchy equivalent stress, σ^{eq}, at the last increment for the smooth round bar specimen subjected to the uniaxial tensile test. 207
9.10 Comparison between the effective Cauchy stress-equivalent strain response for three different Gauss points from the macro-scale analysis and the unit cell micro-scale analysis, employing both the literature and calibrated properties. 208
9.11 Schematic representation of the final configurations and the middle-plane contours illustrating the ABS total porosity and cohesive elements damage of the PC/ABS unit cell for the three Gauss points analysed, employing the literature properties. 209

9.12 Comparison between the effective Cauchy stress-equivalent strain response for three different Gauss points from the macro-scale analysis and the unit cell micro-scale analysis, without and with cohesive elements. 212
9.13 Comparison between the effective Cauchy stress-equivalent strain response for three different Gauss points from the macro-scale analysis and the unit cell and RVE micro-scale analysis, employing the literature properties. 213
9.14 Schematic representation of the final configurations and the middle-plane contours illustrating the ABS total porosity and cohesive elements damage of the PC/ABS RVE for the three Gauss points analysed, employing the literature properties. 214
9.15 Comparison between the force-displacement response of the smooth round bar specimen predicted by the coupled multi-scale analyses, without and with cohesive elements, and the experimental results conducted by Macedo (2023). 215
9.16 Distribution of the Cauchy equivalent stress, σ^{eq}, at the last increment for the smooth round bar specimen subjected to the uniaxial tensile test. 216

10 Visco-Elastic Visco-Plastic Constitutive Model: Damage Variable 217

10.1 Mesh topology of the PC matrix with voids 2D RVE with a side length of 40 μm. 232
10.2 Effect of the critical accumulated plastic strain, $\bar{\varepsilon}^{p}_{\text{cr}}$ on the microscopic response of PC material with voids. 234
10.3 Damage bands obtained for different values of the critical accumulated plastic strain, $\bar{\varepsilon}^{p}_{\text{cr}}$, shown for the PC matrix with voids 2D RVE. 234
10.4 Mesh topology of PC/ABS 2D RVE with a side length of 50 μm and a volume fraction of 10% of ABS. 236
10.5 Microscopic response of PC/ABS blend with a volume fraction of 10% of ABS for all combinations of damage mechanisms. 237
10.6 Visual representation of the microscopic response of PC/ABS blend with a volume fraction of 10% of ABS for all combinations of damage mechanisms. 237
10.7 Effect of the critical accumulated plastic strain, $\bar{\varepsilon}^{p}_{\text{cr}}$ on the microscopic response of PC/ABS blend with a volume fraction of 10% of ABS with cohesive elements. 239

10.8 Damage localisation obtained for different values of the critical accumulated plastic strain, $\bar{\varepsilon}^{p}_{\mathrm{cr}}$, shown for the PC/ABS 2D RVE with a side length of 50 μm and a volume fraction of 10% of ABS with cohesive elements. 239

A Representative Volume Element Size **263**

A.1 Homogenised First Piola Kirchhoff shear stress, P_{xy}, for different RVE sizes with 10% volume fraction and linear boundary condition. Shaded bounds: standard deviation; and dashed line: standard deviation 10% limit. 264

A.2 Homogenised First Piola Kirchhoff shear stress, P_{xy}, for different RVE sizes with 10% volume fraction and uniform boundary condition. Shaded bounds: standard deviation; and dashed line: standard deviation 10% limit. 265

A.3 Homogenised First Piola Kirchhoff shear stress, P_{xy}, for different RVE sizes with 10% volume fraction and periodic boundary condition. Shaded bounds: standard deviation; and dashed line: standard deviation 10% limit. 266

A.4 Homogenised First Piola Kirchhoff shear stress, P_{xy}, for different RVE sizes with 20% volume fraction and periodic boundary condition. Shaded bounds: standard deviation; and dashed line: standard deviation 10% limit. 267

A.5 Homogenised First Piola Kirchhoff shear stress, P_{xy}, for different RVE sizes with 30% volume fraction and periodic boundary condition. Shaded bounds: standard deviation; and dashed line: standard deviation 10% limit. 268

A.6 Homogenised First Piola Kirchhoff shear stress, P_{xx}, for different RVE sizes with 10% volume fraction and periodic boundary condition. Shaded bounds: standard deviation; black dashed line: standard deviation 10% limit; red data: 5 samples; and blue data: 3 samples. 269

A.7 Homogenised First Piola Kirchhoff shear stress, P_{xx}, for different RVE sizes with 20% volume fraction and periodic boundary condition. Shaded bounds: standard deviation; and dashed line: standard deviation 10% limit. 270

A.8 Homogenised First Piola Kirchhoff shear stress, P_{xx}, for different RVE sizes with 30% volume fraction and periodic boundary condition. Shaded bounds: standard deviation; black dashed line: standard deviation 10% limit; red data: 5 samples; and blue data: 3 samples. 271
A.9 Homogenised First Piola Kirchhoff shear stress, P_{yy}, for different RVE sizes with 10% volume fraction and periodic boundary condition. Shaded bounds: standard deviation; black dashed line: standard deviation 10% limit; red data: 5 samples; and blue data: 3 samples. 272
A.10 Homogenised First Piola Kirchhoff shear stress, P_{yy}, for different RVE sizes with 20% volume fraction and periodic boundary condition. Shaded bounds: standard deviation; black dashed line: standard deviation 10% limit; red data: 5 samples; and blue data: 3 samples. 273
A.11 Homogenised First Piola Kirchhoff shear stress, P_{yy}, for different RVE sizes with 30% volume fraction and periodic boundary condition. Shaded bounds: standard deviation; and dashed line: standard deviation 10% limit. 274
A.12 Homogenised First Piola Kirchhoff shear stress, P_{xy}, for different RVE sizes with 10% volume fraction and mortar periodic boundary condition. Shaded bounds: standard deviation; black dashed line: standard deviation 10% limit; red data: 5 samples; and blue data: 3 samples. 275
A.13 Homogenised First Piola Kirchhoff shear stress, P_{xy}, for different RVE sizes with 20% volume fraction and mortar periodic boundary condition. Shaded bounds: standard deviation; black dashed line: standard deviation 10% limit; red data: 5 samples; and blue data: 3 samples. 276
A.14 Homogenised First Piola Kirchhoff shear stress, P_{xy}, for different RVE sizes with 30% volume fraction and mortar periodic boundary condition. Shaded bounds: standard deviation; and dashed line: standard deviation 10% limit. 277

B Finite Elements **279**

B.1 Schematic representation of the two-dimensional 3-node linear finite element. 280

B.2 Schematic representation of the two-dimensional 6-node quadratic finite element. 281
B.3 Schematic representation of the two-dimensional 4-node linear finite element. 282
B.4 Schematic representation of the two-dimensional 8-node quadratic finite element. 283
B.5 Schematic representation of the two-dimensional 9-node quadratic finite element. 284
B.6 Schematic representation of the three-dimensional 4-node linear finite element. 285
B.7 Schematic representation of the three-dimensional 10-node quadratic finite element. 286
B.8 Schematic representation of the three-dimensional 5-node linear finite element. 287
B.9 Schematic representation of the three-dimensional 6-node linear finite element. 288
B.10 Schematic representation of the three-dimensional 8-node linear finite element. 289
B.11 Schematic representation of the three-dimensional 20-node quadratic finite element. 290

C Representative Volume Element Size **291**

C.1 Schematic representation of the two-dimensional 4-node linear finite element. 291
C.2 Schematic representation of the two-dimensional 6-node quadratic finite element. 292
C.3 Schematic representation of the three-dimensional 6-node linear finite element. 294
C.4 Schematic representation of the three-dimensional 12-node quadratic finite element. 295
C.5 Schematic representation of the three-dimensional 8-node linear finite element. 296
C.6 Schematic representation of the three-dimensional 16-node quadratic finite element. 297

LIST OF TABLES

4 PC/ABS Polymer Blend **79**

4.1 Examples of process-structure-property-performance dimensions involved in the engineering design space of PC/ABS polymer blends given the ICME computational framework. 89

5 Size of the Representative Volume Element (RVE) **91**

5.1 Material properties of the finite strain visco-elastic visco-plastic constitutive model. 105
5.2 Material properties of the PC matrix and ABS particles employed. . 106

6 Cohesive Zone Model **143**

6.1 Constitutive cohesive model input parameters. 157

7 Cohesive Elements Generation in an RVE **159**

7.1 Average CPU time (over ten realisations for each case) for generating the RVE - Analysis 1. 172
7.2 Average CPU time (over ten realisations for each case) for generating the cohesive elements - Analysis 1. 172
7.3 Average CPU time (over ten realisations for each case) for generating the cohesive elements - Analysis 2. 174

8 Numerical Analysis on the Influence of Cohesive Elements **181**

8.1 Constitutive cohesive model input parameters. 187

9 Cohesive Zone Model Parameters Calibration **195**

9.1 Material properties of the visco-elastic-visco-plastic model calibrated from the uniaxial tensile test. 206

9.2 Material properties of the PPR cohesive zone model calibrated from the comparison between the macro-scale and micro-scale analysis. 208

10 Visco-Elastic Visco-Plastic Constitutive Model: Damage Variable 217

10.1 Convergence table of the mixed tensile-shear numerical response of the 2D PC matrix with voids RVE. Normalised equilibrium residual evolution at increment 100 and state update normalised residual evolution at one Gauss point subjected to the highest value of the damage variable during each global iteration. Convergence tolerance set to 1.0×10^{-8}. 235

NOTATION

Abbreviations

1D	One-dimensional
2D	Two-dimensional
3D	Three-dimensional
ABS	Acrylonitrile-butadiene-styrene
AN	Acrylonitrile
BO	Bayesian Optimisation
BPA	Bisphenol-A
BVP	Boundary Value Problem
CM2S	Computational Multi-Scale Modeling of Solids and Structures
CMT	Continuum Mechanics Theory
CPU	Central Processing Unit
CZM	Cohesive Zone Model
DOF	Degrees of Freedom
FEM	Finite Element Method
GP	Gauss point
inc	Increment
ICME	Integrated Computational Materials Engineering
LINKS	Large Strain Non-Linear Finite Element Analysis of
MSM	Multi-scale Models
MSM-H	Multi-scale Models based on Computational Homogenisation
MSE	Mean Squared Error
NRMSE	Normalised Root Mean Squared Error
PB	Polybutadiene
PC	Polycarbonate
PPR	Park-Paulino-Roesler
RMSE	Root Mean Squared Error
ROM	Reduced-Order Models

RVE	Representative Volume Element
SAN	Styrene-Acrylonitrile
SEM	Scanning Electron Microscopy
XFEM	Upper Confidence Bounds

General Notation

a	Scalar
$\boldsymbol{a}$	First-order tensor
$\boldsymbol{A}$	Second-order tensor
a, A	Fourth-order tensor
$\mathbf{a}$	Finite Element Method vector
$\mathbf{A}$	Finite Element Method matrix
$\mathscr{A}$	Body, set or space
$\boldsymbol{\varphi}_*(\bullet)$	Push forward
$\boldsymbol{\varphi}_*^{-1}(\bullet)$	Push back

Indices

$\dot{(\bullet)}$	First-order time derivative
$\ddot{(\bullet)}$	Second-order time derivative
$\hat{(\bullet)}$	Incremental constitutive function
$\bar{(\bullet)}$	Prescribed variable
$\overline{(\bullet)}$	Mean quantity
$\tilde{(\bullet)}$	Fluctuation quantity
$(\bullet)_0$	Reference configuration, initial time
$(\bullet)_\mathrm{c}$, $(\bullet)^\mathrm{coh}$	Cohesive components/variables
$(\bullet)_\mathrm{cr}$	Critical quantity
$(\bullet)_\mathrm{D}$	Driving component of the PC/ABS rheological model
$(\bullet)_\mathrm{d}$	Deviatoric component
$(\bullet)_\mathrm{H}$	Hardening component of the PC/ABS rheological model
$(\bullet)_\mathrm{h}$	Hydrostatic component
$(\bullet)_\mathrm{iso}$	Isochoric quantity
$(\bullet)_\mathrm{vol}$	Volumetric quantity

$(\bullet)_n$	General increment, Variables at time step n
$(\bullet)_{n+1}$	Variables at time step $n+1$
$(\bullet)_{\mathrm{n}}$	Normal interfacial components
$(\bullet)_{\mathrm{t}}$	Tangential interfacial components
$(\bullet)_\mu$	Micro-scale
$(\bullet)^{\,\mathrm{ext}}$	Exterior
$(\bullet)^{\,\mathrm{int}}$	Interior
$(\bullet)^{-1}$	Inverse
$(\bullet)^S$	Symmetric
$(\bullet)^T$	Transpose
$(\bullet)^0$	Initial guess of the Newton-Raphson Method
$(\bullet)^e$	Element quantity, Elastic component
$(\bullet)^{\mathrm{eq}}$	Equivalent quantity
$(\bullet)^k$	General iteration of the Newton-Raphson Method
$(\bullet)^g$	Global quantity
${}^h(\bullet)$	Discretised
$(\bullet)^p$	Plastic component
$(\bullet)^t$	History of $(\bullet)$ at $\boldsymbol{X}$ up to instant t
$(\bullet)^{\mathrm{trial}}$	Elastic trial state

Operators

$\det[\bullet]$	Determinant
$\mathrm{diag}[\bullet]$	Diagonal
$\mathrm{div}[\bullet]$	Divergence
$\exp[\bullet]$	Natural exponential function
$\ln[\bullet]$	Logarithm
$\mathrm{tr}[\bullet]$	Matrix trace
$\nabla[\bullet]$	Gradient
$\Delta(\bullet)$	Incremental quantity
$\delta(\bullet)$	Iterative quantity
$d(\bullet)$	Infinitesimal
$\partial(\bullet)/\partial a$	Partial derivative with respect to a
$d(\bullet)/da$	Total derivative with respect to a

$\boldsymbol{\varphi}_*(\bullet)$	Push-forward operator
$\boldsymbol{\varphi}_*^{-1}(\bullet)$	Pull-back operator
$\mathsf{A}(\bullet)$	Finite Element Method assembly operator
$\lvert(\bullet)\rvert$	Scalar norm (absolute value)
$\lVert(\bullet)\rVert$	Frobenius norm
$(\bullet)\otimes(\bullet)$	Tensorial product
$(\bullet)\cdot(\bullet)$	Tensorial single contraction
$(\bullet):(\bullet)$	Tensorial double contraction
$(\bullet)*(\bullet)$	Appropriate product

Variables

a	Area
$\mathbf{a}$	Spatial consistent tangent modulus
A	Eyring-related function
A_0	Fundamental vibration temperature factor
$\boldsymbol{A}$	Set of thermodynamical forces
$\mathbf{A}$	Material consistent tangent modulus
$\boldsymbol{b}$	Body forces
$\boldsymbol{B}$	Left Cauchy-Green strain tensor
$\mathbf{B}$	Discrete symmetric gradient operator
$\mathscr{B}$	General body
C_r	Rubbery modulus
$\boldsymbol{C}$	Right Cauchy-Green strain tensor, constraint matrix
D	Damage variable
D_∞	Saturation value of the softening parameter
$\boldsymbol{D}$	Symmetric component of the velocity gradient
$\mathbf{D}^{\text{ve}}$	Fourth-order visco-elastic relaxation tensor
$\dot{e}$	Specific internal energy
$\boldsymbol{e}^{(m)}$	Strain tensor from the Eulerian family
$\boldsymbol{e}_i$	Deformed configuration orthonormal basis
$\boldsymbol{e}_i^*$	Eigenvectors of the left stretch tensor
E	Young's modulus
E_∞	Long term Young's modulus

$\boldsymbol{E}^{(2)}$	Green-Lagrange strain tensor
$\boldsymbol{E}^{(m)}$	Strain tensor from the Lagrange family
$\boldsymbol{E}_i$	Reference configuration orthonormal basis
$\boldsymbol{E}_i^*$	Eigenvectors of the right stretch tensor
$\mathscr{E}$	Euclidean space
f	Void volume fraction (or porosity)
f_0	Initial void volume fraction (or porosity)
f_r	Total porosity from nucleation (rubber porosity)
$\dot{f}_N$	Rate of nucleation of new voids
$\dot{f}_g$	Rate of nucleation of existing voids
$\mathbf{f}$	Vector of forces
$\boldsymbol{F}$	Deformation gradient
g_j	Temperature-dependent relaxation time of j -th visco- elastic relaxation mode
$\boldsymbol{g}$	Spatial gradient of the temperature field
G	Shear modulus
G_r	Shear modulus of the rubber particles
G_∞	Long-term elastic modulus
$\mathbf{G}$	Discrete gradient operator
h	Scalar influencing the softening slope
H	Hardening modulus
ΔH	Activation energy
I	Scalar invariants
$\boldsymbol{I}$	Second-order identity tensor
$\mathbf{I}$	Fourth-order identity tensor
J	Deformation gradient determinant, invariant
$\boldsymbol{J}$	Jacobian matrix
$k_{\max}$	Maximum number of iterations
K	Bulk modulus
K_r	Bulk modulus of the rubber particles
$\boldsymbol{K}_T$	Global tangent stiffness matrix
$\mathscr{K}$	Set of kinematically admissible macroscopic displacements
$\mathscr{K}_\mu$	Set of kinematically admissible minimally constrained microscopic displacement fields

l_{macro}	Macroscopic characteristic dimension
l_{micro}	Characteristic dimension of the microstructure heterogeneities
l_{RVE}	Characteristic dimension of the RVE
$\boldsymbol{L}$	Velocity gradient
$\mathscr{L}$	Symmetry group, set of rotations, Loss function, Langevin function
$\boldsymbol{m}$	Unitary vector normal to the surface or boundary in the reference configuration
n	Number of sampling points
n_{dof}	Number of degrees of freedom
n_{elem}	Number of finite elements
n_{V}	Number of visco-elastic relaxation modes
$\boldsymbol{n}$	Unitary vector normal to the surface or boundary in the deformed configuration
N_i	Shape function associated with node i
$\mathbf{N}$	Interpolation matrix
$\sqrt{N}$	Limiting chain extensibility
$\mathscr{O}^+$	Proper orthogonal group
p	Hydrostatic pressure
p^*	Superimposed hydrostatic pressure
P	Total hydrostatic pressure
$\boldsymbol{P}$	First Piola-Kirchhoff stress tensor
q_1, q_2	Heuristic parameters
$\boldsymbol{q}$	Heat flux vector, center of rotation
$\boldsymbol{Q}$	Orthogonal second-order rotation tensor
r	Density of heat production
$\mathbf{r}$	Residual force vector
R^*	Rubber particles radii
R^*	Universal gas constant
$\boldsymbol{R}$	Rotation tensor, residual vector
$\mathscr{R}$	Real number domain
s	Specific entropy
$\boldsymbol{S}$	Second Piola-Kirchhoff stress tensor
t	Instant of time, total number of tests
$\boldsymbol{t}$	Cauchy stress vector, Surface forces; Cohesive stress vector

T	Absolute temperature
T_g	Glass transition temperature
$\boldsymbol{u}$	Displacement field
$\tilde{\boldsymbol{u}}$	Displacement fluctuation field
$\boldsymbol{U}$	Right stretch tensor
$\mathscr{U}$	n-dimension vector space associated with $\mathscr{E}$
v	Volume
v^*	Shear activation volume
$\boldsymbol{v}$	Velocity field
$\boldsymbol{V}$	Left stretch tensor
$\mathscr{V}$	Set of virtual displacements
w	Gaussian quadrature weights
W	Power
$\boldsymbol{W}$	Skew component of the velocity gradient
$\boldsymbol{x}$	Spatial macroscopic position vector, vector of material parameters
$\boldsymbol{X}$	Material macroscopic position vector, candidate solutions
$\boldsymbol{y}$	Spatial microscopic position vector
$\boldsymbol{Y}$	Material microscopic position vector
α	Contraction/dilation ratio, main transition, PPR - shape parameter
α_{p}	PPR - Contact penalty factor
$\boldsymbol{\alpha}$	Set of internal variables
Γ	Fracture surface in the deformed configuration, Energy constant of the PPR model, Surface energy of the rubber
β	PPR - shape parameter
$\boldsymbol{\beta}$	Set of microscopic internal variables
δ	Final crack opening width
δ_{ij}	Kronecker delta
$\boldsymbol{\Delta}$	Displacement jump/gap
$\delta\boldsymbol{\Delta}$	Virtual separation vector
ε	Infinitesimal strain tensor
$\dot{\varepsilon}$	Strain rate
ε_r, s_r	Mean and standard deviation for the nucleation law

ε_{tol}	Convergence tolerance
$\dot{\varepsilon}_{\text{th}}$	Threshold strain rate
$\bar{\varepsilon}^p$	Accumulated plastic strain
$\bar{\varepsilon}^p_{\text{cr}}$	Critical accumulated plastic strain
$\boldsymbol{\varepsilon}$	Deformation quantity
η	Viscosity function
$\boldsymbol{\eta}$	Virtual displacements, virtual displacement fluctuations
θ	Temperature field
$\boldsymbol{\Theta}$	Dependency matrix
λ_i	Eigenvalues of both the right and left stretch tensor, Prescribed load factor, Initial slope indicator of the PPR model
$\lambda_{g,\,j}$	Visco-elastic relaxation time sensitivity
μ	Pressure coefficient
ν	Poisson's ratio
ν_∞	Long term Poisson's ratio
$\boldsymbol{\xi}$	Natural coordinate
ρ	Material density
σ_y	Yield stress
σ_d	Deviatoric stress tensor
σ_{eff}	Effective Cauchy Stress
$\boldsymbol{\sigma}$	Second-order symmetric Cauchy stress tensor
$\boldsymbol{\tau}$	Kirchhoff stress tensor
$\boldsymbol{\tau}_{\text{D}}$	Driving component of the Kirchhoff stress tensor
$\boldsymbol{\tau}_{\text{H}}$	Hardening component of the Kirchhoff stress tensor
$\boldsymbol{\tau}_{\text{T}}$	Total Kirchhoff stress tensor
$\boldsymbol{\tau}^*$	Damaged Kirchhoff stress tensor
Υ	Natural normalised domain
$\boldsymbol{\varphi}$	Motion
ϕ	Fracture energy
$\bar{\phi}$	Energy release rate
Φ	Dashpot potential
ψ	Specific free energy, strain-energy function
$\boldsymbol{\Psi}$	Potential fracture energy
Ω	Body domain in the current configuration

$\partial\Omega$	Body domain boundary in the current configuration
Ω_0	Body domain in the reference configuration
$\partial\Omega_0$	Body domain boundary in the reference configuration
$\Omega^{(e)}$	Finite element domain

CHAPTER 1

INTRODUCTION

1.1 Motivation

The PC/ABS blends, ternary blends of polycarbonate (PC) and acrylonitrile-butadiene-styrene (ABS), are one of the most successful commercial polymer blends. These blends exhibit a wide range of compositions (e.g., amount of PC, amount of rubber in ABS) and microstructure morphologies (e.g., particulate structure, co-continuous lamellar structure), allowing them to meet diverse application requirements across industries such as automotive and consumer electronics (Lombardo et al., 1994). The key factor contributing to their success is the "synergistic effect" observed under specific compositions, where the blends demonstrate superior macroscopic behaviour and characteristics compared to their individual constituents (Chiang and Hwung, 1987; Chun et al., 1991). Notably, one of the main characteristics is the enhanced toughness in notched applications.

This improved toughness and synergistic effect are believed to originate from the various deformation and damage micromechanisms, including rubber particle cavitation, plastic void growth, crazing, and debonding at the interface between PC and ABS. However, due to the complexity of the PC/ABS ternary blend, which depends on multiple material parameters and manufacturing conditions such as ABS structure, ABS content, rubber content in ABS, strain rate, and temperature, a comprehensive understanding of the dominant deformation mechanisms and their occurrence remains elusive, even despite the extensive research carried out through the years in the polymer field (Greco, 1996, 1999; Greco et al., 1994; Chun et al., 1991; Inberg, 2001; Ishikawa, 1995; Wildes et al., 1999; Lombardo et al., 1994; Nigam et al., 2005; Tan et al., 2006). Moreover, the existing literature contains inconclusive and contradictory findings, indicating the need for further experimental work and modelling to unravel the failure behaviour of PC/ABS blends (Suarez et al., 1984; Khan et al.,

2005; Hassan and Wong, 2005).

Therefore, given these blends' highly complex and non-linear behaviour, it is easy to understand the paramount importance of developing a suitable Integrated Computational Materials Engineering (ICME) framework with a micromechanical approach to gain a deeper understanding of their local deformation and failure behaviour. Consequently, enabling the accurate and efficient design and optimisation of PC/ABS polymer blend compositions for specific use cases. A fundamental aspect in this endeavour of accurately predicting the macroscopic behaviour is the paradigm of multi-scale modelling. This entails characterising the constituents, elucidating the mechanisms at each length scale, and comprehending the interactions between these scales. Nonetheless, formulating a constitutive continuum model that accurately predicts the thermomechanical behaviour of PC/ABS blends is a challenging task that has evolved over the years.

For instance, in previous studies, constitutive models accounting for visco-plastic strains, softening-rehardening behaviour, and plastic dilatation were used to study the plastic strain patterns and toughening mechanisms in function of the microstructure and their interrelation (Seelig and van der Giessen, 2002). The influence of blend composition and morphology on the local stress distribution, plastic zone development, crack propagation, and fracture toughness evolution at a stationary crack tip were numerically analysed in Seelig and Van der Giessen (2007). In Fang et al. (2009), a one-dimensional phenomenological constitutive model was proposed to describe the rate-dependent large-strain deformation behaviour under uniaxial tension. The compression behaviour during monotonic and cyclic loading was described using a rate-dependent J_2 plasticity model by Wang et al. (2016). The responses of four different constitutive models were compared to investigate the rate/temperature-dependent deformation at various strain rates and temperatures by Wang et al. (2018). In Hund and Seelig (2019), two visco-plasticity models were compared to examine the influence of PC/ABS ratio and ABS rubber content on the mechanical response. More recently, building upon the developments in previous studies, Carvalho Alves et al. (2023) proposed a finite strain visco-elastic visco-plastic constitutive model (three-dimensional) constitutive model to forecast the non-linear behaviour of rubber-toughened amorphous polymers and extended to account for void nucleation, the interaction between voids, and the evolution of the voids' geometry. This model serves as the starting point and cornerstone for the research presented in this dissertation.

Over the decades, these efforts have contributed to the field in extensively investigating the impact of blend composition, morphology, manufacturing conditions, rubber particle cavitation, and plastic void growth on the mechanical behaviour of the blend. However, a common denominator between all these studies is the neglect of any impact of the interface between the PC and ABS constituents on the blend behaviour, i.e., perfect adherence between the two constituents is assumed. Therefore, the present dissertation aims to address this literature gap by examining the interface's influence on the mechanical behaviour of PC/ABS blends. It seeks to comprehensively understand the interface and identify the parameters that characterise its behaviour. To the best of the author's knowledge, this research fills a critical knowledge gap in the field, as no previous study has focused on the interface and its impact on the constitutive behaviour of PC/ABS blends.

The interface debonding process can be conceptualised as a fracture problem, where all potential fracture paths correspond to the interface between the constituents. Various numerical models have been developed in the literature to simulate this phenomenon, including the extended finite element method (XFEM) and cohesive zone models (CZM). These approaches can be attributed to the initial works by Needleman (1987) and Tvergaard (1990, 1991). Moreover, when all possible fracture paths are known in advance, the choice of CZM becomes natural due to its elegant implementation. Specifically, cohesive zone models allow for the explicit representation of the interface behaviour by defining cohesive laws, which govern the interface's initiation, growth, and eventual failure.

In this context, to achieve a comprehensive description of all damage mechanisms present in PC/ABS blends, only the development of a model that considers the shear-yielding mechanism, a plastic deformation mechanism, within the PC matrix remains outstanding. This can be accomplished by introducing a damage variable that quantifies the reduction in load-carrying capacity due to the presence and evolution of defects. Non-local formulations, including gradient-type and integral-type theories (De Borst and Mühlhaus, 1992; PEERLINGS et al., 1996; Peerlings et al., 2001; Jirásek and Patzák, 2002; Andrade et al., 2014, 2011), have gained significant attention in recent decades due to their ability to mitigate the loss of ellipticity in the governing equilibrium equations within a local continuum framework (Jirásek, 1998; Jirásek and Rolshoven, 2003; Bažant and Jirásek, 2002; Bažant and Pijaudier-Cabot, 1988; Bažant and Lin, 1988). However, local damage formulations are still being employed due to their simplicity and lower computational costs.

The primary focus of this dissertation is to enhance the understanding of the deformation mechanisms and their impact on the behaviour of PC/ABS blends, with the aim of enabling the development of customised materials and predicting their ideal composition for specific applications. While the primary focus is on PC/ABS blends, the numerical tools and methodologies developed in this dissertation can also be extended to other classes of materials.

1.2 Objectives

The main goal of the present dissertation can be summarised as follows:

Expand the knowledge associated with the microscopic deformation and damage mechanisms of PC/ABS blends, which govern their complex macroscopic behaviour, through the detailed numerical analysis of their challenging constitutive behaviour.

To achieve this goal, the following steps have been devised:

- Review and understand the constitutive models, namely the visco-elastic visco-plastic model and the Park-Paulino-Roesler (PPR) potential-based cohesive model, for accurately capturing the mechanical behaviour of PC/ABS blends;
- Generate 2D and 3D Representative Volume Elements (RVEs) for three PC/ABS blends in the mass fraction range known for exhibiting interesting synergistic effects (90/10, 80/20, 70/30) using the in-house AMINO program;
- Conduct mesh and RVE size sensitivity finite element analyses to determine the optimal size and mesh for both 2D and 3D RVEs of the three PC/ABS blends, excluding cohesive elements;
- Develop a Python tool to incorporate zero-thickness cohesive interface elements around each ABS particle in preexisting finite element RVEs, and ensure seamless integration between its output files and Links' input files;
- Extract reference values for the material parameters of the PPR potential-based cohesive model from the literature and identify experimental tests suitable for determining these parameters;

- Perform a comprehensive parametric study to assess the influence of each material parameter of the PPR potential-based cohesive model on the constitutive behaviour of the PC/ABS material under a given loading condition;
- Conduct a parametric study, using the reference literature values, to examine the loading conditions most affected by including cohesive elements by presenting colour maps illustrating the differences between RVE responses with and without ideal interfaces;
- Define a numerical optimisation-based calibration strategy using the in-house parameter identification program, piglot, to determine the authentic material parameters of the PPR potential-based cohesive model;
- Evaluate the models' predictive ability and the calibration procedure's validity by comparing coupled multi-scale finite element analysis against experimental results, both with and without cohesive elements;
- Formulate and implement an extension of the visco-elastic visco-plastic constitutive model to incorporate a damage variable that quantifies the accumulation of defects in the PC matrix. Linearise the system of residual equations at local and global levels to ensure asymptotic quadratic convergence rates.

1.3 Computational Framework

The numerical implementations and simulations presented in this dissertation are conducted using several in-house programs developed by the CM2S (Computational Multi-Scale Modelling of Solids and Structures) research group (Figure 1.1(a)). The main program is Links (Large Strain Implicit Non-Linear Analysis of Solids Linking Scales) (Figure 1.1(b)), which is a modern Fortran-based finite element program capable of solving single-scale (macro and micro analysis) and multi-scale coupled problems. This program started with the integration of three independent codes: HYPLAS (de Souza Neto et al., 2008), MSP, and CMSP (Reis, 2014); and is still under development. More recently, thermomechanical, dynamic and contact analysis are also enabled.



(a) CM2S. (b) `Links`. (c) Piglot.

Figure 1.1: Research group and finite element program logotypes.

The generation and discretisation of all high-fidelity periodic PC/ABS Representative Volume Elements (RVEs) utilised in this dissertation is enabled by using the AMINO (Adaptive Multi-temperature Isokinetic Method) program. Developed by the CM2S research group in the works of Vila-Chã et al. (2021); Ferreira et al. (2022), AMINO is an in-house program that incorporates a novel computational generation method for particle-reinforced materials within a time-driven molecular dynamics framework. Furthermore, the program seamlessly integrates with Links, bridging AMINO's output files with Links' input files.

The piglot (Parameter Identification via Global Optimisation) (Figure 1.1(c)), another in-house program developed by the CM2S research group, is used for the parameter calibration procedures. This toolbox offers an automated parameter identification solution for macro-, micro-, and constitutive responses through direct numerical simulation using the finite element method. The introduction and details of this program can be found in the works of Coelho (2022).

Adding to this, this dissertation presents the development of a new Python tool that enables the generation of zero-thickness two- and three-dimensional cohesive interface elements within preexisting discretised finite element RVEs. In this study, the tool is used in conjunction with the AMINO program; however, it is important to note that any other RVE generation code could have been utilised.

1.4 Document Structure

In this section, the overall structure of the dissertation is presented. The dissertation is organised into several chapters, each addressing the objectives outlined. The chapters are designed to provide a comprehensive and sequential account of the global history, where the data and conclusions from each chapter are accumulated and utilised in subsequent chapters. Towards the end of the document, the main conclusions are synthesised, and future research directions are proposed. This is followed by a section containing references and any relevant appendices to the dissertation.

It is important to note that the literature review and state-of-the-art are integrated throughout all the chapters rather than being presented extensively at the beginning of the dissertation. By adopting this approach, the relevant literature is discussed in context, enhancing the flow and coherence of the overall narrative. Furthermore, a consistent notation system is

employed throughout all chapters, whose variables and symbols' meanings are appropriately defined in the text upon their initial introduction.

Chapter 2 - Continuum Mechanics Theory and Finite Element Method

This chapter, along with Chapter 3, lays the groundwork by providing a comprehensive review of the fundamental concepts and methods essential for the subsequent dissertation chapters. This chapter focuses specifically on the fundamental concepts of continuum mechanics and the finite element method (FEM) in the context of solids undergoing finite deformations. It covers key topics such as the kinematics of the continuum body, strain and stress concepts, conservation principles, and the formulation of the initial boundary value problem. It also discusses the weak formulation, its discretisation in time and space, and its numerical integration necessary for FEM solutions.

Chapter 3 - First-order Computational Homogenisation Multi-Scale Models

This chapter provides a concise overview of the fundamental concepts of first-order hierarchical multi-scale models based on computational homogenisation, enabling a better understanding of material behaviour and deformation mechanisms at different length scales. It introduces the concept of the Representative Volume Element (RVE), explores the admissible kinematical boundary conditions applicable to it, and discusses the microscopic weak equilibrium equations and their numerical formulation.

Chapter 4 - PC/ABS Polymer Blend

This chapter provides a concise introduction to the materials within the scope of this work, namely PC/ABS polymer blends and their main constituents. Each constituent is briefly described, including their manufacturing processes, applications, and key characteristics and limitations. Special emphasis is given to the material behaviour of ABS, highlighting the concept of rubber toughening. The chapter concludes with a more detailed description of PC/ABS polymer blends, explaining the motivation behind their use and study. It further discusses the different microstructures observed in PC/ABS blends, process conditions, and subsequently delves into the description of their deformation and damage mechanisms, which are the main focus of this dissertation.

Chapter 5 - Size of the Representative Volume Element (RVE)

This chapter focuses on the essential task of determining the optimal size of RVEs that strikes a balance between computational affordability and statistical representativity of micro-scale singularities. Firstly, the generation and meshing process of high-fidelity RVEs, conforming to statistical distributions based on experimental data on PC/ABS blends with particle morphology microstructure, are described. This is followed by the formulation of a visco-elastic visco-plastic constitutive model that incorporates void nucleation, providing a comprehensive framework for accurately capturing the mechanical behaviour of the PC/ABS blend. Subsequently, 2D and 3D numerical studies are conducted on the PC/ABS blend, focusing on three distinct volume fractions of ABS (10%, 20%, and 30%), and the results obtained are thoroughly discussed. Furthermore, mesh discretisation analyses are performed, in both 2D and 3D, to determine an appropriate level of discretisation that ensures high-quality solutions and to verify the convergence of the response. This chapter serves as a crucial foundation for the subsequent chapters, as the chosen RVE sizes established here will be carried forward throughout the remainder of the dissertation. Additionally, an appendix (Appendix A) is included to justify and demonstrate the presented data and conclusions, offering supplementary results.

Chapter 6 - Cohesive Zone Model

This chapter, in conjunction with Chapter 7, establishes the necessary foundation for studying the influence of interfaces between the PC matrix and ABS particles on the constitutive behaviour of the PC/ABS blend. The focus of this chapter is to provide a brief explanation of the theory behind incorporating cohesive elements in a finite element framework, both in 2D and 3D formulations. The chapter begins by presenting both linear and quadratic versions of cohesive elements. It then provides a concise review of traction-separation laws, with particular emphasis on describing the Park-Paulino-Roesler (PPR) potential-based cohesive model, which is chosen to describe the constitutive behaviour of the cohesive elements. Furthermore, the chapter addresses the mechanisms for handling unloading/reloading scenarios, the theory of computational contact mechanics in cohesive elements, and the incorporation of an energetically based damage variable for output purposes. To supplement this chapter, two appendices are included, compiling essential information on continuum elements (Appendix B) and cohesive elements (Appendix C).

Chapter 7 - Cohesive Elements Generation in an RVE

This chapter introduces and explains the Python program developed for generating and incorporating zero-thickness cohesive interface elements into preexisting discretised finite element RVEs. It begins with a brief overview of the software used to generate the RVEs to which the cohesive elements will be added. Next, the thought process, important considerations for building this new program, and the various optimisation procedures employed are outlined. The chapter then presents several numerical applications that demonstrate the performance of the code in generating cohesive interface elements within complex and diverse RVEs. Additionally, two numerical assessments are conducted to showcase the efficiency and robustness of the program.

Chapter 8 - Numerical Analysis on the Influence of Cohesive Elements

This chapter examines the influence on the constitutive behaviour of the PC/ABS blend of incorporating cohesive elements at the interfaces between its constituents. It begins with a comprehensive literature review and state-of-the-art analysis, focusing on understanding and characterising the interfacial properties and the deduction of approximate values for the PPR cohesive model properties of the PC/ABS interface. Subsequently, a thorough parametric study is conducted to investigate the impact of these parameters on the constitutive behaviour of the PC/ABS material. This study provides insights into the sensitivity of different parameters and identifies the ones that have the most significant impact. Furthermore, an extensive parametric study is carried out to assess the loading conditions that are most affected by the inclusion of cohesive elements. The results obtained from each analysis are discussed in detail.

Chapter 9 - Cohesive Zone Model Parameters Calibration

This chapter focuses on determining the authentic parameters of the PPR cohesive zone model for the PC/ABS blend through numerical calibration techniques and analyses the material's behaviour based on experimental data. Due to the complexity and computational cost of coupled multi-scale finite element analysis, this chapter starts by providing a concise summary of the main steps and simplifications of the alternative method used. Secondly, the experimental setup, specimen geometry, and test conditions are described in detail. Thirdly, a brief review of calibration techniques for obtaining material parameters is presented, along with the calibration tool used in this study. The computational setup for all numerical analyses, including macro-scale,

micro-scale, and coupled multi-scale analysis, is outlined. Finally, the results of each analysis are presented, accompanied by a comprehensive discussion and explanation of the obtained results. It is important to emphasise that this chapter encompasses all the information gathered throughout the dissertation. To complement this chapter, two appendices are included, providing detailed information about the geometry of the specimens used in the experimental tests (Appendix D) and the technical specifications concerning the PC/ABS material used in these specimens (Appendix E).

Chapter 10 - Visco-Elastic Visco-Plastic Constitutive Model: Damage Variable

This chapter focuses on enhancing the visco-elastic visco-plastic constitutive model presented in Chapter 5 by incorporating a damage variable that quantifies the reduction in load-carrying capacity caused by defects in the PC matrix. It begins with a brief literature review of different damage models, specifically focusing on the explicit local damage model chosen for integration into the constitutive model. The chapter then describes the implementation of the visco-elastic visco-plastic constitutive model, including the computation of the state update procedure and consistent tangent operator. These implementation details are crucial for integrating the explicit local damage model. Three studies are conducted to evaluate various aspects of the explicit local damage model, including its efficiency, numerical robustness, and its impact on the constitutive behaviour of the PC/ABS blend. With the completion of this final chapter, a comprehensive numerical description of all damage mechanisms present in the PC/ABS blend is now possible. Additionally, an appendix (Appendix F) is included, providing relevant mathematical derivations to facilitate the implementation of the model.

Chapter 11 - Conclusions and Future Research

In this chapter, the main conclusions of the present dissertation are summarised, providing a comprehensive overview of the findings. Additionally, a conclusive assessment is presented, evaluating the challenges addressed and highlighting their significance in the research context. Lastly, future research perspectives are established and discussed, outlining potential avenues for further investigation.

CHAPTER 2

CONTINUUM MECHANICS THEORY AND FINITE ELEMENT METHOD

The continuum mechanics theory (CMT) assumes that matter's discrete atomic and molecular structure can be neglected by considering the body as a continuum if guaranteed that its length is sufficiently larger than its atomic structure. Continuum bodies can be subdivided into infinitesimal elements without losing the properties of the bulk material, which makes this theory particularly interesting for most engineering applications since modelling an object's behaviour becomes drastically simpler. This theory is the polar opposite of quantum physics, where molecular and atomistic theories rely on a discrete particle approach, which leads to overcomplicated theories and makes them impractical for most engineering purposes.

Generally, when applied to complex geometries, continuum mechanics theories lead to equations that are impracticable to be solved, and therefore numerical approximation schemes are often employed. The Finite Element Method (FEM) is the most used approximation technique. By applying a spatial discretisation of the matter and interpolating the relevant fields, the weak form of the problem can be solved.

The following Chapter reviews the basic concepts of continuum mechanics and the Finite Element Method (FEM) for the solution of an initial boundary value equilibrium problem. This provides the necessary groundwork for the remainder of this dissertation since both are fundamental tools to mathematically describe and, subsequently, overcome the challenges posed by material characterisation and modelling. This Chapter also serves as a guide for the definitions and nomenclatures used throughout the work.

The topics to be developed were mainly based on the approach presented

by the textbook of de Souza Neto et al. (2008). However, for a more profound and extensive explanation of the concepts and methods presented, the following literature can be consulted: (Holzapfel, 2000), (Tadmor et al., 2011), (Belytschko et al., 2014), (Bertram, 2012), (Bonet and Wood, 2008), (Bower, 2009), (Haupt, 2002), (Wriggers, 2008), (Zienkiewicz et al., 2014) and (Zienkiewicz et al., 2013).

2.1 Deformation Kinematics

The kinematics of deformation provides the tools to establish the possible deformation states of the continuum without reference/connection to their cause. The relation between deformation and the applied loads or the stress state that the body is subjected to is not yet treated. It is important to note that inertial effects are not considered in this dissertation.

2.1.1 Deformation Mapping Function

Let $\mathscr{B}$ be a deformable continuum body occupying an open region Ω_0 of the three-dimensional (3D) Euclidean space $\mathscr{E}$, with a regular boundary $\partial\Omega_0$ in its reference configuration (see Figure 2.1). The reference configuration corresponds to an undeformed state prior to loading at time instant t_0. The need to define a reference configuration comes from the fact that upon deformation, a continuum body can assume an infinite number of configurations. Therefore, a reference configuration is needed to compare all the others and gauge the deformations. In this reference configuration, let $\boldsymbol{X}$ denote the position of an arbitrary infinitesimal volume (particle) of the body in space, such that $\boldsymbol{X} \in \Omega_0$.

A smooth univocal time-dependent mapping function expresses the deformation/motion of body $\mathscr{B}$,

$$\boldsymbol{\varphi} : \Omega_0 \times \mathscr{R} \rightarrow \mathscr{E}, \tag{2.1}$$

which, for a given instant of time t, maps the initial position of every infinitesimal volume (particle) $\boldsymbol{X}$ in the reference configuration to its new position $\boldsymbol{x}$ in the deformed configuration (volume Ω with boundary $\partial\Omega$) as[1]

$$\boldsymbol{x} = \boldsymbol{\varphi}\left(\boldsymbol{X}, t\right). \tag{2.2}$$

[1] In the present report, the orthonormal basis associated with the reference configuration, $\boldsymbol{E}_i$, i=1,2,3, and with the deformed configuration, $\boldsymbol{e}_i$, i=1,2,3, are taken to be coincident, i.e., $\boldsymbol{x} = x_i \boldsymbol{E}_i = x_i \boldsymbol{e}_i$.

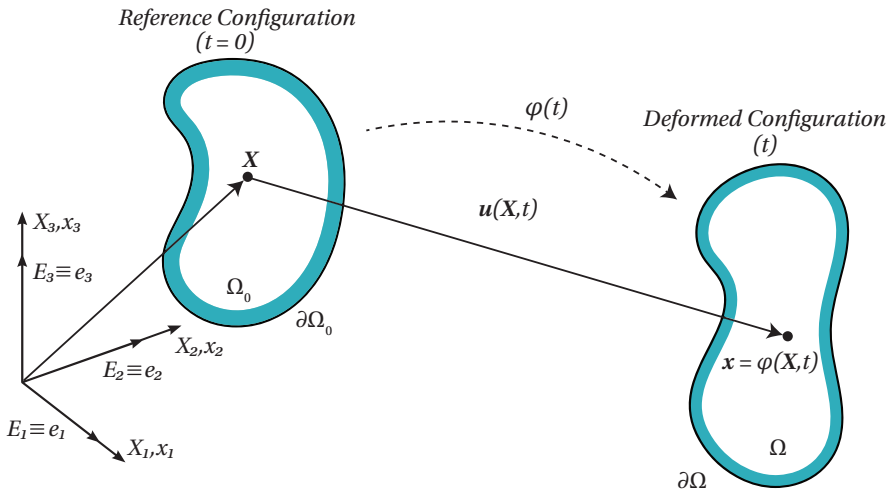


Figure 2.1: Deformation of a generic continuum body $\mathscr{B}$.

The displacement vector field is the difference between the deformed and reference configurations of the particle's position and can be defined as

$$\boldsymbol{u}\left(\boldsymbol{X},t\right)=\boldsymbol{\varphi}\left(\boldsymbol{X},t\right)-\boldsymbol{X}, \tag{2.3}$$

and the velocity field as

$$\boldsymbol{v}\left(\boldsymbol{X},t\right)=\dot{\boldsymbol{u}}\left(\boldsymbol{X},t\right)=\frac{\partial\boldsymbol{\varphi}\left(\boldsymbol{X},t\right)}{\partial t}. \tag{2.4}$$

Furthermore, since the motion is assumed to be uniquely invertible, the initial position $\boldsymbol{X}$ in the reference configuration can be directly obtained as

$$\boldsymbol{X}=\boldsymbol{\varphi}^{-1}\left(\boldsymbol{X},t\right)=\boldsymbol{x}-\boldsymbol{u}\left(\boldsymbol{\varphi}^{-1}\left(\boldsymbol{x},t\right),t\right). \tag{2.5}$$

It is important to note that motion does not necessarily imply deformation and, on the contrary, can be associated with a rigid-body motion. In the case of rigid-body displacements, the distance between the particles is preserved since the change in shape does not occur. Moreover, as schematically represented in Figure 2.2, this type of motion can further be subdivided into translation, rotation or a combination of both:

- **Rigid translation**: The displacement vector is constant in space, in other words, independent of $\boldsymbol{X}$, such that

$$\boldsymbol{x}=\boldsymbol{X}+\boldsymbol{u}\left(t\right); \tag{2.6}$$

- **Rigid rotation**: Generic rotation around a fixed point $\boldsymbol{q}$ (center of rotation - always remains in the same position) given by a second-order rotational tensor $\boldsymbol{R}(t)$, such that

$$\boldsymbol{x} = \boldsymbol{q} + \boldsymbol{R}(t)\left(\boldsymbol{X} - \boldsymbol{q}\right); \tag{2.7}$$

- **Combination of rigid translation and rotation**: Any rigid-body displacement may be interpreted as a rigid translation superimposed on a rigid rotation R about q, such that

$$\boldsymbol{x} = \boldsymbol{\varphi}\left(\boldsymbol{q}, t\right) + \boldsymbol{R}(t)\left(\boldsymbol{X} - \boldsymbol{q}\right). \tag{2.8}$$

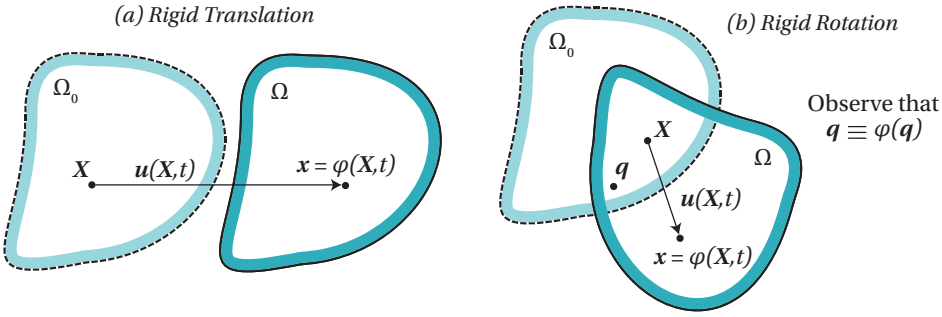


Figure 2.2: Schematic of the two types of rigid-body motion of a continuum body: a) rigid translation; b) rigid rotation.

2.1.2 Material and Spatial Descriptions

When dealing with finite deformation, the system's kinematics of body $\mathscr{B}$ under analysis can be characterised by looking from a particle at the reference configuration or a position on the deformed configuration. Therefore, two approaches can be defined to describe the properties under study:

- **Lagrangian description (material description)**: Expresses any field (scalar, vectorial or tensorial) defined over the body as a function of the reference configuration $\boldsymbol{X}$, defined over the domain Ω_0. In other words, it studies the behaviour of a fixed material point as time evolves. For example, despite being naturally associated with the deformed configuration, the material velocity field can be defined as presented by Equation 2.4;
- **Eulerian description (spatial description)**: Expresses any field (scalar, vectorial or tensorial) defined over the body as a function of the deformed

configuration $\boldsymbol{x}$, defined over the domain Ω. It is equivalent to fixing a point in space and following its evolution. Similarly, the velocity field can also be derived for the spatial description as

$$\boldsymbol{v}\left(\boldsymbol{x},t\right)=\dot{\boldsymbol{u}}\left(\boldsymbol{\varphi}^{-1}\left(\boldsymbol{x},t\right),t\right). \tag{2.9}$$

The operators push-forward, $\boldsymbol{\varphi}_{*}\left[\bullet\right]$, and pull-back, $\boldsymbol{\varphi}_{*}^{-1}\left[\bullet\right]$ (where $\boldsymbol{a}\left[\bullet\right]$ implies an operation that will be evaluated according to the operand) allow establishing a relation between quantities defined in material and spatial descriptions. These can be applied to different operators, such as the divergence and the gradient. For example, let a be a generic field defined in both material and spatial descriptions as

$$a\left(\boldsymbol{X},t\right)=a\left(\boldsymbol{\varphi}\left(\boldsymbol{X},t\right),t\right),\qquad a\left(\boldsymbol{x},t\right)=a\left(\boldsymbol{\varphi}^{-1}\left(\boldsymbol{x},t\right),t\right). \tag{2.10}$$

The material and spatial gradients, ∇_0 and ∇, respectively, are defined as

$$\nabla_0 a=\frac{\partial}{\partial\boldsymbol{X}}a\left(\boldsymbol{X},t\right),\qquad \nabla a=\frac{\partial}{\partial\boldsymbol{x}}a\left(\boldsymbol{x},t\right), \tag{2.11}$$

where the derivatives are taken concerning the reference and deformed configuration accordingly. If a is, for instance, a generic first-order tensor $\boldsymbol{a}$, the material and spatial divergences, div_0 and div, respectively, are defined as

$$\mathrm{div}_0\left[\boldsymbol{a}\right]=\mathrm{tr}\left[\nabla_0\boldsymbol{a}\right],\qquad \mathrm{div}\left[\boldsymbol{a}\right]=\mathrm{tr}\left[\nabla\boldsymbol{a}\right]. \tag{2.12}$$

2.1.3 Deformation Gradient

An essential quantity in finite deformations analyses is the deformation gradient, $\boldsymbol{F}$, which is a second-order tensor. From a physical point of view, it characterises the body's shape change from the reference to the deformed configuration. In order to capture this phenomenon, it is compulsory to consider two neighbouring material particles separated by an infinitesimal distance $d\boldsymbol{X}$. After the motion, these two particles, denoted by $\boldsymbol{X}$ and $\boldsymbol{X}+d\boldsymbol{X}$, are $\boldsymbol{x}$ and $\boldsymbol{x}+d\boldsymbol{x}$, respectively (see Figure 2.3). In other words, the deformation gradient allows us to relate the infinitesimal material distance $d\boldsymbol{X}$ and its deformed counterpart $d\boldsymbol{x}$ as

$$d\boldsymbol{x}=\boldsymbol{F}d\boldsymbol{X}. \tag{2.13}$$

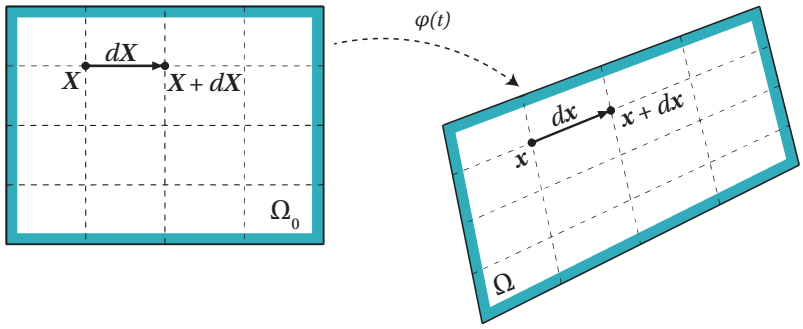


Figure 2.3: Deformation gradient: deformation of two neighbouring particles

The concept of the deformation mapping function can be used to express the deformation gradient in terms of the material gradient, and Equation 2.13 can be rewritten as

$$\boldsymbol{F}\left(\boldsymbol{X},t\right)=\nabla_0\boldsymbol{\varphi}\left(\boldsymbol{X},t\right)=\frac{\partial\boldsymbol{x}}{\partial\boldsymbol{X}}. \tag{2.14}$$

Furthermore, by substituting Equation 2.3 into Equation 2.14, it is possible to simplify the deformation gradient as a function of the displacement field

$$\boldsymbol{F}\left(\boldsymbol{X},t\right)=\boldsymbol{I}+\nabla_0\boldsymbol{u}\left(\boldsymbol{X},t\right), \tag{2.15}$$

where $\boldsymbol{I}$ denotes the second-order identity tensor.

2.1.4 Isochoric/Volumetric Decomposition

The deformation gradient can be conveniently decomposed into an isochoric, $\boldsymbol{F}_{\text{iso}}$, and a volumetric, $\boldsymbol{F}_{\text{vol}}$, component, as represented in Figure 2.4:

- **Isochoric deformation**: is a volume-preserving deformation, i.e., the continuum body volume is constant before and after deformation; it only changes shape;
- **Volumetric deformation**: consists of a uniform contraction/dilation in all directions, i.e., the continuum body shape remains constant; it only changes volume. Note that $\boldsymbol{F}_{\text{vol}}$ is a spherical tensor

  $$\boldsymbol{F}_{\text{vol}}=\alpha\boldsymbol{I}, \tag{2.16}$$

  where α represents the contraction/dilation ratio (defined as $\alpha=l/L$), l the final distance (in a particular direction) between two neighbouring

particles and L its corresponding reference quantity, so that $\boldsymbol{F}$ can be rewritten as:

$$\boldsymbol{F} = \boldsymbol{F}_{\text{iso}}\boldsymbol{F}_{\text{vol}} = \boldsymbol{F}_{\text{vol}}\boldsymbol{F}_{\text{iso}}. \tag{2.17}$$

The determinant of the deformation gradient, J, represents, locally, the volume change ratio, and is defined as

$$J = \det(\boldsymbol{F}) = \frac{\mathrm{d}v}{\mathrm{d}v_0}, \tag{2.18}$$

where $\mathrm{d}v_0$ is an infinitesimal volume of the body in its reference configuration and $\mathrm{d}v$ the infinitesimal volume after deformation.

Note that this deformation gradient, J, cannot be either null (it is physically impossible for the infinitesimal volume to collapse) or negative. By this logic, J needs to be a positive scalar. According to the definitions of isochoric and volumetric deformations, it can be concluded that

$$J = \det(\boldsymbol{F}) = \det\left(\boldsymbol{F}_{\text{iso}}\right)\det\left(\boldsymbol{F}_{\text{vol}}\right) = 1 \cdot \alpha^3, \tag{2.19}$$

and, as a result, these components can be defined as

$$\boldsymbol{F}_{\text{iso}} = \left(J\right)^{-\frac{1}{3}}\boldsymbol{F}, \qquad \boldsymbol{F}_{\text{vol}} = \left(J\right)^{\frac{1}{3}}\boldsymbol{I}. \tag{2.20}$$

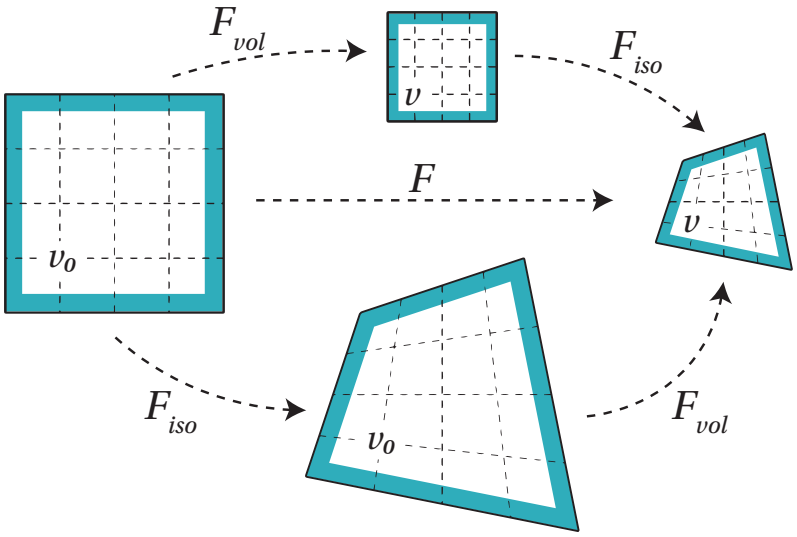


Figure 2.4: Isochoric and volumetric decompositions.

2.1.5 Polar Decomposition

In a more general approach, the deformation gradient tensor includes not only a shape-change component but also a rotation component. Whereas the shape-change component comprises length changes (stretching) and angle changes (shearing), the rotational component does not directly affect the deformation process. Therefore, it is helpful to apply the *polar decomposition theorem* to $\boldsymbol{F}$ in order to decompose it into these two different deformation modes

$$\boldsymbol{F} = \boldsymbol{R}\boldsymbol{U} = \boldsymbol{V}\boldsymbol{R}, \tag{2.21}$$

where $\boldsymbol{R}$ is the local orthogonal rotation tensor (unstrained component) and $\boldsymbol{U}$ and $\boldsymbol{V}$ are the right and left stretch tensors (strained component), respectively. Straining happens when the distance between two points in the body changes upon deformation. Therefore, in the absence of strain, i.e., unstrained state, the tensors $\boldsymbol{U}$ and $\boldsymbol{V}$ are identical to $\boldsymbol{I}$. On the other hand, if straining occurs, the stretch tensors deviate from the identity tensor.

From a physical standpoint, the right polar decomposition ($\boldsymbol{F} = \boldsymbol{R}\boldsymbol{U}$) corresponds to a stretch mapping followed by a rotation, whereas in the left polar decomposition ($\boldsymbol{F} = \boldsymbol{V}\boldsymbol{R}$), the rotation is followed by the stretch mapping (see Figure 2.5). Nonetheless, it is important to understand that the right stretch tensor is a material quantity, whereas the left stretch tensor is a spatial entity. Both $\boldsymbol{U}$and $\boldsymbol{V}$ are symmetric positive definite tensors and can be related by the rotation tensor

$$\boldsymbol{V} = \boldsymbol{R}\boldsymbol{U}\boldsymbol{R}^T. \tag{2.22}$$

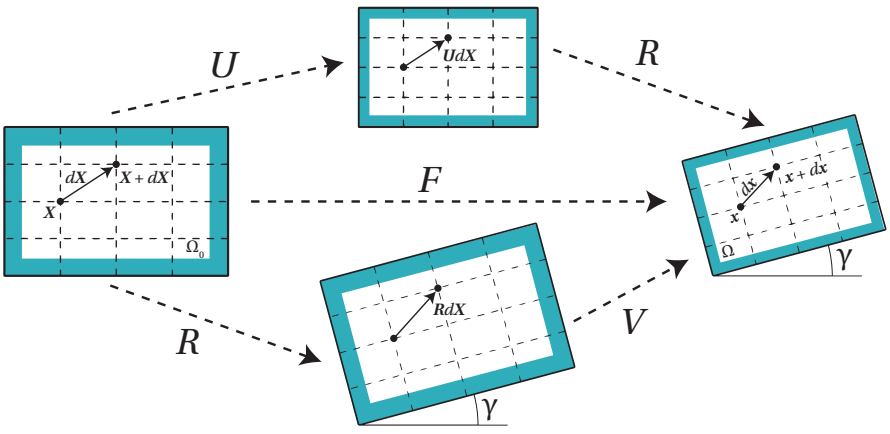


Figure 2.5: Polar decompositions of the deformation gradient.

Moreover, the right and left stretch tensors can also be defined as

$$\boldsymbol{U} = \sqrt{\boldsymbol{C}}, \qquad \boldsymbol{V} = \sqrt{\boldsymbol{B}}, \tag{2.23}$$

where $\boldsymbol{C}$ and $\boldsymbol{B}$ are the right and left Cauchy-Green strain tensors which are, in turn, defined as

$$\boldsymbol{C} = \boldsymbol{U}^2 = \boldsymbol{F}^T\boldsymbol{F}, \qquad \boldsymbol{B} = \boldsymbol{V}^2 = \boldsymbol{F}\boldsymbol{F}^T. \tag{2.24}$$

If the definition of $\boldsymbol{F}$ presented in Equation 2.15 is introduced in the former expressions, they can be rewritten as a function of the displacement gradient

$$\boldsymbol{C} = \boldsymbol{I} + \nabla_0(\boldsymbol{u}) + \left[\nabla_0(\boldsymbol{u})\right]^T + \left[\nabla_0(\boldsymbol{u})\right]^T \cdot \nabla_0(\boldsymbol{u}), \tag{2.25}$$

$$\boldsymbol{B} = \boldsymbol{I} + \nabla_0(\boldsymbol{u}) + \left[\nabla_0(\boldsymbol{u})\right]^T + \nabla_0(\boldsymbol{u}) \cdot \left[\nabla_0(\boldsymbol{u})\right]^T. \tag{2.26}$$

As seen as though $\boldsymbol{U}$ and $\boldsymbol{V}$ are symmetric tensors, they admit spectral decomposition, and may be represented as

$$\boldsymbol{U} = \sum_{i=1}^{3} \lambda_i \boldsymbol{E}_i^* \otimes \boldsymbol{E}_i^*, \qquad \boldsymbol{V} = \sum_{i=1}^{3} \lambda_i \boldsymbol{e}_i^* \otimes \boldsymbol{e}_i^*, \tag{2.27}$$

where $\lambda_i, i = 1,2,3$ denote the eigenvalues of both $\boldsymbol{U}$ and $\boldsymbol{V}$, i.e., the principal stretches, and $\boldsymbol{E}_i^*$ and $\boldsymbol{e}_i^*$ are the eigenvectors of $\boldsymbol{U}$ and $\boldsymbol{V}$, respectively. These eigenvectors also define, in the same order, the Lagrangian and Eulerian principal directions, and their triads, $\left\{\boldsymbol{E}_1^*, \boldsymbol{E}_2^*, \boldsymbol{E}_3^*\right\}$ and $\left\{\boldsymbol{e}_1^*, \boldsymbol{e}_2^*, \boldsymbol{e}_3^*\right\}$, form two orthogonal bases related through the rotational tensor

$$\boldsymbol{E}_i^* = \boldsymbol{R}\boldsymbol{e}_i^*. \tag{2.28}$$

The local stretching from a material particle can also be expressed as a superposition of stretches along the three mutually orthogonal directions. From the definitions of both right and left Cauchy-Green strain tensors, it is obtained

$$\boldsymbol{C} = \sum_{i=1}^{3} \lambda_i^2 \boldsymbol{E}_i^* \otimes \boldsymbol{E}_i^*, \qquad \boldsymbol{B} = \sum_{i=1}^{3} \lambda_i^2 \boldsymbol{e}_i^* \otimes \boldsymbol{e}_i^*. \tag{2.29}$$

2.2 Strain Tensors

In a local sense, pure rotations can be separated from pure stretches by employing the polar decomposition of the deformation gradient. However, the resulting tensors, $\boldsymbol{U}$ and $\boldsymbol{V}$, are irrational functions of the deformation gradient, and consequently, they can be challenging to obtain. Thus, the right and left

Cauchy-Green tensors, $\boldsymbol{C}$ and $\boldsymbol{B}$, are a much more attractive solution to define strain measures.

If a measure of the deformation magnitude is taken, such as

$$\begin{aligned} \|\partial \boldsymbol{x}\| - \|\partial \boldsymbol{X}\| &= \partial \boldsymbol{x} \cdot \partial \boldsymbol{x} - \partial \boldsymbol{X} \cdot \partial \boldsymbol{X} \\ &= \boldsymbol{F}\partial \boldsymbol{X} \cdot \boldsymbol{F}\partial \boldsymbol{X} - \partial \boldsymbol{X} \cdot \partial \boldsymbol{X} \\ &= \left(\boldsymbol{C} - \boldsymbol{I}\right) \partial \boldsymbol{X} \cdot \partial \boldsymbol{X} \\ &= 2\boldsymbol{E}^{(2)} \partial \boldsymbol{X} \cdot \partial \boldsymbol{X}, \end{aligned} \tag{2.30}$$

it can be concluded that a strain measure can be established regarding the difference between the Cauchy-Green strain tensor and the identity tensor, which aligns with the definition that a strain will deviate the stretch tensor from the identity tensor. $\boldsymbol{E}^{(2)}$ is the Green-Lagrange strain tensor, and is defined by

$$\boldsymbol{E}^{(2)} = \frac{1}{2}\left(\boldsymbol{C} - \boldsymbol{I}\right). \tag{2.31}$$

It is important to note that the Green-Lagrange strain tensor is a particular case of the Lagrangian strain tensors family when $m = 2$. In fact, the Lagrangian family is one of the two main families of strain tensors often employed in continuum mechanics and is defined in terms of the right stretch tensor as

$$\boldsymbol{E}^{(m)} = \begin{cases} \frac{1}{m}\left(\boldsymbol{U}^m - \boldsymbol{I}\right), & m \neq 0, \\ \ln\left[\boldsymbol{U}\right], & m = 0, \end{cases} \tag{2.32}$$

where $m \in \mathbb{R}$ and $\ln[\bullet]$ denotes the tensor logarithm of $[\bullet]$.

The other family of strain tensors is the Eulerian family, which is, in turn, defined by the left stretch tensor

$$\boldsymbol{e}^{(m)} = \begin{cases} \frac{1}{m}\left(\boldsymbol{V}^m - \boldsymbol{I}\right), & m \neq 0, \\ \ln\left[\boldsymbol{V}\right], & m = 0. \end{cases} \tag{2.33}$$

Furthermore, the Lagrangian and Eulerian strain tensors, similarly to Equation 2.22, can be related by the rotation tensor

$$\boldsymbol{e}^{(m)} = \boldsymbol{R}\boldsymbol{E}^{(m)}\boldsymbol{R}^T. \tag{2.34}$$

Another particular case besides the Green-Lagrange strain tensor for $m = 2$ is the material and spatial logarithmic strain tensors for $m = 0$

$$\boldsymbol{E}^{(0)} = \ln[\boldsymbol{U}] = \sum_{i=1}^{3} \lambda_i \boldsymbol{E}_i^* \otimes \boldsymbol{E}_i^*, \tag{2.35}$$

$$\boldsymbol{e}^{(0)} = \ln[\boldsymbol{V}] = \sum_{i=1}^{3} \lambda_i \boldsymbol{e}_i^* \otimes \boldsymbol{e}_i^*. \tag{2.36}$$

To finalise this topic, it is crucial to establish the bridge between the theory presented so far and the infinitesimal strain theory, which employs the infinitesimal strain tensor ε, one of the most used deformation measures in introductory engineering courses. The assumption of very small displacement gradients simplifies the strain tensor, since the reference and the current configurations are supposed to be coincident, and the quadratic terms of the right and left Cauchy-Green strain tensors can be ignored. As a consequence, the left and right strain tensors become formally equivalent

$$\boldsymbol{C} \approx \boldsymbol{B} \approx \boldsymbol{I} + \nabla_0(\boldsymbol{u}) + \left[\nabla_0(\boldsymbol{u})\right]^T, \tag{2.37}$$

$$\boldsymbol{U} \approx \boldsymbol{V}. \tag{2.38}$$

If the former Equation 2.37 is combined with Equations 2.32 and 2.33, definitions of the Lagrangian and Eulerian strain tensors, respectively, for any m under small strains, the following relation is obtained

$$\varepsilon \approx \boldsymbol{E}^{(m)} \approx \boldsymbol{e}^{(m)}, \tag{2.39}$$

where the infinitesimal strain tensor ε is a linear functional of $\boldsymbol{u}$

$$\varepsilon = \frac{1}{2}\left[\nabla_0(\boldsymbol{u}) + \left[\nabla_0(\boldsymbol{u})\right]^T\right]. \tag{2.40}$$

2.3 Forces and Stresses

Up until this point, all focus was on studying the tools available to describe the possible deformations a body can undergo. Hence, no reference was made to the concept of forces acting on it, which are fundamental for establishing the physical and constitutive laws. From a mechanical point of view, forces can be subdivided into two classes:

- **Volume (or body) forces**: forces exerted on the body's interior (ex., magnetic and gravitational forces);

- **Surface forces:** forces exerted on the body's boundary (ex., result from interactions with the neighbourhood) and forces transmitted across its interior (ex., arise from internal interactions between its adjacent parts).

The spotlight will be on the mathematical description of the surface forces, which are associated with the concept of stress and can be described by different stress tensors, either in the material or spatial description.

2.3.1 Cauchy Stress Tensor

Cauchy's theorem allows the establishment of a linear relation between the Cauchy stress vector, $\boldsymbol{t}\left(\boldsymbol{x},\boldsymbol{n}\right)$, and the unitary outward vector, $\boldsymbol{n}$, normal to the deformed surface.

$$\boldsymbol{t}(\boldsymbol{x},\boldsymbol{n}) = \boldsymbol{\sigma}(\boldsymbol{x})\,\boldsymbol{n}, \tag{2.41}$$

where $\boldsymbol{\sigma}(\boldsymbol{x})$ is the second-order symmetric Cauchy stress tensor. It is a symmetric tensor due to the angular momentum balance and is established in the deformed configuration of the solid (measured in force per unit of deformed area).

It is also convenient to define the following three scalar invariants for the Cauchy stress tensor

$$I_1 = \mathrm{tr}(\boldsymbol{\sigma}), \tag{2.42}$$

$$I_2 = \frac{1}{2}\left[\left(\mathrm{tr}(\boldsymbol{\sigma})\right)^2 - \mathrm{tr}\left(\boldsymbol{\sigma}^2\right)\right], \tag{2.43}$$

$$I_3 = \det(\boldsymbol{\sigma}). \tag{2.44}$$

2.3.2 Piola-Kirchhoff Stress Tensors

The First Piola-Kirchhoff stress tensor, $\boldsymbol{P}$, is the material counterpart of the Cauchy stress tensor and, likewise, establishes a linear dependence between the stress vector, $\boldsymbol{t}_0\left(\boldsymbol{X},\boldsymbol{m}\right)$, and the unitary outward vector, $\boldsymbol{m}$, normal to the undeformed surface

$$\boldsymbol{t}_0\left(\boldsymbol{X},\boldsymbol{m}\right) = \boldsymbol{P}(\boldsymbol{X})\,\boldsymbol{m}. \tag{2.45}$$

The stress vector $\boldsymbol{t}_0$ is measured in force per unit of undeformed area and can be related to $\boldsymbol{t}$ by the relation between the infinitesimal areas of the spatial, da, and material, da_0, configurations

$$\boldsymbol{t}_0 = \frac{da}{da_0}\boldsymbol{t}. \tag{2.46}$$

Additionally, unlike the Cauchy stress tensor, the First Piola-Kirchhoff stress tensor is generally nonsymmetric and can be related to the former by

$$\boldsymbol{P} = J\boldsymbol{\sigma}\boldsymbol{F}^{-T}. \tag{2.47}$$

In contrast to the first Piola-Kirchhoff stress tensor, the second Piola-Kirchhoff stress tensor, $\boldsymbol{S}$, is symmetric

$$\boldsymbol{S} = J\boldsymbol{F}^{-1}\boldsymbol{\sigma}\boldsymbol{F}^{-T}. \tag{2.48}$$

2.3.3 Kirchhoff Stress Tensor

Even though the first Piola-Kirchhoff is generally nonsymmetric, it can be rewritten in terms of a symmetric tensor, the Kirchhoff stress tensor, $\boldsymbol{\tau}$,

$$\boldsymbol{P} = \boldsymbol{\tau}\boldsymbol{F}^{-T}. \tag{2.49}$$

Note that the Kirchhoff stress tensor symmetry results from the fact that the Cauchy stress tensor is symmetric

$$\boldsymbol{\tau} = J\boldsymbol{\sigma}. \tag{2.50}$$

2.3.4 Deviatoric/Hydrostatic Decomposition

In some applications for the purpose of constitutive modeling (such as metal plasticity), it is more convenient to split the Cauchy stress tensor in terms of a deviatoric component $\boldsymbol{\sigma}_d$ (volume-preserving component) and a spherical/volumetric $p\boldsymbol{I}$ component

$$\boldsymbol{\sigma} = \boldsymbol{\sigma}_d - p\boldsymbol{I}, \tag{2.51}$$

where p denotes the hydrostatic pressure/stress

$$p = -\frac{1}{3}\mathrm{tr}\,(\boldsymbol{\sigma})\,. \tag{2.52}$$

Being $\boldsymbol{A}$ a generic second-order tensor and given that

$$\mathrm{tr}\,[\boldsymbol{A}] = \boldsymbol{A} : \boldsymbol{I}, \tag{2.53}$$

the hydrostatic stress tensor can also be obtained as

$$p\boldsymbol{I} = -\frac{1}{3}\left(\boldsymbol{I} \otimes \boldsymbol{I}\right) : \boldsymbol{\sigma}, \tag{2.54}$$

and the traceless symmetric deviatoric stress tensor as

$$\boldsymbol{\sigma}_d = \boldsymbol{\sigma} + p\boldsymbol{I} = \boldsymbol{I}_d : \boldsymbol{\sigma}, \tag{2.55}$$

where

$$\boldsymbol{I}_d = \boldsymbol{I} - \frac{1}{3}\left(\boldsymbol{I} \otimes \boldsymbol{I}\right). \tag{2.56}$$

2.4 Fundamental Laws of Thermodynamics

In this dissertation, the analyses developed are restrained to purely mechanical problems, i.e., neglecting the thermal effects. However, despite this, in continuum mechanics, the fundamental laws of thermodynamics and mass and momentum conservation principles have always to be satisfied. Throughout this section, only a brief introduction to these principles is provided.

2.4.1 Principle of Mass Conservation

This principle states that during motion, mass is a conserved quantity, it cannot be produced or destroyed. Mathematically, this corresponds to

$$\dot{\rho} + \rho\ \mathrm{div}\left[\dot{\boldsymbol{u}}\left(\boldsymbol{x}\right)\right] = 0, \tag{2.57}$$

where ρ is the material density measured in mass per unit of deformed volume.

2.4.2 Principle of Linear Momentum Conservation

Considering the deformed configuration, spatial description, the conservation of linear momentum can be expressed, with boundary conditions established by Cauchy's theorem, by

$$\begin{cases} \operatorname{div}\left[\boldsymbol{\sigma}\left(\boldsymbol{x}\right)\right] + \boldsymbol{b} = \rho\ddot{\boldsymbol{u}}\left(\boldsymbol{x}\right), & \forall \boldsymbol{x} \in \Omega, \\ \boldsymbol{t}\left(\boldsymbol{x}, \boldsymbol{n}\right) = \boldsymbol{\sigma}\left(\boldsymbol{x}\right)\boldsymbol{n}, & \forall \boldsymbol{x} \in \partial\Omega, \end{cases} \tag{2.58}$$

where $\boldsymbol{b}$ is the body forces field expressed per unit of deformed volume. The first equality of Equation 2.58 is also known as Cauchy's equation of motion. Equivalently, a material description can also be used

$$\begin{cases} \operatorname{div}_0\left[\boldsymbol{P}\left(\boldsymbol{x}\right)\right] + \boldsymbol{b}_0 = \rho_0\ddot{\boldsymbol{u}}\left(\boldsymbol{X}\right), & \forall \boldsymbol{X} \in \Omega, \\ \boldsymbol{t}_0\left(\boldsymbol{X}, \boldsymbol{m}\right) = \boldsymbol{P}\left(\boldsymbol{X}\right)\boldsymbol{m}, & \forall \boldsymbol{X} \in \partial\Omega, \end{cases} \tag{2.59}$$

where $\boldsymbol{b}_0$ is the body forces field expressed per unit of undeformed volume

$$\boldsymbol{b}_0 = J\boldsymbol{b}, \tag{2.60}$$

and ρ_0 is the material density measured in mass per unit of undeformed volume

$$\rho_0 = J\rho. \tag{2.61}$$

Equations 2.58 and 2.59 define, respectively, the spatial and material strong forms of equilibrium, or local or pointwise equilibrium equations, since they have to satisfy equilibrium at every material particle of the continuum body. Furthermore, these equations establish a connection between the forces and stresses with the displacements of the body.

2.4.3 First Law of Thermodynamics

The first law of thermodynamics expresses energy conservation in the continuum and postulates, in detail, that "the rate of internal energy equals the sum of the stress power and heat production subtracted to the spatial divergence of the heat flux" expressed per unit of deformed volume. Mathematically, this corresponds to

$$\rho\dot{e} = \boldsymbol{\sigma} : \boldsymbol{D} + \rho r - \operatorname{div}\left[\boldsymbol{q}\right], \tag{2.62}$$

where $\dot{e}$ is the specific internal energy, r is the density of heat production, $\boldsymbol{q}$ is the heat flux vector and the double contraction $\boldsymbol{\sigma} : \boldsymbol{D}$ is the stress power per unit of deformed volume.

2.4.4 Second Law of Thermodynamics

The second law of thermodynamics expresses the directionality of thermodynamic processes or, in other words, the irreversibility of entropy production. Numerically, this corresponds to an inequality

$$\rho \dot{s} + \operatorname{div}\left[\frac{\boldsymbol{q}}{\theta}\right] - \frac{\rho r}{\theta} \geq 0, \tag{2.63}$$

where θ the temperature field and s is the specific entropy.

2.4.5 Clausius-Duhem Inequality

The Clausius-Duhem inequality results from the combination of the first (Equation 2.62) and second (Equation 2.63) laws of thermodynamics

$$\rho \dot{s} + \operatorname{div}\left[\frac{\boldsymbol{q}}{\theta}\right] - \frac{1}{\theta}\left(\rho \dot{e} - \boldsymbol{\sigma} : \boldsymbol{D} + \operatorname{div}\left[\boldsymbol{q}\right]\right) \geq 0. \tag{2.64}$$

Alternatively, it can also be expressed as

$$\boldsymbol{\sigma} : \boldsymbol{D} - \rho\left(\dot{\psi} + s\dot{\theta}\right) - \frac{1}{\theta}\boldsymbol{q} \cdot \boldsymbol{g} \geq 0, \tag{2.65}$$

where ψ and $\boldsymbol{g}$ are, respectively, the specific free energy and the temperature gradient

$$\psi = e - \theta s, \tag{2.66}$$

$$\boldsymbol{g} = \nabla\theta, \tag{2.67}$$

and where it was used the identity

$$\operatorname{div}\left[\frac{\boldsymbol{q}}{\theta}\right] = \frac{1}{\theta}\operatorname{div}\left[\boldsymbol{q}\right] - \frac{1}{\theta^2}\boldsymbol{q} \cdot \nabla\theta. \tag{2.68}$$

From a physical standpoint, the left-hand side of Equation 2.65 represents the energy dissipation per unit of deformed volume. Alternatively, Clausius-Duhem inequality in terms of the material configuration, i.e., dissipation per unit of reference volume, is

$$\boldsymbol{\tau} : \boldsymbol{D} - \rho_0\left(\dot{\psi} + s\dot{\theta}\right) - \frac{J}{\theta}\boldsymbol{q} \cdot \boldsymbol{g} \geq 0. \tag{2.69}$$

2.5 Constitutive Theory

The balance principles introduced in the previous Section are valid for any continuum body, regardless of its material. However, two bodies subjected to the same set of forces may deform differently if their materials differ. Therefore, since the material of the body plays a crucial role in its response, there is a need to define constitutive models which allow distinguishing between the various types of materials.

A constitutive model is a set of equations establishing the relationship between strains and stresses for a particular material. As a starting point, it is essential to provide the definitions of the thermokinetic process of a body $\mathscr{B}$, which is a pair of fields

$$\left\{\boldsymbol{\varphi}\left(\boldsymbol{X},t\right),\theta\left(\boldsymbol{X},t\right)\right\}, \tag{2.70}$$

and of the calorodynamic process of body $\mathscr{B}$, which is the following set of fields

$$\left\{\boldsymbol{\sigma}\left(\boldsymbol{X},t\right),e\left(\boldsymbol{X},t\right),s\left(\boldsymbol{X},t\right),r\left(\boldsymbol{X},t\right),\boldsymbol{b}\left(\boldsymbol{X},t\right),\boldsymbol{q}\left(\boldsymbol{X},t\right)\right\}, \tag{2.71}$$

satisfying the principle of linear momentum conservation and the first and second laws of thermodynamics.

2.5.1 Constitutive Axioms

Independently of the material of the body, any constitutive model must verify three fundamental axioms:

- **Thermodynamic determinism**: Postulates that "the history of the thermokinetic process to which a neighbourhood of a point $\boldsymbol{X}$ of $\mathscr{B}$ has been subjected determines a calorodynamic process for $\mathscr{B}$ at $\boldsymbol{X}$". A particularly interesting case is the case of a simple material for which the local history of $\boldsymbol{F}$, θ and $\boldsymbol{g}$ dictates the history of the thermokinetic process. Thus, concluding that this principle predicts the existence of constitutive functionals $\mathfrak{F}$, $\mathfrak{G}$, $\mathfrak{H}$ and $\mathfrak{J}$ dependent on these histories, such that, for a material point $\boldsymbol{X}$, the calorodynamic process is defined as

$$\boldsymbol{\sigma}(t) = \mathfrak{F}\left(\boldsymbol{F}^t, \theta^t, \boldsymbol{g}^t\right), \tag{2.72}$$

$$\psi(t) = \mathfrak{G}\left(\boldsymbol{F}^t, \theta^t, \boldsymbol{g}^t\right), \tag{2.73}$$

$$s(t) = \mathfrak{H}\left(\boldsymbol{F}^t, \theta^t, \boldsymbol{g}^t\right), \tag{2.74}$$

$$\boldsymbol{q}(t) = \mathfrak{J}\left(\boldsymbol{F}^t, \theta^t, \boldsymbol{g}^t\right), \tag{2.75}$$

where the thermokinetic process satisfies the Clausius-Duhem inequality and $(\bullet)^t$ denotes the history of $(\bullet)$ at $\boldsymbol{X}$ up to instant t. It is important to note that just four of the six fields that compose a calorodynamic process are specified, as it is considered that the body forces $\boldsymbol{b}$ and the heat supply r are known external interactions of the body with its neighbourhood. In fact, $\boldsymbol{b}$ are determined by the momentum equilibrium, and the first law of thermodynamics determines r. Lastly, a constitutive functional was allocated for the specific free energy ψ instead of the specific energy e;

- **Material objectivity**: Postulates that the material response is independent of the observer. A motion $\boldsymbol{\varphi}^*$ is related to motion $\boldsymbol{\varphi}$ by a change in the observer if the following relation is satisfied

$$\boldsymbol{\varphi}^*\left(\boldsymbol{X}, t\right) = \boldsymbol{y}(t) + \boldsymbol{Q}(t)\left[\boldsymbol{\varphi}\left(\boldsymbol{X}, t\right) - \boldsymbol{X}_0\right], \tag{2.76}$$

where $\boldsymbol{y}(t)$ is an arbitrary spatial point, $\boldsymbol{Q}(t)$ is an orthogonal second-order tensor representing a rotation and $\boldsymbol{\varphi}\left(\boldsymbol{X}, t\right) - \boldsymbol{X}_0$ is the position vector of $\boldsymbol{\varphi}\left(\boldsymbol{X}, t\right)$ relative to an arbitrary origin $\boldsymbol{X}_0$. Note that, motion $\boldsymbol{\varphi}^*$ defines a rigid relative motion between the two observers. Accordingly, this principle requires the constitutive functionals previously defined (Equations 2.72 to 2.75) to verify

$$\boldsymbol{\sigma}^*(t) = \mathfrak{F}\left(\boldsymbol{F}^{t*}, \theta^t, \boldsymbol{g}^{t*}\right), \tag{2.77}$$

$$\psi(t) = \mathfrak{G}\left(\boldsymbol{F}^{t*}, \theta^t, \boldsymbol{g}^{t*}\right), \tag{2.78}$$

$$s(t) = \mathfrak{H}\left(\boldsymbol{F}^{t*}, \theta^t, \boldsymbol{g}^{t*}\right), \tag{2.79}$$

$$\boldsymbol{q}^*(t) = \mathfrak{J}\left(\boldsymbol{F}^{t*}, \theta^t, \boldsymbol{g}^{t*}\right). \tag{2.80}$$

Observe that the generic vectorial $\boldsymbol{a}$ and generic tensorial $\boldsymbol{A}$ fields corresponding to motion $\boldsymbol{\varphi}^*$ are given, respectively, by

$$\boldsymbol{a}^* = \boldsymbol{Q}\boldsymbol{a}, \tag{2.81}$$

$$\boldsymbol{A}^* = \boldsymbol{Q}\boldsymbol{a}\boldsymbol{Q}^T. \tag{2.82}$$

In contrast, the scalar fields are independent of the observer, i.e., for a generic scalar a

$$a^* = a; \tag{2.83}$$

- **Material Symmetry**: Postulates that the symmetries of the constitutive functionals need to be consistent with the symmetries of the material. The symmetry group of a solid material is the set of rotations of the reference configuration for which the response functionals of the constitutive model remain unchanged. This leads to the following relations

$$\mathfrak{F}\left(\boldsymbol{F}^t, \theta^t, \boldsymbol{g}^t\right) = \mathfrak{F}\left(\left[\boldsymbol{F}\boldsymbol{Q}\right]^t, \theta^t, \boldsymbol{g}^t\right), \tag{2.84}$$

$$\mathfrak{G}\left(\boldsymbol{F}^t, \theta^t, \boldsymbol{g}^t\right) = \mathfrak{G}\left(\left[\boldsymbol{F}\boldsymbol{Q}\right]^t, \theta^t, \boldsymbol{g}^t\right), \tag{2.85}$$

$$\mathfrak{H}\left(\boldsymbol{F}^t, \theta^t, \boldsymbol{g}^t\right) = \mathfrak{H}\left(\left[\boldsymbol{F}\boldsymbol{Q}\right]^t, \theta^t, \boldsymbol{g}^t\right), \tag{2.86}$$

$$\mathfrak{J}\left(\boldsymbol{F}^t, \theta^t, \boldsymbol{g}^t\right) = \mathfrak{J}\left(\left[\boldsymbol{F}\boldsymbol{Q}\right]^t, \theta^t, \boldsymbol{g}^t\right), \tag{2.87}$$

which must be verified for any time-independent rotation tensor $\boldsymbol{Q}$ belonging to the material symmetry group. The symmetry group, $\mathscr{L}$ of a material body $\mathscr{B}$, is a set of rotations such that $\boldsymbol{R} \in \mathscr{L}$ and is a subset of the proper orthogonal group $\mathscr{O}^+$. This is particularly interesting for the case of isotropic solids, where the symmetry group coincides with the proper orthogonal group leading to the well-known behaviour that the response of isotropic materials remains the same in all directions.

2.5.2 Thermodynamics with Internal Variables

The constitutive equations previously presented (Equations 2.72 to 2.75) show the dependence of the constitutive functionals upon the histories of $\boldsymbol{F}$, θ and $\boldsymbol{g}$. However, due to their general character, they bear limited practical utility in modelling real materials undergoing real thermodynamical processes. Therefore, it is imperative to adopt a far more compelling description, which will be based on thermodynamics with internal variables.

In essence, this description postulates that the thermodynamic state of

a given material particle ($\boldsymbol{\sigma}$, ψ, s and $\boldsymbol{q}$), defined at a given instant of the calorodynamic process, is assumed to be entirely defined by the instantaneous values of a finite number of state variables

$$\left\{\boldsymbol{F},\theta,\boldsymbol{g},\boldsymbol{\alpha}\right\}, \tag{2.88}$$

and, consequently, past histories do not need to be recorded. Therefore, becoming clear that the accuracy of the constitutive model will highly depend on the appropriate choice of the set of internal variables since these need to contain all the essential information about the material's thermodynamical history. In the above set of state variables, $\boldsymbol{\alpha}$ represents a set of scalar and tensorial internal variables associated with dissipative mechanisms.

Following this hypothesis, the specific free energy can be expressed in terms of the state variables proposed. However, in order to verify the second law of thermodynamics, it cannot be a function of $\boldsymbol{g}$, and the principle of thermodynamic determinism becomes

$$\boldsymbol{\sigma}(t) = \boldsymbol{\sigma}\left(\boldsymbol{F},\theta,\boldsymbol{g},\boldsymbol{\alpha}\right), \tag{2.89}$$

$$\psi(t) = \psi\left(\boldsymbol{F},\theta,\boldsymbol{\alpha}\right), \tag{2.90}$$

$$s(t) = s\left(\boldsymbol{F},\theta,\boldsymbol{g},\boldsymbol{\alpha}\right), \tag{2.91}$$

$$\boldsymbol{q}(t) = \boldsymbol{q}\left(\boldsymbol{F},\theta,\boldsymbol{g},\boldsymbol{\alpha}\right). \tag{2.92}$$

By applying the derivation chain rule, the derivative to time of ψ is

$$\dot{\psi} = \frac{\partial\psi}{\partial t} = \frac{\partial\psi}{\partial\boldsymbol{F}} : \dot{\boldsymbol{F}} + \frac{\partial\psi}{\partial\theta}\dot{\theta} + \sum_k \frac{\partial\psi}{\partial\alpha_k} * \dot{\alpha}_k, \tag{2.93}$$

where $*$ denotes the appropriate product operation depending on the nature of $\dot{\alpha}_k$ (scalar, vectorial or tensorial).

Replacing the above equation (Equation 2.93), and adopting the velocity gradient to set the work conjugacy as

$$\boldsymbol{\sigma} : \boldsymbol{D} = \boldsymbol{\sigma} : \boldsymbol{L} = \boldsymbol{\sigma} : \dot{\boldsymbol{F}}\boldsymbol{F}^{-1} = \boldsymbol{\sigma}\boldsymbol{F}^{-T} : \boldsymbol{F}, \tag{2.94}$$

the Clausius-Duhem inequality can be reduced in terms of power per unit of deformed volume to

$$\left(\boldsymbol{\sigma}\boldsymbol{F}^{-T} - \rho\frac{\partial\psi}{\partial\boldsymbol{F}}\right) : \dot{\boldsymbol{F}} - \rho\left(s + \frac{\partial\psi}{\partial\theta}\right)\dot{\theta} - \rho\sum_k \frac{\partial\psi}{\partial\alpha_k} * \dot{\alpha}_k - \frac{1}{\theta}\boldsymbol{q}\cdot\boldsymbol{g} \geq 0. \tag{2.95}$$

Equivalently, the Clasius-Duhem inequality can also be written in terms of power per unit reference/undeformed volume as

$$\left(\boldsymbol{P}-\rho_0\frac{\partial\psi}{\partial\boldsymbol{F}}\right):\dot{\boldsymbol{F}}-\rho_0\left(s+\frac{\partial\psi}{\partial\theta}\right)\dot{\theta}-\rho_0\sum_k\frac{\partial\psi}{\partial\alpha_k}*\dot{\alpha}_k-\frac{J}{\theta}\boldsymbol{q}\cdot\boldsymbol{g}\geq 0. \tag{2.96}$$

The axiom of thermodynamic determinism imposes that the Clausius-Duhem inequality must hold for any thermokinetic process in both the material and spatial descriptions. In particular, for a process where the temperature is uniform throughout the body ($\boldsymbol{g}=0$), there are no dissipative mechanisms ($\boldsymbol{\alpha}=0$) and the deformation gradient is constant in time ($\dot{\boldsymbol{F}}=0$), the Clausius-Duhem inequality is reduced to

$$\rho\left(s+\frac{\partial\psi}{\partial\theta}\right)\dot{\theta}\geq 0. \tag{2.97}$$

As seen as though $\dot{\theta}$ is arbitrary, the only way of satisfying this inequality for any process is if

$$s=-\frac{\partial\psi}{\partial\theta}. \tag{2.98}$$

This equation is known as the entropy constitutive relation. Similarly, by repeating the same procedure for the material Clausius-Duhem inequality, but now for the case of a uniform temperature across the body, the following expression for the first Piola-Kirchhoff is obtained

$$\boldsymbol{P}=\rho_0\frac{\partial\psi}{\partial\boldsymbol{F}}. \tag{2.99}$$

This equation is known as the stress constitutive equation, and can also be represented, alternatively, in terms of the Cauchy stress tensor

$$\boldsymbol{\sigma}=\rho\frac{\partial\psi}{\partial\boldsymbol{F}}\boldsymbol{F}^T. \tag{2.100}$$

Furthermore, suppose the set of thermodynamical forces $\boldsymbol{A}$ is defined as

$$\boldsymbol{A}=\{A_k\},\qquad A_k=\rho_0\frac{\partial\psi}{\partial\alpha_k},\quad \text{with } \alpha_k\in\boldsymbol{\alpha}, \tag{2.101}$$

and it is replaced in conjunction with the expressions of $\boldsymbol{P}$ (Equation 2.99) and s (Equation 2.98) into the material Clausius-Duhem inequality. In that case, a

more compact form is obtained

$$\boldsymbol{A} * \dot{\boldsymbol{\alpha}} - \frac{J}{\theta}\boldsymbol{q}\cdot\boldsymbol{g} \geq 0. \tag{2.102}$$

Nevertheless, constitutive equations for the internal variables and the thermal term must be formulated to fully characterise the constitutive model

$$\dot{\boldsymbol{\alpha}} = f\left(\boldsymbol{F},\theta,\boldsymbol{g},\boldsymbol{\alpha}\right), \tag{2.103}$$

$$\frac{1}{\theta}\boldsymbol{q} = g\left(\boldsymbol{F},\theta,\boldsymbol{g},\boldsymbol{\alpha}\right). \tag{2.104}$$

The choice of these constitutive functions is very restrictive since the Clausius-Duhem inequality must be satisfied for any process. An efficient and mathematically convenient way of ensuring its satisfaction consists in defining a non-negative scalar-valued function, termed as dissipation potential

$$\Xi = \Xi\left(\boldsymbol{A},\boldsymbol{g};\boldsymbol{F},\theta,\boldsymbol{\alpha}\right). \tag{2.105}$$

The state variables $\boldsymbol{F}$, θ and α appear as parameters and the potential Ξ is assumed to be non-negative, convex concerning each A_k and $\boldsymbol{g}$, and null at the origin ($\{\boldsymbol{A},\boldsymbol{g}\} = \{0,0\}$). In addition, by introducing the hypothesis of normal dissipation, the flux variables can be determined by

$$\dot{\alpha}_k = -\frac{\partial\Xi}{\partial A_k}, \tag{2.106}$$

$$\frac{1}{\theta}\boldsymbol{q} = -\frac{\partial\Xi}{\partial\boldsymbol{g}}. \tag{2.107}$$

2.5.3 Mechanical Constitutive Initial Value Problem

In purely mechanical problems, all thermal effects are neglected. Consequently, the corresponding constitutive model based on internal variables simplifies to

$$\boldsymbol{P} = \rho_0\frac{\partial\Psi}{\partial\boldsymbol{F}}, \tag{2.108}$$

$$\Psi = \Psi\left(\boldsymbol{F},\boldsymbol{\alpha}\right), \tag{2.109}$$

$$\dot{\boldsymbol{\alpha}} = f\left(\boldsymbol{F},\boldsymbol{\alpha}\right). \tag{2.110}$$

Hence, the generic constitutive problem reduces to the fundamental mechanical constitutive initial value problem in the spatial description

Problem 2.1 | Spatial mechanical constitutive initial value problem.

Given the initial values of the internal variables, $\boldsymbol{\alpha}\left(t_0\right)$, and the history of the deformation gradient

$$\boldsymbol{F}(t), \quad t \in \left[t_0, t_f\right], \tag{2.111}$$

find the functions for $\boldsymbol{\sigma}(t)$ and $\boldsymbol{\alpha}(t)$ such that the constitutive equations

$$\boldsymbol{\sigma} = \rho \frac{\partial \Psi}{\partial \boldsymbol{F}} \boldsymbol{F}^T, \tag{2.112}$$

$$\Psi = \Psi\left(\boldsymbol{F}, \boldsymbol{\alpha}\right), \tag{2.113}$$

$$\dot{\boldsymbol{\alpha}} = f\left(\boldsymbol{F}, \boldsymbol{\alpha}\right), \tag{2.114}$$

are satisfied for every $t \in \left[t_0, t_f\right]$.

or, alternatively, in the material description

Problem 2.2 | Material mechanical constitutive initial value problem.

Given the initial values of the internal variables, $\boldsymbol{\alpha}\left(t_0\right)$, and the history of the deformation gradient

$$\boldsymbol{F}(t), \quad t \in \left[t_0, t_f\right], \tag{2.115}$$

find the functions for $\boldsymbol{P}(t)$ and $\boldsymbol{\alpha}(t)$ such that the constitutive equations

$$\boldsymbol{P} = \rho_0 \frac{\partial \Psi}{\partial \boldsymbol{F}} \boldsymbol{F}^T, \tag{2.116}$$

$$\Psi = \Psi\left(\boldsymbol{F}, \boldsymbol{\alpha}\right), \tag{2.117}$$

$$\dot{\boldsymbol{\alpha}} = f\left(\boldsymbol{F}, \boldsymbol{\alpha}\right), \tag{2.118}$$

are satisfied for every $t \in \left[t_0, t_f\right]$.

To summarise the exposition of the topic, moving forward, the equations will be presented mainly in the spatial description. However, as demonstrated, they may also be expressed equivalently in the material description.

2.6 Weak Equilibrium Equations

Section 2.4 presented the strong (point-wise, local or differential) forms of the equilibrium equations, Equations 2.58 and 2.59, respectively, in the spatial and material descriptions. However, obtaining the exact solution to these equations is exceptionally challenging or even practically impossible for real engineering problems. Therefore, the majority of the numerical methods employ variational principles to obtain an approximate solution to the corresponding weak equilibrium equations.

The weak or global form results from a relaxation of the strong form, where the equilibrium equations are no longer satisfied punctually but instead are satisfied in an average sense by doing an integration over the body volume. In this work, the Virtual Work Principle will be used to derive a spatial, a material and a quasi-static formulation of the weak equilibrium equations.

2.6.1 Spatial Formulation

The principle of virtual work, in a spatial description, states that a body $\mathscr{B}$ is in equilibrium if, and only if, the Cauchy stress tensor, $\boldsymbol{\sigma}$, satisfies

$$\int_{\Omega} \left[\boldsymbol{\sigma} : \nabla \boldsymbol{\eta} - \left(\boldsymbol{b} - \rho \ddot{\boldsymbol{u}} \right) \cdot \boldsymbol{\eta} \right] d\upsilon - \int_{\partial\Omega} \boldsymbol{t} \cdot \boldsymbol{\eta} \, da = 0, \quad \forall \boldsymbol{\eta} \in \mathscr{V}, \tag{2.119}$$

where $\boldsymbol{\eta}$ is the virtual displacement vector and $\mathscr{V}$ is the space of virtual displacements of the body, defined by the space of sufficiently regular arbitrary displacements

$$\boldsymbol{\eta} : \Omega \rightarrow \mathscr{U}, \tag{2.120}$$

with $\mathscr{U}$ being the n-dimension vector space associated with $\mathscr{E}$. Note that, if the stress field is sufficiently smooth, the virtual work equation is equivalent to the strong equilibrium equation.

2.6.2 Material Formulation

Alternatively, for the material description, the Virtual Work Principle states that a body $\mathscr{B}$ is in equilibrium if, and only if, the First Piola-Kirchhoff stress tensor, $\boldsymbol{P}$, satisfies

$$\int_{\Omega_0} \left[\boldsymbol{P} : \nabla_0 \boldsymbol{\eta} - \left(\boldsymbol{b}_0 - \rho_0 \ddot{\boldsymbol{u}} \right) \cdot \boldsymbol{\eta} \right] d\upsilon - \int_{\partial\Omega_0} \boldsymbol{t}_0 \cdot \boldsymbol{\eta} \, da = 0, \quad \forall \boldsymbol{\eta} \in \mathscr{V}. \tag{2.121}$$

In this case, $\mathscr{V}$ is defined by

$$\boldsymbol{\eta} : \Omega_0 \rightarrow \mathscr{U}. \tag{2.122}$$

2.6.3 Quasi-Static Formulation

As previously stated, the inertial effects are not considered, leading to the quasi-static formulation of the weak form. With this simplification, Equations 2.119 and 2.121 are reduced to

$$\int_{\Omega} \left[\boldsymbol{\sigma} : \nabla \boldsymbol{\eta} - \boldsymbol{b} \cdot \boldsymbol{\eta} \right] dv - \int_{\partial\Omega} \boldsymbol{t} \cdot \boldsymbol{\eta} da = 0, \quad \forall \boldsymbol{\eta} \in \mathscr{V}, \tag{2.123}$$

and,

$$\int_{\Omega_0} \left[\boldsymbol{P} : \nabla_0 \boldsymbol{\eta} - \boldsymbol{b}_0 \cdot \boldsymbol{\eta} \right] dv - \int_{\partial\Omega_0} \boldsymbol{t}_0 \cdot \boldsymbol{\eta} da = 0, \quad \forall \boldsymbol{\eta} \in \mathscr{V}, \tag{2.124}$$

respectively. In both cases, it can be seen that the terms involving time derivatives were neglected.

2.7 Quasi-Static Initial Value Problem

After developing all the necessary definitions and formulations, it is now possible to formulate the weak form of the quasi-static mechanical constitutive initial value problem. Consider a body $\mathscr{B}$ of a generic material characterised by a given constitutive model whose internal variables are known at the initial time t_0. Additionally, this body is subjected to a prescribed history of body forces $\boldsymbol{b}(\boldsymbol{X}, t)$, with $t \in \left[t_0, t_f \right]$, and the following boundary conditions (see Figure 2.6):

- **Natural (or Neumann) boundary condition**: the history of the surface traction $\boldsymbol{t}(\boldsymbol{X}, t)$ is defined over the portion of the boundary of $\mathscr{B}$ that occupies the region $\partial\Omega_{\text{traction},0}$ in its reference configuration ($\boldsymbol{X} \in \partial\Omega_{\text{traction},0}$);
- **Essential (or Dirichlet) boundary condition**: the motion is a function defined over the portion of the boundary of $\mathscr{B}$ that occupies the region $\partial\Omega_{\text{motion},0}$ in its reference configuration. Assuming $\partial\Omega_{\text{motion},0} \cap \partial\Omega_{\text{traction},0} = \phi$, the motion over $\partial\Omega_{\text{motion},0}$ is expressed as

$$\bar{\varphi}(\boldsymbol{X}, t) = \boldsymbol{X} + \bar{\boldsymbol{u}}(\boldsymbol{X}, t), \quad \boldsymbol{X} \in \partial\Omega_{\text{motion},0}, \quad t \in \left[t_0, t_f \right], \tag{2.125}$$

  where $\bar{\boldsymbol{u}}$ is the prescribed boundary displacement vector. Consequently, these sufficiently regular displacements that satisfy the essential boundary

condition allow defining a set of kinematically admissible displacements of $\mathscr{B}$

$$\mathscr{X} = \Big\{ \boldsymbol{u} : \Omega_0 \times \mathscr{R} \to \mathscr{U} \mid \boldsymbol{u}\left(\boldsymbol{X}, t\right) = \bar{\boldsymbol{u}}\left(\boldsymbol{X}, t\right), \quad t \in \left[t_0, t_f\right], \ \ \boldsymbol{X} \in \partial\Omega_{\text{motion},0} \Big\}. \tag{2.126}$$

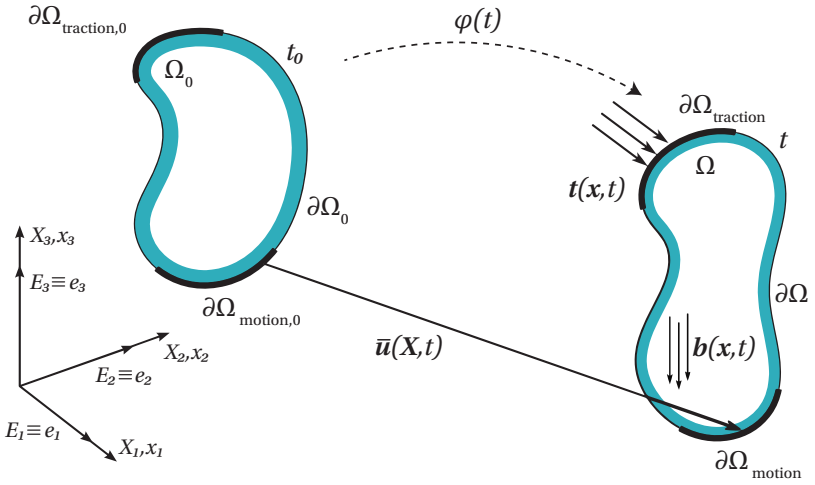


Figure 2.6: Representation of the initial boundary value problem.

The weak form of the quasi-static mechanical constitutive initial boundary value problem can thus be stated in the spatial description as

Problem 2.3 | Spatial quasi-static mechanical initial boundary value problem.

Find a kinematically admissible displacement function, $\boldsymbol{u} \in \mathscr{X}$, such that for every $t \in \left[t_0, t_f\right]$, the body $\mathscr{B}$ is in equilibrium as stated by the Virtual Work Principle

$$\int_\Omega \left[\boldsymbol{\sigma} : \nabla\boldsymbol{\eta} - \boldsymbol{b}\cdot\boldsymbol{\eta}\right] dv - \int_{\partial\Omega} \boldsymbol{t}\cdot\boldsymbol{\eta}\, da = 0, \quad \forall \boldsymbol{\eta} \in \mathscr{V}, \tag{2.127}$$

where the space of virtual displacements at time t is defined by

$$\mathscr{V} = \left\{ \boldsymbol{\eta} : \Omega \to \mathscr{U} \mid \boldsymbol{\eta} = \boldsymbol{0} \quad \text{in} \quad \partial\Omega_{\text{motion},0} \right\}, \tag{2.128}$$

and, at each point of $\mathscr{B}$, the Cauchy stress tensor is the solution to the spatial mechanical constitutive initial value problem.

2.8 Finite Element Method

As previously stated, obtaining a universal analytical solution for the weak form of the quasi-static initial boundary value problem is practically impossible, given the broad spectrum of geometries and constitutive models needed to be considered. Therefore, approximation methods need to be employed, being the Finite Element Method (FEM), the most popular numerical technique used to solve the equilibrium problem within solid mechanics. Very briefly, this method is based on two central numerical approximations:

- **Temporal discretisation**: the original time-continuum constitutive equations are transformed into incremental (time-discrete) ones, allowing to solve path-dependent and path-independent constitutive relations in a straightforward way;
- **Spatial discretisation**: the domain of the body is subdivided into finite-dimensional elements, establishing the weak form in terms of a function on nodal values. Associated with this discretisation is the appropriate choice of the interpolation functions.

The introduction of these approximations transforms the original initial boundary value problem into a set of incremental (generally non-linear) algebraic finite element equations. The main steps of the FEM are presented in Figure 2.7.

2.8.1 Time Discretisation

The behaviour of most engineering materials can only be accurately described by path-dependent constitutive models, i.e., the material stress state depends on the deformation history to which the material has been subjected. Therefore, it can not depend solely on the instantaneous value of strains, and the adoption of an internal variable-based constitutive model is inevitable. As previously seen, the internal variables store information about the intrinsic material state.

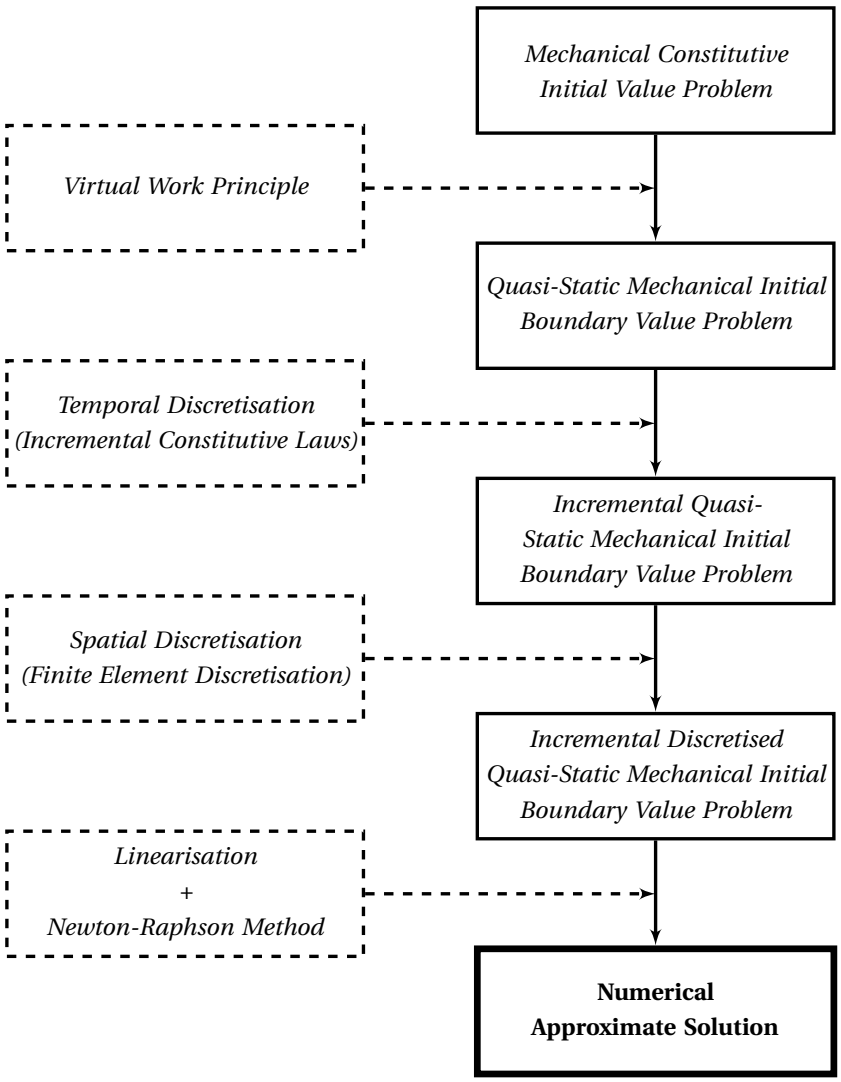


Figure 2.7: Schematic representation of the different tools (left column) and steps (right column) of the FEM.

To numerically deal with this problem, it is essential to use an appropriate numerical algorithm to integrate over time the constitutive equations. Very briefly, these algorithms consist of a time (or, in quasi-static problems, pseudo-time) discretisation of the domain $\left[t_0, t_f\right]$ in a given number of subintervals, along with the assumption of a specific deformation path for each subinterval, in which the equilibrium equations must be satisfied. Considering the mechanical constitutive initial boundary value problem and the generic time increment $\left[t_n, t_{n+1}\right]$, the following two requirements are imposed:

- **Cauchy and First Piola-Kirchhoff stress tensors**: From the axiom of thermodynamic determinism, the stress $\boldsymbol{\sigma}_{n+1}$ must be uniquely determined by the prescribed deformation gradient $\boldsymbol{F}_{n+1}$ at instant t_{n+1}

$$\boldsymbol{\sigma}_{n+1} = \hat{\boldsymbol{\sigma}}\left(\boldsymbol{F}_{n+1}, \boldsymbol{\alpha}_n\right), \tag{2.129}$$

  where $\hat{\boldsymbol{\sigma}}$ is the incremental constitutive function for the Cauchy stress tensor. Similarly, the First Piola-Kirchhoff stress tensor $\boldsymbol{P}_{n+1}$ must also be uniquely determined by the prescribed deformation gradient $\boldsymbol{F}_{n+1}$ at instant t_{n+1}

$$\boldsymbol{P}_{n+1} = \hat{\boldsymbol{P}}\left(\boldsymbol{F}_{n+1}, \boldsymbol{\alpha}_n\right), \tag{2.130}$$

  where $\hat{\boldsymbol{P}}$ is the incremental constitutive function for the First Piola-Kirchhoff stress tensor. For both cases, it is assumed that the set of internal variables $\boldsymbol{\alpha}_n$ is known at time t_n.

- **Set of internal variables**: Assuming, once again, that the set of internal variables $\boldsymbol{\alpha}_n$ is known at time t_n, the set of internal variables $\boldsymbol{\alpha}_{n+1}$ must be uniquely determined by the prescribed deformation gradient $\boldsymbol{F}_{n+1}$ at instant t_{n+1}

$$\boldsymbol{\alpha}_{n+1} = \hat{\boldsymbol{\alpha}}\left(\boldsymbol{F}_{n+1}, \boldsymbol{\alpha}_n\right), \tag{2.131}$$

  where $\hat{\boldsymbol{\alpha}}$ is the incremental constitutive function for the set of internal variables.

Note that, as the strain increments are reduced, the incremental constitutive functions are expected to converge to the exact solution. Furthermore, these generally non-linear functions are considered as path independent within one increment, i.e., within each subinterval, $\boldsymbol{\alpha}_n$ is assumed constant, and they are a function of $\boldsymbol{F}_{n+1}$ alone.

In short, with the introduction of the numerical integration scheme, the incremental time discrete expressions, that update the stresses and the internal variables of the model, substitute the original time-continuum constitutive laws. Therefore, the weak form of the quasi-static mechanical constitutive initial boundary value problem can be stated in the spatial description as

Problem 2.4 | Spatial incremental quasi-static mechanical initial boundary value problem.

Given the set of internal variables $\boldsymbol{\alpha}_n$ at time t_n, the prescribed body and traction force fields $\boldsymbol{b}_{n+1}$ and $\boldsymbol{t}_{n+1}$ at time t_{n+1}, and the prescribed deformation gradient $\boldsymbol{F}_{n+1}$ at time t_{n+1}, find the kinematically admissible displacement field $\boldsymbol{u}_{n+1} \in \mathscr{X}_{n+1}$ such that the body $\mathscr{B}$ is in equilibrium as stated by the Virtual Work Principle

$$\int_{\Omega_{n+1}} \left[\hat{\boldsymbol{\sigma}} \left(\boldsymbol{F}_{n+1}, \boldsymbol{\alpha}_n \right) : \nabla \boldsymbol{\eta} - \boldsymbol{b}_{n+1} \cdot \boldsymbol{\eta} \right] dv - \int_{\partial\Omega_{n+1}} \boldsymbol{t}_{n+1} \cdot \boldsymbol{\eta} \, da = 0, \quad \forall \boldsymbol{\eta} \in \mathscr{V}, \tag{2.132}$$

where the space of virtual displacements at time t_{n+1} is defined by

$$\mathscr{X}_{n+1} = \left\{ \{ \boldsymbol{u} : \Omega \times \mathscr{R} \to \mathscr{U} \mid \boldsymbol{u}_{n+1}(\boldsymbol{X}) = \bar{\boldsymbol{u}}_{n+1}(\boldsymbol{X}), \quad \boldsymbol{X} \in \partial\Omega_{\text{motion},0} \right\}. \tag{2.133}$$

2.8.2 Spatial Discretisation

Spatial discretisation, also called finite element discretisation, is the starting point of the application of the Finite Element Method. Where the continuum domain Ω of a generic body $\mathscr{B}$ is divided into a finite set of n_{elem} non-overlapping subdomains called finite elements, occupying a region $\Omega^{(e)}$. Therefore, the discretised domain, ${}^h\Omega$, is an approximation of the continuum domain

$$\Omega \approx {}^h\Omega = \bigcup_{e=1}^{n_{\text{elem}}} \Omega^{(e)}. \tag{2.134}$$

It is important to emphasise that the space of virtual displacements $\mathscr{V}$ and the space of kinematically admissible displacement fields $\mathscr{X}$ must also take their discretised forms denoted by ${}^h\mathscr{V}$ and ${}^h\mathscr{X}$.

Interpolation functions

Consider a generic finite element (e) with a set of n_{nodes} nodes, where each node i has associated an interpolation/shape function, $N_i^{(e)}$. These functions perform the field interpolations inside the element domain $\Omega^{(e)}$ and must verify the Kronecker delta property, independently of the type of element used,

$$N_i^{(e)}\left(\boldsymbol{x}_j\right) = \delta_{ij} = \begin{cases} 1, & \text{if } j = i, \\ 0, & \text{if } j \neq i. \end{cases} \tag{2.135}$$

This property expresses that the shape function associated with node i has a unit value at i and a null value at all other nodes of the element.

Let $a(\boldsymbol{x})$ be a generic field defined over the region $\Omega^{(e)}$. The interpolation of $a(\boldsymbol{x})$ at any point $\boldsymbol{x}$ inside the element is defined by the element shape functions $N_i^{(e)}$ as (see Figure 2.8)

$$a(\boldsymbol{x}) \approx^h a(\boldsymbol{x}) = \sum_{i=1}^{n_{\text{nodes}}} a\left(\boldsymbol{x_i}\right) N_i^{(e)}(\boldsymbol{x}). \tag{2.136}$$

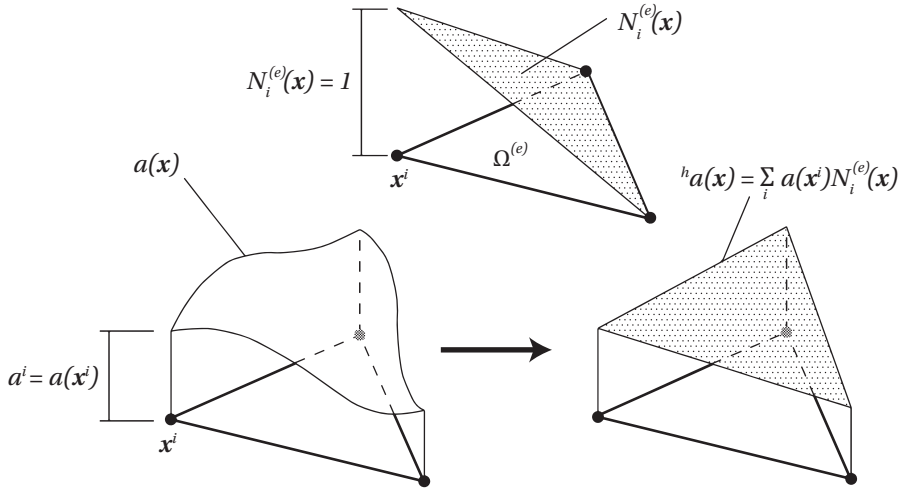


Figure 2.8: Finite element interpolation - element shape function.
Source: (de Souza Neto et al., 2008)

If the generic field $a(\boldsymbol{x})$ is instead defined over the global domain Ω, the interpolation of $a(\boldsymbol{x})$ at any point $\boldsymbol{x}$ is defined by the global shape functions N_i^g as (see Figure 2.9)

$$a(\boldsymbol{x}) \approx^h a(\boldsymbol{x}) = \sum_{i=1}^{n_{\text{points}}} a\left(\boldsymbol{x_i}\right) N_i^g(\boldsymbol{x}), \tag{2.137}$$

where i denotes a global node and n_{points} the total number of nodes in the finite element mesh. The global shape functions also satisfy the Kronecker delta property (Equation 2.135).

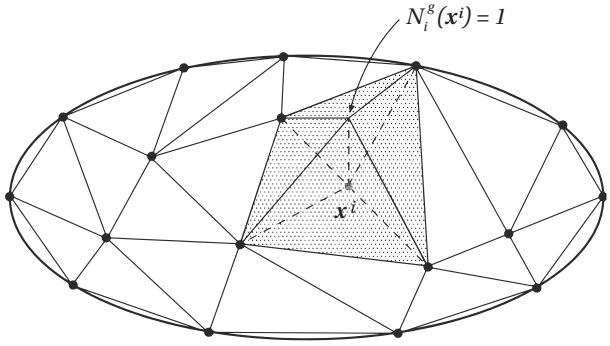


Figure 2.9: Finite element interpolation - global shape function.
Source: (de Souza Neto et al., 2008)

With the introduction of the above interpolation procedure, the discretised spaces of virtual displacements, ${}^h\mathscr{V}$ and ${}^h\mathscr{X}$, can be defined a

$$ {}^h\mathscr{V} = \left\{ {}^h\boldsymbol{\eta}(\boldsymbol{x}) = \sum_{i=1}^{n_{\text{points}}} \boldsymbol{\eta}\left(\boldsymbol{x}_i\right) N_i^g(\boldsymbol{x}) \mid \boldsymbol{\eta}\left(\boldsymbol{x}_i\right) = \mathbf{0}, \quad \text{if } \boldsymbol{x}_i \in \partial\Omega_{\text{motion},0} \right\}, \tag{2.138} $$

$$ {}^h\mathscr{X} = \left\{ {}^h\boldsymbol{u}(\boldsymbol{x}) = \sum_{i=1}^{n_{\text{points}}} \boldsymbol{u}\left(\boldsymbol{x}_i\right) N_i^g(\boldsymbol{x}) \mid \boldsymbol{u}\left(\boldsymbol{x}_i\right) = \bar{\boldsymbol{u}}\left(\boldsymbol{x}_i\right), \quad \text{if } \boldsymbol{x}_i \in \partial\Omega_{\text{motion},0} \right\}. \tag{2.139} $$

Interpolation matrix

For a generic element (e), its interpolation matrix $\mathbf{N}^{(e)}$ is given by

$$ \mathbf{N}^{(e)}(\boldsymbol{x}) = \left[\operatorname{diag}\left[N_1^{(e)}(\boldsymbol{x})\right] \quad \operatorname{diag}\left[N_2^{(e)}(\boldsymbol{x})\right] \quad \ldots \quad \operatorname{diag}\left[N_{n_{\text{nodes}}}^{(e)}(\boldsymbol{x})\right] \right], \tag{2.140} $$

where $\operatorname{diag}\left[N_i^{(e)}(\boldsymbol{x})\right]$ denotes the $n_{\text{dof}} \times n_{\text{dof}}$ diagonal matrix associated with node i, with n_{dof} being the number of degrees of freedom in the node,

$$ \operatorname{diag}\left[N_i^{(e)}(\boldsymbol{x})\right] = \begin{bmatrix} N_i^{(e)}(\boldsymbol{x}) & 0 & \ldots & 0 \\ 0 & N_i^{(e)}(\boldsymbol{x}) & \ldots & 0 \\ \vdots & \vdots & \ldots & \vdots \\ 0 & 0 & \ldots & N_i^{(e)}(\boldsymbol{x}) \end{bmatrix}_{n_{\text{dof}} \times n_{\text{dof}}}. \tag{2.141} $$

Nonetheless, to derive the discretised form of the virtual work equation, it is more convenient to assemble the global shape functions in the so-called

global interpolation matrix. This matrix is defined analogously to $\mathbf{N}^{(e)}$, though considering all n_{points} [2] nodes within the finite element mesh:

$$\mathbf{N}^g(\boldsymbol{x}) = \left[\text{diag}\left[N_1^g(\boldsymbol{x})\right] \quad \text{diag}\left[N_2^g(\boldsymbol{x})\right] \quad \dots \quad \text{diag}\left[N_{n_{\text{points}}}^g(\boldsymbol{x})\right]\right], \tag{2.142}$$

where $\text{diag}\left[N_i^g(\boldsymbol{x})\right]$ denotes the $n_{\text{dof}} \times n_{\text{dof}}$ diagonal matrix associated with node i, with n_{dof} being the number of degrees of freedom in the node,

$$\text{diag}\left[N_i^g(\boldsymbol{x})\right] = \begin{bmatrix} N_i^g(\boldsymbol{x}) & 0 & \dots & 0 \\ 0 & N_i^g(\boldsymbol{x}) & \dots & 0 \\ \vdots & \vdots & \dots & \vdots \\ 0 & 0 & \dots & N_i^g(\boldsymbol{x}) \end{bmatrix}_{n_{\text{dof}} \times n_{\text{dof}}} . \tag{2.143}$$

A fundamental aspect of the finite element method is the capacity to approximate the displacement field $\boldsymbol{u}(\boldsymbol{x})$ by its discretised counterpart ${}^h\boldsymbol{u}(\boldsymbol{x})$ over the entire domain, i.e., at any point $\boldsymbol{x}$,

$$\boldsymbol{u}(\boldsymbol{x}) \approx {}^h\boldsymbol{u}(\boldsymbol{x}) = \mathbf{N}^g(\boldsymbol{x})\,\mathbf{u}, \quad {}^h\boldsymbol{u} \in {}^h\mathscr{X}, \tag{2.144}$$

where $\mathbf{u}$ is the global vector of nodal displacements, given by

$$\mathbf{u} = \left[u_1^1 \quad \dots \quad u_{n_{\text{dof}}}^1 \quad \dots \quad u_1^{n_{\text{points}}} \quad \dots \quad u_{n_{\text{dof}}}^{n_{\text{points}}}\right]. \tag{2.145}$$

Discrete gradient operators

In order to discretise the incremental initial boundary value problem, there is the need to introduce two critical operators, which are the global discrete symmetric gradient operator $\mathbf{B}^g$, and the global discrete spatial gradient operator $\mathbf{G}^g$. The type of problem that will be solved affects the format of these matrices. For instance, for two-dimensional (2D) problems where a cartesian coordinate system is employed, these matrices are given by:

[2] $n_{\text{points}} < n_{\text{elem}} \times n_{\text{nodes}}$, since adjacent elements share nodes

$$\mathbf{B}^g = \begin{bmatrix} \frac{\partial N_1^g}{\partial x} & 0 & \frac{\partial N_2^g}{\partial x} & 0 & \dots & \frac{\partial N_{n_{\text{points}}}^g}{\partial x} & 0 \\ 0 & \frac{\partial N_1^g}{\partial y} & 0 & \frac{\partial N_2^g}{\partial y} & \dots & 0 & \frac{\partial N_{n_{\text{points}}}^g}{\partial y} \\ \frac{\partial N_1^g}{\partial y} & \frac{\partial N_1^g}{\partial x} & \frac{\partial N_2^g}{\partial y} & \frac{\partial N_2^g}{\partial x} & \dots & \frac{\partial N_{n_{\text{points}}}^g}{\partial y} & \frac{\partial N_{n_{\text{points}}}^g}{\partial x} \end{bmatrix}, \tag{2.146}$$

and

$$\mathbf{G}^g = \begin{bmatrix} \frac{\partial N_1^g}{\partial x} & 0 & \frac{\partial N_2^g}{\partial x} & 0 & \dots & \frac{\partial N_{n_{\text{points}}}^g}{\partial x} & 0 \\ 0 & \frac{\partial N_1^g}{\partial x} & 0 & \frac{\partial N_2^g}{\partial x} & \dots & 0 & \frac{\partial N_{n_{\text{points}}}^g}{\partial x} \\ \frac{\partial N_1^g}{\partial y} & 0 & \frac{\partial N_2^g}{\partial y} & 0 & \dots & \frac{\partial N_{n_{\text{points}}}^g}{\partial y} & 0 \\ 0 & \frac{\partial N_1^g}{\partial y} & 0 & \frac{\partial N_2^g}{\partial y} & \dots & 0 & \frac{\partial N_{n_{\text{points}}}^g}{\partial y} \end{bmatrix}. \tag{2.147}$$

Discrete boundary value problem

The spatial incremental quasi-static mechanical constitutive initial boundary value problem can be rewritten by applying the aforementioned finite element discretisation, resulting in

$$\begin{aligned} \int_{h\Omega} \left[\hat{\boldsymbol{\sigma}}^T \left(\boldsymbol{F}_{n+1}, \boldsymbol{\alpha}_n \right) \mathbf{B}^g \boldsymbol{\eta} - \mathbf{b}_{n+1} \cdot \mathbf{N}^g \boldsymbol{\eta} \right] dv \\ - \int_{\partial^h \Omega_{\text{traction}}} \mathbf{t}_{n+1} \cdot \mathbf{N}^g \boldsymbol{\eta} \, da = 0, \quad \forall \boldsymbol{\eta} \in {}^h\mathcal{V}, \end{aligned} \tag{2.148}$$

or ultimately in

$$\begin{aligned} \left\{ \int_{h\Omega} \left[\left(\mathbf{B}^g \right)^T \hat{\boldsymbol{\sigma}} \left(\boldsymbol{\alpha}_n, \boldsymbol{F}_{n+1} \right) - \left(\boldsymbol{N}^g \right)^T \cdot \mathbf{b}_{n+1} \right] dv \right. \\ \left. - \int_{\partial^h \Omega_{\text{traction}}} \left(\boldsymbol{N}^g \right)^T \cdot \mathbf{t}_{n+1} \, da \right\}^T \boldsymbol{\eta} = 0, \quad \forall \boldsymbol{\eta} \in {}^h\mathcal{V}. \end{aligned} \tag{2.149}$$

As seen as though the above equation must be satisfied for all $\boldsymbol{\eta} \in {}^h\mathcal{V}$, the term inside the curly braces must be null. Therefore, the incremental quasi-static mechanical discretised constitutive initial boundary value problem can be stated in the spatial description as

Problem 2.5 | Spatial incremental discretised quasi-static mechanical initial boundary value problem.

Given the set of internal variables $\boldsymbol{\alpha}_n$ at time t_n, the prescribed body and traction force fields $\mathbf{b}_{n+1}$ and $\mathbf{t}_{n+1}$ at time t_{n+1}, and the prescribed deformation gradient $\boldsymbol{F}_{n+1}$ at time t_{n+1}, find the kinematically admissible nodal displacement field $\mathbf{u}_{n+1} \in^h \mathscr{X}_{n+1}$ such that the body $\mathscr{B}$ is in equilibrium as stated by the Virtual Work Principle

$$\mathbf{r}\left(\mathbf{u}_{n+1}\right) = \mathbf{f}^{\text{int}}\left(\mathbf{u}_{n+1}\right) - \mathbf{f}^{\text{ext}}_{n+1} = \mathbf{0}, \tag{2.150}$$

where $\boldsymbol{f}^{int}$ and $\boldsymbol{f}^{ext}_{n+1}$ are the global vectors of internal and external forces defined as

$$\mathbf{f}^{\text{int}} = \int_{h\Omega} \left(\mathbf{B}^g\right)^T \hat{\boldsymbol{\sigma}}\left(\boldsymbol{F}_{n+1}, \boldsymbol{\alpha}_n\right) d\upsilon, \tag{2.151}$$

$$\mathbf{f}^{\text{ext}}_{n+1} = \int_{h\Omega} \left(\mathbf{N}^g\right)^T \mathbf{b}_{n+1} d\upsilon + \int_{\partial^h\Omega_{\text{traction}}} \left(\boldsymbol{N}^g\right)^T \mathbf{t}_{n+1} da. \tag{2.152}$$

Element force vectors

In finite element computations, the global vectors of internal and external forces are normally obtained by an assemblage of their elemental counterparts as

$$\mathbf{f}^{\text{int}} = \mathop{\mathsf{A}}_{e=1}^{n_{\text{elem}}} \left(\mathbf{f}^{\text{int}}\right)^{(e)}, \tag{2.153}$$

$$\mathbf{f}^{\text{ext}}_{n+1} = \mathop{\mathsf{A}}_{e=1}^{n_{\text{elem}}} \left(\mathbf{f}^{\text{ext}}\right)^{(e)}, \tag{2.154}$$

where the elemental vectors in the spatial description are defined as

$$\left(\mathbf{f}^{\text{int}}\right)^{(e)} = \int_{h\Omega^{(e)}} \mathbf{B}^T \hat{\boldsymbol{\sigma}}\left(\boldsymbol{F}_{n+1}, \boldsymbol{\alpha}_n\right) d\upsilon, \tag{2.155}$$

$$\left(\mathbf{f}^{\text{ext}}\right)^{(e)} = \int_{h\Omega^{(e)}} \mathbf{N}^T \mathbf{b}_{n+1} d\upsilon + \int_{\partial^h\Omega^{(e)}_{\text{traction}}} \mathbf{N}^T \mathbf{t}_{n+1} da, \tag{2.156}$$

and in the material description as

$$\left(\mathbf{f}^{\text{int}}\right)^{(e)} = \int_{h\Omega^{(e)}_0} \mathbf{G}^T \hat{\mathbf{P}}\left(\boldsymbol{F}_{n+1}, \boldsymbol{\alpha}_n\right) d\upsilon, \tag{2.157}$$

$$\left(\mathbf{f}^{\text{ext}}\right)^{(e)} = \int_{{}^{h}\Omega_0^{(e)}} \mathbf{N}^T \mathbf{b}_{0,n+1}\, dv + \int_{\partial^h \Omega^{(e)}_{\text{traction},0}} \mathbf{N}^T \mathbf{t}_{0,n+1}\, da. \tag{2.158}$$

Note that the matrices **N**, **B** and **G** are, respectively, the elemental interpolation matrix, the symmetric elemental gradient operator and the discrete elemental gradient operator. Moreover, the finite element assembly operator, A, implies that each component of the global force, associated with a particular global node, is the result of the sum of the element force vectors of all elements that share that global node.

2.8.3 Numerical Integration

The exact integrals of Equations 2.155 and 2.156 over the element domain are generally unfeasible to solve. Therefore, numerical methods need to be employed to compute an approximate solution, being the Gaussian Quadrature Method, the method typically used in the FEM framework.

Very briefly, if a mapping $\boldsymbol{x}$ from the local/natural normalised domain onto the element domain exists ($\boldsymbol{x} : \Upsilon \rightarrow \Omega^{(e)}$) (see Figure 2.10), the Gaussian Quadrature Method approximates the integral of a generic function $a(\boldsymbol{x})$ over the element domain $\Omega^{(e)}$ by evaluating the function on n_{gp} Gauss points

$$\int_{\Omega^{(e)}} a(\boldsymbol{x})\, d\boldsymbol{x} = \int_{\Upsilon} a\left(\boldsymbol{x}\left(\boldsymbol{\xi}\right)\right) j\left(\boldsymbol{\xi}\right) d\boldsymbol{\xi} \approx \sum_{i=1}^{n_{gp}} w_i\, a\left(\boldsymbol{x}\left(\boldsymbol{\xi}_i\right)\right) j\left(\boldsymbol{\xi}_i\right), \tag{2.159}$$

where $\boldsymbol{\xi}_i$, $i = 1, 2, \ldots, n_{gp}$ are positions of the Gauss sampling points in natural coordinates, i.e., in the domain Υ, w_i the corresponding weights, and $j\left(\boldsymbol{\xi}\right)$ the determinant of the transformation Jacobian

$$j\left(\boldsymbol{\xi}\right) = \det\left[\frac{\partial \boldsymbol{x}}{\partial \boldsymbol{\xi}}\right]. \tag{2.160}$$

Additionally, it is important to point out that the Gaussian Quadrature can also be applied to integrals over the boundaries $\partial\Omega$.

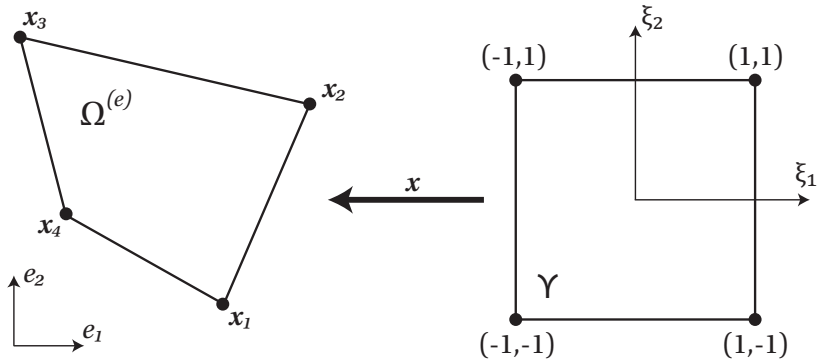


Figure 2.10: Representation of the mapping from the local/natural normalised domain onto the element domain, for a 4-noded bilinear quadratic element.

2.8.4 Proportional Loading

Until this point, no development was made on how to define/compute the body forces $\boldsymbol{b}_{n+1}$ and the traction forces $\boldsymbol{t}_{n+1}$ at time t_{n+1}. A possible approach consists of adopting a proportional loading scheme in which the mentioned fields, at any given instant t_{n+1}, are proportional to the prescribed constant body forces $\bar{\boldsymbol{b}}$ and traction forces $\bar{\boldsymbol{t}}$, i.e., the loading is applied proportionally, $\lambda(t)$,

$$\boldsymbol{b}_{n+1} = \lambda_{n+1}\bar{\boldsymbol{b}} \tag{2.161}$$

$$\boldsymbol{t}_{n+1} = \lambda_{n+1}\bar{\boldsymbol{t}} \tag{2.162}$$

where λ_{n+1} is the prescribed load factor at time t_{n+1}. Since the prescribed fields are constant in time and λ_{n+1} is a scalar, the body and traction forces preserve their direction throughout the deformation process.

According to the proportional loafing scheme, the main steps required to solve the incremental equilibrium equation are summarised in Algorithm 1.

Algorithm 1: Solution of the incremental equilibrium equation by adopting a proportional loading scheme.

(i) Compute and assemble the elemental external forces vector

$$\mathbf{f}_{\text{total}}^{\text{ext}} = \mathop{\mathsf{A}}_{e=1}^{n_{\text{elem}}} \left(\mathbf{f}_{\text{total}}^{\text{ext}}\right)^{(e)}$$

(ii) Set up the proportional loading curve, $\lambda(t)$

(iii) Initialise the increment counter, $n := 0$

(iv) Set the load factor at the end of $\left[t_n, t_{n+1}\right]$, $\lambda_{n+1} = \lambda\left(t_{n+1}\right)$

(v) Solve the non-linear equilibrium equation (Algorithm 2)

$$\mathbf{r}\left(\mathbf{u}_{n+1}\right) = \mathbf{f}^{\text{int}}\left(\mathbf{u}_{n+1}\right) - \lambda_{n+1}\mathbf{f}_{\text{total}}^{\text{ext}} = \mathbf{0}$$

(vi) Check if the total load was applied

if $\left(n+1 < n_{incr}\right)$ **then**

- Update incremental counter, $n := n+1$, and go to step (iv)

else

- Exit

end

2.8.5 Newton-Raphson Method

The Newton–Raphson algorithm is a robust and efficient iterative scheme for solving the generally non-linear equilibrium equation (Equation 2.150). Its applicability attractiveness is mainly due to its quadratic rates of asymptotic convergence.

Very briefly, the Newton-Raphson method consists of linearising the non-linear incremental discretised equilibrium equation on the current iterative value. Each iteration solves this linearised equation and obtains an approximate solution. Afterwards, this estimate is used as the linearisation point for the next iteration, and the procedure is repeated until the error of the solution is below a given tolerance.

The linearised version of the spatial equilibrium equation, whose derivation can be seen in detail in de Souza Neto et al. (2008), is given by

$$\left\{\int_{{}^h\Omega}\left(\mathbf{G}^g\right)^T\mathbf{a}\mathbf{G}^g\,dv\right\}\delta\boldsymbol{u}\cdot\boldsymbol{\eta}=-\left\{\int_{{}^h\Omega}\left[\left(\mathbf{B}^g\right)^T\hat{\boldsymbol{\sigma}}\left(\boldsymbol{F}_{n+1},\boldsymbol{\alpha}_n\right)-\left(\mathbf{N}^g\right)^T\mathbf{b}_{n+1}\right]dv - \int_{\partial^h\Omega_{\text{traction}}}\left(\mathbf{N}^g\right)^T\mathbf{t}_{n+1}\,da\right\}\cdot\boldsymbol{\eta},\qquad\forall\boldsymbol{\eta}\in{}^h\mathscr{V}, \tag{2.163}$$

where $\mathbf{a}$ is the consistent spatial tangent modulus (fourth-order tensor),

$$\mathsf{a}_{ijkl}=\frac{1}{J}\frac{\partial\tau_{ij}}{\partial F_{km}}F_{lm}-\sigma_{ij}\delta_{jk}, \tag{2.164}$$

and since the linearised version of the spatial equilibrium equation must be satisfied for any $\forall\boldsymbol{\eta}\in{}^h\mathscr{V}$, it can be simplified

$$\left\{\int_{{}^h\Omega}\left(\mathbf{G}^g\right)^T\mathbf{a}\mathbf{G}^g\,dv\right\}\delta\boldsymbol{u}=-\left\{\int_{{}^h\Omega}\left[\left(\mathbf{B}^g\right)^T\hat{\boldsymbol{\sigma}}\left(\boldsymbol{F}_{n+1},\boldsymbol{\alpha}_n\right)-\left(\mathbf{N}^g\right)^T\mathbf{b}_{n+1}\right]dv - \int_{\partial^h\Omega_{\text{traction}}}\left(\mathbf{N}^g\right)^T\mathbf{t}_{n+1}\,da\right\},\qquad\forall\boldsymbol{\eta}\in{}^h\mathscr{V}. \tag{2.165}$$

In contrast, the linearised version of the material equilibrium equation, is given by

$$\left\{\int_{{}^h\Omega_0}\left(\mathbf{G}^g\right)^T\mathbf{A}\mathbf{G}^g\,dv\right\}\delta\boldsymbol{u}\cdot\boldsymbol{\eta}=-\left\{\int_{{}^h\Omega_0}\left[\left(\mathbf{G}^g\right)^T\hat{\mathbf{P}}\left(\boldsymbol{F}_{n+1},\boldsymbol{\alpha}_n\right)-\left(\mathbf{N}^g\right)^T\mathbf{b}_{0,n+1}\right]dv - \int_{\partial^h\Omega_{\text{traction},0}}\left(\mathbf{N}^g\right)^T\mathbf{t}_{0,n+1}\,da\right\}\cdot\boldsymbol{\eta},\qquad\forall\boldsymbol{\eta}\in{}^h\mathscr{V}, \tag{2.166}$$

where $\mathbf{A}$ is the consistent material tangent modulus (fourth-order tensor),

$$\mathsf{A}_{ijkl}=\frac{\partial P_{ij}}{\partial F_{kl}}, \tag{2.167}$$

which can be related to its spatial counterpart by

$$\mathsf{a}_{ijkl}=\frac{1}{J}\mathsf{A}_{ijkl}F_{jm}F_{ln}, \tag{2.168}$$

and since the linearised version of the material equilibrium equation must also be satisfied for any $\forall\boldsymbol{\eta}\in{}^h\mathscr{V}$, it can be simplified

$$\left\{\int_{h\Omega_0}\left(\mathbf{G}^g\right)^T\mathbf{A}\mathbf{G}^g\,dv\right\}\delta\boldsymbol{u}=-\left\{\int_{h\Omega_0}\left[\left(\mathbf{G}^g\right)^T\hat{\mathbf{P}}\left(\boldsymbol{F}_{n+1},\boldsymbol{\alpha}_n\right)-\left(\mathbf{N}^g\right)^T\mathbf{b}_{0,n+1}\right]dv - \int_{\partial^h\Omega_{\text{traction},0}}\left(\mathbf{N}^g\right)^T\mathbf{t}_{0,n+1}\,da\right\},\qquad \forall\boldsymbol{\eta}\in{}^h\mathcal{V}. \tag{2.169}$$

In more detail, the generic Newton-Raphson iteration (k) consists of solving the following system of linear equations for $\delta\mathbf{u}^{(k)}$

$$\mathbf{K}_T^{(k-1)}\delta\mathbf{u}^{(k)}=-\mathbf{r}^{(k-1)}, \tag{2.170}$$

where $\mathbf{r}^{(k-1)}$ is the residual force vector

$$\mathbf{r}\left(\mathbf{u}_{n+1}^{(k-1)}\right)=\mathbf{f}^{\text{int}}\left(\mathbf{u}_{n+1}^{(k-1)}\right)-\mathbf{f}_{n+1}^{\text{ext}}, \tag{2.171}$$

and $\mathbf{K}_T$ is the global tangent stiffness matrix, which represents the term in curly brackets on the left-hand side of Equation 2.165,

$$\mathbf{K}_T=\int_{h\Omega}\left(\mathbf{G}^g\right)^T\mathbf{a}\mathbf{G}^g\,dv=\left.\frac{\partial\mathbf{r}}{\partial\mathbf{u}_{n+1}}\right|_{\mathbf{u}_{n+1}^{(k-1)}}, \tag{2.172}$$

or Equation 2.169

$$\mathbf{K}_T=\int_{h\Omega_0}\left(\mathbf{G}^g\right)^T\mathbf{A}\mathbf{G}^g\,dv=\left.\frac{\partial\mathbf{r}}{\partial\mathbf{u}_{n+1}}\right|_{\mathbf{u}_{n+1}^{(k-1)}}. \tag{2.173}$$

As in the cases of the global internal and external forces vectors, the global tangent stiffness matrix can also be obtained by the assemblage of all element tangent stiffness matrices

$$\mathbf{K}_T=\bigwedge_{e=1}^{n_{\text{elem}}}\mathbf{K}_T^{(e)}. \tag{2.174}$$

After solving the system of linear equations and obtaining $\delta\mathbf{u}$, the global nodal displacement vector can be updated

$$\mathbf{u}_{n+1}^{(k)}=\mathbf{u}_n+\Delta\mathbf{u}_{n+1}^{(k)}, \tag{2.175}$$

where $\Delta\mathbf{u}_{n+1}^{(k)}$ is the global incremental nodal displacement vector

$$\Delta\mathbf{u}_{n+1}^{(k)}=\Delta\mathbf{u}_{n+1}^{(k-1)}+\delta\mathbf{u}, \tag{2.176}$$

resulting in

$$\mathbf{u}_{n+1}^{(k)} = \mathbf{u}_{n+1}^{(k-1)} + \delta\mathbf{u}. \tag{2.177}$$

The iterative process is repeated until the imposed a priori convergence criterion, i.e., imposition of an equilibrium convergence tolerance ϵ_{tol}, is satisfied at an iteration (m)

$$\frac{\left|\mathbf{r}^{(m)}\right|}{\left|\mathbf{f}_{n+1}^{\text{ext}}\right|} \leq \epsilon_{\text{tol}}. \tag{2.178}$$

Lastly, it is important to point out that the Newton-Raphson Method requires the definition of an initial guess $\mathbf{u}_{n+1}^{(0)}$. A standard procedure involves taking the converged displacement vector, at the end of the previous increment, as the initial guess for the current one

$$\mathbf{u}_{n+1}^{(0)} = \mathbf{u}_n. \tag{2.179}$$

To facilitate the comprehension of the Newton-Raphson Method, its iterative cycle is schematically represented in Figure 2.11 and presented in the pseudo-code format in Algorithm 2.

Algorithm 2: Newton-Raphson Method steps for solving a given increment of the non-linear equilibrium equation.

(i) Initialise iterative counter, $k := 1$

(ii) Set initial guess for displacements, $\mathbf{u}_{n+1}^{0} = \mathbf{u}_n$

(iii) Compute initial residual force vector

$$\mathbf{r}\left(\mathbf{u}_{n+1}^{(0)}\right) = \mathbf{f}^{\text{int}}\left(\mathbf{u}_n\right) - \lambda_{n+1}\mathbf{f}_{\text{total}}^{\text{ext}}$$

(iv) Compute consistent spatial tangent modulus

$$\mathrm{a}_{ijkl} = \frac{1}{J}\mathrm{A}_{imkn}F_{jm}F_{ln}$$

(v) Compute and assemble elemental tangent stiffness matrices

$$\mathbf{K}_T^{(e)} = \sum_{i=1}^{n_{\text{gauss}}} w_i \mathbf{G}_i^T \mathbf{a}_i \mathbf{G}_i j_i, \qquad \mathbf{K}_T = \bigwedge_{e=1}^{n_{\text{elem}}} \mathbf{K}_T^{(e)}$$

(vi) Increment iteration counter, $k := k + 1$

(vii) Solve the equilibrium system of equations

$$\delta\mathbf{u} = -\mathbf{K}_T^{-1}\left(\mathbf{u}_n^{(k-1)}\right)\mathbf{r}\left(\mathbf{u}_n^{(k-1)}\right)$$

(viii) Update displacements

$$\mathbf{u}_{n+1}^{(k)} = \mathbf{u}_{n+1}^{(k-1)} + \delta\mathbf{u}$$

(ix) Update deformation gradient

$$\boldsymbol{F}_{n+1} = \left[\boldsymbol{I} - \nabla\mathbf{u}_{n+1}^{(k)}\right]^{-1}$$

(x) Update stresses and other state variables

$$\boldsymbol{\sigma}_{n+1} = \hat{\boldsymbol{\sigma}}\left(\boldsymbol{F}_{n+1}, \boldsymbol{\alpha}_n\right), \qquad \boldsymbol{\alpha}_{n+1} = \hat{\boldsymbol{\alpha}}\left(\boldsymbol{F}_{n+1}, \boldsymbol{\alpha}_n\right)$$

(xi) Compute and assemble elemental internal forces vectors:

$$\left(\mathbf{f}^{\text{int}}\right)^{(e)} = \sum_{i=1}^{n_{\text{gauss}}} w_i \mathbf{B}_i^T \hat{\boldsymbol{\sigma}}_i j_i, \qquad \mathbf{f}^{\text{int}} = \bigwedge_{e=1}^{n_{\text{elem}}} \left(\mathbf{f}^{\text{int}}\right)^{(e)}$$

(xii) Update residual force vector

$$\mathbf{r}\left(\mathbf{u}_{n+1}^{(k)}\right) = \mathbf{f}^{\text{int}}\left(\mathbf{u}_{n+1}^{(k)}\right) - \lambda_{n+1}\mathbf{f}_{total}^{\text{ext}}$$

(xiii) Check for convergence

if *converged* **then**

- Update incremental solution, $(\bullet)_{n+1} = (\bullet)_{n+1}^{(k)}$

else

- Go to step (iv), or exit

end

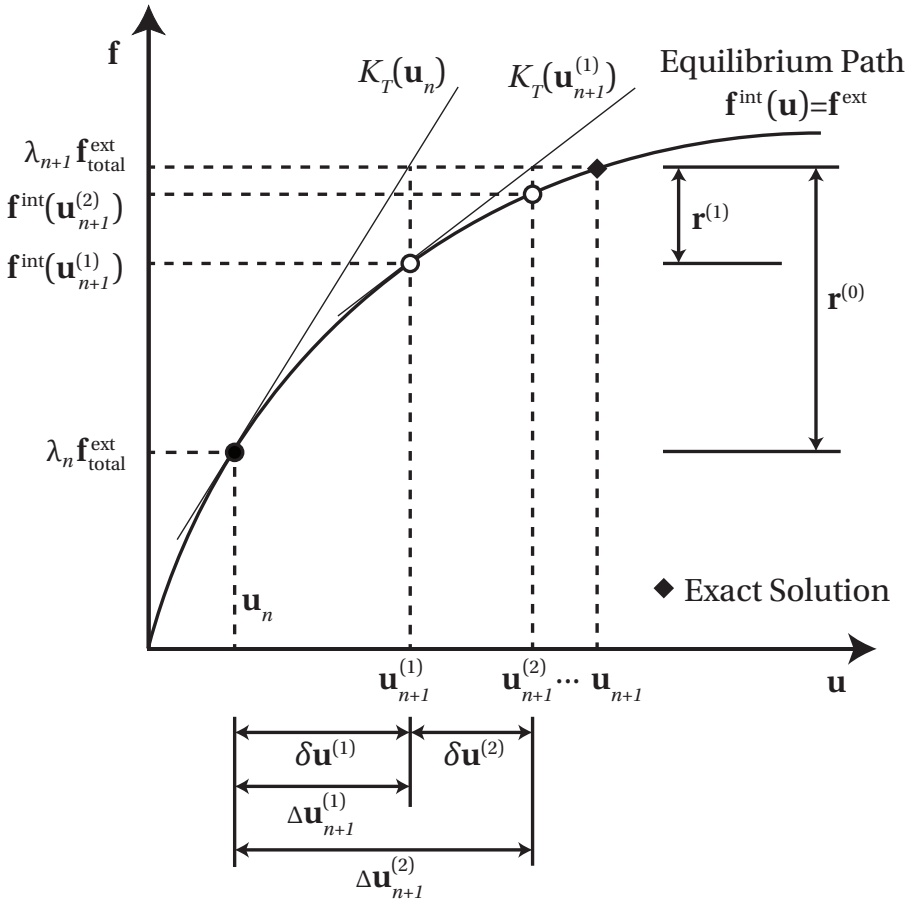


Figure 2.11: Representation of the Newton- Raphon Method iterative cycle for a given increment n of the equilibrium equation - one degree of freedom.

Source: (Ferreira, 2022)

Page intentionally left blank

CHAPTER 3

FIRST-ORDER COMPUTATIONAL HOMOGENISATION MULTI-SCALE MODELS

In Chapter 2, the continuum mechanics theory was introduced, where bodies are assumed to be continuous distributions of matter, neglecting their discontinuities and atomic structure. However, a solid's behaviour is highly influenced by its microstructure. Therefore, a macroscopic constitutive model may not be adequate when addressing materials with very complex microstructures or when many flaws or damages are present. Theoretically, these issues could be resolved instantaneously using a typical finite element analysis, where the mesh size is less than the size of the heterogeneities. Nonetheless, if the size of the heterogeneities is minimal, the simulation is practically impossible owing to the disproportionately high number of degrees of freedom.

In order to introduce the microstructure's impacts on the material's response, Multi-scale Models (MSM) are typically employed, comprising an analysis with at least two scales involved. So, a microscopic problem, where the presence of heterogeneities is taken into account, is used to determine the constitutive behaviour of a macroscopic point. Furthermore, to directly link up the two scale problems, an averaging technique called Homogenisation is used, resulting in the particular scheme of Multi-Scale Models based on Computational Homogenisation (MSM-H). Another designation for this method is Coupled Multi-scale Finite Element Analysis since it involves the bi-directional coupling of two simultaneous and concurrent simulations. With this approach, almost ideal accuracy levels can be obtained, and since the micro-scale is significantly greater than the atomic structure of the materials, the basics of CMT will be valid at both sizes.

The following sections will briefly review the presented topic, laying down all the necessary groundwork. Thus, for a more thorough explanation of the kinematical variational formulation of small and large strain first-order multi-scale solid constitutive models de Souza Neto and Feijó (2006) must be consulted. Moreover, Gitman et al. (2007) assemble potential definitions of an RVE and Watanabe and Terada (2010) differentiate coupled and decoupled micro-macro techniques.

3.1 First-order Computational Homogenisation

First-order computational homogenisation is a technique that allows the development of a multi-scale model of a material or structure on the notion that by averaging the material's behaviour at a smaller scale, the material's behaviour at a larger one can be predicted.

The definition of a Representative Volume Element (RVE) of the material is the initial step in developing a first-order computational homogenisation model. The RVE is a volume of material that is both tiny enough to accurately represent the material's microstructure and big enough to statistically include all essential microstructure characteristics. Afterwards, a finite element analysis is used to obtain the microscopic properties over the RVE, and lastly, by employing their volumetric averages, the corresponding macroscopic counterparts are derived.

As previously seen in Section 2.8.3, the integrals over the element domain are solved numerically using the Gaussian Quadrature Method, where the stress incremental constitutive function is determined in the Gauss integration points. At this step, the transition between the macro and micro scales occurs, and the stress incremental constitutive function is substituted by the solution of the microscopic equilibrium problem over the RVE for the corresponding Gauss integration point. Thus, the total number of RVEs equals the total number of integration points necessary to integrate the macro-scale finite element domain.

The formulation applied is a first-order formulation, which implies that only the first term of the Taylor series of the transformation between the reference and the deformed configurations is taken into account. Moreover, when employing this method, it should also be highlighted that (Kouznetsova et al., 2004):

1. It is an approximation technique, and it cannot fully capture the complexity of the material's microstructure. As a result, the precision of the predictions obtained relies on the size of the RVE and the quality of the computational model used to mimic the material's behaviour within

the RVE;

2. In certain circumstances, it could be necessary to apply higher-order computational homogenisation techniques, considering how the microstructure of the material's higher-order terms affects its effective properties. Nonetheless, despite achieving more accurate results for certain materials and loading conditions, it is much more computationally expensive.

3.1.1 Representative Volume Element

As previously mentioned, in order to develop a MSM-H scheme, Representative Volume Elements are crucial as they enable continuum properties associated with the material particle $\boldsymbol{X}$ to be predicted in terms of the microstructure of the particle's infinitesimal neighbourhood (which may include cracks, voids, inclusions, grain boundaries and other defects) (Nemat-Nasser and Hori, 1993). Hill (1963) was the first to introduce the term RVE, defining it as a sample of material having enough microscopic defects to render the mechanical properties independent of boundary values and a structure that is, on average, representative of the whole material.

The scale separation principle serves as the cornerstone for establishing an RVE. It specifies that the characteristic dimension of the RVE should be much smaller than the macro-scale characteristic dimension but large enough to be representational of the material's microstructure (i.e., notably greater than its heterogeneities) (Hashin, 1983). The scale separation principle is defined by:

$$l_{micro} \ll l_{\mathrm{RVE}} \ll l_{macro}, \tag{3.1}$$

where l_{micro} is the average length of the micro-constituents, l_{RVE} is the RVE's size, and l_{macro} is the macro-scale length (see Figure 3.1).

It is important to remember that this principle simply provides relative dimensions and that the size of the continuum body and the analysis' goals will determine the absolute dimensions of the RVEs (they might be very small or very large). The size of an RVE is indeed a topic of major concern, and various studies have been conducted in recent years. For instance, characterising materials with intricate microstructures would require significantly large RVEs, incompatible with the existing computational resources. To circumvent this constraint, Kanit et al. (2003) suggested that numerous microstructural realisations of smaller RVEs were employed instead, to analyse the homogenised behaviour. Further research on the issue may be found in the works of Gitman et al. (2007) and

Kanit et al. (2003). In summation, it must be kept in mind that, to conserve CPU time and memory, RVEs should be as small as feasible while yet comprising a very high number of micro-constituents.

The subscript $(\cdot)_\mu$ will be used to denote fields pertaining to the micro-scale in order to differentiate them from the macro-scale entities. Furthermore, the micro-scale coordinates are given by $\boldsymbol{y}$ for the spatial description and $\boldsymbol{Y}$ for the material one.

3.2 Large Strain Multi-Scale Constitutive Models

As previously indicated, each integration point $\boldsymbol{x}$ of the continuum macroscopic body has an RVE linked to it, and by volume averaging the response throughout the deformed RVE's domain, the solution is obtained at each point. Furthermore, the interchange of strain and stress levels between the macro and micro scales is what allows the establishment of the connection between them, as illustrated in Figure 3.1.

The scale transition theory, which serves as a fundamental presumption underlying hierarchical multi-scale models, is built upon three main pillars: the Principle of Scales Separation, which is inherently linked to the RVE characteristic dimension; the kinematic multi-scale relations, which include the kinematic insertion and homogenisation procedures; and the Principle of Multi-scale Virtual Power (generalisation of the Hill-Mandel macro-homogeneity principle), which establishes the energetic equivalence between both scales and the stress homogenisation.

The micro-scale problem is triggered by the deformation gradient $\boldsymbol{F}(\boldsymbol{x},t)$, which also limits how it may be solved by placing boundary constraints on the RVE. Afterwards, having the microscopic equilibrium problem already been solved, the return to the macro-scale occurs with the computation of the macro-scale stress tensor (the first Piola-Kirchhoff stress tensor), $\boldsymbol{P}(\boldsymbol{x},t)$, and the consistent tangent modulus, $\mathbf{A}(\boldsymbol{x},t)$, as volume averages of their microscopic counterparts. Lastly, the macro-scale solution procedure may then be carried out as usual.

Throughout this section, it is observed that applying a homogenised deformation gradient at the micro-scale limits the resolution of the microscopic problem. Moreover, the RVE is subject to extra constraints due to the energy linkage across scales. From these constraints, numerous boundary conditions for the microscopic problem will be developed and addressed.

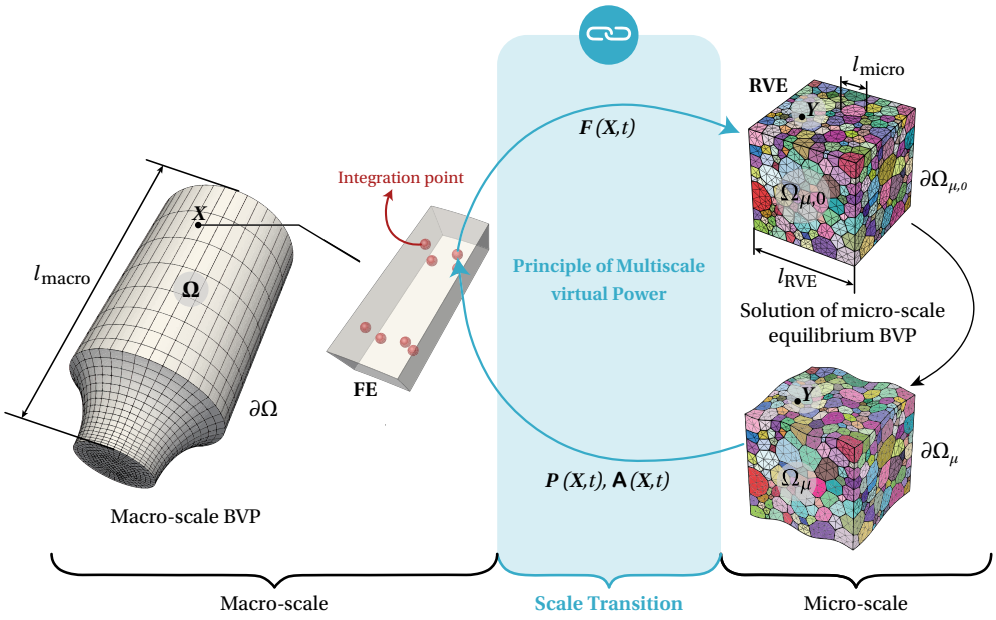


Figure 3.1: Schematic of multi-scale model based on first-order homogenisation models. Source: (Ferreira, 2022)

3.2.1 Homogenisation

The process of upscaling microscopic kinematic quantities to their equivalents at the macro-scale is known as kinematic homogenisation. In a general case, a field $a(\boldsymbol{X},t)$ at a point $\boldsymbol{X}$ of the macro-scale can be obtained from the volume average of its microscopic counterparts $a_\mu(\boldsymbol{Y},t)$ over the RVE domain by

$$a(\boldsymbol{X},t) = \frac{1}{v_{\mu,0}} \int_{\Omega_{\mu,0}} a_\mu(\boldsymbol{Y},t)\, dv, \tag{3.2}$$

where $v_{\mu,0}$ is the RVE's volume in the reference configuration. Accordingly, the definition of the homogenised or macro-scale deformation gradient, $\boldsymbol{F}(\boldsymbol{X},t)$, which drives the micro-scale deformation, is given by

$$\boldsymbol{F}(\boldsymbol{X},t) = \frac{1}{v_{\mu,0}} \int_{\Omega_{\mu,0}} \boldsymbol{F}_\mu(\boldsymbol{Y},t)\, dv, \tag{3.3}$$

or, recalling that the microscopic deformation gradient is given by Equation 2.15,

$$\boldsymbol{F}(\boldsymbol{X},t) = \boldsymbol{I} + \frac{1}{v_{\mu,0}} \int_{\Omega_{\mu,0}} \nabla_0 \boldsymbol{u}_\mu(\boldsymbol{Y},t)\, dv. \tag{3.4}$$

Moreover, the preceding integral over the RVE's domain, $\Omega_{\mu,0}$, can be transformed into an integral over the RVE's boundary, $\partial\Omega_{\mu,0}$, by employing Gauss's theorem

$$\boldsymbol{F}\left(\boldsymbol{X},t\right)=\boldsymbol{I}+\frac{1}{v_{\mu,0}}\int_{\partial\Omega_{\mu,0}}\boldsymbol{u}_{\mu}\left(\boldsymbol{Y},t\right)\otimes\boldsymbol{n}_{\mu,0}\left(\boldsymbol{Y}\right)da, \tag{3.5}$$

where $\boldsymbol{n}_{\mu,0}$ is the unitary vector normal to the RVE's boundary in its reference configuration. With this expression, the macroscopic deformation gradient can be established as a function of the microscopic displacement field across the RVE's boundary.

A similar approach may also be adopted for the first Piola-Kirchhoff stress tensor, where its homogenised field becomes

$$\boldsymbol{P}\left(\boldsymbol{X},t\right)=\frac{1}{v_{\mu,0}}\int_{\Omega_{\mu,0}}\boldsymbol{P}_{\mu}\left(\boldsymbol{Y},t\right)dv. \tag{3.6}$$

3.2.2 RVE Kinematics

As stated before, the potential microscopic displacements field is constrained by the imposition of a macroscopic deformation gradient, Equation 3.5. Hence, for the microscopic displacements field, $\boldsymbol{u}_{\mu}$, to be kinematically admissible, it has to satisfy the following requirement

$$\boldsymbol{u}_{\mu}\in\mathscr{K}_{\mu}^{*}, \tag{3.7}$$

where $\mathscr{K}_{\mu}^{*}$ is the minimally constrained set of kinematically admissible microscopic displacements, which in turn is given by

$$\begin{aligned}\mathscr{K}_{\mu}^{*}\equiv\Bigg\{\boldsymbol{u}_{\mu},\ \text{sufficiently regular}\ \Bigg|\\ \int_{\partial\Omega_{\mu,0}}\boldsymbol{u}_{\mu}\left(\boldsymbol{Y},t\right)\otimes\boldsymbol{n}_{\mu,0}\left(\boldsymbol{Y}\right)da=v_{\mu,0}\left[\boldsymbol{F}\left(\boldsymbol{X},t\right)-\boldsymbol{I}\right]\Bigg\}.\end{aligned} \tag{3.8}$$

Without loss of generality, the microscopic kinematically admissible displacements field can be decomposed into two components: the sum of its linear part, which depends on the prescribed deformation gradient, and the sum of the displacement fluctuations, $\tilde{\boldsymbol{u}}$,

$$\boldsymbol{u}_{\mu}\left(\boldsymbol{Y},t\right)=\left[\boldsymbol{F}\left(\boldsymbol{X},t\right)-\boldsymbol{I}\right]\boldsymbol{Y}+\tilde{\boldsymbol{u}}_{\mu}\left(\boldsymbol{Y},t\right)=\boldsymbol{u}_{\mu}^{\text{linear}}+\tilde{\boldsymbol{u}}_{\mu}\left(\boldsymbol{Y},t\right). \tag{3.9}$$

It becomes then clear that the displacement fluctuations are the unknown variable in the microscopic equilibrium problem, since the linear component of the microscopic displacements field only depends on the downscaled deformation gradient, which is assumed to be constant throughout the RVE's domain. Additionally, an expression for the microscopic deformation gradient is found by substituting the prior equation into Equation 2.15

$$\begin{aligned}\boldsymbol{F}_\mu\left(\boldsymbol{Y},t\right) &= \boldsymbol{I}+\nabla_0\left[\left[\boldsymbol{F}\left(\boldsymbol{X},t\right)-\boldsymbol{I}\right]\boldsymbol{Y}+\tilde{\boldsymbol{u}}_\mu\left(\boldsymbol{Y},t\right)\right]\\ &= \boldsymbol{I}+\left[\boldsymbol{F}\left(\boldsymbol{X},t\right)-\boldsymbol{I}\right]\boldsymbol{I}+\nabla_0\tilde{\boldsymbol{u}}_\mu\left(\boldsymbol{Y},t\right)\\ &= \boldsymbol{F}\left(\boldsymbol{X},t\right)+\nabla_0\tilde{\boldsymbol{u}}_\mu\left(\boldsymbol{Y},t\right).\end{aligned} \tag{3.10}$$

As a result, the microscopic deformation gradient may also be decomposed into two components: the prescribed deformation gradient, which represents homogeneous deformation, and the strain fluctuation field. Coupling this expression with Equation 3.3 yields

$$\boldsymbol{F}\left(\boldsymbol{X},t\right)=\boldsymbol{F}\left(\boldsymbol{X},t\right)+\frac{1}{v_{\mu,0}}\int_{\Omega_{\mu,0}}\nabla_0\tilde{\boldsymbol{u}}_\mu\left(\boldsymbol{Y},t\right)dv. \tag{3.11}$$

Thus, becoming evident that the minimal kinematic admissible constraint is specified as

$$\int_{\Omega_{\mu,0}}\nabla_0\tilde{\boldsymbol{u}}_\mu\left(\boldsymbol{Y},t\right)dv=\boldsymbol{0}, \tag{3.12}$$

or, by employing once again Gauss's theorem, as

$$\int_{\partial\Omega_{\mu,0}}\tilde{\boldsymbol{u}}_\mu\left(\boldsymbol{Y},t\right)\otimes\boldsymbol{n}_{\mu,0}\left(\boldsymbol{Y}\right)da=\boldsymbol{0}. \tag{3.13}$$

The previous expression allows defining the set of kinematically admissible minimally constrained microscopic displacement fluctuations as

$$\tilde{\mathcal{K}}_\mu^*\equiv\left\{\tilde{\boldsymbol{u}}_\mu,\ \text{sufficiently regular}\ \middle|\ \int_{\partial\Omega_{\mu,0}}\tilde{\boldsymbol{u}}_\mu\left(\boldsymbol{Y},t\right)\otimes\boldsymbol{n}_{\mu,0}\left(\boldsymbol{Y}\right)da=\boldsymbol{0}\right\}. \tag{3.14}$$

3.2.3 Hill-Mandel Principle

The Principle of Multi-scale Virtual Power degenerates into the Hill-Mandel principle and establishes the link between field properties from both the macro and micro-scales by invoking an energy conservation principle. Specifically,

it postulates that the macroscopic virtual stress power must be equivalent to microscopic homogenised virtual power such that

$$\boldsymbol{P}\left(\boldsymbol{X},t\right):\delta\boldsymbol{F}\left(\boldsymbol{X},t\right)=\frac{1}{v_{\mu,0}}\int_{\Omega_{\mu,0}}\boldsymbol{P}_{\mu}\left(\boldsymbol{Y},t\right):\delta\boldsymbol{F}_{\mu}\left(\boldsymbol{Y},t\right)dv. \tag{3.15}$$

This expression must be satisfied for any virtual macro-scale $\delta\boldsymbol{F}\left(\boldsymbol{X},t\right)$ and micro-scale $\delta\boldsymbol{F}_{\mu}\left(\boldsymbol{Y},t\right)$ deformation gradient. Moreover, coupling this expression with Equation 3.10 yields

$$\begin{aligned}\boldsymbol{P}\left(\boldsymbol{X},t\right):\delta\boldsymbol{F}\left(\boldsymbol{X},t\right)&=\frac{1}{v_{\mu,0}}\int_{\Omega_{\mu,0}}\boldsymbol{P}_{\mu}\left(\boldsymbol{Y},t\right):\left[\delta\boldsymbol{F}\left(\boldsymbol{X},t\right)+\nabla_0\boldsymbol{\eta}_{\mu}\left(\boldsymbol{Y},t\right)\right]dv,\\&=\boldsymbol{P}\left(\boldsymbol{X},t\right):\delta\boldsymbol{F}\left(\boldsymbol{X},t\right)+\frac{1}{v_{\mu,0}}\int_{\Omega_{\mu,0}}\boldsymbol{P}_{\mu}\left(\boldsymbol{Y},t\right):\nabla_0\boldsymbol{\eta}_{\mu}\left(\boldsymbol{Y},t\right)dv,\end{aligned} \tag{3.16}$$

where $\boldsymbol{\eta}_{\mu}$ is the virtual microscopic displacement fluctuations. From this expression, it can be shown that the Hill-Mandel principle places restrictions on the virtual microscopic displacement fluctuations and the first Piola-Kirchhoff stress tensor,

$$\int_{\Omega_{\mu,0}}\boldsymbol{P}_{\mu}\left(\boldsymbol{Y},t\right):\nabla_0\boldsymbol{\eta}_{\mu}\left(\boldsymbol{Y},t\right)dv=\boldsymbol{0}. \tag{3.17}$$

The micro-scale equilibrium problem can thus be stated in the spatial description as

Problem 2.6 | Spatial quasi-static micro-scale mechanical initial boundary value problem.

For a given macro-scale spatial particle $\boldsymbol{x}$ and the associated macro-scale deformation gradient $\boldsymbol{F}\left(\boldsymbol{x},t\right)$, find a kinematically admissible microscopic displacement fluctuation function, $\tilde{\boldsymbol{u}}\in\mathscr{K}_{\mu}$, such that, for every $t\in\left[t_0,t_f\right]$, the RVE is in equilibrium, as stated by the Virtual Work Principle

$$\int_{\Omega_{\mu}}\boldsymbol{\sigma}_{\mu}\left(\boldsymbol{y},t\right):\nabla\boldsymbol{\eta}_{\mu}dv=0,\qquad\forall\boldsymbol{\eta}_{\mu}\in\mathscr{K}_{\mu}, \tag{3.18}$$

where the space of virtual displacements fluctuation, $\mathscr{K}_{\mu}$, at time t, is defined by the set of kinematically admissible displacement fluctuations constrained by the adopted micro-scale boundary condition.

Recalling the Principle of Virtual Work, described in Section 2.6, it is feasible to deduce that the microscopic body and traction forces do not produce work

$$\int_{\partial\Omega_{\mu,0}}\boldsymbol{t}_{\mu,0}\left(\boldsymbol{Y},t\right)\cdot\boldsymbol{\eta}_{\mu}\left(\boldsymbol{Y},t\right)da=\boldsymbol{0}, \tag{3.19}$$

$$\int_{\partial\Omega_{\mu,0}} \boldsymbol{b}_{\mu,0}\left(\boldsymbol{Y},t\right)\cdot\boldsymbol{\eta}_{\mu}\left(\boldsymbol{Y},t\right)d\upsilon=\boldsymbol{0}. \tag{3.20}$$

These conditions suggest that the microscopic body and traction forces are considered reaction forces which emerge from the enforcement of the kinematical constraints imposed on the microscopic displacement field.

As a consequence, and by neglecting the inertia effects, the strong form of the micro-scale equilibrium equations may be established in the material description as

$$\begin{cases} \mathrm{div}_{Y}\boldsymbol{P}_{\mu}\left(\boldsymbol{Y},t\right)+\boldsymbol{b}_{\mu,0}\left(\boldsymbol{Y},t\right)=\boldsymbol{0}, & \forall\,\boldsymbol{Y}\in\Omega_{\mu,0}, \\ \boldsymbol{P}_{\mu}\left(\boldsymbol{Y},t\right)\boldsymbol{n}_{\mu,0}\left(\boldsymbol{Y},t\right)-\boldsymbol{t}_{\mu,0}\left(\boldsymbol{Y},t\right)=\boldsymbol{0}, & \forall\,\boldsymbol{Y}\in\Omega_{\mu,0}, \end{cases} \tag{3.21}$$

or, alternatively, in the spatial description as

$$\begin{cases} \mathrm{div}_{y}\boldsymbol{\sigma}_{\mu}\left(\boldsymbol{y},t\right)+\boldsymbol{b}_{\mu}\left(\boldsymbol{y},t\right)=\boldsymbol{0}, & \forall\,\boldsymbol{y}\in\Omega_{\mu}, \\ \boldsymbol{\sigma}_{\mu}\left(\boldsymbol{y},t\right)\boldsymbol{n}_{\mu}\left(\boldsymbol{y},t\right)-\boldsymbol{t}_{\mu}\left(\boldsymbol{y},t\right)=\boldsymbol{0}, & \forall\,\boldsymbol{y}\in\Omega_{\mu}. \end{cases} \tag{3.22}$$

Note that, if the right-hand side of Equation 3.6 is integrated by parts and the strong form of the micro-scale equilibrium problem is introduced (Equation 3.21), Equation 3.6 may be rewritten as a boundary integral,

$$\boldsymbol{P}\left(\boldsymbol{X},t\right)=\frac{1}{\upsilon_{\mu,0}}\int_{\partial\Omega_{\mu,0}}\boldsymbol{t}_{\mu,0}\otimes\boldsymbol{Y}\,da. \tag{3.23}$$

Subsequently, the homogenised first Piola-Kirchhoff stress tensor and the homogenised deformation gradient can be used to represent the Cauchy stress tensor

$$\boldsymbol{\sigma}=\frac{1}{J}\boldsymbol{P}\boldsymbol{F}^{T}. \tag{3.24}$$

3.2.4 Micro-Scale Boundary Conditions

One of the most crucial elements of a multi-scale model is the appropriate selection of a micro-scale boundary condition since the microscopic displacement field is strongly affected by the type of restrictions imposed on the RVE boundary. The chosen boundary condition has to match the unique characteristics of the microstructure, i.e., it must constrain the solution of the microscopic equilibrium problem such that the model may accurately reflect the actual behaviour of the solid.

The set of kinematically admissible minimally constrained microscopic displacement $\mathscr{K}_\mu^*$ and the associated set of displacement fluctuations $\tilde{\mathscr{K}}_\mu^*$ were already established in Section 3.2.2, and in order to fulfilL these requirements, the RVE may be subjected to four distinct kinds of constraints:

- Taylor model;
- Linear boundary condition;
- Periodic boundary condition (most commonly applied);
- Uniform boundary traction model.

The models are arranged in decreasing order of the degree of restriction, with the Taylor model enforcing the highest restrictions, increasing the stiffness of the RVE, and the uniform traction model being the least restrictive. This last one is identical to the minimally constrained set of admissible kinematic displacement fluctuations.

$$\tilde{\mathscr{K}}_\mu^{\text{Taylor}} \subset \tilde{\mathscr{K}}_\mu^{\text{Linear}} \subset \tilde{\mathscr{K}}_\mu^{\text{Periodic}} \subset \tilde{\mathscr{K}}_\mu^{\text{U. Traction}} \tag{3.25}$$

Taylor model

The Taylor hypothesis is the most straightforward and restrictive boundary condition of the four presented models, leading to overestimated stiffness matrices of heterogeneous materials. It imposes null displacement fluctuations over the entire domain of the RVE (see Figure 3.2),

$$\tilde{\boldsymbol{u}}_\mu\left(\boldsymbol{Y},t\right)=\boldsymbol{0}, \quad \forall \boldsymbol{Y}\in\Omega_{\mu,0}. \tag{3.26}$$

Such condition immediately satisfies Equations 3.13, 3.19 and 3.20. As a result, the microscopic displacement field $\boldsymbol{u}_\mu$ is linearly dependent on the reference position $\boldsymbol{Y}$

$$\boldsymbol{u}_\mu\left(\boldsymbol{Y},t\right)=\left[\boldsymbol{F}\left(\boldsymbol{X},t\right)-\boldsymbol{I}\right]\boldsymbol{Y}=\boldsymbol{u}_\mu^{\text{linear}}, \quad \forall \boldsymbol{Y}\in\Omega_{\mu,0}. \tag{3.27}$$

Furthermore, the microscopic deformation gradient is constant and coincides with its macroscopic counterpart, and therefore, the RVE is not capable of deforming freely enough to define geometric or material heterogeneities

$$\boldsymbol{F}\left(\boldsymbol{X},t\right)=\boldsymbol{F}_\mu\left(\boldsymbol{Y},t\right). \tag{3.28}$$

Lastly, the set of kinematically admissible microscopic displacement fluctuations minimally constrained by the Taylor model is given by

$$\tilde{\mathscr{K}}_{\mu}^{\text{Taylor}} \equiv \left\{ \tilde{\boldsymbol{u}}_{\mu},\ \text{sufficiently regular} \;\middle|\; \tilde{\boldsymbol{u}}_{\mu}\left(\boldsymbol{Y},t\right)=\boldsymbol{0},\quad \forall \boldsymbol{Y}\in\Omega_{\mu,0} \right\}. \tag{3.29}$$

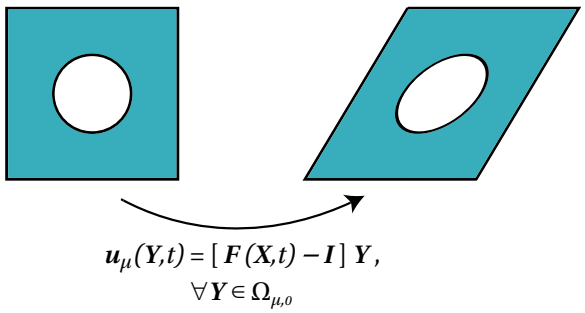


Figure 3.2: Micro-scale Taylor boundary condition model.

In light of the above, one significant drawback of the Taylor model is that it neglects the mechanical interactions between the RVE heterogeneities. Therefore, it may be rather inadequate when dealing with multiphase materials, given that the strain field near the boundary between solid phases may significantly affect the macroscopic behaviour of the material.

Linear boundary condition

The linear boundary condition relaxes Taylor's hypothesis by imposing the null microscopic displacements fluctuations only on the boundary of the RVE (see Figure 3.3),

$$\tilde{\boldsymbol{u}}_{\mu}\left(\boldsymbol{Y},t\right)=\boldsymbol{0},\quad \forall \boldsymbol{Y}\in\partial\Omega_{\mu,0}. \tag{3.30}$$

Note that, the displacement $\boldsymbol{u}_{\mu}$ on the boundary continues to be linearly dependent on $\boldsymbol{Y}$. This boundary condition continues to satisfy Equations 3.13 and 3.19; however, Equation 3.20 is only verified in the absence of body forces and accelerations. This is a plausible assumption in a quasi-static formulation, where inertial effects are disregarded, and in the absence of other body forces.

In accordance, the set of kinematically admissible microscopic displacement

fluctuations minimally constrained by the linear boundary condition is given by

$$\mathscr{K}_{\mu}^{\text{Linear}} \equiv \left\{ \tilde{\boldsymbol{u}}_{\mu},\ \text{sufficiently regular} \;\middle|\; \tilde{\boldsymbol{u}}_{\mu}\left(\boldsymbol{Y},t\right)=\boldsymbol{0},\quad \forall\,\boldsymbol{Y}\in\partial\Omega_{\mu,0} \right\}. \tag{3.31}$$

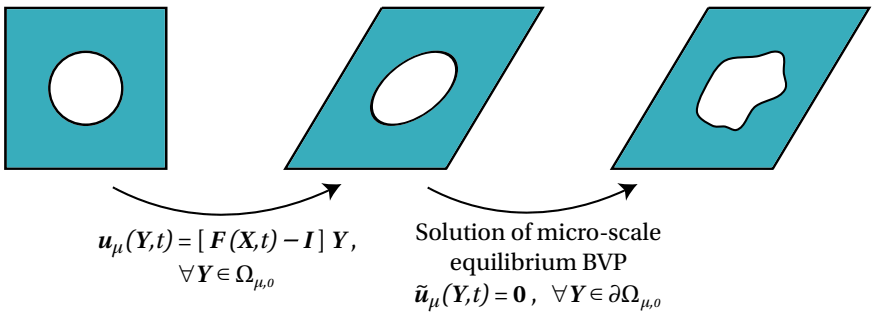


Figure 3.3: Micro-scale linear boundary condition.

Periodic boundary condition

The periodic boundary condition is generally used to describe the behaviour of materials having periodic/repetitive microstructures. It is assumed that a periodic structure maintains its periodicity under deformation. So, the fundamental premise behind this condition is that opposite sides of the RVE boundary must be compatible with respect to displacement if a pattern of identical RVEs can replicate the microstructure (see Figure 3.4) (Speirs, 2007).

In light of this, suppose that the RVE boundary is split into d equal pair groups in such a way that

$$\partial\Omega_{\mu,0} = \bigcup_{i=1}^{d} \partial\Omega_{\mu,0,i}, \qquad \partial\Omega_{\mu,0,i} = \left(\Gamma_{i}^{-} \cup \Gamma_{i}^{+}\right). \tag{3.32}$$

Each point on the positive side, $\boldsymbol{Y}^{+}\in\Gamma_{i}^{+}$, of each group $\partial\Omega_{\mu,0,i}$ has a pair on the opposite negative side, $\boldsymbol{Y}^{-}\in\Gamma_{i}^{-}$. Additionally, the unitary vectors $\boldsymbol{n}^{+}$ and $\boldsymbol{n}^{-}$, respectively normal to Γ_{i}^{+} and Γ_{i}^{-}, must be antisymmetric ($\boldsymbol{n}^{+}=\boldsymbol{n}^{-}$), such that the periodic boundary condition is given by

$$\tilde{\boldsymbol{u}}_{\mu}\left(\boldsymbol{Y}^{+},t\right) = \tilde{\boldsymbol{u}}_{\mu}\left(\boldsymbol{Y}^{-},t\right). \tag{3.33}$$

This expression reflects that the displacement fluctuations are equal on opposing sides of the RVE boundary

In accordance, the set of kinematically admissible microscopic displacement fluctuations minimally constrained by the periodic boundary condition is given by

$$\mathscr{K}_{\mu}^{\text{Periodic}} \equiv \Big\{ \tilde{\boldsymbol{u}}_{\mu},\ \text{sufficiently regular} \ \Big| \ \tilde{\boldsymbol{u}}_{\mu}\left(\boldsymbol{Y}^{+},t\right) = \tilde{\boldsymbol{u}}_{\mu}\left(\boldsymbol{Y}^{-},t\right),\ \ \forall \boldsymbol{Y}^{+} \in \partial\Omega_{\mu,0}^{+},\ \forall \boldsymbol{Y}^{-} \in \partial\Omega_{\mu,0}^{-} \Big\}. \tag{3.34}$$

Moreover, it is possible to demonstrate that the aforementioned constraint can only be met if the traction forces field is anti-periodic, i.e.,

$$\boldsymbol{t}_{\mu,0}\left(\boldsymbol{Y}^{+},t\right) = \boldsymbol{t}_{\mu,0}\left(\boldsymbol{Y}^{-},t\right). \tag{3.35}$$

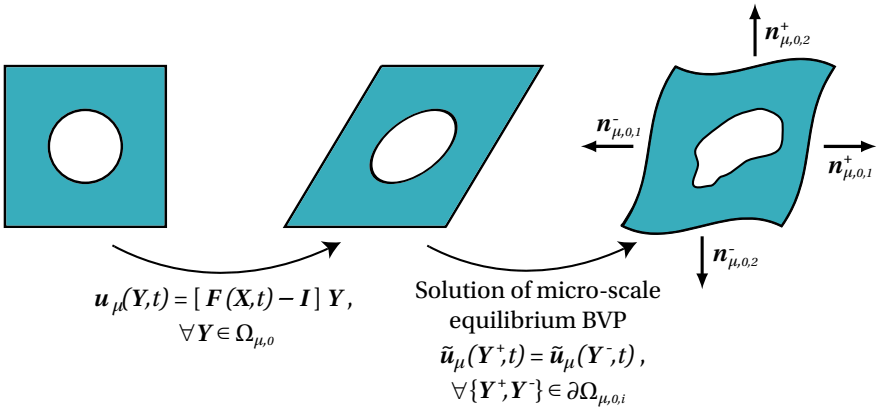


Figure 3.4: Micro-scale periodic boundary condition.

The periodic boundary model implies neither periodicity in the micro-heterogeneities nor in the distribution of the micro-singularities over the RVE. Furthermore, the RVE's periodic repetition is not necessarily global, which indicates that the macroscopic body may not be made up of the recurrence of a single RVE. The periodicity could only be local (Guedes and Kikuchi, 1990).

Uniform boundary traction model

Lastly, the uniform boundary traction model is the least restrictive one, mandating only that the minimal restriction specified by Equation 3.13 must be met (see Figure 3.5). This indicates that the set of kinematically acceptable microscopic displacement fluctuations constrained by the uniform traction boundary condition is equivalent to the set of kinematically admissible

minimally constrained microscopic displacement fluctuations,

$$\mathscr{K}_{\mu}^{\text{U. Traction}} \equiv \left\{ \tilde{\boldsymbol{u}}_{\mu},\ \text{sufficiently regular} \ \middle|\ \int_{\partial\Omega_{\mu,0}} \tilde{\boldsymbol{u}}_{\mu}\left(\boldsymbol{Y},t\right) \otimes \boldsymbol{n}_{\mu,0}\left(\boldsymbol{Y}\right) da = \boldsymbol{0} \right\}. \tag{3.36}$$

Moreover, it is possible to demonstrate that the traction along the RVE boundary is uniform and equal to the homogenised traction, i.e.,

$$\boldsymbol{t}_{\mu,0}\left(\boldsymbol{Y},t\right) = \boldsymbol{P}_{\mu}\left(\boldsymbol{Y},t\right)\boldsymbol{n}_{\mu,0}\left(\boldsymbol{Y},t\right) = \boldsymbol{P}\left(\boldsymbol{X},t\right)\boldsymbol{n}_{\mu,0}\left(\boldsymbol{Y},t\right), \quad \forall \boldsymbol{Y} \in \partial\Omega_{\mu,0}. \tag{3.37}$$

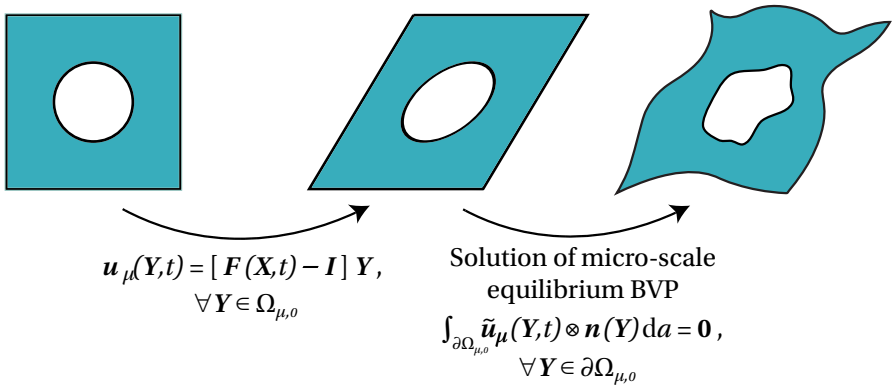


Figure 3.5: Micro-scale uniform traction boundary condition.

It should be noted that, this type of kinematical restriction may provide unrealistic or nonsensical results when dealing with large strains, as spurious effects may occur (Coenen et al., 2012).

Convergence of the boundary condition models

As explained, the suggested models have various degrees of restrictions, which result in different material responses. In general terms, when compared to the effective response, the stiffness is often underestimated for uniform traction and overestimated for linear and periodic boundary conditions. Additionally, as also seen, the RVE size affects the accuracy of the properties obtained through homogenisation. Being that the homogenised attributes converge to their effective value as the RVE's size grows. A smaller RVE will have fewer heterogeneities, leading to their response differing from the typical macroscopic one (Terada et al., 2000).

The impact of the RVE size and the boundary conditions are both shown schematically in Figure 3.6. As the RVE's size grows, the periodic boundary condition converges to the actual value more quickly. Therefore, in comparison to the other models, smaller RVEs (and, hence, less computational effort) are needed to obtain results with similar accuracy. An upper and a lower bound of the periodic boundary condition are defined, respectively, by the linear boundary condition and the uniform traction one.

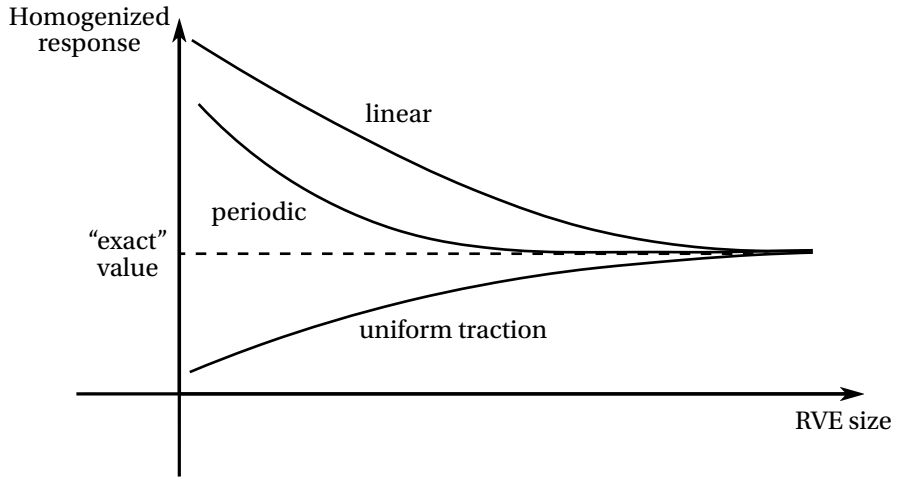


Figure 3.6: Convergence of homogenised characteristics at varied boundary conditions and RVE sizes.

3.3 Numerical Formulation

The microscopic weak equilibrium equations are susceptible to a numerical solution based on the finite element method. This approach was already presented in Section 2.8 to address the macroscopic equilibrium problem. However, for this particular case, extra numerical processing is needed to impose the micro-scale boundary conditions as well as to obtain the homogenised consistent tangent modulus.

3.3.1 Time Discretisation

The methodology applied in Section 2.8.1, which adopts an algorithm based on approximated incremental constitutive functions, is also used for the time discretisation of the micro-scale equilibrium. Likewise, considering the time

increment $\left[t_n, t_{n+1}\right]$, the same conditions stated in Equations 2.129-2.131 must be satisfied. The microscopic internal variables will be represented by $\boldsymbol{\beta}$.

By applying the aforementioned time discretisation to the incremental version of the micro-scale equilibrium problem, it can then be stated in the spatial description as

Problem 2.7 | Spatial incremental quasi-static micro-scale mechanical initial boundary value problem.

For a given macro-scale spatial particle $\boldsymbol{x}$, the associated macro-scale deformation gradient $\boldsymbol{F}\left(\boldsymbol{x}, t\right)$ at t_{n+1} and the set of internal variables $\boldsymbol{\beta}_n$ at t_n, find the kinematically admissible microscopic displacement fluctuations, $\tilde{\boldsymbol{u}}_{\mu,n+1} \in \tilde{\mathscr{K}}_{\mu,n+1}$, such that the RVE is in equilibrium as stated by the Principle of Multi-scale Virtual Power

$$\int_{\Omega_\mu} \hat{\boldsymbol{\sigma}}_\mu \left(\boldsymbol{F}_{\mu,n+1}, \boldsymbol{\beta}_n\right) : \nabla \boldsymbol{\eta}_\mu \, dv = 0, \qquad \forall \boldsymbol{\eta}_\mu \in \mathscr{K}_\mu, \tag{3.38}$$

where the space of virtual displacement fluctuations, $\mathscr{K}_{\mu,n+1}$, at time t_{n+1}, is defined by the set of kinematically admissible displacement fluctuations constrained by the adopted micro-scale boundary condition.

3.3.2 Spatial Discretisation

The spatial discretised incremental quasi-static micro-scale initial BVP can be stated in the spatial and material descriptions as

Problem 2.8 | Spatial discretised quasi-static micro-scale mechanical initial boundary value problem.

For a given macro-scale spatial particle $\boldsymbol{x}$, the associated macro-scale deformation gradient $\boldsymbol{F}\left(\boldsymbol{x}, t\right)$ at t_{n+1} and the set of internal variables $\boldsymbol{\beta}_n$ at t_n, find the kinematically admissible microscopic nodal displacement fluctuations, $\tilde{\mathbf{u}}_{\mu,n+1} \in {}^h\tilde{\mathscr{K}}_{\mu,n+1}$, such that the RVE is in equilibrium as stated by the Principle of Multi-scale Virtual Power

$$\mathbf{f}_\mu^{\text{int}} \left(\tilde{\mathbf{u}}_{\mu,n+1}\right) = \mathbf{0}, \tag{3.39}$$

where $\mathbf{f}_\mu^{\text{int}}$ is the global vector of internal forces defined as

$$\mathbf{f}_\mu^{\text{int}} = \int_{{}^h\Omega_\mu} \left(\mathbf{B}^g\right)^T \hat{\boldsymbol{\sigma}} \left(\boldsymbol{F}_{\mu,n+1}, \boldsymbol{\beta}_n\right) dv. \tag{3.40}$$

3.3.3 Newton-Raphson Algorithm

Applying the Newton-Raphson Method once again to address the typically non-linear micro-scale equilibrium problem is possible. It is crucial to note at this point that Equation 3.39 is entirely general regarding the micro-scale boundary conditions. Therefore, different methods, such as the Lagrange multipliers or the condensation techniques, have been suggested to enforce it. The condensation process will be the one employed going forward due to its ease of use and the way it accounts for the micro-scale boundary conditions without adding a considerable degree of complexity to the linearisation of the micro-scale equilibrium problem.

The Condensation Method begins by dividing the degrees of freedom into four separate groups.

- ***Interior (i)*** *- Related to the nodes in the interior of the RVE;*
- ***Boundary (b)*** *- Related to the nodes in the boundary of the RVE:*
  - ***Free (f)*** *- whose displacement fluctuation is free;*
  - ***Dependent (d)*** *- whose displacement fluctuation depends on free degrees of freedom;*
  - ***Prescribed (p)*** *- whose displacement fluctuation is null by prescription to avoid rigid body motion.*

Accordingly, the global vector of nodal displacements fluctuations, the virtual displacements and the internal forces can be re-arranged, respectively, as

$$\tilde{\boldsymbol{u}}_\mu = \begin{Bmatrix} \tilde{\mathbf{u}}_\mu^i \\ \tilde{\mathbf{u}}_\mu^f \\ \tilde{\mathbf{u}}_\mu^d \\ \tilde{\mathbf{u}}_\mu^p \end{Bmatrix}, \quad \boldsymbol{\eta}_\mu = \begin{Bmatrix} \boldsymbol{\eta}_\mu^i \\ \boldsymbol{\eta}_\mu^f \\ \boldsymbol{\eta}_\mu^d \\ \boldsymbol{\eta}_\mu^p \end{Bmatrix}, \quad \mathbf{f}_\mu^{\text{int}} = \begin{Bmatrix} \mathbf{f}_\mu^i \\ \mathbf{f}_\mu^f \\ \mathbf{f}_\mu^d \\ \mathbf{f}_\mu^p \end{Bmatrix}. \tag{3.41}$$

Similar to the analysis done for the macro-scale, the linearised version of the spatial micro-scale equilibrium equation is provided $\forall \boldsymbol{\eta}_\mu \in {}^h\mathcal{V}_\mu$ by

$$\boldsymbol{\eta}_\mu^T \left\{ \left\{ \int_{{}^h\Omega_\mu} \left(\mathbf{G}^g\right)^T \mathbf{a} \mathbf{G}^g \, dv \right\} \delta\tilde{\mathbf{u}}_\mu + \int_{{}^h\Omega_\mu} \left(\mathbf{B}^g\right)^T \hat{\boldsymbol{\sigma}}_\mu \left(\boldsymbol{F}_{\mu,n+1}, \boldsymbol{\beta}_n \right) dv \right\} = 0, \tag{3.42}$$

or, alternatively, in the material description by

$$\boldsymbol{\eta}_{\mu}^{T}\left\{\left\{\int_{{}^{h}\Omega_{\mu,0}}\left(\mathbf{G}^{g}\right)^{T}\mathbf{A}\mathbf{G}^{g}\,dv\right\}\delta\tilde{\mathbf{u}}_{\mu}+\int_{{}^{h}\Omega_{\mu,0}}\left(\mathbf{B}^{g}\right)^{T}\hat{\mathbf{P}}_{\mu}\left(\boldsymbol{F}_{\mu,n+1},\boldsymbol{\beta}_{n}\right)dv\right\}=0. \quad (3.43)$$

Remembering that the spatial and material descriptions define the global tangent stiffness matrix, respectively, as

$$\mathbf{K}_{T}=\int_{{}^{h}\Omega_{\mu}}\left(\mathbf{G}^{g}\right)^{T}\mathbf{a}\mathbf{G}^{g}\,dv, \quad (3.44)$$

$$\mathbf{K}_{T}=\int_{{}^{h}\Omega_{\mu,0}}\left(\mathbf{G}^{g}\right)^{T}\mathbf{A}\mathbf{G}^{g}\,dv, \quad (3.45)$$

and after considering the degrees of freedom split, it is feasible to rewrite both linearised equilibrium equations[1] as

$$\begin{Bmatrix}\boldsymbol{\eta}_{\mu}^{i}\\ \boldsymbol{\eta}_{\mu}^{f}\\ \boldsymbol{\eta}_{\mu}^{d}\\ \boldsymbol{\eta}_{\mu}^{p}\end{Bmatrix}^{T}\left\{\begin{bmatrix}\boldsymbol{k}^{ii} & \boldsymbol{k}^{if} & \boldsymbol{k}^{id} & \boldsymbol{k}^{ip}\\ \boldsymbol{k}^{fi} & \boldsymbol{k}^{ff} & \boldsymbol{k}^{fd} & \boldsymbol{k}^{fp}\\ \boldsymbol{k}^{di} & \boldsymbol{k}^{df} & \boldsymbol{k}^{dd} & \boldsymbol{k}^{dp}\\ \boldsymbol{k}^{pi} & \boldsymbol{k}^{pf} & \boldsymbol{k}^{pd} & \boldsymbol{k}^{pp}\end{bmatrix}\begin{Bmatrix}\Delta\tilde{\mathbf{u}}_{\mu}^{i}\\ \Delta\tilde{\mathbf{u}}_{\mu}^{f}\\ \Delta\tilde{\mathbf{u}}_{\mu}^{d}\\ \Delta\tilde{\mathbf{u}}_{\mu}^{p}\end{Bmatrix}+\begin{Bmatrix}\mathbf{f}_{\mu}^{i}\\ \mathbf{f}_{\mu}^{f}\\ \mathbf{f}_{\mu}^{d}\\ \mathbf{f}_{\mu}^{p}\end{Bmatrix}\right\}=0,\quad\forall\boldsymbol{\eta}_{\mu}\in{}^{h}\mathcal{V}_{\mu}. \quad (3.46)$$

Employing the condensation method, the micro-scale boundary conditions can now be introduced. Firstly, the appropriate prescribed boundary degrees of freedom (p) are chosen to prevent rigid body motions. Next, the dependent degrees of freedom (d) are chosen in consideration of the imposed boundary conditions. And finally, the relation between the dependent and the free degrees of freedom is established,

$$\tilde{\mathbf{u}}_{\mu}^{d}=\boldsymbol{\Theta}\tilde{\mathbf{u}}_{\mu}^{f}, \quad (3.47)$$

where $\boldsymbol{\Theta}$ is the dependency matrix. Taking into account this relation together with the fact that $\tilde{\mathbf{u}}_{\mu}^{p}=0$ yields

$$\begin{Bmatrix}\boldsymbol{\eta}_{\mu}^{i}\\ \boldsymbol{\eta}_{\mu}^{f}\\ \boldsymbol{\Theta}\boldsymbol{\eta}_{\mu}^{f}\end{Bmatrix}^{T}\left\{\begin{bmatrix}\boldsymbol{k}^{ii} & \boldsymbol{k}^{if} & \boldsymbol{k}^{id}\\ \boldsymbol{k}^{fi} & \boldsymbol{k}^{ff} & \boldsymbol{k}^{fd}\\ \boldsymbol{k}^{di} & \boldsymbol{k}^{df} & \boldsymbol{k}^{dd}\end{bmatrix}\begin{Bmatrix}\Delta\tilde{\mathbf{u}}_{\mu}^{i}\\ \Delta\tilde{\mathbf{u}}_{\mu}^{f}\\ \boldsymbol{\Theta}\Delta\tilde{\mathbf{u}}_{\mu}^{f}\end{Bmatrix}+\begin{Bmatrix}\mathbf{f}_{\mu}^{i}\\ \mathbf{f}_{\mu}^{f}\\ \mathbf{f}_{\mu}^{d}\end{Bmatrix}\right\}=0,\quad\forall\boldsymbol{\eta}_{\mu}\in{}^{h}\mathcal{V}_{\mu}. \quad (3.48)$$

[1]The computation of the global stiffness matrices and vectors of internal forces is accomplished according to the spatial or material description.

Afterwards, by applying condensation to vector $\Delta\tilde{\mathbf{u}}_\mu$ yields

$$\begin{Bmatrix} \boldsymbol{\eta}_\mu^i \\ \boldsymbol{\eta}_\mu^f \\ \boldsymbol{\Theta}\boldsymbol{\eta}_\mu^f \end{Bmatrix}^T \left\{ \begin{bmatrix} \boldsymbol{k}^{ii} & \boldsymbol{k}^{if} & \boldsymbol{k}^{id}\boldsymbol{\Theta} \\ \boldsymbol{k}^{fi} & \boldsymbol{k}^{ff} & \boldsymbol{k}^{fd}\boldsymbol{\Theta} \\ \boldsymbol{k}^{di} & \boldsymbol{k}^{df} & \boldsymbol{k}^{dd}\boldsymbol{\Theta} \end{bmatrix} \begin{Bmatrix} \Delta\tilde{\mathbf{u}}_\mu^i \\ \Delta\tilde{\mathbf{u}}_\mu^f \end{Bmatrix} + \begin{Bmatrix} \mathbf{f}_\mu^i \\ \mathbf{f}_\mu^f \\ \mathbf{f}_\mu^d \end{Bmatrix} \right\} = 0, \quad \forall \boldsymbol{\eta}_\mu \in {}^h\mathcal{V}_\mu, \tag{3.49}$$

and applying the same procedure to vector $\boldsymbol{\eta}$ results in

$$\begin{Bmatrix} \boldsymbol{\eta}_\mu^i \\ \boldsymbol{\eta}_\mu^f \end{Bmatrix}^T \left\{ \begin{bmatrix} \boldsymbol{k}^{ii} & \boldsymbol{k}^{if} + \boldsymbol{k}^{id}\boldsymbol{\Theta} \\ \boldsymbol{k}^{fi} + \boldsymbol{\Theta}^T\boldsymbol{k}^{di} & \boldsymbol{k}^{ff} + \boldsymbol{k}^{fd}\boldsymbol{\Theta} + \boldsymbol{\Theta}^T\boldsymbol{k}^{df} + \boldsymbol{\Theta}^T\boldsymbol{k}^{dd}\boldsymbol{\Theta} \end{bmatrix} \begin{Bmatrix} \Delta\tilde{\mathbf{u}}_\mu^i \\ \Delta\tilde{\mathbf{u}}_\mu^f \end{Bmatrix} + \begin{Bmatrix} \mathbf{f}_\mu^i \\ \mathbf{f}_\mu^f + \boldsymbol{\Theta}^T\mathbf{f}_\mu^d \end{Bmatrix} \right\} = 0, \quad \forall \boldsymbol{\eta}_\mu \in {}^h\mathcal{V}_\mu. \tag{3.50}$$

Since the equality must hold for every $\boldsymbol{\eta}_\mu \in {}^h\mathcal{V}_\mu$, each Newton-Raphson Method iteration (k) consists of solving the following system of linear equations

$$\begin{bmatrix} \boldsymbol{k}^{ii} & \boldsymbol{k}^{if} + \boldsymbol{k}^{id}\boldsymbol{\Theta} \\ \boldsymbol{k}^{fi} + \boldsymbol{\Theta}^T\boldsymbol{k}^{di} & \boldsymbol{k}^{ff} + \boldsymbol{k}^{fd}\boldsymbol{\Theta} + \boldsymbol{\Theta}^T\boldsymbol{k}^{df} + \boldsymbol{\Theta}^T\boldsymbol{k}^{dd}\boldsymbol{\Theta} \end{bmatrix}^{(k-1)} \begin{Bmatrix} \Delta\tilde{\mathbf{u}}_\mu^i \\ \Delta\tilde{\mathbf{u}}_\mu^f \end{Bmatrix} = - \begin{Bmatrix} \mathbf{f}_\mu^i \\ \mathbf{f}_\mu^f + \boldsymbol{\Theta}^T\mathbf{f}_\mu^d \end{Bmatrix}^{(k-1)}. \tag{3.51}$$

$\Delta\tilde{\mathbf{u}}$ is identified by solving Equation 3.54 and applying Equation 3.47. Then, in each cycle, the global vector of nodal displacement fluctuations is updated by

$$\tilde{\mathbf{u}}_{\mu,n+1}^{(k)} = \tilde{\mathbf{u}}_{\mu,n+1}^{(k-1)} + \Delta\tilde{\mathbf{u}}_\mu. \tag{3.52}$$

When the solution $\mathbf{u}_{\mu,n+1}^{(k)}$ fulfills a certain convergence criterion, the iterative procedure comes to an end. Take note that Equation 3.9 determines $\mathbf{u}_{\mu,n+1}^{(k)}$.

3.3.4 Dependency Matrix

The system of linear equations for the RVE equilibrium set in Equation 3.54 remains general despite introducing the dependency matrix as a valuable means of enforcing the micro-scale boundary conditions. Therefore, the dependency matrix will next be presented specifically for each boundary condition.

Linear boundary condition

The RVE boundary is subjected to a null displacement fluctuation field imposed by the linear boundary condition, thus $\tilde{\mathbf{u}}_\mu^b = \tilde{\mathbf{u}}_\mu^f = \tilde{\mathbf{u}}_\mu^d = \mathbf{0}$. The specification of the dependency matrix, $\boldsymbol{\Theta}$, is thus unnecessary, and the system of equations is only reduced to

$$\boldsymbol{k}^{ii} \Delta \tilde{\mathbf{u}}_\mu^i = -\mathbf{f}_\mu^i. \tag{3.53}$$

As a result, the inner degrees of freedom, $\tilde{\mathbf{u}}_\mu^i$, are the only unknowns. The RVE boundary's imposed restriction automatically prevents rigid body movements, so no interior degrees of freedom need to be specified.

Periodic boundary condition

Each pair of boundary edges or surfaces for the periodic boundary condition is divided into two sides. One is categorised as "negative" and is associated with the free degrees of freedom, and the other as "positive" and is related to the dependent degrees of freedom. If the displacement fluctuation vectors, $\tilde{\mathbf{u}}_\mu^f$ and $\tilde{\mathbf{u}}_\mu^d$, are arranged in such a one-to-one relation, then the identity matrix serves as the dependency matrix ($\boldsymbol{\Theta} = \boldsymbol{I}$). The set of equations may then be simplified to

$$\begin{bmatrix} \boldsymbol{k}^{ii} & \boldsymbol{k}^{i-} + \boldsymbol{k}^{i+} \\ \boldsymbol{k}^{-i} + \boldsymbol{k}^{+i} & \boldsymbol{k}^{--} + \boldsymbol{k}^{-+} + \boldsymbol{k}^{+-} + \boldsymbol{k}^{++} \end{bmatrix}^{(k-1)} \begin{Bmatrix} \Delta \tilde{\mathbf{u}}_\mu^i \\ \Delta \tilde{\mathbf{u}}_\mu^f \end{Bmatrix} = - \begin{Bmatrix} \mathbf{f}_\mu^i \\ \mathbf{f}_\mu^- + \mathbf{f}_\mu^+ \end{Bmatrix}^{(k-1)}. \tag{3.54}$$

Note that the RVE boundary corners are prescribed with null displacement fluctuations to prevent rigid body motions and comply with the periodicity requirement.

Uniform boundary traction model

In contrast to the other models, the uniform traction boundary condition requires a precise description of the dependency matrix and does not allow for the system of equations to be further simplified. First, the restriction imposed by the displacement fluctuations must be spatially discretised in a finite element sense resulting in

$$\int_{h\Omega_{\mu,o}} \left(\mathbf{N}^b\right)^g \tilde{\mathbf{u}}_\mu^b \otimes \boldsymbol{n}\, da = \mathbf{0}. \tag{3.55}$$

It is feasible to demonstrate that the previously discretised requirement may be rewritten as

$$\mathbf{C}\tilde{\mathbf{u}}_\mu^b = \mathbf{0}, \tag{3.56}$$

where $\mathbf{C}$ is the constraint matrix, which can be assembled from its elemental counterparts as

$$\mathbf{C} = \mathop{\mathsf{A}}_{e=1}^{n_{\text{elem}}} \mathbf{C}^{(e)}. \tag{3.57}$$

In turn, the elemental constraint matrix for 2D problems is given by

$$\mathbf{C}^{(e)} = \begin{bmatrix} \dots & \int N_i n_1 & 0 & \dots \\ \dots & 0 & \int N_i n_2 & \dots \\ \dots & \int N_i n_2 & 0 & \dots \\ \dots & 0 & \int N_i n_1 & \dots \end{bmatrix}, \tag{3.58}$$

where N_i is the shape function associated with node i, and n_j are the components of the unitary vector normal do the boundary of the RVE, $\boldsymbol{n}$.

So, one may conclude that the number of dependent degrees of freedom is determined by the number of linear constraints imposed by the uniform traction boundary condition (ex: 4 for 2D and 9 for 3D problems). So, it is practical to divide the constraint matrix as

$$\begin{bmatrix} \mathbf{C}^f & \mathbf{C}^d \end{bmatrix} \begin{Bmatrix} \tilde{\mathbf{u}}_\mu^f \\ \tilde{\mathbf{u}}_\mu^d \end{Bmatrix} = \mathbf{0}, \tag{3.59}$$

where $\mathbf{C}^d$ is a square matrix, allowing rewriting the above expression to

$$\tilde{\mathbf{u}}_\mu^d = -\left[\mathbf{C}^d\right]^{-1} \left[\mathbf{C}^f\right] \tilde{\mathbf{u}}^f. \tag{3.60}$$

Lastly, the dependency matrix may be expressed as

$$\boldsymbol{\Theta} = -\left[\mathbf{C}^d\right]^{-1} \left[\mathbf{C}^f\right], \tag{3.61}$$

and must only be established once during the problem initialisation, after which it does not change. Moreover, the dependent degrees of freedom must be carefully chosen to guarantee the nonsingularity of the dependent constraint matrix, $\mathbf{C}^d$. Moreover, only the prescription of 2 or 3 appropriate degrees of

freedom is needed to prevent rigid body translation, as the minimum kinematic acceptable constraint automatically constrains rigid body rotation.

3.3.5 Homogenised Stress Tensor

It is possible to compute the first Piola-Kirchhoff stress tensor by discretising Equation 3.23 as

$$\mathbf{P}\left(\boldsymbol{X}, t\right) = \frac{1}{v_{\mu,0}} \mathbf{D}^b \mathbf{f}_\mu^b, \tag{3.62}$$

where $\mathbf{f}_\mu^b$ is the vector of internal nodal forces associated with the boundary nodes, and $\mathbf{D}^b$ is the boundary reference nodal coordinates matrix

$$\mathbf{D}^b = \begin{bmatrix} \mathbf{D}_1 & \mathbf{D}_2 & \dots & \mathbf{D}_{n_b}, \end{bmatrix}. \tag{3.63}$$

In turn, n_b is the number of boundary nodes and $\mathbf{D}_i$ is the i^{th} reference node coordinates matrix defined in 2D problems as

$$\mathbf{D}_i = \begin{bmatrix} Y_1 \boldsymbol{I} \\ Y_2 \boldsymbol{I} \end{bmatrix}_i, \tag{3.64}$$

and in 3D ones as

$$\mathbf{D}_i = \begin{bmatrix} Y_1 \boldsymbol{I} \\ Y_2 \boldsymbol{I} \\ Y_3 \boldsymbol{I} \end{bmatrix}_i. \tag{3.65}$$

3.3.6 Homogenised Consistent Tangent Modulus

The Newton-Raphson methodology iterative at the macro-scale still requires a tangent matrix compatible with the state updating mechanism once the micro-scale equilibrium problem has been solved and the macro-scale stress tensor has been computed. At each integration point, the material's consistent tangent modulus is defined as

$$\mathbf{A} = \frac{\partial \boldsymbol{P}}{\partial \mathbf{F}}, \tag{3.66}$$

and in the discretised domain as

$$\mathbf{A} = \frac{\partial \boldsymbol{P}}{\partial \mathbf{F}} = \frac{1}{v_{\mu,0}} \mathbf{D}^b \frac{\partial \mathbf{f}_\mu^b}{\partial \mathbf{F}}, \tag{3.67}$$

By employing the condensation procedure to partition the degrees of freedom and the derivation chain rule, it is viable to express

$$\begin{aligned}\mathbf{A} &= \frac{1}{v_{\mu,0}}\mathbf{D}^b \frac{\partial \mathbf{f}_\mu^b}{\partial \mathbf{u}_\mu}\frac{\partial \mathbf{u}_\mu}{\partial \mathbf{F}} \\ &= \frac{1}{v_{\mu,0}}\mathbf{D}^b \left[\frac{\partial \mathbf{f}_\mu^b}{\partial \mathbf{u}_\mu^i}\frac{\partial \mathbf{u}_\mu^i}{\partial \mathbf{F}} + \frac{\partial \mathbf{f}_\mu^b}{\partial \mathbf{u}_\mu^f}\frac{\partial \mathbf{u}_\mu^f}{\partial \mathbf{F}} + \frac{\partial \mathbf{f}_\mu^b}{\partial \mathbf{u}_\mu^d}\frac{\partial \mathbf{u}_\mu^d}{\partial \mathbf{F}} + \frac{\partial \mathbf{f}_\mu^b}{\partial \mathbf{u}_\mu^p}\frac{\partial \mathbf{u}_\mu^p}{\partial \mathbf{F}}\right] \\ &= \frac{1}{v_{\mu,0}}\mathbf{D}^b \left[\mathbf{K}^{bi}\frac{\partial \mathbf{u}_\mu^i}{\partial \mathbf{F}} + \mathbf{K}^{bf}\frac{\partial \mathbf{u}_\mu^f}{\partial \mathbf{F}} + \mathbf{K}^{bd}\frac{\partial \mathbf{u}_\mu^d}{\partial \mathbf{F}} + \mathbf{K}^{bp}\frac{\partial \mathbf{u}_\mu^p}{\partial \mathbf{F}}\right].\end{aligned} \tag{3.68}$$

Equation 3.9 microscopic displacement field's spatial discretisation enables a generic definition of the derivatives of interest as

$$\frac{\partial \mathbf{u}_\mu^{(\cdot)}}{\partial \mathbf{F}} = \left(\mathbf{D}^{(\cdot)}\right)^T + \frac{\partial \tilde{\mathbf{u}}_\mu^{(\cdot)}}{\partial \mathbf{F}}, \tag{3.69}$$

with $(\cdot)$ denoting a given group of nodes. Substituting this expression in Equation 3.68 results in

$$\begin{aligned}\mathbf{A} = \frac{1}{v_{\mu,0}}\mathbf{D}^b \Bigg[\mathbf{K}^{bi}\frac{\partial \tilde{\mathbf{u}}_\mu^i}{\partial \mathbf{F}} + \mathbf{K}^{bf}\frac{\partial \tilde{\mathbf{u}}_\mu^f}{\partial \mathbf{F}} + \mathbf{K}^{bd}\frac{\partial \tilde{\mathbf{u}}_\mu^d}{\partial \mathbf{F}} + \mathbf{K}^{bp}\frac{\partial \tilde{\mathbf{u}}_\mu^p}{\partial \mathbf{F}} + \mathbf{K}^{bi}\left(\mathbf{D}^i\right)^T + \\ \mathbf{K}^{bf}\left(\mathbf{D}^f\right)^T + \mathbf{K}^{bd}\left(\mathbf{D}^d\right)^T + \mathbf{K}^{bp}\left(\mathbf{D}^p\right)^T\Bigg],\end{aligned} \tag{3.70}$$

which has the following matricial notation

$$\mathbf{A} = \frac{1}{v_{\mu,0}}\mathbf{D}^b \left[\begin{bmatrix}\mathbf{K}^{bi} & \mathbf{K}^{bf} & \mathbf{K}^{bd}\end{bmatrix} \begin{bmatrix}\frac{\partial \tilde{\mathbf{u}}_\mu^i}{\partial \mathbf{F}} \\ \frac{\partial \tilde{\mathbf{u}}_\mu^f}{\partial \mathbf{F}} \\ \frac{\partial \tilde{\mathbf{u}}_\mu^d}{\partial \mathbf{F}}\end{bmatrix} + \mathbf{K}^B\mathbf{D}^T\right], \tag{3.71}$$

where $\mathbf{K}^B$ is the boundary-related stiffness matrix

$$\mathbf{K}^B = \begin{bmatrix}\mathbf{k}^{fi} & \mathbf{k}^{ff} & \mathbf{k}^{fd} & \mathbf{k}^{fp} \\ \mathbf{k}^{di} & \mathbf{k}^{df} & \mathbf{k}^{dd} & \mathbf{k}^{dp} \\ \mathbf{k}^{pi} & \mathbf{k}^{pf} & \mathbf{k}^{pd} & \mathbf{k}^{pp}\end{bmatrix}, \tag{3.72}$$

and $\mathbf{D}$ is the total reference nodal coordinates matrix

$$\mathbf{D} = \begin{bmatrix} \mathbf{D}^i & \mathbf{D}^f & \mathbf{D}^d & \mathbf{D}^p \end{bmatrix}. \tag{3.73}$$

Lastly, by using, once again, the condensation procedure and recalling Equation 3.47, the homogenised consistent tangent modulus becomes straightforward by recognising that when the RVE is at equilibrium, it is feasible to write

$$\mathbf{A} = \frac{1}{v_{\mu,0}} \mathbf{D}^b \left[\begin{bmatrix} \mathbf{K}^{bi} & \mathbf{K}^{bf} & \mathbf{K}^{bd}\boldsymbol{\Theta} \end{bmatrix} \begin{bmatrix} \frac{\partial \tilde{\mathbf{u}}_\mu^i}{\partial \mathbf{F}} \\ \frac{\partial \tilde{\mathbf{u}}_\mu^f}{\partial \mathbf{F}} \end{bmatrix} + \mathbf{K}^B \mathbf{D}^T \right]. \tag{3.74}$$

The derivatives of the displacement fluctuations must then be evaluated in order to the deformation gradient, to establish the homogenised material consistent tangent modulus fully. This may be done

$$\frac{\partial}{\partial \mathbf{F}} \begin{bmatrix} \mathbf{f}_\mu^i \\ \mathbf{f}_\mu^f + \boldsymbol{\Theta}^T \mathbf{f}_\mu^d \end{bmatrix} = \mathbf{0}. \tag{3.75}$$

Afterwards, with a linearisation and condensation process identical to the one previously provided leads to the following system of linear equations

$$\begin{aligned} \begin{bmatrix} \boldsymbol{k}^{ii} & \boldsymbol{k}^{if} + \boldsymbol{k}^{id}\boldsymbol{\Theta} \\ \boldsymbol{k}^{fi} + \boldsymbol{\Theta}^T \boldsymbol{k}^{di} & \boldsymbol{k}^{ff} + \boldsymbol{k}^{fd}\boldsymbol{\Theta} + \boldsymbol{\Theta}^T \boldsymbol{k}^{df} + \boldsymbol{\Theta}^T \boldsymbol{k}^{dd}\boldsymbol{\Theta} \end{bmatrix}^{(k-1)} \begin{Bmatrix} \frac{\partial \tilde{\mathbf{u}}_\mu^i}{\partial \mathbf{F}} \\ \frac{\partial \tilde{\mathbf{u}}_\mu^f}{\partial \mathbf{F}} \end{Bmatrix} = \\ - \left[\begin{bmatrix} \mathbf{K}^I \\ \mathbf{K}^F + \boldsymbol{\Theta}^T \mathbf{K}^D \end{bmatrix} \mathbf{D}^T \right]^{(k-1)}, \end{aligned} \tag{3.76}$$

where

$$\mathbf{K}^\bullet = \begin{bmatrix} \mathbf{k}^{\bullet i} & \mathbf{k}^{\bullet f} & \mathbf{k}^{\bullet d} & \mathbf{k}^{\bullet p} \end{bmatrix}. \tag{3.77}$$

The necessary derivatives to calculate the homogenised material consistent tangent modulus are provided by the solution of the preceding system of linear equations.

CHAPTER 4

PC/ABS POLYMER BLEND

The current Chapter briefly introduces the materials in this work's scope: ternary blends of polycarbonate (PC) and acrylonitrile-butadiene-styrene (ABS), the latter being a binary blend of styrene-acrylonitrile (SAN) and polybutadiene (PB). As schematically represented in Figure 4.1, the PC/ABS blends are composed of a PC matrix with randomly distributed ABS particles, which are, in turn, composed of a SAN matrix with PB particles. In short, blends are materials consisting of several components, which combined lead to a macroscopically distinguishable behaviour and characteristics from those presented by their constituents individually. The following information is based mainly on the books (Greco, 1996) and (Hund, 2022) and on the PhD thesis (Inberg, 2001) and (Ferreira, 2022), which can be consulted for a more detailed development of the topic.

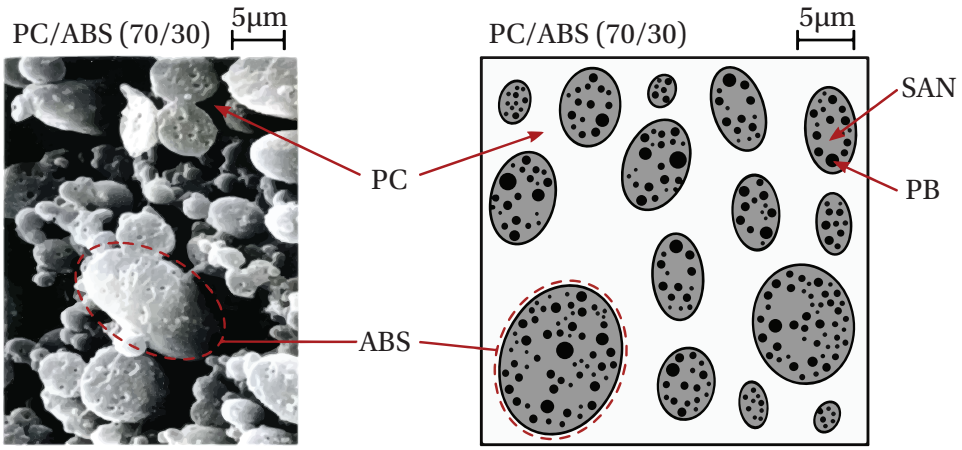


Figure 4.1: Schematic representation of a PC/ABS (70/30) microstructure, evidencing the three phases of the ternary blend. SEM micrograph (PC matrix etched with a NaOH aqueous solution) taken from Greco (1996).

Source: (Ferreira, 2022)

The PC/ABS blends are one of the most successful commercial polymer blends, being available in various compositions to meet the requirements of their applications. Their main technological applications are in the automotive sector (e.g., middle console, lower instrumental panel, overhead console, structural components) and consumer electronics (e.g., electrical connectors and adapters, housings, portable hand-held devices such as phones and flashlights, keyboards). In addition, they are also one of the most suitable materials for conceptual modelling and functional prototyping through three-dimensional (3D) printing.

4.1 Polycarbonate (PC)

Nowadays, PC leads as one of the essential engineering polymeric materials since its first synthesis in 1898 and first production 50 years later, with a worldwide demand of around 4.5 million tons (corresponding to a 2.8-billion-dollar industry) in 2021. It is a linear amorphous glassy thermoplastic and, like all polymeric materials, is a macromolecular material. There are two different types of PC consisting of polyesters of carbonic acid with aliphatic or aromatic (bisphenol-A) dihydroxy compounds, of which the latter, PC-BPA, is the most important for commercial blends with ABS (Figure 4.2 presents its structure).

Commonly, PC manufacturing processes include injection, structural foam and blow moulding, extrusion and vacuum forming. Its main applications/industries are: automotive (e.g., dashboards, headlight lenses, windscreens, exterior cladding), electronics (e.g., connectors, housings, battery casing), packaging (e.g., medical industry, dispensers, bottles, food containers), optical media (e.g., eye protection and swimming goggles, bulletproof glasses) and construction sectors.

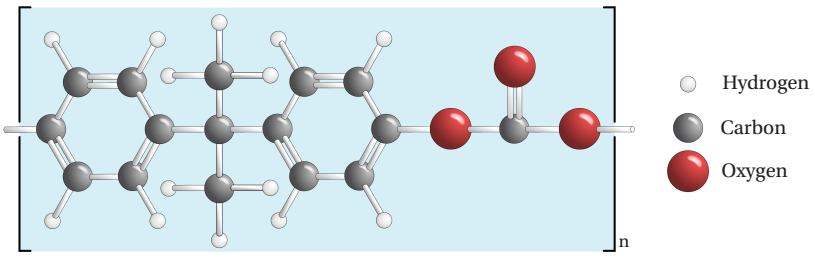
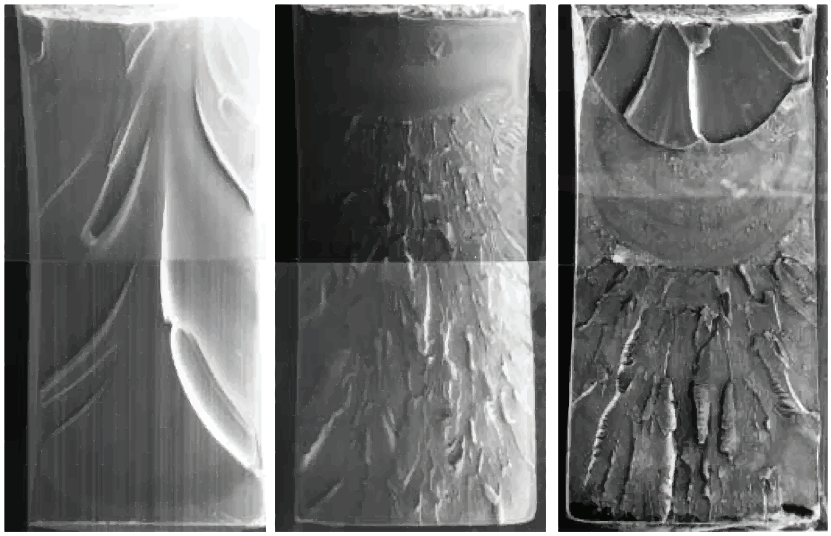


Figure 4.2: Schematic of the molecular structure of the Bisphenol-A Polycarbonate (PC) - repeat unit (molecular conformation is not considered).

Source: (Ferreira, 2022)

It is also worth mentioning that PC shows three modes of failure, as represented in Figure 4.3: (a) entirely ductile, characterised by clearly visible deformation lines at the fracture surface; (b) entirely brittle, characterised by a mirror zone close to the notch tip, followed by an increasingly rough surface, showing signs of mackerel and hackle regions; (c) mixed mode, where the first part of the surface shows ductile-fracture signs and the rest shows brittle-fracture signs (Inberg, 2001).



(a) (b) (c)

Figure 4.3: SEM pictures of fracture surfaces of notched PC specimens, notch at the top. a) ductile, test conditions: 10^{-5} m/s, -50 °C; b) brittle, test conditions: 1 m/s, -20 °C; c) mixed mode, test conditions: 10^{-5} m/s, -60 °C.

Source: (Inberg, 2001)

4.1.1 Properties

Their wide range of applications results from their excellent mechanical, thermal, optical and electric properties, among which can be highlighted (Inberg, 2001; Ferreira, 2022):

1. Good overall mechanical resistance;
2. High unnotched impact resistance;
3. High toughness and ductile fracture in many conditions.;
4. High heat distortion temperature and dimensional stability;
5. Transparency and UV filtration;
6. Glare reduction;
7. Durability and recyclability.

Nonetheless, despite the features defined above, some significant drawbacks restrict the spectrum of its application:

1. Brittle fracture and subsequent losses in toughness at low temperatures, in thick-walled applications, and in the presence of minor defects and scratches. Specifically, sharp microscopic cracks can emerge when the material is exposed to the environment, a phenomenon called environmental stress cracking. In other words, PC provides a high-notch sensitivity and a low-notched impact resistance;
2. Processability issues due to its high melt viscosity, notably in the injection moulding of thin wall products;
3. Low chemical resistance;

4.2 Acrylonitrile-Butadiene-Styrene (ABS)

A widely used solution to mitigate the previously mentioned drawbacks is blending PC with rubber particles. However, this is only practical in applications where the loss of transparency is not important, and therefore a more commercially successful combination is PC blended with acrylonitrile-butadiene-styrene (ABS) (Hund, 2022).

ABS is a binary polymer blend containing an amorphous elastomeric component, usually polybutadiene (PB) or a polybutadiene-based copolymer, in the form of particles well dispersed in an amorphous glassy thermoplastic matrix of styrene-acrylonitrile (SAN) (Figure 4.4 presents its structure). Its main application fields/industries are: home appliances, the construction sector, transportation and automotive industries, electronics and others (Greco, 1996; Hund, 2022; Inberg, 2001; Ferreira, 2022).

ABS can be produced by several methods (such as mechanical blending, polymerisation by emulsion, suspension polymerisation, and bulk polymerisation), which allow it to have high flexibility when tailoring its properties and characteristics to its end-use (e.g., blend composition, molecular weight, degree of grafting, morphology, and rubber particle size). Nonetheless, irrespective of the process chosen, the ABS morphology is still characterised by a rubbery phase dispersed in a SAN matrix (Figure 4.1), resulting from the grafting of SAN onto the PB-phase rubber (Greco, 1996; Ferreira, 2022).

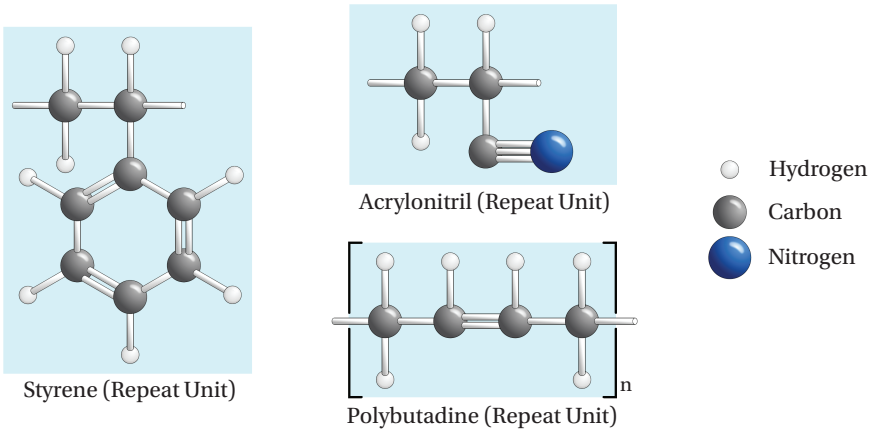


Figure 4.4: Schematic of the molecular structure of the Acrylonitrile-Butadiene-Styrene (ABS) - repeat unit (molecular conformation is not considered).
Source: (Ferreira, 2022)

4.2.1 Rubber-Toughened Polymer Blends

As previously mentioned, the rubber-toughening technique allows for the improvement of the toughness of a polymer by blending it with rubber particles, as is the case of ABS. When subjected to tensile loadings, SAN fails in a brittle manner. However, by adding rubber particles, this brittle failure can be suppressed, and its fracture toughness and notch resistance can drastically increase. Thereby, ABS belongs to the rubber-toughened materials class. The blend parameters, like the matrix properties, rubber volume fraction, particle size and shape, influence the blend's performance. For example, the maximum fracture toughness is obtained by a rubber volume fraction of around 20 – 30 % (Hund, 2022).

Added rubber particles enable energy dissipation throughout a larger part of the material volume at many sites, resulting in the above-mentioned toughening of the material. The brittle behaviour of PC under certain conditions is due to this materials' inability to dissipate energy over an extended volume, and, consequently, it fails due to localised mechanisms such as crazing (Hund, 2022).

The deformation mechanisms that allow energy dissipation throughout a larger part of the material volume are: (1) rubber particle cavitation; (2) matrix shear-yielding; and, (3) distributed crazing. Matrix shear-yielding and distributed crazing are the main mechanisms of inelastic deformation and energy dissipation in ABS. The prevalence of one mechanism over the other depends on conditions such as the blend morphology, the loading conditions, the local stress, the particle size and the amount of rubber particle cavitation.

For instance, smaller rubber particles and lower loading rates favour matrix shear-yielding, while higher deformation rates lead to distributed crazing. As a result of this multiple factors dependency, it is still not totally clear which mechanism contributes more to the increase in fracture toughness (Hund, 2022).

Rubber particle cavitation precedes the other mechanisms, since the rubber particles cavitate upon low hydrostatic stress inside them, and is fundamental in promoting the delocalisation of plastic deformation. In the literature, it is noted that cavitation occurs at a macroscopic hydrostatic stress of around 8 - 20 MPa (Hund, 2022).

4.2.2 Properties

Similarly to PC, ABS has excellent mechanical, chemical and electric properties that explain its wide range of applications (Greco, 1996):

1. High rigidity;
2. High impact resistance, even at low temperatures;
3. Low notch sensitivity;
4. Low cost;
5. Good processability;
6. Good insulating properties;
7. Good abrasion and strain resistance;
8. High dimensional stability;
9. Excellent surface quality.

However, like any other material, it also has some limitations:

1. Poor weathering resistance;
2. Easily scratchable;
3. Low heat distortion temperature;
4. Stress cracking in the presence of some greases.

4.3 PC/ABS Blends

The success of the PC/ABS blends is related to the fact that under specific compositions, they present better properties when compared with their neat constituents, exhibiting the good individual characteristics of both and even elevating them. This phenomenon is referred to as the "synergistic effect" and is only possible due to three main reasons (Hund, 2022; Inberg, 2001; Ferreira, 2022):

- **Complementary properties**: ABS and PC have several mechanical, thermal and chemical properties that complement each other. For instance, ABS's low-notch sensitivity and high impact resistance, even at low temperatures, are carried over to the blend. It is important to remember that these were the main limitations of PC applications. ABS also lowers the high viscosity of the melt flow of neat PC and, subsequently, improves the processability conditions of the final blend. Simultaneously, the beneficial thermal properties of PC are also retained. However, given that ABS is opaque, this blend is not suitable for optical applications where neat PC transparency is required;
- **Compatibility**: The PC and ABS are completely immiscible both in the melting and solid states, being possible to blend them by simple melt-mixings in standard equipment. In more complex techniques used in the toughening of incompatible systems, PC/ABS blends do generally not need the addition of interfacial compatibilising agents due to the good interaction (good interfacial strength) between PC and SAN constituents;
- **Production cost**: Since ABS is cheaper than PC, the addition of ABS lowers the material cost of the product, and in this way, ABS is also used as a filler.

4.3.1 Morphology

PC/ABS blends feature a hierarchical microstructure since the ABS phase contains another phase in the form of rubber particles. Nonetheless, the phase morphology of PC/ABS blends is shaped by the two immiscible phases, PC and ABS, and strongly depends on the blending and manufacturing conditions. Therefore, depending on each constituent fraction, two types of morphologies can be distinguished (see Figure 4.5) (Hund, 2022; Inberg, 2001; Ferreira, 2022).

Blends rich in PC (ABS mass fractions less than 30 %) exhibit a phase-matrix morphology referred to as a sea-island or particulate structure. The ABS domains can be characterised as ellipsoidal-shaped particles with a few micrometres, typically around 5 μm, spatially arranged in clusters and embedded in a PC matrix. In the case of more balanced PC/ABS fractions (ABS mass fractions of about 45 - 55 %), the ABS clusters become progressively more connected, and morphologies with two continuous interpenetrating phases form (PC and ABS lamellas of a few micrometres.) (Hund, 2022; Inberg, 2001; Ferreira, 2022).

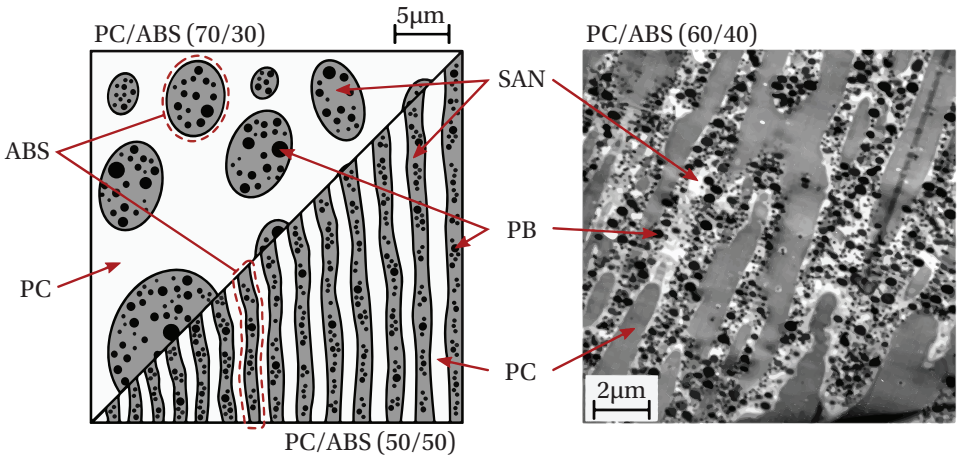


Figure 4.5: Schematic representation of two different types of PC/ABS morphologies. A sea-island structure is shown for PC/ABS (70/30) and a co-continuous lamellar structure for PC/ABS (50/50).

Source: (Ferreira, 2022)

In today's industry, the injection moulding process is the most important manufacturing process for the material under study; therefore, only the influences of this process on morphology are presented. Injection-moulded parts from blends of immiscible components exhibit a distinct morphology anisotropy from the melt flow direction and a gradient from the part's surface to its core. The cooling rate decreases with increasing distance from the mould walls, giving the melt more time to relax and approach the energetically favourable equilibrium state. For PC-rich blends, the ABS particles are oriented and elongated in the injection direction due to shear stresses during the injection moulding process. However, despite this elongation, the PB rubber particles, contained in the SAN, remain round, which is in line with the low viscosity of SAN during the injection. On the other hand, for the cases of more balanced PC/ABS fractions, the lamellar structure is often enhanced by the injection moulding process (Hund, 2022; Inberg, 2001; Ferreira, 2022).

In the remainder of this dissertation, the focus will be on the ABS mass fraction range where the most interesting synergistic effects occur regarding its technological application, which corresponds to the PC/ABS sea-island morphology, in other words, PC-rich blends.

4.3.2 Deformation and Damage Mechanisms

The deformation and damage mechanisms play a significant role in the toughening of PC/ABS blends for the optimal mass fractions of each component. However, their occurrence and predominance in PC/ABS blends are still far from being completely understood, and the results found in the literature appear to be inconclusive and, in some cases, contradictory depending on the experimental parameters (e.g., blending conditions, blend morphology and composition, and deformation path history). Nonetheless, it is broadly accepted that the microstructure damage begins in the ABS domains or at their interface with the PC matrix, delamination.

Three mechanisms can be distinguished within the ABS domains (represented in Figure 4.6): multiple crazing, dilatational bands, and internal cavitation of the rubber particles. Next, a brief description of the different deformation and damage phenomena occurring in PC/ABS polymer blends is presented, rather than discussing the prevalence of each mechanism over the other (Ferreira, 2022).

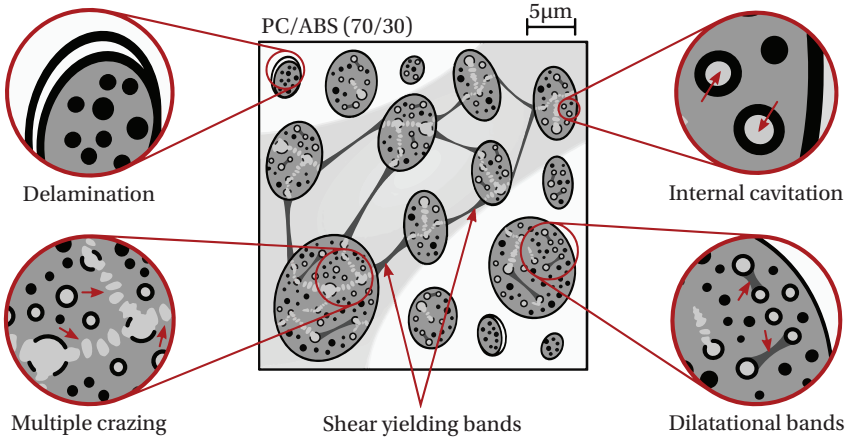


Figure 4.6: Schematic of the deformation and damage mechanisms occurring in a PC/ABS blend with sea-island structure.

Source: (Ferreira, 2022)

Rubber particle internal cavitation is connected with the void nucleation within PB rubber particles, followed by their collapse. It also precedes the other damage mechanisms since cavitated particles may act as initiation sites for both multiple crazing and shear-yielding on the SAN phase. When the largest rubber particles cavitate, they generally lead to the formation of a craze, and the multiple crazing mechanisms take place. This craze then expands and propagates, and further crazes are formed as a consequence of the cavitation

of smaller neighbouring rubber particles owing to the stresses of the first craze. Finally, crazes next to one other may merge and eventually fracture at sufficiently high strains. Simultaneously, shear deformations may localise into zones of high strain by strain-softening of the material. These shear bands can be initiated and connect the cavitated rubber particles, resulting in dilatational bands (Ferreira, 2022).

In competition with the rubber particle internal cavitation happening in the ABS domains are the void formation caused by the interface failure between PC and ABS. This phenomenom is inherently tied to the PC/SAN interfacial strength, and its comparison with the dilatational stress required to cavitate the PB rubber particles may determine which phenomenon prevails. When the multiple crazes propagating in the SAN phase reach the PC/SAN interface, the shear-yielding of the PC matrix may start in the points of highest strain concentrations. These shear-yielding bands can ultimately bridge the space between ABS domains. Nevertheless, craze propagation into the PC matrix is also seen under specific circumstances, with PC fracturing in a brittle manner (Ferreira, 2022).

In summary, the deformation of PC/ABS blends can be described by the following phases (Inberg, 2001):

1. Voids form by internal cavitation of the rubber in the ABS phase;
2. Crazes form in the SAN phase and propagate until they reach the PC phase;
3. Yielding of the PC phase occurs, and shear bands form from the ABS domains at the point of highest stress concentration. The shear bands can eventually span the distance between ABS domains;
4. Possibility of decohesion at high strains at the PC and ABS interface.

4.3.3 Process-Structure-Property-Performance Dimensions

After the description of the PC/ABS polymer blend and its constituents, it is evident why this heterogeneous material's precise and accurate design and optimisation requires a suitable Integrated Computational Materials Engineering (ICME) computational framework. Furthermore, the development of the underlying process-structure-property-performance relationships, summarised in Table 4.1, and the accurate numerical modelling of the thermomechanical behaviour of PC/ABS involves the exploration of a high-dimensional engineering design space. Under these circumstances, the data-driven approaches recently established in the computational mechanics field are very advantageous (Ferreira, 2022).

Table 4.1: Examples of process-structure-property-performance dimensions involved in the engineering design space of PC/ABS polymer blends given the ICME computational framework.

Process
ABS processing method (e.g., emulsion, suspension or bulk polymerisation);
PC/ABS blending process (e.g., miscibility, melt temperature and viscosity);
PC/ABS manufacturing process (e.g., injection molding, extrusion, fused deposition);
...
Structure
SAN and PB content (%) in ABS;
PB cross-linking level, particles size distribution and morphology (e.g., core-shell);
Type of ABS (SAN/PB grafting);
ABS(%) content in PC/ABS;
PC/ABS morphology (particulate or co-continuous);
PC/SAN interface strength/adhesion;
...
Property
Effective elastic properties (e.g., tensile modulus, bulk modulus);
Visco-elasto-plastic properties (e.g., yield stress, strain-softening, strain hardening);
Dependency of loading conditions (e.g., temperature, strain rate and pressure);
Fracture strength and toughness (e.g., thickness, notch sensitivity);
Interplay and predominance of several deformation and damage mechanisms;
Impact strength and shatter resistance;
Glass transition temperature and melting point;
Thermal conductivity and distortion resistance;
...
Performance
Ability to satisfy application requirements and constraints;
Reliability under service conditions and compliance with safety standards;
Durability (e.g., resistance to water, UV radiation and chemicals, flammability);
Processing costs (e.g., energy, CO2 footprint and water consumption);
Recycling and end of life (e.g., recycling fraction, CO2 footprint, biodegradability);
...

Source: (Ferreira, 2022).

Page intentionally left blank

CHAPTER 5

SIZE OF THE REPRESENTATIVE VOLUME ELEMENT (RVE)

The method used for the implementation of the multi-scale model was the first-order computational homogenisation, as described in Chapter 3. This approach cannot completely capture the intricacy of the material's microstructure since, as previously indicated, it is just an approximation technique. Therefore the accuracy of the predictions obtained highly depends on the size/representativity of the RVE and the quality of the computational model used to simulate the behaviour of the material within the RVE.

The scale separation principle serves as the cornerstone for establishing an RVE. It specifies that the characteristic dimension of the RVE should be much smaller than the macro-scale characteristic length but large enough to represent the material's microstructure (i.e., notably greater than its heterogeneities). However, this principle simply provides relative dimensions. Furthermore, the material's response must be independent of the boundary conditions chosen for an RVE to be representative.

It is crucial to find the appropriate equilibrium between an RVE that is computationally affordable and concurrently statistically representative of the micro-scale singularities. Even more, if the RVE is included in a global macroscopic analysis, where several microscopic simulations are conducted. In this scenario, a large RVE, which requires a lot of computational capacity to be analysed, would become impractical.

It is also imperative to emphasise that an RVE can vanish in the presence of strain localisation and discontinuities at the micro-scale (Gitman et al., 2007; Phu Nguyen et al., 2010). This is of paramount significance throughout the study since, as will be seen in Section 5.2, the PC/ABS material exhibits a strain-softening stage and, as demonstrated by Gitman et al. (2007), a material exhibiting this behaviour can lose the "representative" properties, making

impossible to identify an RVE. This is caused by the fact that the material in softening can lose statistical homogeneity due to localisation.

The scientific community has employed a variety of techniques over the last decades to calculate the RVE size, ranging from image processing techniques (Graham and Yang, 2003; Shan and Gokhale, 2002; Grimal et al., 2011) to analytical (Drugan and Willis, 1996; Sebsadji and Chouicha, 2012) and statistical (Kanit et al., 2003; Gitman et al., 2007) ones. In this context, emerges this Chapter which presents a study based on statistical analysis and numerical experiments to detect the ideal size of the RVEs for PC/ABS blends in the mass fraction range where the most interesting synergistic effects occur (between 10 to 30% of ABS - PC-rich blends).

5.1 High-Fidelity RVE

In Section 4.3, the composition and morphology of the PC/ABS polymer blend have been thoroughly described. In short, PC-rich blends exhibit a particulate phase-matrix morphology, as presented in Figure 4.5, where the ABS particles are typically characterised as ellipsoidal-shaped particles oriented and elongated in the injection direction. As previously mentioned, the injection moulding process is this material's most important manufacturing process. However, despite this elongation, the PB rubber particles present in the SAN continue to be spherical.

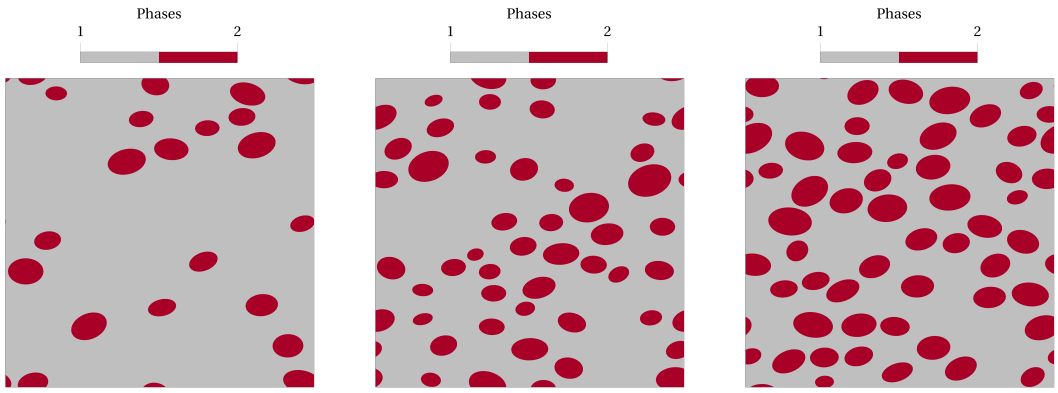
Typically, when modelling PC/ABS blends, only two material phases are taken into account: (1) the PC matrix phase, which is constitutively treated as an amorphous glassy thermoplastic, and (2) the ABS particles phase, which is constitutively treated as a porous amorphous glassy thermoplastic to account for the internal cavitation of the PB rubber particles. Considering that the stiffness of PB rubber particles is substantially lower than that of the SAN matrix surrounding them and that they cavitate at a very low-stress level, this modelling technique is possible from a physical viewpoint. Consequently, all PC/ABS RVEs will be examined based on this simplification (Ferreira, 2022).

AMINO, software used to create the RVEs, is able to build high-fidelity PC/ABS RVEs with the PB rubber particles embedded in the ABS domains, as illustrated in (Ferreira, 2022). Nevertheless, a large amount of processing power would be required to produce the RVE and solve the micro-scale equilibrium problem. Additionally, owing to the microscopic topological characteristics associated with the PB rubber particles and the PB/SAN interfaces, a suitable spatial discretisation would be highly refined, resulting in a problem of

tremendous dimensions.

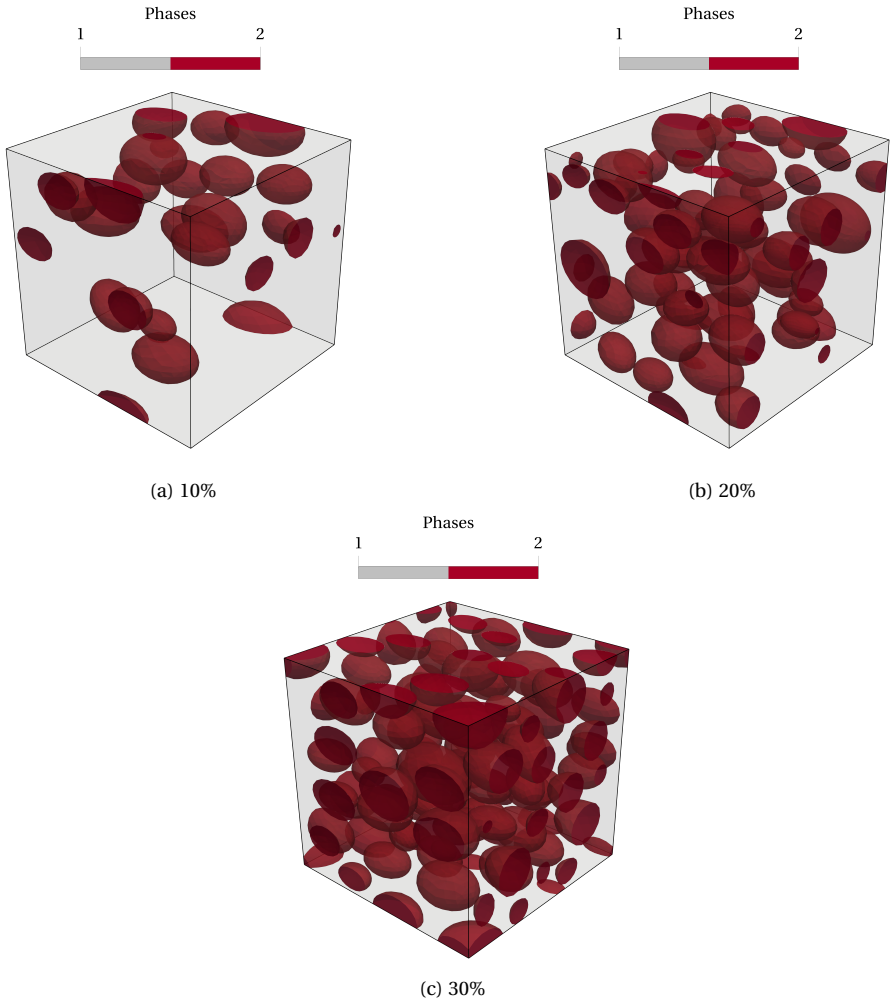
Quantitatively and in conformity with experimental data, the microstructure characteristics for PC/ABS blends with particle morphology follow the following statistical distributions, as summarised by Ferreira (2022). Normal distributions define both the major axis of the ABS elliptical/ellipsoidal particles, $N(5.0,\ 1.0^2)$ μm, and the ratio between it and the other(s) principal axes, $N(1.5,\ 0.1^2)$. This last distribution takes on several discrete values between 1.5, moderate elongation, and 2.3, high elongation. The rotation angle of the ABS elliptical/ellipsoidal particles similarly follows a normal distribution, $N(0.1,\ 0.2^2)$ rad, and is constrained to be oriented around the x-axis (supposed injection moulding direction). Each of these features mimics the projected elongation and alignment of the ABS domains with respect to the direction of injection moulding. While the PB particles inside the ABS are not modelled, the geometrical parameters characterising them are also provided for the purpose of completeness. Therefore, spherical particles with a radius following a normal distribution, $N(0.25,\ 0.1^2)$ μm, can be utilised to simulate the rubber phase.

It is of paramount significance to note that Ferreira (2022) demonstrated that AMINO could produce all the essential microstructures effectively and unsupervisedly, considering the various ABS content (%) values, RVE sizes, geometrical ratios of the ABS particles, and desired orientations. Figures 5.1 and 5.2 illustrate 2D and 3D RVEs for three discrete values of the ABS (%) content in the mass fraction range where the most interesting synergistic effects occur (between 10 to 30% of ABS - PC-rich blends).



(a) 10% (b) 20% (c) 30%

Figure 5.1: PC/ABS high-fidelity 2D RVEs for various ABS(%) contents with a particulate morphology using AMINO. The RVEs have the same side length of 50μm.



(a) 10%

(b) 20%

(c) 30%

Figure 5.2: PC/ABS high-fidelity 3D RVEs for various ABS(%) contents with a particulate morphology using AMINO. The RVEs have a side length of 20 μm.

5.2 Material Model

The mechanical properties and behaviour of thermoplastics are particularly susceptible to temperature, strain rate, pressure, and age, in addition to the inherent dependence on the underlying chemical and physical attributes. For temperatures below the glass transition temperature and small deformations, they exhibit a visco-elastic mechanical behaviour, a conjunction of elastic and viscous characteristics. Whereas viscous behaviour refers to time-dependent deformations (and recovery) driven by molecular-level relaxation processes, elastic behaviour is related to instantaneous (time-independent) deformations (and recovery) (Ferreira et al., 2023).

Most molecular movements are constrained to vibration and short-range rotations at temperatures substantially lower than the glass transition temperature, resulting in an essentially elastic mechanical behaviour (rigid solid material). Viscous effects, which introduce molecular relaxation mechanisms, begin when the temperature rises and approaches the glass transition temperature (rubbery solid material). Ultimately, when the deformation exceeds a certain threshold, the material either breaks (brittle behaviour) or undergoes irreversible time-dependent viscous inelastic deformations (visco-plasticity behaviour) before breaking (Ferreira et al., 2023).

In order to have a better understanding of the PC/ABS behaviour, Figure 5.3 illustrates the characteristic visco-elastic visco-plastic behaviour of an amorphous thermoplastic subjected to a uniaxial compression monotonic loading. The true compressive stress-strain response can be clearly divided into four distinct stages (A-D). The initial phase when it is essentially linear elastic (A), followed by a non-linear visco-elastic behaviour up to the yield point (B). The true stress decreases with increasing deformation once the yield point is crossed and the material suffers visco-plastic deformation (C). This phenomenon, known as strain-softening, characterises the inherent post-yielding behaviour of most amorphous thermoplastics. Eventually, upon saturation of the softening process, the material presents a non-linear strain hardening up to failure (D) (Ferreira et al., 2023). Several experimental data that verify this behaviour and its sensitivity to temperature and strain rate can be examined in Ferreira et al. (2023) and Wang et al. (2016).

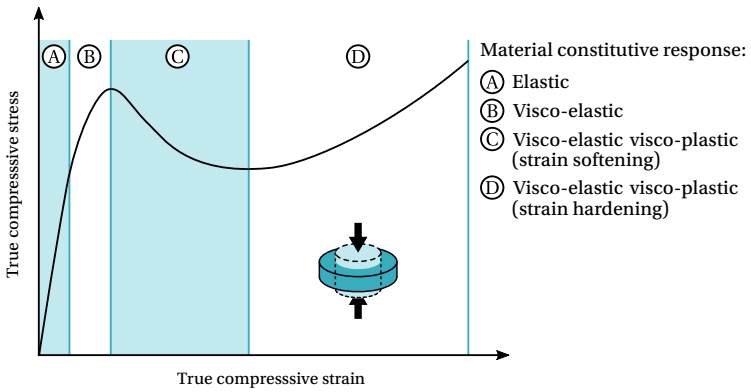


Figure 5.3: Typical constitutive behaviour of amorphous thermoplastics when subjected to uniaxial compression loading.

Source: (Ferreira et al., 2023)

This Section briefly outlines the visco-elastic visco-plastic constitutive model employed in this study to accurately predict the mechanical behaviour of the PC/ABS. The constitutive model presented is proposed by Carvalho Alves et al. (2023) and is an extension of (Ferreira et al., 2023) in order to forecast the non-linear behaviour of rubber-toughened amorphous polymers accounting for void nucleation, the interaction between voids, and the evolution of the voids' geometry. The original model, which includes both visco-elasticity and visco-plasticity (strain-softening and strain hardening), expresses the behaviour of amorphous thermoplastics during isothermal deformation processes at finite stresses below the glass transition temperature. The information presented in the following sections is entirely sourced from (Carvalho Alves et al., 2023).

5.2.1 Rheological Model

The one-dimensional rheological model of the visco-elastic visco-plastic constitutive model, schematically shown in Figure 5.4, consists of two main elements connected in parallel:

- **The driving element** (upper branch), is composed of two components linked in series. The first component is a linear spring, which is coupled to n_V Maxwell elements in parallel, each representing a relaxation mode of the material's (rate-dependent) viscoelastic response. The second component is a dashpot that characterises the visco-plastic behaviour and is driven by a modified version of the Gurson's potential;
- **The entropic resistance to chain alignment element** (lower branch), Langevin spring characterising the strain hardening.

In view of the above, the total stress, $\boldsymbol{\tau}_T$, is additively decomposed into the stress contributions of the two main components as

$$\boldsymbol{\tau}_T = \boldsymbol{\tau}_D + \boldsymbol{\tau}_H. \tag{5.1}$$

From here on, the subscripts $(\cdot)_D$ and $(\cdot)_H$ will be applied to the driving and hardening components, respectively.

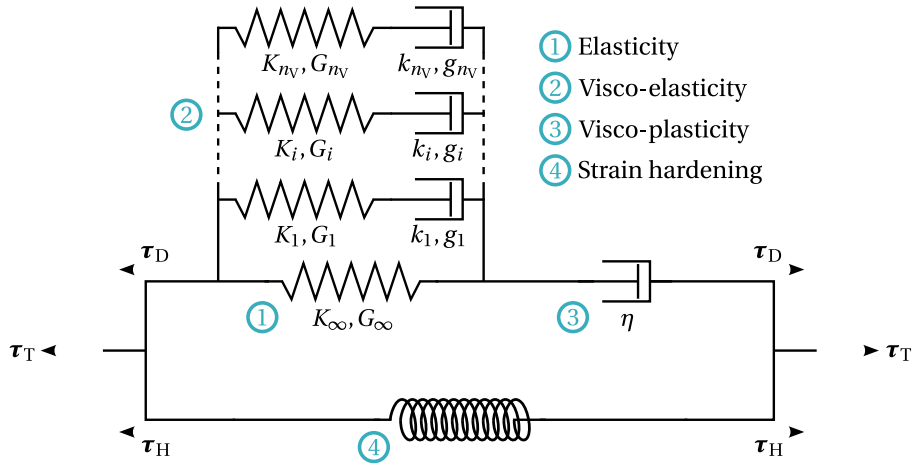


Figure 5.4: Rheological model of the formulated visco-elastic visco-plastic constitutive model. Source: (Ferreira et al., 2023)

5.2.2 Kinematics

The deformation gradient, $\boldsymbol{F}$, is applied equally to the two model components, as shown in Figure 5.4,

$$\boldsymbol{F} = \boldsymbol{F}_{\mathrm{D}} = \boldsymbol{F}_{\mathrm{H}}. \tag{5.2}$$

Moreover, considering the classical Lee multiplicative decomposition of the deformation gradient, it can also be stated as

$$\boldsymbol{F} = \boldsymbol{F}^e \boldsymbol{F}^p, \tag{5.3}$$

where $\boldsymbol{F}^e$ denotes the visco-elastic deformation gradient and $\boldsymbol{F}^p$ its plastic counterpart.

Attending to the multiplicative decomposition (Equation 5.3), the velocity gradient in the driving element becomes

$$\boldsymbol{L} = \boldsymbol{L}^e + \boldsymbol{F}^e \boldsymbol{L}^p \left(\boldsymbol{F}^e\right)^{-1}, \tag{5.4}$$

where $\boldsymbol{L}^e = \dot{\boldsymbol{F}}^e \left(\boldsymbol{F}^e\right)^{-1}$ is the elastic velocity gradient (defined in the deformed configuration), and $\boldsymbol{L}^p = \dot{\boldsymbol{F}}^p \left(\boldsymbol{F}^p\right)^{-1}$ is the plastic velocity gradient (defined in the intermediate configuration). Thus, the operator $\boldsymbol{F}^e(\cdot)\left(\boldsymbol{F}^e\right)^{-1}$ is a push-forward operator of the plastic velocity gradient to the deformed configuration. Notice that the plastic velocity gradient can be further decomposed into a symmetric component, $\boldsymbol{D}^p$, which represents the rate of plastic stretching, and a skew

component, $\boldsymbol{W}^p$, which represents the rate of plastic spin, as

$$\boldsymbol{L}^p = \boldsymbol{D}^p + \boldsymbol{W}^p. \tag{5.5}$$

Since the plastic flow is assumed to be irrotational, the spin tensor becomes null, $\boldsymbol{W}^p = \boldsymbol{0}$, and the plastic isotropy hypothesis is satisfied.

The spatially rotated rate of plastic deformation, $\tilde{\boldsymbol{D}}^p$, will be used to derive the plastic flow rule. Therefore, it is also convenient to establish this quantity

$$\tilde{\boldsymbol{D}}^p = \boldsymbol{R}^e \boldsymbol{D}^p \left(\boldsymbol{R}^e\right)^T, \tag{5.6}$$

where $\boldsymbol{D}^p$ is rotated to the deformed configuration employing the elastic rotation tensor $\boldsymbol{R}^e = \boldsymbol{F}^e \left[\left(\boldsymbol{F}^e\right)^T \boldsymbol{F}^e\right]^{-1/2}$. Consequently, by substituting this quantity (Equation 5.6) in Equation 5.5 and afterwards rearranging the resultant equation in regard to the rate of plastic deformation, one gets the constitutive equation for the plastic deformation gradient

$$\dot{\boldsymbol{F}}^p = \left(\boldsymbol{R}^e\right)^T \tilde{\boldsymbol{D}}^p \boldsymbol{R}^e \boldsymbol{F}^p. \tag{5.7}$$

Lastly, the spatial logarithmic strain tensor is adopted as a suitable strain measure and is established as

$$\varepsilon^e = \ln\left[\boldsymbol{V}^e\right] = \frac{1}{2}\ln\left[\boldsymbol{B}^e\right], \tag{5.8}$$

where $\boldsymbol{V}^e$ is the elastic left stretch tensor and $\boldsymbol{B}^e = \boldsymbol{F}^e \left(\boldsymbol{F}^e\right)^T$ is the elastic left Cauchy-Green strain tensor.

5.2.3 Prediction of Damage Linked to the Rubber Particles' Internal Cavitation

Two scales are presupposed to account for the internal rubber particle cavitation phenomena. The macro-scale, where the material is a continuum, and the micro-scale, which explicitly considers the discrete rubber particles in the polymer matrix. The dashpot in the driving element is expressed as the following potential:

$$\Phi^* = \left(\tau_{\mathrm{D}}^{\mathrm{eq}}\right)^2 + 2 f q_1 \left(\tau_\mu^{\mathrm{eq}}\right)^2 \cosh\left(q_2 \frac{\mathrm{tr}\left(\boldsymbol{\tau}_{\mathrm{D}}\right)}{2\sqrt{3}\tau_\mu^{\mathrm{eq}}}\right) - \left(\tau_\mu^{\mathrm{eq}}\right)^2 \left(1 + q_1^2 f^2\right) = 0, \tag{5.9}$$

where q_1 and q_2 are heuristic parameters used to account for the interaction between voids, $\tau_{\mathrm{D}}^{\mathrm{eq}}$ is the macroscopic equivalent stress in the driving element, and τ_{μ}^{eq} is the microscopic equivalent stress, denoting the equivalent tensile flow strength of the polymeric matrix of the voided material. Note that, $\tau_{\mathrm{D}}^{\mathrm{eq}}$ is expressed as

$$\tau_{\mathrm{D}}^{\mathrm{eq}} = \sqrt{\frac{1}{2}\boldsymbol{\tau}_{\mathrm{D},d} : \boldsymbol{\tau}_{\mathrm{D},d}}, \tag{5.10}$$

being $\boldsymbol{\tau}_{\mathrm{D},d}$ the deviatoric part of the driving Kirchhoff stress tensor.

The driving Kirchhoff stress tensor is defined as

$$\boldsymbol{\tau}_{\mathrm{D}} = \int_0^t \mathbf{D}^{ve}\left(t - t^*\right) : \frac{\partial \varepsilon^e\left(t^*\right)}{\partial t^*}\, \mathrm{d}t^*, \tag{5.11}$$

where $\mathbf{D}^{ve}$ is the visco-elasticity isotropic fourth-order relaxation tensor characterised by

$$\mathbf{D}^{ve}(t) = 2G(t)\mathbf{I}_d + K_{\infty}\boldsymbol{I} \otimes \boldsymbol{I}, \tag{5.12}$$

with $\mathbf{I}_d$ being the fourth-order deviatoric identity tensor, $\boldsymbol{I}$ the second-order identity tensor and $G(t)$ the shear modulus visco-elastic relaxation function, which in turn is defined as a Prony series expansion

$$G(t) = G_{\infty} + \sum_{j=1}^{n_{\mathrm{V}}} G_j \exp\left[-\frac{t}{g_j}\right]. \tag{5.13}$$

Note that G_{∞} denotes the long-term elastic modulus, G_j the shear moduli associated with the j-th visco-elastic relaxation mode, and g_j the j-th visco-elastic relaxation time mode.

Moreover, it is feasible to establish the visco-elastic relaxation time dependency on the strain rate as

$$g_j\left(\dot{\varepsilon}^{\mathrm{eq}}\right) = g_{j,T}\left(\dot{\varepsilon}^{\mathrm{eq}}\right)^{-\lambda_{g,j}}, \quad j = 1, \ldots, n_{\mathrm{V}}, \tag{5.14}$$

where $g_{j,T}$ is constant, and $\lambda_{g,j}$ represents the shear relaxation time strain rate sensitivity, and given that the spatial logarithmic equivalent strain rate can be stated as

$$\dot{\varepsilon}^{\mathrm{eq}} = \frac{1}{\Delta t}\sqrt{\frac{2}{3}\Delta\varepsilon : \Delta\varepsilon}. \tag{5.15}$$

The heuristic parameter, q_1, is assumed to evolve with the void volume fraction, f, in order to represent the anticipated features of void growth

$$q_1 = q_{10} - q_{11} f, \tag{5.16}$$

where q_{10} and q_{11} are material parameters. It should be noted that the evolution of the void volume fraction, $\dot{f}$, has been adjusted to account for the rate of nucleation of new voids, $\dot{f}_N$, as well as the evolution of the porosity of existing voids, $\dot{f}_g$, as

$$\dot{f} = \dot{f}_g + \dot{f}_N, \tag{5.17}$$

in turn, the evolution of the porosity of existing voids is given by

$$\dot{f}_g = 3(1-f)\tilde{D}^p_h, \tag{5.18}$$

and the rate of nucleation of new voids is given by a dependence on the volumetric strain rate, $\dot{\varepsilon}_{\text{vol}} = \dot{\boldsymbol{\varepsilon}} : \boldsymbol{I}$, as

$$\dot{f}_N = \frac{f_r}{s_r\sqrt{2\pi}} \exp\left[-\frac{1}{2}\left(\frac{\varepsilon_{\text{vol}} - \varepsilon_r}{s_r}\right)^2\right] \dot{\varepsilon}_{\text{vol}}, \tag{5.19}$$

where f_r is the total volume fraction that can be nucleated, which for rubber-toughened glassy polymers is equivalent to the volume content of rubber.

Furthermore, the nucleation criteria developed by Bucknall et al. (1994) can be used to calculate the mean, ε_r, and standard deviation values, s_r. This criterion indicates that: *for a given particle radius, the critical strain for cavitation to occur is given by*

$$\left(\varepsilon^e_{R,\text{vol}}\right)_{\min} = 2\left(\frac{2\Gamma}{K_r R}\right)^{3/4} + \frac{3}{2}\frac{G_r}{K_r} F\left(\lambda_f\right), \tag{5.20}$$

where K_r is the bulk modulus of the rubber particles, G_r shear modulus of the rubber particles, and R the rubber particles radii. Moreover, two additional energy terms are introduced due to the void nucleation and growth: a surface energy term, where Γ is the surface energy of the rubber; and a stretching term, $F\left(\lambda_f\right)$, representing the work done in stretching concentrical spherical membranes surrounding the growing void, up to a maximum stretch of λ_f.

5.2.4 The Visco-Plastic Constitutive Formulation

The spatially rotated rate of plastic deformation tensor, $\tilde{\boldsymbol{D}}^p$, which can be additively decomposed into a deviatoric, $\tilde{\boldsymbol{D}}^p_d$, and a hydrostatic component, $\tilde{D}^p_h \boldsymbol{I}$, is used to simulate the visco-plastic flow. Moreover, by employing the modified Gurson potential in Equation 5.9 as the plastic flow potential, the

corresponding viscoplastic flow rule is postulated as

$$\tilde{\boldsymbol{D}}^p = \Lambda \frac{\partial \Phi^*}{\partial \boldsymbol{\tau}_{\mathrm{D}}}, \tag{5.21}$$

where Λ is a scalar multiplier, which can be computed from the equivalence between the macroscopic plastic power, $\dot{W}^p$, and the microscopic plastic power, $\dot{W}^p_\mu$, dissipated in the polymer matrix, defined ad

$$\dot{W}^p = \boldsymbol{\tau}_{\mathrm{D}} \tilde{\boldsymbol{D}}^p = \boldsymbol{\tau}_{\mathrm{D}} \Lambda \frac{\partial \Phi^*}{\partial \boldsymbol{\tau}_{\mathrm{D}}}, \tag{5.22}$$

$$\dot{W}^p_\mu = (1-f)\boldsymbol{\tau}_\mu : \tilde{\boldsymbol{D}}^p_\mu = (1-f)\tau^{\mathrm{eq}}_\mu \dot{\gamma}_\mu = (1-f)\frac{\left(\tau^{\mathrm{eq}}_\mu\right)^2}{\eta_\mu}. \tag{5.23}$$

The Eyring visco-plastic flow model is used to construct the viscosity function, η_μ, as

$$\eta_\mu = A\tau^{\mathrm{eq}}_\mu \left(\sinh\left(\frac{\tau^{\mathrm{eq}}_\mu}{\tau^*} \right) \right)^{-1}, \tag{5.24}$$

being τ^*_i the characteristic stress given by

$$\tau^*_i = \frac{R^* T}{v^*_i}, \quad i = \alpha, \beta, \tag{5.25}$$

where $R^* = 8.3144598(48)$ kg m^2 mol^{-1} K^{-1} s^{-2} is the universal gas constant, T the absolute temperature and v^*_i the shear activation volume. Returning to Equation 5.24, A is an Eyring-related function expressed as

$$A = A_0 \exp\left[\frac{\Delta H}{R^* T} + \frac{\mu P_\mu}{\tau^*} - D_\infty \left(1 - \exp\left(-\sqrt{\frac{3}{2}} \frac{h\bar{\varepsilon}^p_\mu}{D_\infty} \right) \right) \right], \tag{5.26}$$

with ΔH being the activation energy, μ the pressure coefficient, P_μ the total hydrostatic pressure, D_∞ the saturation value of the softening parameter, h the softening slope, and $\bar{\varepsilon}^p_\mu$ the accumulated plastic strain. Subsequently, the accumulated plastic strain is given by

$$\bar{\varepsilon}^p_\mu = \frac{1}{\sqrt{3}} \frac{1}{A} \sinh\left(\frac{\tau^{\mathrm{eq}}_\mu}{\tau^*} \right), \tag{5.27}$$

and the total hydrostatic pressure by

$$P_\mu = p^* + p_\mu = p^* - \frac{1}{3}\mathrm{tr}\left(\tau_\mu\right), \tag{5.28}$$

where p^* is the superimposed hydrostatic pressure and p_μ the hydrostatic pressure. From a physical standpoint, it makes sense to choose an average or homogenised counterpart of p_μ, described as $p_\mu \approx p$. The hydrostatic pressure generated in the matrix viscosity function is thus supposed to be determined as $p_\mu = p$ and $P_\mu = P$ moving forward.

The modified Gurson potential can be derived to produce

$$\frac{\partial \Phi^*}{\partial \boldsymbol{\tau}_\mathrm{D}} = \boldsymbol{\tau}_{\mathrm{D},d} + \frac{1}{\sqrt{3}} q_1 q_2 f \tau_\mu^{\mathrm{eq}} \sinh\left(q_2 \frac{\mathrm{tr}\left(\boldsymbol{\tau}_\mathrm{D}\right)}{2\sqrt{3}\tau_\mu^{\mathrm{eq}}}\right) \boldsymbol{I}, \tag{5.29}$$

and the scalar multiplier, Λ, can be determined by the equivalence of the plastic work between scales ($\dot{W}^p = \dot{W}_\mu^p$),

$$\Lambda = (1-f)\frac{\left(\tau_\mu^{\mathrm{eq}}\right)^2}{\eta_\mu}\left(\boldsymbol{\tau}_{\mathrm{D},d} : \boldsymbol{\tau}_{\mathrm{D},d} + \frac{1}{\sqrt{3}} q_1 q_2 f \tau_\mu^{\mathrm{eq}} \sinh\left(q_2 \frac{\mathrm{tr}\left(\boldsymbol{\tau}_\mathrm{D}\right)}{2\sqrt{3}\tau_\mu^{\mathrm{eq}}}\right) \mathrm{tr}\left(\boldsymbol{\tau}_\mathrm{D}\right)\right)^{-1}. \tag{5.30}$$

Subsequently, the viscoplastic flow rule is established as

$$\tilde{\boldsymbol{D}}^p = \Lambda\left(\boldsymbol{\tau}_{\mathrm{D},d} + \frac{1}{\sqrt{3}} q_1 q_2 f \tau_\mu^{\mathrm{eq}} \sinh\left(q_2 \frac{\mathrm{tr}\left(\boldsymbol{\tau}_\mathrm{D}\right)}{2\sqrt{3}\tau_\mu^{\mathrm{eq}}}\right) \boldsymbol{I}\right), \tag{5.31}$$

where the deviatoric and hydrostatic components are, respectively,

$$\tilde{\boldsymbol{D}}_d^p = \Lambda \boldsymbol{\tau}_{\mathrm{D},d}, \tag{5.32}$$

$$\tilde{D}_h^p \boldsymbol{I} = \Lambda \frac{1}{\sqrt{3}} q_1 q_2 f \tau_\mu^{\mathrm{eq}} \sinh\left(q_2 \frac{\mathrm{tr}\left(\boldsymbol{\tau}_\mathrm{D}\right)}{2\sqrt{3}\tau_\mu^{\mathrm{eq}}}\right) \boldsymbol{I}. \tag{5.33}$$

Lastly, returning to Equation 5.17, the evolution of the void volume fraction becomes

$$\dot{f} = 3(1-f)\tilde{D}_h^p + \frac{f_r}{s_r\sqrt{2\pi}} \exp\left[-\frac{1}{2}\left(\frac{\varepsilon_{\mathrm{vol}} - \bar{\varepsilon}_r}{s_r}\right)^2\right] \dot{\varepsilon}_{\mathrm{vol}}. \tag{5.34}$$

5.2.5 Strain Hardening

The stress in the non-linear hardening component is considered to be deviatoric and characterised using the eight-chain model provided by Arruda and Boyce (1993a),

$$\boldsymbol{\tau}_{\mathrm{H}} = \frac{C_{\mathrm{R}}}{3}\frac{\sqrt{N}}{\lambda^{p}_{\mathrm{chain}}}\mathscr{L}^{-1}\left(\frac{\lambda^{p}_{\mathrm{chain}}}{\sqrt{N}}\right)\boldsymbol{B}_{d,\,\mathrm{iso}}\,, \tag{5.35}$$

where $\sqrt{N}$ is the limiting chain extensibility and C_{R} the rubbery modulus, which is defined as

$$C_{\mathrm{R}} = nkT, \tag{5.36}$$

with n denoting the number of chains per unit volume, k the Boltzmann's constant, and T the absolute temperature. Additionally, $\mathscr{L}^{-1}$ represents the inverse of the Langevin function, $\lambda^{p}_{\mathrm{chain}}$ the stretch on a chain in the eight-chain network, and $\boldsymbol{B}_{d,\,\mathrm{iso}}$ the deviatoric component of the isochoric left Cauchy-Green tensor

$$\mathscr{L}^{-1} = \coth(x) - \frac{1}{x}, \tag{5.37}$$

$$\lambda^{p}_{\mathrm{chain}} = \sqrt{\frac{\mathrm{tr}\left(\boldsymbol{B}_{\,\mathrm{iso}}\right)}{3}}, \tag{5.38}$$

$$\boldsymbol{B}_{d,\,\mathrm{iso}} = \boldsymbol{B}_{\,\mathrm{iso}} : \mathbf{I}_{d}, \qquad \text{with } \boldsymbol{B}_{\,\mathrm{iso}} = \left(\det(\mathbf{F})\right)^{-\frac{2}{3}}\mathbf{F}\mathbf{F}^{T}. \tag{5.39}$$

5.2.6 No Rubber Phase Model

Lastly, it is important to refer that if no rubber phase is considered, $f_r = 0$ and $f = 0$, the derivative of the modified Gurson potential in the viscoplastic flow rule in Equation 5.31 is simplified to

$$\frac{\partial \Phi^{*}}{\partial \boldsymbol{\tau}_{\mathrm{D}}}(f=0) = \boldsymbol{\tau}_{\mathrm{D},d}, \tag{5.40}$$

and the scalar multiplier, Λ, in Equation 5.30 to

$$\Lambda(f=0) = \frac{\left(\tau^{\mathrm{eq}}_{\mu}\right)^{2}}{\eta_{\mu}}\frac{1}{\boldsymbol{\tau}_{\mathrm{D},d} : \boldsymbol{\tau}_{\mathrm{D},d}} = \frac{\left(\tau^{\mathrm{eq}}_{\mu}\right)^{2}}{\eta_{\mu}}\frac{1}{2\left(\tau^{\mathrm{eq}}_{\mu}\right)^{2}} = \frac{1}{\eta_{\mu}}. \tag{5.41}$$

With this, the viscoplastic flow rule becomes

$$\tilde{\boldsymbol{D}}^{p} = \frac{\boldsymbol{\tau}_{\mu,d}}{2\eta_{\mu}}. \tag{5.42}$$

5.2.7 Material Properties

The constitutive model material properties are outlined in Table 5.1, and the actual properties employed in the subsequent studies for the PC and ABS phases are provided in Table 5.2. All properties were acquired from in-house experimental data (by the CM2S research group at the Faculty of Engineering of the University of Porto), where a suitable two-stage optimisation-based calibration procedure was employed to acquire them through a series of uniaxial compression tests. Ferreira et al. (2023) can be referred to for a more detailed development of the methodology involved in this procedure. However, notice that the information shown must be adapted to the previously described updated constitutive model.

The calibration procedure is based on uniaxial compression tests of cylindrical specimens because, unlike standard uniaxial tensile tests, both necking and crazing can be suppressed. This allows inferring the intrinsic strain softening and strain hardening characteristic of the post-yielding behaviour. Moreover, all tests were done under isothermal deformation at a constant strain rate and temperature, owing to the material's sensitivity to them. The various combinations of strain rate and temperatures tested encompass the complete range of interest in terms of engineering application of the constitutive model (Ferreira et al., 2023).

Table 5.1: Material properties of the finite strain visco-elastic visco-plastic constitutive model.

Category	**Notation**	**Designation**
Mechanical	ρ	Density
Thermal	T	Absolute temperature
Elastic	E_∞	Long term Young's modulus
	ν_∞	Long term Poisson's ratio
Yielding	ΔH	Activation energy
	v^*	Shear activation volume
	A_0	Fundamental vibration temperature factor
	p^*	Superimposed hydrostatic pressure
	μ	Pressure coefficient
Post-Yielding	D_∞	Saturation value of the softening parameter
	h	Scalar influencing the softening slope
	$\sqrt{N}$	Limiting chain extensibility
	C_r	Rubbery modulus
Porosity	f_0	Initial void volume fraction (or porosity)
	q_{10}, q_{11}, q_2	Heuristic parameters to capture the evolution of geometry of the voids
	f_r	Total porosity from nucleation (rubber porosity)
	ε_r, s_r	Mean and standard deviation for the nucleation law
Visco-Elastic	n_V	Number of visco-elastic relaxation modes
	G_j	Shear modulus of j-th visco-elastic relaxation mode
	g_j	Temperature-dependent relaxation time of j-th visco-elastic relaxation mode
	$\lambda_{g,j}$	Visco-elastic relaxation time sensitivity

Table 5.2: Material properties of the PC matrix and ABS particles employed.

Property	SI Units	PC	ABS
ρ	kg/m^3	1.200×10^3	1.200×10^3
T	K	2.980×10^3	2.980×10^3
E_∞	Pa	3.008×10^8	7.625×10^3
ν_∞	-	0.390	0.390
ΔH	J/mol	2.508×10^5	1.581×10^5
v^*	m^3/mol	3.558×10^{-3}	0.952×10^{-3}
A_0	s	3.359×10^{-15}	8.733×10^{-16}
p^*	Pa	1.000×10^5	1.000×10^5
μ	-	4.802×10^{-2}	1.171×10^{-1}
D_∞	-	2.948×10^1	1.130×10^1
h	-	3.138×10^2	1.901×10^2
$\sqrt{N}$	-	1.200	1.718
C_r	Pa	8.000×10^6	5.563×10^6
f_0	%	0.000	0.000
q_{10}, q_{11}, q_2	-	1.690, 1.000, 0.920	2.000, 1.500, 0.500
f_r	%	0.000	1.000×10^{-1}
ε_r	-	1.888×10^{-3}	1.888×10^{-3}
s_r	-	2.058×10^{-4}	2.058×10^{-4}
n_V	-	1	1
G_1	Pa	1.089×10^9	8.622×10^8
g_1	-	3.276×10^{-2}	5.768×10^{-2}
$\lambda_{g,1}$	-	9.686×10^{-1}	8.394×10^{-1}

5.3 RVE Size

This Section presents a statistical approach, in conjunction with numerical simulations, to determine the optimal RVEs' size, which enables to have excellent representativity of the material under investigation. Three distinct volume fractions of ABS are considered, namely 10%, 20% and 30% (volume fraction range where the most interesting synergistic effects occur).

The scheme for RVEs size determination is as follows. First, several samples of RVEs are generated, following the statistical distributions presented in Section 5.1, for the different sizes of each volume fraction. Then, the samples are submitted to various loading schemes, and the stress-deformation graphs and correspondent first Piola-Kirchhoff stress tensor component, i.e.,

stress component in the loading direction, are extracted. Lastly, the five best samples are selected, and the average behaviour of the material is analysed. By employing multiple samples, the probability of an outlier impacting the final results will be significantly minimised, and a more accurate RVE optimal size can be determined. The material is evaluated first with 2D RVEs and subsequently with 3D ones. Alongside the graphical visualisation of the data, three criteria are taken into account in the process of determining the RVEs' optimal size (the first two criteria were based on the study done by Mirkhalaf et al. (2016)):

1. A predetermined percentage should be the upper limit for the standard deviation of the average deformation behaviour. This condition makes sure that, for a given size, changing the realisation does not noticeably impact the deformation behaviour. In this study, it was established a limit of 10% for the fluctuation of the first Piola–Kirchhoff stress tensor component correspondent to the examined load,

$$S_{P_k} = \sqrt{\frac{1}{n-1}\sum_{i=1}^{n}\left(P_k^i - \overline{P_k}\right)^2} \;\leq\; 0.1 \times \overline{P_k}, \quad k \in \{xx, yy, xy\}, \tag{5.43}$$

   where S_{P_k} is the standard deviation, k depends on the loading scheme, n is the number of samples, P_k^i is the ith value of the first Piola–Kirchhoff stress tensor and $\overline{P_k}$ is the mean value which is given by

$$\overline{P_k} = \sum_{i=1}^{n}\frac{P_k^i}{n}. \tag{5.44}$$

2. Compared to the average response of the following RVE size, the average behaviour of all realisations of the same RVE size must fall within a predefined error. This condition assures that no substantial change in the deformation behaviour is detected when the sample size is increased. Again, a 10% fluctuation is chosen as the upper limit

$$\text{Error}\,(\%) = \frac{\left|\overline{P_k}^{j+1} - \overline{P_k}^{j}\right|}{\overline{P_k}^{j+1}} \;\leq\; 10\%, \tag{5.45}$$

   where j denotes the current RVE size and $j+1$ the following size.
3. The computational cost must be within a reasonable limit to make future research feasible. No limit was defined beforehand.

Unlike what was done in this study, in (Mirkhalaf et al., 2016), the first two criteria were applied to the first invariant of the first Piola–Kirchhoff stress tensor. Nonetheless, the authors established that both scenarios could reach equivalent outcomes.

This approach makes it easy to conduct a statistical analysis because it eliminates the need to individually study the deformation's elastic, yield, and softening regimes. Additionally, all conceivable criteria are covered, such as the slope of the graph in various deformation regimes, the strain at which the material yields and the energy dissipated.

It is important to note that, the computational implementation of the constitutive model takes into account any explicit dependency of the material properties on the strain rate in contrast to the temperature (which is assumed to be at room temperature). Therefore, a specific strain rate value must be specified for the simulations, namely $\dot{\varepsilon} = 0.001\ \mathrm{s}^{-1}$. The isothermal deformation condition, to which the material properties were calibrated, is thus guaranteed.

5.3.1 2D RVE Size

The 2D analysis's findings are presented in this section. Three separate deformation gradients are applied under the assumption of a plain strain state, describing a uniaxial loading along xx (direction of injection moulding), a uniaxial loading along yy, and a shear across xy denoted as

$$\text{Uniaxial along } xx\text{:} \quad \boldsymbol{F} = \begin{bmatrix} 1.20 & 0.00 \\ 0.00 & 1.00 \end{bmatrix}, \tag{5.46}$$

$$\text{Uniaxial along } yy\text{:} \quad \boldsymbol{F} = \begin{bmatrix} 1.00 & 0.00 \\ 0.00 & 1.20 \end{bmatrix}, \tag{5.47}$$

$$\text{Shear across } xy\text{:} \quad \boldsymbol{F} = \begin{bmatrix} 1.00 & 0.15 \\ 0.00 & 1.00 \end{bmatrix}. \tag{5.48}$$

Void nucleation within PB rubber particles does not occur for uniaxial compression loads, and since this phenomenon is of relevance in terms of engineering application, it was opted to solely apply tensile loadings. Additionally, by applying the two uniaxial tensile loads in perpendicular directions, it is also feasible to examine the predicted anisotropy of the material. Observe that, under shear, nucleation still develops, but it is not so substantial as for traction.

Preliminary simulations using microstructural samples smaller than 10 μm showed that the RVE size could not be less than 10 μm. Consequently, this value is the first volume element size to begin the investigation. Five RVE sizes were selected to be examined, namely, 10 μm, 25 μm, 50 μm, 75 μm and 100 μm. Since first-order computational homogenisation is applied, the results are independent of the RVE's size, so one can either increase the size of the RVE while maintaining the same particle dimensions or reduce the particle dimensions while maintaining the same RVE size. The first technique was chosen because it allows the degree of discretisation of the particles to be kept constant more easily.

Note that, the finite element analyses are carried out with the microstructure being discretised in a nonconform TRI6 mesh with 3 Gauss integration points. Figure 5.5 depicts the five RVE sizes in the study for the 10% volume fraction, enabling a better understanding of their magnitude and representativity. The degree of refinement of the matrix was set to be high enough so as not to impact the findings produced. Thereafter, having determined the appropriate size for the representativeness of the RVE, the impact of the mesh discretisation level is assessed in Section 5.3.3.

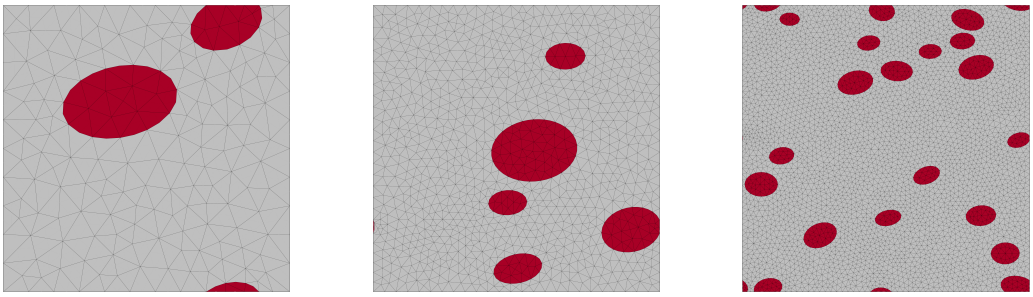
In order to carry out a thorough analysis of the data acquired and to be able to apply the three criteria indicated above, four distinct graphs are shown for each combination of volume fraction and loading scheme:

1. The average response of five samples for each size (red), coupled with the corresponding standard deviation (shaded) and the pre-defined 10% limit of standard deviation (black). Since high deformation gradients were applied, certain combinations could not achieve these high values for all samples. Consequently, the average response of only three samples is also displayed (blue). (see Figures 5.6, 5.10, 5.14, 5.19, 5.23, 5.27, 5.31, 5.35, 5.39, 5.43 and 5.47 and Appendix A.1);
2. The comparison of the average response for all five RVE sizes, enabling to more readily observe the convergence of behaviour as the size rises and to better comprehend the evolution between them (see Figures 5.7, 5.11, 5.15, 5.20, 5.24, 5.28, 5.32, 5.36, 5.40, 5.44 and 5.48);
3. The measure of the difference, i.e., error, between the average behaviour of one RVE size with the next closest size, in order to the deformation gradient (see Figures 5.8, 5.12, 5.16, 5.21, 5.25, 5.29, 5.33, 5.37, 5.41, 5.45 and 5.49);
4. The average CPU time of the five samples for all five RVE sizes. Note that the implementation is neither parallelised nor optimised, and just one

CPU core was employed (the computational resources are the same as the ones presented in Section 7.3) (see Figures 5.9, 5.13, 5.17, 5.22, 5.26, 5.30, 5.34, 5.38, 5.42, 5.46 and 5.50).

As stated in Section 3.2.4, in principle, as the RVE's size grows, the periodic boundary condition converges to the actual value more rapidly than the others. Consequently, smaller RVEs (and, therefore, less computational effort) are required to obtain results with the same precision. With this in mind, it was decided to implement this boundary condition (bc) to carry out the RVE representativeness analysis.

For the sake of completeness, and to verify that what was stated in Section 3.2.4 actually holds true, a study of all three boundary conditions (linear, uniform and periodic) was performed for the 10% volume fraction under shear across *xy*. Hence, a fifth graph emerges for this particular case (see Figure 5.18), intending to prove Figure 3.6, i.e., that an upper and lower limit of the periodic boundary condition are specified, respectively, by the linear boundary condition and the uniform traction one. For this study, four different points of the deformation gradient were chosen, both in the elastic and plastic zones.



(a) 10 μm (b) 25 μm (c) 50 μm

(d) 75 μm (e) 100 μm

Figure 5.5: Various 2D realisations with volume fraction equal to 10% and different volume element sizes.

Shear across *xy*

- 10% volume fraction - linear boundary condition

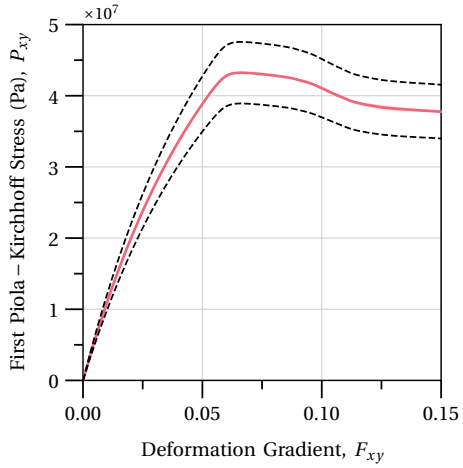


Figure 5.6: Homogenised First Piola Kirchhoff shear stress, P_{xy}, for the 50 µm RVE size with 10% volume fraction and linear boundary condition. Shaded bounds: standard deviation; and dashed line: standard deviation 10% limit.

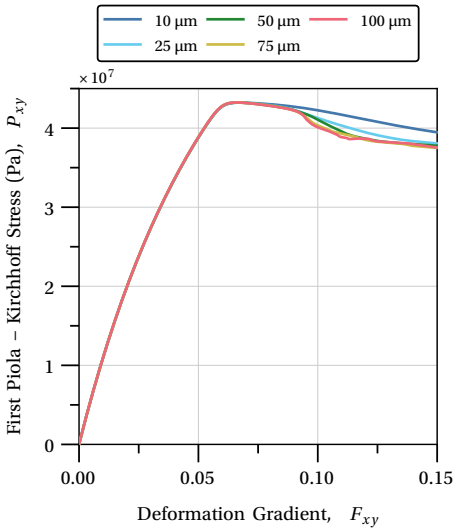


Figure 5.7: Comparison of the Homogenised First Piola Kirchhoff shear stress, P_{xy}, for different RVE sizes with 10% volume fraction and linear boundary condition.

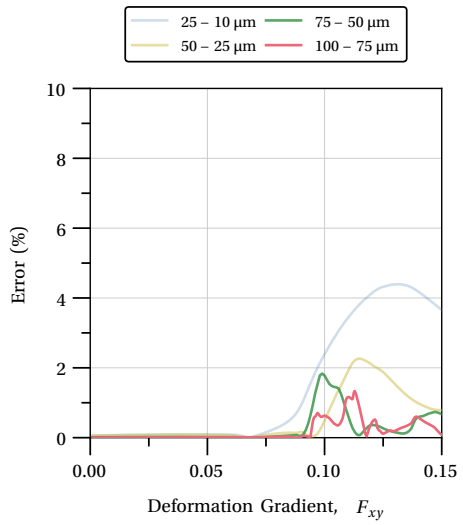


Figure 5.8: Variance in behaviour between one RVE size and the next closest RVE size.

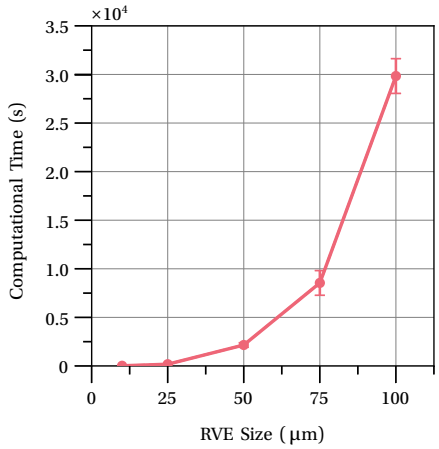


Figure 5.9: Average CPU time of the samples with 10% volume fraction and linear boundary condition under shear across *xy* for different RVE sizes.

- 10% volume fraction - uniform boundary condition

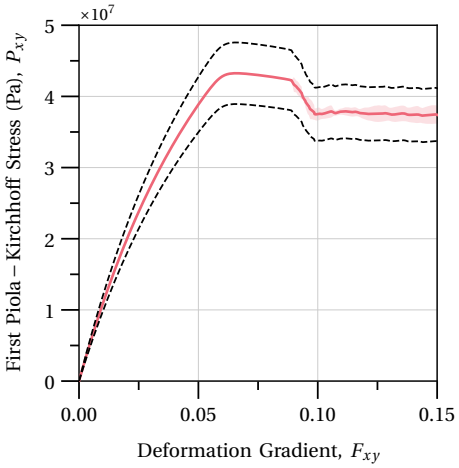


Figure 5.10: Homogenised First Piola Kirchhoff shear stress, P_{xy}, for the 50 µm RVE size with 10% volume fraction and uniform boundary condition. Shaded bounds: standard deviation; and dashed line: standard deviation 10% limit.

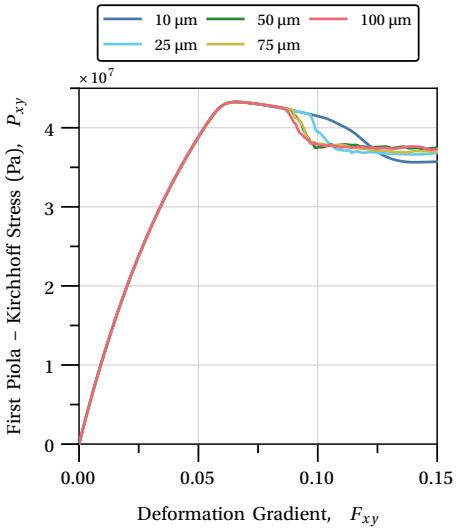


Figure 5.11: Comparison of the Homogenised First Piola Kirchhoff shear stress, P_{xy}, for different RVE sizes with 10% volume fraction and uniform boundary condition.

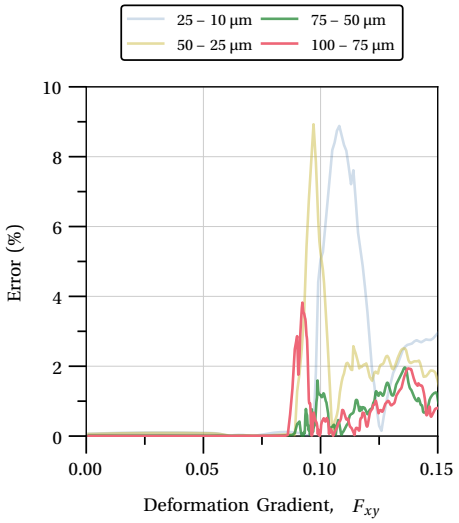


Figure 5.12: Variance in behaviour between one RVE size and the next closest RVE size.

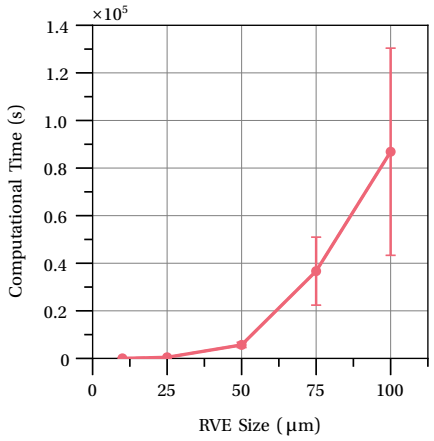


Figure 5.13: Average CPU time of the samples with 10% volume fraction and uniform boundary condition under shear across *xy* for different RVE sizes.

- 10% volume fraction - periodic boundary condition

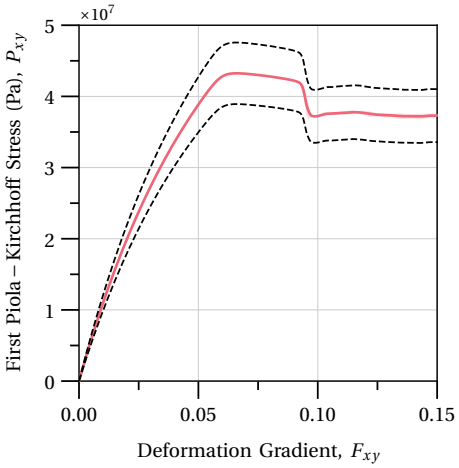


Figure 5.14: Homogenised First Piola Kirchhoff shear stress, P_{xy}, for the 50 µm RVE size with 10% volume fraction and periodic boundary condition. Shaded bounds: standard deviation; and dashed line: standard deviation 10% limit.

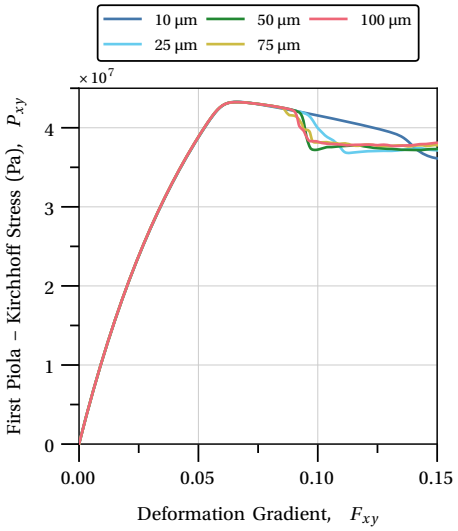


Figure 5.15: Comparison of the Homogenised First Piola Kirchhoff shear stress, P_{xy}, for different RVE sizes with 10% volume fraction and periodic boundary condition.

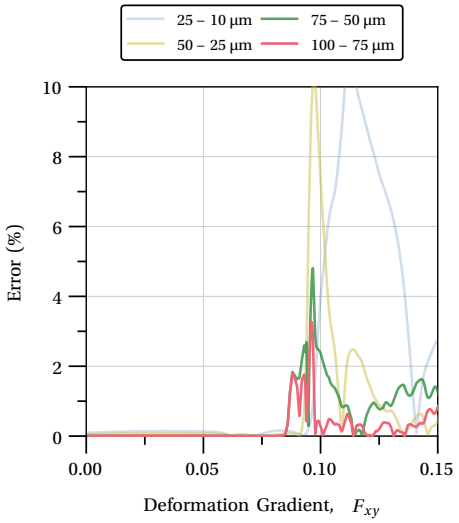


Figure 5.16: Variance in behaviour between one RVE size and the next closest RVE size.

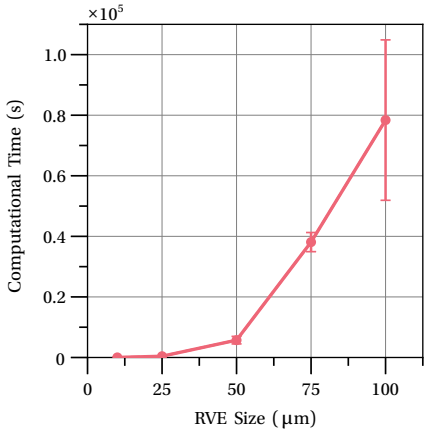
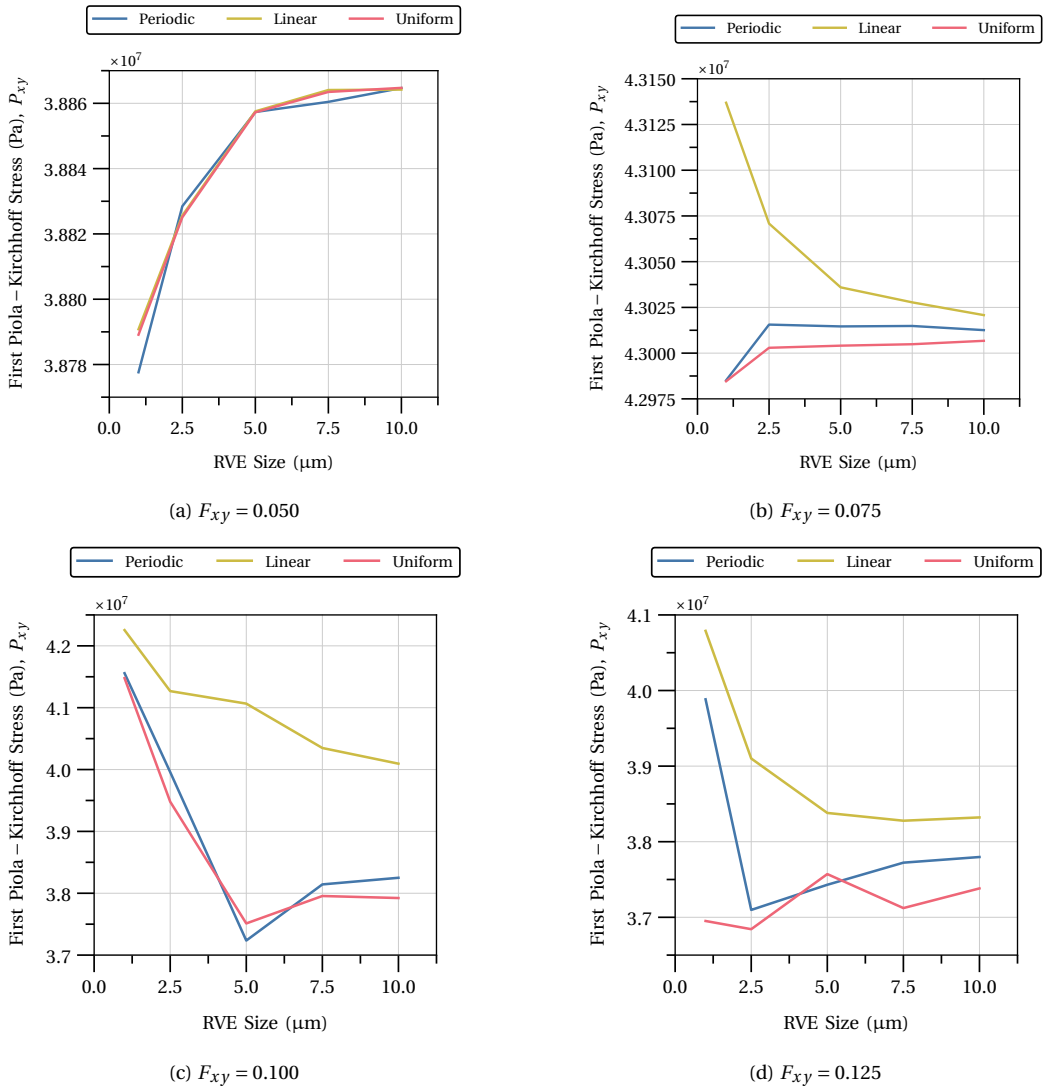


Figure 5.17: Average CPU time of the samples with 10% volume fraction and periodic boundary condition under shear across *xy* for different RVE sizes.

- Convergence of the boundary condition models



(a) $F_{xy} = 0.050$

(b) $F_{xy} = 0.075$

(c) $F_{xy} = 0.100$

(d) $F_{xy} = 0.125$

Figure 5.18: Homogenised First Piola Kirchhoff shear stress, P_{xy}, computed with distinct boundary conditions, for different RVE sizes with 10% volume fraction at four time instants.

- 20% volume fraction - periodic boundary condition

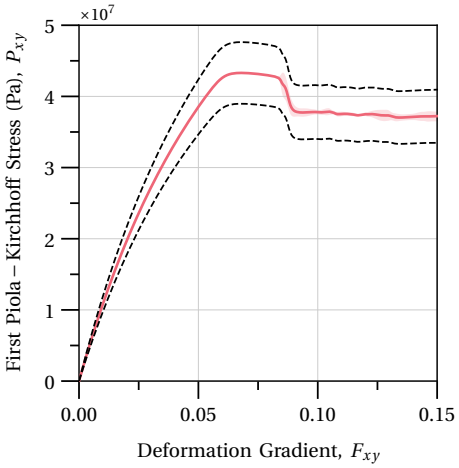


Figure 5.19: Homogenised First Piola Kirchhoff shear stress, P_{xy}, for the 50 µm RVE size with 20% volume fraction and periodic boundary condition. Shaded bounds: standard deviation; and dashed line: standard deviation 10% limit.

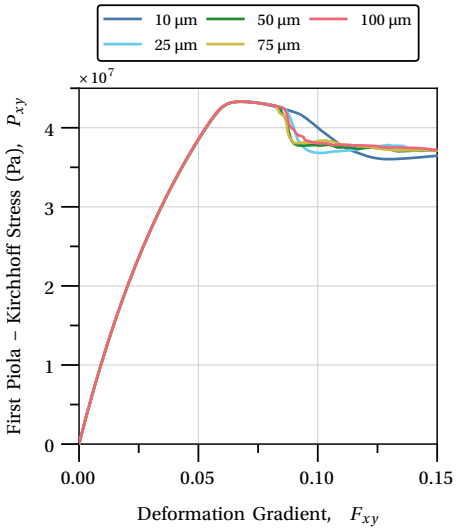


Figure 5.20: Comparison of the Homogenised First Piola Kirchhoff shear stress, P_{xy}, for different RVE sizes with 20% volume fraction and periodic boundary condition.

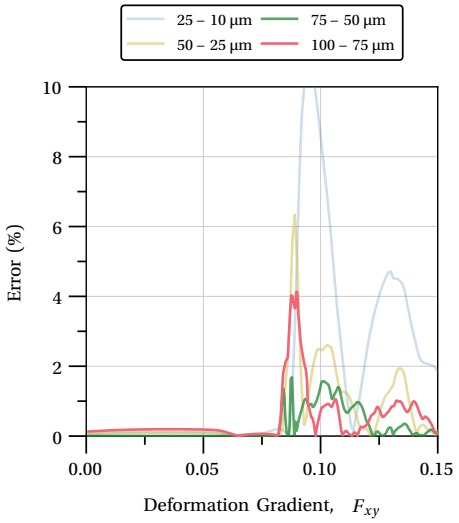


Figure 5.21: Variance in behaviour between one RVE size and the next closest RVE size.

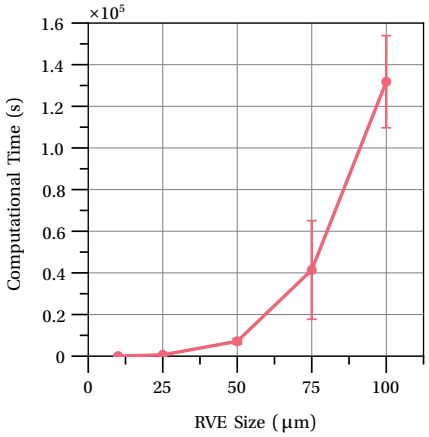


Figure 5.22: Average CPU time of the samples with 20% volume fraction and periodic boundary condition under shear across *xy* for different RVE sizes.

- 30% volume fraction - periodic boundary condition

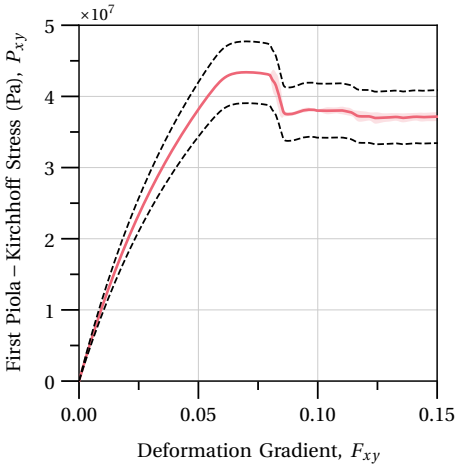


Figure 5.23: Homogenised First Piola Kirchhoff shear stress, P_{xy}, for the 50 µm RVE size with 30% volume fraction and periodic boundary condition. Shaded bounds: standard deviation; and dashed line: standard deviation 10% limit.

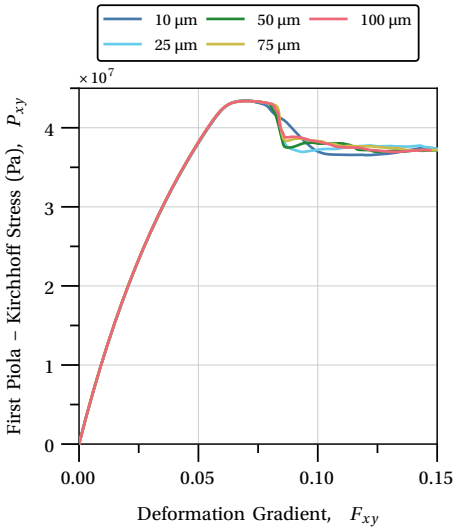


Figure 5.24: Comparison of the Homogenised First Piola Kirchhoff shear stress, P_{xy}, for different RVE sizes with 30% volume fraction and periodic boundary condition.

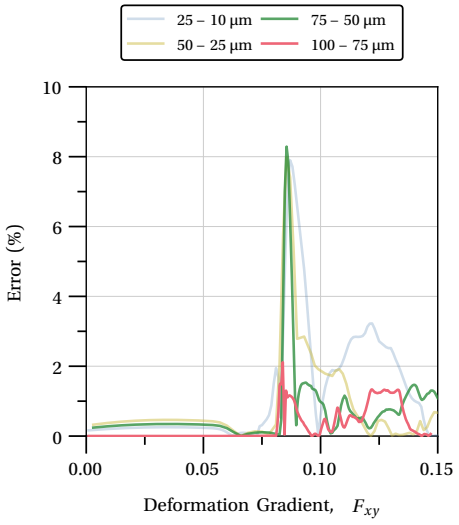


Figure 5.25: Variance in behaviour between one RVE size and the next closest RVE size.

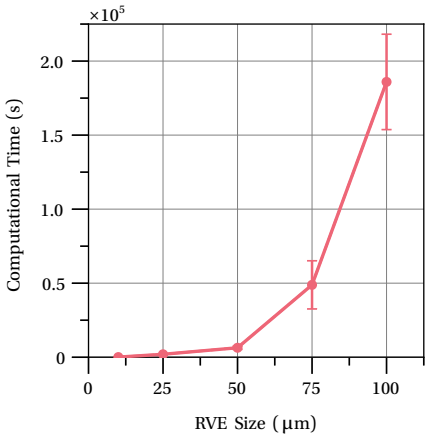


Figure 5.26: Average CPU time of the samples with 30% volume fraction and periodic boundary condition under shear across *xy* for different RVE sizes.

Uniaxial loading along *xx*

- 10% volume fraction - periodic boundary condition

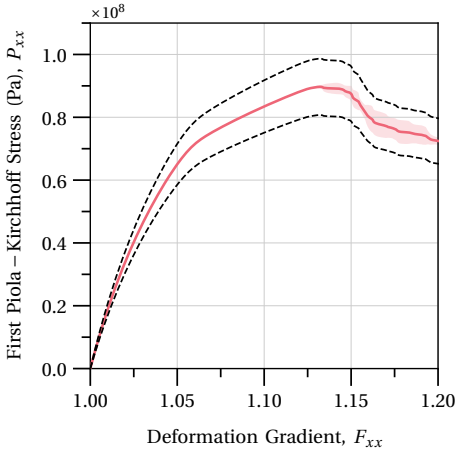


Figure 5.27: Homogenised First Piola Kirchhoff shear stress, P_{xx}, for the 50 µm RVE size with 10% volume fraction and periodic boundary condition. Shaded bounds: standard deviation; black dashed line: standard deviation 10% limit; red data: 5 samples; and blue data: 3 samples.

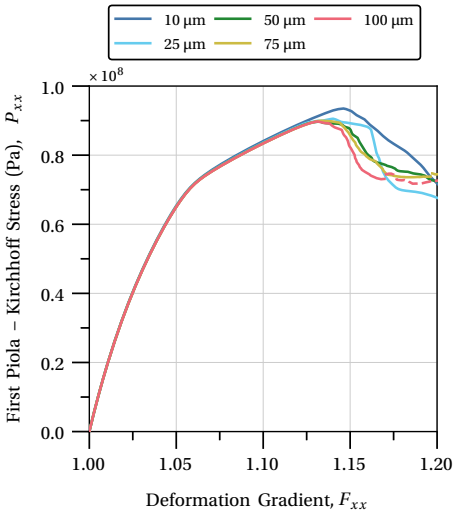


Figure 5.28: Comparison of the Homogenised First Piola Kirchhoff shear stress, P_{xx}, for different RVE sizes with 10% volume fraction and periodic bc. Solid line: 5 samples; and dashed line: 3 samples

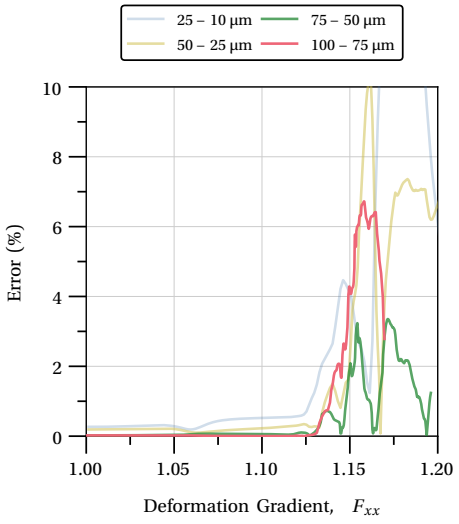


Figure 5.29: Variance in behaviour between one RVE size and the next closest RVE size.

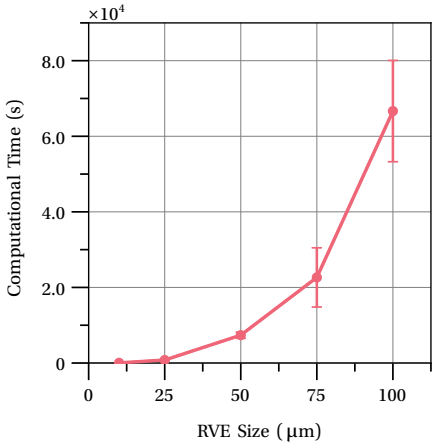


Figure 5.30: Average CPU time of the samples with 10% volume fraction and periodic boundary condition under uniaxial loading along *xx* for different RVE sizes.

- 20% volume fraction - periodic boundary condition

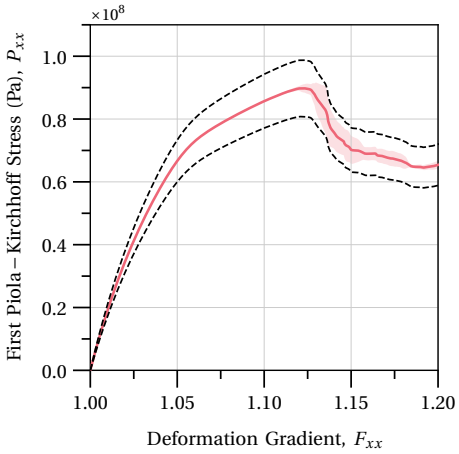


Figure 5.31: Homogenised First Piola Kirchhoff shear stress, P_{xx}, for the 50 µm RVE size with 20% volume fraction and periodic boundary condition. Shaded bounds: standard deviation; and dashed line: standard deviation 10% limit.

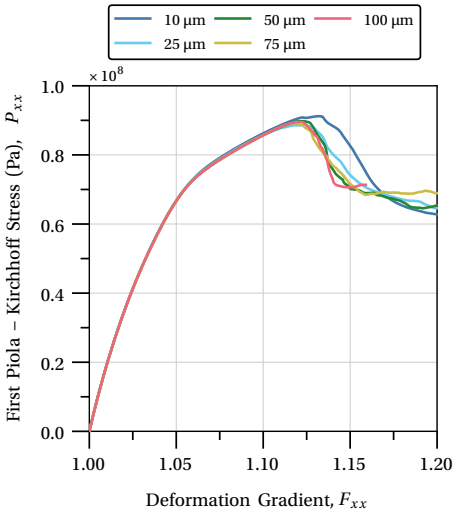


Figure 5.32: Comparison of the Homogenised First Piola Kirchhoff shear stress, P_{xx}, for different RVE sizes with 20% volume fraction and periodic boundary condition.

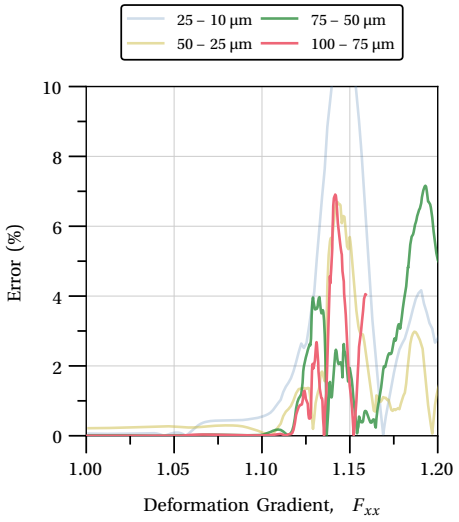


Figure 5.33: Variance in behaviour between one RVE size and the next closest RVE size.

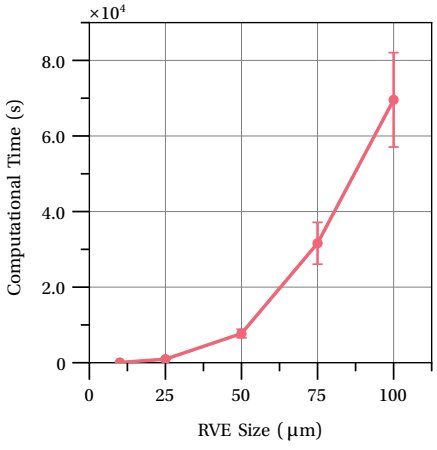


Figure 5.34: Average CPU time of the samples with 20% volume fraction and periodic boundary condition under uniaxial loading along *xx* for different RVE sizes.

- 30% volume fraction - periodic boundary condition

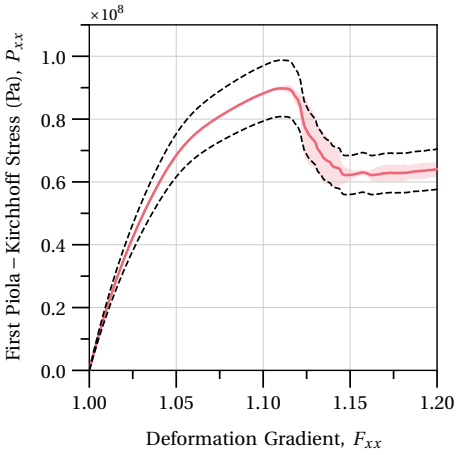


Figure 5.35: Homogenised First Piola Kirchhoff shear stress, P_{xx}, for the 50 µm RVE size with 30% volume fraction and periodic boundary condition. Shaded bounds: standard deviation; black dashed line: standard deviation 10% limit; red data: 5 samples; and blue data: 3 samples.

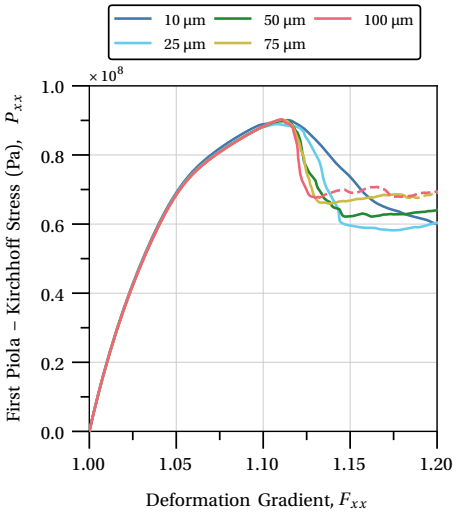


Figure 5.36: Comparison of the Homogenised First Piola Kirchhoff shear stress, P_{xx}, for different RVE sizes with 30% volume fraction and periodic bc. Solid line: 5 samples; and dashed line: 3 samples.

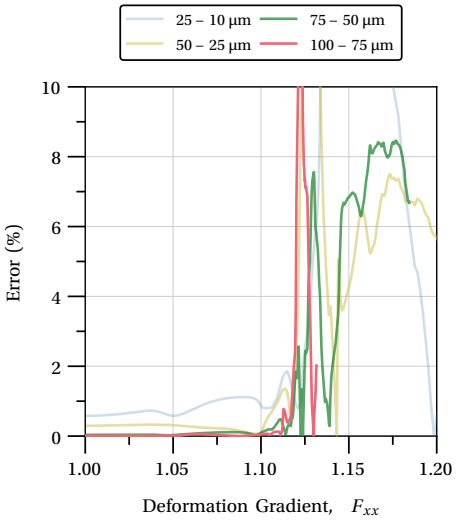


Figure 5.37: Variance in behaviour between one RVE size and the next closest RVE size.

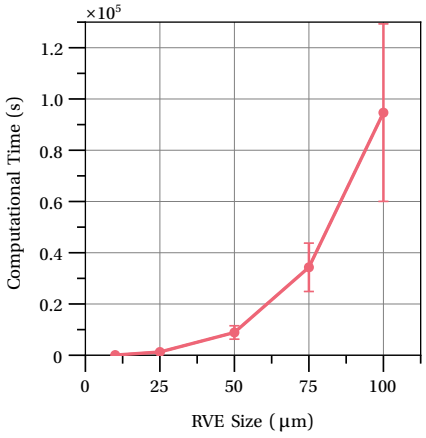


Figure 5.38: Average CPU time of the samples with 30% volume fraction and periodic boundary condition under uniaxial loading along *xx* for different RVE sizes.

Uniaxial loading along *yy*

- 10% volume fraction - periodic boundary condition

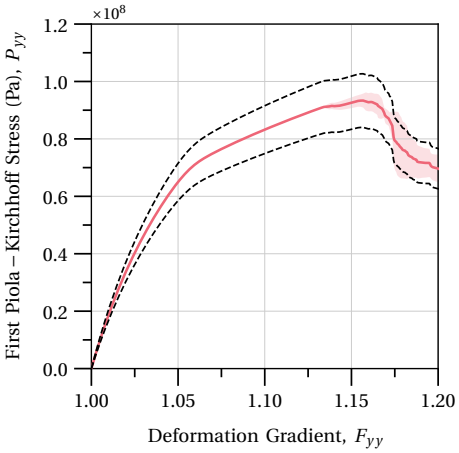


Figure 5.39: Homogenised First Piola Kirchhoff shear stress, P_{yy}, for the 50 µm RVE size with 10% volume fraction and periodic boundary condition. Shaded bounds: standard deviation; black dashed line: standard deviation 10% limit; red data: 5 samples; and blue data: 3 samples.

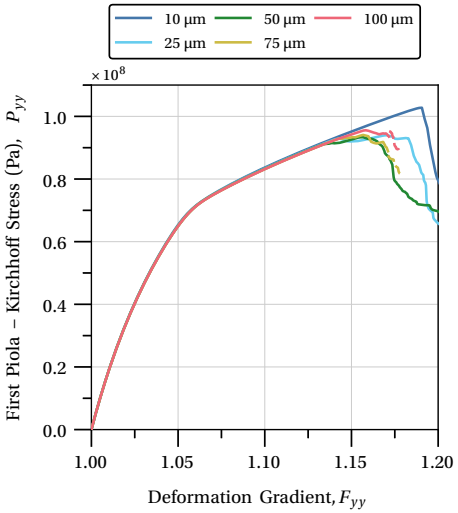


Figure 5.40: Comparison of the Homogenised First Piola Kirchhoff shear stress, P_{yy}, for different RVE sizes with 10% volume fraction and periodic bc. Solid line: 5 samples; and dashed line: 3 samples.

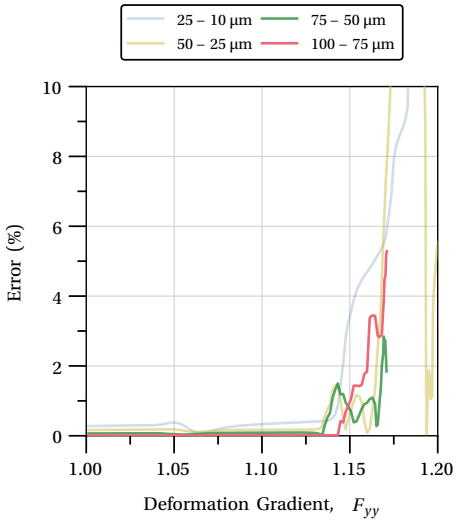


Figure 5.41: Variance in behaviour between one RVE size and the next closest RVE size.

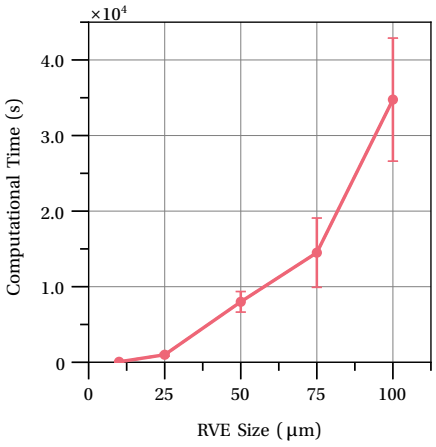


Figure 5.42: Average CPU time of the samples with 10% volume fraction and periodic boundary condition under uniaxial loading along *yy* for different RVE sizes.

- 20% volume fraction - periodic boundary condition

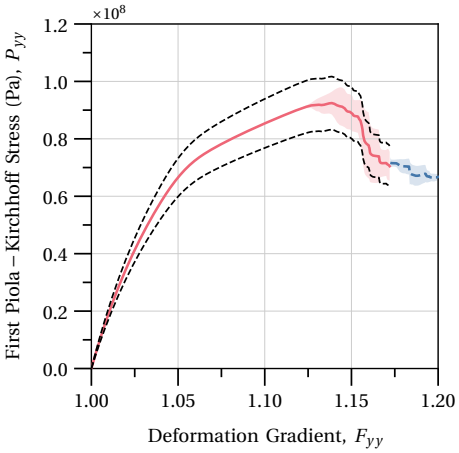


Figure 5.43: Homogenised First Piola Kirchhoff shear stress, P_{yy}, for the 50 µm RVE size with 20% volume fraction and periodic boundary condition. Shaded bounds: standard deviation; black dashed line: standard deviation 10% limit; red data: 5 samples; and blue data: 3 samples.

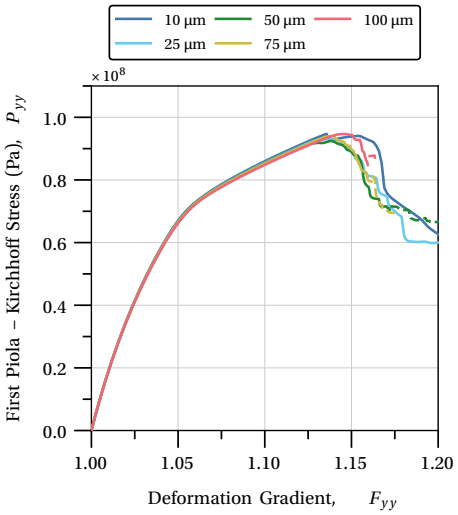


Figure 5.44: Comparison of the Homogenised First Piola Kirchhoff shear stress, P_{yy}, for different RVE sizes with 20% volume fraction and periodic bc. Solid line: 5 samples; and dashed line: 3 samples.

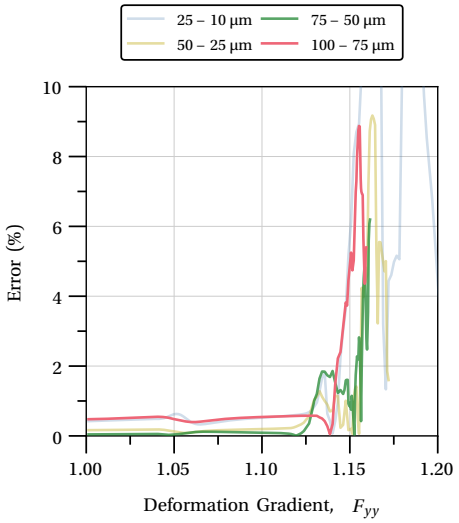


Figure 5.45: Variance in behaviour between one RVE size and the next closest RVE size.

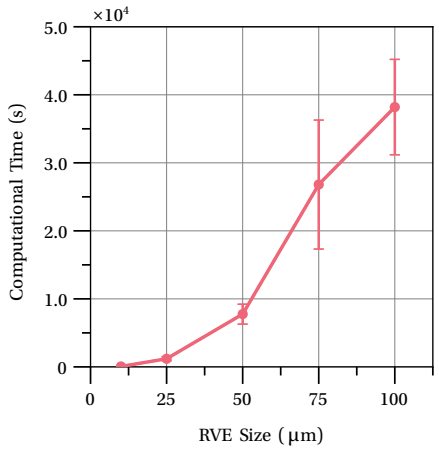


Figure 5.46: Average CPU time of the samples with 20% volume fraction and periodic boundary condition under uniaxial loading along *yy* for different RVE sizes.

- 30% volume fraction - periodic boundary condition

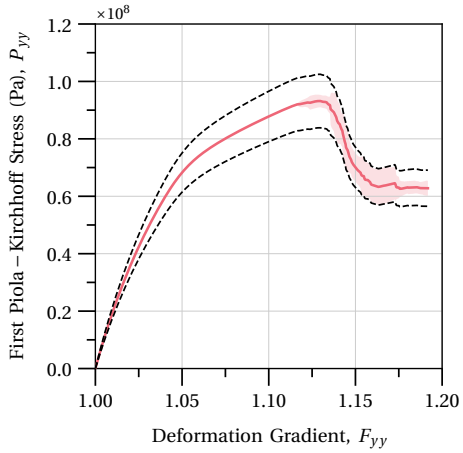


Figure 5.47: Homogenised First Piola Kirchhoff shear stress, P_{yy}, for the 50 µm RVE size with 30% volume fraction and periodic boundary condition. Shaded bounds: standard deviation; and dashed line: standard deviation 10% limit.

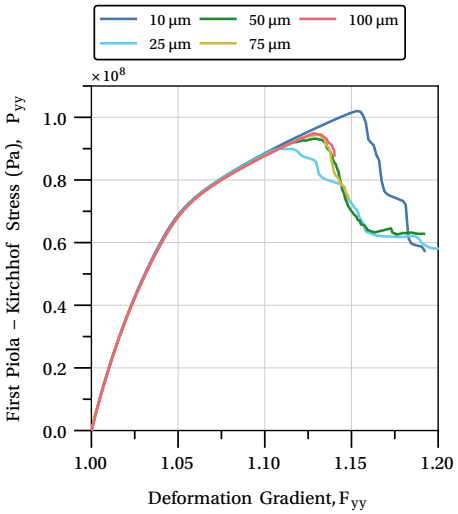


Figure 5.48: Comparison of the Homogenised First Piola Kirchhoff shear stress, P_{yy}, for different RVE sizes with 30% volume fraction and periodic boundary condition.

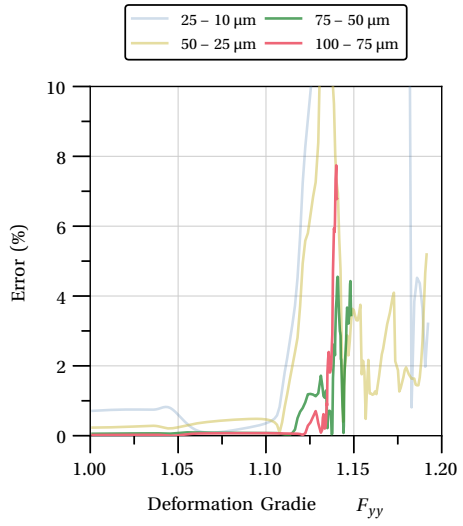


Figure 5.49: Variance in behaviour between one RVE size and the next closest RVE size.

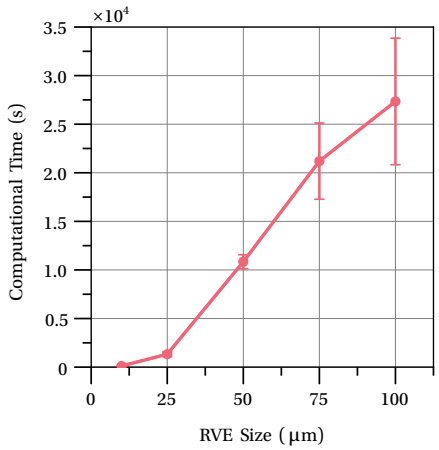


Figure 5.50: Average CPU time of the samples with 30% volume fraction and periodic boundary condition under uniaxial loading along *yy* for different RVE sizes.

5.3.2 2D RVE Size - Discussion

The applied deformation gradients for the three loads are quite high, hence extra caution is required in the analysis of the obtained results. Beyond certain deformation values, the ABS particles begin to deform significantly, as void nucleation within PB rubber particles starts to occur (as seen in Figures 5.51 and 5.52). Thus, the presented values are purely numerical and no longer have physical significance. This detail explains why the simulations stopped earlier with the increased RVE size. As the RVE size increases, the number of ABS particles and the degree of nucleation also increases accordingly, making it increasingly difficult for the simulator to interpret all the distortions correctly. Therefore, this is a sign that the representativeness of the RVE is clearly increasing with its size. It is worth noting that this phenomenon is not visualised for shear since, for this load, the nucleation phenomenon is much less relevant compared to the tensile loads, as can be seen in Figures 5.51, 5.52, and 5.53.

One aspect to consider while determining the representative size for the RVE is the computational cost associated with it, which is of even greater importance given the time constraints of the present study. As can be seen, regardless of the volume fraction and load combination, the computational cost increases exponentially. For a difference of one order of magnitude between RVE sizes (from 10 μm to 100 μm), the simulation time can differ by almost four orders of magnitude. This difference is more noticeable for the shear load since, as already mentioned, for the tensile loads, as the size increases, the simulation stops (rupture occurs) for increasingly smaller deformation gradients, and the last simulation steps take longer due to the computation of the nucleation phenomenon.

The first criterion mentioned for the analysis was to define a maximum variation of 10% for the standard deviation of the average deformation behaviour. As observed for all the examples analysed, regardless of the RVE size used, the fluctuation between the various samples is practically zero for the two initial zones, i.e., in the linear elastic zone and the visco-elastic zone up to the yield point. Thus, if the behaviour of interest is simply up to the yield point, regardless of the load and volume fraction, the smaller RVE size can accurately characterise the material behaviour. Nevertheless, if a more in-depth analysis is required after the yield point (as in the current research), it is necessary to perform more extensive analyses.

As initially introduced, when a material exhibits a strain-softening behaviour, an RVE may not exist, i.e., the material response does not converge as the RVE size increases. Fortunately, this is not observed for PC/ABS, as can be seen by

the clear convergence of the material's response for the three examined loads. Instead, it only exhibits a greater variation between different realisations for the same RVE size.

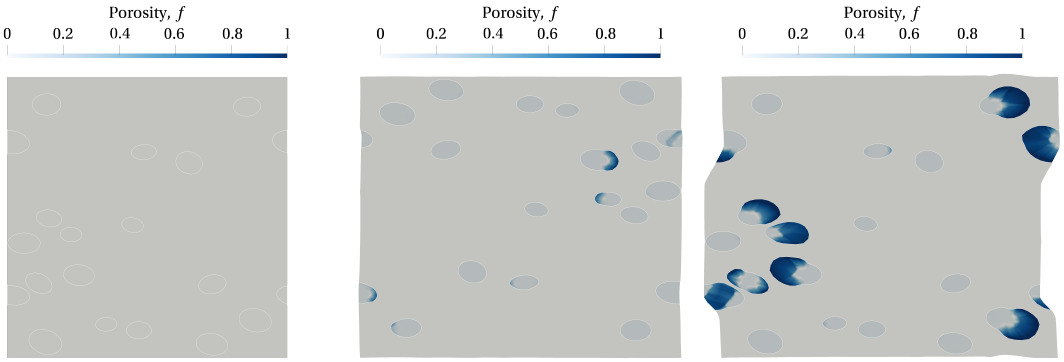


Figure 5.51: Time evolution of the nucleation phenomenon and deformation of a 10% volume fraction RVE under uniaxial loading along *xx*.

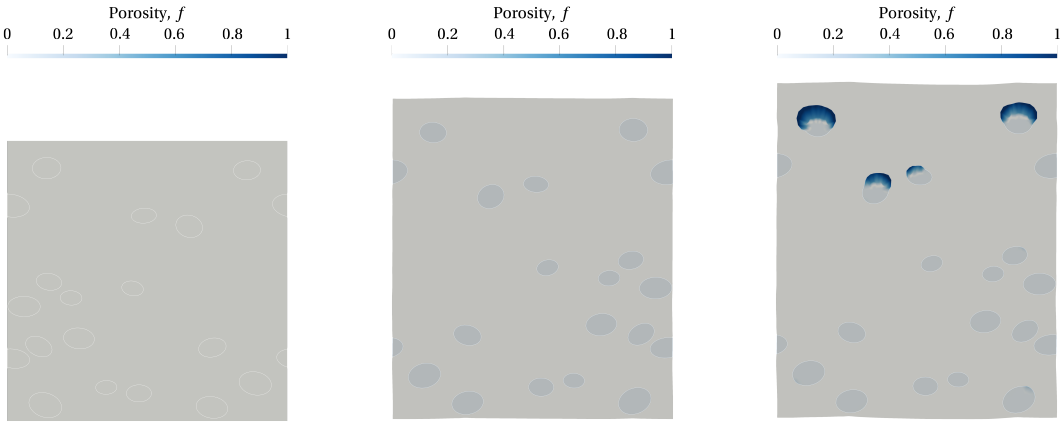


Figure 5.52: Time evolution of the nucleation phenomenon and deformation of a 10% volume fraction RVE under uniaxial loading along *xx*.

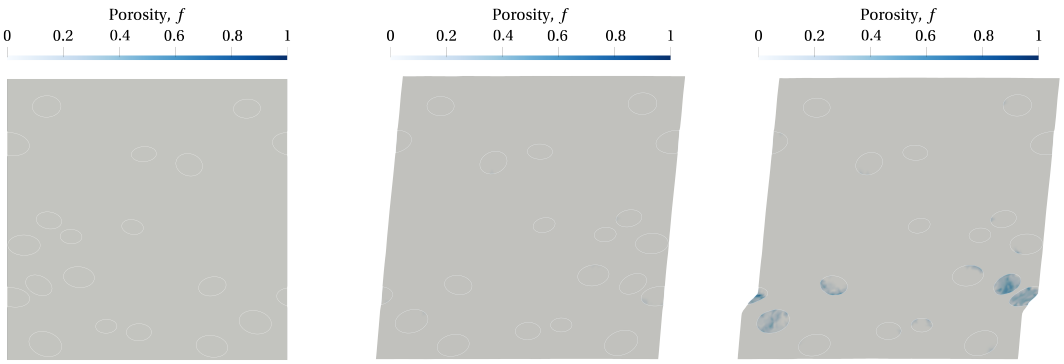


Figure 5.53: Time evolution of the nucleation phenomenon and deformation of a 10% volume fraction RVE under uniaxial loading along *xx*.

For shear, it can be seen that both the error in the average behaviour between consecutive sizes and the respective standard deviations show a considerable reduction up to the size of 50 μm. This is the minimum size that satisfies the first two criteria for all volume fractions. Above this value, the improvement in describing the material behaviour begins to be minimal, to which is added the fact that the computational cost increases drastically, becoming counterproductive. Consequently, it can be stated that the size of the Representative Volume Element can be considered as 50 μm for the shear load for all three volume fractions.

It should be noted that when subjected to shear, the material describes two softening zones. An early phase when predominantly visco-plastic deformation occurs, followed by a second phase where the stress decreases more drastically owing to the simultaneous occurrence of internal cavitation of the PB rubber particles and subsequent formation of voids within the ABS. In this last softening phase, the highest variation in the average behaviour of PC/ABS occurs, as factors such as the geometry, arrangement, and spacing of the particles strongly impact the occurrence of this phenomenon. After that, non-linear strain hardening occurs, and the response tends to stabilise again.

In contrast, for tensile loads, both in the *xx* and *yy* directions, the effects of nucleation begin to be immediately noticeable after the yield point. Therefore, two zones of softening with distinct degrees of stress decay are not observed. As for the case of shear, in this phase, due to the formation of voids, there is substantial variability in deformation behaviour, which only drops below the predefined value of 10%, in general for all scenarios, for RVE sizes bigger than 50 μm, inclusive. Above this magnitude, the fluctuations remain at practically constant percentages, with a little improvement that becomes impractical given the rise in processing effort.

As for the case of shear, the difference in average behaviour between successive sizes is extremely significant up to the size of 50 μm, after which the improvement in characterising the material behaviour starts to be insignificant. Thus, it can be stated that the size of the Representative Volume Element can be considered again as 50 μm for all three volume fractions.

A crucial aspect that can already be detected at this stage of the study is the anisotropy of the material between the injection direction (*xx*) and its perpendicular direction (*yy*). First, it is verified that the yield point is higher in the *yy* direction, a feature that can be explained by the fact that the resistant area of the abs particles is bigger (the particles are elongated in the injection direction). Second, it is verified that, on the other hand, the nucleation

phenomena is more prominent in this direction, as can be recognised by the rupture of the material at an earlier stage in the softening zone.

Regarding the different PC/ABS ratios, it is also possible to analyse some behavioural distinctions at this stage. The most noteworthy distinction is that the deformation value at which the yield point occurs decreases as the proportion of ABS increases. This difference is most substantial between values of 10 and 20% ABS, becoming progressively smaller for higher volume fractions of ABS. Nonetheless, the initial yield stress, which is the highest stress value before the material softening, remains unchanged.

It is essential to highlight that what makes this entire analysis feasible is the fact that the material behaviour clearly converges with the increase in RVE size. This aspect is reinforced by the analysis of Figure 5.18, where it can be noted that the other two boundary conditions encompass the periodic boundary condition and that they converge to a specific value. This behaviour is verified for the four distinct zones of its characteristic behaviour. Moreover, the convergence of the material response is only verified for larger RVE sizes beyond the yield point.

5.3.3 2D RVE Mesh

A mesh convergence analysis is carried out to determine a level of mesh discretisation that ensures solutions of adequate quality for the simulations going forward and to confirm whether or not there is a convergence of the response as the level of discretisation increases. This is also an important consideration when defining an RVE since numerical solutions to localisation problems may show an inherent mesh dependence. For example, the mesh spacing determines the minimum width of the band of localised deformation, leading to less dissipated energy the finer the mesh. Hence, the material's response might not converge for progressive finer meshes (Needleman, 1988; Forest and Lorentz, 2004).

This study is only performed after the study of the ideal size of representativity of the RVE, since this way, it is ensured that the response to which the study converges, if observed, is, in fact, the true behaviour of the material. In addition, it is more effective to tailor the mesh size to the actual representative size of the RVE, as different sizes can have different optimal discretisation levels. Just one volume fraction, namely 10% volume fraction, is investigated, as the conclusions obtained can be easily extrapolated and applied to all the others. The boundary condition employed was the periodic one, for the reasons described in Section 5.3.1.

With the possibility of the mesh dependence problem in mind, two loads with distinct nucleation levels are analysed: shear across *xy* (lower levels of damage) and uniaxial loading along yy (higher levels of damage). Thus, it is possible to evaluate, respectively, the influence of mesh size on the description of the material behaviour for its four phases, with the least possible influence of damage mechanisms, and the study of convergence, or lack thereof, for the case where nucleation is prominent.

As seen in the preceding section, the RVE with a side length of 50 μm is the minimum size that ensures good representativity. Therefore, five realisations of this RVE for each mesh discretisation level are computed. The corresponding results are compiled in Figures 5.54 and 5.58, where the x-axis displays the deformation gradient component in the loading direction and the y-axis the respective first Piola-Kirchhoff stress tensor component. Each line of the graph indicates a level of refinement of the mesh, denoted by their average total number of elements. Moreover, the standard deviation of the average deformation behaviour (see Figures 5.55 and 5.59), the error between the average behaviour of one level of mesh discretisation with the next closest one (see Figures 5.56 and 5.60) and the average CPU time for each level (see Figure 5.57) are also presented.

Shear across *xy*

By analysing Figures 5.54 to 5.56, it can be verified that there are no significant changes in the characterisation of the material behaviour between the coarsest mesh (3000 elements - below this value, the AMINO program cannot generate valid RVEs) and the finest mesh (11000 elements). Figure 5.54 shows that all lines depict the same development for the four zones of the material, with only slight differences in the final softening phase (the zone with the most pronounced stress reduction). However, this is explained by the fact that this zone presents the most considerable variation for the standard deviation of the average deformation behaviour (see Figure 5.55), with a fluctuation value of 6%, which is equal for all five levels of discretisation. Moreover, Figure 5.56 also shows that the error of the average behaviour between consecutive levels of discretisation presents a maximum of only 4% for all cases, also in this zone. As described previously, this is related to the occurrence of the nucleation phenomenon.

It can therefore be concluded that when damage mechanisms are less important, the minimum level of mesh refinement can be employed without compromising the obtained results. It is worth noting that even though this

degree of discretisation presents the highest standard deviation of the 5 cases in the hardening zone, this value does not surpass 2%.

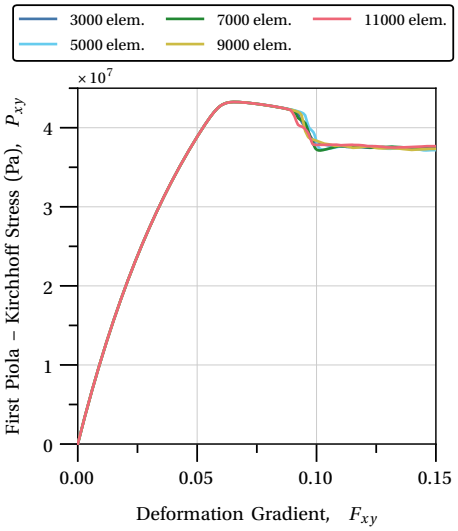


Figure 5.54: Comparison of the Homogenised First Piola Kirchhoff shear stress, P_{xy}, of RVEs with different mesh discretisation levels for 10% volume fraction and periodic boundary condition.

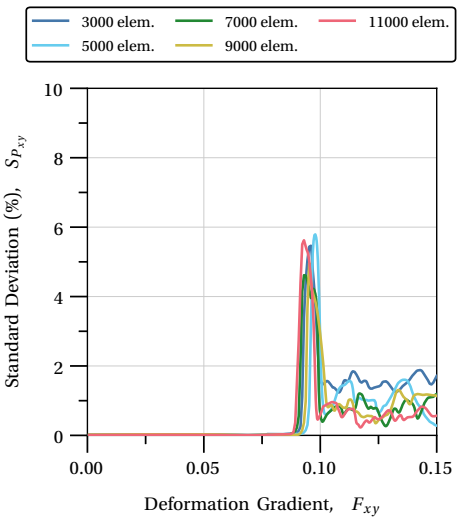


Figure 5.55: Standard deviation of the Homogenised First Piola Kirchhoff shear stress, P_{xy}, of RVEs with different mesh discretisation levels for 10% volume fraction and periodic boundary condition.

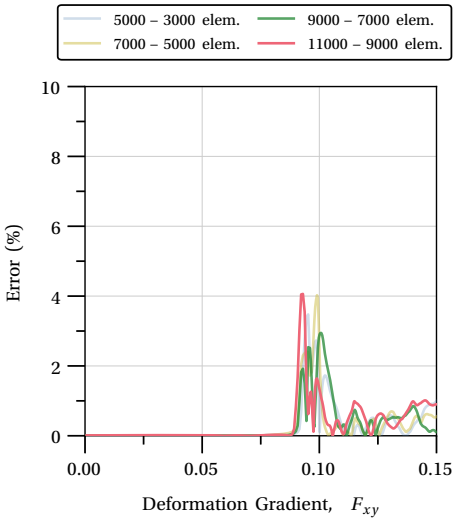


Figure 5.56: Variance in behaviour between one level of mesh discretisation and the next closest level.

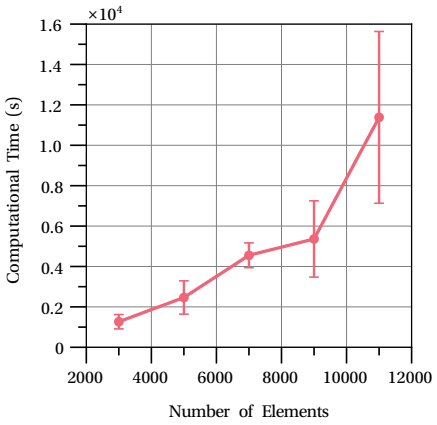


Figure 5.57: Average CPU time of the samples with 10% volume fraction and periodic boundary condition under shear across xy for different mesh discretisation levels.

Uniaxial loading along *yy*

In contrast, when nucleation is the primary phenomenon, the minimum level of mesh refinement can no longer be used (see Figure 5.58). However, it is possible to observe a definite convergence of the material response with increasing mesh discretisation level, thus avoiding the problem of inherent mesh dependence.

Taking this into account and considering that the computational cost increases considerably with the number of elements (see Figure 5.57), the optimal level of mesh refinement that can be employed in the simulations moving forward without compromising the obtained results is around 5000 to 7000 elements. Presenting a maximum variation for the standard deviation of the average deformation behaviour of 5% (see Figure 5.59) and an error of the average behaviour between consecutive discretisation levels of only 1% (see Figure 5.60). Lastly, since the RVE with 7000 elements was utilised in the previous analysis, it is confirmed that previously obtained findings are reliable and accurate.

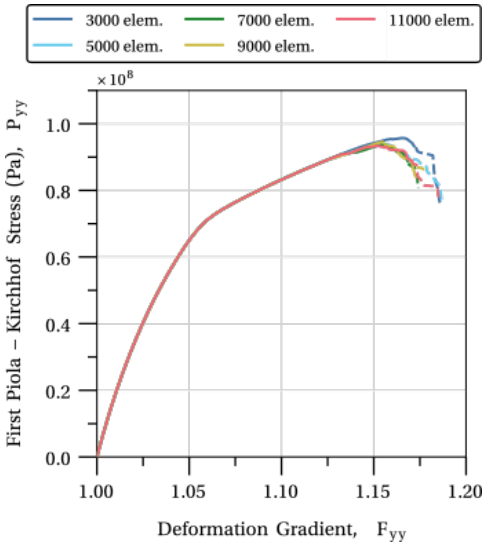


Figure 5.58: Comparison of the Homogenised First Piola Kirchhoff shear stress, P_{yy}, of RVEs with different mesh discretisation levels for 10% volume fraction and periodic boundary condition. Solid line: 5 samples; and dashed line: 3 samples.

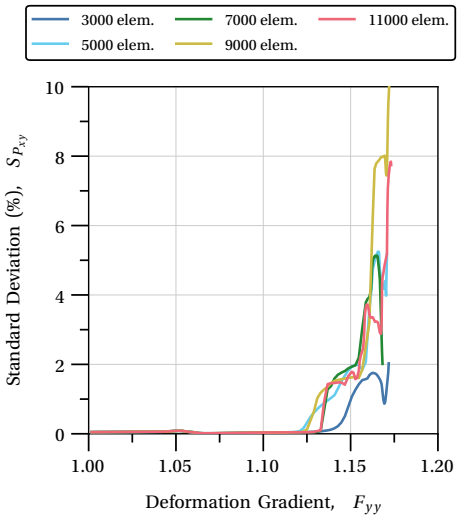


Figure 5.59: Standard deviation of the Homogenised First Piola Kirchhoff shear stress, P_{yy}, of RVEs with different mesh discretisation levels for 10% volume fraction and periodic boundary condition.

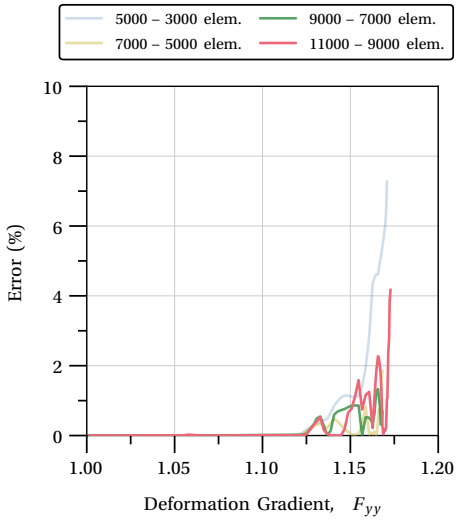


Figure 5.60: Variance in behaviour between one level of mesh discretisation and the next closest level.

5.3.4 3D RVE Size

The 3D analysis's findings are presented in this section. As it was shown that the same size of RVE could be employed for the three evaluated loads in the 2D analysis, there was a definite convergence of the material response, and since the 3D simulations require a greater computational effort, it was decided to analyse just one deformation gradient, namely shear across xy denoted as

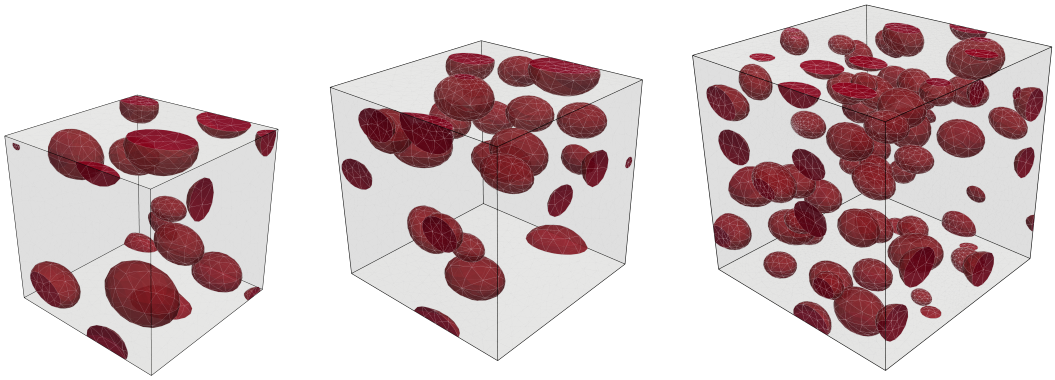
$$\text{Shear across } xy: \quad \boldsymbol{F} = \begin{bmatrix} 1.00 & 0.15 & 0.00 \\ 0.00 & 1.00 & 0.00 \\ 0.00 & 0.00 & 1.00 \end{bmatrix}. \tag{5.49}$$

This load was selected for analysis because, as previously shown, nucleation is not as prominent under shear. On this basis, the four main zones of the typical PC/ABS response can be analysed. Moreover, given the ABS particles' distribution and geometry, it can easily be assessed that the behaviour of the material in the new dimension (zz) will be very similar to that of the behaviour described in the direction yy for the 2D analysis, as it is also perpendicular to the injection direction (xx).

Preliminary simulations using microstructural samples smaller than 15 µm showed that the RVE size could not be less than 15 µm. Consequently, this value is the first volume element size to begin the investigation. In addition to this size, 2 more RVE sizes are evaluated: 20 µm and 25 µm. Unfortunately, a size

of 25 μm demands very high computational resources; therefore, it will only be studied for the 10% volume fraction.

The finite element analyses are carried out with the microstructure being discretised in a nonconform TETRA10 mesh with 4 Gauss integration points. Figure 5.61 depicts the three initial RVE sizes in the study for the 10% volume fraction, enabling a better understanding of their magnitude and representativity. The degree of refinement of the matrix was maintained constant for all three sizes so as not to impact the findings produced. Thereafter, having determined the appropriate size for the representativeness of the RVE, the impact of the mesh discretisation level is assessed in Section 5.3.6. Note, however, that, unlike the 2D study, the mesh refinement level is now lower to enable the study of bigger RVE sizes within an acceptable time frame.



(a) 15 μm (b) 20 μm (c) 25 μm

Figure 5.61: Various 3D realisations with volume fraction equal to 10% and different volume element sizes.

As demonstrated in Sections 5.3.1 and 5.3.2, as the RVE's size grows, the periodic boundary condition converges to the actual value more rapidly than the remainings. Consequently, smaller RVEs (and, therefore, less computational effort) are required to obtain results with the same precision. With this in mind, it was decided to employ this boundary condition once again to carry out the 3D analysis.

Nonetheless, for 3D situations, either owing to the increased complexity of the RVE geometry itself or due to the introduction of a third dimension, even though the generated microstructures display geometrical periodicity, the associated discretisation results in non-conform non-periodic meshes. This is a concern since meshes must comply on opposing RVE sides in the standard finite element implementation of periodic boundary conditions. Moreover, mesh generation fulfilling this requirement can become rather cumbersome.

Hence, Rodrigues Lopes et al. (2021) suggested an alternative technique based on a mortar formulation to efficiently impose periodic boundary conditions over complex RVEs at finite strains with randomly generated finite element meshes. The mortar periodic boundary condition can be considered a mesh tying problem between opposite RVE faces. The mapping and segmentation procedures are based on geometric projection and the intersection of elements in intermediate planes, where integration points are established. Refer to the mentioned reference for a more profound development on the subject, from its implementation to its numerical assessment.

The major drawback of this strategy is the enormous processing power required. For example, for a particular discretisation of an RVE, the mortar periodic condition takes 11h 30min to complete the entire simulation, while the linear boundary condition only takes a mere 14min. However, it should be noted that the linear condition did not exhibit the expected behaviour beyond the yield point, which is the reason why this study was not undertaken using this condition.

In order to overcome this adversity, and after several numerical experiments, it was found that using an iterative solver, namely WSMP (Watson Sparse Matrix Program) (Gupta, 2002b,a), was much faster for tackling the problems under consideration. Returning to the preceding example, it was possible to cut the computational time of the direct solver from 11h 30min to only 1h 1m by employing the aforementioned iterative solver.

Very succinctly, direct methods provide a solution to the linear system of equations in a finite number of steps without requiring any starting estimate. Typically, the solution of a system of equations can easily be determined using a forward or backward substitution algorithm, after reducing the coefficients matrix to a triangular form. In this sense, direct solvers give exact solutions to the detriment of being computationally expensive for large systems. On the other hand, iterative methods solve the systems of linear equations iteratively by refining an initial guess of the solution to the system until a convergence condition is reached. This way, they can be much quicker and consume less memory. Nevertheless, one must always proceed cautiously when employing an iterative solution since convergence is not assured or can be extremely slow in many circumstances.

In order to carry out a thorough analysis of the data acquired and to be able to apply the three criteria indicated, the same four types of graphs described for the 2D analysis (see Section 5.3.1) are used (presented in Figures 5.62 to 5.73 and Appendix A.2).

Shear across *xy*

- 10% volume fraction - mortar periodic boundary condition

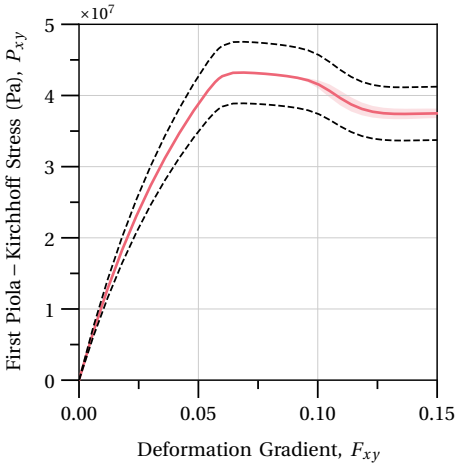


Figure 5.62: Homogenised First Piola Kirchhoff shear stress, P_{xy}, for the 15 µm RVE size with 10% volume fraction and mortar periodic boundary condition. Shaded bounds: standard deviation; black dashed line: standard deviation 10% limit; red data: 5 samples; and blue data: 3 samples.

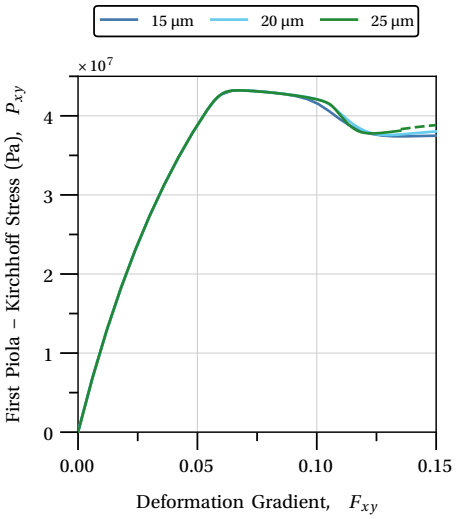


Figure 5.63: Comparison of the Homogenised First Piola Kirchhoff shear stress, P_{xy}, for different RVE sizes with 10% volume fraction and mortar periodic boundary condition.

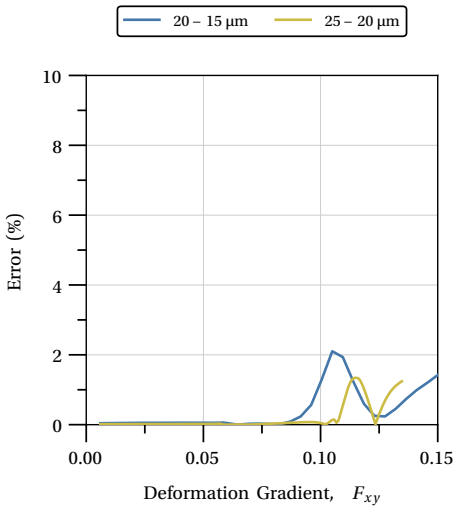


Figure 5.64: Variance in behaviour between one RVE size and the next closest RVE size.

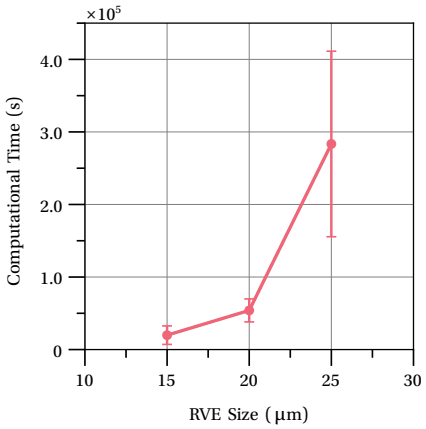


Figure 5.65: Average CPU time of the samples with 10% volume fraction and mortar periodic boundary condition under shear across *xy* for different RVE sizes.

- 20% volume fraction - mortar periodic boundary condition

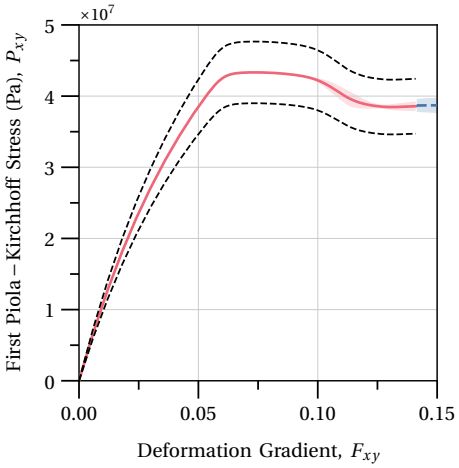


Figure 5.66: Homogenised First Piola Kirchhoff shear stress, P_{xy}, for the 15 µm RVE size with 20% volume fraction and mortar periodic boundary condition. Shaded bounds: standard deviation; black dashed line: standard deviation 10% limit; red data: 5 samples; and blue data: 3 samples.

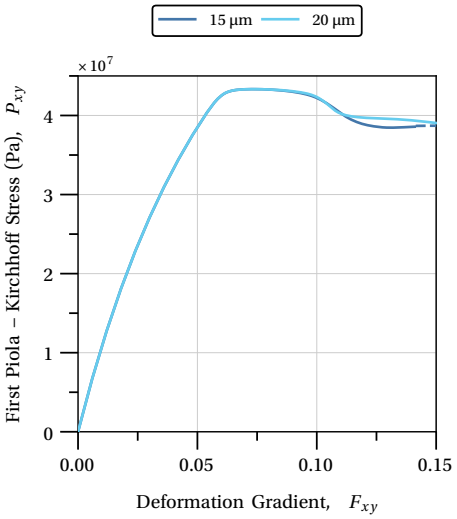


Figure 5.67: Comparison of the Homogenised First Piola Kirchhoff shear stress, P_{xy}, for different RVE sizes with 20% volume fraction and mortar periodic boundary condition.

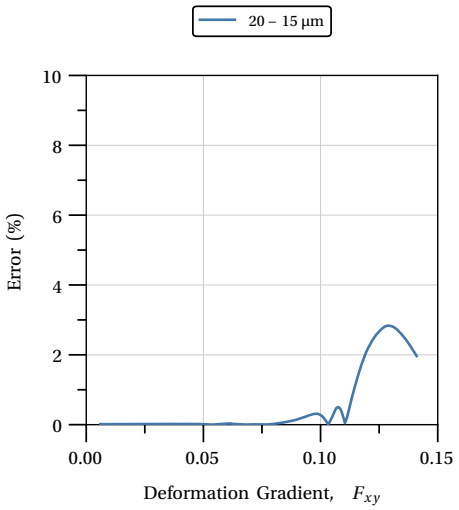


Figure 5.68: Variance in behaviour between one RVE size and the next closest RVE size.

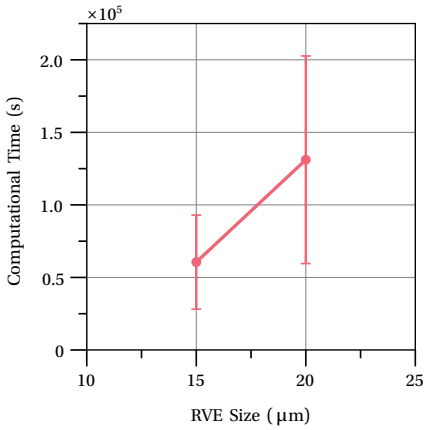


Figure 5.69: Average CPU time of the samples with 20% volume fraction and mortar periodic boundary condition under shear across *xy* for different RVE sizes.

- 30% volume fraction - mortar periodic boundary condition

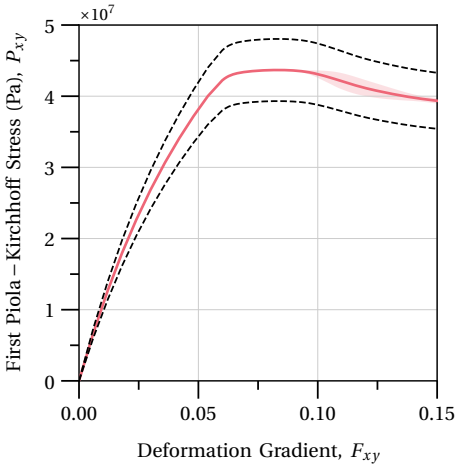


Figure 5.70: Homogenised First Piola Kirchhoff shear stress, P_{xy}, for the 15 µm RVE size with 30% volume fraction and mortar periodic boundary condition. Shaded bounds: standard deviation; and dashed line: standard deviation 10% limit.

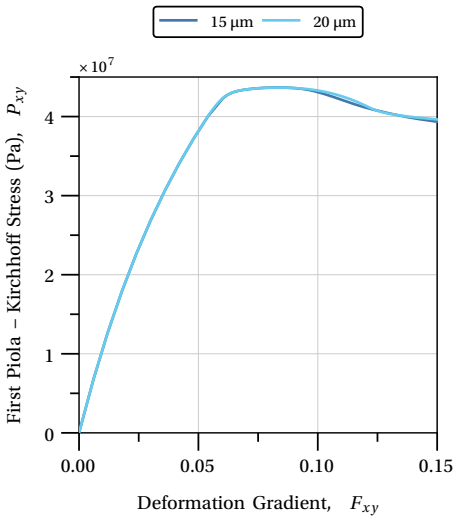


Figure 5.71: Comparison of the Homogenised First Piola Kirchhoff shear stress, P_{xy}, for different RVE sizes with 30% volume fraction and mortar periodic boundary condition.

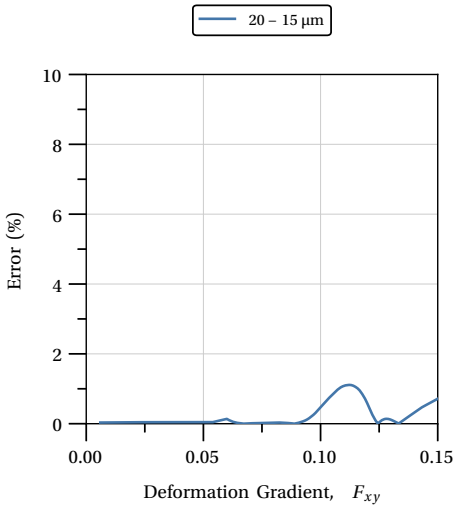


Figure 5.72: Variance in behaviour between one RVE size and the next closest RVE size.

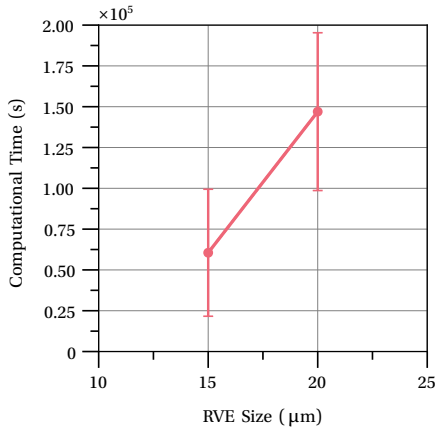


Figure 5.73: Average CPU time of the samples with 30% volume fraction and mortar periodic boundary condition under shear across *xy* for different RVE sizes.

5.3.5 3D RVE Size - Discussion

As highlighted in the 2D representativity study, the computational cost is one of the main limitations of this work. This aspect is considerably more prominent in the 3D analysis, where, as seen in Figures 5.65, 5.69, and 5.73, it increases much more sharply than in the 2D. In fact, for an RVE with a dimension of 15 μm and a volume fraction of 10% (the simplest case), the average simulation time is approximately 7 hours, peaking over 3 days and 12 hours for a size of 25 μm. That is, for a dimensional increase of 10 μm, the duration rose by approximately 11 times. In addition, the memory required to execute the simulations also rises, diminishing the capacity to do several simulations simultaneously for sizes bigger than 15, leading to an even higher increase in the overall time necessary to execute all the simulations. It should also be noted that the computing effort increases with increasing ABS volume fraction.

Considering the reported data, analysing an RVE size bigger than 15 μm becomes impracticable, and thus this size is selected as the representative size for the three volume fractions in the subsequent analyses. The evolution of the deformation for the studied load, shear across *xy*, and selected RVE size is illustrated in Figure 5.74.

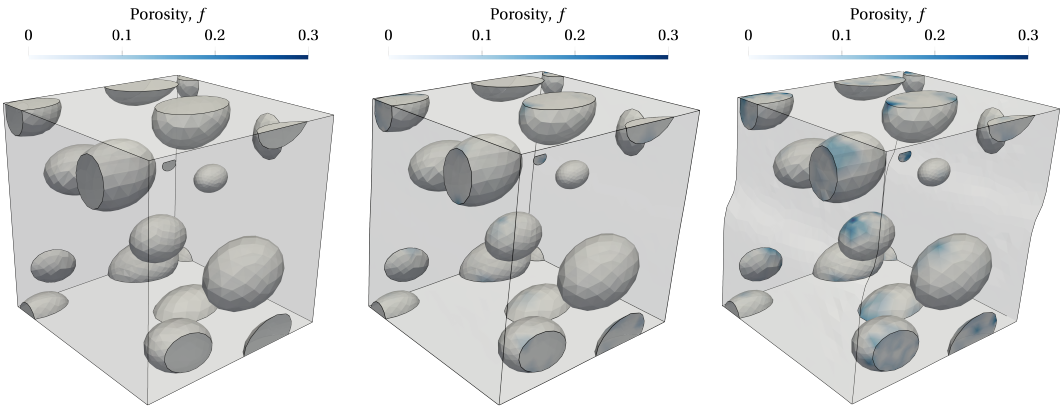


Figure 5.74: Time evolution of the nucleation phenomenon and deformation of a 10% volume fraction RVE under shear across *xy*.

By analysing Figures 5.63, 5.67, and 5.71, it can be observed that there is a deviation in behaviour between the representative size of 15 μm and the next size of 20 μm, solely in the final softening zone and in the hardening zone. Comparatively, in the first mentioned zone, the representative size presents a smoother softening evolution, but the stress value at the beginning and end of softening is practically identical to the following sizes. In the second-mentioned

zone, the representative size does not have the same ability to describe the hardening effect, as there is not such a notable stress increase.

Nonetheless, the two established criteria (a maximum variation of 10% for the standard deviation of the average deformation behaviour; and, a maximum error of 10% in the average behaviour between successive sizes) are fulfilled, even after considering these variations in the material behaviour description. The error reaches only a maximum value of 3% for a volume fraction of 20%, presenting lower values for the other two fractions (see Figures 5.64, 5.68, and 5.72), and the values for the standard deviation of the average deformation behaviour between samples is also minimum.

When analysing the 2D and 3D RVEs, it is observed that there are no distinctions in characterising the evolution of the material behaviour up to the yield point. However, after this point, the second softening phase (the zone with a more pronounced decrease in stress) is no longer described in the same manner. The two primary aspects are that this phase starts, on average, at a higher deformation level in the 3D analysis for all three PC/ABS ratios, and its evolution is smoother. Nonetheless, in both experiments, the ultimate stress after softening, the beginning of hardening, is practically the same.

One of the fundamental causes for the first reported disparity is assuming the plain strain state in the 2D analysis, although it is not the most accurate assumption. This can be immediately noticed from the geometry and arrangement of ABS particles. Thus, it can be concluded that the 3D RVE presents more accurate results. The second disparity reported comes from employing an RVE with a diameter less than the ideal, as previously mentioned.

5.3.6 3D RVE Mesh

A 3D mesh convergence analysis is also conducted to define a level of mesh discretisation that ensures solutions of appropriate quality for the simulations moving forward. This study is only performed after the study of the ideal size of representativity of the RVE, since it is more effective to tailor the mesh size to the actual representative size of the RVE, as different sizes can have different optimal discretisation levels.

Just one volume fraction, namely 10% volume fraction, under shear across xy will be investigated, as the conclusions obtained can be easily extrapolated and applied to all the others. The same boundary condition was employed, the mortar periodic boundary condition, for the reasons described in Section 5.3.4. Furthermore, only one load is studied, as it has already been demonstrated for

the 2D case that there is convergence in the material response with respect to mesh size.

For this scenario, as seen in the preceding section, the RVE with a side length of 15 μm is the minimum size that ensures good representativity. Five realisations of this RVE for each mesh discretisation level are computed. The corresponding results are compiled in Figures 5.75 to 5.78 (the same four graphs described for the 2D analysis (see Section 5.3.3) are used).

Similar to what was discovered in the investigation of RVE size, under shear across *xy*, the material behaviour between the coarsest mesh (10000 elements - discretisation applied in the previous analysis) and the finest mesh (30000 elements) displays only slight changes in the final softening and hardening zones. In other words, the differences begin to develop during the initiation of the nucleation phenomena.

While it is observed that a finer mesh leads to a more accurate description of the material behaviour, to which is added the fact that this difference is expected to be more significant for tensile loads, it is also associated with longer simulation times and greater memory demands. For instance, the computational time evolves approximately linearly, almost doubling for every 10000 elements. Consequently, opting for a mesh discretisation level greater than the coarsest one analysed transforms future analyses impracticable.

However, even when adopting a coarser mesh, it is only observed a peak difference of 4% compared to the behaviour of a finer mesh and a peak standard deviation of 5% between realisations. In addition to presenting more than satisfactory results, this behaviour variation occurs during the final softening phase, a zone typically linked with a greater deviation (where nucleation occurs).

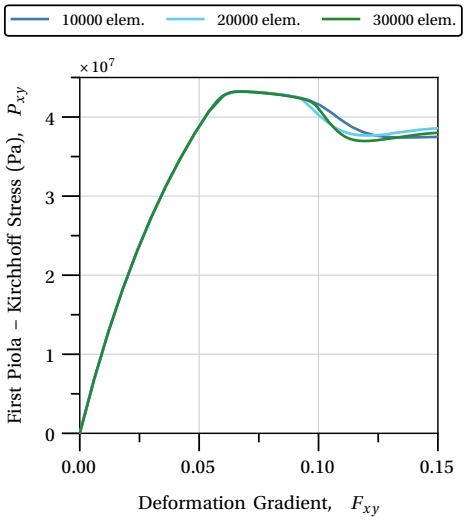


Figure 5.75: Comparison of the Homogenised First Piola Kirchhoff shear stress, P_{xy}, of RVEs with different mesh discretisation levels for 10% volume fraction and periodic mortar boundary condition.

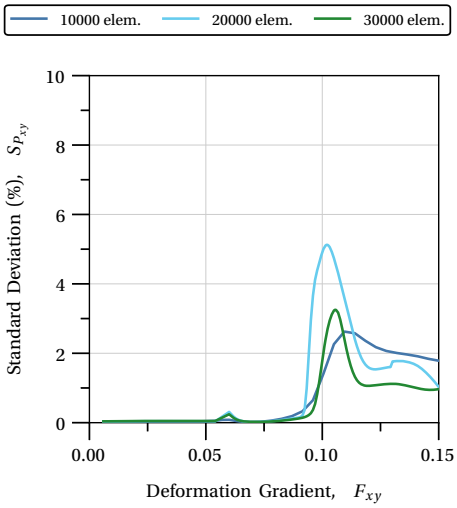


Figure 5.76: Standard deviation of the Homogenised First Piola Kirchhoff shear stress, P_{xy}, of RVEs with different mesh discretisation levels for 10% volume fraction and periodic mortar boundary condition.

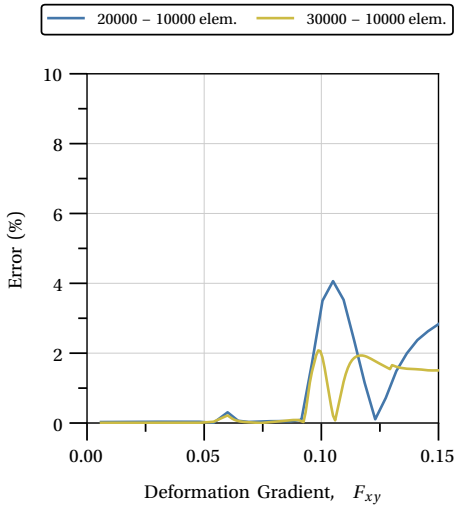


Figure 5.77: Variance in behaviour between one level of mesh discretisation and the next closest level.

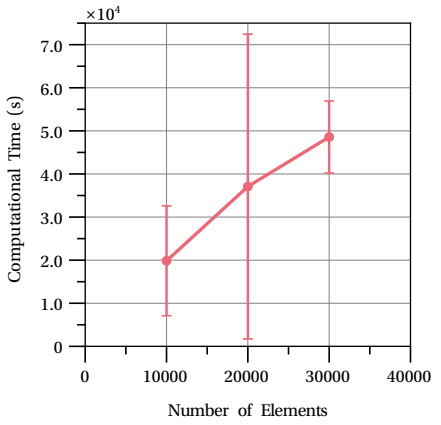


Figure 5.78: Average CPU time of the samples with 10% volume fraction and periodic mortar boundary condition under shear across xy for different mesh discretisation levels.

5.3.7 Remark on the Periodic Boundary Condition - 3D

After some modifications to the RVE generation programme, AMINO, code, it was possible to generate RVEs with periodic meshes. However, this was only attainable for a volumetric fraction of 10% and 20% of ABS with a side length of 15 μm. Figures 5.79 to 5.82 present the results obtained for this boundary condition under shear across xy and their comparison with the condition applied in the experiments presented before, mortar periodic.

As can be observed, there is a slight difference in the material behaviour description as the more pronounced softening zone begins, reaching a maximum difference value of 5% between the two boundary conditions. The periodic boundary condition is the one that presents a behaviour most similar to the expected one.

The difference in results between the simulations could have been caused by the parameter α, associated with the strategy to modify the non-mortar quadratic shape functions associated with triangular elements (Popp et al., 2012), not being set to the most suitable value for the problem. However, after conducting a parametric study, it was concluded that the default value of 10^{-5}, used by Rodrigues Lopes et al. (2021), was the most appropriate.

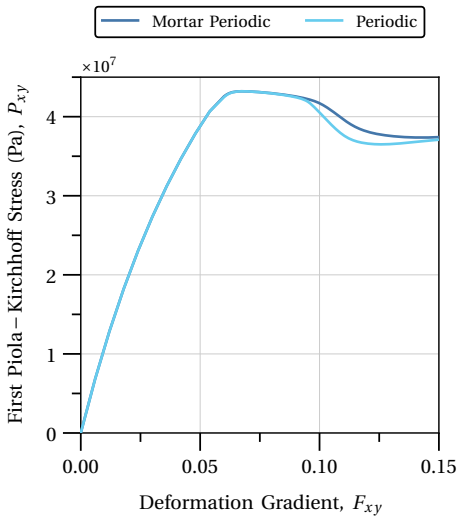


Figure 5.79: Comparisons between the average stress-deformation of the samples with 10% volume fraction for the mortar periodic and periodic boundary conditions.

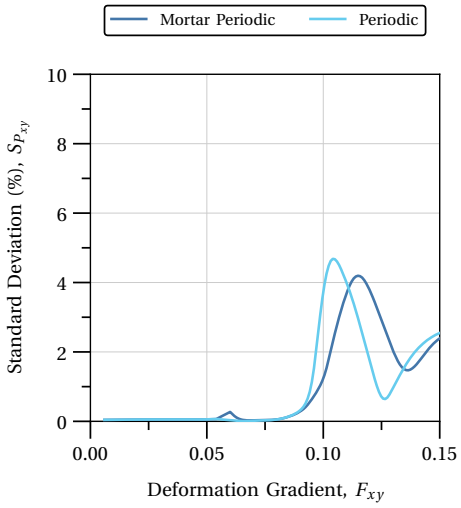


Figure 5.80: Comparison between the standard deviation of the average stress-deformation of the samples with 10% volume fraction for the mortar periodic and periodic boundary conditions.

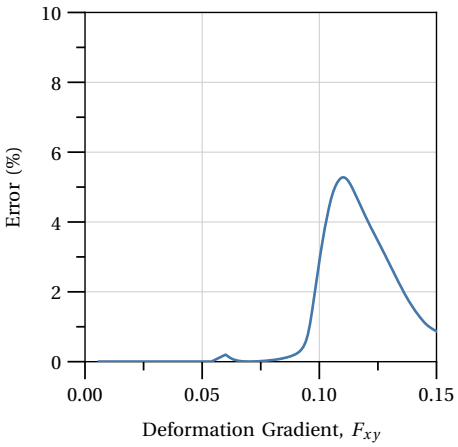


Figure 5.81: Variance in behaviour between the mortar periodic and periodic boundary conditions.

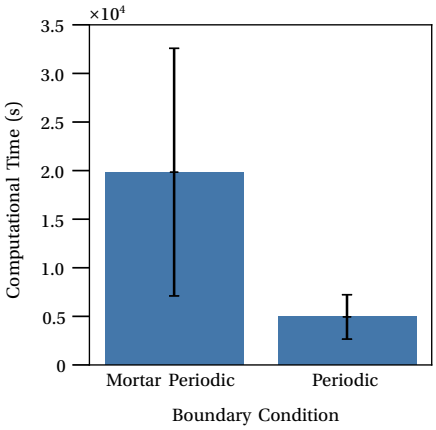


Figure 5.82: Comparison between the average CPU time of the samples with 10% volume fraction for the mortar periodic and periodic boundary conditions.

Moreover, the mortar periodic condition involves tying the mesh between opposite faces of the RVE, which is an approximate method and not 100% accurate. Since the discretisation of the 3D RVEs used was not the most refined, a small portion of a particle remaining on the border of the RVE could result in a highly deformed mesh that would lead to the mapping and segmentation procedures not occurring in the most precise way. This can be confirmed by the results in Figure 5.83, where the RVE in Figure 5.83(a) has a small particle on the border, unlike the RVE in Figure 5.83(b).

Lastly, this difference in response can also demonstrate, although not guaranteed, that the dimension of the RVE chosen is still not the one that best represents the material. The material's response must be independent of the boundary conditions adopted for an RVE to be representative.

Therefore, considering that the periodic condition best characterises the PC/ABS evolution and that computational time reduces by approximately 4 times, in future studies, this boundary condition is implemented whenever PC/ABS with a 10% and 20% ratio is studied.

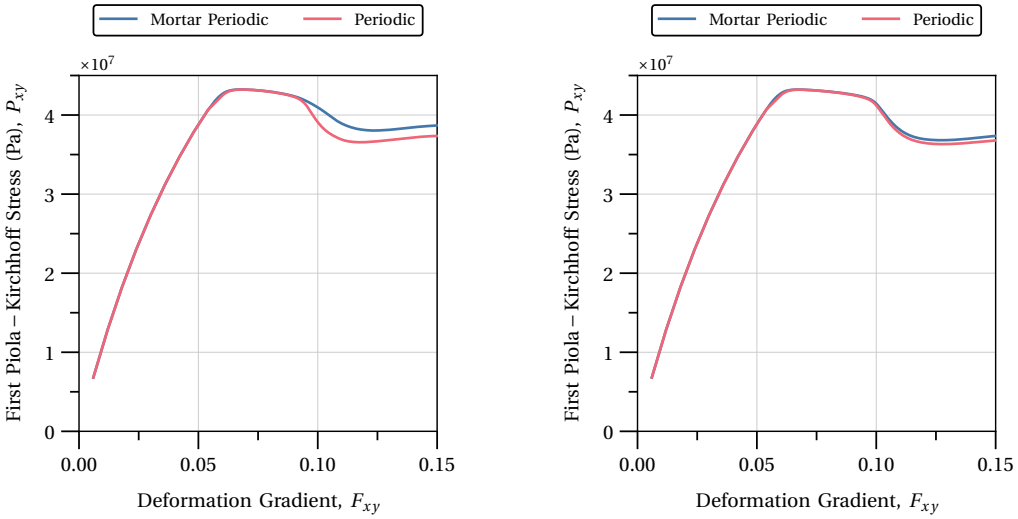


Figure 5.83: Comparisons between the stress-deformation of the samples with 10% volume fraction for the mortar periodic and periodic boundary conditions; (a) With small particle on the border; (b) Without small particle on the border.

CHAPTER 6

COHESIVE ZONE MODEL

The deformation and damage mechanisms of PC/ABS blends were previously described in Chapter 4, where it was pointed out that they begin predominantly in the ABS domains or at their interface with the PC matrix. Consequently, in order to identify which phenomena dominates, it is of paramount relevance to study the PC/SAN interfacial strength and its comparison with the dilatational stress necessary to cavitate the PB rubber particles.

This analysis can be conducted using the numerical models provided in the previous chapters; perfect bonding between the particles and the matrix is considered. However, it can be further enhanced by incorporating cohesive zone models (CZM) into the microscopic problem of a Coupled Multi-scale Finite Element Analysis. Thus, this Chapter will briefly explain the theory behind these models. Subsequently, in the last chapters, after the necessary calibration, it will be evaluated if its implementation dramatically affects the accuracy and quality of the final simulation results.

6.1 Model for Onset and Propagation of Fracture

A discrete approach to fracture is utilised in cohesive zone models; hence the crack is idealised as a surface in three dimensions or a line in two dimensions (one dimension lower). In a finite element framework, this is generally modelled using cohesive elements. All the material degradation takes place in these elements, unlike the continuum elements, which are not affected throughout the analysis (unless a constitutive damage model is also used for the bulk material). Because of this, the problem is broken into two parts (as indicated in Figure 6.1) (de Carvalho, 2022):

- **Continuum elements** are represented using a constitutive model that connects stresses and strains. It is independent of the employed cohesive model (e.g., elastic, hyperelastic, viscoelastic, elastoplastic, etc.);

- **Cohesive elements** are modelled using a cohesive model that relates a displacement gap (material separation) with a traction vector. A traction-separation law (TSL) often defines this.

As a result, while the equilibrium equations are solved using both models, they are independent of one another.

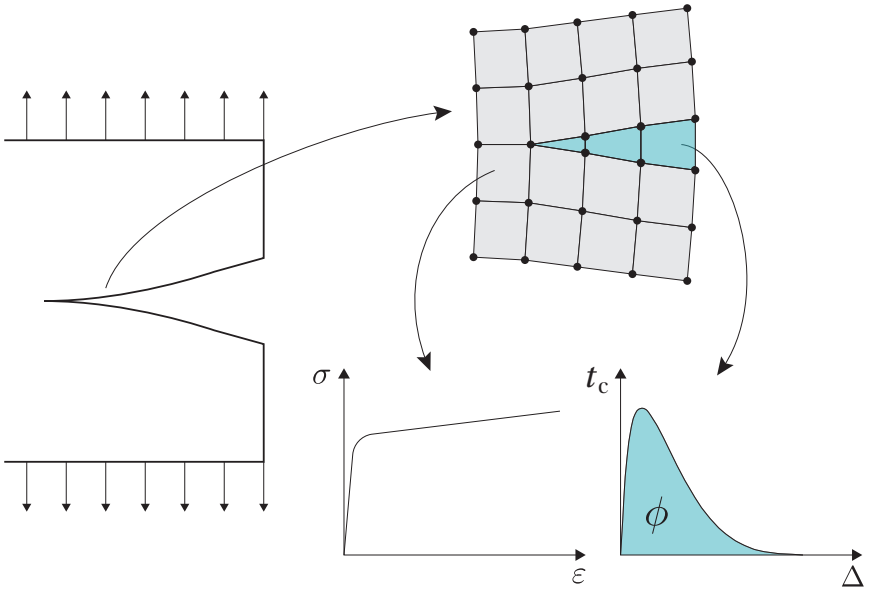


Figure 6.1: Continuum and cohesive elements and respective constitutive laws.
Source: (de Carvalho, 2022)

The gap may increase for a given cohesive element until it reaches a critical level where the cohesive stresses become null. This cohesive component is now excluded from the study, and the bulk material is considered fully separated. Before this vital moment is reached, the surrounding bulk material experiences unloading during the traction-separation law's softening phase.

6.2 Boundary Value Problem

The weak equilibrium equation for a quasi-static deformation, as discussed in Section 2.6, is stated in the spatial description as

$$\int_{\Omega} \left[\boldsymbol{\sigma} : \nabla \boldsymbol{\eta} - \boldsymbol{b} \cdot \boldsymbol{\eta} \right] dv - \int_{\partial\Omega} \boldsymbol{t} \cdot \boldsymbol{\eta} \, da = 0, \quad \forall \boldsymbol{\eta} \in \mathscr{V}. \tag{6.1}$$

Now, with the incorporation of the cohesive elements, a new term arises in the internal work

$$\int_{\Omega} \left[\boldsymbol{\sigma} : \nabla \boldsymbol{\eta} - \boldsymbol{b} \cdot \boldsymbol{\eta} \right] dv - \int_{\partial\Omega} \boldsymbol{t} \cdot \boldsymbol{\eta} \, da + \int_{\Gamma} \boldsymbol{t}_{\mathrm{c}} \cdot \delta \boldsymbol{\Delta} \, da = 0, \quad \forall \boldsymbol{\eta} \in \mathscr{V}. \tag{6.2}$$

Furthermore, this new weak equilibrium equation can be rearranged as

$$\int_{\Omega} \boldsymbol{\sigma} : \nabla \boldsymbol{\eta} \, dv + \int_{\Gamma} \boldsymbol{t}_{\mathrm{c}} \cdot \delta \boldsymbol{\Delta} \, da = \int_{\Omega} \boldsymbol{b} \cdot \boldsymbol{\eta} \, dv + \int_{\partial\Omega} \boldsymbol{t} \cdot \boldsymbol{\eta} \, da, \quad \forall \boldsymbol{\eta} \in \mathscr{V}, \tag{6.3}$$

where $\delta \boldsymbol{\Delta}$ is the virtual separation vector and $\boldsymbol{t}_{\mathrm{c}}$ is the cohesive stress vector, both of which are functions of the virtual displacements. Additionally, the left and right sides denote, respectively, the internal and external work. The first term on the left-hand side of the equation refers to the internal force of the bulk material, while the second term refers to the internal cohesive force of the cohesive elements, which is integrated into the fracture surface's deformed configuration, Γ (see Figure 6.2). Lastly, on the right-hand side, the terms correspond to the external work of the volumetric and surface forces, respectively (de Carvalho, 2022).

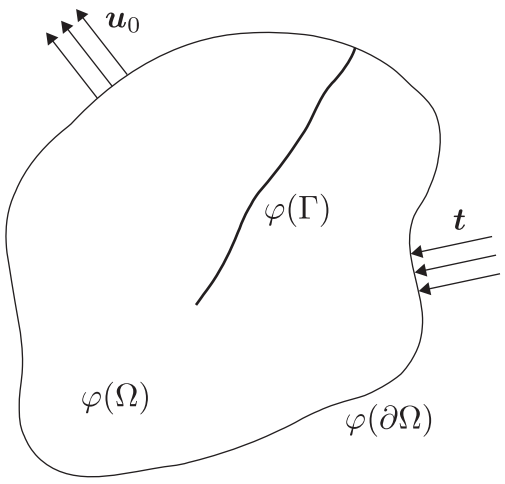


Figure 6.2: Continuum body with a crack in the deformed configuration.
Source: (de Carvalho, 2022)

Note that the internal work related to the bulk material forces in a cohesive element and the internal work related to the internal cohesive forces in a continuum element are both zero. As a result, the internal force vectors and the associated tangent stiffness matrices can be isolated.

The implementation details, such as the finite element discretisation of the equilibrium equation, can be consulted in the following literature: (Park and Paulino, 2012) and (de Carvalho, 2022). After this discretisation is performed, Equation 6.2 becomes

$$\boldsymbol{\eta}^T \left[\int_{\Omega^\mathrm{d}} \left(\mathbf{B}^T \boldsymbol{\sigma} - \mathbf{N}^T \boldsymbol{b} \right) d\upsilon - \int_{\partial\Omega^\mathrm{d}} \mathbf{N}^T \boldsymbol{t}\, da + \int_{\Gamma^\mathrm{d}} \mathbf{B}_\mathrm{c}^T \boldsymbol{t}_\mathrm{c}\, da = 0 \right], \quad \forall \boldsymbol{\eta} \in \mathscr{V}^\mathrm{d}, \tag{6.4}$$

and the cohesive force vector and tangent stiffness matrix are defined as

$$\mathbf{f}^\mathrm{coh} \equiv \int_{\Gamma^\mathrm{d}} \mathbf{B}_\mathrm{c}^T \boldsymbol{t}_\mathrm{c}\, da, \tag{6.5}$$

$$\mathbf{K}^\mathrm{coh} \equiv \frac{\partial \mathbf{f}^\mathrm{coh}}{\partial \mathbf{u}} = \int_{\Gamma^\mathrm{d}} \mathbf{B}_\mathrm{c}^T \frac{\partial \boldsymbol{t}_\mathrm{c}}{\partial \boldsymbol{\Delta}} \frac{\partial \boldsymbol{\Delta}}{\partial \mathbf{u}}\, da = \int_{\Gamma^\mathrm{d}} \mathbf{B}_\mathrm{c}^T \frac{\boldsymbol{t}_\mathrm{c}}{\partial \boldsymbol{\Delta}} \mathbf{B}_\mathrm{c}\, da, \tag{6.6}$$

where the adopted traction-separation constitutive model determines everything related to the traction vector.

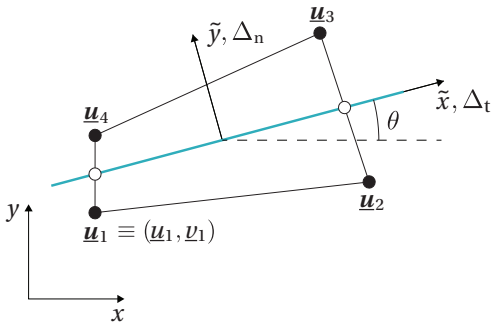
6.3 Cohesive Elements

In 2D, a linear cohesive element is identical to a quadrilateral linear element, as illustrated in Figure 6.3(a). Thus, it is comprised of four nodes, each with two degrees of freedom, yielding eight degrees of freedom in total per element. Consequently, its location is fully described by its eight nodal displacement variables commonly expressed in a global coordinate system. In addition to the linear element, a quadratic quadrangular cohesive element can also be defined, which is defined by six nodes, i.e., it has a total of twelve degrees of freedom (see Figure 6.3(b)). It is essential to point out that, unlike continuum elements, only the tangential direction is made quadratic in cohesive elements, while the normal direction remains linear. This demands the continuous monitoring of the normal and tangential directions of the element(de Carvalho, 2022).

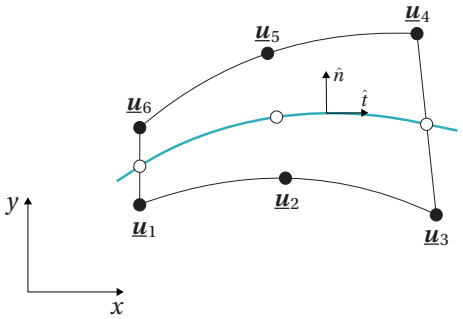
As illustrated in the remaining portion of Figure 6.3, the same idea also holds true for 3D cohesive elements, where there are three degrees of freedom per node due to the extra dimension. The white circles in the middle lines/planes, shown in Figure 6.3, represent the position of the middle plane nodes.

An essential aspect of cohesive elements is that Equations 6.5 and 6.6 are integrated in a space one dimension lower, i.e., 3D cohesive elements are integrated on a surface, and 2D elements are computed over a line. As a result, the cohesive elements' shape functions must likewise be connected to that

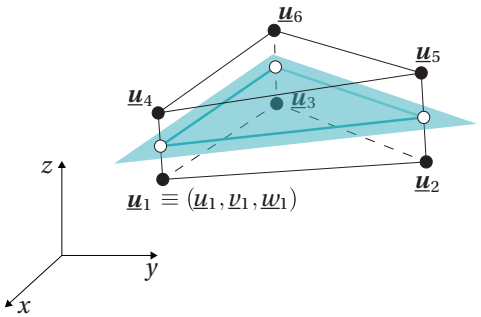
lower-dimensional space (presented in Appendix B for all cohesive elements used in this work). Moreover, as presented by Ortiz and Pandolfi (1999), for the case of large displacement analyses, all geometric operations are performed on the middle surface of the element (represented in blue in Figure 6.3), whose choice is unique regarding traction continuity, as stated by Mosler and Scheider (2011).



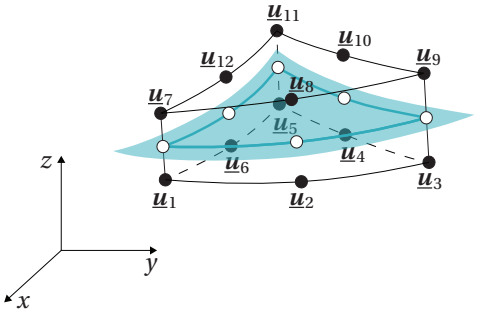
(a) COH2D4: 4-node linear element



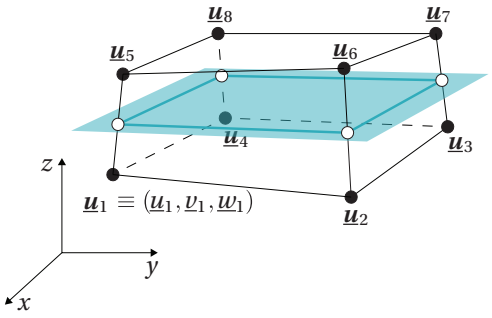
(b) COH2D6: 6-node quadratic element



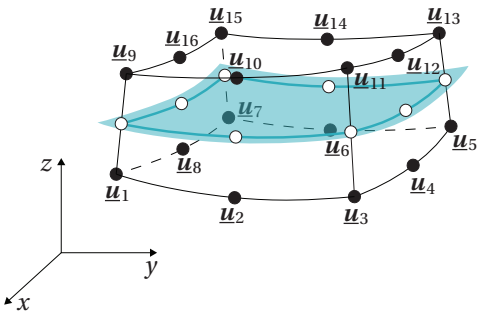
(c) COH3D6: 6-node linear element



(d) COH3D12: 12-node quadratic element



(e) COH3D8: 8-node linear element



(f) COH3D16: 16-node quadratic element

Figure 6.3: Schematic representation of 2D and 3D cohesive elements with respective node displacements defined in the local coordinate system.

Source: (de Carvalho, 2022)

The coordinates of the middle plane nodes, $\mathbf{x}^{\mathrm{m}}$, are derived via a linear interpolation of the coordinates of their corresponding node pairs, which can be estimated using the local displacement-separation matrix, $\mathbf{L}^{\mathrm{e}}$ (presented in Appendix C for all cohesive elements used in this work) (de Carvalho, 2022)

$$\mathbf{x}^{\mathrm{m}} = \frac{1}{2}\overset{+}{\mathbf{L}}^{\mathrm{e}}\mathbf{x}^{\mathrm{e}}, \tag{6.7}$$

where $\overset{+}{\mathbf{L}}^{\mathrm{e}}$ denotes a matrix with the absolute values of each component of $\mathbf{L}^{\mathrm{e}}$ ($\overset{+}{\mathbf{L}}^{\mathrm{e}}_{ij} = |\mathbf{L}^{\mathrm{e}}_{ij}|$), and $\mathbf{x}^{\mathrm{e}}$ the vector of the element coordinates. This vector stores the element's coordinates in the deformed configuration, which depending on whether a 2D or a 3D element is considered, becomes (x_1, y_1, ..., x_n, y_n) and (x_1, y_1, z_1, ..., x_n, y_n, z_n), respectively. Note that n denotes the number of nodes of the cohesive element. It is also crucial to point out that the order of the nodes is defined in a counter-clockwise manner (see Figure 6.3).

6.4 Constitutive Cohesive Model

The cohesive stresses (traction vector) must be established in order to calculate the internal force vector and the tangent stiffness matrix for the cohesive element. In the CZM strategy, as previously mentioned, cohesive stresses are seen as a function of material separation and are determined by a traction-separation law. However, first, it is important to realise that there are typically three distinct fracture modes (schematically represented in Figure 6.4), which need to be included in the model (de Carvalho, 2022):

- **Mode I** (Opening Mode) - tensile stress normal to the crack plane;
- **Mode II** (Sliding Mode) - in-plane shear stress acting parallel to the crack plane and perpendicular to the crack front;
- **Mode III** (Tearing Mode) - out-of-plane shear stress acting parallel to the crack plane and parallel to the crack front.

Before proceeding with the development of the topic, it is vital to offer specific key definitions. First, fracture initiation is associated with the interface strength, i.e., the maximum stress an interface element can withstand or the peak stress in the traction-separation law. Second, fracture propagation is connected to the fracture toughness of the interface material, i.e., to the area under the traction-separation law curve. Third, the area under the curve expresses the energy release rate for a particular displacement gap, which, when it is equal to the fracture toughness of the material, the traction is lowered to zero, and a new crack surface is produced.

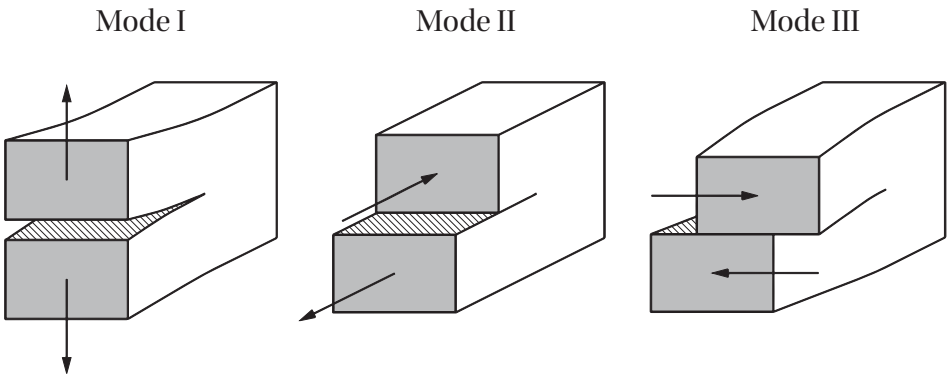


Figure 6.4: Schematic representation of the three fracture modes.
Source: (de Carvalho, 2022)

6.4.1 Loading Modes

Pure Mode Loading

For pure mode loading, fracture initiation takes place when the stress state at a particular interface develops a traction equal to the maximum traction the interface can withstand

$$t_i = \sigma_{\max_i}, \tag{6.8}$$

where i denotes the fracture mode I, II or III. Furthermore, if the energy release rate, $\bar{\phi}_i$, equals the fracture toughness, ϕ_i, of a given mode, fracture propagation occurs (de Carvalho, 2022)

$$\bar{\phi}_i = \phi_i \tag{6.9}$$

Mix Mode Loading

Coupling effects must be taken into consideration in the model if a mixed mode loading occurs instead. One technique for tackling this issue is to develop a scalar that is a function of the numerous tractions and energy release rates (for the distinct modes) in order to foresee fracture initiation and propagation. For a more comprehensive and detailed discussion of the issue, the following literature can be referenced: (Travesa et al., 2006), (Lin Ye, 1988) and (Benzeggagh and Kenane, 1996).

6.4.2 Traction-Separation Laws

The cohesive traction separation law is represented by three primary parameters: the maximum strength, the separation at failure and its shape. Regarding its shape, a few examples are: (1) exponential form (Barenblatt, 1962); (2) polynomial form (Needleman, 1987); (3) constant form (Dugdale, 1960); (4) tri-linear form (Tvergaard and Hutchinson, 1992); (5) linear form (Camacho and Ortiz, 1996); and (6) bi-linear form (Geubelle and Baylor, 1998). With these specified, the dissipated energy per cohesive element can be computed.

Extrinsic and intrinsic procedures are the two major approaches to implement cohesive zone models within a finite element framework (shown in Figure 6.5). The extrinsic approach (Camacho and Ortiz, 1996) follows the physical model of the contact (i.e., the material is regarded to be initially rigid), and the cohesive elements are inserted during the simulation. The second approach, the intrinsic one (Xu and Needleman, 1994) assumes an initial elastic regime before damage initiation, and the cohesive elements are inserted, where necessary, before the simulation starts. This provides for a simpler numerical implementation. However, the drawback of this last technique is that it can result in artificial compliance if the analysis's overall cohesive element density rises (de Carvalho, 2022). In this work, intrinsic cohesive elements will be adopted.

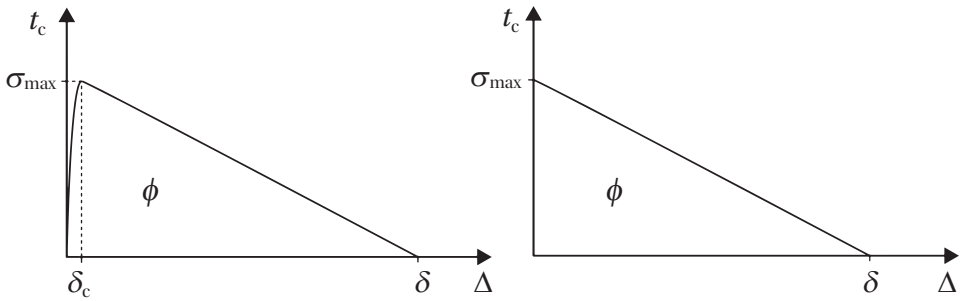


Figure 6.5: Different formulations to implement cohesive zone models.
Source: (de Carvalho, 2022)

This artificial compliance is owing to the fact that the intrinsic cohesive elements can be considered as a series of springs embedded in the continuum material. Consequently, one may anticipate changes in material behaviour with and without the introduction of these elements, even though it is intended that the behaviour of the overall material prior to crack initiation is not affected. One strategy to mitigate this difficulty is to specify the elastic phase with sufficiently

high stiffness, which on the other hand, leads to issues in the convergence of the problem and significant traction oscillations within the cohesive fracture zone (de Carvalho, 2022).

6.4.3 PPR (Park-Paulino-Roesler) Potential-Based Model

The cohesive constitutive models can be split into two primary categories: nonpotential-based and potential-based models. Just the PPR (Park-Paulino-Roesler) potential-based model is discussed in this study as it is the model implemented in `Links`, and from which further analyses are carried out (see Mosler and Scheider (2011) and Park and Paulino (2013) and references cited therein for an extensive review about the other models not explored).

To be compatible with thermodynamics, potential-based models must be derived from potential energy. Due to the physical nature of fracture energy potentials, the cohesive interactions (traction forces) are established by the first derivative in order to a given distance (displacement jump), and the second derivative establishes the constitutive relationship (material tangent stiffness). As a consequence, the traction vector is as follows

$$\mathbf{t}_c = \frac{\partial \boldsymbol{\Psi}}{\partial \boldsymbol{\Delta}}, \qquad \boldsymbol{\Psi} = \boldsymbol{\Psi}(\boldsymbol{\Delta}), \tag{6.10}$$

with $\boldsymbol{\Psi}$ denoting the potential fracture energy, which is a function of the displacement jump/gap, $\boldsymbol{\Delta}$ (de Carvalho, 2022).

In order to solve the fundamental drawbacks of already established traction-separation laws, specifically when the fracture energies are different (anisotropic failure) for the outlined modes, Park et al. (2009) proposed a unified potential-based cohesive model. This is a concern for mixed-mode fracture problems, as one needs to consider identical fracture energy regardless of the loading mode. This model includes distinct modes I and II [1] properties and relies on normal and tangential separation ($\boldsymbol{\Delta}_n$, $\boldsymbol{\Delta}_t$). Additionally, it is governed by the well-known physical macroscopic fracture parameters of cohesive strength (σ_{max}, τ_{max}) and fracture energies (ϕ_n, ϕ_t). Besides this, by specifying initial slope indicators (λ_n, λ_t) and shape parameters (α, β), one has greater control over the elastic and softening domains (de Carvalho, 2022).

[1] Modes II and III are modelled with the same tangential fracture properties.

For this model, the potential of cohesive fracture is defined as

$$\begin{aligned}\Psi\left(\Delta_{\mathrm{n}},\Delta_{\mathrm{t}}\right)=\min\left(\phi_{\mathrm{n}},\phi_{\mathrm{t}}\right)+\left[\Gamma_{\mathrm{n}}\left(1-\frac{\Delta_{\mathrm{n}}}{\delta_{\mathrm{n}}}\right)^{\alpha}\left(\frac{m}{\alpha}+\frac{\Delta_{\mathrm{n}}}{\delta_{\mathrm{n}}}\right)^{m}+\left\langle\phi_{\mathrm{n}}-\phi_{\mathrm{t}}\right\rangle\right]\\ \times\left[\Gamma_{\mathrm{t}}\left(1-\frac{\left|\Delta_{\mathrm{t}}\right|}{\delta_{\mathrm{t}}}\right)^{\beta}\left(\frac{n}{\beta}+\frac{\left|\Delta_{\mathrm{t}}\right|}{\delta_{\mathrm{t}}}\right)^{n}+\left\langle\phi_{\mathrm{t}}-\phi_{\mathrm{n}}\right\rangle\right],\end{aligned} \tag{6.11}$$

where $\langle\cdot\rangle$ denotes the Macaulay brackets, δ the final crack opening width, Γ an energy constant and m and n are non-dimensional parameters (de Carvalho, 2022)

$$\Gamma_{\mathrm{n}}=\left(-\phi_{\mathrm{n}}\right)^{\frac{\langle\phi_{\mathrm{n}}-\phi_{\mathrm{t}}\rangle}{\phi_{\mathrm{n}}-\phi_{\mathrm{t}}}}\left(\frac{\alpha}{m}\right)^{m}\quad\xrightarrow{\phi_{\mathrm{n}}=\phi_{\mathrm{t}}}\quad\Gamma_{\mathrm{n}}=-\phi_{\mathrm{n}}\left(\frac{\alpha}{m}\right)^{m}, \tag{6.12a}$$

$$\Gamma_{\mathrm{t}}=\left(-\phi_{\mathrm{t}}\right)^{\frac{\langle\phi_{\mathrm{t}}-\phi_{\mathrm{n}}\rangle}{\phi_{\mathrm{t}}-\phi_{\mathrm{n}}}}\left(\frac{\beta}{n}\right)^{n}\quad\xrightarrow{\phi_{\mathrm{n}}=\phi_{\mathrm{t}}}\quad\Gamma_{\mathrm{t}}=\left(\frac{\beta}{n}\right)^{n}. \tag{6.12b}$$

$$m=\frac{\alpha(\alpha-1)\lambda_{\mathrm{n}}^{2}}{1-\alpha\lambda_{\mathrm{n}}^{2}}, \tag{6.13a}$$

$$n=\frac{\beta(\beta-1)\lambda_{\mathrm{t}}^{2}}{1-\beta\lambda_{\mathrm{t}}^{2}}. \tag{6.13b}$$

Moreover, it is crucial to highlight that this potential was constructed with the following fracture boundary conditions in mind (Park et al., 2009):

- Full normal separation happens when either the normal separation reaches the normal final crack opening width, δ_{n}, or the tangential separation reaches the tangential conjugate final crack opening width, $\bar{\delta}_{\mathrm{t}}$

$$t_{\mathrm{n}}\left(\delta_{\mathrm{n}},\Delta_{\mathrm{t}}\right)=0,\quad t_{\mathrm{n}}\left(\Delta_{\mathrm{n}},\bar{\delta}_{\mathrm{t}}\right)=0; \tag{6.14}$$

- Full tangential separation happens when either the tangential separation reaches the tangential final crack opening width, δ_{t}, or the normal separation reaches the normal conjugate final crack opening width, $\bar{\delta}_{\mathrm{n}}$

$$t_{\mathrm{t}}\left(\Delta_{\mathrm{n}},\delta_{\mathrm{t}}\right)=0,\quad t_{\mathrm{n}}\left(\bar{\delta}_{\mathrm{n}},\Delta_{\mathrm{t}}\right)=0; \tag{6.15}$$

- The area under the traction-separation functions corresponds to the fracture toughness of the respective fracture mode

$$\phi_{\mathrm{n}} = \int_0^{\delta_{\mathrm{n}}} t_{\mathrm{n}}\left(\Delta_{\mathrm{n}}, 0\right) \mathrm{d}\Delta_{\mathrm{n}}, \quad \phi_{\mathrm{t}} = \int_0^{\delta_{\mathrm{t}}} t_{\mathrm{t}}\left(0, \Delta_{\mathrm{t}}\right) \mathrm{d}\Delta_{\mathrm{t}}; \tag{6.16}$$

- The traction-separation functions are maximum when the critical opening widths are reached, $\delta_{\mathrm{n_c}}$ and $\delta_{\mathrm{t_c}}$

$$\left.\frac{\partial t_{\mathrm{n}}\left(\Delta_{\mathrm{n}}, \Delta_{\mathrm{t}}\right)}{\partial \Delta_{\mathrm{n}}}\right|_{\Delta_{\mathrm{n}}=\delta_{\mathrm{n_c}}} = 0, \quad \left.\frac{\partial t_{\mathrm{t}}\left(\Delta_{\mathrm{n}}, \Delta_{\mathrm{t}}\right)}{\partial \Delta_{\mathrm{t}}}\right|_{\Delta_{\mathrm{t}}=\delta_{\mathrm{t}}} = 0; \tag{6.17}$$

- The maximum tractions correspond to the fracture mode cohesive strengths, when considering pure loads

$$t_{\mathrm{n}}\left(\delta_{\mathrm{n_c}}, 0\right) = \sigma_{\max}, \quad t_{\mathrm{t}}\left(0, \delta_{\mathrm{t_c}}\right) = \tau_{\max}. \tag{6.18}$$

According to the first two boundary conditions, the softening domain is confined by a pair of final crack opening widths (δ_{n} and δ_{t}) and conjugate final crack opening widths ($\bar{\delta}_{\mathrm{n}}$ and $\bar{\delta}_{\mathrm{t}}$). While the latter considers mixed-mode conditions and allows for having distinct fracture energies, the former merely depends on the properties of the respective fracture mode. Figure 6.6 illustrates the cohesive interaction zone (de Carvalho, 2022).

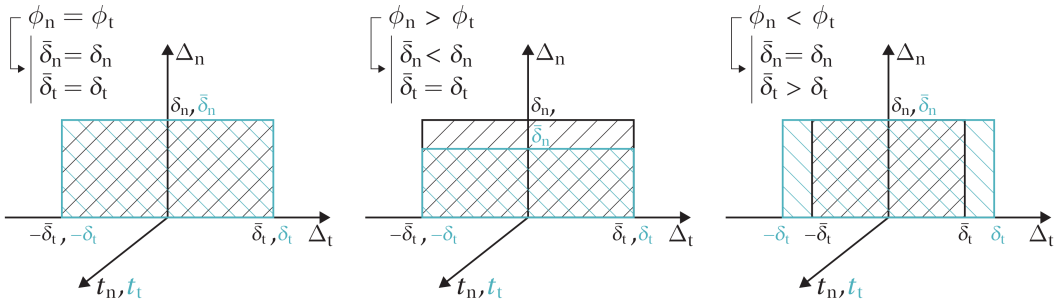


Figure 6.6: Graphic representation of the cohesive interaction zones for the different fracture toughness combinations. The black and blue regions, respectively, define the domains where the normal and tangential tractions are positive and acceptable.
Source: (de Carvalho, 2022)

Referring to Figure 6.6, it can be observed that the tangential softening region is specified as $0 \leq \Delta_{\mathrm{n}} \leq \delta_{\mathrm{n}}$ and $-\bar{\delta}_{\mathrm{t}} \leq \Delta_{\mathrm{t}} \leq \bar{\delta}_{\mathrm{t}}$, while the normal softening region is defined as $0 \leq \Delta_{\mathrm{n}} \leq \bar{\delta}_{\mathrm{n}}$ and $-\delta_{\mathrm{t}} \leq \Delta_{\mathrm{t}} \leq \delta_{\mathrm{t}}$. However, in practice, the normal softening domain can be simplified to $0 \leq \Delta_{\mathrm{n}} \leq \delta_{\mathrm{n}}$, $-\delta_{\mathrm{t}} \leq \Delta_{\mathrm{t}} \leq \delta_{\mathrm{t}}$ and $t_{\mathrm{n}}\left(\Delta_{\mathrm{n}}, \Delta_{\mathrm{t}}\right) \geq 0$ and the tangential counterpart to $0 \leq \Delta_{\mathrm{n}} \leq \delta_{\mathrm{n}}, -\delta_{\mathrm{t}} \leq \Delta_{\mathrm{t}} \leq \delta_{\mathrm{t}}$ and $t_{\mathrm{t}}\left(\Delta_{\mathrm{n}}, \Delta_{\mathrm{t}}\right) \geq 0$ (de Carvalho, 2022).

The ratio of the critical crack opening width to the final crack opening width is expressed by the initial slope indicators, λ_n and λ_t (Park et al., 2009)

$$\lambda_n = \frac{\delta_{n_c}}{\delta_n}, \tag{6.19a}$$

$$\lambda_t = \frac{\delta_{t_c}}{\delta_t}. \tag{6.19b}$$

Using these indicators, it is possible to have complete control over the initial elastic stiffness associated with each fracture mode, individually. As previously indicated, one of the drawbacks of the use of intrinsic cohesive elements is the introduction of artificial compliance, which can now be lowered by applying small values of λ_n and λ_t. Nevertheless, one must still pay attention to the associated downsides also indicated earlier.

The final crack opening widths are expressed as

$$\delta_n = \frac{\phi_n}{\sigma_{max}} \alpha \lambda_n \left(1-\lambda_n\right)^{\alpha-1} \left(\frac{\alpha}{m}+1\right) \left(\frac{\alpha}{m}\lambda_n + 1\right)^{m-1}, \tag{6.20a}$$

$$\delta_t = \frac{\phi_t}{\tau_{max}} \beta \lambda_t \left(1-\lambda_t\right)^{\beta-1} \left(\frac{\beta}{n}+1\right) \left(\frac{\beta}{n}\lambda_t + 1\right)^{n-1}. \tag{6.20b}$$

Lastly, as shown in Figure 6.7, the model can anticipate different material softening responses, including brittle, plateau, and quasi-brittle responses, depending on the shape parameters that are employed. For instance, $\alpha = \beta = 2$ can be used to depict a linear softening behaviour. Then, by reducing the shape parameter's value, the traction-separation law's format becomes more concave. Hence, it is predicted that the value of the ultimate crack opening width will decrease if the fracture toughness remains the same (it is not reflected in Figure 6.7) (de Carvalho, 2022).

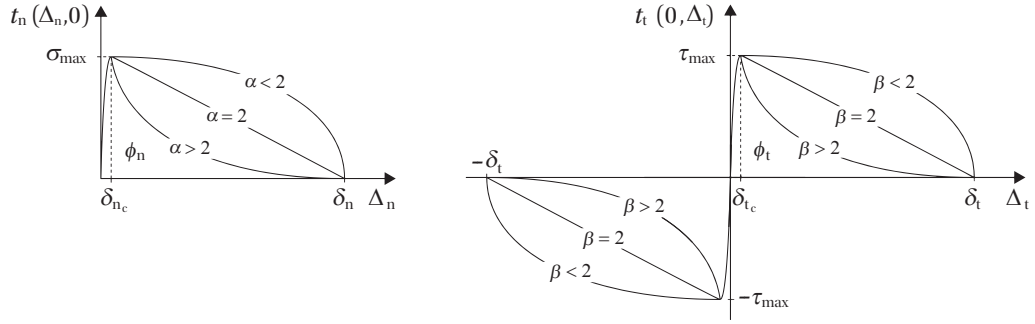


Figure 6.7: Graphical depiction of the PPR cohesive zone model for varying values of α and β. Source: (Park et al., 2009)

6.4.4 Unloading/Reloading Model

The behaviour of the cohesive elements during unloading scenarios also needs to be addressed. In this instance, the terms "loading" and "unloading" relate to a rise or fall in the displacement jump, respectively. It is vital to note that a cohesive element could be unloaded in one direction while being loaded in another.

The two main mechanisms for handling unloading are ductile unloading and cleavage unloading. The former exhibits an unloading/reloading relationship analogous to that observed in elastoplastic materials (i.e., it has the same stiffness as the elastic domain). The latter exhibits a decrease in the elastic stiffness of the material as the amount of damage it undergoes rises (de Carvalho, 2022). For more information on the topic, the following literature can be accessed (Scheider, 2001) and (Park, 2009).

Furthermore, unloading/reloading can be modeled either in a coupled or uncoupled way. If the coupled method is employed, an internal variable must be established to retain the history of loading

$$\eta\left(\Delta_{\mathrm{n}}, \Delta_{\mathrm{t}}\right) = \sqrt{\Delta_{\mathrm{n}}^2 + \Delta_{\mathrm{t}}^2}. \tag{6.21}$$

However, if the uncoupled approach is employed, two internal variables must be used to store the maximum displacement in each direction independently (de Carvalho, 2022)

$$\eta_{\mathrm{n}_{\max}} = \Delta_{\mathrm{n}_{\max}}, \quad \eta_{\mathrm{t}_{\max}} = \Delta_{\mathrm{t}_{\max}}. \tag{6.22}$$

As it is assumed that the fracture process is reversible in the elastic domain, it is crucial to notice that these variables are not updated there. Hence, in scenario $\Delta_{\mathrm{n}} > \delta_{\mathrm{n_c}}$ and $\Delta_{\mathrm{n}} > \eta_{\mathrm{n}_{\max}}$, the value of the internal variable is updated to represent the new normal separation, and the normal traction is computed using the softening traction-separation law. However, if $\Delta_{\mathrm{n}} > \delta_{\mathrm{n_c}}$ and $\Delta_{\mathrm{n}} < \eta_{\mathrm{n}_{\max}}$, the normal unloading/reloading relationship is considered. Identical conditions apply to the tangential direction, except in this situation, the absolute value of the tangential separation must be utilised (de Carvalho, 2022).

The approach implemented in `Links` is the uncoupled cleavage unloading (linear to the origin), which is defined by

$$t_{\mathrm{n}}^{\mathrm{u}}\left(\Delta_{\mathrm{n}},\Delta_{\mathrm{t}}\right)=t_{\mathrm{n}}\left(\eta_{\mathrm{n}_{\max}},\Delta_{\mathrm{t}}\right)\left(\frac{\Delta_{\mathrm{n}}}{\eta_{\mathrm{n}_{\max}}}\right)^{\alpha_{\mathrm{u}}} \tag{6.23a}$$

$$t_{\mathrm{t}}^{\mathrm{u}}\left(\Delta_{\mathrm{n}},\Delta_{\mathrm{t}}\right)=t_{\mathrm{t}}\left(\Delta_{\mathrm{n}},\eta_{\mathrm{t}_{\max}}\right)\left(\frac{\left|\Delta_{\mathrm{t}}\right|}{\eta_{\mathrm{t}_{\max}}}\right)^{\beta_{\mathrm{u}}}\frac{\Delta_{\mathrm{t}}}{\left|\Delta_{\mathrm{t}}\right|}, \tag{6.23b}$$

where α_{u} and β_{u} are additional shape parameters, which allow for finer control of the shape of the unloading/reloading states. For the linear-to-origin case, $\alpha_{\mathrm{u}}=\beta_{\mathrm{u}}=1$ (de Carvalho, 2022).

6.4.5 Contact

Lastly, to fully define the cohesive model, it is necessary to implement computational contact mechanics in the cohesive elements to prevent negative normal separation. A more complex contact methodology can be consulted in (Popp et al., 2010); still, for simplicity, it will merely be quickly described the implementation of a penalty method to ensure $\Delta_{\mathrm{n}}\geq\eta$.

For this method, a penalty parameter, α_{p}, needs to be established, which is frequently related to the stiffness of the interface in the normal direction. Having created this parameter, the normal traction is computed as

$$t_{\mathrm{n}}=\alpha_{\mathrm{p}}\Delta_{\mathrm{n}},\quad \text{for } \Delta_{\mathrm{n}}<0, \tag{6.24}$$

where the penalty parameter is the stiffness at zero separation

$$\alpha_{\mathrm{p}}=\left.\frac{\partial^2\Psi\left(\Delta_{\mathrm{n}},\Delta_{\mathrm{t}}\right)}{\partial\Delta_{\mathrm{n}}^2}\right|_{\Delta_{\mathrm{n}}=\Delta_{\mathrm{t}}=0}. \tag{6.25}$$

Smaller continuum element interpenetrations are caused by higher values of α_{p}, yet as with any penalty technique, the higher the α_{p} value, the lower is method's convergence. Note that the contact condition must always be verified, even in the event of failure. The neighboring continuum components cannot be allowed to penetrate one another, even if the interface element has entirely collapsed.

6.4.6 Model Parameters

In summary, nine input parameters are required to describe the numerical model for the implementation of cohesive elements, which have been described throughout Section 6.4 and are compiled in Table 6.1.

Table 6.1: Constitutive cohesive model input parameters.

Notation	Designation
ϕ_{n}	Normal fracture energy
ϕ_{t}	Tangencial fracture energy
$\sigma_{\max}$	Normal cohesive strength
$\tau_{\max}$	Tangencial cohesive strength
λ_{n}	Initial slope indicators
λ_{t}	
α	Shape parameters
β	
α_{p}	Contact penalty factor
-	Unloading type: Irreversible or Reversible

6.4.7 Damage Variable for Post-Processing

To facilitate the post-processing phase of finite element analysis, it is crucial to have a scalar quantity that can effectively convey the state of cohesive elements. However, the potential-based PPR cohesive model presented in this study does not compute any damage-related variable. To address this issue, de Carvalho (2022) introduced three scalar damage variables based purely on energetic quantities: one for the normal direction (D_{n}), one for the tangential direction (D_{t}), and one that encompasses both (D).

It is worth noting that, under pure mode loading conditions, the dissipated energy at the point of complete failure is equivalent to the fracture toughness of the respective mode, as indicated by Equation 6.9. However, under mixed mode loading conditions, the area under the traction-separation law in a given direction is lower than the respective fracture toughness. This is due to the fact that when the displacement in a particular direction increases, the energy that a material dissipates in another direction diminishes. Thus, it is necessary to define an effective fracture toughness for a given fracture mode i, denoted by ϕ_i^{eff}. Accordingly, the damage variable for each direction is defined as the ratio between the energy release rate ($\bar{\phi}_i$) and the effective fracture toughness

$$D_{\mathrm{n}} = \frac{\bar{\phi}_n}{\phi_n^{\mathrm{eff}}}, \qquad D_{\mathrm{t}} = \frac{\bar{\phi}_t}{\phi_t^{\mathrm{eff}}}, \tag{6.26}$$

where $D_{\mathrm{n}} \in \left[0,\, 1\right]$ and $D_{\mathrm{t}} \in \left[0,\, 1\right]$.

Lastly, the combined damage variable is computed as a weighted arithmetic mean of the damage variables for each direction,

$$D = \xi D_{\mathrm{n}} + (1-\xi) D_{\mathrm{t}}, \tag{6.27}$$

where $D \in \left[0,\, 1\right]$ and ξ is a weight factor that represents the proportion of the normal direction energy release rate to the total energy release rate:

$$\xi = \frac{\bar{\phi}_n}{\bar{\phi}_n + \bar{\phi}_t}. \tag{6.28}$$

Under pure normal loading conditions, $\xi = 1$ and $D = D_{\mathrm{n}}$. On the other hand, if a pure tangential loading condition is applied, $\xi = 0$ and $D = D_{\mathrm{t}}$. Moreover, the variable ξ can also be used during the post-processing phase to assess the significance of each fracture mode in the progression of a given crack.

CHAPTER 7

COHESIVE ELEMENTS GENERATION IN AN RVE

After establishing the cohesive zone models in Chapter 6, this Chapter aims to present and explain the program developed to generate the necessary zero-thickness cohesive interface elements in preexisting discretised finite element RVEs. This contribution fills the gap in the literature that, to the best of the author's knowledge, there is only one similar open-source, available program (Nguyen, 2014). The decision was made to develop an in-house program in order to substantially simplify and provide more flexibility in the integration process with the other internal programs currently in place. Moreover, this allowed us to implement all the desired features, some of which may not be available in currently available programs.

The developed code can generate two and three-dimensional, linear and quadratic cohesive elements (given in Appendix C) from all various kinds of continuum elements (provided in Appendix B). Additionally, one can also insert cohesive elements along any number of materials, allowing even the alternative of applying them solely to the interface between materials specified by the user.

Several methods to improve the program's effectiveness and resilience are also shown, and in the end, several examples are provided together with a performance study of the whole program.

7.1 RVE Generation

The conceived code is essentially a pre-processing script that inserts cohesive elements into an already-existing finite element mesh. Thus, it is essential first to define the software used to generate the RVE to which the elements will be added to. The program used was AMINO (Adaptive Multi-temperature Isokinetic

Method), which, for the interested reader, is presented in all its detail in (Vila-Chã et al., 2021) and (Ferreira et al., 2022). It is important to bear in mind that the software developed is independent of the AMINO program; thus it can also be used for other programs which produce FEM meshes either on macro or micro scale.

The generation of high-fidelity RVEs that closely resemble the material's true microstructure is critical for achieving accurate predictive capabilities. Thus Vila-Chã et al. (2021) developed a new flexible, robust, and efficient computational generation method for particle-reinforced materials based on a geometrical generation method characterised by an adaptive multi-temperature isokinetic time-driven molecular dynamics scheme. An extensive review of the many microstructure generation methods (such as methods based on reconstruction from experimental data or physics-based generation methods) can be consulted in (Bargmann et al., 2018).

Considering flexibility and robustness, the method effectively handles any number of material phases, multiple particle types (disks and ellipses in 2D; and spheres, ellipsoids, and cylinders in 3D - Figure 7.1) and the inherent diversity of particle-reinforced heterogeneous materials. Still related to the flexibility of the program, it is possible to specify any given number of particles or volume fraction for each phase. Another essential element is that its performance is not reliant on the cumbersome calibration of parameters based on numerical experience. Finally, its efficiency is attributed to producing hundreds or thousands of high-fidelity RVEs in a reasonable time for the complete spectrum of microstructure descriptors (Vila-Chã et al., 2021; Ferreira et al., 2022).

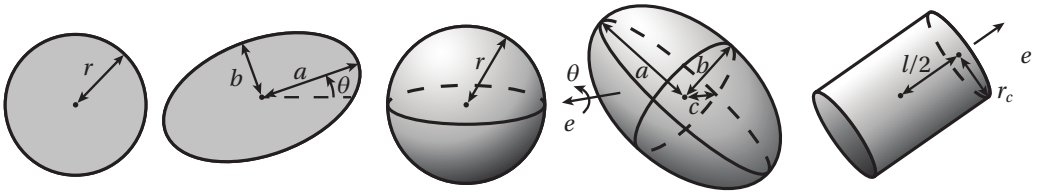


Figure 7.1: Admissible particle types generated by AMINO. From left to right: a disk, an ellipse, a sphere, an ellipsoid and a cylinder.

Source: (Vila-Chã et al., 2021)

The arrangement of all particle types is fully defined by their geometric centre, and their geometrical microstructure descriptors (also shown in 7.1) are established by (Vila-Chã et al., 2021; Ferreira et al., 2022):

- **Disk** (2D) and **sphere** (3D): radius, r;

- **Ellipse** (2D): major and minor primary semi-axes, a and b. The orientation is determined by the angle that the main axis makes with the positive x semi-axis, θ;
- **Ellipsoid** (3D): three major semi-axes, a, b and c. The spatial orientation is established by a predetermined rotation axis, $\boldsymbol{e}$, and a rotation angle around that same axis, θ. The reference orientation is the one where the three primary axes are parallel to the three coordinate axes;
- **Cylinder** (3D): length, l and base radius, r_c. The orientation is immediately supplied by its axis, $\boldsymbol{e}$.

In the general case of ellipses and ellipsoids, alternative parameters can also be specified to geometrically define these particles (e.g., length ratios between principal axes).

Moreover, all geometrical microstructure descriptors can be specified as a fixed prescribed value, i.e., equal for all particles in that phase, or following a given statistical distribution. Three types of statistical distributions are considered: (1) a uniform distribution, for which lower and upper bounds must be prescribed; (2) a discrete distribution, for which each value along with its probability must be prescribed; and (3) a Gaussian distribution, for which the mean and standard deviation must be prescribed (Vila-Chã et al., 2021; Ferreira et al., 2022).

Regarding the final configuration, microstructure periodicity is effectively handled and two features are incorporated to assist the spatial mesh discretisation of the RVE.

7.1.1 Output File

In order to grasp the developed code and where the essential information originates from, it is appropriate to describe the relevant data accessible in the output file of the AMINO program, that is, the data available in the generated RVE file. In summary, the file includes the following bits of information:

- **Analyse type**: from which one may determine whether it is either 2D or 3D;
- **Element types**: the total number and name of the type of element utilised are present (all continuum element types are presented in Appendix B). Each one has a unique identifying number;
- **Materials**: all material properties are mentioned. However, for the current scenario, simply their ID number is required;

- **Element groups**: result from combining the element types with the materials. Each element group is specified by its ID, followed by the ID of the element type and finally, the ID of the material (e.g., [1 2 3] - group 1, element 2, and material 3);
- **Nodes**: each node has its own ID number, in front of which its spatial coordinates are supplied;
- **Elements**: each element also has its unique ID, which is followed by the element group to which it belongs and by its connectivities (i.e., the node IDs that compose it). The node IDs form the node matrix that can be consulted for all implemented continuum elements in Appendix B.

7.2 Cohesive Elements Generation

In this section, the pre-processing program is explained in its full complexity (the key blocks are summarised in Figure 7.2). The program starts by reading the discretised finite element RVE, which includes the data specified in Section 7.1.1. It then identifies all elements in the interface between the desired materials and their associated interface edges or faces for the case of 2D and 3D, respectively (from this point forward, both these terms will be referred to as facets). After that, it constructs all needed interface components and adjusts the continuum elements' connectivities to update them to the new nodes implemented. Lastly, it exports the output file with the modified RVE mesh, which now contains the 2D or 3D interface elements. In the following sections, the main algorithms' blocks will be presented in depth.

7.2.1 Adjacent Elements Detection

The algorithm that enables the identification of all elements in the interface between the desired materials and their corresponding interface facets is summarised in Figure 7.3. In words, the initial stage is to link each element to its corresponding material (Step 1 in Figure 7.3). This step is vital because each element is recognised by its group, and various groups can have the same material (this can happen when numerous element types are utilised). Without this association, cohesive elements would be inserted between the same material. Afterwards, all facets from the elements of one material are compared with those of the other materials, and if there is a match, that pair of elements establishes an interface (Step 5 in Figure 7.3).

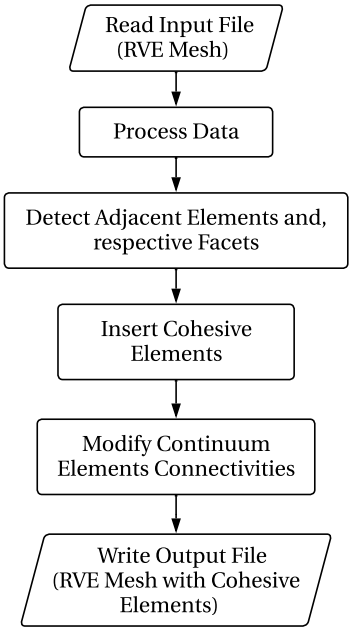


Figure 7.2: Flowchart illustrating the primary blocks of the program.

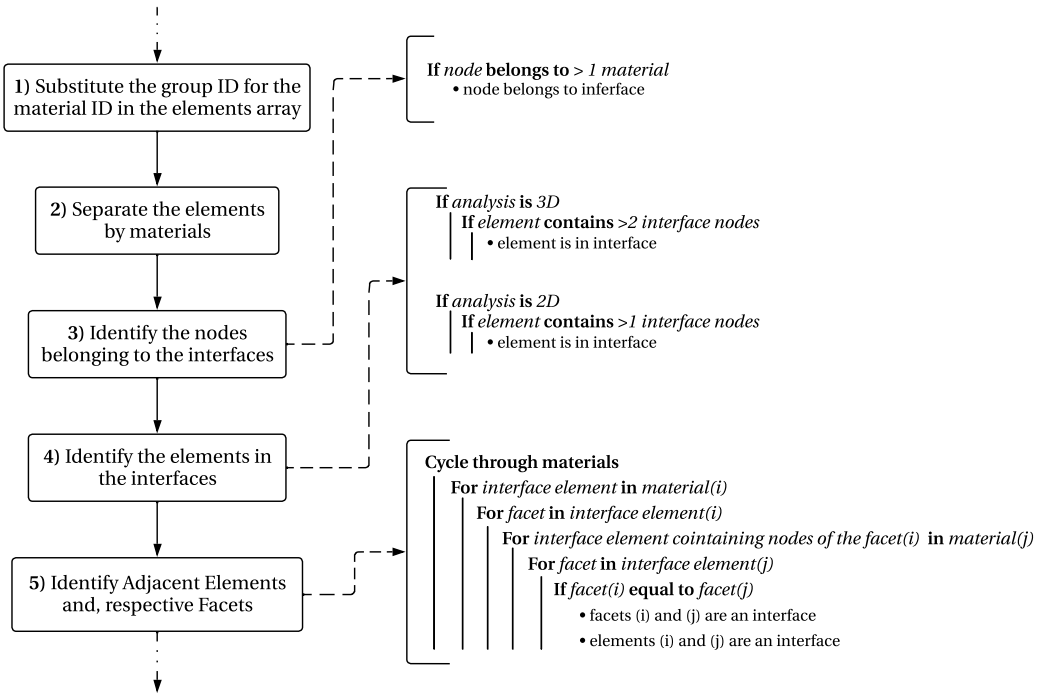


Figure 7.3: Flowchart depicting the basic logic underlying the interface detection block.

The algorithm's performance was crucial throughout its development since it needed to generate the cohesive elements in a reasonable amount of time to ensure its application was feasible (detailed statistical analyses are presented in Section 7.3). Thus, steps 2) to 4) of Figure 7.3 arise.

In essence, this process entails building a matrix of zeros, with each row denoting one of the mesh's n nodes and each column denoting one of its m materials (a representation of this matrix is shown in Figure 7.4). All nodes are first examined, and if they belong to an element of a given material, the zero is converted to a one. After that, each row is counted, and if k is greater than one, the node is at an interface (i.e., the node belongs to more than one material). Finally, the elements can be filtered to include just those containing these interface nodes, resulting in the interface elements (the filter criteria are presented in Figure 7.3). As a result, the elements analysed in step 5) are drastically reduced.

$$
\begin{array}{c|c}
 & \begin{array}{cccc} \text{mat.1} & \text{mat.2} & \dots & \text{mat.m} \end{array} \\
\begin{array}{c} \text{node 1} \\ \text{node 2} \\ \dots \\ \text{node n} \end{array} & \left[\begin{array}{cccc} 1 & 0 & \dots & 0 \\ 0 & 1 & \dots & 1 \\ \vdots & \vdots & \ddots & \vdots \\ 0 & 0 & \dots & 0 \end{array}\right] \begin{array}{c} \longrightarrow \\ \longrightarrow \\ \vdots \\ \longrightarrow \end{array} \begin{array}{c} k1 \\ k2 \\ \\ kn \end{array}
\end{array}
$$

Figure 7.4: Representation of the identification matrix of the interface nodes.

The filtering criteria applied in step 4) are based on:

- **2D linear analysis**: the elements' interfaces are edges with two nodes. Therefore only elements with at least two interface nodes can belong to one. All 2D linear continuum element types considered are shown in Figure 7.5;

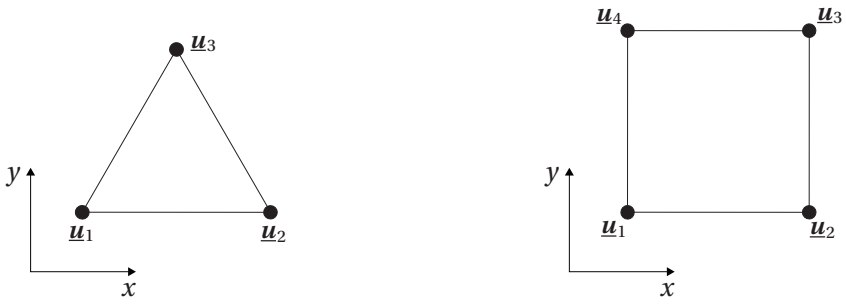


Figure 7.5: Schematic representation of the admissible 2D linear continuum element types read by the code. From left to right: TRI3 and QUAD4

- **2D quadratic analysis**: the elements' interfaces are edges with three nodes. However, if the two end nodes belong to an interface, the middle one must also belong. Consequently, the quadratic elements are handled as linear (i.e., the middle node is omitted); hence elements with more than one interface node can belong to one. All 2D quadratic continuum element types considered are shown in Figure 7.6;

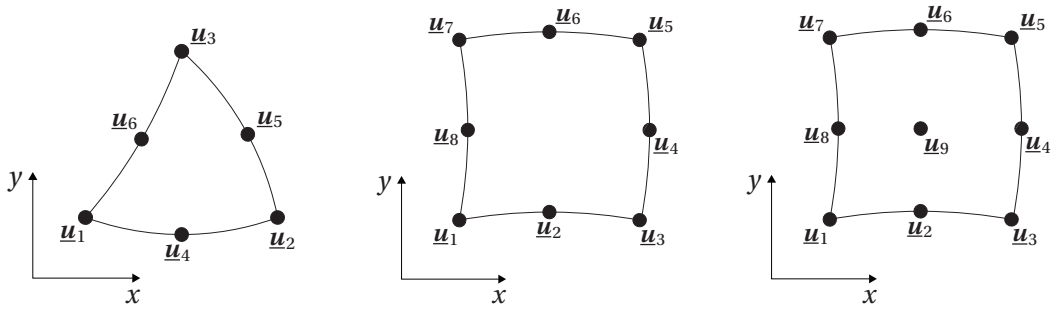


Figure 7.6: Schematic representation of the admissible 2D quadratic continuum element types read by the code. From left to right: TRI6, QUAD8 and QUAD9

- **3D linear analysis**: the elements' interfaces are faces with two nodes per edge. Therefore only elements with at least three interface nodes can belong to one. All 3D linear continuum element types considered are shown in Figure 7.7;

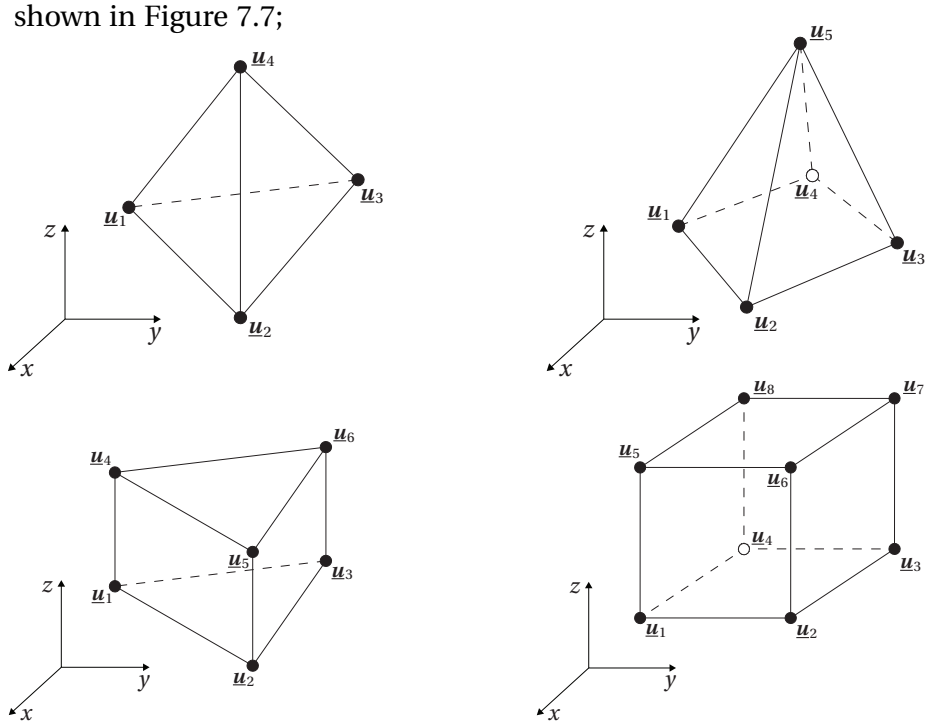


Figure 7.7: Schematic representation of the admissible 3D linear continuum element types read by the code. From left to right: TETRA4 and PYRA5; WEDGE6 and HEXA8.

- **3D quadratic analysis**: the elements' interfaces are edges with three nodes. However, as for the 2D case, the intermediate nodes can also be ignored, and the problem can be treated as linear. Hence elements with more than two interface nodes can belong to one. All 3D quadratic continuum element types considered are shown in Figure 7.7.

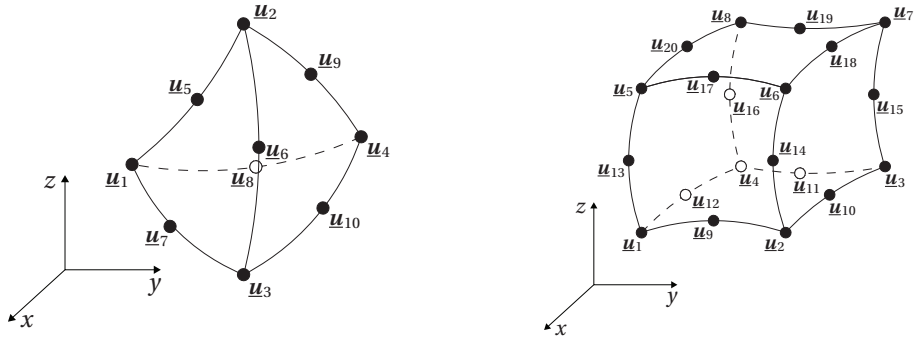


Figure 7.8: Schematic representation of the admissible 3D quadratic continuum element types read by the code. From left to right: TETRA10 and HEXA20.

The simple detail of treating the quadratic elements as linear strongly impacts the processing time, yielding considerable savings in the order of 200%. Moreover, it is vital to stress that the resulting elements may not necessarily form an interface despite matching the aforementioned requirements. Nonetheless, it still constitutes a significant step towards improving and speeding up the process. Figure 7.9 presents an example of one of these circumstances for a 2D linear scenario, simplest case. As can be seen, element number ① establishes no interface while having four interface nodes.

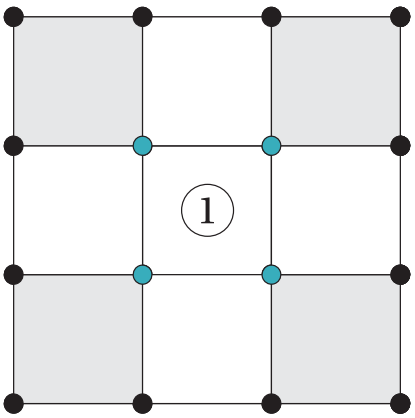


Figure 7.9: Graphical representation of a 2D linear element with interface nodes that does not form an interface.

The algorithm developed can also be extended to scenarios other than merely generating cohesive elements at the interface between distinct materials. For example, in a mesh with just one material, two different IDs can be assigned to it, and the programme will perform the same procedure described before. This second ID may be allocated to specific elements in the mesh in order to, for example, mimic the path of a fracture. This approach extends beyond what is covered in this work.

7.2.2 Cohesive Elements Creation

After all interfaces have been established, the cohesive elements can finally be inserted into the mesh. Defining the normal and tangential directions of the cohesive elements is highly critical to achieving the proper behaviour of the material. This formulation presents several peculiarities between 2D and 3D analyses; thus, each instance will be treated individually. Nonetheless, in both circumstances, one of the elements preserves its original connectivities in each pair of interface elements while the other has them updated.

In 2D studies (shown in Figure 7.10), continuum and cohesive elements are always specified in a counter-clockwise manner (refer to appendixes B and C for the full definition of all implemented element types). Hence, to properly build the cohesive element and make the program as generic as feasible, the interface facet from the continuum element is first inverted to generate the cohesive element edge, followed by the insertion of additional nodes. Through these stages, the cohesive element is established.

As previously said, one of the interface components has its nodes modified; thus, it is of essential significance to save and build the correct link between the old connectivities and the new ones (see Figure 7.10). Furthermore, in the establishing of the other cohesive components, this association library also enables to evaluate whether another neighbouring cohesive element has already altered the nodes. This avoids the production of duplicated nodes.

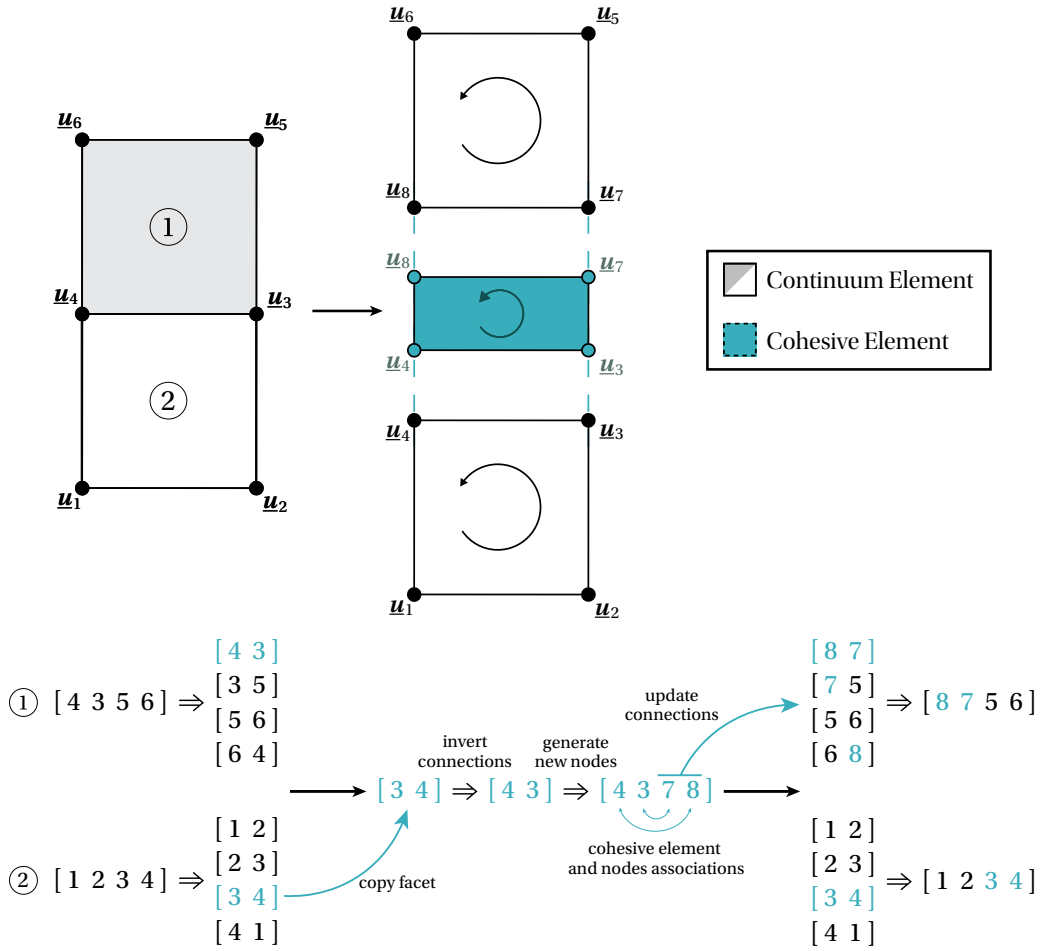


Figure 7.10: Graphic representation of the cohesive elements generation process - 2D analysis.

For 3D studies, continuum and cohesive elements are defined differently, which makes the procedure slightly more challenging (shown in Figure 7.11) (refer to appendixes B and C for the full definition of all implemented element types). Similarly to the 2D continuum elements, the 3D ones have all their faces specified in the counter-clockwise direction, which in the 3D space amounts to having all normals facing the outside. In contrast, cohesive elements can be defined either clockwise or counter-clockwise. It simply needs to be assured that the first face is defined with its normal towards the inside and the second towards the outside, i.e., in the same direction as the first. Additionally, as can be seen in Figure 7.11, the association between the old and new connectivities is also different, owing to this particularity.

With this stated, to generate the cohesive element, the interface facet from the continuum element, unlike in 2D, is immediately passed on to the cohesive one. In geometric terms, it is simple to comprehend this implementation

because since the normal of the continuous element must be to the outside, when duplicating it straight to the cohesive, the face of the latter will be, as requested, to the inside. Subsequently, there merely has to be additional care while establishing the new nodes and their links, to guarantee the proper orientation of the second face (see Figure 7.11).

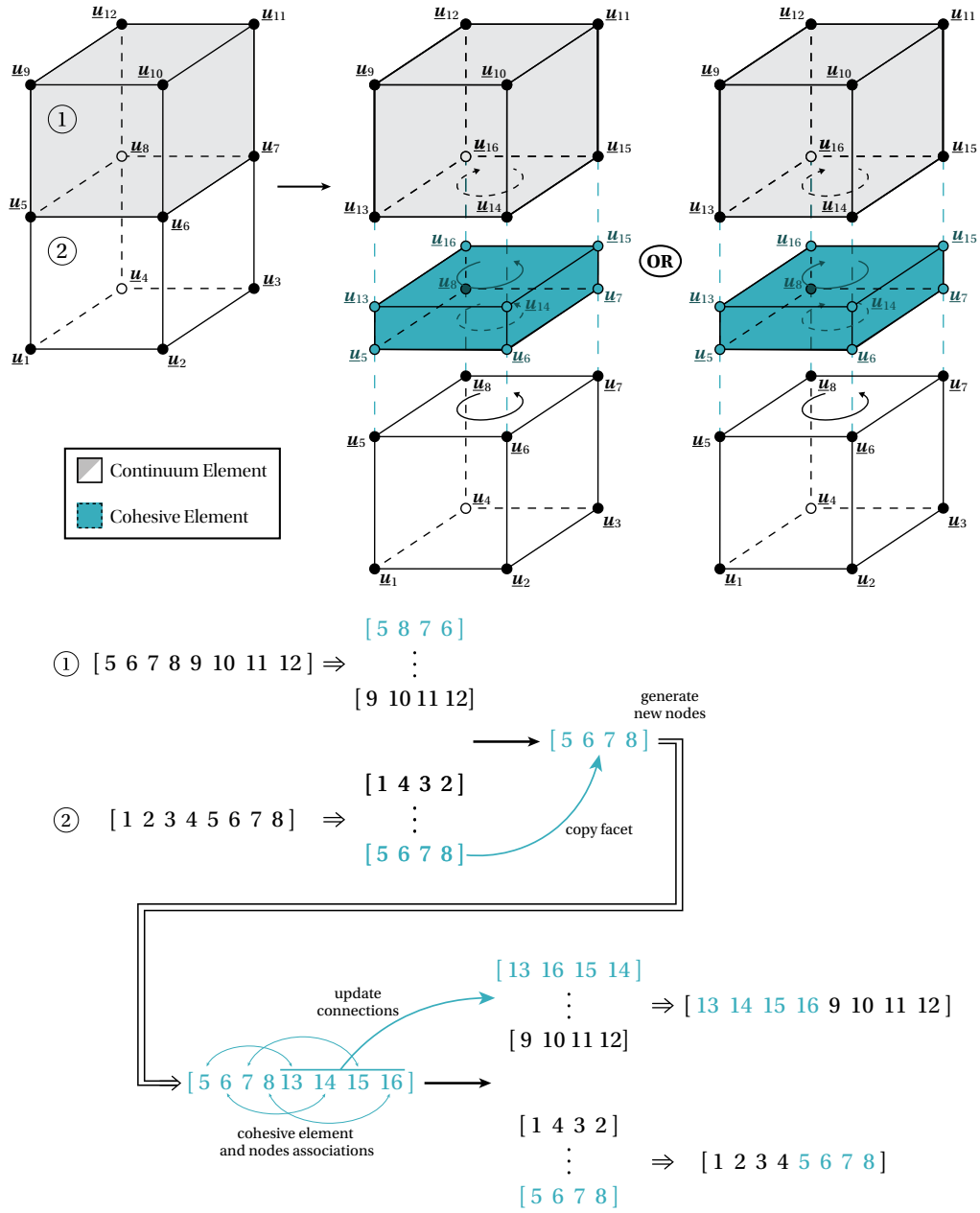


Figure 7.11: Graphic representation of the cohesive elements generation process - 3D analysis.

Lastly, it is also crucial to discuss a peculiar scenario that occurs mainly when RVEs with more than two materials are evaluated. Figure 7.12, depicts the referred scenario for a basic 2D analysis with three distinct materials. As can be noticed, when three distinct materials meet at a node, there is an intricacy in forming the cohesive elements, which was decided to be addressed by leaving an empty space, this is, this region has zero stiffness. This approach stems from the fact that when the size of this area is significant enough to impact the material's behaviour, the cohesive elements surrounding it would have collapsed long ago. Moreover, as mentioned numerous times, the specification of the normal direction of the cohesive elements is vitally critical, and, in this location, there is no normal direction that would make physical sense.

There are more particular examples linked to partitioning numerous junctions in a FE mesh, especially in 3D situations, which can be read in detail in (Zhang et al., 2012). The authors also provide additional strategies to solve these challenges, although their execution, aside from being time-consuming and complex, show minor changes in the final response of the material.

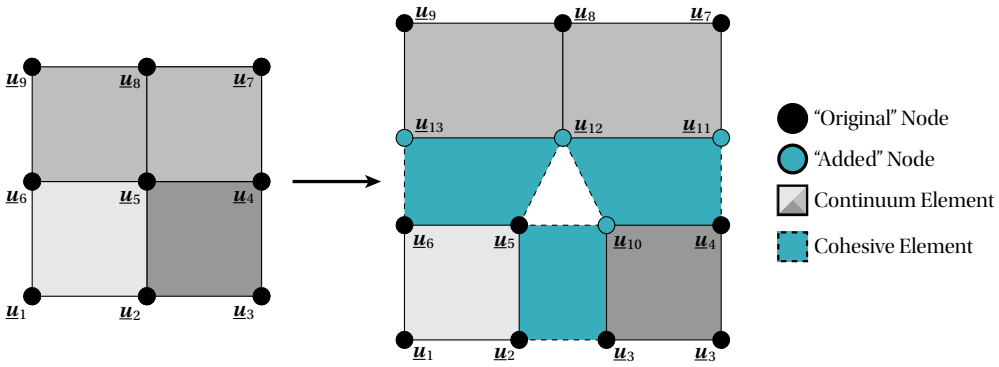


Figure 7.12: Schematic representation of a 2D case when empty spaces are generated.

7.2.3 Output File

With everything set, the next step is to write the output file with the modified discretised finite element RVEs containing the zero-thickness cohesive interface elements. To design this new file, the initial RVE file is taken, and the following information about the cohesive elements is added: the material; the type of cohesive elements established; the groups to which it belongs, as noted above, it comprises the combination of material and element type; the new nodes generated; and, the new cohesive elements. In addition, as described in the previous chapter, the previously specified continuum elements' connectivities also need to be updated.

As a last note, because this programme aims to establish zero-thickness cohesive interface elements, the new nodes generated have the exact same coordinates as their corresponding original nodes of the continuum element.

7.3 Numerical Assessment

The implementation of the proposed code is conducted in Python (Python3.8 version), and all the numerical results provided in this research are achieved in a computer with the following computational resources: Intel ® Core™ i7-12700H Processor 2.30 GHz (24M Cache, up to 4.7GHz, 6P + 8E cores). Moreover, its implementation is neither parallelised nor optimised, and just one CPU core is employed.

7.3.1 Analysis 1 - Number of Elements

Only RVEs containing ellipsoids (some examples are shown in Figures 7.16 and 7.17) are examined in the study since the code is blind to the geometry and distribution of the particles; therefore, the findings obtained can be generalised to all other types of particles. It solely depends on the number of elements, nodes, materials and dimensionality of the analysis. The same scenario is applied to the type of finite element employed in the study. While the TRI3 and TETRA4 elements were employed for 2D and 3D problems respectively, and their quadratic counterparts, the findings can be generalised to all other element types.

The research aimed to evaluate the programme's execution time for 2D and 3D scenarios and linear and quadratic meshes, resulting in a total of four unique combinations. To ensure that the research was as fair as feasible for each of the four analyses, the RVEs generator's input parameters were iteratively adjusted to progressively increase the number of continuum elements, while always maintaining a 10% ratio between them and the number of interfaces (i.e., the number of cohesive elements after the execution of the elaborated code). In other words, a mesh with 1000 continuous elements will have 100 cohesive elements, and so forth. Additionally, given the random nature of each RVE realisation, ten samples for each particular instance were generated, and their CPU times were averaged to provide the most precise and reliable results.

The CPU times observed are described for the generation of the RVEs in Table 7.1 and for the generation of the cohesive elements (processing time of the implemented code) in Table 7.2 and Figure 7.13. Lastly, Figure 7.14 provides

the ratio between the generation time of the RVE and the cohesive elements. It is vital to note that the generation of the RVE has significant fluctuations in processing time depending on the starting parameters employed. Hence, this ratio is only presented in order to have a rough figure for subsequent studies.

Table 7.1: Average CPU time (over ten realisations for each case) for generating the RVE - Analysis 1.

Number Elements	**Time (s)**	**2D**		**3D**	
		Linear	**Quadratic**	**Linear**	**Quadratic**
1000	Mean	8.51×10^{-1}	9.00×10^{-1}	7.12×10^{-1}	4.84×10^{0}
	Std. Dev.	3.14×10^{-1}	3.27×10^{-1}	3.78×10^{-1}	9.37×10^{0}
10000	Mean	6.97×10^{0}	1.17×10^{1}	1.59×10^{0}	5.04×10^{1}
	Std. Dev.	8.86×10^{-1}	1.44×10^{0}	1.90×10^{-1}	6.59×10^{1}
25000	Mean	1.51×10^{1}	3.94×10^{1}	8.79×10^{0}	2.42×10^{2}
	Std. Dev.	2.40×10^{-1}	5.85×10^{0}	1.23×10^{0}	2.44×10^{2}
50000	Mean	3.42×10^{1}	1.82×10^{2}	1.70×10^{1}	1.33×10^{3}
	Std. Dev.	2.49×10^{0}	35.13×10^{1}	1.51×10^{0}	9.50×10^{2}
75000	Mean	5.35×10^{1}	2.83×10^{2}	2.66×10^{1}	1.52×10^{3}
	Std. Dev.	1.62×10^{0}	2.26×10^{1}	2.81×10^{0}	1.01×10^{3}
100000	Mean	7.77×10^{1}	4.67×10^{2}	3.26×10^{1}	3.11×10^{3}
	Std. Dev.	3.20×10^{0}	3.12×10^{1}	2.21×10^{0}	1.54×10^{3}
250000	Mean	2.56×10^{2}	2.92×10^{3}	1.03×10^{2}	5.44×10^{3}
	Std. Dev.	8.28×10^{0}	5.46×10^{2}	5.36×10^{0}	3.68×10^{3}

Table 7.2: Average CPU time (over ten realisations for each case) for generating the cohesive elements - Analysis 1.

Number Elements	**Time (s)**	**2D**		**3D**	
		Linear	**Quadratic**	**Linear**	**Quadratic**
1000	Mean	4.01×10^{-2}	4.91×10^{-2}	4.65×10^{-2}	5.25×10^{-2}
	Std. Dev.	1.22×10^{-2}	4.38×10^{-3}	3.65×10^{-2}	1.79×10^{-2}
10000	Mean	1.89×10^{0}	1.38×10^{0}	1.58×10^{0}	1.75×10^{0}
	Std. Dev.	2.18×10^{-1}	3.99×10^{-1}	1.91×10^{-1}	5.42×10^{-1}
25000	Mean	6.55×10^{0}	7.04×10^{0}	9.93×10^{0}	1.01×10^{1}
	Std. Dev.	9.35×10^{-2}	2.63×10^{-1}	1.99×10^{0}	1.37×10^{0}
50000	Mean	2.73×10^{1}	2.70×10^{1}	3.85×10^{1}	3.98×10^{1}
	Std. Dev.	1.40×10^{0}	6.22×10^{-1}	3.48×10^{0}	5.80×10^{0}
75000	Mean	5.96×10^{1}	6.04×10^{1}	8.56×10^{1}	9.04×10^{1}
	Std. Dev.	4.67×10^{0}	1.78×10^{0}	1.25×10^{1}	9.87×10^{0}
100000	Mean	1.05×10^{2}	1.07×10^{2}	1.45×10^{2}	1.57×10^{2}
	Std. Dev.	6.24×10^{0}	2.93×10^{0}	8.07×10^{0}	5.07×10^{0}
250000	Mean	6.56×10^{2}	6.99×10^{2}	1.02×10^{3}	1.04×10^{3}
	Std. Dev.	1.39×10^{1}	1.00×10^{1}	7.11×10^{1}	7.82×10^{1}

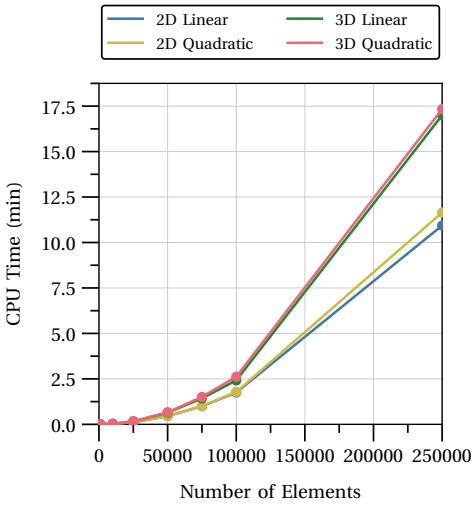


Figure 7.13: Average CPU time (over ten realisations for each case) for generating the cohesive elements - Analysis 1.

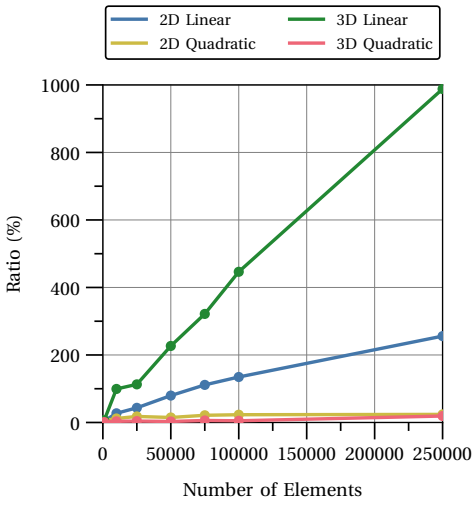


Figure 7.14: Ratio between the average CPU time (over ten realisations for each case) for generating the RVE and the cohesive elements - Analysis 1.

Concerning the cohesive elements generation, the CPU time increases roughly exponentially as the number of elements increases. Nevertheless, given that even an RVE with 100000 elements is already regarded as a large one, the proposed code achieves extremely satisfactory processing times for both 2D and 3D problems (the most challenging case, 3D quadratic problem, takes less than 3 minutes). As was to be predicted, 3D meshes take longer to process than 2D meshes, even though the number of elements is the same. This is because the number of nodes in the mesh increases substantially as well as the number of facets to be analysed per element (for example, for the case under study, the TRI3 element (2D) has a total of 3 facets, each with two nodes, while the TETRA4 element (3D) has a total of 4 facets, each with three nodes).

Moreover, owing to the optimisation procedures previously presented, namely the one denoted in Section 7.2.1, both linear and quadratic problems present identical execution times. This leads to very different ratios between the RVE generation time over the cohesive element generation time. This is due to the fact that contrary to what was managed to be implemented, the RVEs generating program requires more computational resources for the quadratic cases.

Lastly, it can be validated by the standard deviation values presented in Tables 7.1 and 7.2 that the code to generate cohesive elements is significantly more robust and consistent.

7.3.2 Analysis 2 - Number of Materials

Another aspect worth studying regarding the performance of the developed code is how it behaves as the number of materials increases. Even though the present work only analyses microstructures with two materials (PC/ABS), considerable effort was put into optimising the program for its usage in microstructures with multiple materials. This way, the program is ready to be employed in any circumstance.

For this second study, microstructures of polycrystalline materials containing 2, 20, 100, 200, and 1000 materials were generated (some examples are shown in Figures 7.18 to 7.21). Once again, TRI3 and TETRA4 elements and their quadratic counterparts were employed for the 2D and 3D scenarios. Moreover, to ensure that the research was as fair as possible, the total number of mesh elements was maintained constant and equal to 50000 for all cases under study. Considering the random nature of each RVE realisation, ten samples for each particular instance were created, and their CPU times were averaged to provide the most precise and reliable results.

The CPU times observed are described for the generation of the cohesive elements (processing time of the implemented code) in Table 7.3 and Figure 7.15. For the microstructure with 1000 materials, it was not possible to generate a 3D RVE with only 50000 elements; hence there are no values for this specific case.

Table 7.3: Average CPU time (over ten realisations for each case) for generating the cohesive elements - Analysis 2.

Number Materials	**Time (s)**	**2D**		**3D**	
		Linear	**Quadratic**	**Linear**	**Quadratic**
2	Mean	1.10×10^{0}	2.11×10^{0}	3.72×10^{0}	5.12×10^{0}
	Std. Dev.	3.71×10^{-1}	3.50×10^{-1}	6.04×10^{-1}	1.06×10^{-1}
20	Mean	5.66×10^{0}	7.01×10^{0}	2.00×10^{1}	2.79×10^{1}
	Std. Dev.	7.67×10^{-1}	9.05×10^{-1}	1.11×10^{0}	3.12×10^{0}
100	Mean	1.09×10^{1}	1.45×10^{1}	4.32×10^{1}	5.46×10^{1}
	Std. Dev.	2.22×10^{-1}	1.41×10^{-1}	5.92×10^{-1}	1.25×10^{-1}
200	Mean	2.93×10^{1}	4.39×10^{1}	1.02×10^{2}	1.54×10^{2}
	Std. Dev.	6.32×10^{0}	5.85×10^{0}	1.85×10^{1}	9.24×10^{0}
1000	Mean	2.82×10^{2}	3.97×10^{2}	–	–
	Std. Dev.	1.66×10^{1}	2.07×10^{1}	–	–

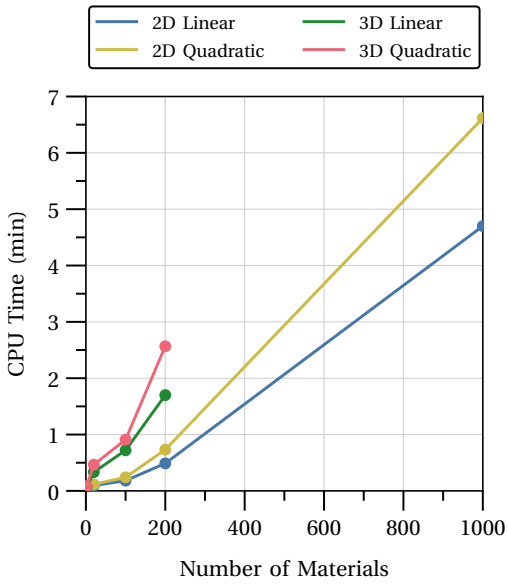


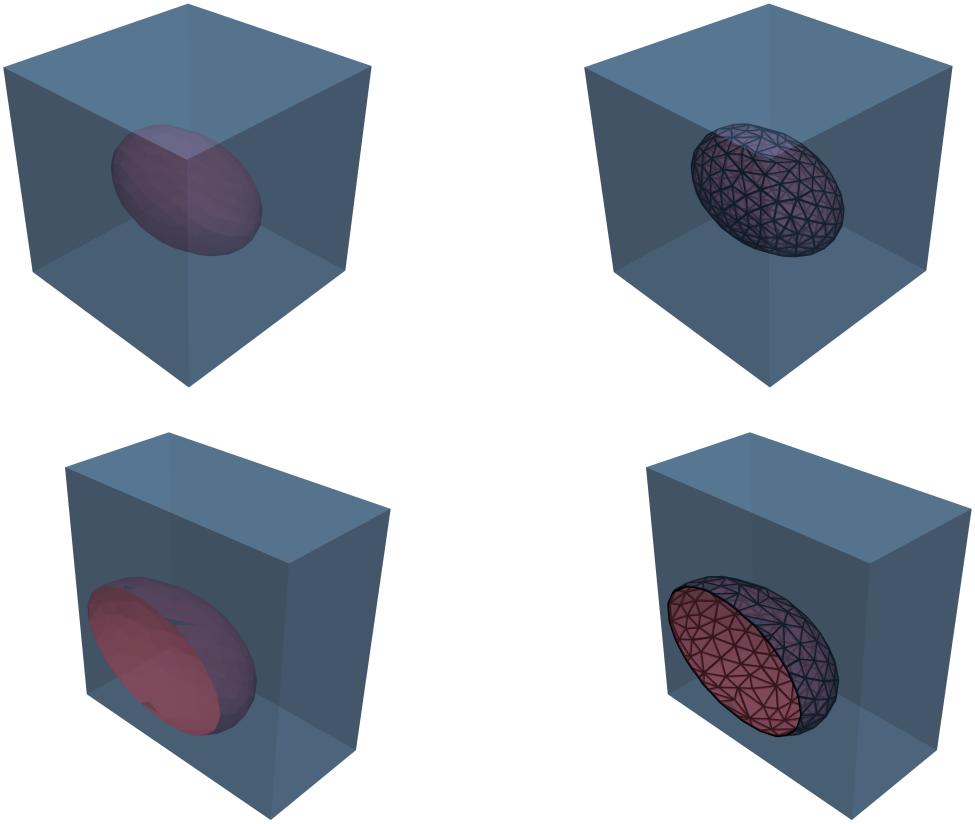
Figure 7.15: Average CPU time (over ten realisations for each case) for generating the cohesive elements - Analysis 2.

Similarly to the previous study, the CPU time increases roughly exponentially as the number of materials increases, with 3D meshes taking longer to process than 2D ones for the same number of elements. It is important to emphasise that 200 materials is already a very high number, and any RVE beyond this value is purely academic and serves only the purpose of demonstrating the capacity of the generated code. For example, a 2D quadratic RVE with 1000 materials takes less than 7 minutes to generate the cohesive elements.

7.4 Application Examples

This Section demonstrates the code's performance in generating cohesive interface elements in several complex and miscellaneous RVEs. These vary from the simplest example of just two materials to more complex ones with several materials and from one to multiple particles, both in two and three dimensions.

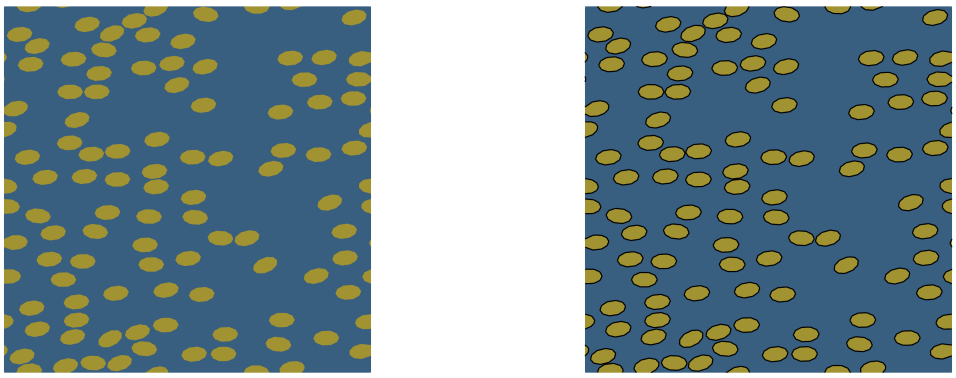
The first example is an RVE containing one particle material phase both in 2D and 3D (see Figures 7.17 and 7.16, respectively). The cohesive elements are depicted here and in the following examples in black. The thickness of the line has been scaled such that its correct location is noticeable. In reality, as previously explained, the implemented cohesive elements present zero thickness in the initial instant.



(a) RVE generated through AMINO.

(b) RVE with cohesive elements.

Figure 7.16: Example of a 3D RVE with two material phases. Different colours correspond to different material phases.



(a) RVE generated through AMINO.

(b) RVE with cohesive elements.

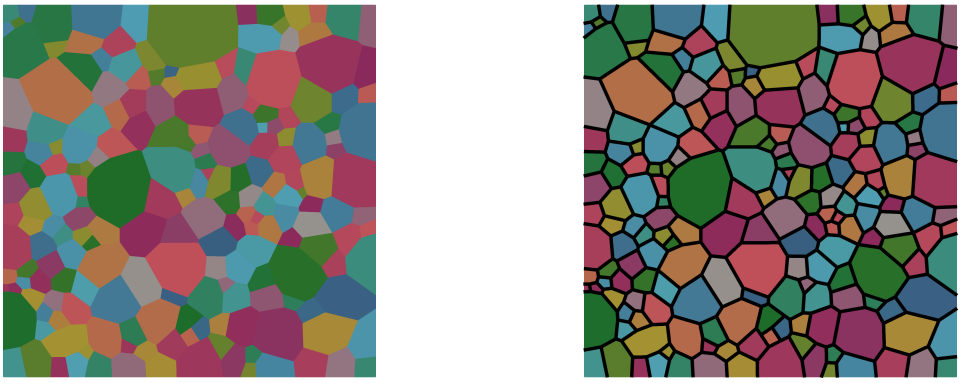
Figure 7.17: Example of a 2D RVE with two material phases. Different colours correspond to different material phases.

The second and third examples are an RVE of a polycrystalline material, both in 2D (see Figures 7.18 and 7.19) and 3D (see Figures 7.20 and 7.21). These examples are meant to illustrate that the programme can also be used in more complicated scenarios with many materials, accurately detecting the boundaries of each one.



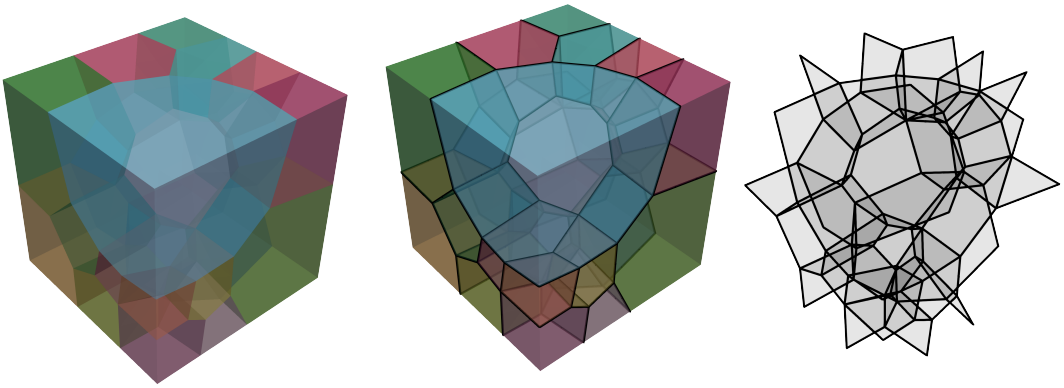
(a) RVE generated through AMINO. (b) RVE with cohesive elements. (c) Cohesive elements.

Figure 7.18: Example of a 2D RVE with twenty material phases. Different colours correspond to different material phases.



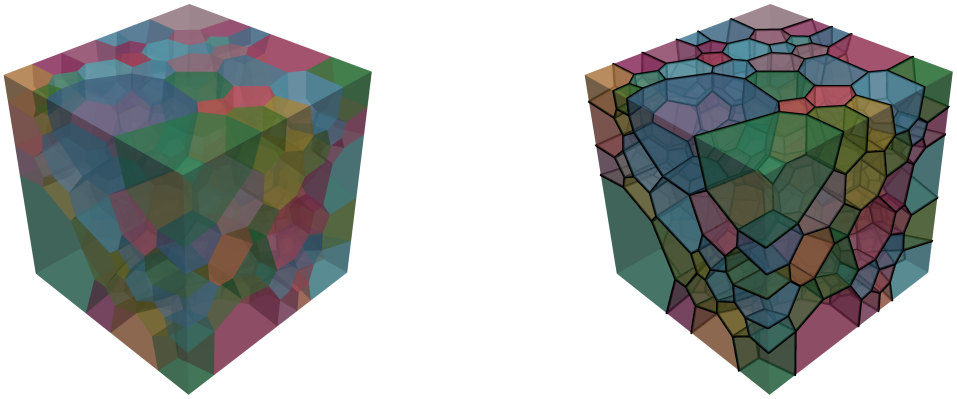
(a) RVE generated through AMINO. (b) RVE with cohesive elements.

Figure 7.19: Example of a 2D RVE with two hundred material phases. Different colours correspond to different material phases.



(a) RVE generated through AMINO. (b) RVE with cohesive elements. (c) Cohesive elements.

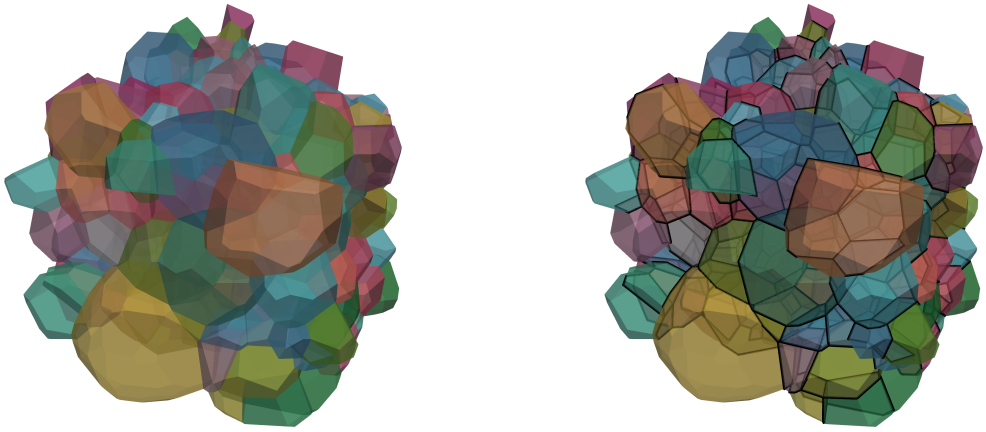
Figure 7.20: Example of a 3D RVE with twenty material phases. Different colours correspond to different material phases.



(a) RVE generated through AMINO. (b) RVE with cohesive elements.

Figure 7.21: Example of a 3D RVE with two hundred material phases. Different colours correspond to different material phases.

Only perfectly squared (2D) and cubic (3D) RVEs with unitary side lengths were presented until this point. However, any random geometry can be used. Figure 7.22 illustrates one of these examples for a 3D case with 200 materials.



(a) RVE without cohesive elements.

(b) RVE with cohesive elements.

Figure 7.22: Example of a 3D RVE with two hundred material phases and a random geometry. Different colours correspond to different material phases.

Another feature that is crucial to depict, given its high degree of relevance, as highlighted repeatedly throughout the chapter, is the normals of the cohesive elements. Returning to the example shown in Figure 7.18, a polycrystalline material with 20 materials, results in Figure 7.23, where its normals are now included.

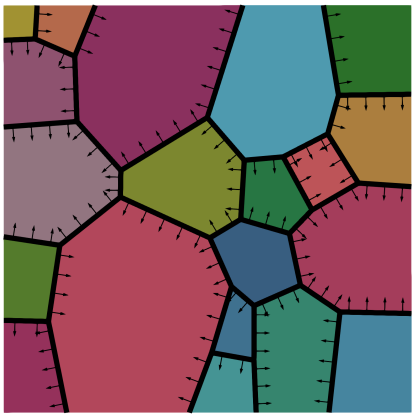
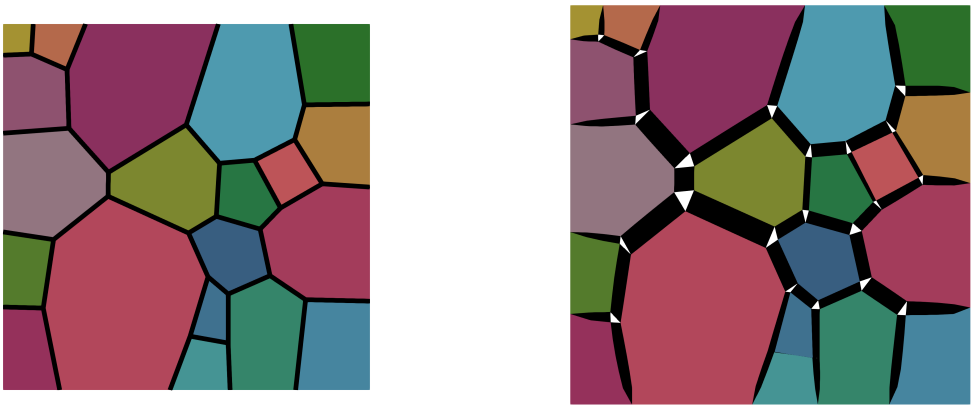


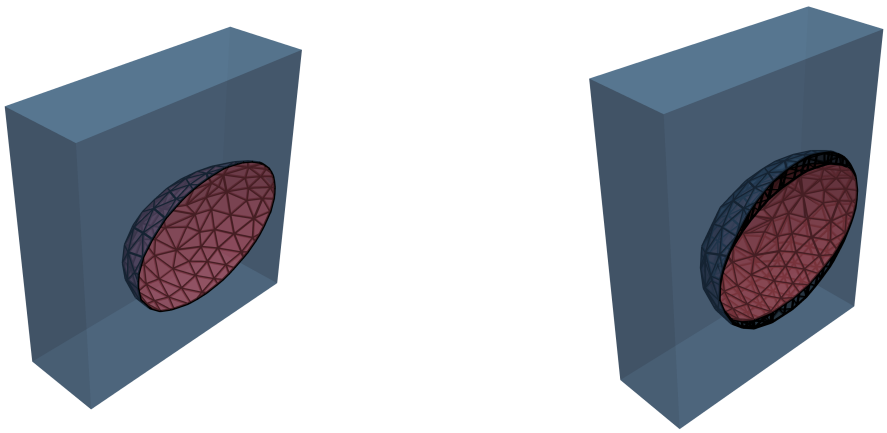
Figure 7.23: Example of a 2D RVE with twenty material phases, with the cohesive elements normals depicted. Different colours correspond to different material phases.

Lastly, to demonstrate that the cohesive elements are accurately described, the final instant of an RVE being tractioned is provided for a 2D (see Figure 7.24) and 3D (see Figure 7.25) example. For the 2D example, a traction force was applied in the X and Y directions, whereas for the 3D case, it was just applied in the Z direction. As can be seen, the cohesive components start to expand as predicted. Notice, however, that the strain scale has been extrapolated to a very high number in order to be able to see these components' behaviour.



(a) RVE initial configuration (b) RVE final configuration

Figure 7.24: Example of a 2D RVE with twenty material phases being tractioned in the X and Y directions. Different colours correspond to different material phases.



(a) RVE initial configuration (b) RVE final configuration

Figure 7.25: Example of a 2D RVE with two material phases being tractioned in the Z direction. Different colours correspond to different material phases.

CHAPTER 8

NUMERICAL ANALYSIS ON THE INFLUENCE OF COHESIVE ELEMENTS

In this chapter, the impact of the introduction of cohesive elements in the RVE of PC/ABS is studied. The PC/ABS polymer blend is modelled by the finite strain visco-elastic visco-plastic constitutive model (described in Section 5.2), while the cohesive elements follow the PPR potential-based cohesive zone model (discussed in Section 6.4).

Only 2D analyses are conducted since, as observed in Section 5.3.1, the computing cost of 3D studies is significantly higher. Consequently, it was decided to only conduct more in-depth research in 2D, assuming that the conclusions derived may be equally applicable to the 3D scenario.

8.1 Constitutive Cohesive Model Properties

Very specialised approaches are needed to comprehend and detect interfacial characteristics, and sometimes only a combination of these methods may be beneficial. The most common interface analysis methods are compiled in (Stamm, 2008), along with the properties that may be gathered from each method. However, as can be seen, for example, in this reference and (Schneider, 2008), experimental tests and studies present in the literature are mainly focused on composite materials and fibre-reinforced materials.

Even though PC/ABS is a polymer that has been extensively investigated in the literature over the years, the study of its interface properties and implementation of CZM is limited or non-existent. Likewise, there is very little development for particulate polymer blends, mainly due to their inherent difficulty in studying the interface in detail and with precision.

Krishnan (2020) addresses this knowledge gap, estimating the cohesive zone model parameters through a series of direct experimental methodologies for smart particulate polymer composites, specifically for elastomeric mechanoluminescent composites. The main issue with this study is the enormous amount of time required to conduct all the experiments, making this approach impractical in the current framework. Additionally, some tests entail specific characteristics of the material under study that cannot be replicated for PC/ABS. Other studies on particulate polymers may provide information on the properties employed, but often little detail is given about the methods used to obtain them (Nafar Dastgerdi et al., 2015, 2014; Hosseini et al., 2017).

In subsequent stages of this research, the objective is to determine the precise properties of the interface between PC and ABS necessary for implementing the CZM. However, at this stage, approximate values for these properties are sufficient for the objectives of the analysis. Furthermore, the properties outlined in this Section will provide a valuable foundation for further investigation into the actual properties of the interface.

8.1.1 Fracture Energy

As previously stated, ABS is a binary blend consisting of Styrene-Acrylonitrile (SAN) and Polybutadiene (PB). As such, the interfacial properties of ABS are determined by the bonding between PC and SAN. In order to evaluate the fracture toughness of this interface, Kim and Kim (2003) conducted experiments using an asymmetric double cantilever beam geometry.

The experimental procedure involved drying PC and SAN in a vacuum furnace at 100°C for 24 hours. Subsequently, the polymers were compression moulded using a chrome-plated mould to form rectangular plates with dimensions of 50x10x2 mm (length x width x thickness). The samples were then joined in their respective moulds at 190°C for 2 hours, with slight pressure applied to ensure proper adhesion. After completion of the joining procedure, the samples were cooled in the mould for 3 hours to reach room temperature and prevent the formation of thermal stresses (Kim and Kim, 2003).

The asymmetric double-cantilever beam test geometry was chosen to avoid crack propagation towards the more compliant material, as seen as though SAN presents a lower crazing stress than PC. To introduce the desired asymmetry, the SAN plate was firmly attached to a 5-mm glass plate. Moreover, a symmetric double cantilever beam geometry would yield a shear mode (K_{II}) component in the stress intensity factor near the crack tip, which would considerably impact the fracture toughness (Kim and Kim, 2003; Janarthanan et al., 1993). The

implications of mixed modes on fracture toughness are discussed in detail in Xu et al. (1991); Charalambides et al. (1990).

Subsequently, the fracture toughness was evaluated by inserting a single-edge razor blade at the interface and applying a constant velocity of 4 μm/s using a stepping motor (as shown in Figure 8.1). Finally, the crack length ahead of the wedge was measured using an optical microscope after a 24-hour period of crack propagation (Kim and Kim, 2003).

Figure 8.2 depicts the fracture toughness between PC and SAN as a function of SAN copolymers' acrylonitrile (AN) content (only the curve without compatibilizer is relevant for the current study). The maximum adhesion energy of approximately 40 J/m^2 is attained when the AN content is around 24% by weight. Therefore, this value will be considered for the fracture toughness of PC/ABS, given that it represents the optimal adhesion properties. Although the PPR potential-based model distinguishes between modes I and II properties, this study only determines the fracture toughness for mode I. However, since the approximate properties are sufficient for this stage of the study, it is assumed that the fracture toughness is equal for both modes ($\phi_n = \phi_t = 40$ J/m^2).

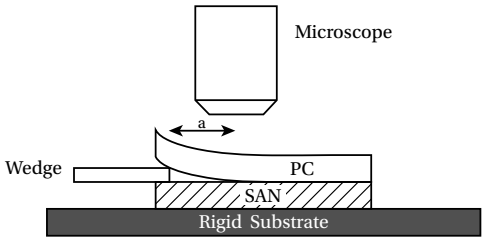


Figure 8.1: Geometry of the asymmetric double-cantilever beam test used in the calculation of the interfacial fracture toughness.
Source: (Janarthanan et al., 1993) - Adapted

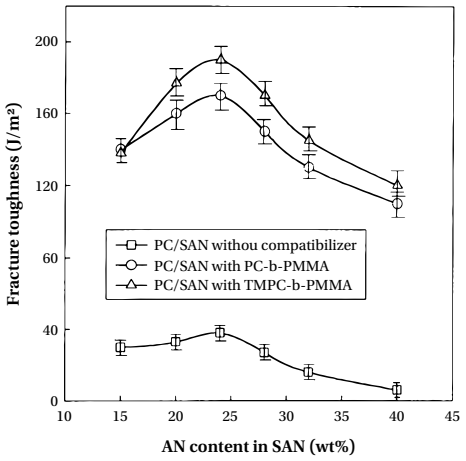


Figure 8.2: Fracture toughness, and respective standard deviation, for PC/SAN adhesive joint as a function of AN content of SAN copolymers.
Source: (Kim and Kim, 2003)

8.1.2 Cohesive Strength

A thorough literature review did not yield any experimental cohesive strength values for the bonding between the PC matrix and ABS particles. However, Inberg (2001) suggests that a standard dumbbell specimen produced by injection moulding, with a weld line in the centre, resulting from injecting material from both sides of the mould, and subjected to a tensile test (perpendicular to the weld line), can offer an indication of the interfacial strength.

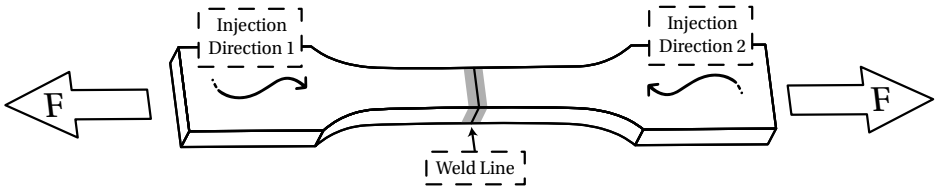


Figure 8.3: Standard dumbbell specimen with a weld line in the centre, to determine the interfacial strength.

Semba and Hamada (1999) investigated the relationship between the PC/ABS blend ratio and the strength of the weld line, as shown in Figure 8.4. The study found that the weld line strength remained mostly constant, at around 40 MPa, for an ABS content ranging from 20 to 80%. On the other hand, Lim et al. (2008) explored the impact of the injection moulding temperature and the addition of unmodified SPMMA (styrene/n-phenyl maleimide/maleic anhydride) terpolymer on the weld line strength of PC/ABS blends with a 6/4 ratio. The results, shown in Figure 8.5, indicate that the weld line strength decreases with increasing injection moulding temperature, with a decrease from 44 MPa at 280 ^{o}C to 42 MPa at 240 ^{o}C (only the data for 0% SPMIMA content is relevant for this study).

Both Semba and Hamada (1999) and Lim et al. (2008) utilised a standard dumbbell specimen as described by Inberg. However, the tensile experiments were carried out under slightly varied conditions. Specifically, Semba and Hamada (1999) conducted the tests at room temperature using a universal testing equipment (Instron 4206) with a cross-head speed of 1.0 mm/min and a gauge length of 115 mm. Conversely, Lim et al. (2008) employed universal tensile machine (Instron 4467) operating at a 5 mm/min cross-head speed under similar conditions. Detailed information regarding the injection moulding processing conditions can be found in the respective articles.

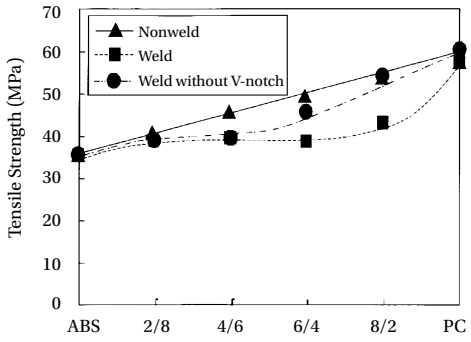


Figure 8.4: Relation between weld line strength and PC/ABS blend ratio.
Source: (Semba and Hamada, 1999)

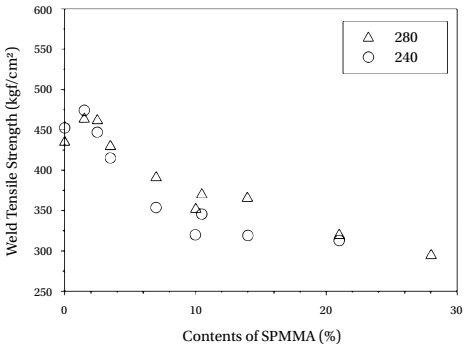


Figure 8.5: Influence of injection moulding temperature on the weld line strength of PC/ABS.
Source: (Lim et al., 2008)

By drawing a parallel to the cohesive strength of the PC/ABS interface, and considering that these values are obtained from a tensile test with load perpendicular to the weld line, it is possible to approximate the value of the normal cohesive strength to 40 MPa. Furthermore, the tangential cohesive strength can be approximated by employing the Tresca criteria, as carried out by Despringre et al. (2016), where it is set as half the value of the normal cohesive strength, i.e., 20 MPa. However, it is crucial to note that this assumption may not always hold true, depending on the particular material and testing conditions. Nevertheless, this estimate is acceptable in the absence of more comprehensive data.

8.1.3 Remaining Parameters

The significance of the shape of the traction-separation equations, as characterised by the initial slope indicators and shape parameters, in describing the material response is still not well-established in the existing literature, with different authors and materials leading to distinct conclusions.

Most of the literature holds that independent parameters such as cohesive energies and strengths suffice to capture the cohesive behaviour of materials. For instance, as reported by (Alfano et al., 2011), shape parameters and slope indicators do not substantially affect the numerical outcomes of predicted peel-force versus displacement curves for Al/epoxy T-peel joints.

However, an alternative view was presented by (Chandra et al., 2002), who argued that the form of the traction-separation equations for CZMs is also critical in characterising the macroscopic mechanical response of metal-ceramic composite systems. Specifically, the appropriate shape of the equations

must be carefully selected, considering the material system and inelastic micromechanical processes, to produce meaningful results.

Since detailed information regarding the form of the traction-separation law for PC/ABS is lacking, a linear softening behaviour is considered by setting $\alpha = \beta = 2$. This parameter choice results in an intermediate behaviour between concave (α and $\beta > 2$) and convex (α and $\beta > 2$) forms. It is essential to note that by adopting this linear softening behaviour, the PPR CZM becomes equivalent to the bilinear CZM. Furthermore, as reported in (Chandra et al., 2002), the bilinear CZM was the best suited, for their case study, to reproduce the mechanical macroscopic response and failure process.

The initial slope indicators measure cohesive stiffness by conveying the critical crack opening width ratio to the final crack opening width. This ratio controls the cohesive elastic domain and influences the amount of artificial elastic deformation. Consequently, a higher initial slope can be attained using lower ratio values. Therefore, in general, smaller values within the range of numerical stability for the intrinsic cohesive zone model, [0.005-0.025], are preferred to minimise artificial elastic deformation and ensure numerical stability (Park et al., 2009; Cerrone et al., 2014).

Given that the initial slope indicators have a relatively negligible impact on the numerical findings, as demonstrated by Vargas et al. (2019), a constant value of 0.01 has been chosen for this parameter. This figure falls within the range of numerical stability and is one of the most frequently employed in the literature. This way, it is possible to minimise artificial elastic deformation while ensuring numerical stability by selecting a value that is neither too small nor excessive.

The irreversible unloading model was selected over the reversible one. This decision was based on the fact that the reversible model is not as well-grounded from a physics point of view, as noted by (de Carvalho, 2022). Therefore, using the irreversible method is generally regarded as the most appropriate approach.

Lastly, a value of one was chosen for the contact penalty factor as it was the one that led to the best overall results from previous analyses done within the CM2S research group. All PPR cohesive zone model parameters employed in the following study for the PC and ABS interphase are summarised in Table 8.1.

Table 8.1: Constitutive cohesive model input parameters.

Parameter	SI Units	PC/ABS Interface
ϕ_n	J/m^2	40
ϕ_t	J/m^2	40
σ_{max}	MPa	40
τ_{max}	MPa	20
λ_n	-	0.01
λ_t	-	0.01
α	-	2
β	-	2
α_p	-	1
Unloading type	-	Irreversible

8.2 CZM Properties Analysis

In this section, a thorough parametric study is performed to investigate the impact of the PPR cohesive parameters (i.e., cohesive strengths, fracture energies, shape parameters, and slope indicators) on the constitutive behaviour of PC/ABS material. To conduct this analysis, a 2D square RVE with a side length of 50 μm (representative size found in Section 5.3.2) and a volume fraction of 10% ABS is subjected to a uniaxial load along *xx*.

The main objective of this analysis is to gain a greater sensitivity to the parameters that have the most significant impact on the material behaviour. To this extent, only one type of load was employed in the study. The selected load was chosen based on its ability to exert greater stress on the matrix/particle interface and because the nucleation phenomenon is less prevalent in this direction compared to the *yy* direction. Thus, allowing for a more comprehensive study of cohesive element behaviour.

The base PPR cohesive parameters used in this study are presented in Table 8.1. The parametric study revolves around varying one pair of properties (one pair corresponds to the normal and tangential component) while keeping the others constant and equal to the base values. Figure 8.6 is presented as a reference to illustrate the difference in behaviour between PC/ABS with and without cohesive elements. It is important to note that the selected cohesive parameters are only approximations (they may not represent the actual values accurately) chosen to investigate the overall behaviour of the material accounting for particle/matrix debonding. The evolution of the deformation for

the RVE with cohesive elements is illustrated in Figure 8.7.

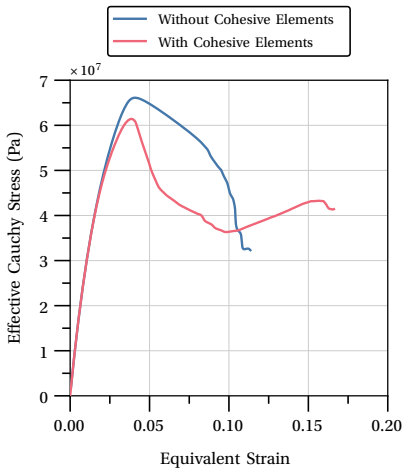


Figure 8.6: Comparison of the microscopic response of PC/ABS with and without cohesive elements.

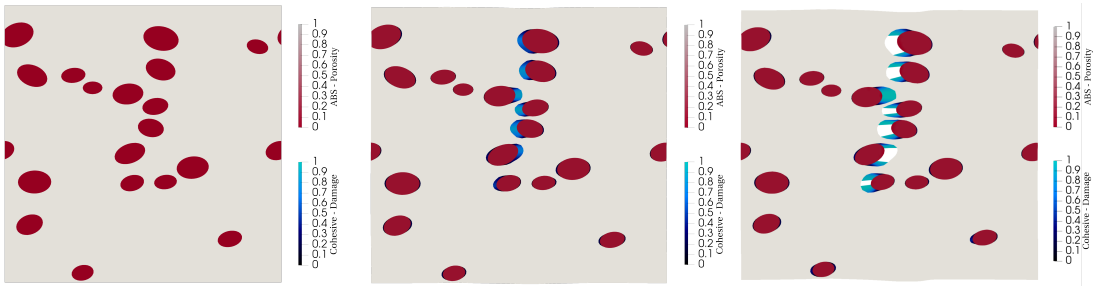


Figure 8.7: Time evolution of the nucleation and debonding phenomena and deformation of a 10% volume fraction RVE under uniaxial loading along *xx*.

The following figures, Figures 8.8 to 8.11, represent the parametric study for each pair of properties. Figures 8.8 and 8.9 are subdivided into three graphs, which are organised as follows: 1) Each graph maintains the normal component constant while the tangential component is varied; 2) In the set of three graphs, each colour represents a different value of the normal component, while the tangential component is kept constant.

Firstly the influence of $\sigma_{\max}$ and $\tau_{\max}$ on the material response is studied by varying both variables independently between 20, 40, and 80 MPa, resulting in a total of nine combinations (see Figure 8.8). The findings of this study reveal that an increase in the cohesive strength of the interface debonding relation, either tangential or normal, has a significant effect primarily by increasing the elastic limit stress. However, the higher cohesive strength resulting from a

fixed cohesive energy leads to a smaller final normal separation, causing full debonding to occur earlier.

In particular, an increase in the tangential component produces a higher slope in both the softening and hardening regions, resulting in lower stress levels at the end of the softening process. Conversely, the stress reached at the end of the softening process remains relatively stable, irrespective of the value of the normal component.

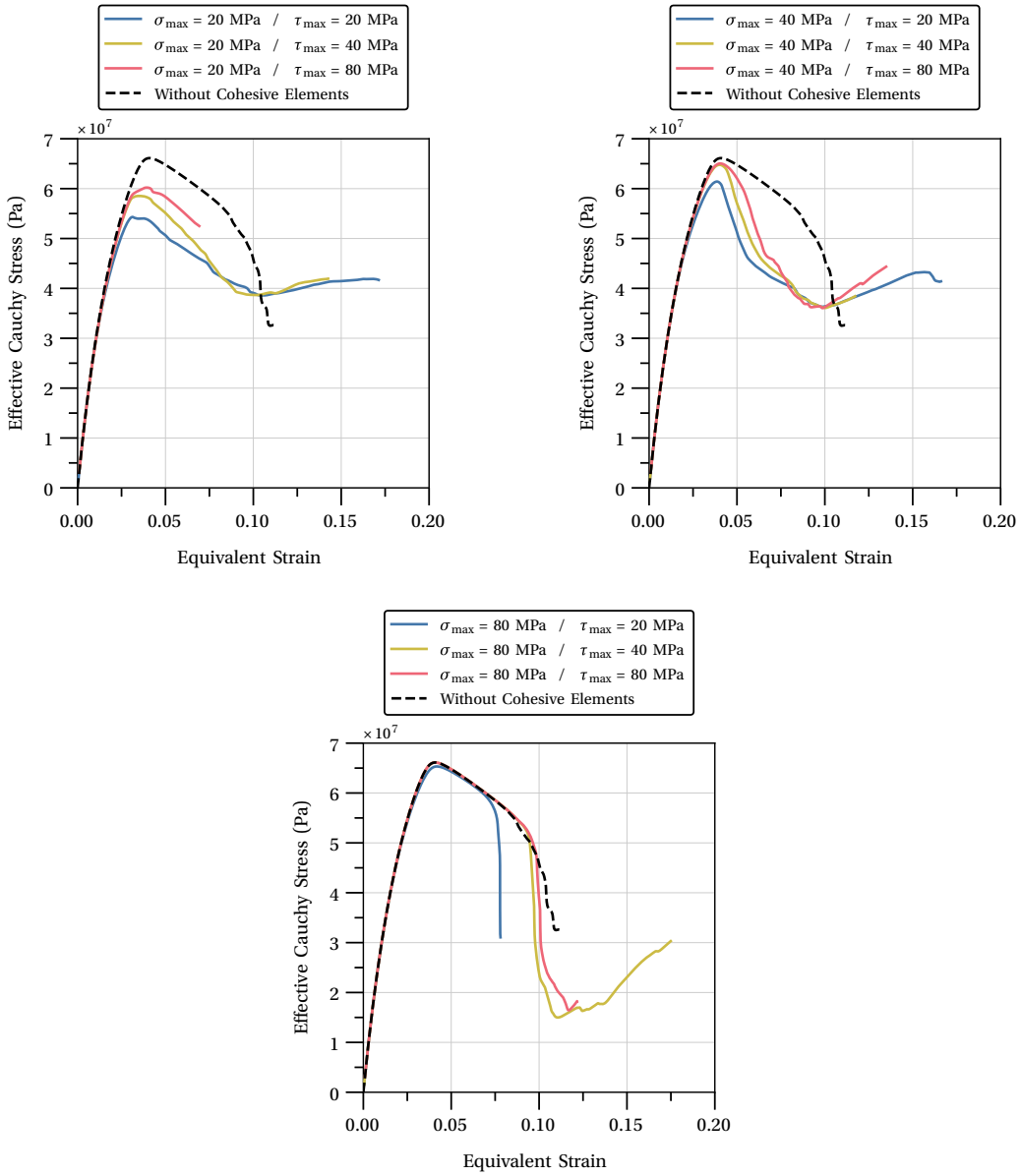


Figure 8.8: Effect of the cohesive strengths on the microscopic response of PC/ABS.

Next, the effect of the fracture energies was investigated by varying each one independently between 20, 40, and 80 J/m^2, as shown in Figure 8.9. As the cohesive strengths are held constant, an increase in the fracture energies requires more energy to separate the particle and the matrix, resulting in an increase in the area under the curve (global dissipated energy) and a decrease in the slope of the post-peak region. This implies that an increase in fracture energy leads to less pronounced strain-softening. Additionally, as ϕ_n increases, the softening to hardening transition stress value tends to be higher, with an increasing difference for higher values of ϕ_t. Nonetheless, the region of non-linear hardening remains mostly unaffected.

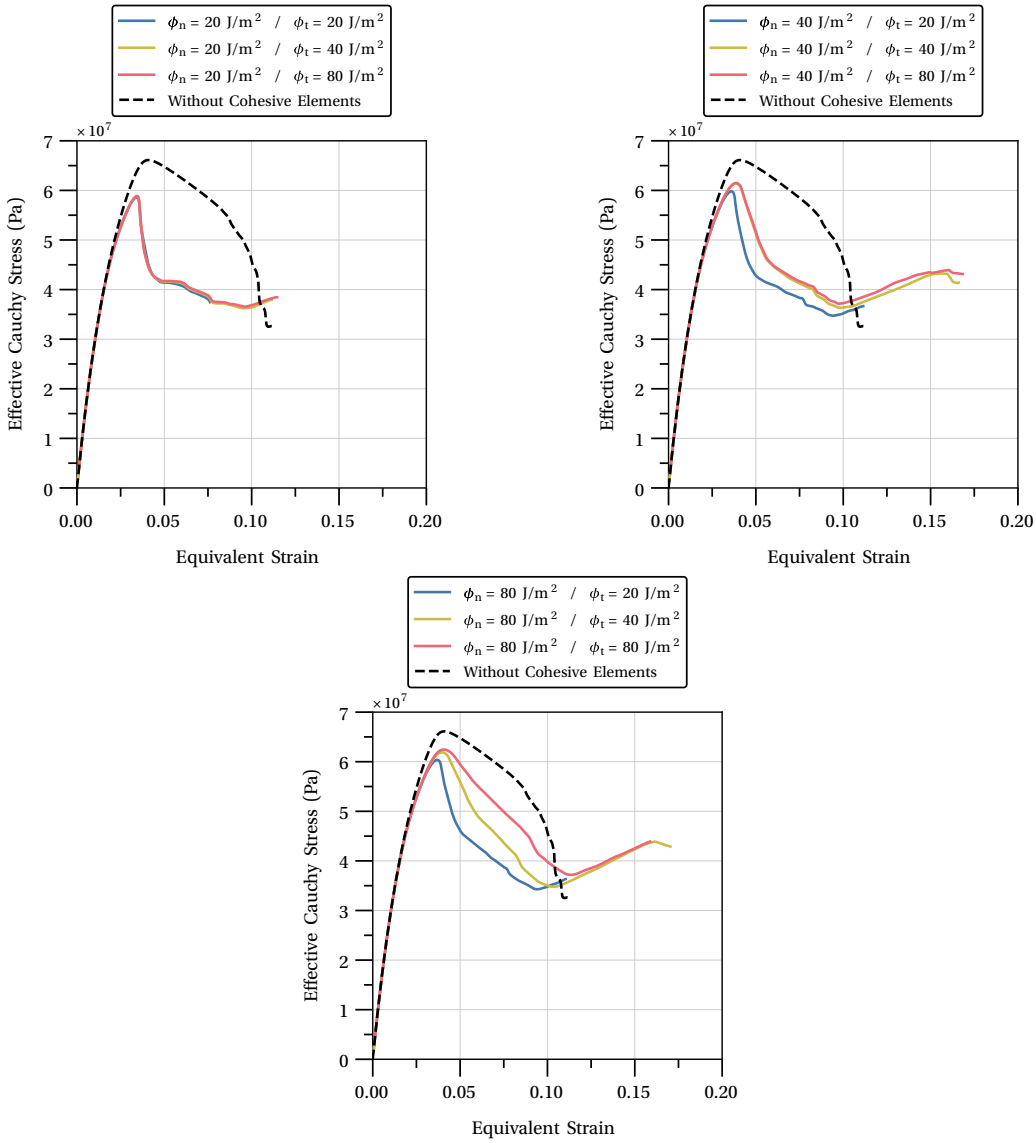


Figure 8.9: Effect of the fracture energies on the microscopic response of PC/ABS.

Finally, the effect of different values of the initial slope indicators and shape parameters is presented in Figures 8.10 and 8.11. The initial slope parameters were varied within the range of numerical stability, i.e., 0.005, 0.01, and 0.025, and the shape parameters were varied between convex ($\alpha = \beta = 1.5$), linear ($\alpha = \beta = 2$), and concave ($\alpha = \beta = 4$) forms. The analysis reveals that their values are practically irrelevant in characterising the material behaviour. This implies that the numerical results are most sensitive to the cohesive strengths and fracture energies, being only necessary to identify/calibrate these four parameters of the nine total parameters of the PPR potential-based cohesive zone model.

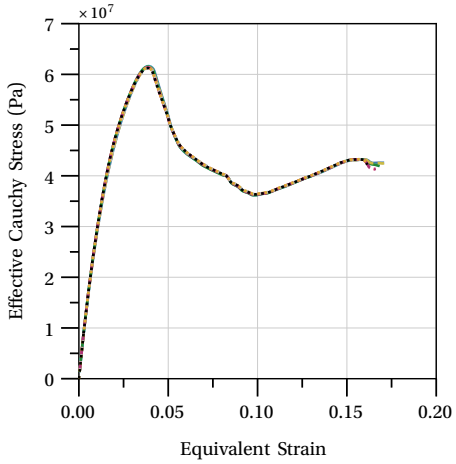


Figure 8.10: Effect of the initial slope indicators on the microscopic response of PC/ABS. A total of 9 different combinations are represented.

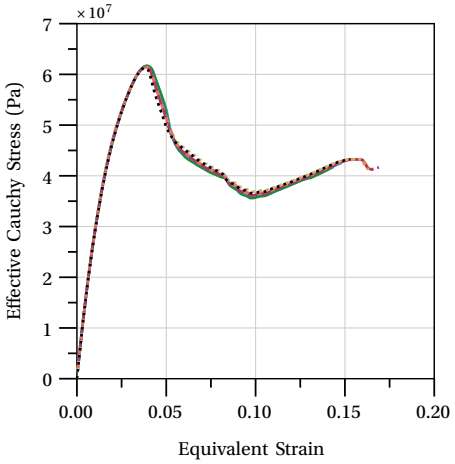


Figure 8.11: Effect of the shape parameters on the microscopic response of PC/ABS. A total of 9 different combinations are represented.

8.3 Loading Schemes Analysis

An extensive parametric study is conducted, where a specific RVE, 2D square RVE with a side length of 50 μm (representative size) and a volume fraction of 10% of ABS, is subjected to several loading schemes prescribed by means of the deformation gradient $\boldsymbol{F}$. This parametric analysis provides a set of numerical experimental data that allows for greater sensitivity regarding which type of loadings are most affected by the inclusion of cohesive elements.

The loading conditions are given by the following two deformation gradients

$$\boldsymbol{F}_x = \boldsymbol{I} + \begin{bmatrix} \mathrm{C1} & \mathrm{C2} \\ 0 & 1 \end{bmatrix} \qquad \text{and} \qquad \boldsymbol{F}_y = \boldsymbol{I} + \begin{bmatrix} 1 & \mathrm{C2} \\ 0 & \mathrm{C1} \end{bmatrix}, \tag{8.1}$$

where $\boldsymbol{I}$ is the second-order identity tensor, and C2 and C1 are independent loading variables that define the shear and traction components, respectively. The following bounds were set to the independent loading variables

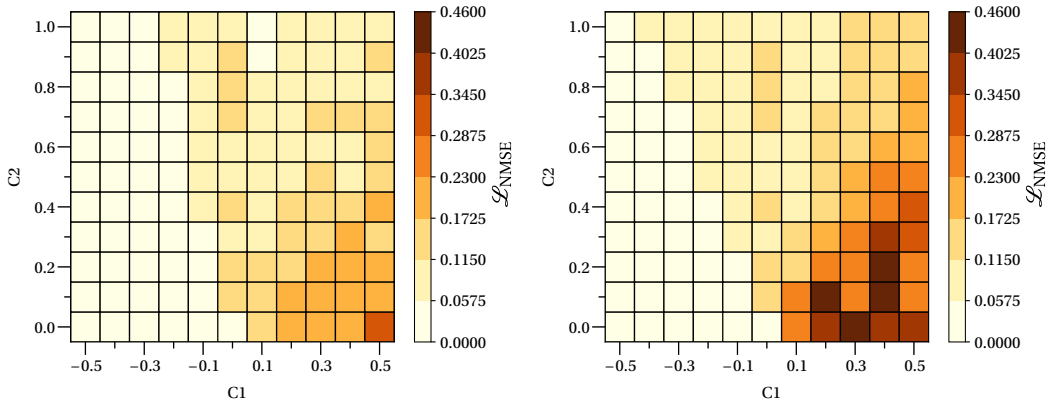
$$\mathrm{C1} \in \left[-0.5,\, 0.5\right] \qquad \text{and} \qquad \mathrm{C2} \in \left[0,\, 1\right]. \tag{8.2}$$

A vital aspect concluded from the analysis of Section 5.3 is the anisotropy of the material between the injection direction, *xx*, (see Figure 8.12(a)) and its perpendicular direction, *yy* (see Figure 8.12(b)). Therefore, one deformation gradient was defined for each direction, making it possible to assess the importance of cohesive elements according to the direction of the tensile loading. The C1 value was varied within the intervals described above, such that both compressive and traction loads can be studied.

To conduct this analysis, it is imperative to employ a suitable comparison function. In this regard, the error function proposed by Ferreira et al. (2023) was modified to quantify the dissimilarity in describing the RVE with and without cohesive elements. The approach in (Ferreira et al., 2023) applies the discrete version of an integrated normalised mean squared error (NMSE) loss function to a calibration procedure, which was adapted to the specific case presented as follows:

$$\mathscr{L}_{\mathrm{NMSE}} = \left[\frac{1}{n_s}\sum_{i=1}^{n_s}\left(\sigma_{\mathrm{eff}} - \sigma_{\mathrm{eff_c}}\right)^2\right]\left[\sum_{i=1}^{n_s}\left(\sigma_{\mathrm{eff}}\right)^2\right]^{-1} \tag{8.3}$$

where n_s is the number of discrete sampling points (each associated with a discrete value of the equivalent strain), and σ_{eff} and $\sigma_{\mathrm{eff_c}}$ are the effective Cauchy stresses without and with cohesive elements, respectively. The utilisation of this method is primarily motivated by the fact that various loading schemes can exhibit substantial variations in their maximum and average stress values. By utilising this function, the resultant value is normalised, thereby enabling meaningful comparisons across different scales.



(a) (b)

Figure 8.12: Sensitivity analysis of the loading schemes most impacted by incorporating cohesive elements at the interface between PC and ABS: (a) Traction along *xx*; (b) Traction along *yy*.

As anticipated, this study reveals that the impact of incorporating cohesive elements at the interface between ABS particles and the PC matrix can be clearly distinguished into two distinct regions, irrespective of the direction of the applied deformation gradient. The results, as illustrated in Figure 8.12, indicate that, for compression loading, including cohesive elements leads to a minor or even negligible change in the material behaviour, as demonstrated in Figure 8.13. Conversely, the material response is significantly altered for tensile loading, as shown in Figure 8.14. Based on these findings, it can be inferred that including cohesive elements is dispensable when studying PC/ABS under compression. This conclusion is further supported by the significant increase in computational cost, which on average rises by 3000%, with the extent of increase being higher or lower depending on the degree of compression.

Conversely, when subjected to traction, including cohesive elements becomes crucial in accurately depicting the material behaviour. Nevertheless, it should be acknowledged that the cohesive element properties employed in this study are only approximations and may not precisely reflect the actual values. Consequently, if the cohesive strengths and fracture toughness values are, in fact, higher, the influence of incorporating cohesive elements will diminish, as evidenced in Section 8.2. Notably, despite the considerable impact on the material response, the increase in computational cost is, on average, only 400%. This observation can be attributed to the fact that in compression, unlike tension, significant computational effort is needed to compute contact mechanics to prevent negative normal separation.

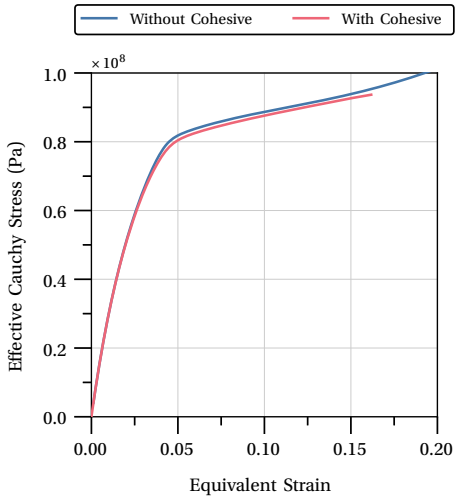


Figure 8.13: Comparison of the microscopic response of PC/ABS with and without cohesive elements under compression along *yy*. Specifically, C1 = −0.5 and C2 = 0.0.

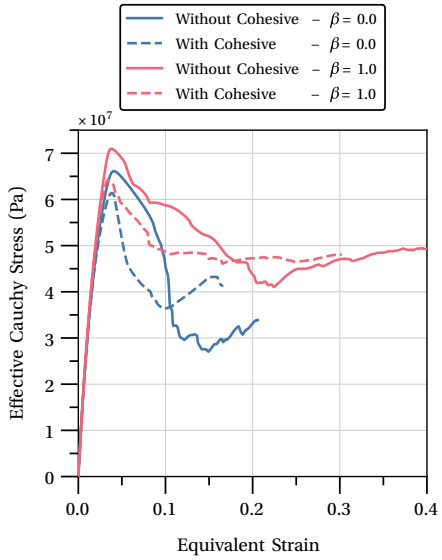


Figure 8.14: Comparison of the microscopic response of PC/ABS with and without cohesive elements under traction along *xx*. Specifically, C1 = 0.5 and C2 = 0.0 or 1.0.

Further examination of the graphs in the tensile loading zone reveals two key findings. Firstly, the influence of cohesive elements is significantly greater for loadings in the *yy* direction than in the *xx* direction. This observation can be primarily attributed to the fact that the resistant area of ABS particles is larger in the *yy* direction (owing to the elongation of the particles in the *xx* direction), which consequently results in an expansion of the area of cohesive elements under tension and enhances their influence.

Secondly, the influence of cohesive elements decreases with an increase in the shear component. It should be noted that while Figure 8.12 may suggest a substantial decrease in the influence of cohesive elements with an increase in the shear component, in reality, this decrease is not as significant. In fact, cohesive elements continue to play a fundamental role in describing the material behaviour, as demonstrated in Figure 8.14. As discussed in Section 5.3.2, material rupture occurs later under shear due to less prominent nucleation phenomena. This observation can be attributed to the low shear modulus of the rubber, which hinders the nucleation and growth of voids under shear loading. Consequently, the material exhibits increased stiffness. Furthermore, the material behaviour converges to the same value, irrespective of whether cohesive elements are included or not, during the hardening phase, thus explaining why the error displayed in the graphs diminishes with an increase in shear.

CHAPTER 9

COHESIVE ZONE MODEL PARAMETERS CALIBRATION

Chapter 8 has established that the incorporation of cohesive elements at the interface between the ABS particles and the PC matrix results in a notable modification of the PC/ABS constitutive behaviour, particularly in the case of tensile loadings. Building on this finding, the present chapter aims to determine the authentic parameters of the PPR cohesive zone model by employing numerical calibration techniques and by analysing the material's true response under uniaxial traction. Numerical calibration was chosen for determining these properties because, as discussed previously, their determination through exclusively direct experimental procedures has proved to be highly challenging for particulate polymer blends.

Ideally, a coupled multi-scale finite element analysis, which involves a series of microscopic problems to determine the constitutive behaviour of each macroscopic point, would provide almost ideal accuracy levels, when identifying the four parameters of the PPR cohesive zone model (ϕ_n, ϕ_t, σ_{max} and τ_{max}) that have the most influence on the material behaviour characterisation. However, such an approach is computationally expensive and impractical, even with simplified mesh structures at both macro and micro levels. Even more so, each simulation corresponds solely to one iteration of the calibration process, which involves a minimum of 100 iterations to achieve desirable outcomes.

To overcome this challenge, an alternative method is developed that allows determining the properties of the interfaces between PC/ABS (micro-scale behaviour) through the response obtained from the material in uniaxial tensile experimental tests (macro-scale behaviour). The implemented procedure involves a multi-scale analysis approach where macro- and micro-scale behaviours are decoupled from each other, meaning that the two problems are treated and analysed separately. This approach enables us to identify the four

parameters of the PPR cohesive zone model that have the most influence on material behaviour characterisation while also reducing computational costs. A succinct summary of the main steps of this analysis can be found in Figure 9.1.

The first step involves obtaining the actual response of the material through uniaxial tensile experimental tests, as described in Section 9.1. Following this, a numerical simulation is carried out, referred to as the Macro-scale Problem, which reproduces the same conditions as the real test. A constitutive model that can accurately describe the load-displacement curve obtained from the experimental test is applied to the specimen at this stage. To achieve this, the visco-elastic visco-plastic constitutive model presented in Section 5.2 is chosen. The calibration process is then carried out to obtain the model parameters that allow for the numerical response to be the closest to the actual response. These new parameters will be quite different from those applied to the PC and ABS since they intend to describe the material as a whole (a kind of homogeneous material); that is, they describe, simultaneously, the PC, the ABS, and their interface.

After calibrating the properties and obtaining the numerical response at the macro-scale, n Gauss points are selected from the specimen mesh, and their deformation gradient history is stored during the simulation. It is important to note that the deformation gradient obtained is independent of the chosen constitutive model; it only needs to be able to describe the real behaviour of the material with the least complexity and computational cost possible. The next step involves studying the material behaviour at the micro-scale by considering the response obtained at the macro-scale. A 3D RVE of PC/ABS is generated to which the deformation gradients are applied. With the response of the RVE for different deformation gradients, the calibration process is carried out once again to determine the missing properties of the PPR cohesive zone model.

The credibility and accuracy of this methodology are rooted in the calibration of the macro-scale response to match the experimental test results, which enables the effective stress-equivalent strain curves of the n Gauss points to correspond to the actual behaviour of the material at the micro-scale. Consequently, by applying the deformation gradients of these n Gauss points to the RVE, the response of the RVE must be identical to the response obtained from the macro-scale, with the only unknowns being the interface parameters.

Lastly, after obtaining the actual properties of the CZM, a Coupled Multi-scale Finite Element Analysis is conducted to validate the results. In this final stage, the load-displacement curve obtained is anticipated to resemble its corresponding curve from the experimental tests closely. This final step is of

paramount significance, considering that the entire process involves a series of simplifications and approximations that attempt to replicate the coupled analysis's results with a significant reduction in computational cost.

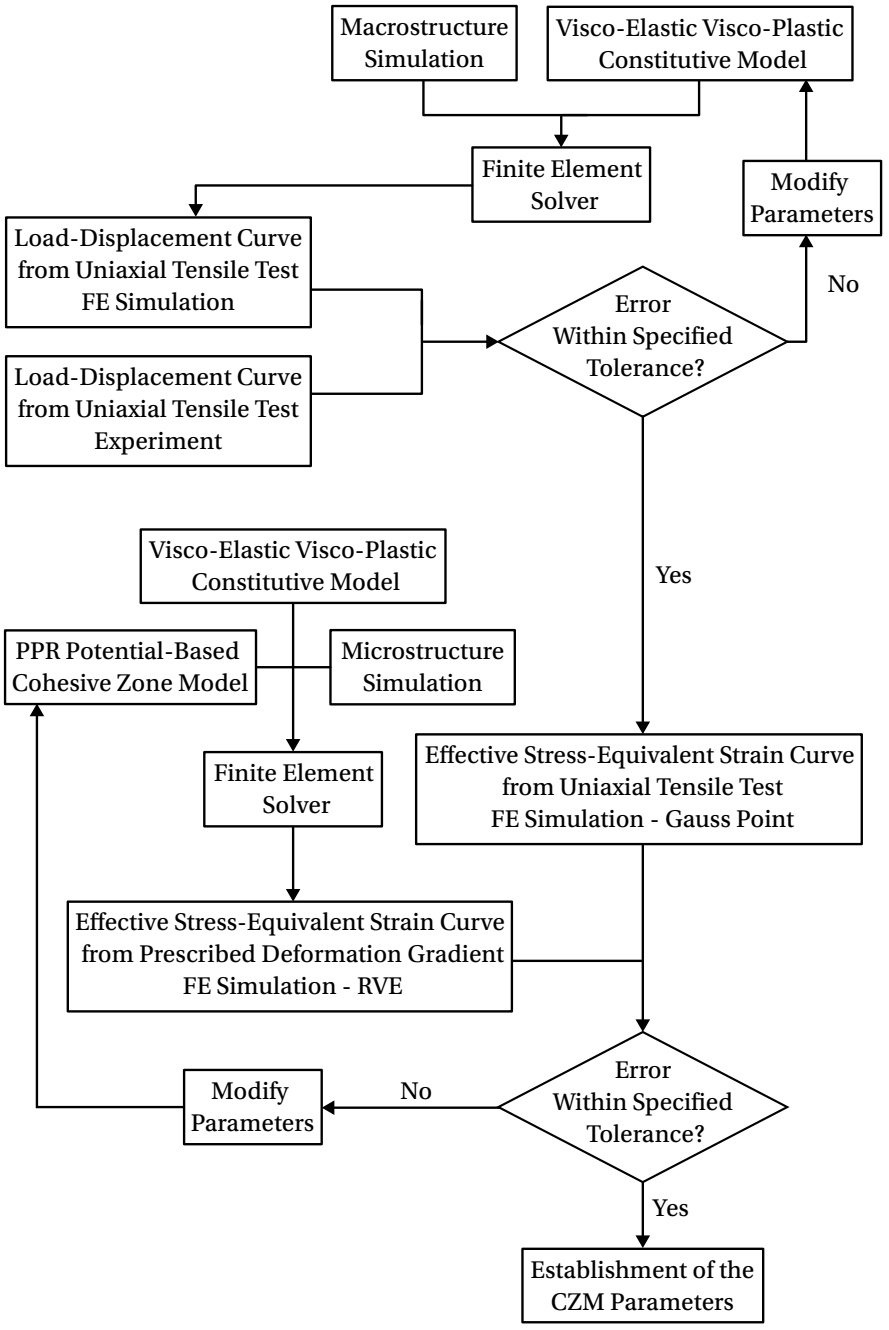


Figure 9.1: Cohesive Zone Model parameters calibration procedure.

9.1 Experimental Testing Setup

The experimental methods and setup required for determining the parameters of the PPR cohesive zone model are presented in this section. All experiments were conducted at the Faculty of Engineering of the University of Porto by Macedo (2023). The mechanical tests included uniaxial tensile tests performed at room temperature using an MTS 810 servo-hydraulic testing machine and an MTS load cell (serial No. 526958) calibrated up to 10 kN (see Figure 9.2). The crosshead speed was maintained constant at $\dot{u}$ = 0.0125 mm/s for all tests.

The smooth round bar specimen geometry, depicted in Figure 9.3, was used for the uniaxial tensile tests. Each end of the specimen had a threaded clamping zone with a nominal length of 30 mm. To manufacture the specimens, larger cylindrical bars with a diameter of 14 mm and a length of 125 mm were first injected with their *yy* axis aligned with the direction of material flow, followed by their machining according to the technical drawing presented in Appendix D.



Figure 9.2: Uniaxial tensile tests: MTS 810 servo-hydraulic testing system.

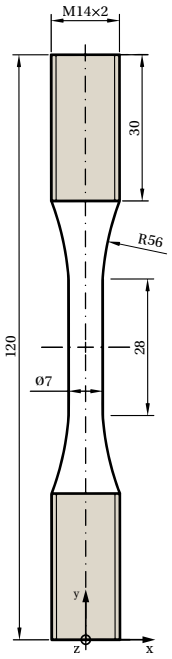


Figure 9.3: Geometry of tensile test specimen - smooth round bar.

Afterwards, to eliminate residual stresses in the specimen and recover its true properties, the specimens were subjected to a thermal treatment cycle schematically shown in Figure 9.4. This cycle involved annealing the specimens

by heating them in a furnace to the glass transition temperature for 1 hour and holding that temperature for 2 hours. The samples were then slowly cooled in the furnace over 8 hours to room temperature (T_{room} = 25 °C). The PC/ABS specimen was annealed at T_{g} = 100 °C, as the glass transition temperatures T_{g} of PC and SAN are around T_{g} = 150 °C and T_{g} = 105 °C, respectively (MARK, 1999). Finally, it should be noted that the specimens were fabricated for an 80/20 PC/ABS ratio, whose technical specifications are presented in Appendix E.

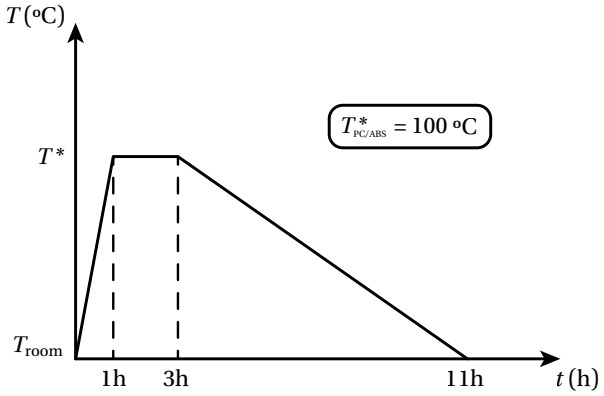


Figure 9.4: Thermal cycle used for the thermal treatment of the PC/ABS test specimens.

9.2 Calibration Procedure

The piglot (Parameter Identification via Global Optimisation) tool, introduced in Coelho (2022), was employed in this chapter to conduct the necessary parameter identification. This toolbox provides an automated parameter identification solution for macro-, micro-, and constitutive responses by utilising direct numerical simulation via the finite element method. The procedure is formulated as a gradient-free optimisation problem, in which an objective function that accounts for the distance between predicted and reference responses is minimised. During the parameter identification process, the toolset queries multiple responses from the FEM program to guide the search towards the optimum solution.

One notable feature of this tool is its ability to simultaneously compare several responses, either from the same FEM analysis or from different cases. As a result, it is possible to calibrate material properties using multiple experimental loadings concurrently.

9.2.1 Optimisation Problem

In summary, an optimisation problem seeks to find the optimal values $\boldsymbol{\theta}^*$ that provide the best fit for the incremental response $\hat{y}^i(t)$ in comparison to the reference response $y^i(t)$. This problem can be formulated as an optimisation problem, such that

$$\boldsymbol{\theta}^* = \arg\min_{\boldsymbol{\theta}\in\mathscr{B}} \; J(\boldsymbol{\theta}), \tag{9.1}$$

where $J(\boldsymbol{\theta})$ represents a cost function that is uniquely dependent on the material parameters and must be minimised, and $\mathscr{B}$ denotes the domain of the parameters. Note that the incremental finite element procedure defines a function f^i for a given quantity of interest i of the form

$$\hat{y}^i(t) = f^i(t, \boldsymbol{\theta}), \tag{9.2}$$

where $\boldsymbol{\theta}$ represents the material parameters that need to be identified. For notational convenience, the function dependencies are relaxed, as they are typically not only dependent on the material parameters and time (Coelho, 2022).

In addition, for multi-objective optimisation, where several fields and/or loading conditions can be simultaneously analysed, the following expression is derived

$$J(\boldsymbol{\theta}) = \sum_{i=1}^{N_L} \mathscr{L}^i \left(y^i, f^i \right), \tag{9.3}$$

where $\mathscr{L}^i$ denotes a loss/cost function on the reference and predicted functionals for the i-th field, and N_L is the number of fields to consider. The tool also enables executing all input files in parallel to speed up the total loss evaluation. As the shape and expression of the cost function are generally unknown, extracting its derivatives is challenging, which restricts the family of optimisation methods to derivative-free methods (Coelho, 2022).

In practice, only a sampled response of the functionals $\hat{y}^i$ and y^i is known. However, to directly compare the sampled responses, both the predicted and reference responses must be sampled on the same time grid. In piglot, all loss values are computed using an interpolated prediction response on the reference grid. The choice of using the reference grid is preferable, as the reference grid does not vary for different function calls, whereas the predicted grid may not necessarily remain constant for all parameters (Coelho, 2022).

9.2.2 Loss Functions

The appropriate use and choice of the loss function is a critical aspect of every optimisation problem. In this particular work, the vector loss function is employed

$$\mathscr{L}^i_{\text{vector}_n}(\boldsymbol{\theta}) = \frac{\hat{y}^i_n - y^i_n}{y^i_n}. \tag{9.4}$$

For a more in-depth review of the many types and variants of the most relevant loss functions, refer to Coelho (2022). It should be noted that if more than one input file needs to be run, the total loss returned to the optimisation procedure is the average of the losses of all analyses.

9.2.3 Integration with Finite Element Analysis

The input data for the finite element analysis is provided via an input file containing the parameters that need to be identified. In this way, the first step to obtaining the predicted response is to write an appropriate input file compatible with piglot. This is achieved by employing a template substitution technique. Specifically, for the unknown parameters to be optimised, a placeholder with a unique name is introduced in the input file instead of their numerical value. Simultaneously, in the driver Python script, the parameters are specified with four fields in the presented order: (1) unique name, (2) initial value, (3) lower bound, and (4) upper bound (Coelho, 2022).

9.2.4 Optimisation Algorithm

To select the most suitable optimisation method for parameter identification, several methods were integrated into piglot, including population-based methods (genetic algorithm (GA), particle swarm optimisation (PSO), and artificial ecosystem-based optimisation (AOA)), sampling-based methods (Bayesian optimisation (BO), Lipschitz optimisation (LIPO), DIRECT, and partition-based random search (PRS)), and stochastic gradient methods (simultaneous perturbation stochastic approximation (SPSA) and adaptive moment estimation SPSA (AdamSPSA)). In Coelho (2022), LIPO was found to be the most efficient method based on the number of iterations, function calls, and elapsed time. However, currently, BO can be considered a more efficient method given the correct pre-processing of the data, reason why it was the method employed in the following analyses.

BO is an optimisation technique that employs the Bayesian approach to set a prior over the objective function and combines it with evidence to obtain a posterior function. This allows for a utility-based selection of the next observation to make on the objective function, which takes into account both exploration (sampling from regions of high uncertainty) and exploitation (sampling regions likely to offer an improvement over the current best observation). BO is particularly beneficial when function evaluations are expensive, derivatives are not accessible, or the problem is non-convex. Furthermore, it can incorporate prior knowledge about the problem to aid in directing the sampling and balance exploration and exploitation of the search space (Balandat et al., 2020; Brochu et al., 2010). For a more detailed discussion of BO, please refer to the mentioned literature.

9.3 Computational Setting

9.3.1 Macro-scale Analysis

The uniaxial tensile test, detailed in Section 9.1, is simulated using a one-eighth portion of a smooth round bar specimen. Suitable symmetric boundary conditions are applied to this portion, which is also discretised into a finite element mesh consisting of 20-node hexahedral elements (comprising 3888 elements and 17929 nodes) with reduced integration (8 Gauss integration points), as depicted in Figure 9.5. It is important to note that the specimen mesh is optimised to minimise the total number of elements. To achieve this, a coarser mesh is employed in the clamping zone, while a more refined mesh is implemented in the necking zone, the zone of primary interest. By modelling only one-eighth of the specimen and optimising the overall mesh, both computational costs and simulation time are significantly reduced. Moreover, the loading conditions are imposed through a prescribed total (traction) displacement on the upper surface, incrementally applied over 200 increments.

Multiple Gauss points are selected from the modelled specimen to record their deformation gradient histories. However, for the micro-scale analysis, only three specific points are chosen. These points are strategically located in zones of utmost importance for characterising the micro-scale behaviour, exhibiting distinct behaviours that allow for more accurate results when determining the parameters of the PPR cohesive zone model. These three points are illustrated in Figure 9.5.

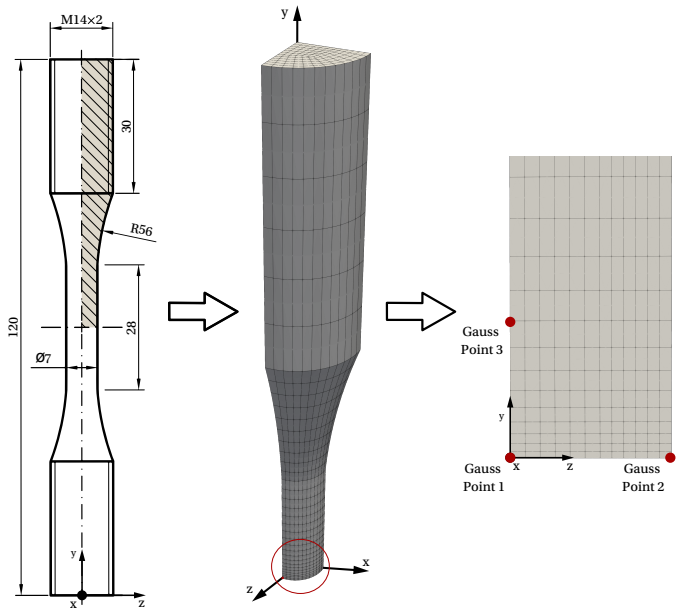


Figure 9.5: Finite element model of one-eighth of the tensile test specimen - smooth round bar; and selected Gauss points.

9.3.2 Micro-scale Analysis

After conducting preliminary tests, it was found that employing an RVE with a dimension of 15 µm, the smallest feasible size as discussed in Section 5.3.5, was impractical as an initial approach for the calibration process, even only at the micro-scale. Each iteration required a minimum of 3 hours, and in some instances, the duration exceeded 12 hours. Consequently, an alternative initial approach is required to represent the PC/ABS at the micro-scale.

A widely adopted strategy for characterising the arrangement of atoms or molecules in crystalline materials involves using unit cells, which represent the smallest periodic unit in a periodic structure. Drawing a parallel to continuum micromechanics, this concept can be applied to approximate the arrangement of at least two distinct constituents, as is the present case. The significant advantage of employing a unit cell approach to approximate the complex morphologies of PC/ABS blends is the substantial reduction in computational effort compared to more intricate and commonly utilised representations of the microstructure, such as the aforementioned RVEs (Hund, 2022). In fact, when utilising unit cells, each iteration of the calibration procedure generally fluctuates between 5 minutes and, in extreme cases, 1 hour.

However, it is essential to note that unit cells cannot accurately describe

the material response to the same extent as an RVE, as evidenced by the results presented in Chapter 5. Nevertheless, the unit cells are solely used to obtain an initial approximation of the desired properties, enabling subsequent calibration with the appropriate RVE while significantly reducing the search space. Consequently, this approach facilitates accelerating the overall process.

In more comprehensive detail, the unit cell (depicted in Figure 9.6) is discretised into a finite element mesh (comprising 1194 elements and 2117 nodes), specifically consisting of 856 10-node tetrahedral elements with reduced integration (employing 4 Gauss integration points) and 338 12-node 3D quadratic cohesive elements (COH3D12) with 6 Gauss integration points. The geometry of the unit cell is intentionally designed to elongate the ABS particle along the *yy* axis, which aligns with the injection direction of the smooth round bar specimen and for it to have a volume fraction of 20% of the total volume. The size of the unit cell is defined as 5.813 μm to maintain the particle's dimension and geometry consistent with reality, as described in Section 5.1. This consistency is crucial as the size effect influences the cohesive zone model.

Furthermore, the RVE, also elongated in the *yy* axis and featuring an ABS volume fraction of 20%, is illustrated in Figure 9.7 and has a dimension of 15 μm. Its finite element mesh consists of 16013 elements and 25808 nodes, including 13613 10-node tetrahedral elements with reduced integration (utilising 4 Gauss integration points) and 2400 12-node 3D quadratic cohesive elements (COH3D12) with 6 Gauss integration points. Moreover, in both cases, the loading conditions are imposed by utilising the deformation gradient history obtained from the selected Gauss points.

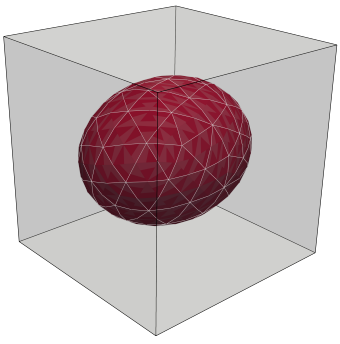


Figure 9.6: Geometry of the unit cell with a side length of 5.813 μm and an ABS volume fraction of 20%.

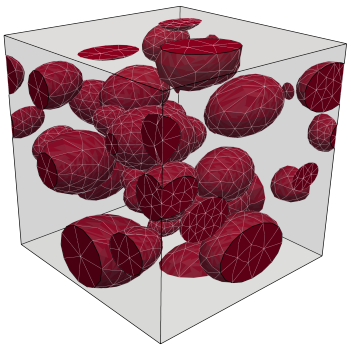


Figure 9.7: Geometry of the RVE with a side length of 15 μm and an ABS volume fraction of 20%.

9.3.3 Coupled Multi-scale Analysis

As previously discussed, a Coupled Multi-scale Finite Element Analysis involves a series of microscopic problems to determine the constitutive behaviour of each macroscopic point. Specifically, each Gauss point of the continuum macroscopic smooth round bar specimen has an RVE linked to it, whose problem needs to be solved for each increment at the macro-scale.

It is evident that directly employing the discretised specimen used in the macro-scale analysis would lead to a substantial computational cost. Hence, it becomes crucial to discretise the specimen's geometry again, thereby reducing the total number of elements while ensuring that its macro-scale response aligns with that of the initial specimen using a finer mesh. To accomplish this, the mesh optimisation strategy employed in Section 9.3.1 is utilised again, resulting in a finite element mesh consisting of 168 20-node hexahedral elements with reduced integration (8 Gauss integration points). This corresponds to a remarkable reduction of 2200% in the total number of elements and micro-scale problems to be solved. Expressly, the new discretised mesh requires only 1344 micro-scale simulations per increment, in contrast to the initial requirement of 31104 simulations.

Nonetheless, despite this simplification, the computational cost remains prohibitively high in terms of both CPU time and memory requirements when employing the RVE discussed in Section 9.3.2. Therefore, in order to accommodate the available memory capabilities for the coupled analysis within the remaining time frame, the unit cell, also presented in Section 9.3.2, is chosen as an alternative for the micro-scale.

Analogous to the macro-scale problem, the specimen is subjected to the appropriate symmetric boundary conditions, and the loading conditions are imposed by incrementally applying a prescribed total (traction) displacement on the upper surface over 200 increments.

9.4 Results and Discussion

9.4.1 Macro-scale Analysis

The calibration procedure, which incorporates the mean response of the experimental uniaxial tensile tests, leads to the determination of the material properties presented in Table 9.1. Figure 9.8 demonstrates the comparison between the constitutive model predictions and the experimental results,

specifically the force-displacement curves, indicating a close agreement between the two responses achieved through the utilisation of these calibrated properties. This outcome not only confirms the effectiveness of the proposed calibration procedure but also ensures the attainment of more accurate results in the subsequent calibration stage, which involves obtaining the missing properties of the PPR cohesive zone model. This aspect is crucial, considering all the simplifications implemented in this study.

Furthermore, Figure 9.9 showcases the Cauchy equivalent stress experienced by the smooth round bar specimen. Consistent with the experimental tests, the numerical results portray stress concentrations around the notch, the middle of the specimen, leading to its subsequent necking.

Table 9.1: Material properties of the visco-elastic-visco-plastic model calibrated from the uniaxial tensile test.

Property	**SI Units**	**Value**
ρ	kg/m^3	1.200×10^3
T	K	2.980×10^3
E_∞	Pa	3.134×10^8
ν_∞	-	0.335
ΔH	J/mol	3.205×10^5
v^*	m^3/mol	2.871×10^{-3}
A_0	s	1.110×10^{-34}
p^*	Pa	1.000×10^5
μ	-	1.726×10^{-1}
D_∞	-	9.992
h	-	3.987×10^2
$\sqrt{N}$	-	1.297
C_r	Pa	5.446×10^6
f_0	%	0.000
q_{10}, q_{11}, q_2	-	3.182×10^{-1}, 1.263, 7.207×10^{-1}
f_r	%	2.703×10^{-2}
ε_r	-	1.888×10^{-3}
s_r	-	2.058×10^{-4}
n_{V}	-	1
G_1	Pa	1.823×10^9
g_1	-	1.874×10^{-2}
$\lambda_{g,1}$	-	9.900×10^{-1}

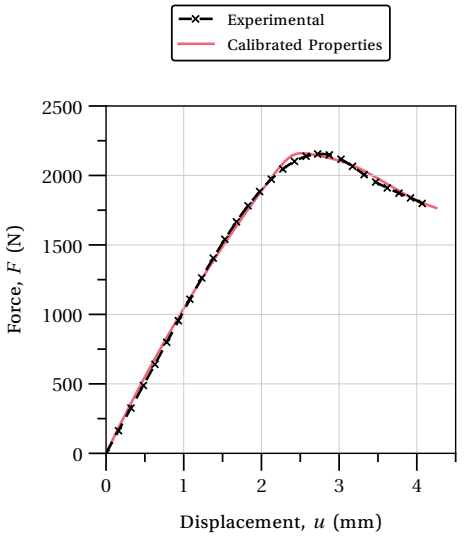


Figure 9.8: Comparison between the force-displacement response of the smooth round bar specimen predicted by the proposed constitutive model and the experimental results conducted by Macedo (2023).

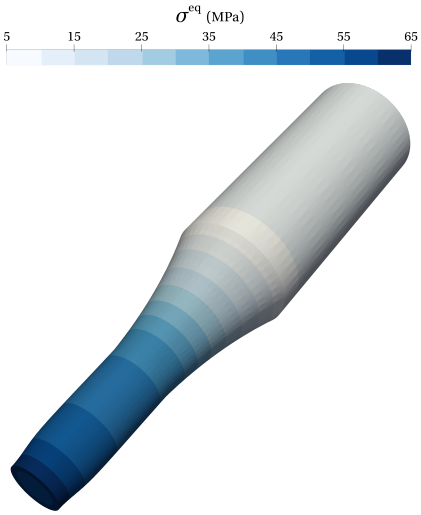


Figure 9.9: Distribution of the Cauchy equivalent stress, σ^{eq}, at the last increment for the smooth round bar specimen subjected to the uniaxial tensile test.

9.4.2 Micro-scale Analysis

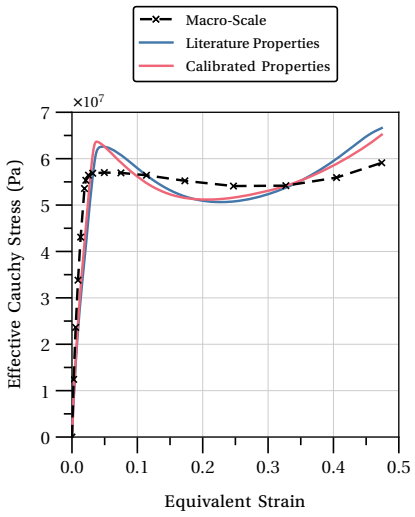
The calibration procedure, comparing the numerical responses of the three selected Gauss points obtained from both the macro-scale and unit cell micro-scale analyses, yields the material properties presented in Table 9.2. As previously stated, the micro-scale is achieved using the deformation gradient history recorded from the macro-scale analysis. Note that only the calibrated properties are shown in Table 9.2, given that the remaining properties are the same as those presented in Table 8.1.

However, as can be observed, the material properties obtained through the calibration process, which effectively minimise the error, lack physical significance and are purely numerical. Specifically, for the normal components of the fracture energy and cohesive strength, both their values were optimised to a minimum, resulting in a significant and nonsensical discrepancy when compared to their tangential components.

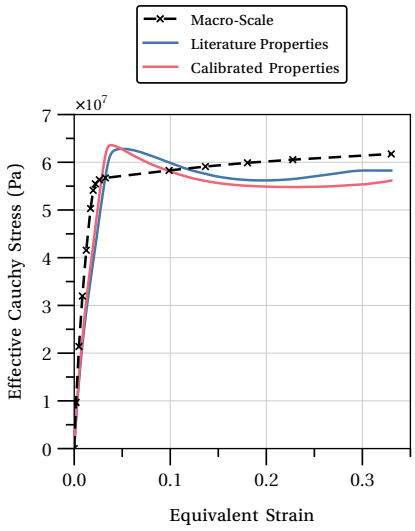
Figure 9.13 presents a comparison between the macro-scale and unit cell micro-scale results, considering both the initial properties derived from the literature and the calibrated properties. Additionally, Figure 9.14 provides a schematic representation of the final configurations for the three Gauss points, considering the utilisation of the properties derived from the literature.

Table 9.2: Material properties of the PPR cohesive zone model calibrated from the comparison between the macro-scale and micro-scale analysis.

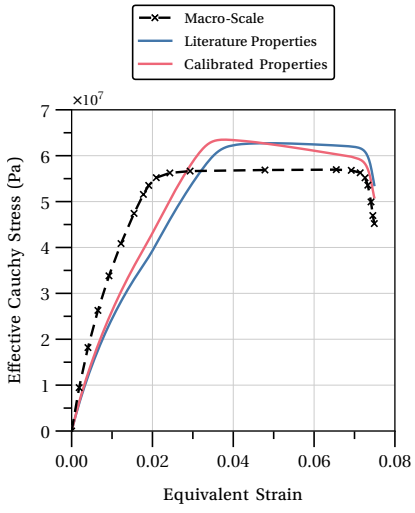
Parameter	SI Units	PC/ABS Interface
ϕ_n	J/m^2	1
ϕ_t	J/m^2	41.489
σ_{max}	MPa	2.552
τ_{max}	MPa	200



(a) Gauss Point 1

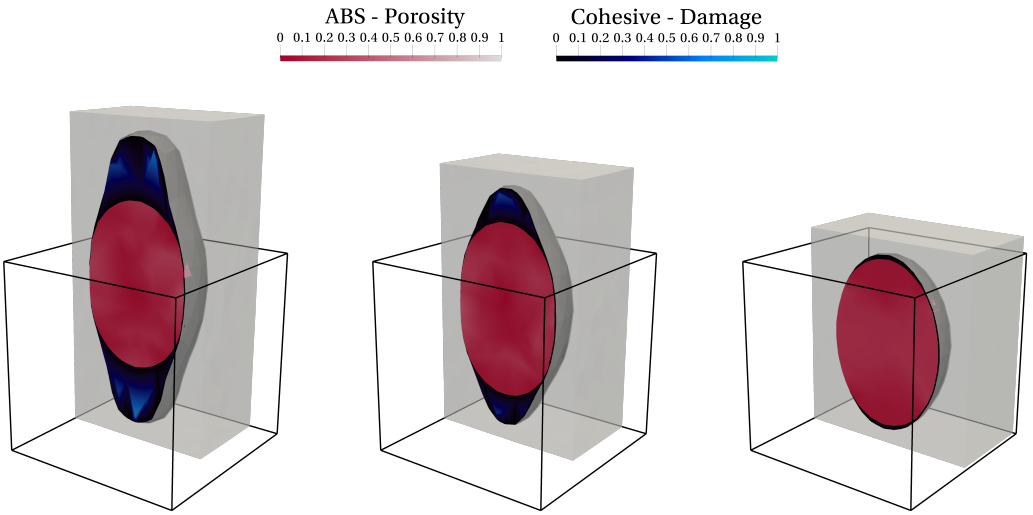


(b) Gauss Point 2



(c) Gauss Point 3

Figure 9.10: Comparison between the effective Cauchy stress-equivalent strain response for three different Gauss points from the macro-scale analysis and the unit cell micro-scale analysis, employing both the literature and calibrated properties.



(a) Gauss Point 1 (b) Gauss Point 2 (c) Gauss Point 3

Figure 9.11: Schematic representation of the final configurations and the middle-plane contours illustrating the ABS total porosity and cohesive elements damage of the PC/ABS unit cell for the three Gauss points analysed, employing the literature properties.

As demonstrated by the results presented in Figure 9.13, achieving a satisfactory fit between the numerical results at the micro-scale and those obtained from the macro-scale problem was not possible, even when using purely numerical values through the calibration process. Consequently, the initial objective of deducing the PC/ABS authentic PPR cohesive zone model parameters could not be accomplished.

Furthermore, it can be stated that the final results obtained are slightly worse than the results obtained from the initially derived literature values. This observation does not imply that the calibration process was poorly executed. In fact, the error between the calibrated and macro-scale curves is indeed smaller compared to the one obtained from the "literature curve". However, considering that the difference in errors between the two curves is minimal, and the "literature curve" exhibits a general trend in closer agreement with the macro-scale curve, coupled with the fact that the calibrated properties lack physical meaning, it is decided to proceed with the literature properties for the coupled multi-scale analysis. It is important to highlight that the use of a different loss function could potentially capture the trend of the curve more effectively. However, due to time constraints, it was not possible to explore this possibility in the present study.

Specifically, when analysing only the "literature curve" compared to the reference curve (obtained from the macro-scale analysis), it can be

observed that the elastic stiffness is underestimated, while the yield stress is overestimated. This difference is more noticeable in the 3rd Gauss point, considering that the total equivalent strain is significantly lower compared to the other three points, resulting in a reduced horizontal scale on the graph. However, it is essential to note that the elastic region is the same for all three Gauss points, as the material remains unchanged. Moreover, in the 3rd Gauss point, the curve follows the same behaviour as the reference curve, with the only difference being the high value of the effective Cauchy stresses due to the overestimated yield stress.

Regarding the 1st Gauss point, there is an overemphasis on the amount of softening followed by an overestimation of the strain hardening. This leads to a highly concave curve that deviates significantly from the intended behaviour. In broad terms, the evolution of the material's behaviour resembles what is observed at the macro-scale but is greatly exaggerated. However, this is not the case for the 2nd Gauss point, where the reference behaviour shows strain hardening after the yield point, while the "literature curve" exhibits softening followed by a slight hardening.

Difficulties in accurately describing the material behaviour at the micro-scale and consequently calibrating micro-scale parameters are commonly encountered in the literature, as evidenced in the works of Hund (2022) and Smit et al. (2000). In the current case, one of the leading causes is the assumption of similar macro (bulk) and micro (phase constituents) material behaviours. As described in Section 5.2.7, the properties used for each PC and ABS constituent were obtained individually through a series of uniaxial compression tests conducted on them as bulk materials. However, the response of a material as a constituent of a microstructure can differ significantly from its macroscopic behaviour in bulk form. Furthermore, it should be noted that the PC and SAN used in the test specimens for calibrating the properties of the individual constituents may differ from the PC and SAN (ABS matrix) used to produce the PC/ABS blend used in the current calibration process.

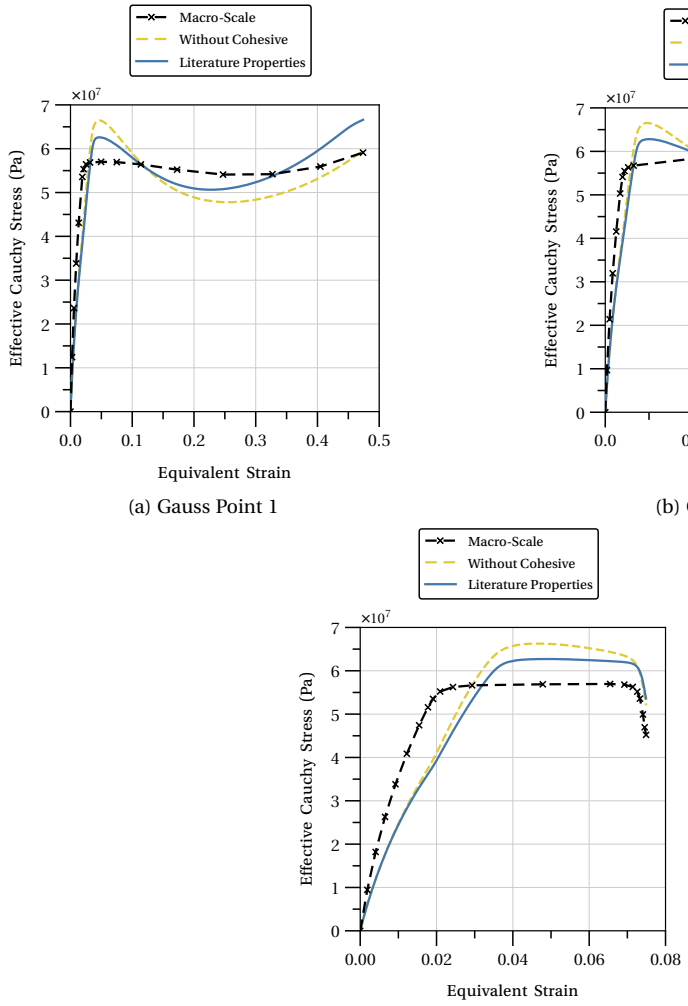
It should also be noted that the response of the material on the macroscopic scale can significantly differ from its response on the micro-scale, primarily due to the size effect phenomena. Therefore, it may not be appropriate to directly compare the curves obtained from the macro-scale numerical analysis with those obtained from the micro-scale analysis.

The analysis of Figure 9.12 further highlights these potential issues, which compares the reference response with the unit cell micro-scale results. The comparison is made considering the literature properties and the unit cell

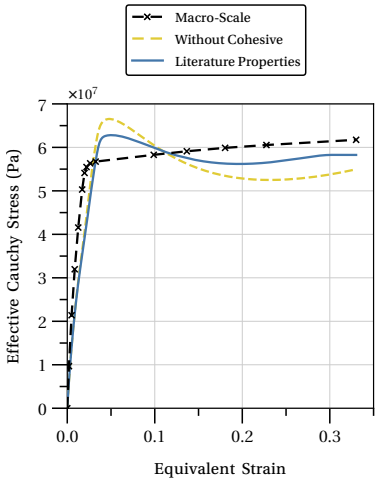
without cohesive elements, i.e., perfect cohesion in the interface.

As observed, it is evident that only in the 3rd Gauss point the response without cohesive elements exceeds the values of the reference curve, while in the other two Gauss points, the material exhibits excessive softening. It is worth noting that the issue of excessive softening had already been observed during the calibration of the ABS properties in the work of (Carvalho Alves et al., 2023).

Moreover, it is important to acknowledge that the inclusion of cohesive elements only allows for describing an additional damage mechanism, specifically the debonding of interfaces, which, as discussed in Section 8.2, leads to an equal or decreased stress response compared to the initial response. Based on these observations, it becomes evident that the calibration process could not achieve satisfactory results right from the beginning.



(a) Gauss Point 1



(b) Gauss Point 2

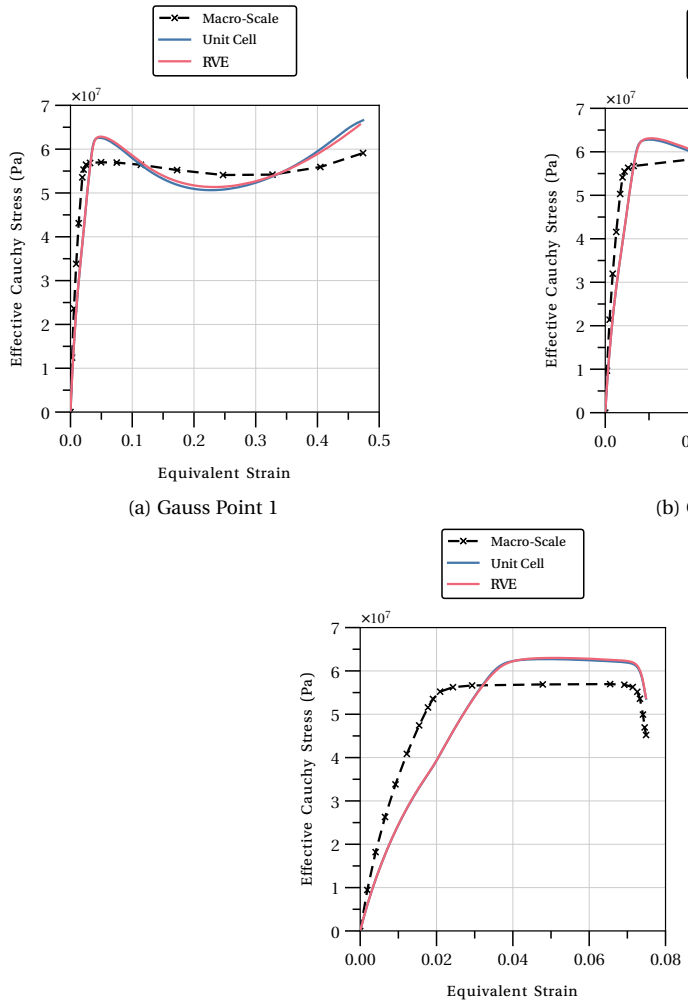
(c) Gauss Point 3

Figure 9.12: Comparison between the effective Cauchy stress-equivalent strain response for three different Gauss points from the macro-scale analysis and the unit cell micro-scale analysis, without and with cohesive elements.

Nonetheless, as can be seen, even if the parameters of the cohesive elements may not be the most accurate ones, the material behaviour described is in closer agreement with the reference response. In other words, cohesive elements undoubtedly allow for a more accurate and realistic response. The two main improvements worth emphasising are the reduction of the overestimation of the yield stress and the smoothing of the softening region.

Lastly, the responses obtained from the micro-scale analysis using the unit cell and the RVE are compared with the reference result in Figure 9.13. Additionally, Figure 9.14 provides a schematic representation of the final configurations of the RVEs for the three Gauss points when utilising the

properties derived from the literature.

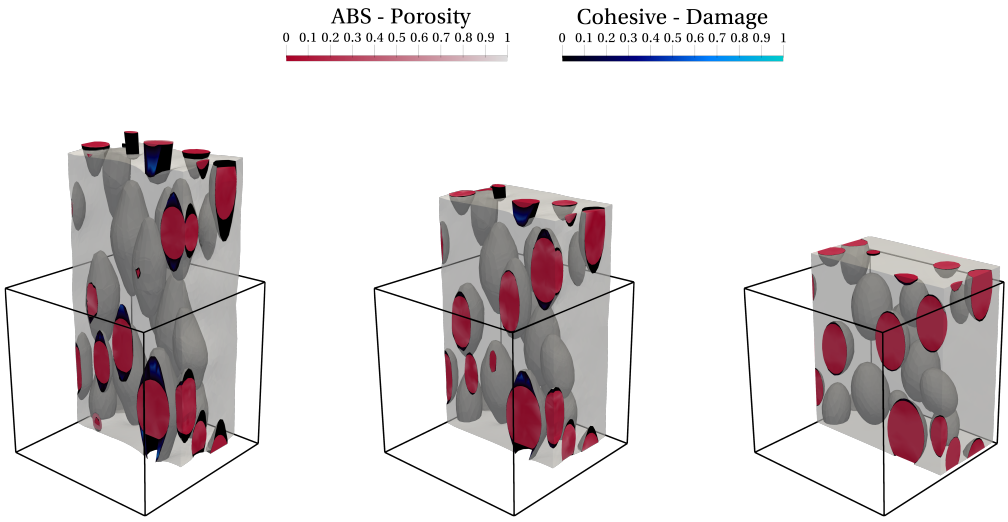


(a) Gauss Point 1

(b) Gauss Point 2

(c) Gauss Point 3

Figure 9.13: Comparison between the effective Cauchy stress-equivalent strain response for three different Gauss points from the macro-scale analysis and the unit cell and RVE micro-scale analysis, employing the literature properties.



(a) Gauss Point 1 (b) Gauss Point 2 (c) Gauss Point 3

Figure 9.14: Schematic representation of the final configurations and the middle-plane contours illustrating the ABS total porosity and cohesive elements damage of the PC/ABS RVE for the three Gauss points analysed, employing the literature properties.

As can be observed from Figure 9.13, the description of the behaviour of the PC/ABS blend using the unit cell or the RVE is very similar. This finding aligns closely with the conclusions drawn in Section 5.3.5, where it was noted that in 3D, the difference in the behaviour description was minimal between different RVE sizes, especially considering that the RVE used in the current study was the smallest possible size. Therefore, it can be stated that the micro-scale calibration results were not significantly affected by the use of a unit cell.

Additionally, this consistency between the unit cell and RVE results provides validation and greater confidence in the results of the coupled multi-scale analysis, as they are expected to be highly similar to those obtained using the RVE.

9.4.3 Coupled Multi-scale Analysis

In order to gain a more realistic understanding of the impact of interfaces, a coupled multi-scale finite element analysis was conducted. Figure 9.15 illustrates a comparison between experimental results and multi-scale modelling results, with and without the consideration of the interfaces. Specifically, the force-displacement curves were examined. Additionally, the Cauchy equivalent stresses in the smooth round bar specimen for each scenario are presented in Figure 9.16. It is important to note that, as previously

mentioned, the cohesive model parameters utilised in this study were based on the literature properties.

As expected within the context of multi-scale analysis, observations and conclusions drawn at the micro-scale are transferred to the macroscopic behaviour of the material. Consequently, similar to the findings from micro-scale calibration, achieving an exact fit between the numerical and experimental results was not possible. However, it is evident that considering the interfaces undoubtedly leads to a more accurate and realistic response, despite the parameters' lack of precision. Furthermore, the same improvements observed previously are confirmed, namely a reduction in the overestimation of the yield stress and the smoothing of the softening region.

The suboptimal results obtained cannot be attributed to the macro-scale simulation itself, as it has been repeatedly emphasised that this approach yields the most satisfactory outcomes. Instead, the challenges lie in accurately describing the microscopic behaviour of the material. These issues have been carefully identified and extensively analysed in Section 9.4.2.

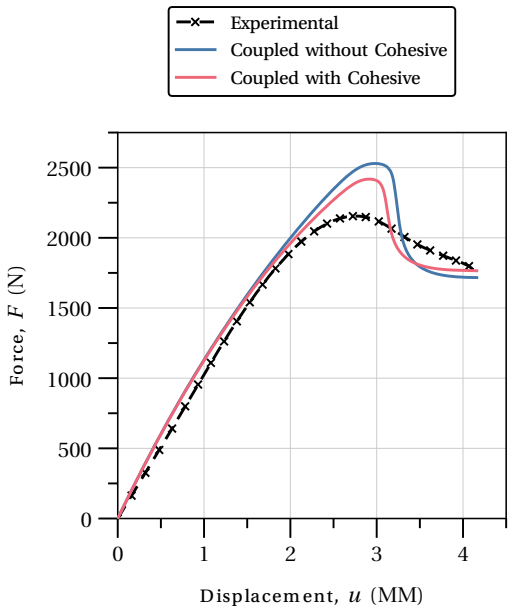
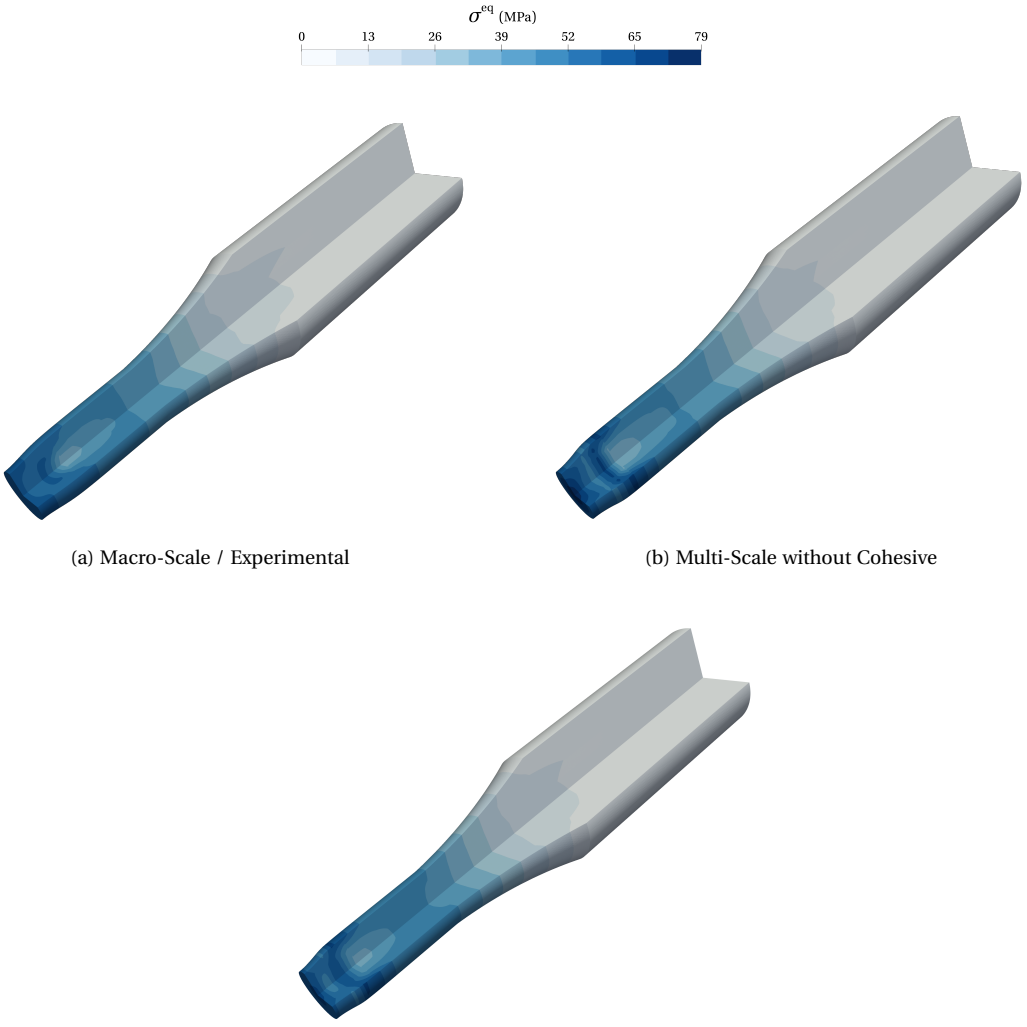


Figure 9.15: Comparison between the force-displacement response of the smooth round bar specimen predicted by the coupled multi-scale analyses, without and with cohesive elements, and the experimental results conducted by Macedo (2023).



(a) Macro-Scale / Experimental

(b) Multi-Scale without Cohesive

(c) Multi-Scale with Cohesive

Figure 9.16: Distribution of the Cauchy equivalent stress, σ^{eq}, at the last increment for the smooth round bar specimen subjected to the uniaxial tensile test.

CHAPTER 10

VISCO-ELASTIC VISCO-PLASTIC CONSTITUTIVE MODEL: DAMAGE VARIABLE

As described in Chapter 4, the primary deformation mechanisms that allow energy dissipation throughout a larger material volume encompass the following: (1) rubber particle cavitation, (2) matrix shear yielding, and (3) multiple crazing. The occurrence of voids within the ABS domains due to rubber particle internal cavitation competes with void formation resulting from PC and ABS interface failure. The prevailing phenomenon is determined by comparing the dilatational stress required for cavitation of PB rubber particles with the strength of the PC/SAN interface. Additionally, when multiple crazes propagate within the SAN phase and reach the PC/SAN interface, shear yielding of the PC matrix can initiate in regions of heightened strain concentrations. Consequently, these shear-yielding bands can potentially bridge the gap between ABS domains.

Up to this point, the current study accounts for and incorporates both void nucleation, interaction among voids, and the evolution of void geometry within the ABS domains, as well as interface failure and debonding between the PC and ABS phases. The former failure mechanism is integrated into the finite strain visco-elastic visco-plastic constitutive model outlined in Section 5.2, while the latter is implemented by introducing cohesive elements that follow the PPR potential-based cohesive zone model presented in Section 6.4.

However, to achieve a comprehensive description of all damage mechanisms present in PC/ABS, the inclusion of a model to study and consider the effects of the shear-yielding mechanism, a plastic deformation mechanism, within the PC matrix remains outstanding. Therefore, this chapter aims to enhance the visco-elastic visco-plastic constitutive model presented in Section 5.2 by introducing a damage variable that quantifies the reduction in load-carrying capacity resulting

from the presence and evolution of defects.

10.1 Explicit Local Damage Model

Incorporating damage variables into material constitutive models introduces softening regimes that can lead to the loss of ellipticity in the governing equilibrium equations within a local continuum framework. This can result in an ill-posed boundary value problem and a finite element solution that becomes dependent on spatial discretisation. One approach to mitigate or prevent this mesh dependence issue is replacing the local damage variable, D, with its non-local counterpart, $\bar{D}$ (Reis et al., 2018). Various non-local formulations have been developed in recent years, aiming to introduce an intrinsic length into standard constitutive models to properly define the localisation zone (Jirásek, 1998; Jirásek and Rolshoven, 2003).

The current model, the finite strain visco-elastic visco-plastic constitutive model, already includes a damage mechanism in the form of void nucleation. However, as demonstrated in Sections 5.3.3 and 5.3.6, it exhibits no mesh dependence in the convergence of its response. This, combined with the previous work on the numerical implementation of this model by Carvalho Alves et al. (2023), led to the decision to employ a local damage law. Apart from its simplicity, this approach also offers lower computational costs compared to the non-local one.

Another important consideration when selecting an appropriate damage model is whether to use an explicit or implicit formulation. In an explicit model, the stress functional is independent of the damage variable, whereas in an implicit model, it becomes a function of the damage variable. The numerical treatment of the latter generally involves highly coupled and nested implementations, often requiring more complex algorithms and is also prone to ill-posed boundary value problems and spatial discretisation dependency (Reis et al., 2018). With these factors in mind, an explicit local damage model is chosen for implementation.

Recalling the principles of thermodynamics with internal variables, it is feasible to define the constitutive functionals governing the evolution of the stress tensor, $\boldsymbol{\tau}$, and the damage variable, D, as functions of various thermodynamic quantities,

$$\boldsymbol{\tau} = \hat{\boldsymbol{\tau}}\{\boldsymbol{\varepsilon},\, \boldsymbol{\alpha}\}, \tag{10.1}$$

$$D = \hat{D}\{\boldsymbol{\varepsilon},\, \boldsymbol{\alpha},\, \boldsymbol{\tau}\}, \tag{10.2}$$

where $\boldsymbol{\varepsilon}$ is a deformation quantity, $\boldsymbol{\alpha}$ a set of internal variables and $\boldsymbol{\tau}$ the effective stress tensor (Reis et al., 2018).

Under the assumption of isotropy, it is possible to introduce an internal damage state variable, D, which represents the degradation of a constituent at the micro-scale. This assumption is particularly applicable in the context of the updated constitutive model being applied exclusively to the PC matrix. For simplicity, variable D influences the total stress, $\boldsymbol{\tau}_{\mathrm{T}}$, affecting both the driving, $\boldsymbol{\tau}_{\mathrm{D}}$, and hardening, $\boldsymbol{\tau}_{\mathrm{H}}$, stress components. As a result, the stress tensor is redefined as its damaged counterpart, $\boldsymbol{\tau}^*$, (Reis et al., 2018)

$$\boldsymbol{\tau}^* = \big(1-D\big)\,\boldsymbol{\tau}_{\mathrm{T}} = \big(1-D\big)\,\big(\boldsymbol{\tau}_{\mathrm{D}} + \boldsymbol{\tau}_{\mathrm{H}}\big)\,. \tag{10.3}$$

It should be noted that D is equal to 0 when the material is in its undamaged condition and equal to 1 when the material is completely damaged. The distinction between the damaged stress tensor and the stress tensor lies in the fact that the former accounts for the internal degradation of the material. In contrast, the latter assumes that the deformation of the material occurs in the absence of internal damage (Lemaitre, 1985).

The implemented damage law is governed by the evolution of the rate of accumulated plastic strain, $\bar{\varepsilon}^p$, influenced by a scalar parameter that can be interpreted as a critical value of the accumulated plastic strain, $\bar{\varepsilon}^p_{\mathrm{cr}}$. This leads to the following formulation (Reis et al., 2018)

$$\dot{D} = \frac{\dot{\bar{\varepsilon}}^p}{\bar{\varepsilon}^p_{\mathrm{cr}}}, \qquad \text{with} \;\; D \in \big[0,\,1\big]\,. \tag{10.4}$$

To maintain physical meaning, it is of utmost importance to upper bound the damage variable to a value of 1, preventing the stress tensor from becoming negative. This occurs when the accumulated plastic strain equalises or exceeds the critical value.

10.2 Computational Implementation

The solution to the constitutive model described in Section 5.2, defined by a set of constitutive equations and initial conditions, cannot be readily determined analytically. Therefore, the use of a numerical algorithm for the integration of the constitutive equations becomes crucial. Note that Carvalho Alves et al. (2023) carried out the numerical implementation of such an algorithm in `Links` and that the modifications and additions necessary to incorporate the damage variable are only presented in Section 10.2.5.

In essence, a mechanical initial boundary value equilibrium problem is solved via a fully implicit elastic predictor/return mapping integration algorithm, where the Finite Element Method is used to formulate it, and the Newton-Raphson Method is used to solve it. The integration algorithm encompasses two distinct procedures: (1) the constitutive state update, required for computing the elemental internal forces; and (2) the computation of the consistent tangent modulus, necessary for calculating the elemental stiffness matrices. It is worth mentioning that Sections 10.2.1 to 10.2.4 are based on the following reference (Carvalho Alves et al., 2023).

10.2.1 Numerical Integration Scheme

The initial step in any computational implementation involves the numerical integration of the constitutive equations over time. This process is achieved by discretising the time domain, denoted as $t \in \left[t_0,\, t_f\right]$, into n_{inc} increments. Consequently, a generic time increment can be expressed as $\left[t_n,\, t_{n+1}\right]$ and $\Delta t = t_{n+1} + t_n$. At time t_n, the values of both the constitutive internal variables, denoted as $\boldsymbol{\alpha}$, and the Kirchhoff stress tensor, denoted as $\boldsymbol{\tau}_{\text{T}}$, are known. However, at time t_{n+1}, both these quantities need to be uniquely determined based on the prescribed deformation gradient, $\boldsymbol{F}_{n+1} = \boldsymbol{F}\left(t_{n+1}\right)$, as

$$\boldsymbol{\tau}_{\text{T},n+1} = \hat{\boldsymbol{\tau}}\left(\boldsymbol{F}_{n+1}, \boldsymbol{\alpha}_n\right), \qquad \boldsymbol{\alpha}_{n+1} = \hat{\boldsymbol{\alpha}}\left(\boldsymbol{F}_{n+1}, \boldsymbol{\alpha}_n\right), \tag{10.5}$$

where $\hat{\boldsymbol{\tau}}$ and $\hat{\boldsymbol{\alpha}}$ denote the incremental constitutive functions. In the subsequent part of this section, the notation $A_{n+1} = A\left(t_{n+1}\right)$ is adopted, where A represents a general time-dependent function.

Firstly, the nucleation law, presented in Equation 5.19, can be analytically integrated over time, yielding the following expression

$$f_{N,n+1} - f_{N,n} = \int_{\varepsilon_{\text{vol},n}}^{\varepsilon_{\text{vol},n+1}} \frac{f_r}{s_r\sqrt{2\pi}} \exp\left[-\frac{1}{2}\left(\frac{\varepsilon_{\text{vol}} - \varepsilon_r}{s_r}\right)^2\right] \mathrm{d}\varepsilon_{\text{vol}}, \tag{10.6}$$

which given the definition of the error function, $\operatorname{erf}(x)$,

$$\operatorname{erf}(x) = \frac{2}{\sqrt{\pi}} \int_0^x \exp\left(-t^2\right) \mathrm{d}t, \tag{10.7}$$

becomes

$$f_{N,n+1} - f_{N,n} = \frac{f_r}{2}\left[\operatorname{erf}\left(\frac{\varepsilon_{\mathrm{vol},n+1} - \varepsilon_r}{\sqrt{2}s_r}\right) - \operatorname{erf}\left(\frac{\varepsilon_{\mathrm{vol},n} - \varepsilon_r}{\sqrt{2}s_r}\right)\right]. \tag{10.8}$$

Then, the incremental formulation of the current model can be expressed by utilising the exponential map integrator, for integrating the visco-plastic flow rule, in conjunction with the conventional implicit Euler scheme, for integrating the remaining rate equations. With this in mind, the incremental version of this model can be stated as: *Given the initial values* $\boldsymbol{F}^e_n$, f_n, $\eta_{\mu,n}$, $\tau^{\mathrm{eq}}_{\mu,n}$ *and* $\bar{\varepsilon}^p_{\mu,n}$ *at the beginning of the time interval* $[t_n, t_{n+1}]$, *and given the prescribed incremental deformation gradient* $\Delta\boldsymbol{F}$ *for this interval, solve the following system of equations*

$$\boldsymbol{F}^e_{n+1} = \Delta\boldsymbol{F}\boldsymbol{F}^e_n\left(\boldsymbol{R}^e_{n+1}\right)^T \exp\left[\Lambda_{n+1}\Delta t\left(\boldsymbol{\tau}_{\mathrm{D},d,n+1} + \frac{1}{\sqrt{3}}q_{1,n+1}q_2 f_{n+1}\tau^{\mathrm{eq}}_{\mu,n+1}\sinh\left(q_2\frac{\operatorname{tr}\left(\boldsymbol{\tau}_{\mathrm{D},n+1}\right)}{2\sqrt{3}\tau^{\mathrm{eq}}_{\mu,n+1}}\right)\boldsymbol{I}\right)\right]\boldsymbol{R}^e_{n+1}, \tag{10.9}$$

$$f_{n+1} = f_n + f_{g,n+1} - f_{g,n} + f_{N,n+1} - f_{N,n}, \tag{10.10}$$

$$\bar{\varepsilon}^p_{\mu,n+1} = \bar{\varepsilon}^p_{\mu,n} + \frac{\sqrt{3}\Delta t}{3\eta_{\mu,n+1}}\tau^{\mathrm{eq}}_{\mathrm{D},\mu,n+1}, \tag{10.11}$$

and

$$\Phi_{n+1} = \left(\tau^{\mathrm{eq}}_{\mathrm{D},n+1}\right)^2 + 2f_{n+1}q_{1,n+1}\left(\tau^{\mathrm{eq}}_{\mu,n+1}\right)^2\cosh\left(q_2\frac{\operatorname{tr}\left(\boldsymbol{\tau}_{\mathrm{D},n+1}\right)}{2\sqrt{3}\tau^{\mathrm{eq}}_{\mu,n+1}}\right) - \left(\tau^{\mathrm{eq}}_{\mu,n+1}\right)^2\left(1 + q^2_{1,n+1}f^2_{n+1}\right) = 0, \tag{10.12}$$

with

$$\Lambda_{n+1} = \left(1 - f_{n+1}\right)\frac{\left(\tau^{\mathrm{eq}}_{\mu,n+1}\right)^2}{\eta_{\mu,n+1}}\left(2\left(\tau^{\mathrm{eq}}_{\mathrm{D},n+1}\right)^2 + \frac{q_{1,n+1}q_2}{\sqrt{3}}f_{n+1}\tau^{\mathrm{eq}}_{\mu,n+1}\sinh\left(\frac{q_2\operatorname{tr}\left(\boldsymbol{\tau}_{\mathrm{D},n+1}\right)}{2\sqrt{3}\tau^{\mathrm{eq}}_{\mu,n+1}}\right)\operatorname{tr}\left(\boldsymbol{\tau}_{\mathrm{D},n+1}\right)\right)^{-1}, \tag{10.13}$$

$$\tau^{\mathrm{eq}}_{\mathrm{D},n+1} = \sqrt{\frac{1}{2}\boldsymbol{\tau}_{\mathrm{D},d,n+1} : \boldsymbol{\tau}_{\mathrm{D},d,n+1}}, \tag{10.14}$$

$$f_{g,n+1} - f_{g,n} = 3\left(1 - f_{n+1}\right)\Lambda_{n+1}\frac{1}{\sqrt{3}}q_{1,n+1}q_2 \\ f_{n+1}\tau^{\mathrm{eq}}_{\mu,n+1}\sinh\left(q_2\frac{\mathrm{tr}\left(\boldsymbol{\tau}_{\mathrm{D},n+1}\right)}{2\sqrt{3}\tau^{\mathrm{eq}}_{\mu,n+1}}\right)\Delta t, \tag{10.15}$$

$$f_{N,n+1} - f_{N,n} = \frac{f_r}{2}\left[\mathrm{erf}\left(\frac{\varepsilon_{\mathrm{vol},n+1} - \varepsilon_r}{\sqrt{2}s_r}\right) - \mathrm{erf}\left(\frac{\varepsilon_{\mathrm{vol},n} - \varepsilon_r}{\sqrt{2}s_r}\right)\right], \tag{10.16}$$

$$q_{1,n+1} = q_{10} - q_{11}f_{n+1}, \tag{10.17}$$

and

$$A_{n+1} = A_0\exp\left[\frac{\Delta H}{R^*T} + \frac{\mu P_{n+1}}{\tau^*} - D_\infty\left(1 - \exp\left(-\sqrt{\frac{3}{2}}\frac{h\bar{\varepsilon}^p_{\mu,n+1}}{D_\infty}\right)\right)\right], \tag{10.18}$$

for the unknowns $\boldsymbol{F}^e_{n+1}$, f_{n+1}, $\eta_{\mu,n+1}$, $\tau^{\mathrm{eq}}_{\mu,n+1}$ and $\bar{\varepsilon}^p_{\mu,n+1}$ with

$$\boldsymbol{\tau}_{\mathrm{T},n+1} = \boldsymbol{\tau}_{\mathrm{D},n+1} + \boldsymbol{\tau}_{\mathrm{H},n+1}, \tag{10.19}$$

$$\boldsymbol{\tau}_{\mathrm{D},n+1} = \boldsymbol{\tau}_{\mathrm{D},\infty,n+1} + \sum_{j=1}^{n_{\mathrm{V}}}\boldsymbol{\tau}_{\mathrm{D},j,n+1}, \tag{10.20}$$

$$\boldsymbol{\tau}_{\mathrm{H},n+1} = \frac{C_{\mathrm{R}}}{3}\frac{\sqrt{N}}{\lambda^p_{\mathrm{chain},n+1}}\mathscr{L}^{-1}\left(\frac{\lambda^p_{\mathrm{chain},n+1}}{\sqrt{N}}\right)\boldsymbol{B}_{d,\mathrm{iso},n+1}, \tag{10.21}$$

where $\boldsymbol{\tau}_{\mathrm{D},\infty,n+1}$ is the stress in the (instantaneous) linear spring, given by

$$\boldsymbol{\tau}_{\mathrm{D},\infty,n+1} = \boldsymbol{\tau}_{\mathrm{D},\infty,n} + \mathbf{D}^e_\infty : \left(\boldsymbol{\varepsilon}^e_{n+1} - \boldsymbol{\varepsilon}^e_n\right), \tag{10.22}$$

and $\boldsymbol{\tau}_{\mathrm{D},j,n+1}$ is the stress in the j-th visco-elastic Maxwell element, given by

$$\boldsymbol{\tau}_{\mathrm{D},j,n+1} = \hat{\omega}_{j,n+1}\boldsymbol{\tau}_{\mathrm{D},j,n} + \breve{\omega}_{j,n+1}2G_j\left(\boldsymbol{\varepsilon}^e_{d,n+1} - \boldsymbol{\varepsilon}^e_{d,n}\right), \tag{10.23}$$

with

$$\hat{\omega}_{j,n+1} = \exp\left[-\frac{\Delta t}{g_{j,n+1}}\right], \qquad \check{\omega}_{j,n+1} = \left(\frac{\Delta t}{g_{j,n+1}}\right)^{-1}\left[1-\exp\left[-\frac{\Delta t}{g_{j,n+1}}\right]\right], \quad (10.24)$$

with $g_{j,n+1} = g_{j,\,\mathrm{T}}\left(\dot{\varepsilon}^{\mathrm{eq}}_{n+1}\right)^{-\lambda_{g,j}}$, and the kinematic relations

$$\boldsymbol{\varepsilon}^{e}_{n+1} = \frac{1}{2}\ln\left[\boldsymbol{F}^{e}_{n+1}\left(\boldsymbol{F}^{e}_{n+1}\right)^{T}\right], \quad (10.25)$$

$$\boldsymbol{R}^{e}_{n+1} = \boldsymbol{F}^{e}_{n+1}\left[\left(\boldsymbol{F}^{e}_{n+1}\right)^{T}\boldsymbol{F}^{e}_{n+1}\right]^{-1/2}, \quad (10.26)$$

$$\boldsymbol{F}^{e}(t) = \boldsymbol{F}_{n+1}\left[\boldsymbol{F}^{p}_{n+1}\right]^{-1}. \quad (10.27)$$

10.2.2 Fully Implicit Elastic Predictor/Return Mapping Algorithm

A fully implicit elastic predictor/return mapping algorithm is presented, aligning with the implicit time discretisation of the equilibrium equations of the constitutive model. The state update process and the computation of the consistent tangent operator are derived using the infinitesimal strain format, incorporating the consistent purely kinematic finite strain extension. Besides its simplicity, this extension retains the crucial characteristics of the formulation of the infinitesimal strain, such as volume-preserving plastic deformations and finite plastic incompressibility.

Let us assume a prescribed incremental displacement $\Delta\boldsymbol{u}$ in the interval $\left[t_n, t_{n+1}\right]$, which leads to the following prescribed incremental deformation gradient

$$\Delta\boldsymbol{F} = \boldsymbol{I} + \nabla_0\Delta\boldsymbol{u}. \quad (10.28)$$

As a result, the deformation gradient and the visco-elastic trial deformation gradient at the instant t_{n+1} can be computed, respectively, as

$$\boldsymbol{F}_{n+1} = \Delta\boldsymbol{F}\boldsymbol{F}_n, \quad (10.29)$$

$$\boldsymbol{F}^{e,\,\mathrm{trial}}_{n+1} = \Delta\boldsymbol{F}\boldsymbol{F}^{e}_n. \quad (10.30)$$

Whereas the spatial logarithmic elastic trial strain can be defined as

$$\boldsymbol{\varepsilon}^{e,\,\mathrm{trial}}_{i,n+1} = \frac{1}{2}\ln\left(\boldsymbol{B}^{e,\,\mathrm{trial}}_{i,n+1}\right), \qquad i = \alpha, \beta, \quad (10.31)$$

where

$$\boldsymbol{B}^{e,\,\text{trial}}_{i,n+1} = \boldsymbol{F}^{e,\,\text{trial}}_{i,n+1}\left(\boldsymbol{F}^{e,\,\text{trial}}_{i,n+1}\right)^T = \Delta\boldsymbol{F}\boldsymbol{F}^e_{i,n}\left(\boldsymbol{F}^e_{i,n}\right)^T\Delta\boldsymbol{F}^T = \Delta\boldsymbol{F}\boldsymbol{B}^e_{i,n}\Delta\boldsymbol{F}^T. \tag{10.32}$$

From Equation 10.9, the following expression is obtained by post-multiplying both sides by $\left(\boldsymbol{R}^e_{n+1}\right)^{-1}$ and after performing some simple algebraic operations

$$\begin{aligned}\boldsymbol{V}^e_{n+1} = \boldsymbol{V}^{e,\,\text{trial}}_{n+1}\,\exp\Bigg[\Lambda_{n+1}\Delta t\Bigg(&\boldsymbol{\tau}_{\text{D},d,n+1} + \\ &\frac{1}{\sqrt{3}}q_{1,n+1}q_2 f_{n+1}\tau^{\text{eq}}_{\mu,n+1}\sinh\left(q_2\frac{\text{tr}\left(\boldsymbol{\tau}_{\text{D},n+1}\right)}{2\sqrt{3}\tau^{\text{eq}}_{\mu,n+1}}\right)\boldsymbol{I}\Bigg)\Bigg],\end{aligned} \tag{10.33}$$

where

$$\boldsymbol{V}^e_{n+1} = \left[\boldsymbol{F}^e_{n+1}\left(\boldsymbol{F}^e_{n+1}\right)^T\right]^{1/2}, \tag{10.34}$$

$$\boldsymbol{V}^{e,\,\text{trial}}_{n+1} = \left[\boldsymbol{F}^{e,\,\text{trial}}_{n+1}\left(\boldsymbol{F}^{e,\,\text{trial}}_{n+1}\right)^T\right]^{1/2}. \tag{10.35}$$

Lastly, by applying logarithms to both sides of the previous equation results

$$\begin{aligned}\boldsymbol{\varepsilon}^e_{n+1} = \boldsymbol{\varepsilon}^{e,\,\text{trial}}_{n+1} + \Lambda_{n+1}\Delta t\Bigg(&\boldsymbol{\tau}_{\text{D},d,n+1} + \\ &\frac{1}{\sqrt{3}}q_{1,n+1}q_2 f_{n+1}\tau^{\text{eq}}_{\mu,n+1}\sinh\left(q_2\frac{\text{tr}\left(\boldsymbol{\tau}_{\text{D},n+1}\right)}{2\sqrt{3}\tau^{\text{eq}}_{\mu,n+1}}\right)\boldsymbol{I}\Bigg).\end{aligned} \tag{10.36}$$

10.2.3 State Update

The infinitesimal visco-plastic flow rule

$$\begin{aligned}\boldsymbol{\varepsilon}^p_{n+1} = \boldsymbol{\varepsilon}^p_n + \Lambda_{n+1}\Bigg(&\boldsymbol{\tau}_{\text{D},d,n+1} + \\ &\frac{1}{\sqrt{3}}q_{1,n+1}q_2 f_{n+1}\tau^{\text{eq}}_{\mu,n+1}\sinh\left(q_2\frac{\text{tr}\left(\boldsymbol{\tau}_{\text{D},n+1}\right)}{2\sqrt{3}\tau^{\text{eq}}_{\mu,n+1}}\right)\boldsymbol{I}\Bigg)\Delta t,\end{aligned} \tag{10.37}$$

is obtained by assuming the additive decomposition of both the spatial logarithmic and the visco-elastic trial logarithmic strain tensors

$$\boldsymbol{\varepsilon} = \boldsymbol{\varepsilon}^e + \boldsymbol{\varepsilon}^p, \tag{10.38}$$

$$\boldsymbol{\varepsilon}^{e,\,\text{trial}}_{n+1} = \Delta\boldsymbol{\varepsilon}_{n+1} + \boldsymbol{\varepsilon}^e_n. \tag{10.39}$$

The state update procedure aims to determine the state variables $\left(\boldsymbol{\varepsilon}^e_{n+1},\ \boldsymbol{\varepsilon}^p_{n+1},\ f_{n+1},\ \eta_{\mu,n+1},\ \tau^{\text{eq}}_{\mu,n+1},\ \text{and}\ \bar{\varepsilon}^p_{\mu,n+1}\right)$ at the instant t_{n+1} using the following return mapping system of equations

$$\begin{cases}
\boldsymbol{\varepsilon}_{n+1} = \boldsymbol{\varepsilon}^e_{n+1} + \boldsymbol{\varepsilon}^p_{n+1} \\
\boldsymbol{\varepsilon}^p_{n+1} = \boldsymbol{\varepsilon}^p_n + \Lambda_{n+1}\left(\boldsymbol{\tau}_{\text{D},d,n+1} + \dfrac{1}{\sqrt{3}} q_{1,n+1} q_2 f_{n+1} \tau^{\text{eq}}_{\mu,n+1} \sinh\left(q_2 \dfrac{\text{tr}\left(\boldsymbol{\tau}_{\text{D},n+1}\right)}{2\sqrt{3}\tau^{\text{eq}}_{\mu,n+1}}\right)\boldsymbol{I}\right)\Delta t \\
f_{n+1} = f_n + 3\Delta t\left(1 - f_{n+1}\right)\dfrac{1}{\sqrt{3}} q_{1,n+1} q_2 f_{n+1} \Lambda_{n+1} \tau^{\text{eq}}_{\mu,n+1} \sinh\left(q_2 \dfrac{\text{tr}\left(\boldsymbol{\tau}_{\text{D},n+1}\right)}{2\sqrt{3}\tau^{\text{eq}}_{\mu,n+1}}\right) \\
\qquad\qquad + \dfrac{f_r}{2}\left[\text{erf}\left(\dfrac{\varepsilon_{\text{vol},n+1} - \varepsilon_r}{\sqrt{2}s_r}\right) - \text{erf}\left(\dfrac{\varepsilon_{\text{vol},n} - \varepsilon_r}{\sqrt{2}s_r}\right)\right] \\
\Phi_{n+1} = \left(\tau^{\text{eq}}_{\text{D},n+1}\right)^2 + 2 f_{n+1} q_{1,n+1}\left(\tau^{\text{eq}}_{\mu,n+1}\right)^2 \cosh\left(q_2 \dfrac{\text{tr}\left(\boldsymbol{\tau}_{\text{D},n+1}\right)}{2\sqrt{3}\tau^{\text{eq}}_{\mu,n+1}}\right) - \\
\qquad\qquad \left(\tau^{\text{eq}}_{\mu,n+1}\right)^2\left(1 + q^2_{1,n+1} f^2_{n+1}\right) = 0 \\
\eta_{\mu,n+1} = A_0 \exp\left[\dfrac{\Delta H}{R^* T} + \dfrac{\mu P_{n+1}}{\tau^*} - D_\infty\left(1 - \exp\left(-\sqrt{\dfrac{3}{2}}\dfrac{h\bar{\varepsilon}^p_{\mu,n+1}}{D_\infty}\right)\right)\right] \dfrac{\tau^{\text{eq}}_{\mu,n+1}}{\sinh\left(\dfrac{\tau^{\text{eq}}_{\mu,n+1}}{\tau^*}\right)} \\
\bar{\varepsilon}^p_{\mu,n+1} = \bar{\varepsilon}^p_{\mu,n} + \dfrac{\sqrt{3}\Delta t}{3\eta_{\mu,n+1}} \tau^{\text{eq}}_{\mu,n+1}
\end{cases} \tag{10.40}$$

with initial conditions $\boldsymbol{\varepsilon}^p_{n+1} = \boldsymbol{\varepsilon}^p_n$, $f_{n+1} = f_n$, $\eta_{\mu,n+1} = \eta_{\mu,n}$, $\tau^{\text{eq}}_{\mu,n+1} = \tau^{\text{eq}}_{\mu,n}$ and $\bar{\varepsilon}^p_{\mu,n+1} = \bar{\varepsilon}^p_{\mu,n}$, and by considering that the elastic trial strain introduced above is given and that the state variables are all known at instant t_n.

The first equation of the return mapping system of equations can be reformulated as a straightforward relationship between the elastic and plastic strain, as

$$\boldsymbol{\varepsilon}^{e}_{n+1} = \boldsymbol{\varepsilon}^{e,\,\text{trial}}_{n+1} - \boldsymbol{\varepsilon}^{p}_{n+1} + \boldsymbol{\varepsilon}^{p}_{n}. \tag{10.41}$$

This is possible because the total logarithmic strain tensor, $\boldsymbol{\varepsilon}_{n+1}$, can be computed in terms of the elastic predictor strain tensor as

$$\boldsymbol{\varepsilon}_{n+1} = \boldsymbol{\varepsilon}^{e,\,\text{trial}}_{i,n+1} + \boldsymbol{\varepsilon}^{p}_{i,n}. \tag{10.42}$$

Furthermore, the mentioned equation can be eliminated from the system of non-linear equations and updated *a posteriori* once the plastic strain tensor is determined. Additionally, the last equation can also be eliminated from the equation system by directly substituting it in the viscosity matrix, $\eta_{\mu,n+1}$.

For a generic 3D problem, the state update process entails solving a system of 9 non-linear equations, which are readily expressed in terms of residual functions as

$$R = \begin{bmatrix} \boldsymbol{R}_1 \\ R_2 \\ R_3 \\ R_4 \end{bmatrix} = \mathbf{0}, \tag{10.43}$$

where

$$\begin{aligned} \boldsymbol{R}_1 = \boldsymbol{\varepsilon}^{p}_{n+1} - \boldsymbol{\varepsilon}^{p}_{n} - \Lambda_{n+1} \Bigg(& \boldsymbol{\tau}_{\mathrm{D},d,n+1} + \\ & \frac{1}{\sqrt{3}} q_{1,n+1} q_2 f_{n+1} \tau^{\text{eq}}_{\mu,n+1} \sinh\left(q_2 \frac{\text{tr}\left(\boldsymbol{\tau}_{\mathrm{D},n+1}\right)}{2\sqrt{3}\tau^{\text{eq}}_{\mu,n+1}} \right) \boldsymbol{I} \Bigg) \Delta t, \end{aligned} \tag{10.44}$$

$$\begin{aligned} R_2 = & f_{n+1} - f_n - 3\Delta t \left(1 - f_{n+1}\right) \frac{1}{\sqrt{3}} q_{1,n+1} q_2 f_{n+1} \Lambda_{n+1} \tau^{\text{eq}}_{\mu,n+1} \\ & \sinh\left(q_2 \frac{\text{tr}\left(\boldsymbol{\tau}_{\mathrm{D},n+1}\right)}{2\sqrt{3}\tau^{\text{eq}}_{\mu,n+1}} \right) - \frac{f_r}{2} \left[\text{erf}\left(\frac{\varepsilon_{\text{vol},n+1} - \varepsilon_r}{\sqrt{2} s_r} \right) - \text{erf}\left(\frac{\varepsilon_{\text{vol},n} - \varepsilon_r}{\sqrt{2} s_r} \right) \right], \end{aligned} \tag{10.45}$$

$$R_3 = \eta_{\mu,n+1} - A_0 \exp\left[\frac{\Delta H}{R^* T} + \frac{\mu P_{n+1}}{\tau^*} - D_\infty \left(1 - \exp\left(-\sqrt{\frac{3}{2}}\frac{h}{D_\infty}\right.\right.\right. \\ \left.\left.\left.\left(\bar{\varepsilon}^p_{\mu,n} + \frac{\sqrt{3}\Delta t}{3\eta_{\mu,n+1}}\tau^{\text{eq}}_{\mu,n+1}\right)\right)\right)\right] \frac{\tau^{\text{eq}}_{\mu,n+1}}{\sinh\left(\frac{\tau^{\text{eq}}_{\mu,n+1}}{\tau^*}\right)}, \tag{10.46}$$

and

$$R_4 = \left(\tau^{\text{eq}}_{n+1}\right)^2 + 2 f_{n+1} q_{1,n+1} \left(\tau^{\text{eq}}_{\mu,n+1}\right)^2 \cosh\left(q_2 \frac{\text{tr}\left(\boldsymbol{\tau}_{\text{D},n+1}\right)}{2\sqrt{3}\tau^{\text{eq}}_{\mu,n+1}}\right) \\ - \left(\tau^{\text{eq}}_{\mu,n+1}\right)^2 \left(1 + q^2_{1,n+1} f^2_{n+1}\right), \tag{10.47}$$

with

$$q_{1,n+1} = q_{10} - q_{11} f_{n+1}, \tag{10.48}$$

and

$$P_{n+1} = p^* - \frac{1}{3}\text{tr}\left(\boldsymbol{\tau}_{\text{D},n+1}\right). \tag{10.49}$$

It is crucial to note that the hardening stress described by Equation 5.35 is purely deviatoric. Therefore, it does not contribute to the total hydrostatic pressure or affect the prediction of plastic strain.

Lastly, the Newton-Raphson iterative approach can be used to determine the return mapping system of equations' solution as

$$\boldsymbol{\alpha}^{(k)}_{n+1} = \boldsymbol{\alpha}^{(k-1)}_{n+1} + \delta\boldsymbol{\alpha}^{(k)}, \tag{10.50}$$

where

$$\delta\boldsymbol{\alpha}^{(k)} = -\mathbf{J}^{-1}\left(\boldsymbol{\alpha}^{(k-1)}_{n+1}\right)\mathsf{R}\left(\boldsymbol{\alpha}^{(k-1)}_{n+1}\right), \tag{10.51}$$

α is the matricial form of the vector of state variables,

$$\boldsymbol{\alpha}_{n+1} = \left[\boldsymbol{\varepsilon}^p_{n+1},\, f_{n+1},\, \eta_{\mu,n+1},\, \tau^{\text{eq}}_{\mu,n+1}\right]^T, \tag{10.52}$$

and $\mathbf{J}$ is the state update Jacobian matrix, given by

$$\mathbf{J} = \frac{\partial \boldsymbol{R}}{\partial \boldsymbol{\alpha}_{n+1}}, \tag{10.53}$$

all state variables are updated accordingly once the solution, $\boldsymbol{\alpha}_{n+1}$, is found. The necessary residual derivatives are included in Appendix F.1 for compactness's sake.

10.2.4 Consistent Tangent Modulus

The linearisation of the elemental internal forces results in the generic finite stresses spatial tangent modulus, a,

$$\left(\mathrm{a}_{ijkl}\right)_{n+1} = \left(\frac{1}{\det[\boldsymbol{F}]}\frac{\partial \tau_{\mathrm{T},ij}}{\partial F_{km}}F_{lm} - \sigma_{\mathrm{T},il}\delta_{jk}\right)_{n+1}, \tag{10.54}$$

where $\boldsymbol{\sigma}_{\mathrm{T},n+1}$ denotes the Cauchy stress tensor,

$$\boldsymbol{\sigma}_{\mathrm{T},n+1} = \frac{1}{\det\left[\boldsymbol{F}_{n+1}\right]}\boldsymbol{\tau}_{\mathrm{T},n+1}. \tag{10.55}$$

Moreover, since the differentiation chain rule can be used to determine the derivative of the total incremental Kirchhoff stress tensor as

$$\frac{\partial \hat{\boldsymbol{\tau}}_{\mathrm{T}}}{\partial \boldsymbol{F}_{n+1}} = \frac{\partial \hat{\boldsymbol{\tau}}_{\mathrm{T}}}{\partial \boldsymbol{\varepsilon}^{e,\,\mathrm{trial}}_{n+1}} : \frac{\boldsymbol{\varepsilon}^{e,\,\mathrm{trial}}_{n+1}}{\partial \boldsymbol{B}^{e,\,\mathrm{trial}}_{n+1}} : \frac{\partial \boldsymbol{B}^{e,\,\mathrm{trial}}_{n+1}}{\partial \boldsymbol{F}_{n+1}}, \tag{10.56}$$

the spatial tangent modulus can also be expressed as

$$\left(\mathrm{a}_{ijkl}\right)_{n+1} = \frac{1}{2\det\left[\boldsymbol{F}_{n+1}\right]}\left(\left[\mathsf{D} : \mathsf{L} : \mathsf{B}\right]_{ijkl}\right)_{n+1} - \left(\sigma_{\mathrm{T},il}\right)_{n+1}\delta_{jk}, \tag{10.57}$$

where

$$\mathsf{D}_{n+1} = \frac{\partial \hat{\boldsymbol{\tau}}_{\mathrm{T}}}{\partial \boldsymbol{\varepsilon}^{e\,\mathrm{trial}}_{n+1}}, \tag{10.58}$$

has the same functional format as the consistent tangent modulus at infinitesimal strains,

$$\mathsf{L}_{n+1} = \frac{\partial \ln\left[\boldsymbol{B}^{e,\,\mathrm{trial}}_{n+1}\right]}{\partial \boldsymbol{B}^{e,\,\mathrm{trial}}_{n+1}}, \tag{10.59}$$

is the derivative of the tensor logarithm function at $\boldsymbol{B}^{e,\,\mathrm{trial}}_{n+1}$, and

$$\left(\mathrm{B}_{mjkl}\right) = \delta_{mk}\left(B^{e,\,\mathrm{trial}}_{jl}\right)_{n+1} + \delta_{jk}\left(B^{e,\,\mathrm{trial}}_{ml}\right)_{n+1}, \tag{10.60}$$

is entirely established by the cartesian components of $\boldsymbol{B}^{e,\,\mathrm{trial}}_{n+1}$.

It is noted that the fourth-order tensor $\mathbf{D}_{n+1}$, which, by application of the differentiation chain rule, can be written as

$$\mathbf{D}_{n+1}^{vevp} = \frac{\partial \hat{\boldsymbol{\tau}}_T}{\partial \boldsymbol{\varepsilon}_{n+1}^{e\,\text{trial}}} = \frac{\partial \hat{\boldsymbol{\tau}}_T}{\partial \boldsymbol{\varepsilon}_{n+1}} : \frac{\partial \boldsymbol{\varepsilon}_{n+1}}{\partial \boldsymbol{\varepsilon}_{n+1}^{e,\,\text{trial}}} = \frac{\partial \hat{\boldsymbol{\tau}}_{\text{T}}}{\partial \boldsymbol{\varepsilon}_{n+1}}, \tag{10.61}$$

is the sole material-related operator for the calculation of the spatial tangent modulus. Moreover, the closed-form of the visco-elastic visco-plastic consistent tangent modulus can be established as

$$\mathbf{D}_{n+1}^{vevp} = \frac{\partial \hat{\boldsymbol{\tau}}_{\text{T}}}{\partial \boldsymbol{\varepsilon}_{n+1}} = \frac{\partial \boldsymbol{\tau}_{\text{D},n+1}}{\partial \varepsilon_{n+1}} + \frac{\partial \boldsymbol{\tau}_{\text{H},n+1}}{\partial \varepsilon_{n+1}}, \tag{10.62}$$

by paying attention to the additive decomposition of the Kirchhoff stress tensor in Equation 5.1 and where the derivative of the driving stress is provided by

$$\begin{aligned}\frac{\partial \boldsymbol{\tau}_{\text{D},n+1}}{\partial \varepsilon_{n+1}} = K_\infty \boldsymbol{I} \otimes \boldsymbol{I} - K_\infty \boldsymbol{I} \otimes \left(\boldsymbol{I} : \frac{\partial \boldsymbol{\varepsilon}_{n+1}^p}{\partial \boldsymbol{\varepsilon}_{n+1}} \right) + 2\bar{G}_{n+1} \mathbf{I}_d - 2\bar{G}_{n+1} \mathbf{I}_d : \frac{\partial \boldsymbol{\varepsilon}_{n+1}^p}{\partial \boldsymbol{\varepsilon}_{n+1}} \\ + \sum_{j=1}^{n_V} \left(\boldsymbol{\tau}_{\text{D},j,n} \otimes \frac{\partial \hat{\omega}_{j,n+1}}{\partial \boldsymbol{\varepsilon}_{n+1}} \right) + 2 \left(\boldsymbol{\varepsilon}_{d,n+1}^e - \boldsymbol{\varepsilon}_{d,n}^e \right) \otimes \frac{\partial \bar{G}_{n+1}}{\partial \boldsymbol{\varepsilon}_{n+1}}.\end{aligned} \tag{10.63}$$

In order to calculate the derivative of the hardening stress, it is advantageous to represent the hardening law in Equation 5.35 using the total spatial logarithmic strain. By considering the definition of the spatial logarithmic strain tensor

$$\boldsymbol{\varepsilon} = \frac{1}{2} \ln \boldsymbol{B}, \tag{10.64}$$

the left Cauchy-Green strain tensor can be expressed in terms of the logarithmic strain as

$$\boldsymbol{B} = \exp(2\boldsymbol{\varepsilon}). \tag{10.65}$$

Additionally, the isochoric left Cauchy-Green strain tensor can be reformulated as

$$\boldsymbol{B}_{\text{iso}} = (\exp\big(2\,\text{tr}(\boldsymbol{\varepsilon})\big))^{-1/3} \exp(2\boldsymbol{\varepsilon}), \tag{10.66}$$

and the stretch on a chain in the eight-chain network as

$$\lambda_{\text{chain}}^p = \sqrt{\frac{1}{3} (\exp\big(2\,\text{tr}(\boldsymbol{\varepsilon})\big))^{-1/3}\,\text{tr}(\exp(2\boldsymbol{\varepsilon}))}, \tag{10.67}$$

by considering the fact that $\det(\boldsymbol{B}) = \big(\det(\boldsymbol{F})\big)^2$, and that

$$\det(\boldsymbol{B}) = \det(\exp(2\boldsymbol{\varepsilon})) = \exp\big(2\,\text{tr}(\boldsymbol{\varepsilon})\big). \tag{10.68}$$

As a result, the derivative of the hardening stress with respect to the total logarithmic strain tensor becomes

$$\frac{\partial \boldsymbol{\tau}_{\mathrm{H},n+1}}{\partial \boldsymbol{\varepsilon}_{n+1}} = -\frac{C_{\mathrm{R}}}{3}\frac{\sqrt{N}}{\left(\lambda^{p}_{\mathrm{chain}}\right)^{2}}\mathscr{L}^{-1}\left(\frac{\lambda^{p}_{\mathrm{chain}}}{\sqrt{N}}\right)\boldsymbol{B}_{d,\,\mathrm{iso}} \otimes \frac{\partial \lambda^{p}_{\mathrm{chain}}}{\partial \boldsymbol{\varepsilon}_{n+1}} + \frac{C_{\mathrm{R}}}{3}\frac{\sqrt{N}}{\lambda^{p}_{\mathrm{chain}}} \boldsymbol{B}_{d,\,\mathrm{iso}} \otimes \frac{\partial}{\partial \boldsymbol{\varepsilon}_{n+1}}\left(\mathscr{L}^{-1}\left(\frac{\lambda^{p}_{\mathrm{chain}}}{\sqrt{N}}\right)\right) + \frac{C_{\mathrm{R}}}{3}\frac{\sqrt{N}}{\lambda^{p}_{\mathrm{chain}}}\mathscr{L}^{-1}\left(\frac{\lambda^{p}_{\mathrm{chain}}}{\sqrt{N}}\right)\mathbf{I}_{d} : \frac{\partial \boldsymbol{B}_{\mathrm{iso}}}{\partial \boldsymbol{\varepsilon}_{n+1}}. \tag{10.69}$$

The necessary derivatives in both Equations 10.63 and 10.69 are included in Appendix F.2 for compactness's sake.

10.2.5 Damage Variable Computation

After detailing the numerical algorithm for integrating the constitutive equations, the implementation of the damage variable within it can now be addressed. This involves three distinct procedures that need to be followed: (1) numerical integration of the damage law over time; (2) modification of the state update procedure; and (3) modification of the computation of the consistent tangent modulus.

Firstly, the numerical integration of the damage law, as described in Equation 10.4, can be analytically performed over time, resulting in the following expression

$$D_{n+1} = \frac{\bar{\varepsilon}^{p}_{\mu,n+1}}{\bar{\varepsilon}^{p}_{\mu,\mathrm{cr}}}, \tag{10.70}$$

where $\bar{\varepsilon}^{p}_{\mu,n+1}$ is given by Equation 10.11. The simplicity of this expression arises from the initial condition where there is no damage, i.e., zero accumulated plastic strain, in the material at time instant t_0, and thus $D_0 = 0$.

Subsequently, the state update procedure needs to be modified to incorporate the influence of the damage variable on the material response. This entails updating the Kirchhoff stress tensor, after solving the return mapping system of equations, by computing the damaged stress tensor, taking into account the current value of the damage variable

$$\boldsymbol{\tau}^{*}_{n+1} = \left(1 - D_{n+1}\right)\boldsymbol{\tau}_{\mathrm{T},\,n+1}. \tag{10.71}$$

Lastly, it is necessary to update the formulation of the consistent tangent modulus, which plays a critical role within the context of the iterative Newton-

Raphson method. Considering the formulation presented in Equation 10.57, the only variable that requires modification is the fourth-order tensor $\mathbf{D}_{n+1}$. Thus, considering the closed-form expression of the visco-elastic visco-plastic consistent tangent modulus, its formulation, presented in Equation 10.62, is replaced by

$$\mathbf{D}^{vevp*}_{n+1} = \frac{\partial \boldsymbol{\tau}^{*}_{n+1}}{\partial \boldsymbol{\varepsilon}_{n+1}} = \left(1 - D_{n+1}\right)\mathbf{D}^{vevp}_{n+1} - \boldsymbol{\tau}_{\mathrm{T},\,n+1} \otimes \frac{\partial D_{n+1}}{\partial \boldsymbol{\varepsilon}_{n+1}}, \tag{10.72}$$

where the derivative of the damage variable with respect to the total logarithmic strain tensor is

$$\frac{\partial D_{n+1}}{\partial \boldsymbol{\varepsilon}_{n+1}} = \frac{1}{\bar{\varepsilon}^{p}_{\mu,\mathrm{cr}}} \frac{\partial \bar{\varepsilon}^{p}_{\mu,n+1}}{\partial \boldsymbol{\varepsilon}_{n+1}}, \tag{10.73}$$

with

$$\frac{\partial \bar{\varepsilon}^{p}_{\mu,n+1}}{\partial \boldsymbol{\varepsilon}_{n+1}} = \frac{\sqrt{3}\Delta t}{3\left(\eta_{\mu,n+1}\right)^{2}} \left(\frac{\partial \tau^{\mathrm{eq}}_{\mathrm{D},\mu,n+1}}{\partial \boldsymbol{\varepsilon}_{n+1}} \eta_{\mu,n+1} - \tau^{\mathrm{eq}}_{\mathrm{D},\mu,n+1} \frac{\partial \eta_{\mu,n+1}}{\partial \boldsymbol{\varepsilon}_{n+1}} \right). \tag{10.74}$$

The remaining derivatives, $\partial \tau^{\mathrm{eq}}_{\mu,n+1} / \partial \boldsymbol{\varepsilon}_{n+1}$ and $\partial \eta_{\mu,n+1} / \partial \boldsymbol{\varepsilon}_{n+1}$, are obtained by solving the system of linear equations in Equation F.55.

10.3 Results and Discussion

In this section, three studies are conducted to evaluate various aspects of the explicit local damage model introduced in the present chapter. Firstly, the efficiency and numerical robustness of the model is assessed (Section 10.3.1). Secondly, the influence of different values for the critical accumulated plastic strain, $\bar{\varepsilon}^{p}_{\mu,\mathrm{cr}}$, on the constitutive behaviour of both the PC material and the PC/ABS blend is investigated (Sections 10.3.1 and 10.3.2, respectively). Lastly, the impact of introducing the damage variable on the constitutive behaviour of the PC/ABS blend is examined (Section 10.3.2). For the PC and ABS constituents, the material properties used in this study are those presented in Section 5.2, and for the cohesive elements, the properties employed are the ones obtained from the literature and described in Section 6.4.

10.3.1 PC Matrix with Voids under Mixed Tensile-Shear

To evaluate the impact of the newly introduced damage model in describing the material's behaviour, a 2D square RVE with a side length of 40 μm is considered.

The RVE consists of a PC matrix with a void volume fraction of 40%, where each void has a circular geometry characterised by a 6 μm radius and is subjected to a mixed tensile-shear loading given by the following deformation gradient

$$\boldsymbol{F} = \begin{bmatrix} 1.00500 & 0.13000 \\ -0.00175 & 0.99800 \end{bmatrix}. \tag{10.75}$$

This choice is motivated by the fact that this combined loading condition, together with voids, promotes more severe plastic deformations within the material. Consequently, it enhances the influence of the damage variable in describing the material's behaviour and enables the evaluation of the model's performance in a more extreme case. Moreover, it is important to remember that the constitutive model is dependent on the strain rate; therefore, a value of $\dot{\varepsilon} = 0.001\ \mathrm{s}^{-1}$ is specified.

The RVE utilised in this study is shown in Figure 10.1, together with its finite element mesh topology. The RVE is spatially discretised in a finite element mesh of 8-node quadrilateral elements with reduced integration (4 Gauss integration points), and the analysis is conducted under the assumption of the plane strain condition. In addition, the Mortar Periodic boundary condition is employed due to the fact that the RVE possesses a periodic microstructure, while its finite element mesh topology does not exhibit periodicity.

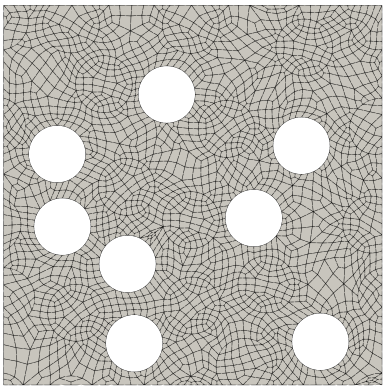


Figure 10.1: Mesh topology of the PC matrix with voids 2D RVE with a side length of 40 μm.

In Figure 10.2, the evolution of the effective Cauchy stress as a function of the equivalent strain for various values of the critical accumulated plastic strain is plotted, while Figure 10.3 visually represents the distribution and evolution of the damage variable within the material as it undergoes deformation. These Figures provide insights into how the material response develops and how damage accumulates and propagates throughout the material.

As anticipated, altering the value of $\bar{\varepsilon}^p_{\text{cr}}$ significantly influences the material's response and damage localisation. Increasing the value of $\bar{\varepsilon}^p_{\text{cr}}$ implies less consideration for the internal degradation of the matrix resulting from defects, leading to material rupture occurring at a later stage, i.e., at higher equivalent strain values and higher stress levels.

Furthermore, as $\bar{\varepsilon}^p_{\text{cr}}$ increases, the yield point becomes higher, and the softening regime becomes less pronounced and more gradual. However, it is essential to note that when $\bar{\varepsilon}^p_{\text{cr}}$ is extremely small, the material fails immediately at the yield point, and no softening is observed. In this scenario, the damage rapidly localises in the zone where plastic deformation initiates, resulting in high values of the damage variable, D, and subsequently close to zero stress values in that zone, ultimately leading to material rupture. Conversely, in extreme cases like $\bar{\varepsilon}^p_{\text{cr}} = 1000$, the damage variable takes insignificant values, and the material essentially recovers its response in the undamaged model. This last observation is crucial as it also confirms the correct damage model implementation.

All these observations can be verified in Figure 10.3, which illustrates how the damage becomes less localised with the increase of $\bar{\varepsilon}^p_{\text{cr}}$. Instead, it spreads over a larger region, with smaller values of D.

The efficiency and robustness of the newly implemented damage model are analysed in Table 10.1, where the numerical convergence of both constitutive state update and global equilibrium iterative scheme (relies on the proper computation of the material consistent tangent modulus) for the PC matrix with voids under mixed tensile-shear loading is presented. This convergence was obtained for $\bar{\varepsilon}^p_{\text{cr}} = 2$ at increment 100 when the total load factor equals 0.5563. As it is possible to observe, Newton-Raphson's expected quadratic convergence rate is obtained, which strongly supports the proper linearisation and computational implementation of the model.

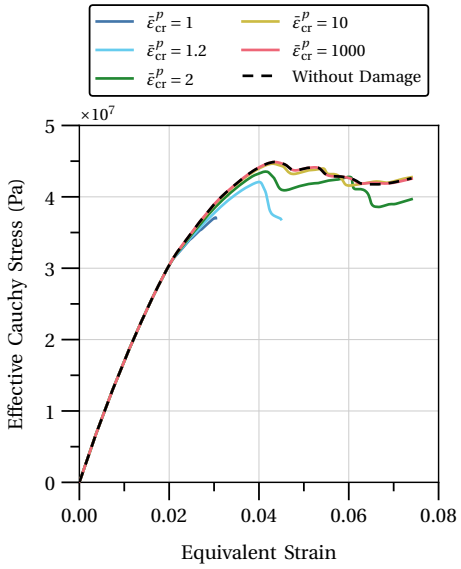
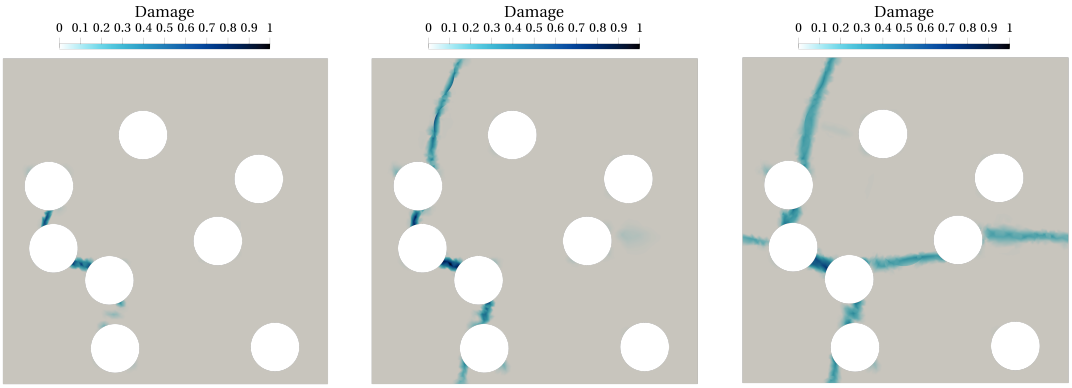
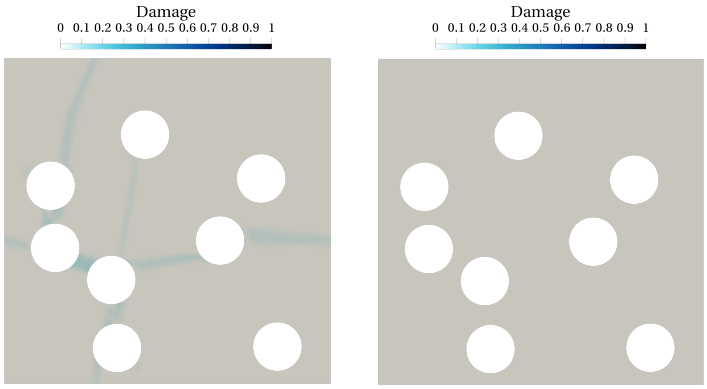


Figure 10.2: Effect of the critical accumulated plastic strain, $\bar{\varepsilon}^p_{cr}$ on the microscopic response of PC material with voids.



(a) $\bar{\varepsilon}^p_{cr} = 1$ (b) $\bar{\varepsilon}^p_{cr} = 1.2$ (c) $\bar{\varepsilon}^p_{cr} = 2$



(d) $\bar{\varepsilon}^p_{cr} = 10$ (e) $\bar{\varepsilon}^p_{cr} = 1000$

Figure 10.3: Damage bands obtained for different values of the critical accumulated plastic strain, $\bar{\varepsilon}^p_{cr}$, shown for the PC matrix with voids 2D RVE.

Table 10.1: Convergence table of the mixed tensile-shear numerical response of the 2D PC matrix with voids RVE. Normalised equilibrium residual evolution at increment 100 and state update normalised residual evolution at one Gauss point subjected to the highest value of the damage variable during each global iteration. Convergence tolerance set to 1.0×10^{-8}.

Global			**State Update**	
Increment	Iteration	Norm. Eq. Res.	Iteration	Norm. Res.
100	⋮	⋮	⋮	⋮
	4	0.2866×10^{-1}	1	0.5551×10^{-1}
			2	0.6005×10^{-3}
			3	0.1849×10^{-7}
			4	0.6212×10^{-15}
	5	0.6085×10^{-3}	1	0.5553×10^{-1}
			2	0.5670×10^{-3}
			3	0.1640×10^{-7}
			4	0.6641×10^{-14}
	6	0.1686×10^{-5}	1	0.5553×10^{-1}
			2	0.5666×10^{-3}
			3	0.1637×10^{-7}
			4	0.8943×10^{-14}
	7	0.5197×10^{-10}	1	0.5553×10^{-1}
			2	0.5666×10^{-3}
			3	0.1637×10^{-7}
			4	0.2083×10^{-14}

10.3.2 PC/ABS under Mixed Tensile-Shear

The main objective of this chapter was to implement a damage model that accounted for the effects of the shear-yielding mechanism within the PC matrix, aiming to comprehensively describe all damage mechanisms present in the PC/ABS blend. After verifying the correct implementation of the model in Section 10.3.1 and conducting a parametric study on the influence of the critical accumulated plastic strain on the response of the PC constituent, this section focuses on studying the overall response of the blend by combining all the models presented in this dissertation.

To accomplish this objective, a 2D square RVE with a side length of 50 μm (representative size) and a volume fraction of 10% of ABS (the particles are elongated in the xx axis) is subjected to a mixed tensile-shear loading, under a strain rate value of $\dot{\varepsilon} = 0.001\ \mathrm{s}^{-1}$, given by the following deformation gradient

$$\boldsymbol{F} = \begin{bmatrix} 1.30 & 0.30 \\ 0.00 & 1.00 \end{bmatrix}. \tag{10.76}$$

In this study, two RVEs are employed, where the first RVE serves as the base configuration, while the second RVE is derived from the first by introducing cohesive elements. Figure 10.4 depicts only one RVE, along with its finite element mesh topology, as both RVEs have the same topology, and in the initial configuration, the cohesive elements cannot be visualised. Both RVE are spatially discretised in a finite element mesh consisting of 6-node triangular elements and the analysis is conducted under the assumption of plane strain condition with periodic boundary condition. In addition to the base elements, the second RVE incorporates 6-node 2D quadratic cohesive elements (COH2D6), specifically in the PC and ABS interface.

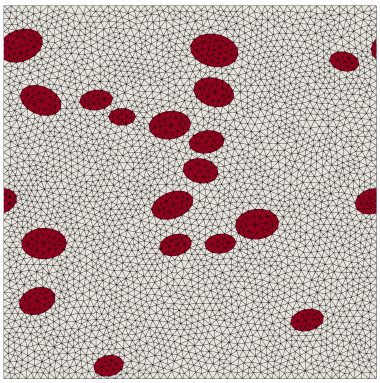


Figure 10.4: Mesh topology of PC/ABS 2D RVE with a side length of 50 μm and a volume fraction of 10% of ABS.

Figures 10.5 and 10.6 provide numerical and visual representations, respectively, of the microscopic response of the PC/ABS blend, considering various combinations of the damage mechanism models. These combinations range from employing only the finite strain visco-elastic visco-plastic constitutive model, which represents the base response of the PC/ABS blend, to incorporating cohesive elements in the interface and introducing damage within the PC matrix. It is important to note that the obtained numerical responses highly depend on the properties assigned to both the PPR potential-based cohesive zone model and the damage model (a value of $\bar{\varepsilon}^{p}_{\mathrm{cr}} = 1.2$ was used in the current study). Nevertheless, the main influences resulting from including these models can still be analysed.

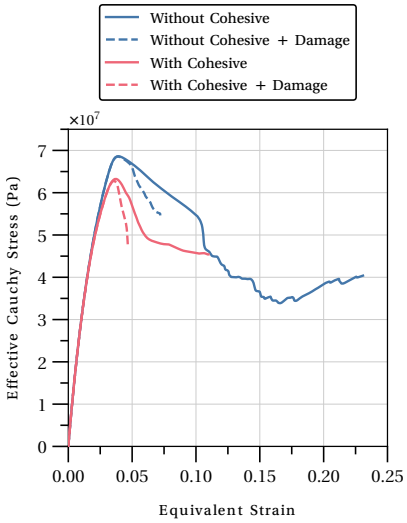
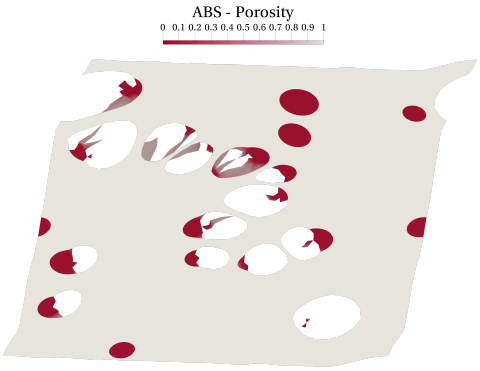
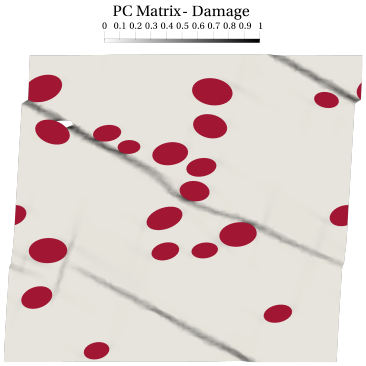


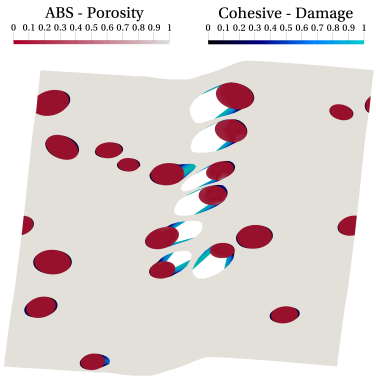
Figure 10.5: Microscopic response of PC/ABS blend with a volume fraction of 10% of ABS for all combinations of damage mechanisms.



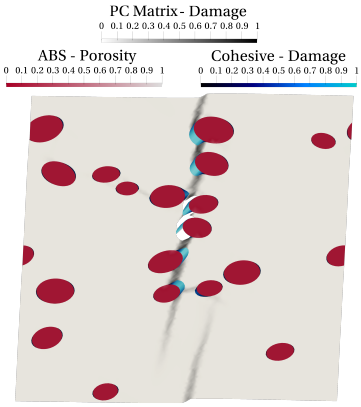
(a) Without Cohesive



(b) Without Cohesive + Matrix Damage



(c) With Cohesive



(d) With Cohesive + Matrix Damage

Figure 10.6: Visual representation of the microscopic response of PC/ABS blend with a volume fraction of 10% of ABS for all combinations of damage mechanisms.

As previously observed in Sections 8.2 and 8.3, including cohesive elements in the interface, representing imperfect bonding between the particles and the matrix, leads, under tensile loading, to more pronounced and intense softening, a decrease in yield stress, and earlier material rupture. Note that the extent of these observations can vary depending on the chosen properties. Currently, when considering damage within the PC matrix, the softening regime becomes even more pronounced for both material responses, with and without cohesive elements, and the material experiences rupture at even lower strain values. However, the yield stress does not appear to vary.

Additionally, Figure 10.6 allows visual analysis of the logical evolution of the material's response with the different model combinations. First, when only the visco-elastic visco-plastic constitutive model is employed, extreme deformation of the ABS particles occurs while void nucleation occurs within the PB rubber particles. Consequently, the presented response becomes predominantly numerical and loses some of its physical significance.

However, incorporating cohesive elements or introducing the damage model produces a more realistic description of the material's behaviour. As a result, the material does not reach such high levels of deformation, and failure occurs earlier. In the case of cohesive elements, it can be observed that the interfaces undergoing debonding follow a distinct path, which, combined with the simultaneous inclusion of the damage variable, leads to a precise localisation of damage along the matrix and the cohesive elements. Furthermore, it is noteworthy that the localisation of damage within the matrix takes completely different paths for cases with and without cohesive elements, indicating a synergistic effect between the two models in capturing the material's behaviour.

With the combination of different models, void nucleation within the PB rubber particles becomes less relevant in describing the material's response. However, as mentioned numerous times, if other properties were used, specifically higher values of $\bar{\varepsilon}^{p}_{\text{cr}}$ together with higher interfacial bonding strength, this could cease to be the case.

Lastly, given the synergistic relationship between the PPR cohesive zone model and the damage model, a second parametric study on the influence of the critical accumulated plastic strain is presented. However, in this case, the main objective is to explore which damage mechanism has a more prominent impact in shaping the PC/ABS blend's microscopic response. To this end, Figure 10.7 plots the evolution of the effective Cauchy stress as a function of the equivalent strain for various values of the critical accumulated plastic strain, while Figure 10.8 visually represents the distribution and evolution of the

damage mechanisms as the RVE undergoes deformation.

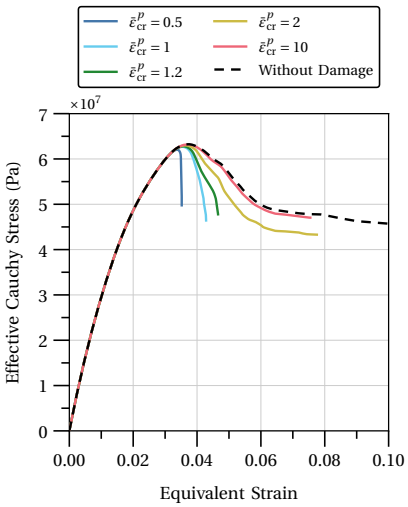
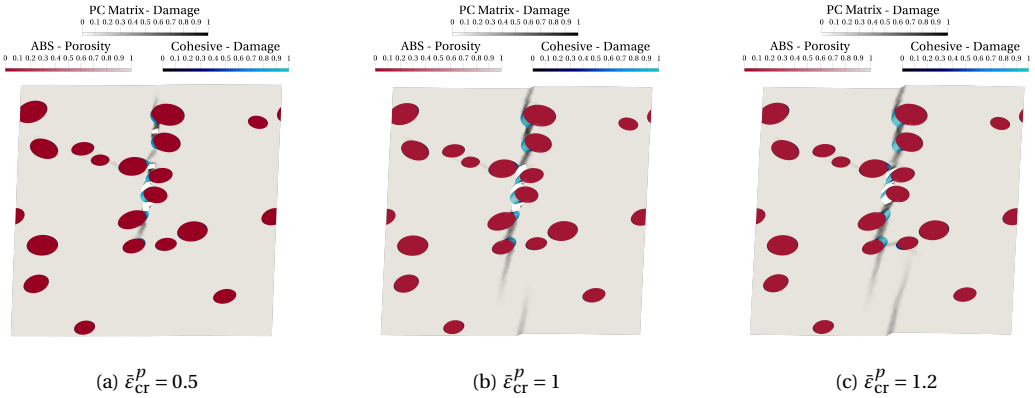
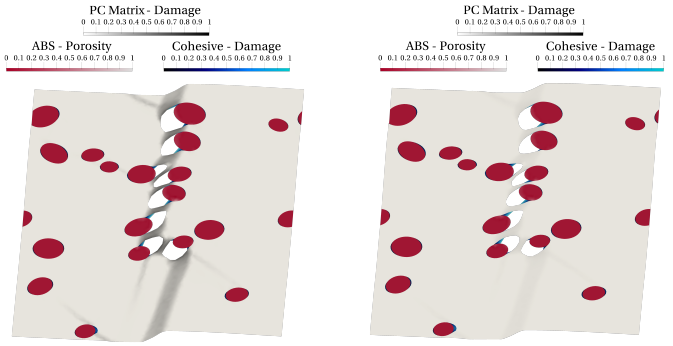


Figure 10.7: Effect of the critical accumulated plastic strain, $\bar{\varepsilon}^p_{cr}$ on the microscopic response of PC/ABS blend with a volume fraction of 10% of ABS with cohesive elements.



(a) $\bar{\varepsilon}^p_{cr} = 0.5$ (b) $\bar{\varepsilon}^p_{cr} = 1$ (c) $\bar{\varepsilon}^p_{cr} = 1.2$



(d) $\bar{\varepsilon}^p_{cr} = 2$ (e) $\bar{\varepsilon}^p_{cr} = 10$

Figure 10.8: Damage localisation obtained for different values of the critical accumulated plastic strain, $\bar{\varepsilon}^p_{cr}$, shown for the PC/ABS 2D RVE with a side length of 50 μm and a volume fraction of 10% of ABS with cohesive elements.

The observations made in Section 10.3.1 align with the conclusions derived from the present study. This is, increasing the value of $\bar{\varepsilon}^p_{\text{cr}}$ leads to material rupture occurring at a later stage, for higher equivalent strain values, and to the softening regime becoming less pronounced and more gradual. However, it is noted that in the PC/ABS blend, the yield point does not vary with the variation of $\bar{\varepsilon}^p_{\text{cr}}$. Therefore, the matrix damage mechanism plays a more crucial role in describing the softening regime and has little effect on yield stress. Moreover, from the studies carried out in Section 8.2, the variation of the yield stress can be attributed mainly to the properties employed in the cohesive elements, i.e., to the matrix-particle interaction and respective debonding.

Specifically, regarding the synergy between the two referenced models, it can be observed that the damage path always passes through the same zone in all cases, with greater damage dispersion as the value of $\bar{\varepsilon}^p_{\text{cr}}$ increases. This is expected because, for higher values, the consideration for the internal degradation of the matrix decreases, resulting in less localised damage in the matrix. Consequently, the cohesive elements and interface debonding play a more significant role. This can be observed by considering that in Figure 10.8(a), with a low value of $\bar{\varepsilon}^p_{\text{cr}}$, the failure mainly occurs in the matrix, while in Figure 10.8(e), with a high value of $\bar{\varepsilon}^p_{\text{cr}}$, the damage is primarily observed at the interface.

Thus, although it is only possible to conclude the influence of each model's properties on describing the behaviour of the PC/ABS blend, without having a clear understanding of the predominant damage mechanism in its response, it can be stated that only a combination of the three models allows for a realistic description of the material. However, it is also evident that this combination leads to a more time-consuming and complex calibration process of the different properties involved.

CHAPTER 11

CONCLUSIONS

11.1 Conclusions

Over the past few decades, extensive research has been conducted to understand the effects of blend composition, morphology, manufacturing conditions, rubber particle cavitation, and plastic void growth on the mechanical behaviour of PC/ABS blends. However, a crucial aspect that has been overlooked in previous studies is the influence of the interface between the PC and ABS constituents on the blend's behaviour. This dissertation aims to address this gap in the existing literature by enhancing the understanding of the impact and significance of the principal microscopic deformation and damage mechanisms that occur in PC/ABS blends, mainly focusing on the debonding process at the interface.

The present study focuses on three PC/ABS blends with mass fractions known to exhibit interesting synergistic effects (90/10, 80/20, 70/30). The objective is to provide a comprehensive numerical description of these blends' constitutive behaviour by examining the interface's influence. To achieve this, a combined approach of modelling and experimental validation is employed at both macro and micro scales in an independent and coupled manner.

To establish a robust theoretical framework for the analyses performed in this dissertation, Chapters 2 and 3 offer an extensive examination of the core principles of continuum mechanics and first-order multi-scale modelling, together with Chapter 4, which concentrates on a meticulous characterisation of the polymer blend under examination, providing detailed insights into its composition and properties. The primary contributions to the aforementioned objectives are described in what follows.

In Chapter 5, a combination of statistical analysis and numerical simulations is employed to determine the optimal size of three PC/ABS blend volume fractions for high-fidelity RVEs. The aim is to strike a balance between

computational affordability and the statistical representativeness of micro-scale singularities. The research successfully achieves this by verifying a clear convergence of the response as the RVE size increases. For the 2D case, a decision is made on when its use becomes counterproductive, meaning that the improvement in describing the material behaviour becomes insignificant compared to the high computational cost. In the 3D case, the limiting factor is the computational cost due to the increased complexity of RVE geometry and time constraints. Therefore, a suboptimal RVE size is established, with the main deviations in behaviour observed in the final softening zone and the hardening zone. Additionally, it is discovered that the computing effort increases as the ABS volume fraction increases. Regarding the mesh sensitivity finite element analyses, the material response demonstrates definite convergence with increasing mesh discretisation levels. This refutes the problem of inherent mesh dependence and ensures that statistical homogeneity is not lost due to damage localisation. These analyses also allow for the determination of the minimum level of mesh discretisation that ensures solutions of appropriate quality for both 2D and 3D cases, thus reducing the computational effort. Furthermore, the study confirms the expected anisotropic behaviour between the particle elongation direction, injection direction, and the other two perpendicular directions through numerical simulations. This is mainly characterised by a lower yield point and less prominent nucleation phenomena in the injection direction. Lastly, slight disparities are observed between the descriptions of 2D and 3D behaviour, primarily attributed to assuming a plain strain state in the 2D analysis. This assumption is easily refuted based on the geometry and arrangement of ABS particles.

To achieve the main goal of this dissertation, in Chapter 7, a new Python tool is developed to incorporate zero-thickness cohesive interface elements around each ABS particle in preexisting finite element RVEs and ensure seamless integration between its output files and Links' input files. Although the development of the tool focuses on its specific application to PC/ABS blends, it is designed to insert cohesive elements along any number of material phases, either on all of them or only between ones specified by the user, and to any type of morphology, as demonstrated through extensive application examples. Moreover, the tool is also capable of generating two-dimensional and three-dimensional, linear and quadratic cohesive elements from various types of continuum elements. Computational cost and efficiency are crucial aspects of any tool, and in this case, they have been significantly improved through extensive code optimisation. The studies conducted to assess the tool's

performance demonstrate extremely low execution times even when drastically increasing the total number of elements and materials. Additionally, owing to the optimisation procedures, both linear and quadratic problems present identical execution times. The low standard deviations observed across different examples further support its efficiency, reliability and robustness.

In Chapter 8, the main research question regarding the impact of the interface between the PC matrix and the ABS particles on describing the behaviour of PC/ABS blends is analysed through three major studies. Firstly, reference values for the material parameters of the PPR potential-based cohesive model are derived from the literature. Since studies of the PC/ABS blend interface and the implementation of cohesive zone modelling to it are limited or non-existent, likewise, for particulate polymer blends, only approximate values for these cohesive parameters are obtained by adapting results from experimental tests conducted for other purposes. Secondly, a parametric study is performed to assess the influence of each material parameter of the PPR potential-based cohesive model on its constitutive behaviour. It is concluded that the behaviour is most sensitive to the cohesive strengths and fracture energies, while the initial slope indicators and shape parameters have practically no influence. Increasing the cohesive strength, either tangential or normal, primarily leads to an increase in the elastic limit stress and earlier occurrence of full debonding. On the other hand, increasing the fracture energies results in a larger area under the curve (global dissipated energy) and a decrease in the slope of the post-peak region, indicating less pronounced strain-softening. Thirdly, a parametric study is conducted to examine the loading conditions most affected by including cohesive elements. It is found that including cohesive elements is not necessary when studying PC/ABS blends under compression. However, it becomes crucial to accurately depict the material behaviour when the material is subjected to traction. Furthermore, it is observed that the influence of incorporating cohesive elements diminishes as the cohesive strengths and fracture toughness values increase, ultimately leading to perfect bonding.

In Chapter 9, an alternative approach to coupled multi-scale finite element analysis is presented and utilised to determine the material parameters of the PPR potential-based cohesive model for PC/ABS blends. This approach involves unit cells and a decoupled procedure. However, despite achieving close agreement between the predictions of the macroscopic constitutive model and the experimental results, a satisfactory fit between the numerical results at the micro-scale and those obtained from the macro-scale problem was not possible. Additionally, the material properties obtained through the calibration process

lack physical significance and are purely numerical. As a result, the initial objective of deducing the authentic PPR cohesive zone model parameters for PC/ABS blends could not be accomplished. The reasons for this lack of success have been carefully analysed and identified. Assumptions such as the similarity of macro (bulk) and micro (phase constituents) material behaviours and the use of different PC and ABS types for the calibration procedures were found to contribute to the inability to achieve satisfactory results from the beginning. Despite this, the inclusion of cohesive elements in the analysis resulted in a material behaviour description that is in closer agreement with the reference response. This indicates that considering cohesive elements allows for a more accurate and realistic response, even if the parameters of the cohesive elements may not be the most accurate. Furthermore, the capability to describe the material behaviour using either a unit cell or an RVE is found to be very similar, which empowers future research in employing this method.

In Chapter 10, an extension of the visco-elastic visco-plastic constitutive model is formulated to incorporate a damage variable that quantifies the accumulation of defects in the PC matrix. The computational aspects of the model, including constitutive state update and consistent tangent modulus, are thoroughly derived and asymptotic quadratic convergence rates are achieved. This supports successful linearisation and computational implementation of the damage extension. Three studies are conducted to evaluate different aspects of the explicit local damage model, leading to the following findings. The matrix damage mechanism plays a pivotal role in describing the behaviour of the softening regime. A reduction in the critical accumulated plastic strain leads to an earlier occurrence of material rupture and the softening regime becomes more pronounced. However, it has little effect on the yield stress of the material. In fact, the variation in yield stress primarily stems from the properties utilised in the cohesive elements, i.e., the matrix-particle interaction and respective debonding. This observation highlights a synergistic effect between the two models (cohesive elements and damage model), in capturing the material's behaviour. While it is only possible to conclude the qualitative influence of each model's properties on describing the PC/ABS blend's behaviour, without having a clear quantitative understanding of each damage mechanism in its response, it can be stated that only a combination of all the models presented throughout the dissertation allows for a realistic description of the PC/ABS blend.

Due to the significant computational costs associated with CPU time and memory requirements of the analyses, coupled with the limited time frame of a Master's dissertation and the ongoing lack of reliable experimental data, it

was not possible to determine the authentic parameters of the PPR cohesive zone model for the PC/ABS blend through numerical calibration techniques. Nevertheless, it is believed that this research has taken a substantial step towards achieving the primary focus of this dissertation, which is to enhance our understanding of the behaviour of the PC/ABS blend. Additionally, important foundations have been laid to address the existing gap in the literature, thereby empowering further research in the field. It is worth noting that the numerical tools and methodologies developed and presented in this dissertation have the potential for extension to other material classes, despite the primary focus on PC/ABS blends.

11.2 Future Research

In the present dissertation, various topics have been covered, but despite thorough coverage, the research is still far from complete. Therefore, the following paragraphs address additional challenges that should be addressed in future research.

Future research related to the present dissertation primarily focuses on the exact identification and physical significance of the four main properties of the PPR cohesive zone model (cohesive strengths and fracture toughness) and the new property introduced in the extension of the visco-elastic visco-plastic constitutive model (critical accumulated plastic strain). As observed, experimental tests and studies on the PC/ABS blend or particulate polymer blends regarding interface analysis are scarce and highly complex. Thus, future research will likely still involve numerical calibration techniques combined with analysing the material's true response under different loading states. While the present dissertation lays the groundwork for future research on this topic, it is important to highlight the increased calibration complexity due to the introduction of this new model and the synergetic effects between the two.

However, before conducting further studies, it is necessary to address the difficulties and challenges encountered. Firstly, the visco-elastic visco-plastic constitutive model properties for the PC and ABS bulk materials need to be further validated. To achieve this, the model should be calibrated to other loading states since the properties employed in the present study were only calibrated for a series of uniaxial compression tests. Secondly, it is crucial to acquire better experimental tests, both in terms of obtaining improved experimental curves and ensuring that the PC and ABS used in the test specimens for calibrating the bulk properties are the same as those used in

the PC/ABS blend employed for the multi-scale calibration process. Thirdly, it is important to reiterate the simplifications made in the alternative method employed to achieve more accurate results. By addressing these issues, the majority of problems affecting the results of the present study can be mitigated. Once all the properties have been determined, a parametric study on all damage mechanisms present in PC/ABS can be performed to analyse their predominance for different load cases.

Another interesting topic that warrants further research is the implementation of a non-local damage formulation instead of the currently employed local approach and a comparison between the two in describing the damage within the PC matrix. This would enable a more in-depth study of the dependence of finite element solutions on spatial discretisation due to damage localisation.

In order to speed up the analysis of the PC/ABS blends, the adoption of reduced-order models (ROM) should be considered. This would not only enable the simulation of a more comprehensive range of loading scenarios and blend ratios, which would help the understanding of their deformation behaviour, but also facilitate the design of new blends for specific engineering applications.

REFERENCES

Alfano, M., Furgiuele, F., Lubineau, G., and Paulino, G. H. (2011). Simulation of debonding in al/epoxy t-peel joints using a potential-based cohesive zone model. *Procedia Engineering*, 10:1760–1765. 11th International Conference on the Mechanical Behavior of Materials (ICM11).

Andrade, F., Andrade Pires, F., and Cesar de Sa, J. (2014). Consistent tangent operators for implicit non-local models of integral type. *Computers & Structures*, 141:59–73.

Andrade, F., de Sá, J. C., and Pires, F. A. (2011). A ductile damage nonlocal model of integral-type at finite strains: Formulation and numerical issues. *International Journal of Damage Mechanics*, 20(4):515–557.

Arruda, E. M. and Boyce, M. C. (1993a). Evolution of plastic anisotropy in amorphous polymers during finite straining. *International Journal of Plasticity*, 9(6):697–720.

Arruda, E. M. and Boyce, M. C. (1993b). A three-dimensional constitutive model for the large stretch behavior of rubber elastic materials. *Journal of the Mechanics and Physics of Solids*, 41(2):389–412.

Balandat, M., Karrer, B., Jiang, D. R., Daulton, S., Letham, B., Wilson, A. G., and Bakshy, E. (2020). Botorch: A framework for efficient monte-carlo bayesian optimization.

Barenblatt, G. (1962). The mathematical theory of equilibrium cracks in brittle fracture. volume 7 of *Advances in Applied Mechanics*, pages 55–129. Elsevier.

Bargmann, S., Klusemann, B., Markmann, J., Schnabel, J. E., Schneider, K., Soyarslan, C., and Wilmers, J. (2018). Generation of 3d representative volume elements for heterogeneous materials: A review. *Progress in Materials Science*, 96:322–384.

Bažant, Z. P. and Jirásek, M. (2002). Nonlocal integral formulations of plasticity and damage: Survey of progress. *Journal of Engineering Mechanics*, 128(11):1119–1149.

Bažant, Z. P. and Lin, F.-B. (1988). Non-local yield limit degradation. *International Journal for Numerical Methods in Engineering*, 26(8):1805–1823.

Bažant, Z. P. and Pijaudier-Cabot, G. (1988). Nonlocal Continuum Damage, Localization Instability and Convergence. *Journal of Applied Mechanics*, 55(2):287–293.

Belytschko, T., Liu, W. K., Moran, B., and Elkhodary, K. (2014). *Nonlinear Finite Elements for Continua and Structures*. John Wiley & Sons, Chichester, 2nd edition.

Benzeggagh, M. and Kenane, M. (1996). Measurement of mixed-mode delamination fracture toughness of unidirectional glass/epoxy composites with mixed-mode bending apparatus. *Composites Science and Technology*, 56(4):439–449.

Bertram, A. (2012). *Elasticity and Plasticity of Large Deformations*. Springer, 3rd edition.

Bonet, J. and Wood, R. D. (2008). *Nonlinear Continuum Mechanics for Finite Element Analysis*. Cambridge University Press, 2nd edition.

Bower, A. F. (2009). *Elasticity and Plasticity of Large Deformations*. CRC Press, 1st edition.

Brochu, E., Cora, V. M., and de Freitas, N. (2010). A tutorial on bayesian optimization of expensive cost functions, with application to active user modeling and hierarchical reinforcement learning.

Bucknall, C. B., Karpodinis, A., and Zhang, X. C. (1994). A model for particle cavitation in rubber-toughened plastics. *Journal of Materials Science*, 29:3377–3383.

Camacho, G. and Ortiz, M. (1996). Computational modelling of impact damage in brittle materials. *International Journal of Solids and Structures*, 33(20):2899–2938.

Carvalho Alves, A. F., Ferreira, B. P., and Andrade Pires, F. (to be submitted 2023). On the modeling of particle cavitation in rubber-toughened amorphous polymers: constitutive extension and fully implicit implementation.

Cerrone, A., Wawrzynek, P., Nonn, A., Paulino, G. H., and Ingraffea, A. (2014). Implementation and verification of the park-paulino-roesler cohesive zone model in 3d. *Engineering Fracture Mechanics*, 120:26–42.

Chandra, N., Li, H., Shet, C., and Ghonem, H. (2002). Some issues in the application of cohesive zone models for metal-ceramic interfaces. *International Journal of Solids and Structures*, 39(10):2827–2855.

Charalambides, P., Cao, H., Lund, J., and Evans, A. (1990). Development of a test method for measuring the mixed mode fracture resistance of bimaterial interfaces. *Mechanics of Materials*, 8(4):269–283.

Chiang, W.-Y. and Hwung, D.-S. (1987). Properties of polycarbonate/acrylonitrile-butadiene-styrene blends. *Polymer Engineering & Science*, 27(9):632–639.

Chun, J.-H., Maeng, K. S., and Suh, K. S. (1991). Miscibility and synergistic effect of impact strength in polycarbonate/abs blends. *Journal of Materials Science*, 26:5347–5352.

Coelho, R. P. C. (2022). A thermodynamically consistent multi-scale model and an efficient numerical framework for mechanically induced martensitic phase transformations. *Seminar - PRODEM, Faculty of Engineering of University of Porto*.

Coenen, E., Kouznetsova, V., and Geers, M. (2012). Novel boundary conditions for strain localization analyses in microstructural volume elements. *International Journal for Numerical Methods in Engineering*, 90(1):1–21.

De Borst, R. and Mühlhaus, H.-B. (1992). Gradient-dependent plasticity: Formulation and algorithmic aspects. *International Journal for Numerical Methods in Engineering*, 35(3):521–539.

de Carvalho, M. V. (2022). *Multi-Scale Modelling of Polycrystalline Materials: Slip Plasticity, Martensitic Transformation and Intergranular Fracture*. PhD thesis, Faculty of Engineering of University of Porto.

de Carvalho, M. V., de Bortoli, D., and Andrade Pires, F. M. (2022). Consistent modeling of the coupling between crystallographic slip and martensitic phase transformation for mechanically induced loadings. *International Journal for Numerical Methods in Engineering*, 123(14):3179–3236.

de Souza Neto, E. and Feijó, R. (2006). Variational foundations of multi-scale constitutive models of solid: Small and large strain kinematical formulation. *LNCC R&D Report*.

de Souza Neto, E. A., Peric, D., and Owen, D. R. J. (2008). *Computational Methods for Plasticity: Theory and Applications*. John Wiley & Sons, Chichester.

Despringre, N., Chemisky, Y., Bonnay, K., and Meraghni, F. (2016). Micromechanical modeling of damage and load transfer in particulate composites with partially debonded interface. *Composite Structures*, 155:77–88.

Drugan, W. and Willis, J. (1996). A micromechanics-based nonlocal constitutive equation and estimates of representative volume element size for elastic composites. *Journal of the Mechanics and Physics of Solids*, 44(4):497–524.

Dugdale, D. (1960). Yielding of steel sheets containing slits. *Journal of the Mechanics and Physics of Solids*, 8(2):100–104.

Fang, Q.-Z., Wang, T., Beom, H., and Zhao, H. (2009). Rate-dependent large deformation behavior of pc/abs. *Polymer*, 50(1):296–304.

Ferreira, B. P. (2022). *Towards Data-driven Multi-scale Optimization of Thermoplastic Blends: Microstructural Generation, Constitutive Development and Clustering-Based Reduced-Order Modeling*. PhD thesis, Faculty of Engineering of University of Porto.

Ferreira, B. P., Carvalho Alves, A. F., and Andrade Pires, F. (2023). An efficient finite strain constitutive model for amorphous thermoplastics: Fully implicit computational implementation and optimization-based parameter calibration. *Computers & Structures*, 281:107007.

Ferreira, B. P., Vila-Chã, J. L., and Pires, F. A. (2022). An adaptive multi-temperature isokinetic method for the rve generation of particle reinforced heterogeneous materials, part ii: Numerical assessment and statistical analysis. *Mechanics of Materials*, 165:104068.

Forest, S. and Lorentz, E. (2004). Localization phenomena and regularization methods. In Besson, J., editor, *Local approach to fracture*, Ecole d'été "Mécanique de l'endommagement et approche locale de la rupture" (MEALOR), juillet 2004, pages 311–371. Les presses de l'ecole des mines de paris.

Geubelle, P. H. and Baylor, J. S. (1998). Impact-induced delamination of composites: a 2d simulation. *Composites Part B: Engineering*, 29(5):589–602.

Gitman, I., Askes, H., and Sluys, L. (2007). Representative volume: Existence and size determination. *Engineering Fracture Mechanics*, 74(16):2518–2534.

Graham, S. and Yang, N. (2003). Representative volumes of materials based on microstructural statistics. *Scripta Materialia*, 48(3):269–274.

Greco, R. (1996). Polycarbonate toughening by abs. In *Advanced Routes for Polymer Toughening*, chapter 9. Elsevier Science, The Netherlands.

Greco, R. (1999). "natural" polymer alloys: Pc/abs systems. In *Polymer Blends and Alloys*, page 289–330. CRC Press.

Greco, R., Astarita, M. F., Dong, L., and Sorrentino, A. (1994). Polycarbonate/abs blends: Processability, thermal properties, and mechanical and impact behavior. *Advances in Polymer Technology*, 13(4):259–274.

Grimal, Q., Raum, K., Gerisch, A., and Laugier, P. (2011). A determination of the minimum size of representative volume elements for the prediction of cortical bone elastic properties. *Biomechanics and modeling in mechanobiology*, 10:925–37.

Guedes, J. M. and Kikuchi, N. (1990). Preprocessing and postprocessing for materials based on the homogenization method with adaptive finite element methods. *Computer Methods in Applied Mechanics and Engineering*, 83(2):143–198.

Gupta, A. (2002a). Improved symbolic and numerical factorization algorithms for unsymmetric sparse matrices. *SIAM Journal on Matrix Analysis and Applications*, 24(2):529–552.

Gupta, A. (2002b). Wsmp: Watson sparse matrix package part ii - direct solution of general sparse systems.

Hashin, Z. (1983). Analysis of composite materials-a survey. *Journal of Applied Mechanics*, 50(3):481–505.

Hassan, A. and Wong, Y. J. (2005). Mechanical properties of high impact abs/pc blends - effect of blend ratio.

Haupt, P. (2002). *Continuum Mechanics and Theory of Materials*. Springer, 2nd edition.

Hill, R. (1963). Elastic properties of reinforced solids: Some theoretical principles. *Journal of the Mechanics and Physics of Solids*, 11(5):357–372.

Holzapfel, G. A. (2000). *Nonlinear Solid Mechanics: A Continuum Approach for Engineering*. John Wiley & Sons, Chichester.

Hosseini, S. A., Saber-Samandari, S., and Maleki Moghadam, R. (2017). Multiscale modeling of interface debonding effect on mechanical properties of nanocomposites. *Polymer Composites*, 38(4):789–796.

Hund, J. (2022). *Characterisation and modelling of PC/ABS blends*. KIT Scientific Publishing, Karlsruhe, 2 edition.

Hund, J. and Seelig, T. (2019). Application of different plasticity models to pc/abs blends within micromechanical approaches. *PAMM*, 19(1):e201900093.

Inberg, J. P. F. (2001). *Fracture of Polycarbonate/ABS Blends*. PhD thesis, University of Twente.

Ishikawa, M. (1995). Stability of plastic deformation and toughness of polycarbonate blended with poly(acrylonitrile-butadiene-styrene) copolymer. *Polymer*, 36(11):2203–2210.

Janarthanan, V., Stein, R. S., and Garrett, P. D. (1993). Effect of oligomers and acrylonitrile content on the interfacial adhesion between pc and san. *Journal of Polymer Science Part B: Polymer Physics*, 31(13):1995–2001.

Jirásek, M. (1998). Nonlocal models for damage and fracture: Comparison of approaches. *International Journal of Solids and Structures*, 35(31):4133–4145.

Jirásek, M. and Rolshoven, S. (2003). Comparison of integral-type nonlocal plasticity models for strain-softening materials. *International Journal of Engineering Science*, 41(13):1553–1602. Damage and failure analysis of materials.

Jirásek, M. and Patzák, B. (2002). Consistent tangent stiffness for nonlocal damage models. *Computers & Structures*, 80(14):1279–1293.

Kanit, T., Forest, S., Galliet, I., Mounoury, V., and Jeulin, D. (2003). Determination of the size of the representative volume element for random composites: statistical and numerical approach. *International Journal of Solids and Structures*, 40(13):3647–3679.

Khan, M. M., Liang, R., Gupta, R., and Agarwal, S. (2005). Rheological and mechanical properties of abs/pc blends. *Korea-Australia rheology journal*, 17.

Kim, J. H. and Kim, C. K. (2003). Changes in the interfacial properties of pc/san blends with compatibilizer. *Journal of Applied Polymer Science*, 89(10):2649–2656.

Kouznetsova, V., Geers, M., and Brekelmans, W. (2004). Multi-scale second-order computational homogenization of multi-phase materials: a nested finite element solution strategy. *Computer Methods in Applied Mechanics and Engineering*, 193(48):5525–5550. Advances in Computational Plasticity.

Krishnan, S. (2020). *Modeling and Characterization of Interfacial Stress Transfer in Mechanoluminescent Smart Particulate Polymer Composites*. PhD thesis, The Ohio State University.

Lemaitre, J. (1985). Coupled elasto-plasticity and damage constitutive equations. *Computer Methods in Applied Mechanics and Engineering*, 51(1):31–49.

Lim, J. C., Cho, K. Y., and Park, J.-K. (2008). Weld line characteristics of pc/abs blend. ii. effect of reactive compatibilizer. *Journal of Applied Polymer Science*, 108(6):3632–3643.

Lin Ye (1988). Role of matrix resin in delamination onset and growth in composite laminates. *Composites Science and Technology*, 33(4):257–277.

Lombardo, B. S., Keskkula, H., and Paul, D. R. (1994). Influence of abs type on morphology and mechanical properties of pc/abs blends. *Journal of Applied Polymer Science*, 54(11):1697–1720.

Macedo, F. P. B. (to be submitted 2023). *Numerical Modelling of Amorphous Polymers: Formulation and Implementation*. PhD thesis, Faculty of Engineering of University of Porto.

MARK, J. E. (1999). *Polymer Data Handbook*.

Mirkhalaf, S., Andrade Pires, F., and Simoes, R. (2016). Determination of the size of the representative volume element (rve) for the simulation of heterogeneous polymers at finite strains. *Finite Elements in Analysis and Design*, 119:30–44.

Mosler, J. and Scheider, I. (2011). A thermodynamically and variationally consistent class of damage-type cohesive models. *Journal of the Mechanics and Physics of Solids*, 59(8):1647–1668.

Nafar Dastgerdi, J., Anbarlooie, B., Marzban, S., and Marquis, G. (2015). Mechanical and real microstructure behavior analysis of particulate-reinforced nanocomposite considering debonding damage based on cohesive finite element method. *Composite Structures*, 122:518–525.

Nafar Dastgerdi, J., Marquis, G., and Salimi, M. (2014). Micromechanical modeling of nanocomposites considering debonding and waviness of reinforcements. *Composite Structures*, 110:1–6.

Needleman, A. (1987). A Continuum Model for Void Nucleation by Inclusion Debonding. *Journal of Applied Mechanics*, 54(3):525–531.

Needleman, A. (1988). Material rate dependence and mesh sensitivity in localization problems. *Computer Methods in Applied Mechanics and Engineering*, 67(1):69–85.

Nemat-Nasser, S. and Hori, M. (1993). *Micromechanics: Overall Properties of Heterogeneous Materials*. Elsevier.

Nguyen, V. P. (2014). An open source program to generate zero-thickness cohesive interface elements. *Advances in Engineering Software*, 74:27–39.

Nigam, I., Nigam, D., and Mathur, G. N. (2005). Effect of rubber content of abs on properties of pc/abs blends. i. rheological, mechanical, and thermal properties. *Polymer-Plastics Technology and Engineering*, 44(5):815–832.

Ortiz, M. and Pandolfi, A. (1999). Finite-deformation irreversible cohesive element for three-dimensional crack-propagation analysis. *International Journal for Numerical Methods in Engineering - INT J NUMER METHOD ENG*, 44:1267–1282.

Park, K. (2009). *Potential-Based Fracture Mechanics Using Cohesive Zone and Virtual Internal Bond Modeling*. PhD thesis, University of Illinois at Urbana-Champaign.

Park, K. and Paulino, G. H. (2012). Computational implementation of the ppr potential-based cohesive model in abaqus: Educational perspective. *Engineering Fracture Mechanics*, 93:239–262.

Park, K. and Paulino, G. H. (2013). Cohesive Zone Models: A Critical Review of Traction-Separation Relationships Across Fracture Surfaces. *Applied Mechanics Reviews*, 64(6). 060802.

Park, K., Paulino, G. H., and Roesler, J. R. (2009). A unified potential-based cohesive model of mixed-mode fracture. *Journal of the Mechanics and Physics of Solids*, 57(6):891–908.

Peerlings, R., Geers, M., de Borst, R., and Brekelmans, W. (2001). A critical comparison of nonlocal and gradient-enhanced softening continua. *International Journal of Solids and Structures*, 38(44):7723–7746.

PEERLINGS, R. H. J., DE BORST, R., BREKELMANS, W. A. M., and DE VREE, J. H. P. (1996). Gradient enhanced damage for quasi-brittle materials. *International Journal for Numerical Methods in Engineering*, 39(19):3391–3403.

Phu Nguyen, V., Lloberas-Valls, O., Stroeven, M., and Johannes Sluys, L. (2010). On the existence of representative volumes for softening quasi-brittle materials - a failure zone averaging scheme. *Computer Methods in Applied Mechanics and Engineering*, 199(45):3028–3038.

Popp, A., Gitterle, M., Gee, M. W., and Wall, W. A. (2010). A dual mortar approach for 3d finite deformation contact with consistent linearization. *International Journal for Numerical Methods in Engineering*, 83(11):1428–1465.

Popp, A., Wohlmuth, B. I., Gee, M. W., and Wall, W. A. (2012). Dual quadratic mortar finite element methods for 3d finite deformation contact. *SIAM Journal on Scientific Computing*, 34(4):B421–B446.

Reis, F., Rodrigues Lopes, I., Andrade Pires, F., and Andrade, F. (2018). Microscale analysis of heterogeneous ductile materials with nonlocal damage models of integral type. *Computers & Structures*, 201:37–57.

Reis, F. J. d. P. (2014). *Multi-Scale Modelling and Analysis of Heterogeneous Solids at Finite Strains*. PhD thesis, Faculty of Engineering of University of Porto.

Rodrigues Lopes, I. A., Ferreira, B. P., and Andrade Pires, F. M. (2021). On the efficient enforcement of uniform traction and mortar periodic boundary conditions in computational homogenisation. *Computer Methods in Applied Mechanics and Engineering*, 384:113930.

Scheider, I. (2001). Cohesive model for crack propagation analyses of structures with elastic-plastic material behavior foundations and implementation. *GKSS research center, Geesthacht*.

Schneider, K. (2008). *Mechanical Properties of Polymers at Surfaces and Interfaces*, pages 139–160. Springer Berlin Heidelberg, Berlin, Heidelberg.

Sebsadji, S. and Chouicha, K. (2012). Determining periodic representative volumes of concrete mixtures based on the fractal analysis. *International Journal of Solids and Structures*, 49(21):2941–2950.

Seelig, T. and van der Giessen, E. (2002). Localized plastic deformation in ternary polymer blends. *International Journal of Solids and Structures*, 39(13):3505–3522.

Seelig, T. and Van der Giessen, E. (2007). Effects of microstructure on crack tip fields and fracture toughness in pc/abs polymer blends. *International Journal of Fracture*, 145.

Semba, T. and Hamada, H. (1999). Weld line strength in pc/abs injection moldings. *International Polymer Processing*, 14(4):365–369.

Shan, Z. and Gokhale, A. M. (2002). Representative volume element for non-uniform micro-structure. *Computational Materials Science*, 24(3):361–379.

Smit, R., Brekelmans, W., and Meijer, H. (2000). Predictive modelling of the properties and toughness of polymeric materials - part i why is polystyrene brittle and polycarbonate tough? *Journal of Materials Science*, 35:2855–2867.

Speirs, D. C. D. (2007). *Characterisation of Materials with Hyperelastic Microstructures through Computational Homogenisation and Optimisation Methods*. PhD thesis, Swansea University.

Stamm, M. (2008). *Polymer Surface and Interface Characterization Techniques*, pages 1–16. Springer Berlin Heidelberg, Berlin, Heidelberg.

Suarez, H., Barlow, J. W., and Paul, D. R. (1984). Mechanical properties of abs/polycarbonate blends. *Journal of Applied Polymer Science*, 29(11):3253–3259.

Tadmor, E. B., Miller, R. E., and Elliott, R. S. (2011). *Continuum Mechanics and Thermodynamics: From Fundamental Concepts to Governing Equations*. Cambridge University Press.

Tan, Z., Xu, X., Sun, S., Zhou, C., Ao, Y., Zhang, H., and Han, Y. (2006). Influence of rubber content in abs in wide range on the mechanical properties and morphology of pc/abs blends with different composition. *Polymer Engineering & Science*, 46(10):1476–1484.

Terada, K., Hori, M., Kyoya, T., and Kikuchi, N. (2000). Simulation of the multi-scale convergence in computational homogenization approaches. *International Journal of Solids and Structures*, 37(16):2285–2311.

Travesa, A., Balanzat, J., de Girona. Departament d'Enginyeria Mecànica i de la Construcció Industrial, U., and de Castro Camanho, P. (2006). *Simulation of Delamination in Composites Under Quasi-static and Fatigue Loading Using Cohesive Zone Models*. Universitat de Girona.

Tvergaard, V. (1990). Effect of fibre debonding in a whisker-reinforced metal. *Materials Science and Engineering: A*, 125(2):203–213.

Tvergaard, V. (1991). Micromechanical modelling of fibre debonding in a metal reinforced by short fibres. In Dvorak, G. J., editor, *Inelastic Deformation of Composite Materials*, pages 99–111, New York, NY. Springer New York.

Tvergaard, V. and Hutchinson, J. W. (1992). The relation between crack growth resistance and fracture process parameters in elastic-plastic solids. *Journal of the Mechanics and Physics of Solids*, 40(6):1377–1397.

Vargas, R., Neggers, J., Canto, R., Rodrigues, J., and Hild, F. (2019). Analysis of a castable refractory using the wedge splitting test and cohesive zone model. *Journal of the European Ceramic Society*, 39(13):3903–3914.

Vila-Chã, J. L., Ferreira, B. P., and Pires, F. A. (2021). An adaptive multi-temperature isokinetic method for the rve generation of particle reinforced heterogeneous materials, part i: Theoretical formulation and computational framework. *Mechanics of Materials*, 163:104069.

Wang, H., Zhang, Y., Huang, Z., Tang, Z., Wang, Y., and Zhou, H. (2018). Establishment and comparison of four constitutive relationships of PC/ABS from low to high uniaxial strain rates. *Mechanics of Time-Dependent Materials*, 22(4):457–481.

Wang, H., Zhou, H., Huang, Z., Zhang, Y., Qiao, H., and Yu, Z. (2016). Experimental investigation and modeling of the mechanical behavior of pc/abs during monotonic and cyclic loading. *Polymer Testing*, 50:216–223.

Watanabe, I. and Terada, K. (2010). A method of predicting macroscopic yield strength of polycrystalline metals subjected to plastic forming by micro-macro de-coupling scheme. *International Journal of Mechanical Sciences*, 52(2):343–355.

Wildes, G., Keskkula, H., and Paul, D. (1999). Fracture characterization of pc/abs blends: effect of reactive compatibilization, abs type and rubber concentration. *Polymer*, 40(25):7089–7107.

Wriggers, P. (2008). *Nonlinear Finite Element Method*. Springer, 1st edition.

Xu, D.-B., Hui, C.-Y., Kramer, E., and Creton, C. (1991). A micromechanical model of crack growth along polymer interfaces. *Mechanics of Materials*, 11(3):257–268.

Xu, X. and Needleman, A. (1994). Numerical simulation of fast crack growth in brittle solids. *Journal of the Mechanics and Physics of Solids*, 42:1397–1434.

Zhang, P., Karimpour, M., Balint, D., and Lin, J. (2012). Cohesive zone representation and junction partitioning for crystal plasticity analyses. *International Journal for Numerical Methods in Engineering*, 92(8):715–733.

Zienkiewicz, O., Taylor, R., and Zhu, J. (2013). *The Finite Element Method: Its Basis and Fundamentals*. Butterworth-Heinemann, 7th edition.

Zienkiewicz, O. C., Taylor, R. L., and Fox, D. (2014). *The Finite Element Method for Solid and Structural Mechanics*. Butterworth-Heinemann, 7th edition.

CONFERENCE TALKS

Amaro, A. D. C., Alves, A. F. C., Carvalho, M. V., and Andrade, F. M. (2023a). Numerical analysis of the impact of interface modeling on the behavior of pc/abs blends. 5th Doctoral Congress in Engineering (DCE23), Porto, Portugal, June, 2023.

Amaro, A. D. C., Alves, A. F. C., Carvalho, M. V., Ferreira, B. P., and Andrade, F. M. (2023b). On the modeling of the interfaces in pc/abs ternary blends. ECCOMAS 7th Young Investigators Conference (YIC23), Porto, Portugal, June, 2023.

Page intentionally left blank

Appendixes

APPENDIX A

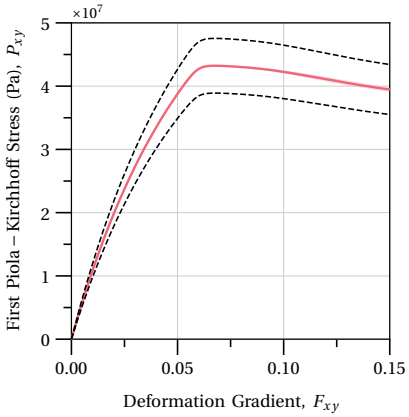
REPRESENTATIVE VOLUME ELEMENT SIZE

This appendix provides supplementary results to demonstrate the data and conclusions presented in Chapter 5. It includes the average response and corresponding standard deviation (shaded) for five samples of each size (represented in red), along with the pre-defined 10% limit of standard deviation (indicated in black). Additionally, due to the application of high deformation gradients, certain combinations could not reach these high values for all samples. As a result, the average response of only three samples is also displayed (shown in blue).

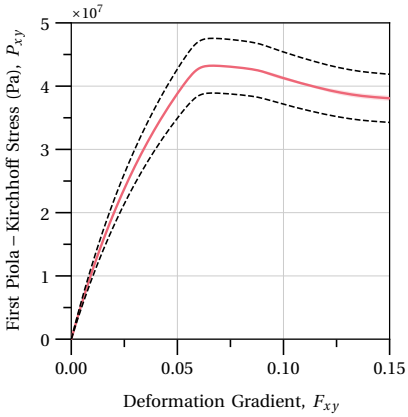
A.1 Two-dimensional RVEs

Shear across *xy*

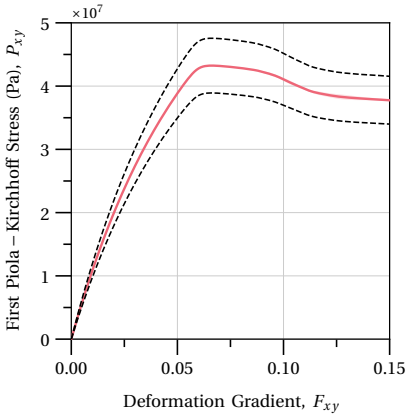
- 10% volume fraction - linear boundary condition



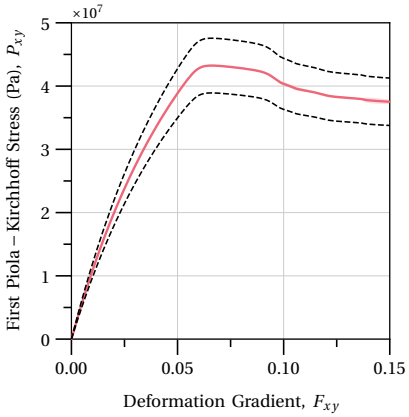
(a) 10 µm



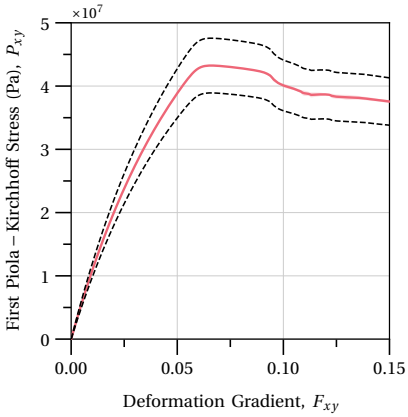
(b) 25 µm



(c) 50 µm



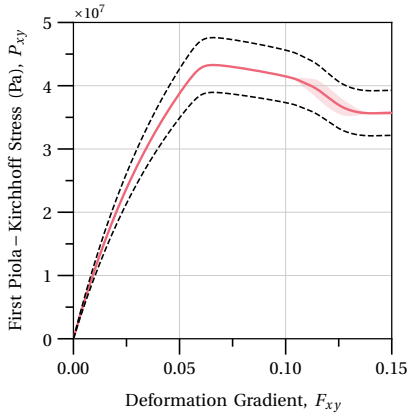
(d) 75 µm



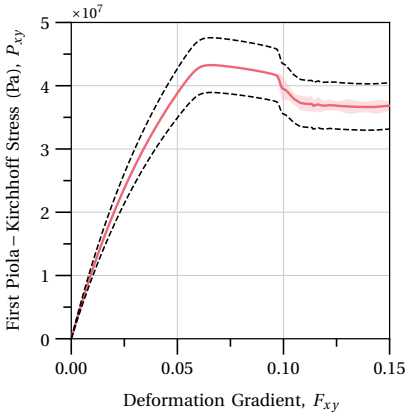
(e) 100 µm

Figure A.1: Homogenised First Piola Kirchhoff shear stress, P_{xy}, for different RVE sizes with 10% volume fraction and linear boundary condition. Shaded bounds: standard deviation; and dashed line: standard deviation 10% limit.

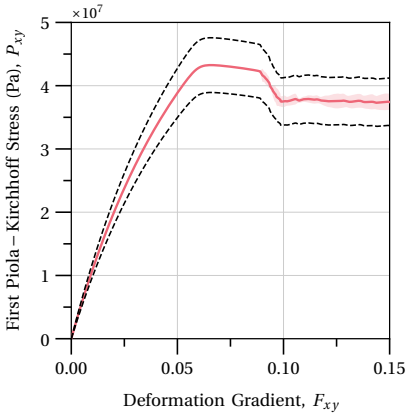
- 10% volume fraction - uniform boundary condition



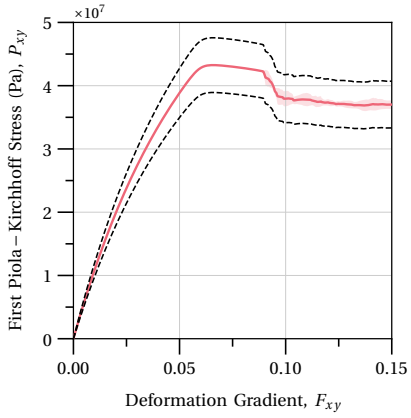
(a) 10 µm



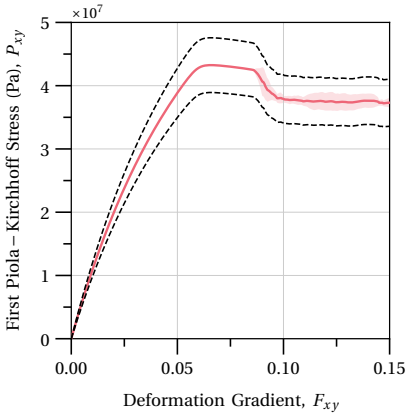
(b) 25 µm



(c) 50 µm



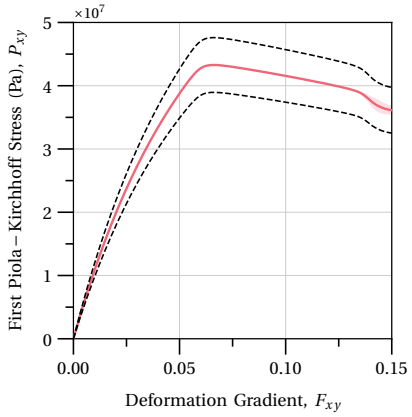
(d) 75 µm



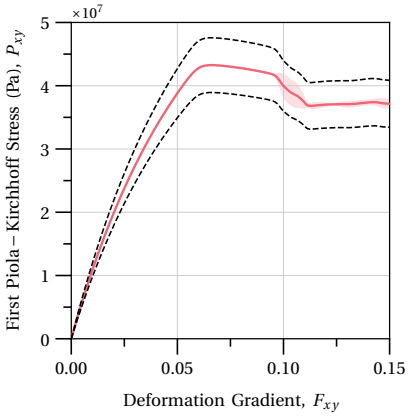
(e) 100 µm

Figure A.2: Homogenised First Piola Kirchhoff shear stress, P_{xy}, for different RVE sizes with 10% volume fraction and uniform boundary condition. Shaded bounds: standard deviation; and dashed line: standard deviation 10% limit.

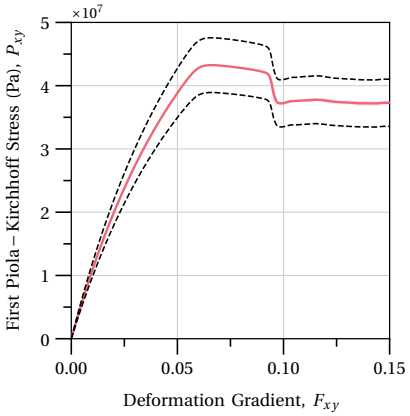
- 10% volume fraction - periodic boundary condition



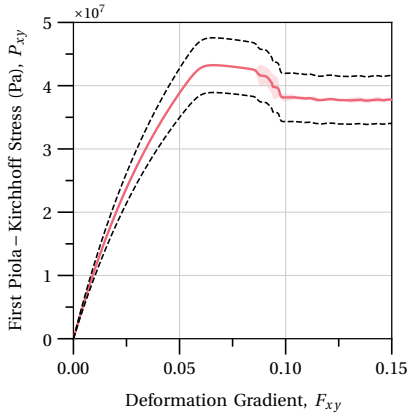
(a) 10 µm



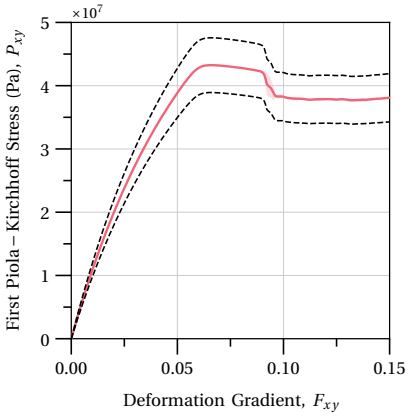
(b) 25 µm



(c) 50 µm



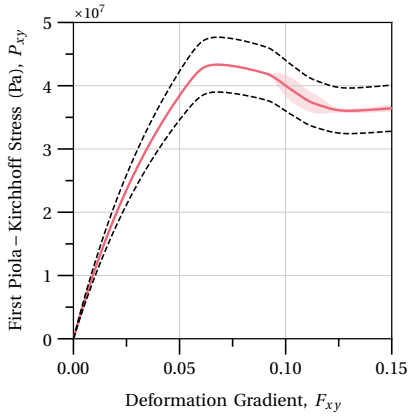
(d) 75 µm



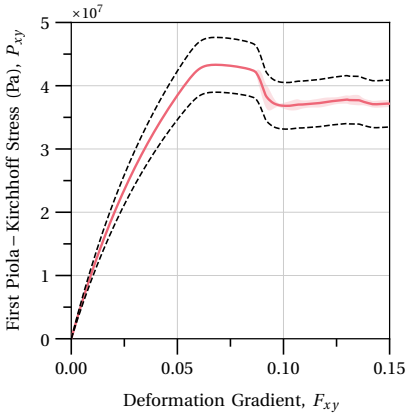
(e) 100 µm

Figure A.3: Homogenised First Piola Kirchhoff shear stress, P_{xy}, for different RVE sizes with 10% volume fraction and periodic boundary condition. Shaded bounds: standard deviation; and dashed line: standard deviation 10% limit.

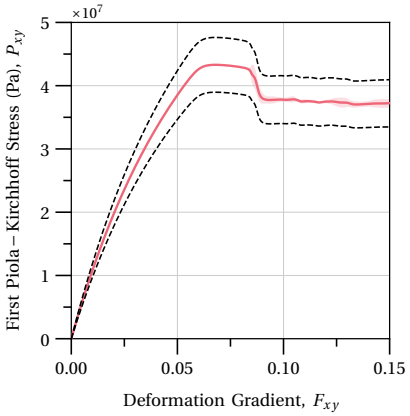
- 20% volume fraction - periodic boundary condition



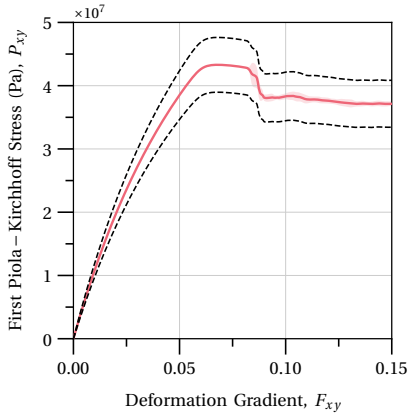
(a) 10 µm



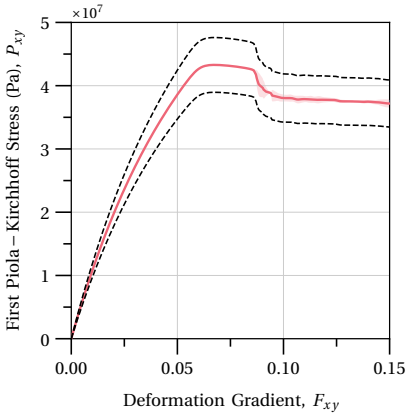
(b) 25 µm



(c) 50 µm



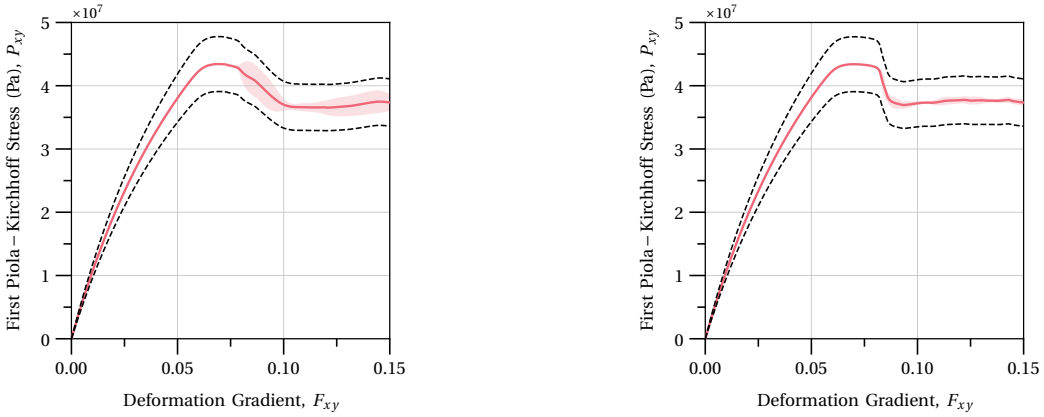
(d) 75 µm



(e) 100 µm

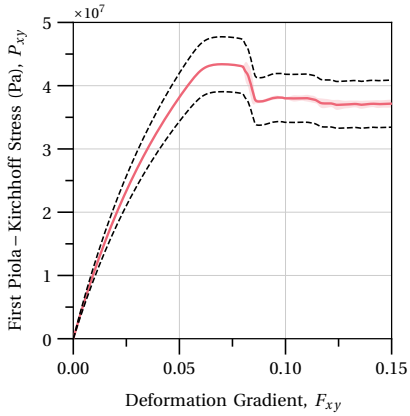
Figure A.4: Homogenised First Piola Kirchhoff shear stress, P_{xy}, for different RVE sizes with 20% volume fraction and periodic boundary condition. Shaded bounds: standard deviation; and dashed line: standard deviation 10% limit.

- 30% volume fraction - periodic boundary condition

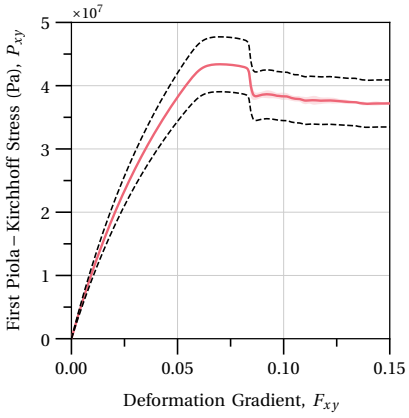


(a) 10 µm

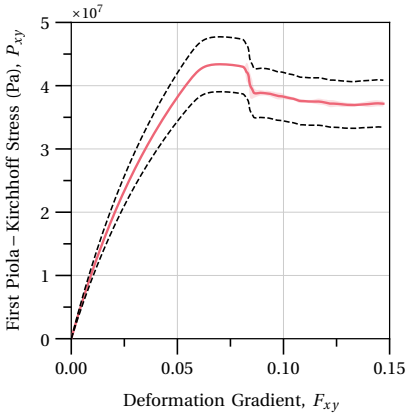
(b) 25 µm



(c) 50 µm



(d) 75 µm

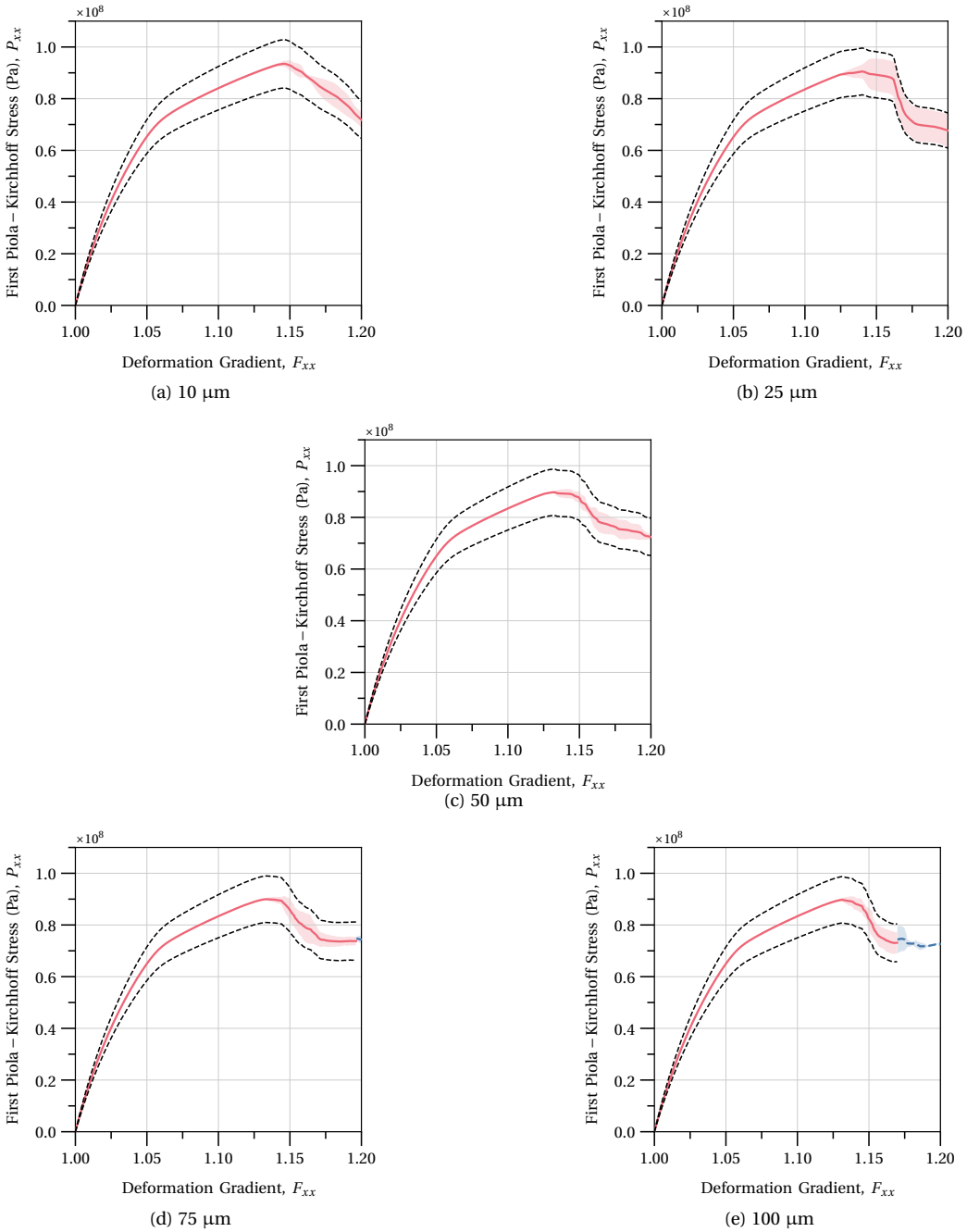


(e) 100 µm

Figure A.5: Homogenised First Piola Kirchhoff shear stress, P_{xy}, for different RVE sizes with 30% volume fraction and periodic boundary condition. Shaded bounds: standard deviation; and dashed line: standard deviation 10% limit.

Uniaxial loading along *xx*

- 10% volume fraction - periodic boundary condition



(a) 10 µm (b) 25 µm

(c) 50 µm

(d) 75 µm (e) 100 µm

Figure A.6: Homogenised First Piola Kirchhoff shear stress, P_{xx}, for different RVE sizes with 10% volume fraction and periodic boundary condition. Shaded bounds: standard deviation; black dashed line: standard deviation 10% limit; red data: 5 samples; and blue data: 3 samples.

- 20% volume fraction - periodic boundary condition

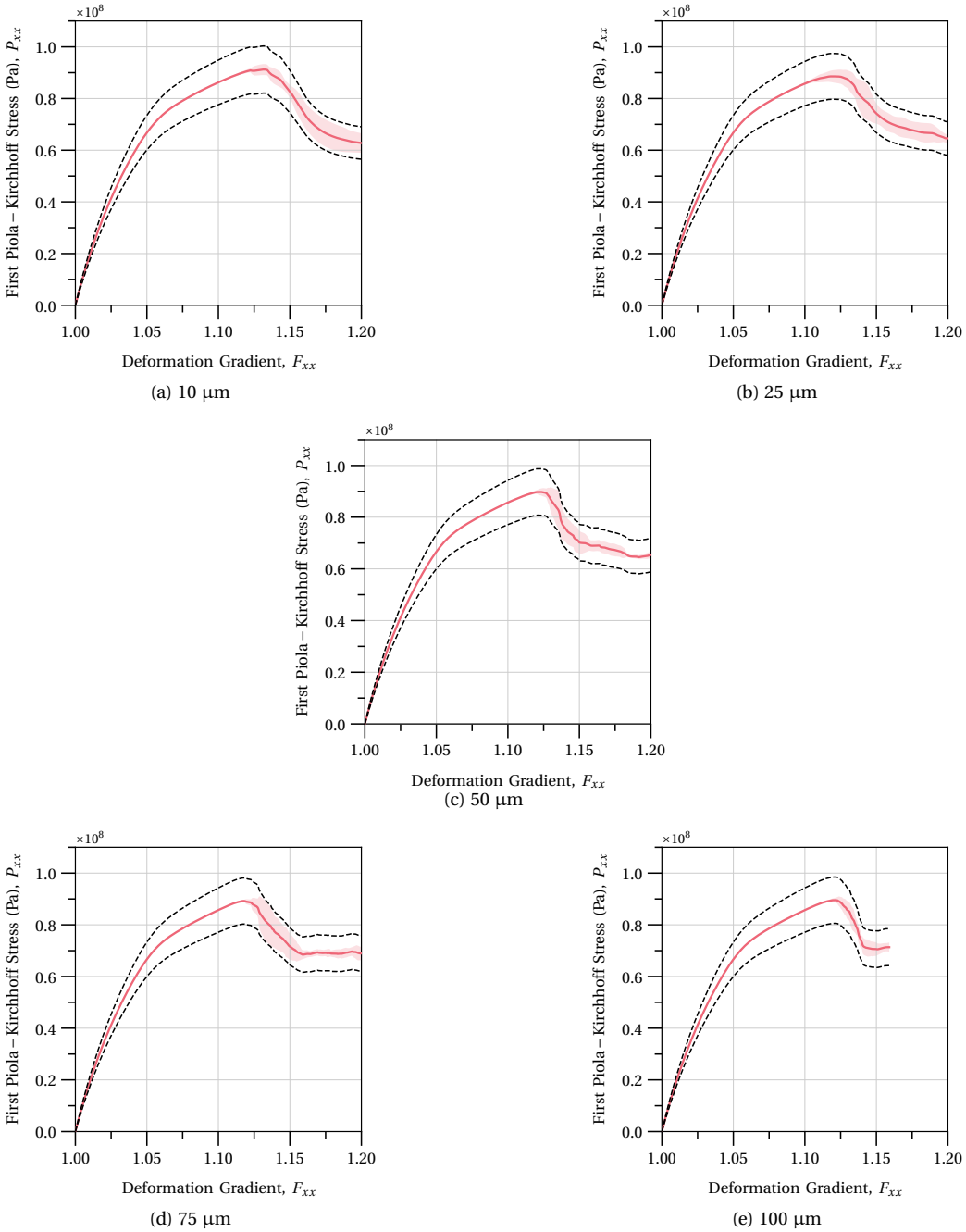
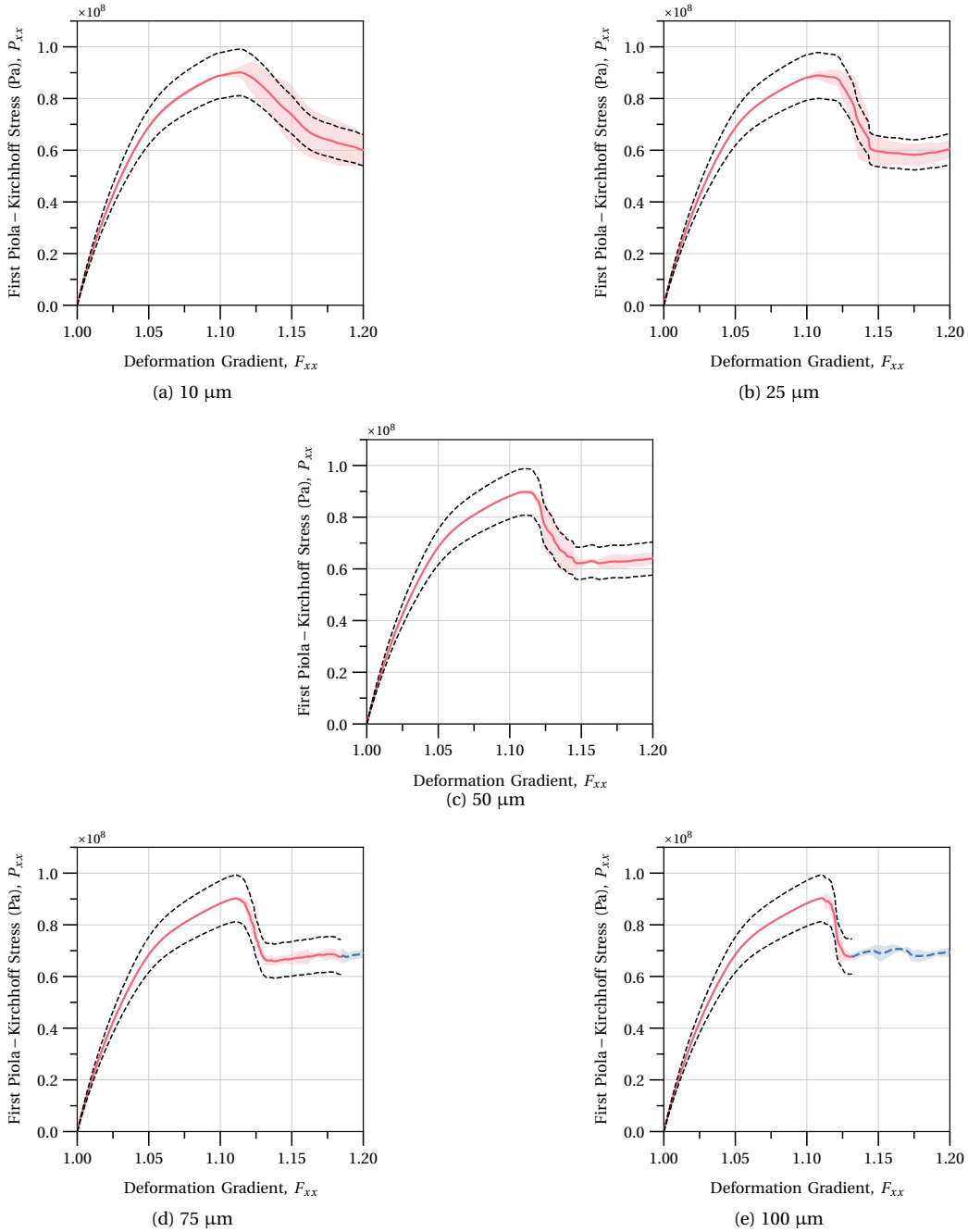


Figure A.7: Homogenised First Piola Kirchhoff shear stress, P_{xx}, for different RVE sizes with 20% volume fraction and periodic boundary condition. Shaded bounds: standard deviation; and dashed line: standard deviation 10% limit.

- 30% volume fraction - periodic boundary condition



(a) 10 µm

(b) 25 µm

(c) 50 µm

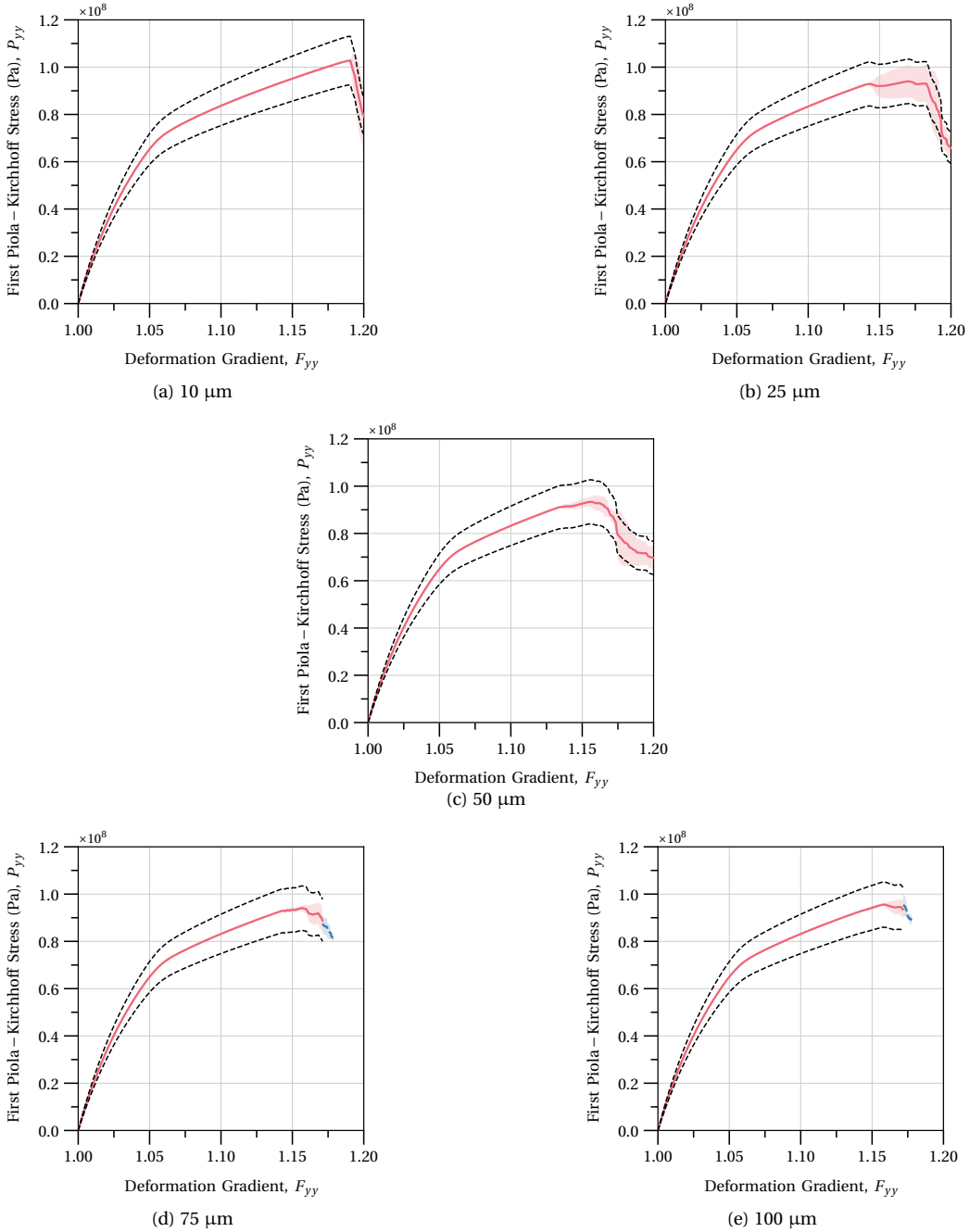
(d) 75 µm

(e) 100 µm

Figure A.8: Homogenised First Piola Kirchhoff shear stress, P_{xx}, for different RVE sizes with 30% volume fraction and periodic boundary condition. Shaded bounds: standard deviation; black dashed line: standard deviation 10% limit; red data: 5 samples; and blue data: 3 samples.

Uniaxial loading along *yy*

- 10% volume fraction - periodic boundary condition



(a) 10 µm

(b) 25 µm

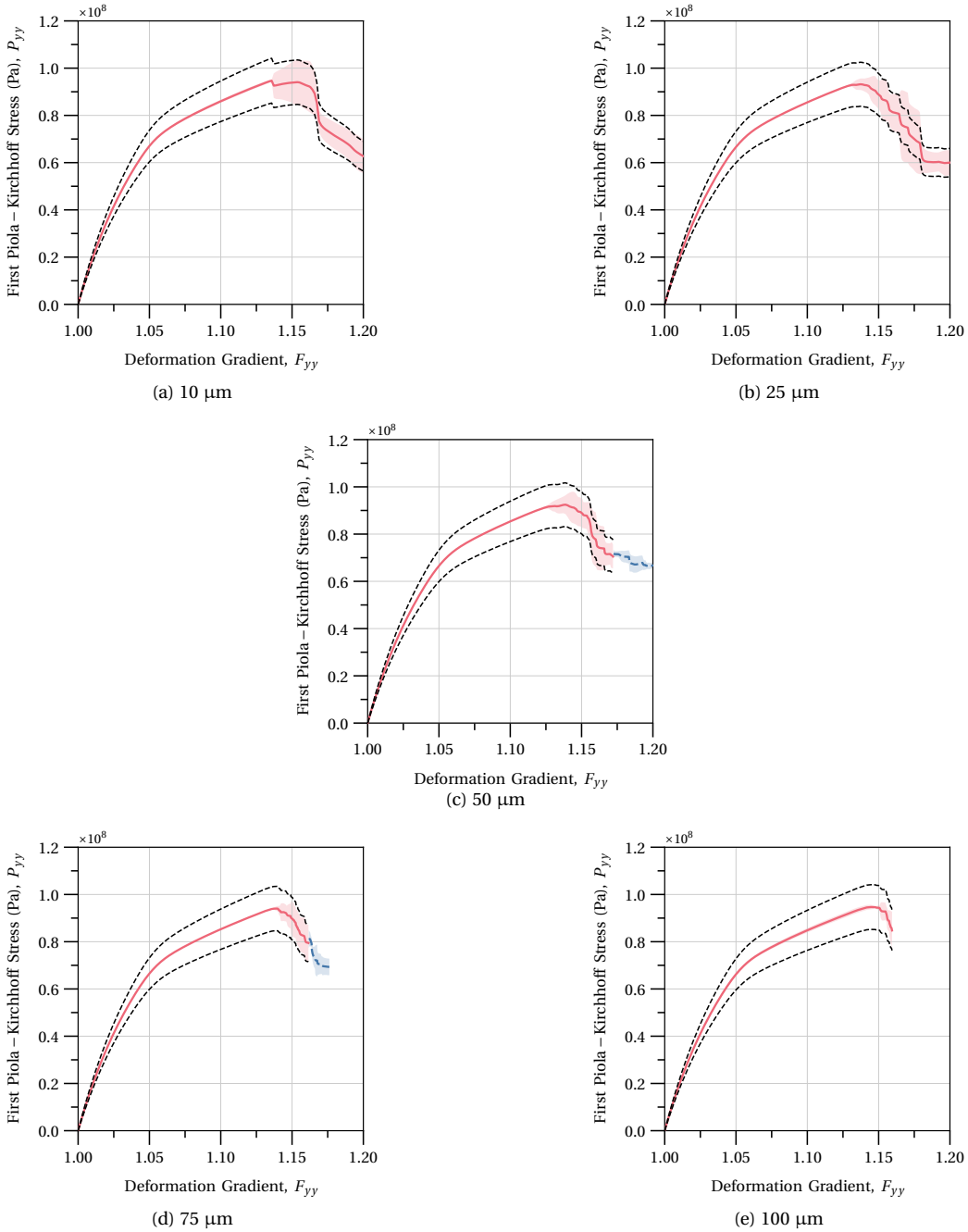
(c) 50 µm

(d) 75 µm

(e) 100 µm

Figure A.9: Homogenised First Piola Kirchhoff shear stress, P_{yy}, for different RVE sizes with 10% volume fraction and periodic boundary condition. Shaded bounds: standard deviation; black dashed line: standard deviation 10% limit; red data: 5 samples; and blue data: 3 samples.

- 20% volume fraction - periodic boundary condition



(a) 10 µm

(b) 25 µm

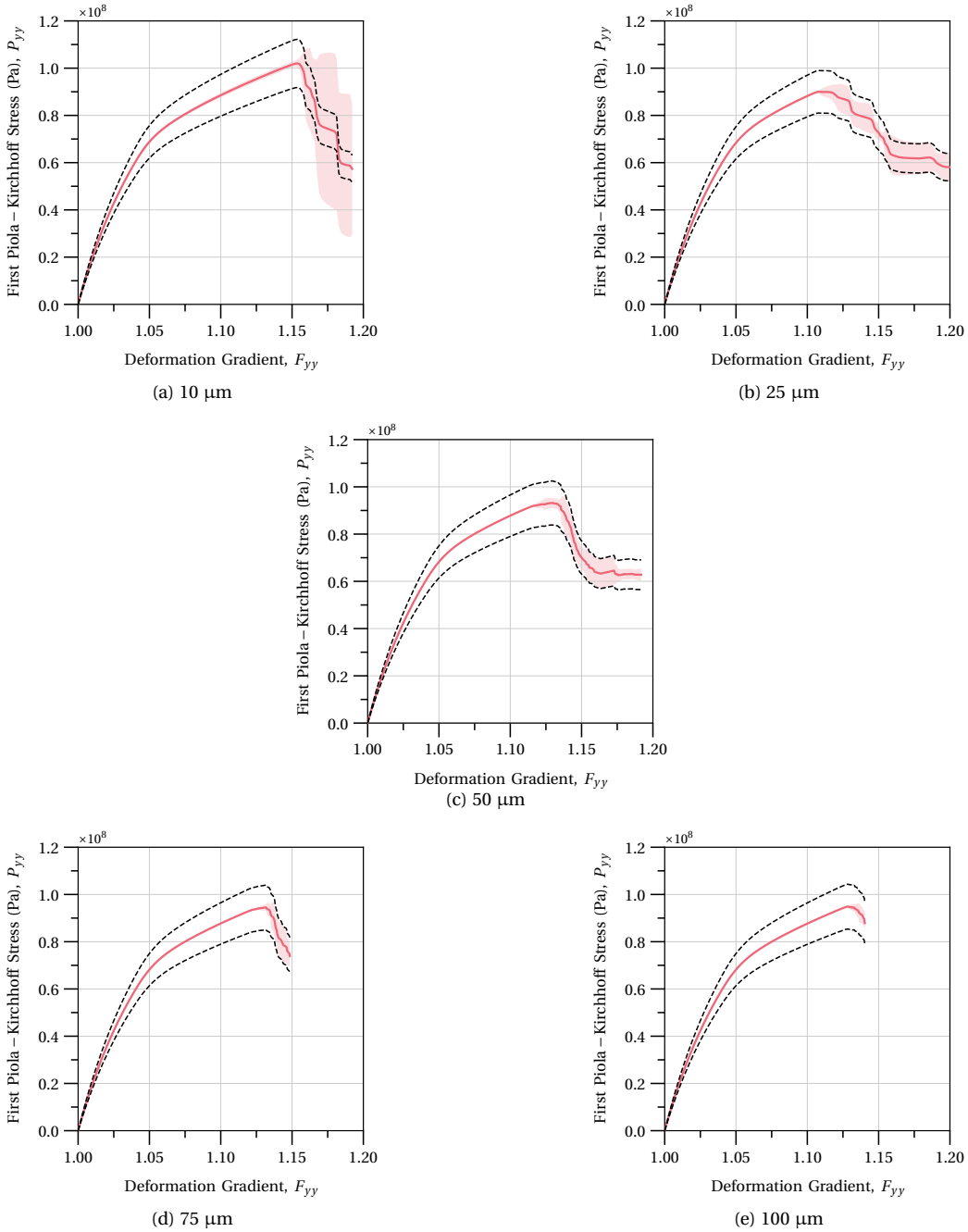
(c) 50 µm

(d) 75 µm

(e) 100 µm

Figure A.10: Homogenised First Piola Kirchhoff shear stress, P_{yy}, for different RVE sizes with 20% volume fraction and periodic boundary condition. Shaded bounds: standard deviation; black dashed line: standard deviation 10% limit; red data: 5 samples; and blue data: 3 samples.

- 30% volume fraction - periodic boundary condition



(a) 10 µm

(b) 25 µm

(c) 50 µm

(d) 75 µm

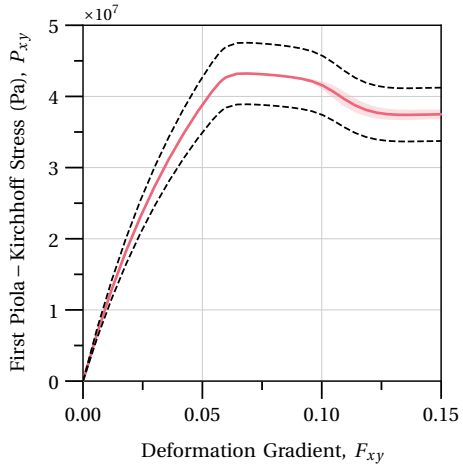
(e) 100 µm

Figure A.11: Homogenised First Piola Kirchhoff shear stress, P_{yy}, for different RVE sizes with 30% volume fraction and periodic boundary condition. Shaded bounds: standard deviation; and dashed line: standard deviation 10% limit.

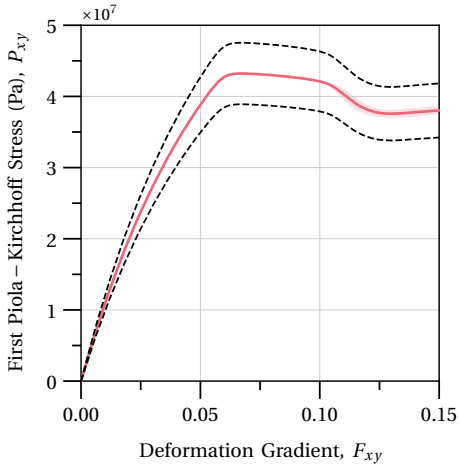
A.2 Three-dimensional RVEs

Shear across *xy*

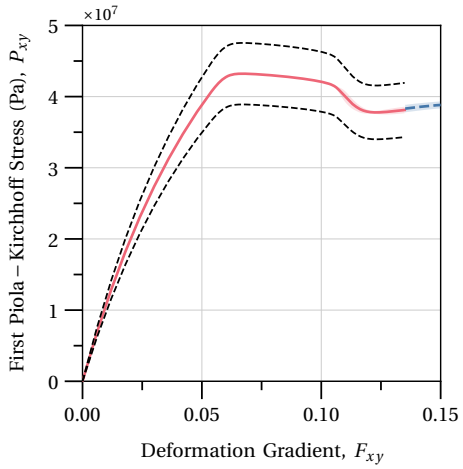
- 10% volume fraction - mortar periodic boundary condition



(a) 15 µm



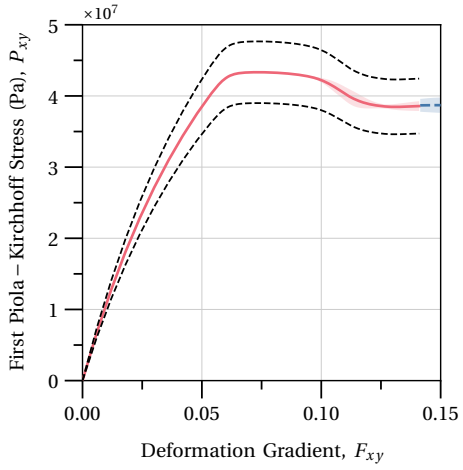
(b) 20 µm



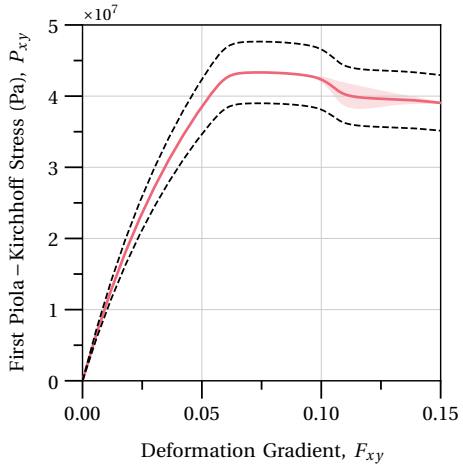
(c) 25 µm

Figure A.12: Homogenised First Piola Kirchhoff shear stress, P_{xy}, for different RVE sizes with 10% volume fraction and mortar periodic boundary condition. Shaded bounds: standard deviation; black dashed line: standard deviation 10% limit; red data: 5 samples; and blue data: 3 samples.

- 20% volume fraction - mortar periodic boundary condition



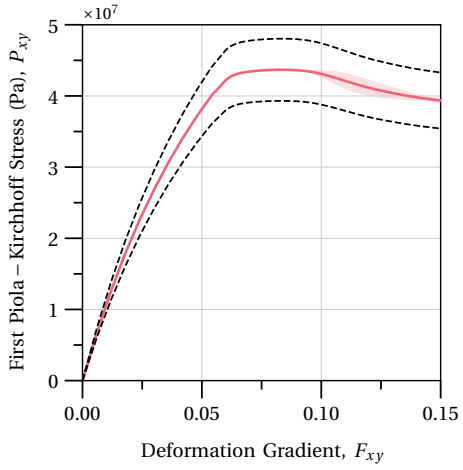
(a) 15 µm



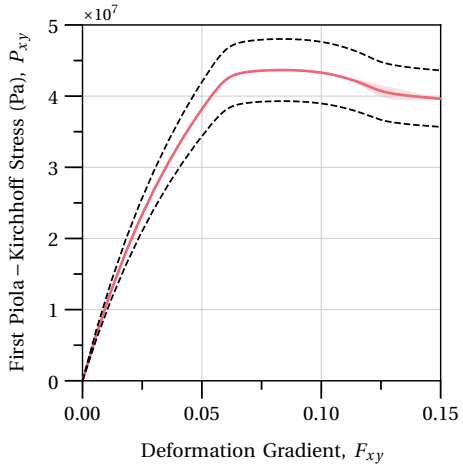
(b) 20 µm

Figure A.13: Homogenised First Piola Kirchhoff shear stress, P_{xy}, for different RVE sizes with 20% volume fraction and mortar periodic boundary condition. Shaded bounds: standard deviation; black dashed line: standard deviation 10% limit; red data: 5 samples; and blue data: 3 samples.

- 30% volume fraction - mortar periodic boundary condition



(a) 15 µm



(b) 20 µm

Figure A.14: Homogenised First Piola Kirchhoff shear stress, P_{xy}, for different RVE sizes with 30% volume fraction and mortar periodic boundary condition. Shaded bounds: standard deviation; and dashed line: standard deviation 10% limit.

Page intentionally left blank

APPENDIX B

FINITE ELEMENTS

This appendix seeks to compile the essential information to implement the continuum elements specified in this work. Hence, a graphical representation of all continuum elements and the matching node matrix is shown as written in the developed code's input file to be read by the developed code. In addition, the facets-nodes matrix (each row represents one facet) for each element is also presented, as it is of utmost importance when correctly defining the cohesive element in the developed code. Note that all facets are defined in a counter-clockwise direction (represented in the following figures with a blue arrow), which in the 3D instance amounts to having all normals in the inside-out direction.

B.1 Two-dimensional Elements

B.1.1 TRI3: 3-node linear element

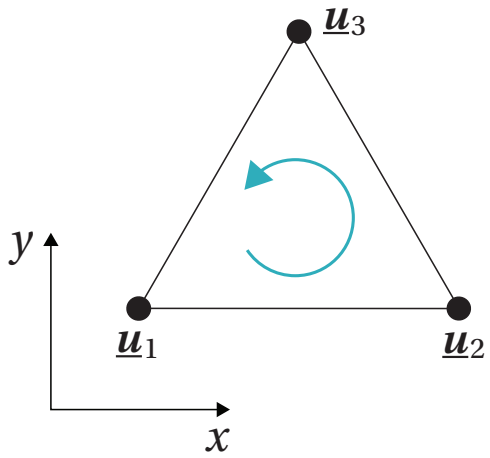


Figure B.1: Schematic representation of the two-dimensional 3-node linear finite element.

- Node Matrix

$$\begin{bmatrix} 1 & 2 & 3 \end{bmatrix} \tag{B.1}$$

- Facets-Nodes Matrix

$$\begin{bmatrix} 1 & 2 \\ 2 & 3 \\ 3 & 1 \end{bmatrix} \tag{B.2}$$

B.1.2 TRI6: 6-node quadratic element

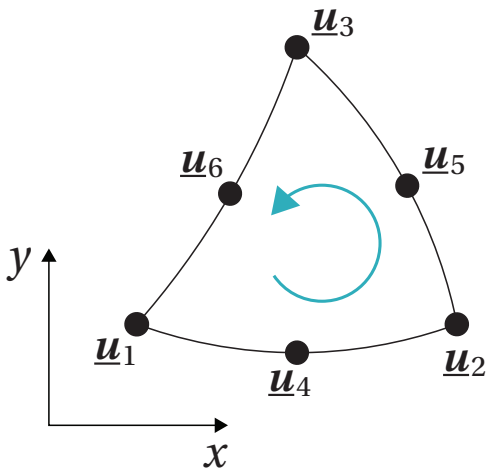


Figure B.2: Schematic representation of the two-dimensional 6-node quadratic finite element.

- Node Matrix

$$\begin{bmatrix} 1 & 2 & 3 & 4 & 5 & 6 \end{bmatrix} \tag{B.3}$$

- Facets-Nodes Matrix

$$\begin{bmatrix} 1 & 4 & 2 \\ 2 & 5 & 3 \\ 3 & 6 & 1 \end{bmatrix} \tag{B.4}$$

B.1.3 QUAD4: 4-node linear element

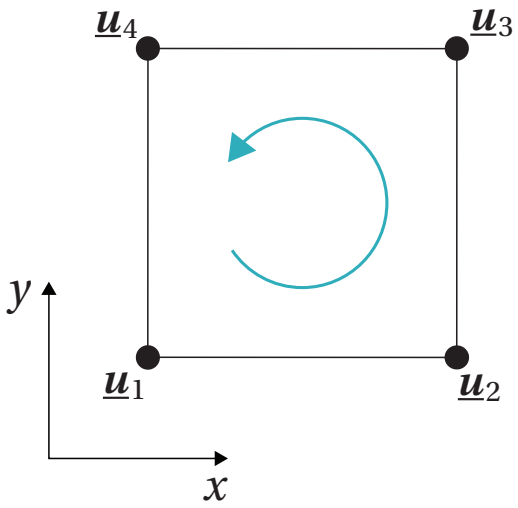


Figure B.3: Schematic representation of the two-dimensional 4-node linear finite element.

- Node Matrix

$$\begin{bmatrix} 1 & 2 & 3 & 4 \end{bmatrix} \tag{B.5}$$

- Facets-Nodes Matrix

$$\begin{bmatrix} 1 & 2 \\ 2 & 3 \\ 3 & 4 \\ 4 & 1 \end{bmatrix} \tag{B.6}$$

B.1.4 QUAD8: 8-node quadratic element

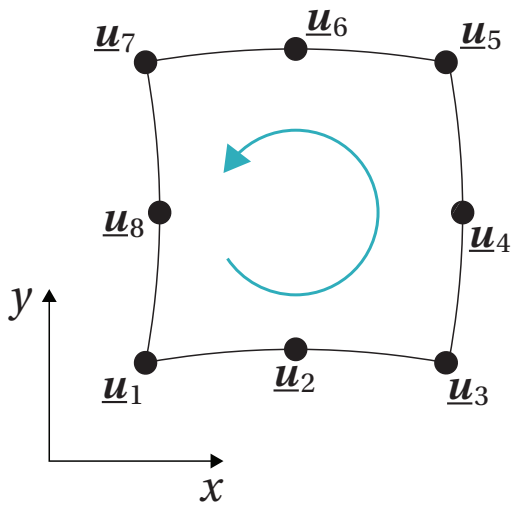


Figure B.4: Schematic representation of the two-dimensional 8-node quadratic finite element.

- Node Matrix

$$\begin{bmatrix} 1 & 2 & 3 & 4 & 5 & 6 & 7 & 8 \end{bmatrix} \tag{B.7}$$

- Facets-Nodes Matrix

$$\begin{bmatrix} 1 & 2 & 3 \\ 3 & 4 & 5 \\ 5 & 6 & 7 \\ 7 & 8 & 1 \end{bmatrix} \tag{B.8}$$

B.1.5 QUAD9: 9-node quadratic element

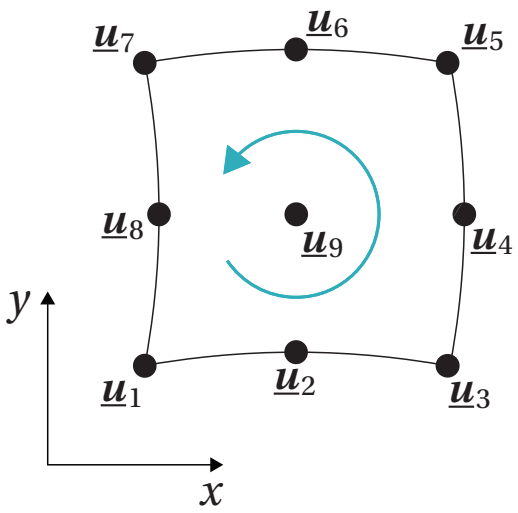


Figure B.5: Schematic representation of the two-dimensional 9-node quadratic finite element.

- Node Matrix

$$\begin{bmatrix} 1 & 2 & 3 & 4 & 5 & 6 & 7 & 8 & 9 \end{bmatrix} \tag{B.9}$$

- Facets-Nodes Matrix

$$\begin{bmatrix} 1 & 2 & 3 \\ 3 & 4 & 5 \\ 5 & 6 & 7 \\ 7 & 8 & 1 \end{bmatrix} \tag{B.10}$$

B.2 Three-dimensional Elements

B.2.1 TETRA4: 4-node linear element

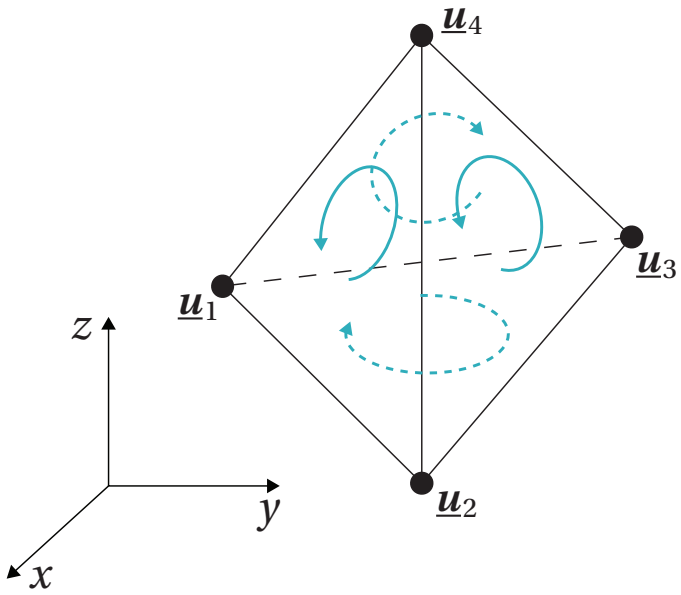


Figure B.6: Schematic representation of the three-dimensional 4-node linear finite element.

- Node Matrix

$$\begin{bmatrix} 1 & 2 & 3 & 4 \end{bmatrix} \tag{B.11}$$

- Facets-Nodes Matrix

$$\begin{bmatrix} 1 & 2 & 4 \\ 2 & 3 & 4 \\ 3 & 1 & 4 \\ 1 & 3 & 2 \end{bmatrix} \tag{B.12}$$

B.2.2 TETRA10: 10-node quadratic element

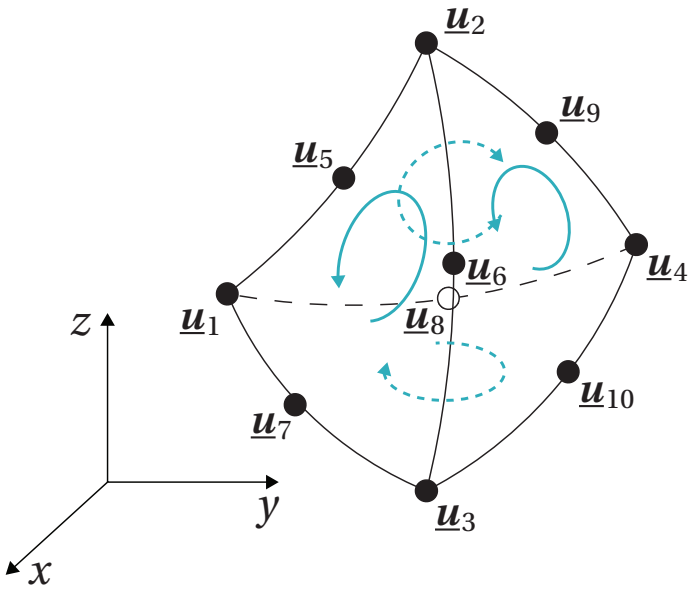


Figure B.7: Schematic representation of the three-dimensional 10-node quadratic finite element.

- Node Matrix

$$\begin{bmatrix} 1 & 2 & 3 & 4 & 5 & 6 & 7 & 8 & 9 & 10 \end{bmatrix} \tag{B.13}$$

- Facets-Nodes Matrix

$$\begin{bmatrix} 1 & 5 & 2 & 9 & 4 & 8 \\ 2 & 6 & 3 & 10 & 4 & 9 \\ 3 & 7 & 1 & 8 & 4 & 10 \\ 1 & 7 & 3 & 5 & 2 & 5 \end{bmatrix} \tag{B.14}$$

B.2.3 PYRA5: 5-node linear element

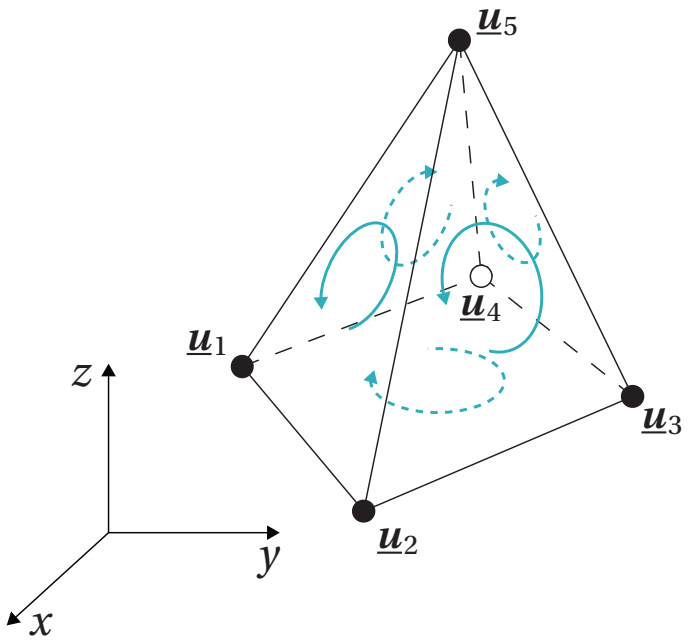


Figure B.8: Schematic representation of the three-dimensional 5-node linear finite element.

- Node Matrix

$$\begin{bmatrix} 1 & 2 & 3 & 4 & 5 \end{bmatrix} \tag{B.15}$$

- Facets-Nodes Matrix

$$\begin{bmatrix} 4 & 3 & 2 & 1 \\ 1 & 2 & 5 & \\ 2 & 3 & 5 & \\ 3 & 4 & 5 & \\ 4 & 1 & 5 & \end{bmatrix} \tag{B.16}$$

B.2.4 WEDGE6: 6-node linear element

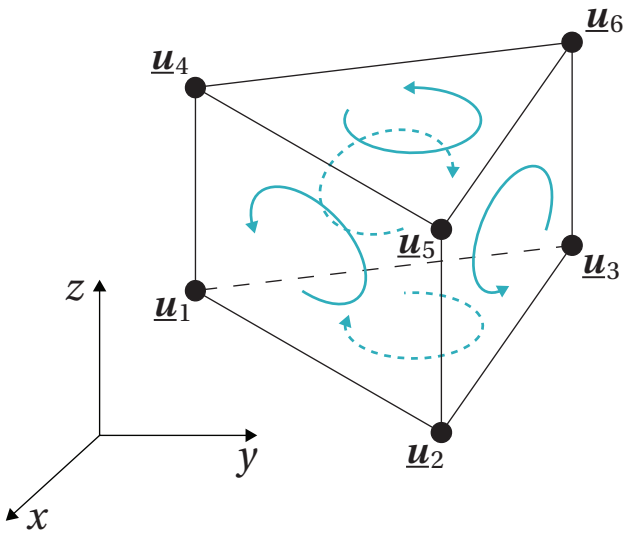


Figure B.9: Schematic representation of the three-dimensional 6-node linear finite element.

- Node Matrix

$$\begin{bmatrix} 1 & 2 & 3 & 4 & 5 & 6 \end{bmatrix} \tag{B.17}$$

- Facets-Nodes Matrix

$$\begin{bmatrix} 1 & 3 & 2 & \\ 4 & 5 & 6 & \\ 1 & 2 & 5 & 4 \\ 2 & 3 & 6 & 5 \\ 3 & 1 & 4 & 6 \end{bmatrix} \tag{B.18}$$

B.2.5 HEXA8: 8-node linear element

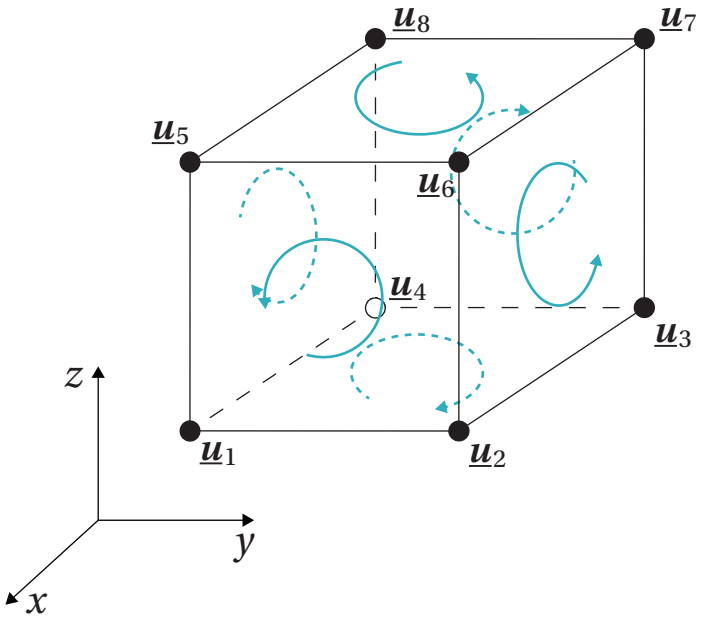


Figure B.10: Schematic representation of the three-dimensional 8-node linear finite element.

- Node Matrix

$$\begin{bmatrix} 1 & 2 & 3 & 4 & 5 & 6 & 7 & 8 \end{bmatrix} \tag{B.19}$$

- Facets-Nodes Matrix

$$\begin{bmatrix} 1 & 4 & 3 & 2 \\ 5 & 6 & 7 & 8 \\ 1 & 2 & 6 & 5 \\ 2 & 3 & 7 & 6 \\ 4 & 8 & 7 & 3 \\ 1 & 5 & 8 & 4 \end{bmatrix} \tag{B.20}$$

B.2.6 HEXA20: 20-node quadratic element

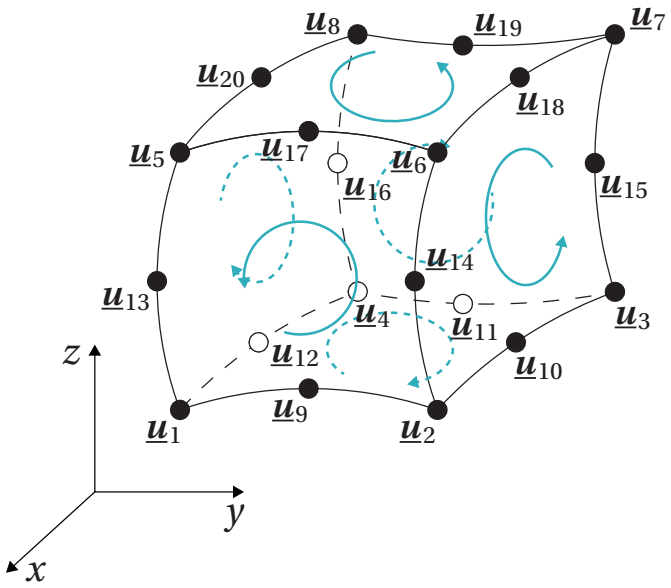


Figure B.11: Schematic representation of the three-dimensional 20-node quadratic finite element.

- Node Matrix

$$[1 \quad 2 \quad 3 \quad 4 \quad 5 \quad 6 \quad 7 \quad 8 \quad 9 \quad 10 \quad 11 \quad 12 \quad 13 \quad 14 \quad 15 \quad 16 \quad 17 \quad 18 \quad 19 \quad 20] \tag{B.21}$$

- Facets-Nodes Matrix

$$\begin{bmatrix} 1 & 12 & 4 & 11 & 3 & 10 & 2 & 9 \\ 5 & 17 & 6 & 18 & 7 & 19 & 8 & 20 \\ 1 & 9 & 2 & 14 & 6 & 17 & 5 & 13 \\ 2 & 10 & 3 & 15 & 7 & 18 & 6 & 14 \\ 5 & 16 & 8 & 19 & 7 & 15 & 3 & 11 \\ 1 & 13 & 5 & 20 & 8 & 16 & 4 & 12 \end{bmatrix} \tag{B.22}$$

APPENDIX C

COHESIVE ELEMENTS

This appendix seeks to compile the essential information to implement the cohesive elements specified in this work. Hence, a graphical representation of all cohesive elements and the matching node matrix is shown as written in the developed code's output file to be read by `Links`. The facets-nodes matrix (each row represents one facet) for each element is also presented, as it is of utmost importance when correctly defining the cohesive element in the developed code. Lastly, the local displacement-separation matrices, which connect the nodal displacements to the normal and tangential separations in the middle plane, and the shape functions matrices, which enable the interpolation of nodal variables in the middle plane to a given dof coordinate, are also shown.

C.1 Two-dimensional Elements

C.1.1 COH2D4: 4-node linear element

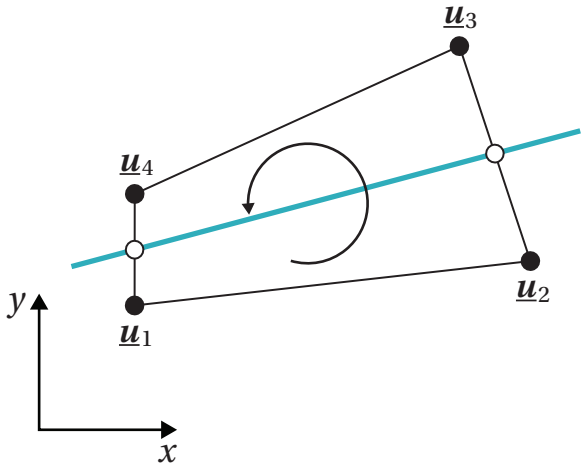


Figure C.1: Schematic representation of the two-dimensional 4-node linear finite element.
Source: (de Carvalho, 2022) - Adapted

- Node Matrix

$$\begin{bmatrix} 1 & 2 & 3 & 4 \end{bmatrix} \tag{C.1}$$

- Facets-Nodes Matrix

$$\begin{bmatrix} 1 & 2 \\ 3 & 4 \end{bmatrix} \tag{C.2}$$

- Local Displacement-Separation Matrix

$$\boldsymbol{L} = \begin{bmatrix} -1 & 0 & 0 & 0 & 0 & 0 & 1 & 0 \\ 0 & -1 & 0 & 0 & 0 & 0 & 0 & 1 \\ 0 & 0 & -1 & 0 & 1 & 0 & 0 & 0 \\ 0 & 0 & 0 & -1 & 0 & 1 & 0 & 0 \end{bmatrix} \tag{C.3}$$

- Shape Functions Matrix

$$\boldsymbol{N} = \begin{bmatrix} N_1 & 0 & N_2 & 0 \\ 0 & N_1 & 0 & N_2 \end{bmatrix}, \quad \begin{Bmatrix} N_1 = \dfrac{1-\xi}{2} \\ N_2 = \dfrac{1+\xi}{2} \end{Bmatrix} \tag{C.4}$$

C.1.2 COH2D6: 6-node quadratic element

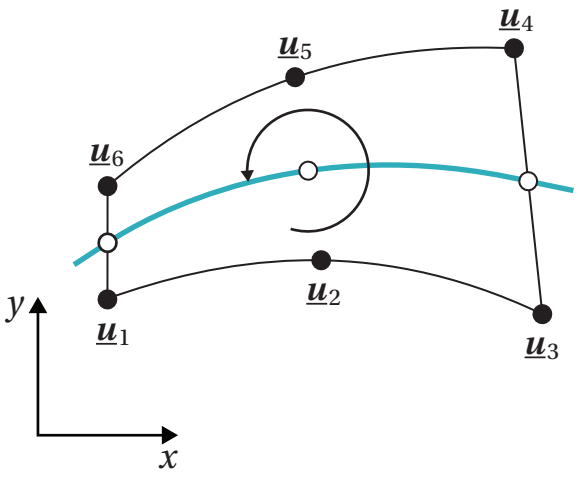


Figure C.2: Schematic representation of the two-dimensional 6-node quadratic finite element.
Source: (de Carvalho, 2022) - Adapted

- Node Matrix

$$\begin{bmatrix} 1 & 2 & 3 & 4 & 5 & 6 \end{bmatrix} \tag{C.5}$$

- Facets-Nodes Matrix

$$\begin{bmatrix} 1 & 2 & 3 \\ 4 & 5 & 6 \end{bmatrix} \tag{C.6}$$

- Local Displacement-Separation Matrix

$$\boldsymbol{L} = \begin{bmatrix} -1 & 0 & 0 & 0 & 0 & 0 & 0 & 0 & 0 & 0 & 1 & 0 \\ 0 & -1 & 0 & 0 & 0 & 0 & 0 & 0 & 0 & 0 & 0 & 1 \\ 0 & 0 & -1 & 0 & 0 & 0 & 0 & 0 & 1 & 0 & 0 & 0 \\ 0 & 0 & 0 & -1 & 0 & 0 & 0 & 0 & 0 & 1 & 0 & 0 \\ 0 & 0 & 0 & 0 & -1 & 0 & 1 & 0 & 0 & 0 & 0 & 0 \\ 0 & 0 & 0 & 0 & 0 & -1 & 0 & 1 & 0 & 0 & 0 & 0 \end{bmatrix} \tag{C.7}$$

- Shape Functions Matrix

$$\boldsymbol{N} = \begin{bmatrix} N_1 & 0 & N_2 & 0 & N_3 & 0 \\ 0 & N_1 & 0 & N_2 & 0 & N_3 \end{bmatrix}, \quad \begin{cases} N_1 = -\dfrac{1}{2}\xi(1-\xi) \\ N_2 = (1-\xi)(1+\xi) \\ N_3 = \dfrac{1}{2}\xi(1+\xi) \end{cases} \tag{C.8}$$

C.2 Three-dimensional Elements

The aforementioned matrices' dimensions, for three-dimensional problems, become too large for a complete representation to be displayed . As a result, they are defined in the following concise form:

$$\boldsymbol{L} = \left[-\boldsymbol{I}_{n^{\mathrm{m}}_{\mathrm{dof}} \times n^{\mathrm{m}}_{\mathrm{dof}}} \;\middle|\; \boldsymbol{I}_{n^{\mathrm{m}}_{\mathrm{dof}} \times n^{\mathrm{m}}_{\mathrm{dof}}} \right] \tag{C.9a}$$

$$\boldsymbol{N} = \left[\boldsymbol{N}_1 \boldsymbol{I}_{3\times 3} \;\middle|\; \ldots \;\middle|\; \boldsymbol{N}_{n^{\mathrm{m}}} \boldsymbol{I}_{3\times 3} \right] \tag{C.9b}$$

C.2.1 COH3D6: 6-node linear element

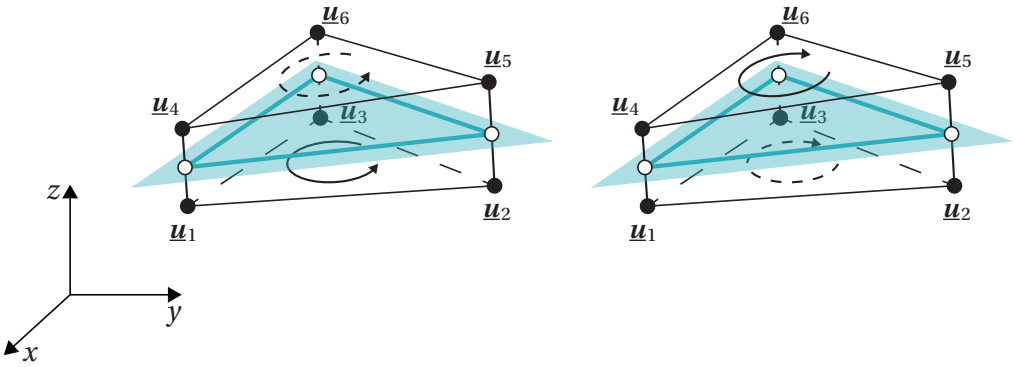


Figure C.3: Schematic representation of the three-dimensional 6-node linear finite element. Source: (de Carvalho, 2022) - Adapted

- Node Matrix

$$\begin{bmatrix} 1 & 2 & 3 & 4 & 5 & 6 \end{bmatrix} \tag{C.10}$$

- Facets-Nodes Matrix

$$\begin{bmatrix} 1 & 2 & 3 \\ 4 & 5 & 6 \end{bmatrix} \quad \text{or} \quad \begin{bmatrix} 4 & 6 & 5 \\ 1 & 3 & 2 \end{bmatrix} \tag{C.11}$$

- Shape Functions

$$\begin{cases} N_1 = 1 - \xi - \eta \\ N_2 = \xi \\ N_3 = \eta \end{cases} \tag{C.12}$$

C.2.2 COH3D12: 12-node quadratic element

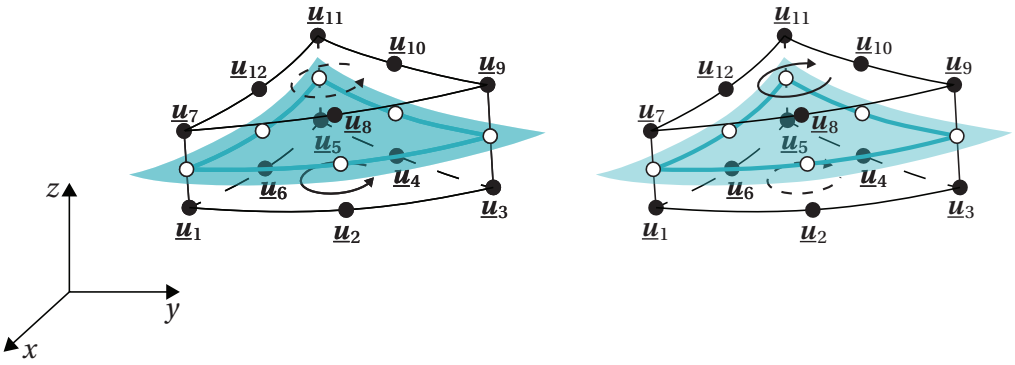


Figure C.4: Schematic representation of the three-dimensional 12-node quadratic finite element. Source: (de Carvalho, 2022) - Adapted

- Node Matrix

$$[1 \quad 2 \quad 3 \quad 4 \quad 5 \quad 6 \quad 7 \quad 8 \quad 9 \quad 10 \quad 11 \quad 12] \tag{C.13}$$

- Facets-Nodes Matrix

$$\begin{bmatrix} 1 & 2 & 3 & 4 & 5 & 6 \\ 7 & 8 & 9 & 10 & 11 & 12 \end{bmatrix} \quad \text{or} \quad \begin{bmatrix} 7 & 12 & 11 & 10 & 9 & 8 \\ 1 & 6 & 5 & 4 & 3 & 2 \end{bmatrix} \tag{C.14}$$

- Shape Functions

$$\begin{cases} N_1 = \frac{1}{4}(1-\xi)(1-\eta), \\ N_2 = \frac{1}{4}(1+\xi)(1-\eta), \\ N_3 = \frac{1}{4}(1+\xi)(1+\eta), \\ N_4 = \frac{1}{4}(1-\xi)(1+\eta). \end{cases} \tag{C.15}$$

C.2.3 COH3D8: 8-node linear element

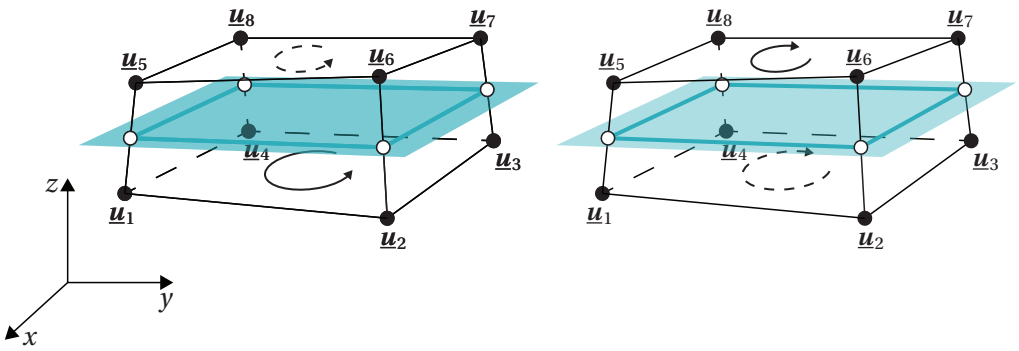


Figure C.5: Schematic representation of the three-dimensional 8-node linear finite element. Source: (de Carvalho, 2022) - Adapted

- Node Matrix

$$\begin{bmatrix} 1 & 2 & 3 & 4 & 5 & 6 & 7 & 8 \end{bmatrix} \tag{C.16}$$

- Facets-Nodes Matrix

$$\begin{bmatrix} 1 & 2 & 3 & 4 \\ 5 & 6 & 7 & 8 \end{bmatrix} \quad \text{or} \quad \begin{bmatrix} 5 & 8 & 7 & 6 \\ 1 & 4 & 3 & 2 \end{bmatrix} \tag{C.17}$$

- Shape Functions

$$\begin{cases} N_1 = (1-2\xi-2\eta)(1-\xi-\eta), \\ N_2 = 4\xi(1-\xi-\eta), \\ N_3 = \xi(2\xi-1), \end{cases} \quad \begin{cases} N_4 = 4\xi\eta \\ N_5 = \eta(2\eta-1), \\ N_6 = 4\eta(1-\xi-\eta). \end{cases} \tag{C.18}$$

C.2.4 COH3D16: 16-node quadratic element

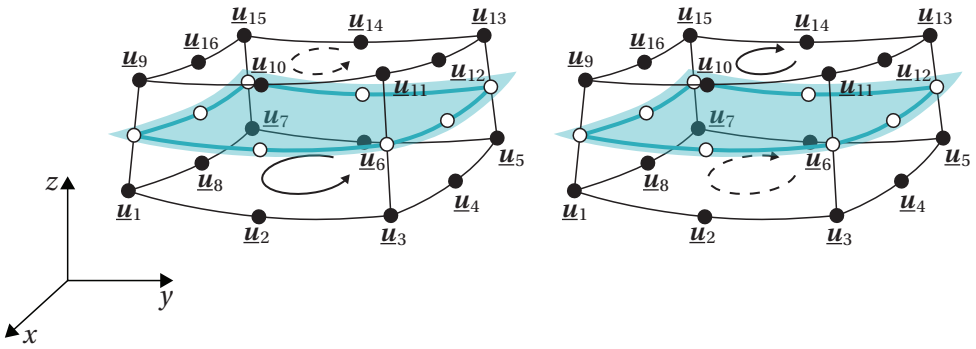


Figure C.6: Schematic representation of the three-dimensional 16-node quadratic finite element. Source: (de Carvalho, 2022) - Adapted

- Node Matrix

$$[1 \quad 2 \quad 3 \quad 4 \quad 5 \quad 6 \quad 7 \quad 8 \quad 9 \quad 10 \quad 11 \quad 12 \quad 13 \quad 14 \quad 15 \quad 16] \tag{C.19}$$

- Facets-Nodes Matrix

$$\begin{bmatrix} 1 & 2 & 3 & 4 & 5 & 6 & 7 & 8 \\ 9 & 10 & 11 & 12 & 13 & 14 & 15 & 16 \end{bmatrix}$$

$$\text{or} \tag{C.20}$$

$$\begin{bmatrix} 1 & 8 & 7 & 6 & 5 & 4 & 3 & 2 \\ 9 & 16 & 15 & 14 & 13 & 12 & 11 & 10 \end{bmatrix}$$

- Shape Functions

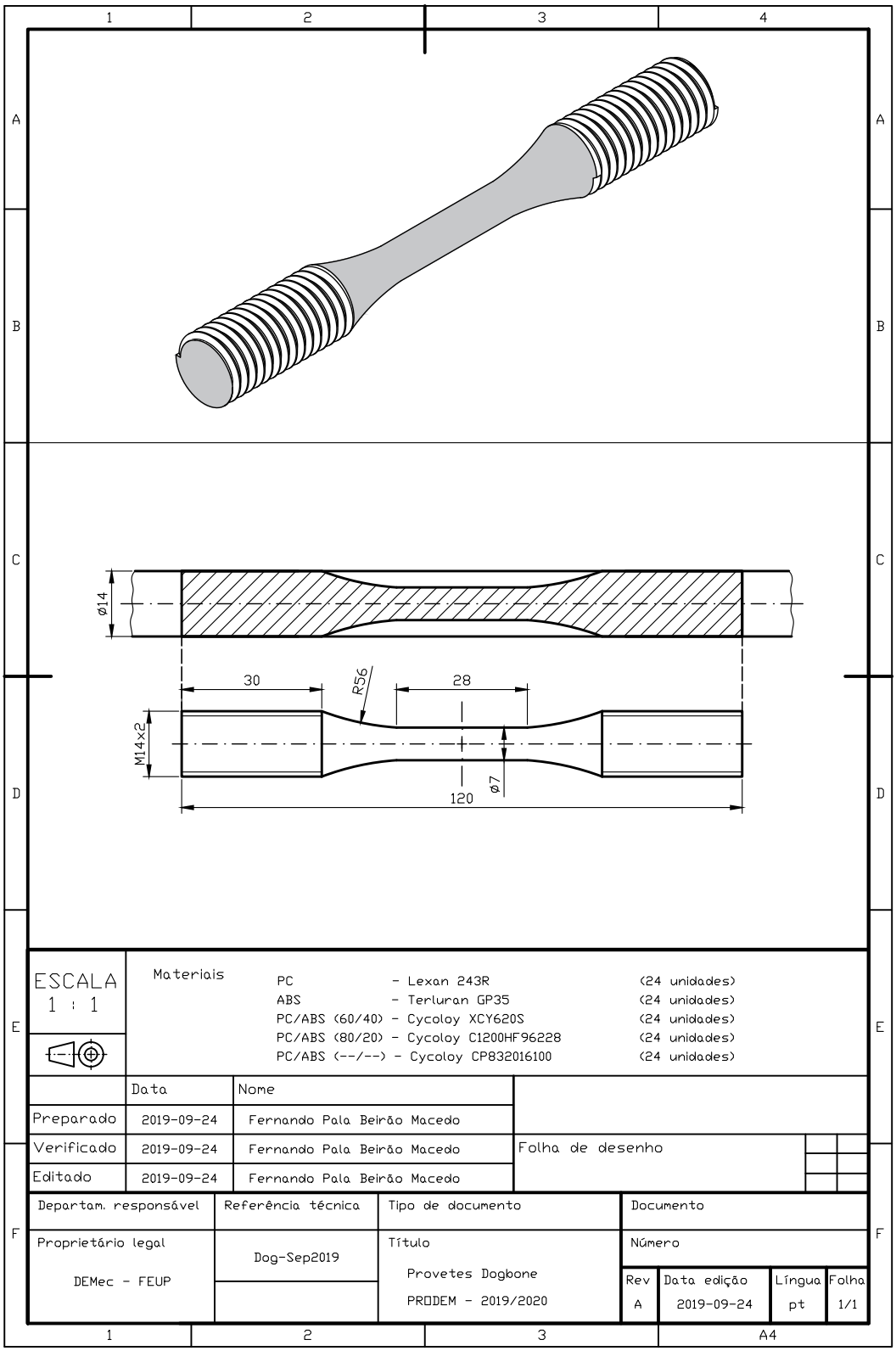
$$\begin{cases} N_1 = -\frac{1}{4}(1-\xi)(1-\eta)(1+\xi+\eta), \\ N_2 = \frac{1}{2}(1-\xi^2)(1-\eta), \\ N_3 = -\frac{1}{4}(1+\xi)(1-\eta)(1-\xi+\eta), \\ N_4 = \frac{1}{2}(1+\xi)(1-\eta^2), \end{cases} \quad \begin{cases} N_5 = -\frac{1}{4}(1+\xi)(1+\eta)(1-\xi-\eta), \\ N_6 = \frac{1}{2}\left(1-\xi^2\right)(1+\eta), \\ N_7 = -\frac{1}{4}(1-\xi)(1+\eta)(1+\xi-\eta), \\ N_8 = \frac{1}{2}(1-\xi)\left(1-\eta^2\right). \end{cases} \tag{C.21}$$

Page intentionally left blank

APPENDIX D

SMOOTH ROUND BAR

In this Appendix the technical drawing concerning the smooth round bar specimen geometry used for the uniaxial tensile tests is presented.


1
2
3
4
A
B
C
D
E
F
ø14
30
R56
28
M14×2
ø7
120
ESCALA
1 : 1
Materiais
PC - Lexan 243R (24 unidades)
ABS - Terluran GP35 (24 unidades)
PC/ABS (60/40) - Cycoloy XCY620S (24 unidades)
PC/ABS (80/20) - Cycoloy C1200HF96228 (24 unidades)
PC/ABS (--/--) - Cycoloy CP832016100 (24 unidades)
Data
Nome
Preparado
2019-09-24
Fernando Pala Beirão Macedo
Verificado
2019-09-24
Fernando Pala Beirão Macedo
Folha de desenho
Editado
2019-09-24
Fernando Pala Beirão Macedo
Departam. responsável
Referência técnica
Tipo de documento
Documento
Proprietário legal
DEMec - FEUP
Dog-Sep2019
Título
Provetes Dogbone
PRODEM - 2019/2020
Número
Rev
A
Data edição
2019-09-24
Língua
pt
Folha
1/1
A4

APPENDIX E

PC/ABS MATERIAL: TECHNICAL SPECIFICATIONS

In this Appendix the technical specifications concerning PC/ABS material of the smooth round bar specimen geometry used for the uniaxial tensile tests is presented.

CYCOLOY™ Resin C1200HF
Europe-Africa-Middle East: COMMERCIAL

CYCOLOY C1200HF is the improved version of CYCOLOY C1200 and has been developed to provide enhanced productivity and surface appearance of the finished parts

TYPICAL PROPERTIES[1]	TYPICAL VALUE	Unit	Standard
MECHANICAL			
Taber Abrasion, CS-17, 1 kg	63	mg/1000cy	SABIC Method
Tensile Stress, yield, 5 mm/min	55	MPa	ISO 527
Tensile Stress, break, 5 mm/min	45	MPa	ISO 527
Tensile Stress, yield, 50 mm/min	55	MPa	ISO 527
Tensile Stress, break, 50 mm/min	45	MPa	ISO 527
Tensile Strain, yield, 5 mm/min	5	%	ISO 527
Tensile Strain, break, 5 mm/min	100	%	ISO 527
Tensile Strain, yield, 50 mm/min	4	%	ISO 527
Tensile Strain, break, 50 mm/min	>50	%	ISO 527
Tensile Modulus, 1 mm/min	2400	MPa	ISO 527
Flexural Stress, yield, 2 mm/min	80	MPa	ISO 178
Flexural Modulus, 2 mm/min	2300	MPa	ISO 178
Hardness, H358/30	96	MPa	ISO 2039-1
Hardness, Rockwell R	115	-	ISO 2039-2
IMPACT			
Izod Impact, unnotched 80*10*3 +23°C	NB	kJ/m²	ISO 180/1U
Izod Impact, unnotched 80*10*3 -30°C	NB	kJ/m²	ISO 180/1U
Izod Impact, notched 80*10*3 +23°C	50	kJ/m²	ISO 180/1A
Izod Impact, notched 80*10*3 -30°C	30	kJ/m²	ISO 180/1A
Izod Impact, unnotched 80*10*4 +23°C	NB	kJ/m²	ISO 180/1U
Izod Impact, unnotched 80*10*4 -30°C	NB	kJ/m²	ISO 180/1U
Izod Impact, notched 80*10*4 +23°C	40	kJ/m²	ISO 180/1A

(1) Typical values only. Variations within normal tolerances are possible for various colors. All values are measured after at least 48 hours storage at 23°C/50% relative humidity. All properties, except the melt volume and melt flow rates, are measured on injection molded samples. All samples tested under ISO test standards are prepared according to ISO 294.

(2) Only typical data for selection purposes. Not to be used for part or tool design.
(3) This rating is not intended to reflect hazards presented by this or any other material under actual fire conditions.
(4) Internal measurements according to UL standards.
(5) Measurements made from laboratory test coupon. Actual shrinkage may vary outside of range due to differences in processing conditions, equipment, part geometry and tool design. It is recommended that mold shrinkage studies be performed with surrogate or legacy tooling prior to cutting tools for new molded article.
(6) Needs hard coat to consistently pass 60 sec Vertical Burn.

Source GMD, last updated:

PLEASE CONTACT YOUR LOCAL SALES OFFICE FOR AVAILABILITY IN YOUR AREA

DISCLAIMER : THE MATERIALS, PRODUCTS AND SERVICES OF SAUDI BASIC INDUSTRIES CORPORATION (SABIC) OR ITS SUBSIDIARIES OR AFFILIATES (SELLER) ARE SOLD SUBJECT TO SELLER S STANDARD CONDITIONS OF SALE, WHICH ARE AVAILABLE UPON REQUEST. INFORMATION AND RECOMMENDATIONS CONTAINED IN THIS DOCUMENT ARE GIVEN IN GOOD FAITH. HOWEVER, SELLER MAKES NO EXPRESS OR IMPLIED REPRESENTATION, WARRANTY OR GUARANTEE (i) THAT ANY RESULTS DESCRIBED IN THIS DOCUMENT WILL BE OBTAINED UNDER END-USE CONDITIONS, OR (ii) AS TO THE EFFECTIVENESS OR SAFETY OF ANY DESIGN OR APPLICATION INCORPORATING SELLER S MATERIALS, PRODUCTS, SERVICES OR RECOMMENDATIONS. UNLESS OTHERWISE PROVIDED IN SELLER S STANDARD CONDITIONS OF SALE, SELLER SHALL NOT BE RESPONSIBLE FOR ANY LOSS RESULTING FROM ANY USE OF ITS MATERIALS, PRODUCTS, SERVICES OR RECOMMENDATIONS DESCRIBED IN THIS DOCUMENT.

Each user is responsible for making its own determination as to the suitability of Seller s materials, products, services or recommendations for the user s particular use through appropriate end-use and other testing and analysis. Nothing in any document or oral statement shall be deemed to alter or waive any provision of Seller s Standard Conditions of Sale or this Disclaimer, unless it is specifically agreed to in a writing signed by Seller. Statements by Seller concerning a possible use of any material, product, service or design do not, are not intended to, and should not be construed to grant any license under any patent or other intellectual property right of Seller or as a recommendation for the use of any material, product, service or design in a manner that infringes any patent or other intellectual property right.

SABIC and brands marked with ™ are trademarks of SABIC or its subsidiaries or affiliates.

© 2016 Saudi Basic Industries Corporation (SABIC).

CYCOLOY™ Resin C1200HF

Europe-Africa-Middle East: COMMERCIAL

TYPICAL PROPERTIES[1]	TYPICAL VALUE	Unit	Standard
IMPACT			
Izod Impact, notched 80*10*4 -30°C	20	kJ/m²	ISO 180/1A
Charpy 23°C, V-notch Edgew 80*10*3 sp=62mm	50	kJ/m²	ISO 179/1eA
Charpy -30°C, V-notch Edgew 80*10*3 sp=62mm	30	kJ/m²	ISO 179/1eA
Charpy 23°C, Unnotch Edgew 80*10*3 sp=62mm	NB	kJ/m²	ISO 179/1eU
Charpy -30°C, Unnotch Edgew 80*10*3 sp=62mm	NB	kJ/m²	ISO 179/1eU
Charpy 23°C, V-notch Edgew 80*10*4 sp=62mm	45	kJ/m²	ISO 179/1eA
Charpy -30°C, V-notch Edgew 80*10*4 sp=62mm	18	kJ/m²	ISO 179/1eA
Charpy 23°C, Unnotch Edgew 80*10*4 sp=62mm	NB	kJ/m²	ISO 179/1eU
Charpy -30°C, Unnotch Edgew 80*10*4 sp=62mm	NB	kJ/m²	ISO 179/1eU
THERMAL			
Thermal Conductivity	0.2	W/m-°C	ISO 8302
CTE, -40°C to 40°C, flow	8.E-05	1/°C	ISO 11359-2
CTE, -40°C to 40°C, xflow	8.E-05	1/°C	ISO 11359-2
Ball Pressure Test, 125°C +/- 2°C	PASSES	-	IEC 60695-10-2
Vicat Softening Temp, Rate B/50	132	°C	ISO 306
Vicat Softening Temp, Rate B/120	134	°C	ISO 306
HDT/Be, 0.45MPa Edgew 120*10*4 sp=100mm	128	°C	ISO 75/Be
HDT/Ae, 1.8 MPa Edgew 120*10*4 sp=100mm	108	°C	ISO 75/Ae
Relative Temp Index, Elec	105	°C	UL 746B
Relative Temp Index, Mech w/impact	80	°C	UL 746B
Relative Temp Index, Mech w/o impact	105	°C	UL 746B
PHYSICAL			
Mold Shrinkage on Tensile Bar, flow (2) (5)	0.5 - 0.7	%	SABIC Method
Density	1.15	g/cm³	ISO 1183
Water Absorption, (23°C/sat)	0.6	%	ISO 62

(1) Typical values only. Variations within normal tolerances are possible for various colors. All values are measured after at least 48 hours storage at 23°C/50% relative humidity. All properties, except the melt volume and melt flow rates, are measured on injection molded samples. All samples tested under ISO test standards are prepared according to ISO 294.

(2) Only typical data for selection purposes. Not to be used for part or tool design.
(3) This rating is not intended to reflect hazards presented by this or any other material under actual fire conditions.
(4) Internal measurements according to UL standards.
(5) Measurements made from laboratory test coupon. Actual shrinkage may vary outside of range due to differences in processing conditions, equipment, part geometry and tool design. It is recommended that mold shrinkage studies be performed with surrogate or legacy tooling prior to cutting tools for new molded article.
(6) Needs hard coat to consistently pass 60 sec Vertical Burn.

Source GMD, last updated:

PLEASE CONTACT YOUR LOCAL SALES OFFICE FOR AVAILABILITY IN YOUR AREA

DISCLAIMER : THE MATERIALS, PRODUCTS AND SERVICES OF SAUDI BASIC INDUSTRIES CORPORATION (SABIC) OR ITS SUBSIDIARIES OR AFFILIATES (SELLER) ARE SOLD SUBJECT TO SELLER S STANDARD CONDITIONS OF SALE, WHICH ARE AVAILABLE UPON REQUEST. INFORMATION AND RECOMMENDATIONS CONTAINED IN THIS DOCUMENT ARE GIVEN IN GOOD FAITH. HOWEVER, SELLER MAKES NO EXPRESS OR IMPLIED REPRESENTATION, WARRANTY OR GUARANTEE (I) THAT ANY RESULTS DESCRIBED IN THIS DOCUMENT WILL BE OBTAINED UNDER END-USE CONDITIONS, OR (II) AS TO THE EFFECTIVENESS OR SAFETY OF ANY DESIGN OR APPLICATION INCORPORATING SELLER S MATERIALS, PRODUCTS, SERVICES OR RECOMMENDATIONS. UNLESS OTHERWISE PROVIDED IN SELLER S STANDARD CONDITIONS OF SALE, SELLER SHALL NOT BE RESPONSIBLE FOR ANY LOSS RESULTING FROM ANY USE OF ITS MATERIALS, PRODUCTS, SERVICES OR RECOMMENDATIONS DESCRIBED IN THIS DOCUMENT.

Each user is responsible for making its own determination as to the suitability of Seller s materials, products, services or recommendations for the user s particular use through appropriate end-use and other testing and analysis. Nothing in any document or oral statement shall be deemed to alter or waive any provision of Seller s Standard Conditions of Sale or this Disclaimer, unless it is specifically agreed to in a writing signed by Seller. Statements by Seller concerning a possible use of any material, product, service or design do not, are not intended to, and should not be construed to grant any license under any patent or other intellectual property right of Seller or as a recommendation for the use of any material, product, service or design in a manner that infringes any patent or other intellectual property right.

SABIC and brands marked with ™ are trademarks of SABIC or its subsidiaries or affiliates.

©2016Saudi Basic Industries Corporation (SABIC).

CYCOLOY™ Resin C1200HF

Europe-Africa-Middle East: COMMERCIAL

TYPICAL PROPERTIES[1]	TYPICAL VALUE	Unit	Standard
PHYSICAL			
Moisture Absorption (23°C / 50% RH)	0.2	%	ISO 62
Melt Volume Rate, MVR at 260°C/2.16 kg	8	cm³/10 min	ISO 1133
Melt Volume Rate, MVR at 260°C/5.0 kg	22	cm³/10 min	ISO 1133
ELECTRICAL			
Comparative Tracking Index (UL) {PLC}	2	PLC Code	UL 746A
Volume Resistivity	>1.E+15	Ohm-cm	IEC 60093
Surface Resistivity, ROA	>1.E+15	Ohm	IEC 60093
Dielectric Strength, in oil, 0.8 mm	35	kV/mm	IEC 60243-1
Dielectric Strength, in oil, 1.6 mm	25	kV/mm	IEC 60243-1
Dielectric Strength, in oil, 3.2 mm	17	kV/mm	IEC 60243-1
Relative Permittivity, 1 MHz	2.7	-	IEC 60250
Dissipation Factor, 50/60 Hz	0.002	-	IEC 60250
Dissipation Factor, 1 MHz	0.007	-	IEC 60250
Comparative Tracking Index	250	V	IEC 60112
Relative Permittivity, 50/60 Hz	2.8	-	IEC 60250
FLAME CHARACTERISTICS			
UL Recognized, 94HB Flame Class Rating (3)	1.2	mm	UL 94
UL Recognized, 94HB Flame Class Rating 2nd value (3)	3	mm	UL 94
Glow Wire Flammability Index 650°C, passes at	1	mm	IEC 60695-2-12
Oxygen Index (LOI)	23	%	ISO 4589

(1) Typical values only. Variations within normal tolerances are possible for various colors. All values are measured after at least 48 hours storage at 23°C/50% relative humidity. All properties, except the melt volume and melt flow rates, are measured on injection molded samples. All samples tested under ISO test standards are prepared according to ISO 294.

(2) Only typical data for selection purposes. Not to be used for part or tool design.
(3) This rating is not intended to reflect hazards presented by this or any other material under actual fire conditions.
(4) Internal measurements according to UL standards.
(5) Measurements made from laboratory test coupon. Actual shrinkage may vary outside of range due to differences in processing conditions, equipment, part geometry and tool design. It is recommended that mold shrinkage studies be performed with surrogate or legacy tooling prior to cutting tools for new molded article.
(6) Needs hard coat to consistently pass 60 sec Vertical Burn.

Source GMD, last updated:

PLEASE CONTACT YOUR LOCAL SALES OFFICE FOR AVAILABILITY IN YOUR AREA

DISCLAIMER : THE MATERIALS, PRODUCTS AND SERVICES OF SAUDI BASIC INDUSTRIES CORPORATION (SABIC) OR ITS SUBSIDIARIES OR AFFILIATES (SELLER) ARE SOLD SUBJECT TO SELLER S STANDARD CONDITIONS OF SALE, WHICH ARE AVAILABLE UPON REQUEST. INFORMATION AND RECOMMENDATIONS CONTAINED IN THIS DOCUMENT ARE GIVEN IN GOOD FAITH. HOWEVER, SELLER MAKES NO EXPRESS OR IMPLIED REPRESENTATION, WARRANTY OR GUARANTEE (i) THAT ANY RESULTS DESCRIBED IN THIS DOCUMENT WILL BE OBTAINED UNDER END-USE CONDITIONS, OR (ii) AS TO THE EFFECTIVENESS OR SAFETY OF ANY DESIGN OR APPLICATION INCORPORATING SELLER S MATERIALS, PRODUCTS, SERVICES OR RECOMMENDATIONS. UNLESS OTHERWISE PROVIDED IN SELLER S STANDARD CONDITIONS OF SALE, SELLER SHALL NOT BE RESPONSIBLE FOR ANY LOSS RESULTING FROM ANY USE OF ITS MATERIALS, PRODUCTS, SERVICES OR RECOMMENDATIONS DESCRIBED IN THIS DOCUMENT.

Each user is responsible for making its own determination as to the suitability of Seller s materials, products, services or recommendations for the user s particular use through appropriate end-use and other testing and analysis. Nothing in any document or oral statement shall be deemed to alter or waive any provision of Seller s Standard Conditions of Sale or this Disclaimer, unless it is specifically agreed to in a writing signed by Seller. Statements by Seller concerning a possible use of any material, product, service or design do not, are not intended to, and should not be construed to grant any license under any patent or other intellectual property right of Seller or as a recommendation for the use of any material, product, service or design in a manner that infringes any patent or other intellectual property right.

SABIC and brands marked with ™ are trademarks of SABIC or its subsidiaries or affiliates.

©2016Saudi Basic Industries Corporation (SABIC).

CYCOLOY™ Resin C1200HF

Europe-Africa-Middle East: COMMERCIAL

PROCESSING PARAMETERS	TYPICAL VALUE	Unit
Injection Molding		
Drying Temperature	100 - 110	°C
Drying Time	3 - 4	hrs
Drying Time (Cumulative)	8	hrs
Maximum Moisture Content	0.02	%
Melt Temperature	275 - 300	°C
Nozzle Temperature	275 - 300	°C
Front - Zone 3 Temperature	260 - 300	°C
Middle - Zone 2 Temperature	255 - 295	°C
Rear - Zone 1 Temperature	250 - 290	°C
Hopper Temperature	60 - 80	°C
Mold Temperature	60 - 90	°C
Back Pressure	0.3 - 0.7	MPa
Screw Speed	40 - 70	rpm
Shot to Cylinder Size	30 - 80	%
Vent Depth	0.038 - 0.076	mm

(1) Typical values only. Variations within normal tolerances are possible for various colors. All values are measured after at least 48 hours storage at 23°C/50% relative humidity. All properties, except the melt volume and melt flow rates, are measured on injection molded samples. All samples tested under ISO test standards are prepared according to ISO 294.

(2) Only typical data for selection purposes. Not to be used for part or tool design.
(3) This rating is not intended to reflect hazards presented by this or any other material under actual fire conditions.
(4) Internal measurements according to UL standards.
(5) Measurements made from laboratory test coupon. Actual shrinkage may vary outside of range due to differences in processing conditions, equipment, part geometry and tool design. It is recommended that mold shrinkage studies be performed with surrogate or legacy tooling prior to cutting tools for new molded article.
(6) Needs hard coat to consistently pass 60 sec Vertical Burn.

Source GMD, last updated:

PLEASE CONTACT YOUR LOCAL SALES OFFICE FOR AVAILABILITY IN YOUR AREA

DISCLAIMER : THE MATERIALS, PRODUCTS AND SERVICES OF SAUDI BASIC INDUSTRIES CORPORATION (SABIC) OR ITS SUBSIDIARIES OR AFFILIATES (SELLER) ARE SOLD SUBJECT TO SELLER S STANDARD CONDITIONS OF SALE, WHICH ARE AVAILABLE UPON REQUEST. INFORMATION AND RECOMMENDATIONS CONTAINED IN THIS DOCUMENT ARE GIVEN IN GOOD FAITH. HOWEVER, SELLER MAKES NO EXPRESS OR IMPLIED REPRESENTATION, WARRANTY OR GUARANTEE (i) THAT ANY RESULTS DESCRIBED IN THIS DOCUMENT WILL BE OBTAINED UNDER END-USE CONDITIONS, OR (ii) AS TO THE EFFECTIVENESS OR SAFETY OF ANY DESIGN OR APPLICATION INCORPORATING SELLER S MATERIALS, PRODUCTS, SERVICES OR RECOMMENDATIONS. UNLESS OTHERWISE PROVIDED IN SELLER S STANDARD CONDITIONS OF SALE, SELLER SHALL NOT BE RESPONSIBLE FOR ANY LOSS RESULTING FROM ANY USE OF ITS MATERIALS, PRODUCTS, SERVICES OR RECOMMENDATIONS DESCRIBED IN THIS DOCUMENT.

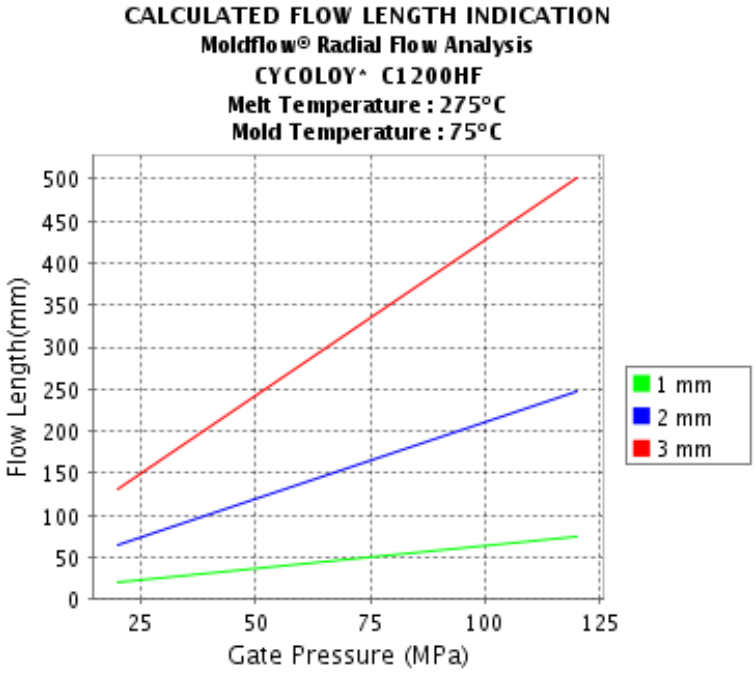
Each user is responsible for making its own determination as to the suitability of Seller s materials, products, services or recommendations for the user s particular use through appropriate end-use and other testing and analysis. Nothing in any document or oral statement shall be deemed to alter or waive any provision of Seller s Standard Conditions of Sale or this Disclaimer, unless it is specifically agreed to in a writing signed by Seller. Statements by Seller concerning a possible use of any material, product, service or design do not, are not intended to, and should not be construed to grant any license under any patent or other intellectual property right of Seller or as a recommendation for the use of any material, product, service or design in a manner that infringes any patent or other intellectual property right.

SABIC and brands marked with ™ are trademarks of SABIC or its subsidiaries or affiliates.

©2016Saudi Basic Industries Corporation (SABIC).

CYCOLOY™ Resin C1200HF

Europe-Africa-Middle East: COMMERCIAL



Note: Technical support is recommended if Gate Pressure is greater than 80 MPa. Contact your local representative.

® Moldflow is a registered trademark of the Moldflow Corporation.

(1) Typical values only. Variations within normal tolerances are possible for various colors. All values are measured after at least 48 hours storage at 23°C/50% relative humidity. All properties, except the melt volume and melt flow rates, are measured on injection molded samples. All samples tested under ISO test standards are prepared according to ISO 294.

(2) Only typical data for selection purposes. Not to be used for part or tool design.
(3) This rating is not intended to reflect hazards presented by this or any other material under actual fire conditions.
(4) Internal measurements according to UL standards.
(5) Measurements made from laboratory test coupon. Actual shrinkage may vary outside of range due to differences in processing conditions, equipment, part geometry and tool design. It is recommended that mold shrinkage studies be performed with surrogate or legacy tooling prior to cutting tools for new molded article.
(6) Needs hard coat to consistently pass 60 sec Vertical Burn.

Source GMD, last updated:

PLEASE CONTACT YOUR LOCAL SALES OFFICE FOR AVAILABILITY IN YOUR AREA

DISCLAIMER : THE MATERIALS, PRODUCTS AND SERVICES OF SAUDI BASIC INDUSTRIES CORPORATION (SABIC) OR ITS SUBSIDIARIES OR AFFILIATES (SELLER) ARE SOLD SUBJECT TO SELLER S STANDARD CONDITIONS OF SALE, WHICH ARE AVAILABLE UPON REQUEST. INFORMATION AND RECOMMENDATIONS CONTAINED IN THIS DOCUMENT ARE GIVEN IN GOOD FAITH. HOWEVER, SELLER MAKES NO EXPRESS OR IMPLIED REPRESENTATION, WARRANTY OR GUARANTEE (i) THAT ANY RESULTS DESCRIBED IN THIS DOCUMENT WILL BE OBTAINED UNDER END-USE CONDITIONS, OR (ii) AS TO THE EFFECTIVENESS OR SAFETY OF ANY DESIGN OR APPLICATION INCORPORATING SELLER S MATERIALS, PRODUCTS, SERVICES OR RECOMMENDATIONS. UNLESS OTHERWISE PROVIDED IN SELLER S STANDARD CONDITIONS OF SALE, SELLER SHALL NOT BE RESPONSIBLE FOR ANY LOSS RESULTING FROM ANY USE OF ITS MATERIALS, PRODUCTS, SERVICES OR RECOMMENDATIONS DESCRIBED IN THIS DOCUMENT.

Each user is responsible for making its own determination as to the suitability of Seller s materials, products, services or recommendations for the user s particular use through appropriate end-use and other testing and analysis. Nothing in any document or oral statement shall be deemed to alter or waive any provision of Seller s Standard Conditions of Sale or this Disclaimer, unless it is specifically agreed to in a writing signed by Seller. Statements by Seller concerning a possible use of any material, product, service or design do not, are not intended to, and should not be construed to grant any license under any patent or other intellectual property right of Seller or as a recommendation for the use of any material, product, service or design in a manner that infringes any patent or other intellectual property right.

SABIC and brands marked with ™ are trademarks of SABIC or its subsidiaries or affiliates.

©2016Saudi Basic Industries Corporation (SABIC).

APPENDIX F

VISCO-ELASTIC VISCO-PLASTIC CONSTITUTIVE MODEL LINEARISATION

This appendix establishes the derivatives necessary for the proposed visco-elastic visco-plastic constitutive model for rubber-toughened amorphous polymers to fully characterise the state update mechanism and the consistent tangent operator. In addition, some auxiliary variables are defined in this context to make the derivatives' presentation more straightforward (Carvalho Alves et al., 2023).

$$v_1 = \boldsymbol{\tau}_{\mathrm{D},d,n+1} : \boldsymbol{\tau}_{\mathrm{D},d,n+1} + \frac{1}{\sqrt{3}} q_{1,n+1} q_2 f_{n+1} \tau^{\mathrm{eq}}_{\mu,n+1} \sinh\left(q_2 \frac{\mathrm{tr}\left(\boldsymbol{\tau}_{\mathrm{D},n+1}\right)}{2\sqrt{3}\tau^{\mathrm{eq}}_{\mu,n+1}} \right) \mathrm{tr}\left(\boldsymbol{\tau}_{\mathrm{D},n+1}\right), \tag{F.1}$$

$$v_2 = \frac{1}{\sqrt{3}} q_{1,n+1} q_2 f_{n+1} \tau^{\mathrm{eq}}_{\mu,n+1} \sinh\left(q_2 \frac{\mathrm{tr}\left(\boldsymbol{\tau}_{\mathrm{D},n+1}\right)}{2\sqrt{3}\tau^{\mathrm{eq}}_{\mu,n+1}} \right), \tag{F.2}$$

$$v_3 = \frac{1}{\sqrt{3}} q_{1,n+1} q_2 f_{n+1} \tau^{\mathrm{eq}}_{\mu,n+1} \cosh\left(q_2 \frac{\mathrm{tr}\left(\boldsymbol{\tau}_{\mathrm{D},n+1}\right)}{2\sqrt{3}\tau^{\mathrm{eq}}_{\mu,n+1}} \right), \tag{F.3}$$

$$v_4 = \cosh\left(q_2 \frac{\mathrm{tr}\left(\boldsymbol{\tau}_{\mathrm{D},n+1}\right)}{2\sqrt{3}\tau^{\mathrm{eq}}_{\mu,n+1}} \right) q_2 \frac{3K_\infty}{2\sqrt{3}\tau^{\mathrm{eq}}_{\mu,n+1}} \mathrm{tr}\left(\boldsymbol{\tau}_{\mathrm{D},n+1}\right) + 3K_\infty \sinh\left(q_2 \frac{\mathrm{tr}\left(\boldsymbol{\tau}_{\mathrm{D},n+1}\right)}{2\sqrt{3}\tau^{\mathrm{eq}}_{\mu,n+1}} \right), \tag{F.4}$$

$$v_5 = \sinh\left(q_2 \frac{\mathrm{tr}\left(\sqrt{3}\boldsymbol{\tau}_{\mathrm{D},n+1}\right)}{2\tau^{\mathrm{eq}}_{\mu,n+1}}\right) - \cosh\left(q_2 \frac{\mathrm{tr}\left(\boldsymbol{\tau}_{\mathrm{D},n+1}\right)}{2\sqrt{3}\tau^{\mathrm{eq}}_{\mu,n+1}}\right) q_2 \frac{\mathrm{tr}\left(\boldsymbol{\tau}_{\mathrm{D},n+1}\right)}{2\sqrt{3}\tau^{\mathrm{eq}}_{\mu,n+1}}, \tag{F.5}$$

$$v_6 = \exp\left[\frac{\Delta H}{RT} + \frac{\mu P_{n+1}}{\tau^*} - D_\infty + D_\infty \exp\left[-\sqrt{\frac{3}{2}}\frac{h}{D_\infty}\left(\bar{\varepsilon}_{\mu,n} + \frac{\sqrt{3}\Delta t}{3\eta_{\mu,n+1}}\tau^{\mathrm{eq}}_{\mu,n+1}\right)\right]\right], \tag{F.6}$$

$$v_7 = D_\infty \exp\left[-\sqrt{\frac{3}{2}}\frac{h}{D_\infty}\left(\bar{\varepsilon}_{\mu,n} + \frac{\sqrt{3}\Delta t}{3\eta_{\mu,n+1}}\tau^{\mathrm{eq}}_{\mu,n+1}\right)\right], \tag{F.7}$$

$$v_8 = \sinh\left(\frac{\tau^{\mathrm{eq}}_{\mu,n+1}}{\tau^*}\right) - \frac{\tau^{\mathrm{eq}}_{\mu,n+1}}{\tau^*}\cosh\left(\frac{\tau^{\mathrm{eq}}_{\mu,n+1}}{\tau^*}\right), \tag{F.8}$$

$$v_9 = 2 f_{n+1} q_{1,n+1}\left[\cosh\left(q_2 \frac{\mathrm{tr}\left(\boldsymbol{\tau}_{\mathrm{D},n+1}\right)}{2\sqrt{3}\tau^{\mathrm{eq}}_{\mu,n+1}}\right) - q_2 \sinh\left(q_2 \frac{\mathrm{tr}\left(\boldsymbol{\tau}_{\mathrm{D},n+1}\right)}{2\sqrt{3}\tau^{\mathrm{eq}}_{\mu,n+1}}\right)\frac{\mathrm{tr}\left(\boldsymbol{\tau}_{\mathrm{D},n+1}\right)}{4\sqrt{3}\tau^{\mathrm{eq}}_{\mu,n+1}}\right], \tag{F.9}$$

$$v_{10} = \frac{\left(\tau^{\mathrm{eq}}_{\mu,n+1}\right)^2}{\eta_{\mu,n+1}}, \tag{F.10}$$

$$v_{11} = q_2 \frac{3K_\infty}{2\sqrt{3}\tau^{\mathrm{eq}}_{\mu,n+1}}, \tag{F.11}$$

$$v_{12} = \frac{1}{\sqrt{3}} q_{1,n+1} q_2 f_{n+1} \tau^{\mathrm{eq}}_{\mu,n+1}, \tag{F.12}$$

$$v_{13} = \sinh\left(\frac{\tau^{\mathrm{eq}}_{\mu,n+1}}{\tau^*}\right), \tag{F.13}$$

$$v_{14} = \frac{1}{\sqrt{3}} q_2 \tau^{\mathrm{eq}}_{\mu,n+1} \sinh\left(q_2 \frac{\mathrm{tr}\left(\boldsymbol{\tau}_{\mathrm{D},n+1}\right)}{2\sqrt{3}\tau^{\mathrm{eq}}_{\mu,n+1}}\right)\left(q_{1,n+1} - q_{11} f_{n+1}\right), \tag{F.14}$$

$$v_{15} = \frac{1}{\sqrt{3}} q_{1,n+1} q_2 f_{n+1} \operatorname{tr}\left(\boldsymbol{\tau}_{\mathrm{D},n+1}\right), \tag{F.15}$$

$$\boldsymbol{v}_{16} = 2\boldsymbol{\tau}_{\mathrm{D},d,n+1} : \boldsymbol{v}_{17}, \tag{F.16}$$

$$\boldsymbol{v}_{17} = \sum_{j=1}^{n_V} \boldsymbol{\tau}_{\mathrm{D},j,n} \otimes \frac{\partial \hat{\omega}_{j,n+1}}{\partial \boldsymbol{\varepsilon}_{n+1}} + 2\left(\boldsymbol{\varepsilon}^e_{d,n+1}\right) \otimes \frac{\partial \bar{G}_{n+1}}{\partial \boldsymbol{\varepsilon}_{n+1}} + 2\bar{G}_{n+1} \mathsf{I}_d, \tag{F.17}$$

$$v_{18} = \frac{f_r}{\sqrt{2\pi} s_{\mathrm{N}}} \exp\left(-\frac{1}{2}\left(\frac{\varepsilon_{\mathrm{vol},n+1} - \varepsilon_{\mathrm{N}}}{s_{\mathrm{N}}}\right)^2\right). \tag{F.18}$$

F.1 State Update Residual Derivative

In this section the derivatives of the residual functions, required for the definition of the Jacobian matrix, are adequately established.

F.1.1 First Residual Derivatives

$$\begin{aligned}\frac{\partial \boldsymbol{R}_1}{\partial \boldsymbol{\varepsilon}^p_{n+1}} = \mathbf{I} - \Delta t\left(1 - f_{n+1}\right) \frac{v_{10}}{\left(v_1\right)^2} \Big(&-2\bar{G}_{n+1} v_1 \mathsf{I}_d - v_1 v_3 v_{11} \boldsymbol{I} \otimes \boldsymbol{I} + \\ &4\bar{G}_{n+1} \boldsymbol{\tau}_{\mathrm{D},d,n+1} \otimes \boldsymbol{\tau}_{\mathrm{D},d,n+1} + v_4 v_{12} \boldsymbol{\tau}_{\mathrm{D},d,n+1} \otimes \boldsymbol{I} + \\ &4\bar{G}_{n+1} v_2 \boldsymbol{I} \otimes \boldsymbol{\tau}_{\mathrm{D},d,n+1} + v_2 v_4 v_{12} \boldsymbol{I} \otimes \boldsymbol{I}\Big),\end{aligned} \tag{F.19}$$

$$\begin{aligned}\frac{\partial \boldsymbol{R}_1}{\partial f_{n+1}} = -\Delta t\, v_{10} \Bigg[&-\frac{\boldsymbol{\tau}_{\mathrm{D},d,n+1} + v_2 \boldsymbol{I}}{v_1} + \frac{\left(1 - f_{n+1}\right)}{\left(v_1\right)^2} \big(v_1 v_{14} \boldsymbol{I} \\ &- v_{14} \operatorname{tr}\left(\boldsymbol{\tau}_{\mathrm{D},n+1}\right) \boldsymbol{\tau}_{\mathrm{D},d,n+1} - \; v_2 v_{14} \operatorname{tr}\left(\boldsymbol{\tau}_{\mathrm{D},n+1}\right) \boldsymbol{I}\big)\Bigg],\end{aligned} \tag{F.20}$$

$$\frac{\partial \boldsymbol{R}_1}{\partial \eta_{\mu,n+1}} = \Delta t\left(1 - f_{n+1}\right) \frac{v_{10}}{v_1} \left(\boldsymbol{\tau}_{\mathrm{D},d,n+1} + v_2 \boldsymbol{I}\right) \frac{1}{\eta_{\mu,n+1}}, \tag{F.21}$$

$$\frac{\partial \boldsymbol{R}_1}{\partial \tau^{\mathrm{eq}}_{\mu,n+1}} = -\Delta t\,(1-f_{n+1})\,\frac{1}{\eta_{\mu,n+1}}\left[2\frac{\tau^{\mathrm{eq}}_{\mu,n+1}}{\nu_1}\left(\boldsymbol{\tau}_{\mathrm{D},d,n+1}+\nu_2\boldsymbol{I}\right)+\frac{\left(\tau^{\mathrm{eq}}_{\mu,n+1}\right)^2}{\left(\nu_1\right)^2}\right.$$
$$\left.\left(\frac{1}{\sqrt{3}}q_{1,n+1}q_2 f_{n+1}\nu_1\nu_5\boldsymbol{I}-\nu_5\nu_{15}\boldsymbol{\tau}_{\mathrm{D},d,n+1}-\nu_2\nu_5\nu_{15}\boldsymbol{I}\right)\right]. \tag{F.22}$$

F.1.2 Second Residual Derivatives

$$\frac{\partial R_2}{\partial \boldsymbol{\varepsilon}^p_{n+1}} = -3\Delta t\left(1-f_{n+1}\right)^2\frac{\nu_{10}}{\left(\nu_1\right)^2}\left(-\nu_1\nu_3\nu_{11}\boldsymbol{I}+\right.$$
$$\left.4\bar{G}_{n+1}\nu_2\boldsymbol{\tau}_{\mathrm{D},d,n+1}+\nu_2\nu_4\nu_{12}\boldsymbol{I}\right), \tag{F.23}$$

$$\frac{\partial R_2}{\partial f_{n+1}} = 1-3\Delta t\left(1-f_{n+1}\right)^2\frac{\nu_{10}}{\left(\nu_1\right)^2}\left(\nu_1\nu_{14}-\nu_2\nu_{14}\ \mathrm{tr}\left(\boldsymbol{\tau}_{\mathrm{D},n+1}\right)\right)+$$
$$6\left(1-f_{n+1}\right)\Delta t\frac{\nu_2\nu_{10}}{\nu_1}, \tag{F.24}$$

$$\frac{\partial R_2}{\partial \eta_{\mu,n+1}} = 3\Delta t\left(1-f_{n+1}\right)^2\nu_{10}\frac{\nu_2}{\nu_1}\frac{1}{\eta_{\mu,n+1}}, \tag{F.25}$$

$$\frac{\partial R_2}{\partial \tau^{\mathrm{eq}}_{\mu,n+1}} = -3\Delta t\frac{\left(1-f_{n+1}\right)^2}{\eta_{\mu,n+1}}\left[2\tau^{\mathrm{eq}}_{\mu,n+1}\frac{\nu_2}{\nu_1}\right.$$
$$\left.+\frac{\left(\tau^{\mathrm{eq}}_{\mu,n+1}\right)^2}{\left(\nu_1\right)^2}\left(\frac{q_{1,n+1}q_2}{\sqrt{3}}f_{n+1}\nu_1\nu_5-\nu_2\nu_5\nu_{15}\right)\right]. \tag{F.26}$$

F.1.3 Third Residual Derivatives

$$\frac{\partial R_3}{\partial \boldsymbol{\varepsilon}^p_{n+1}} = -A_0\nu_6\frac{\tau^{\mathrm{eq}}_{\mu,n+1}}{\nu_{13}}\frac{\mu}{\tau^*}K_\infty\boldsymbol{I}, \tag{F.27}$$

$$\frac{\partial R_3}{\partial f_{n+1}} = 0, \tag{F.28}$$

$$\frac{\partial R_3}{\partial \eta_{\mu,n+1}} = 1 - A_0 \frac{\nu_6 \nu_7}{\nu_{13}} \left(\tau^{\text{eq}}_{\mu,n+1}\right)^2 \frac{1}{\sqrt{2}} \frac{h}{D_\infty} \frac{\Delta t}{\left(\eta_{\mu,n+1}\right)^2}, \tag{F.29}$$

$$\frac{\partial R_3}{\partial \tau^{\text{eq}}_{\mu,n+1}} = -A_0 \left[\frac{\nu_6 \nu_8}{\left(\nu_{13}\right)^2} - \tau^{\text{eq}}_{\mu,n+1} \frac{\nu_6 \nu_7}{\nu_{13}} \frac{1}{\sqrt{2}} \frac{h}{D_\infty} \frac{\Delta t}{\eta_{\mu,n+1}} \right]. \tag{F.30}$$

F.1.4 Fourth Residual Derivatives

$$\frac{\partial R_4}{\partial \boldsymbol{\varepsilon}^p_{n+1}} = -2\bar{G}_{n+1} \boldsymbol{\tau}_{\text{D},d,n+1} - 3\nu_2 K_\infty \boldsymbol{I}, \tag{F.31}$$

$$\frac{\partial R_4}{\partial f_{n+1}} = 2\left(\tau^{\text{eq}}_{\mu,n+1}\right)^2 \left[\left(q_{1,n+1} - q_{11} f_{n+1}\right) \cosh\left(q_2 \frac{\text{tr}\left(\boldsymbol{\tau}_{\text{D},n+1}\right)}{2\sqrt{3}\tau^{\text{eq}}_{\mu,n+1}} \right) - q^2_{1,n+1} f_{n+1} + q_{1,n+1} q_{11} f^2_{n+1} \right], \tag{F.32}$$

$$\frac{\partial R_4}{\partial \eta_{\mu,n+1}} = 0, \tag{F.33}$$

$$\frac{\partial R_4}{\partial \tau^{\text{eq}}_{\mu,n+1}} = 2\tau^{\text{eq}}_{\mu,n+1} \left[\nu_9 - \left(1 + q^2_{1,n+1} f^2_{n+1}\right) \right]. \tag{F.34}$$

$$\tag{F.35}$$

F.2 Consistent Tangent Modulus Derivatives

The visco-elastic visco-plastic consistent tangent modulus of the formulated constitutive model is expressed as

$$\mathbf{D}^{vevp}_{n+1} = \frac{\partial \hat{\boldsymbol{\tau}}_{\text{T}}}{\partial \boldsymbol{\varepsilon}_{n+1}} = \frac{\partial \boldsymbol{\tau}_{\text{D},n+1}}{\partial \boldsymbol{\varepsilon}_{n+1}} + \frac{\partial \boldsymbol{\tau}_{\text{H},n+1}}{\partial \boldsymbol{\varepsilon}_{n+1}}, \tag{F.36}$$

where the derivative of the driving stress is given by

$$\frac{\partial \boldsymbol{\tau}_{\text{D},n+1}}{\partial \boldsymbol{\varepsilon}_{n+1}} = K_\infty \boldsymbol{I} \otimes \boldsymbol{I} - K_\infty \boldsymbol{I} \otimes \left(\boldsymbol{I} : \frac{\partial \boldsymbol{\varepsilon}^p_{n+1}}{\partial \boldsymbol{\varepsilon}_{n+1}} \right) + 2\bar{G}_{n+1} \mathsf{I}_d - 2\bar{G}_{n+1} \boldsymbol{I}_d : \frac{\partial \varepsilon^p_{n+1}}{\partial \boldsymbol{\varepsilon}_{n+1}} + \sum_{j=1}^{n_V} \left(\tau_{\text{D},j,n} \otimes \frac{\partial \hat{\omega}_{j,n+1}}{\partial \boldsymbol{\varepsilon}_{n+1}} \right) + 2\left(\boldsymbol{\varepsilon}^e_{d,n+1} - \boldsymbol{\varepsilon}^e_{d,n} \right) \otimes \frac{\partial \bar{G}_{n+1}}{\partial \boldsymbol{\varepsilon}_{n+1}}, \tag{F.37}$$

and the derivative of the hardening stress by

$$\frac{\partial \boldsymbol{\tau}_{\mathrm{H},n+1}}{\partial \boldsymbol{\varepsilon}_{n+1}} = -\frac{C_\mathrm{R}}{3}\frac{\sqrt{N}}{\left(\lambda^p_{\mathrm{chain}}\right)^2}\mathscr{L}^{-1}\left(\frac{\lambda^p_{\mathrm{chain}}}{\sqrt{N}}\right)\boldsymbol{B}_{d,\,\mathrm{iso}} \otimes \frac{\partial \lambda^p_{\mathrm{chain}}}{\partial \boldsymbol{\varepsilon}_{n+1}} + \frac{C_\mathrm{R}}{3}\frac{\sqrt{N}}{\lambda^p_{\mathrm{chain}}} \boldsymbol{B}_{d,\,\mathrm{iso}} \otimes \frac{\partial}{\partial \boldsymbol{\varepsilon}_{n+1}}\left(\mathscr{L}^{-1}\left(\frac{\lambda^p_{\mathrm{chain}}}{\sqrt{N}}\right)\right) + \frac{C_\mathrm{R}}{3}\frac{\sqrt{N}}{\lambda^p_{\mathrm{chain}}}\mathscr{L}^{-1}\left(\frac{\lambda^p_{\mathrm{chain}}}{\sqrt{N}}\right)\mathbf{I}_d : \frac{\partial \boldsymbol{B}_{\mathrm{iso}}}{\partial \boldsymbol{\varepsilon}_{n+1}}. \tag{F.38}$$

The visco-elasticity-related derivatives are computed as

$$\frac{\partial \hat{\omega}_{j,n+1}}{\partial \boldsymbol{\varepsilon}_{n+1}} = \frac{\Delta t}{g^2_{j,n+1}}\exp\left[-\frac{\Delta t}{g_{j,n+1}}\right]\frac{\partial g_{j,n+1}}{\partial \boldsymbol{\varepsilon}_{n+1}}, \tag{F.39}$$

and

$$\frac{\partial \bar{G}_{n+1}}{\partial \boldsymbol{\varepsilon}_{n+1}} = \sum_{j=1}^{n_\mathrm{V}}\left[\frac{G_j}{\Delta t}\left(1-\exp\left[-\frac{\Delta t}{g_{j,n+1}}\right]\right)\frac{\partial g_{j,n+1}}{\partial \boldsymbol{\varepsilon}_{n+1}} - G_j\frac{g_{j,n+1}}{\Delta t}\frac{\partial \hat{\omega}_{j,n+1}}{\partial \boldsymbol{\varepsilon}_{n+1}}\right], \tag{F.40}$$

where

$$\frac{\partial g_{j,n+1}}{\partial \boldsymbol{\varepsilon}_{n+1}} = -g_{j,T}\lambda_{g,j}\left(\dot{\varepsilon}^{\mathrm{eq}}\right)^{-\left(\lambda_{g,j}+1\right)}\frac{\partial \dot{\varepsilon}^{\mathrm{eq}}_{n+1}}{\partial \boldsymbol{\varepsilon}_{n+1}}, \tag{F.41}$$

and

$$\frac{\partial \dot{\varepsilon}^{\mathrm{eq}}_{n+1}}{\partial \boldsymbol{\varepsilon}_{n+1}} = \frac{1}{\Delta t}\sqrt{\frac{2}{3}}\frac{\Delta \boldsymbol{\varepsilon}_{n+1}}{\left\|\Delta \boldsymbol{\varepsilon}_{n+1}\right\|}. \tag{F.42}$$

Regarding the derivative of the hardening-related terms, the derivative of the stretch in the eight-chain network is given by

$$\begin{aligned}\frac{\partial \lambda^p_{\mathrm{chain}}}{\partial \boldsymbol{\varepsilon}_{n+1}} &= \frac{\partial}{\partial \boldsymbol{\varepsilon}_{n+1}}\sqrt{\frac{1}{3}\left(\det(\boldsymbol{F})\right)^{-2/3}\operatorname{tr}(\exp(2\boldsymbol{\varepsilon}))} \\ &= \frac{1}{2}\frac{1}{\lambda^p_{\mathrm{chain}}}\frac{1}{3}\left(\det(\boldsymbol{F})\right)^{-2/3}\left(-\frac{2}{3}\operatorname{tr}(\exp(2\boldsymbol{\varepsilon}))\boldsymbol{I} + \boldsymbol{I} : \frac{\partial \exp(2\boldsymbol{\varepsilon})}{\partial \boldsymbol{\varepsilon}_{n+1}}\right),\end{aligned} \tag{F.43}$$

in which the derivative of the determinant of the deformation gradient is obtained as

$$\frac{\partial \det(\boldsymbol{F})}{\partial \boldsymbol{\varepsilon}_{n+1}} = \frac{\partial\left(\exp\left(2\operatorname{tr}(\boldsymbol{\varepsilon})\right)\right)^{1/2}}{\partial \boldsymbol{\varepsilon}_{n+1}} = \det(\boldsymbol{F})\boldsymbol{I}. \tag{F.44}$$

The inverse of the Langevin function is computed based on the closed-form

series approximation proposed by Arruda and Boyce (1993b)

$$\mathscr{L}^{-1}(x) \approx 3x + \frac{9}{5}x^3 + \frac{297}{175}x^5 + \frac{1539}{875}x^7. \tag{F.45}$$

In this manner, its derivative becomes

$$\begin{aligned}\frac{\partial}{\partial \boldsymbol{\varepsilon}_{n+1}}\left(\mathscr{L}^{-1}\left(\frac{\lambda^p_{\text{chain}}}{\sqrt{N}}\right)\right) = \Bigg(3 + \frac{27}{5}\left(\frac{\lambda^p_{\text{chain}}}{\sqrt{N}}\right)^2 + \frac{297}{35}\left(\frac{\lambda^p_{\text{chain}}}{\sqrt{N}}\right)^4 + \\ \frac{1539}{125}\left(\frac{\lambda^p_{\text{chain}}}{\sqrt{N}}\right)^6\Bigg)\frac{1}{\sqrt{N}}\frac{\partial \lambda^p_{\text{chain}}}{\partial \boldsymbol{\varepsilon}_{n+1}}.\end{aligned} \tag{F.46}$$

At last, the derivative of the isochoric left Cauchy-Green tensor is given by

$$\begin{aligned}\frac{\partial \boldsymbol{B}_{\text{iso}}}{\partial \boldsymbol{\varepsilon}_{n+1}} = \frac{\partial \left(\det(\boldsymbol{F})\right)^{-2/3}\exp(2\boldsymbol{\varepsilon})}{\partial \boldsymbol{\varepsilon}_{n+1}} &= -\frac{2}{3}\left(\det(\boldsymbol{F})\right)^{-5/3}\exp(2\boldsymbol{\varepsilon})\frac{\partial \det(\boldsymbol{F})}{\partial \boldsymbol{\varepsilon}_{n+1}} + \\ &\left(\det(\boldsymbol{F})\right)^{-2/3}\frac{\partial \exp(2\boldsymbol{\varepsilon})}{\partial \boldsymbol{\varepsilon}_{n+1}} \\ &= -\frac{2}{3}(\det(\boldsymbol{F}))^{-2/3}\exp(2\boldsymbol{\varepsilon})\boldsymbol{I} + \\ &\left(\det(\boldsymbol{F})\right)^{-2/3}\frac{\partial \exp(2\boldsymbol{\varepsilon})}{\partial \boldsymbol{\varepsilon}_{n+1}},\end{aligned} \tag{F.47}$$

where the derivate of the tensor exponential is discussed and established in (de Souza Neto et al., 2008; de Carvalho et al., 2022).

By considering the equilibrium state at t_{n+1}, where the constitutive state update residual functions are null ($\boldsymbol{R} = 0$), the remaining derivatives, $\partial \boldsymbol{\varepsilon}^p_{n+1}/\partial \boldsymbol{\varepsilon}_{n+1}$, $\partial \eta_{\mu,n+1}/\partial \boldsymbol{\varepsilon}_{n+1}$ and $\partial \tau^{\text{eq}}_{\mu,n+1}/\partial \boldsymbol{\varepsilon}_{n+1}$, can be obtained

$$\mathrm{d}\boldsymbol{R} = \frac{\partial \boldsymbol{R}}{\partial \boldsymbol{\alpha}_{n+1}} * \mathrm{d}\boldsymbol{\alpha}_{n+1} + \frac{\partial \boldsymbol{R}}{\partial \boldsymbol{\varepsilon}_{n+1}} * \mathrm{d}\boldsymbol{\varepsilon}_{n+1} = 0, \tag{F.48}$$

where the derivatives $\partial \boldsymbol{R}/\partial \boldsymbol{\alpha}_{n+1}$ and $\partial \boldsymbol{R}/\partial \boldsymbol{\varepsilon}_{n+1}$ are determined from the state update procedure. As a result, the previous equation can be rewritten as

$$\mathsf{J}\mathrm{d}\boldsymbol{\alpha}_{n+1} + \mathsf{G}\mathrm{d}\boldsymbol{\varepsilon}_{n+1} = 0, \tag{F.49}$$

where J is the matricial form of the state update Jacobian matrix, whose derivatives have been previously defined in Appendix F.1 and G is the matricial

form of the residual derivatives

$$\mathsf{G} = \left[\begin{array}{cccc} \dfrac{\partial \boldsymbol{R}_1}{\partial \boldsymbol{\varepsilon}_{n+1}} & \dfrac{\partial R_2}{\partial \boldsymbol{\varepsilon}_{n+1}} & \dfrac{\partial R_3}{\partial \boldsymbol{\varepsilon}_{n+1}} & \dfrac{\partial R_4}{\partial \boldsymbol{\varepsilon}_{n+1}} \end{array} \right]^T, \tag{F.50}$$

given by

$$\begin{aligned} \frac{\partial \boldsymbol{R}_1}{\partial \boldsymbol{\varepsilon}_{n+1}} = -\Delta t \left(1 - f_{n+1}\right) \frac{v_{10}}{\left(v_1\right)^2} \big(& v_1 \boldsymbol{v}_{17} + v_1 v_3 v_{11} \boldsymbol{I} \otimes \boldsymbol{I} - \boldsymbol{\tau}_{\mathrm{D},d,n+1} \otimes \boldsymbol{v}_{16} - \\ & v_4 v_{12} \boldsymbol{\tau}_{\mathrm{D},d,n+1} \otimes \boldsymbol{I} - v_2 \boldsymbol{I} \otimes \boldsymbol{v}_{16} - v_2 v_4 v_{12} \boldsymbol{I} \otimes \boldsymbol{I} \big), \end{aligned} \tag{F.51}$$

$$\frac{\partial R_2}{\partial \boldsymbol{\varepsilon}_{n+1}} = -3\Delta t \left(1 - f_{n+1}\right)^2 \frac{v_{10}}{\left(v_1\right)^2} \left(v_1 v_3 v_{11} \boldsymbol{I} - v_2 \boldsymbol{v}_{16} - v_2 v_4 v_{12} \boldsymbol{I} \right) - v_{18} \boldsymbol{I}, \tag{F.52}$$

$$\frac{\partial R_3}{\partial \boldsymbol{\varepsilon}_{n+1}} = A_0 \frac{v_6}{v_{13}} \tau^{\mathrm{eq}}_{\mu,n+1} \frac{\mu,}{\tau^*} K_\infty \boldsymbol{I}, \tag{F.53}$$

$$\frac{\partial R_4}{\partial \boldsymbol{\varepsilon}_{n+1}} = \frac{1}{2} \boldsymbol{v}_{16} + 3 v_2 K_\infty \boldsymbol{I}. \tag{F.54}$$

Lastly, the solution of this system of linear equations,

$$\mathsf{J} \frac{\mathrm{d}\boldsymbol{\alpha}_{n+1}}{\mathrm{d}\boldsymbol{\varepsilon}_{n+1}} = -\mathsf{G}, \tag{F.55}$$

where $\mathrm{d}\boldsymbol{\alpha}_{n+1}/\mathrm{d}\boldsymbol{\varepsilon}_{n+1}$ is the matricial form of the state variables derivatives

$$\frac{\mathrm{d}\boldsymbol{\alpha}_{n+1}}{\mathrm{d}\boldsymbol{\varepsilon}_{n+1}} = \left[\begin{array}{cccc} \dfrac{\partial \boldsymbol{\varepsilon}^p_{n+1}}{\partial \boldsymbol{\varepsilon}_{n+1}} & \dfrac{\partial f_{n+1}}{\partial \boldsymbol{\varepsilon}_{n+1}} & \dfrac{\partial \eta_{\mu,n+1}}{\partial \boldsymbol{\varepsilon}_{n+1}} & \dfrac{\partial \tau^{\mathrm{eq}}_{\mu,n+1}}{\partial \boldsymbol{\varepsilon}_{n+1}} \end{array} \right]^T, \tag{F.56}$$

yields the required derivatives $\partial \boldsymbol{\varepsilon}^p_{n+1}/\partial \boldsymbol{\varepsilon}_{n+1}$, $\partial \eta_{\mu,n+1}/\partial \boldsymbol{\varepsilon}_{n+1}$ and $\partial \tau^{\mathrm{eq}}_{\mu,n+1}/\partial \boldsymbol{\varepsilon}_{n+1}$.